



SAIP 2018

South African Institute of Physics Conference

PROCEEDINGS OF SAIP2018, **the 63rd Annual Conference of the** **South African Institute of Physics**



63RD ANNUAL CONFERENCE OF THE SOUTH AFRICAN INSTITUTE OF PHYSICS

PROCEEDINGS EDITOR: Prof. Japie Engelbrecht

PUBLISHER: The South African Institute of Physics (SAIP)

COPYRIGHT NOTICE:

Copyright 2019 by the South African Institute of Physics (SAIP)

The Proceedings of SAIP2018, the 63rd Annual Conference of the South African Institute of Physics (SAIP) will only be available electronically on the SAIP website:
www.saip.org.za.

Permission to make digital or hard copies of part or all of this work for personal or classroom use is granted without fee provided that copies are not made or distributed for profit or commercial advantage and that copies bear this notice and the full citation on the first page. Abstracting with credit is permitted. To copy otherwise, to republish, to post on servers, or to distribute to lists, requires specific permissions and/or a fee. Request permissions from the SAIP Office,

Tel. +27 (0)12 841 2655 / 2627,
Fax +27 (0)86 648 8474,
E-mail: info@saip.org.za.

ISBN: 978-0-620-85406-1

SAIP2018

Proceedings of SAIP2018,
the 63rd Annual Conference of the South African Institute
of Physics

Hosted by the University of the Free-State

25 - 29 June 2018

University of the Free-State, Bloemfontein, South Africa

Edited By
Prof. Japie Engelbrecht

TABLE OF CONTENTS

Conference Chairs and Committees	vii
Message from the Conference Chair	viii
Message from the Editor	ix
List of Reviewers	x

FULL RESEARCH PAPERS

DIVISION A – DIVISION FOR PHYSICS OF CONDENSED MATTER AND MATERIALS

Electronic and Optical Properties of Lead-Free Hybrid Perovskite $\text{CH}_3\text{NH}_3\text{SnI}_3$ from First Principles Calculations.	2
<i>I O Abdallah, D P Joubert and M S H Suleiman</i>	
Structural, elastic and electronic properties of binary titanium-based shape memory alloys.	8
<i>M E Baloyi, R Modiba, P E Ngoepe and H R Chauke</i>	
First principles investigation of structural, elastic, electronic and optical properties of Barium seleno-germanate, Ba_2GeSe_4	14
<i>A Barde and D P Joubert</i>	
Growth and structural characterization of germanium on Pt(111)	20
<i>C Dansou, G B Geetha, E Carleschi and B P Doyle</i>	
A numerical study of heterogeneous annealing in a finite one-dimensional geometry	25
<i>J Lethoba, P M Bokov and P A Selyshchev</i>	
ZnO nanoparticles doped with cobalt and indium mechanochemically for methane gas sensing application.	31
<i>M F Manamela, T E Mosuang and B W Mwakikunga</i>	
First principle studies of palladium nanoparticles on titanium dioxide surfaces for catalytic application.	37
<i>A F Mazibuko, R G Diale, H R Chauke and P E Ngoepe</i>	
Effect of temperature on the structure and dynamic properties of metal sulphide nanostructures via molecular dynamics simulation.	44
<i>M A Mehlahe, T G Mametja, T E Letsoalo and P E Ngoepe</i>	
Lattice thermal conductivity of bulk PtTe_2 and PtSe_2	50
<i>H A H Mohammed, D P Joubert and G M D Nguimdo</i>	
Magnetic and physical properties of new hexagonal compounds PrPt_4X ($\text{X} = \text{Ag}, \text{Au}$)	56
<i>M O Ogunbunmi and A M Strydom</i>	
Crystal structure and thermodynamic properties of the non-centrosymmetric PrRu_4Sn_6 caged compound.	62
<i>M O Ogunbunmi and A M Strydom</i>	
Thermoelectric properties of CdGa_2O_4 spinel	68
<i>E Rugut, D P Joubert and G Jones</i>	
The structural, electronic, and optical properties of $\text{CH}_3\text{NH}_3\text{PbI}_3$	74
<i>A S A Sidahmed and D P Joubert</i>	

Structural and optical properties of spin coated graphene oxide films	80
--	----

B C Tladi, R E Kroon and H C Swart

DIVISION B – NUCLEAR, PARTICLE AND RADIATION PHYSICS

A comparative study of the high fluence neutron radiation effects on the properties of plastic scintillator UPS-923A for the TileCal of the ATLAS detector	87
---	----

V Baranov, Y I Davydov, R Erasmus, C O Kureba, J E Mdhuli, B Mellado, G Mokgatitswane, E Sideras-Haddad, I Vasilyev and P N Zhmurin

AdS/CFT predictions for correlations, suppression, and flow of heavy flavours at RHIC and LHC	93
--	----

R Hambrock and W A Horowitz

Performance of missing transverse energy reconstruction in pp collisions at 13 TeV in the diphoton channel with ATLAS	99
--	----

S Liao, B Mellado and X Ruan

Background estimation for multilepton and b-jets analysis at ATLAS at the LHC	105
---	-----

J Monnakgotla, L Mokoena, L Mashishi, Y H Jimenez and B Mellado

Studying the effects of pileup on the leptonic properties in the $H \rightarrow ZZ \rightarrow 4l$ channel using the ATLAS detector	110
---	-----

O Mtintsilana and T Lagouri

Mitigating the effect of fake missing energy using Machine learning technique in the ATLAS experiment	116
--	-----

K G Tomiwa, X Ruan and B Mellado

DIVISION C – PHOTONICS

Measurements of phase distortions through pulse characterization	123
---	-----

G O Dwapanyin, G W Bosman, P H Neethling and E G Rohwer

Using optical tweezers to measure the forces exerted by molecular motors in onion cells	129
--	-----

A Erasmus, G W Bosman, P H Neethling and E G Rohwer

The effect of photobiomodulation at 660 nm on the differentiation of diabetic wounded WS1 human fibroblasts into myofibroblasts	135
--	-----

D R Mokoena, N N Houreld, S S Dhilip Kumar and H Abrahamse

Investigation of a specifically targeted photosynthetic nanoparticle drug delivery system for enhanced photodynamic therapy treatment of metastatic melanoma	141
---	-----

C Naidoo, C A Kruger and H Abrahamse

Simulation of time-domain terahertz ellipsometry measurements towards data extraction	147
--	-----

S Smith, P Neethling and E Rohwer

DIVISION D1 – ASTROPHYSICS

Dark matter gets DAMPE	154
-------------------------------------	-----

G Beck and S Colafrancesco

Probing the intergalactic magnetic field through observations of high-energy gamma rays produced by electromagnetic cascades	160
---	-----

B Bisschof, B van Soelen and P J Meintjes

Gamma-Gamma Absorption in gamma-ray Binaries	166
---	-----

D C du Plooy and B van Soelen

H(α) images of nearby galaxy groups NGC193 and NGC940	172
--	-----

S Hattingh, S I Loubser, A Babul and E O'Sullivan

Star formation histories of Brightest Group Galaxies in CLoGS	178
<i>O C Havenga, S I Loubser, E O'Sullivan, A Babul and A Ratsimbazafy</i>	
Search for Gamma-ray emission in the White Dwarf pulsar of AR Scorpii	184
<i>Q Kaplan, H J van Heerden, P J Meintjes, A Odendaal and R Britto</i>	
The search for gamma-ray emission from AE Aquarii using Fermi-LAT Pass 8 Data pipeline 2008-2018	190
<i>S T Madzime, H J van Heerden, P J Meintjes, A Odendaal and R J Britto</i>	
Did Dark Matter Kill the Dinosaurs?	196
<i>M Sarkis and G Beck</i>	
Probing quantum gravity at low energies	202
<i>J Tarrant, G Beck, and S Colafrancesco</i>	
Implications for gamma-ray production from updated orbital parameters for LMC P3 with SALT/HRS	207
<i>B van Soelen, N Komin, D du Plooy, P V Laisanen and A Kniazev</i>	
DIVISION D2 – SPACE SCIENCE	
dSECS: Including Variometers in Geomagnetic Field Interpolation	212
<i>M J Heyns, S I Lotz and C T Gaun</i>	
DIVISION E – PHYSICS EDUCATION	
The relativistic length transformation: more than a Lorentz contraction	219
<i>R E Kroon</i>	
DIVISION F – APPLIED PHYSICS	
Migration behaviour of selenium implanted into polycrystalline SiC	224
<i>Z A Y Abdalla, T T Hlatshwayo, E G Njoroge, M Mlambo, E Wendler, J B Malherbe</i>	
Photodynamic therapy using Sulfonated Aluminium Phthalocyanine mix for the eradication of cervical cancer: an in vitro study	230
<i>E P Chizenga and H Abrahamse</i>	
Experimental and Numerical Measurement of the thermal performance for parabolic trough solar concentrators	235
<i>K Mohamad and P Ferrer</i>	
Tuning the Bandgap of Bulk Molybdenum Disulphide using Defects	241
<i>P V Mwonga, S R Naidoo, A Quandt and K I Ozoemena</i>	
DFT Study of selected croconate dye molecules for application in dye sensitized solar cells	247
<i>T S Ranwaha, N E Maluta and R R Maphanga</i>	
DIVISION G – THEORETICAL AND COMPUTATIONAL PHYSICS	
Quasi-normal modes of spin-3/2 fields in D-dimensional Reissner-Nordstrom black hole spacetimes using the continued fraction method	254
<i>A S Cornell and G E Harmsen</i>	
Full phase space simulation of the relativistic Boltzmann equation in the context of heavy-ion collisions	259
<i>E W Grunow and A Peshier</i>	
Bose-Einstein condensation from a gluon transport equation	264
<i>B A Harrison and A Peshier</i>	

Quantitative Predictions of Heavy Flavor Photon Bremsstrahlung in Heavy Ion Collisions from AdS/CFT	270
<i>W A Horowitz</i>	
Oscillating cosmological correlations in $f(R)$ gravity	276
<i>N Namane, H Sami and A Abebe</i>	
Using the Ultra-relativistic Quantum Molecular Dynamics (UrQMD) model to extract the thermal conductivity transport coefficient of hadron gas	282
<i>T Nemakhavhani and A Muronga</i>	

Conference Chairs and Committees

SAIP2018 Division Chairs

Division for Physics of Condensed Matter and Materials:

Prof. Japie Engelbrecht (Nelson Mandela Metropolitan University)

Division for Nuclear, Particle and Radiation Physics:

Dr. Simon Mullins (iThemba LABS)

Division for Photonics:

Prof. Andrew Forbes (University of the Witwatersrand)

Division for Astrophysics:

Prof. Christo Venter (North-West University)

Division for Space Science:

Dr. Du Toit Strauss (North-West University)

Division for Physics Education:

Prof. Sam Ramaila (University of Johannesburg)

Division for Applied Physics:

Prof. Ernest van Dyk (Nelson Mandela Metropolitan University)

Division for Theoretical and Computational Physics:

Prof. Kristian Müller-Nedebock (Stellenbosch University)

SAIP2018 Conference Committee

Chairperson:	J J Terblans
Coordinator/Secretariat:	K Cronje, Y Loots, M Lebeko
Social events/Opening/Dinner:	A Odendaal, G H Mhlongo
Plenary speakers/Sponsors:	H C Swart, W D Roos, P J Meintjes
Student affairs:	M M Duvenhage, L F Koao
Winter school on Applications of Luminescence:	L Coetsee-Hugo, R E Kroon, H C Swart
Scientific programme/Web:	R E Kroon, R A Harris
Posters:	S Cronje, D E Motaung
Audio-visual/Wi-Fi/Network:	H J van Heerden, R O Ocaya
Planetarium tour:	M J H Hoffman, D Mangope, P J Meintjes, D P van Jaarsveldt
Physics Bowl:	H Szegedi, B van Soelen, K G Tshabalala, S J Motloung
Teachers Workshop:	M J H Hoffman, D P van Jaarsveldt, O M Ntwaeaborwa, B F
Women in Physics:	Dejene A Odendaal, M M Duvenhage

Proceedings Editorial Committee and Review Panel

Prof. Japie Engelbrecht - Editor

Prof. Deena Naidoo - Education and Condensed Matter

Dr. John Habarulema - Astro & Space

Mr. Brian Masara

Mr. Tebogo Mokhine

Message from the Conference Chair

I am pleased to welcome you to the 63rd Annual Conference of the South African Institute of Physics on behalf of the Physics department, University of the Free State. The department is proud to be part of the South African Institute of Physics and especially to host this year's annual conference.

The department has been part of the annual physics conferences in South Africa since 1953. This happened in the form of many tearoom discussions (in Physics department at the University of the Free State) to start an annual Physics conference in South Africa. This dream was set in motion on 8 May 1953 by Prof CB van Wyk and Prof JHN Loubser by means of a letter circulated to 27 scientists enquiring their views on the organizing of a physics conference for South Africa in 1954. The response was overwhelmingly positive and a physics conference was held in 1954 with about 50 papers presented at the conference. Since then the physics conference has grown to more than 400 papers this year and covers the whole spectrum of physics. Topics range from cutting-edge theoretical research to socially relevant research in teaching and learning physics.

A special word of recognition to late Prof CB van Wyk for his part in founding the annual Physics conference in South Africa and for his family trust still sponsoring plenary speakers.

As HOD of the Physics department I thank all participants for enriching this conference through their presentation and discussion. I hope all delegates will enjoy the content of the conference, renew old friendships, make new friends, get new ideas, and finally have a good time.

Prof JJ (Koos) Terblans
Head of Department: Physics
University of the Free State

Message from the Editor

I had hoped that my second year as Editor would be easier since I thought I knew the ropes. But life remains full of surprises and managing the process of producing the SAIP Conference Proceedings remained an interesting experience.

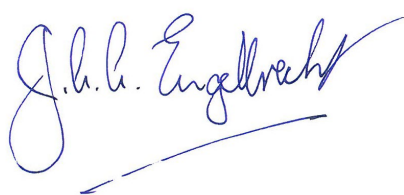
The production of the SAIP Conference Proceedings involves a large number of people: the editorial committee, authors submitting articles, two reviewers for each article and finally the editor. However, process cannot be hurried along, as eventually the SAIP community expects a Proceedings of a standard comparable to that of international journals. I thus remain hugely indebted to the Content Reviewers for their time and due diligence in the review process.

A total of 73 articles were received. Rejection of articles were due to not complying with the required layout, scientific value or not addressing the concerns and suggested corrections of the Reviewers. This was done with the goal of ensuring maintenance of a standard comparable to that of the previous Proceedings, as well as ensuring that the Proceedings will still qualify for subsidy from the DHET.

I again appeal to all students, supervisors and promoters to take much more care in future upon submission of articles to be considered for publication in the Conference Proceedings, to take a greater responsibility in ensuring that articles adhere to the required Layout, and to ensure that articles are proofread before submission to cut down on grammatical and typographical errors. All this will speed up the editorial process and ensure that the Proceedings can be published timeously.

I wish to SINCERELY thank the following persons for their help and assistance:

- The Editorial Committee under the leadership of Prof Deena Naidoo
- Tebogo Mokhe, whose IT skills carried the day – thank you again!
- Mr Brian Masara (CEO of the SAIP) and John Basco Habarulema (Council member for SAIP Conference matters)
- Division Chairs for identifying reviewers, especially those who walked the extra mile to get the reviews done
- All content reviewers who participated and who helped to keep the standard of accepted articles of a high standard.



Editor: SAIP 2018 Conference Proceedings

List of Reviewers

Prof. ALLIE, Saalih	University of Cape Town
Prof. BECK, Geoffrey	University of the Witwatersrand
Prof. BEESHAM, Aroonkumar	University of Zululand
Dr. BOSMAN, Gurthwin	Stellenbosch University
Prof. BOTTCHEER, Markus	North-West University
Prof. BUFFLER, Andy	University of Cape Town
Mrs. BURGER, Liesl	National Laser Centre (CSIR)
Dr. BUTHELEZI, Zinhle	iThemba LABS
Prof. CHITHAMBO, Makaiko	Rhodes University
Prof. CORNELL, Alan	University of Witwatersrand
Prof. CONNELL, Simon	University of Johannesburg
Prof. DEANE, Roger	University of Pretoria / Rhodes University
Mr. DE BEER, Frikkie	South African Nuclear Energy Corporation
Prof. DERRY, Trevor	University of Witwatersrand
Mr. EL-HUSSEIN M.KAMEL, Ahmed	The National Institute of Laser Enhanced Science
Prof. ENGELBRECHT, Japie	Nelson Mandela Metropolitan University
Prof. ERASMUS, Rudolph	University of Witwatersrand
Prof. FERRER, Phil	University of Witwatersrand
Mr. GOVENDER, Nicolin	Nuclear Energy Corporation of South Africa
Prof. HABARULEMA, John Bosco	South African National Space Agency
Dr. HARRIS, Richard	University of the Free State
Dr. HERBERT, Mark	University of the Western Cape
Dr. HEINZ, Ulrich	Ohio State University
Dr. HLATSHWAYO, Thulani	University of Pretoria
Prof. HOROWITZ, William	University of Cape Town
Prof. JOUBERT, Daniel	University of the Witwatersrand
Dr. KARSTEN, Aletta	National Metrology Institute of South Africa
Dr. KEAVENEY, James Michael	Deutsches Elektronen-Synchrotron
Dr. KOTZE, Pieter	South African National Space Agency
Prof. KROON, R. E.	University of the Free State

Prof. KRIEK, Jeanne	University of South Africa
Prof. KRÜGER, Tjaart	University of Pretoria
Dr. KUMAR, Mukesh	University of the Witwatersrand
Mrs. LEE, Claire	University of Johannesburg
Prof. LEE, Mike	Nelson Mandela Metropolitan University
Dr. MAFU, Mhlambululi	Botswana International University of Science and Technology
Dr. MAPASHA, Edwin	University of Pretoria
Dr. MARX, Geneveve	Nelson Mandela Metropolitan University
Prof. MEINTJES, Pieter	University of the Free State
Dr. MEYER, Walter	University of Pretoria
Mr. MOLOTO, Katlego	North West University
Ms. MOODLEY, Nicole	University of Cape Town
Mr. MOTLOUNG, Semuto	Nelson Mandela Metropolitan University
Prof. MURONGA, Azwinndini	University of Johannesburg
Prof. MÜLLER-NEDEBOCK, Kristian	Stellenbosch University
Prof. NAIDOO, Deena	University of the Witwatersrand
Dr. NAYLOR, Wade	South African Institute of Physics
Prof. NEETHLING, Johannes	Nelson Mandela Metropolitan University
Prof. NEETHLING, Pieter	Stellenbosch University
Dr. NEL, Jacqueline	University of Pretoria
Dr. ODENDAAL, Alida	University of the Free-State
Mr. OSANO, Bob	South African Institute of Physics
Prof. PAPKA, Paul	Stellenbosch University
Dr. POTTER, Stephen	South African Astronomical Observatory
Prof. RAZZAQUE, Soebur	University of Johannesburg
Mr. REGIS, Marco	South African Institute of Physics
Prof. ROHWER, Erich	Stellenbosch University
Dr. SKELTON, Rosalind	South African Astronomical Observatory
Dr. SNYMAN, Izak	National Institute for Theoretical Physics
Dr. SOLANS SANCHEZ, Carlos	European Organization for Nuclear Research
Prof. SWART, Hendrik	University of the Free State
Prof. TAME, Mark	University of Kwa-Zulu Natal

Prof. TERBLANS, JJ (Koos)	University of the Free State
Dr. TRUONG, Loan	University of Johannesburg
Dr. URGESSA, Zelalem N.	Nelson Mandela Metropolitan University
Dr. UYS, Hermann	National Laser Centre (CSIR)
Prof. VAN DYK, Ernest	Nelson Mandela Metropolitan University
Prof. VAN SOELEN, Brian	University of the Free State
Prof. VENTER, André	Nelson Mandela Metropolitan University
Dr. VORSTER, Frederik	Nelson Mandela Metropolitan University
Dr. WADIASINGH, Zorawar	North-West University
Prof. WEIGEL, Herbert	Stellenbosch University
Dr. WESTRAADT, Johan	Nelson Mandela Metropolitan University

DIVISION A

Division for Physics of Condensed Matter and Materials

Electronic and Optical Properties of Lead-Free Hybrid Perovskite $\text{CH}_3\text{NH}_3\text{SnI}_3$ from First Principles Calculations

Ibrahim Omer Abdallah^{1,2}, Daniel P Joubert¹, and Mohammed S H Suleiman^{1,3}

¹ The National Institute for Theoretical Physics, School of Physics and Mandelstam Institute for Theoretical Physics, University of the Witwatersrand, Johannesburg, Wits 2050, South Africa.

² Department of Scientific Laboratories, Sudan University of Science and Technology, Khartoum, Sudan.

³ Department of Basic Sciences, Imam Abdulrahman Bin Faisal University, P. O. Box 1982, Dammam, KSA.

E-mail: ibraphysics@gmail.com

Abstract. Organic-inorganic halide perovskites have recently emerged as promising candidates for low cost, high-efficiency solar cells. In this work, the electronic and optical properties of the triclinic lead-free hybrid halide perovskite $\text{CH}_3\text{NH}_3\text{SnI}_3$ as a solar cell absorber has been investigated using density functional theory and many body perturbation theory calculations. Depending on the functional used, our calculated band gaps are 0.82, 1.25 and 1.32 eV, which agree well with the experimental result (1.21 and 1.35) eV. In addition, our calculations show that that $\text{CH}_3\text{NH}_3\text{SnI}_3$ is a direct band gap semiconductor. Many body perturbation theory at the G_0W_0 level of approximation gives a fundamental band gap of 1.54 eV. In order to obtain optical spectra, we carried out Bethe-Salpeter equation calculations on top of non-self-consistent G_0W_0 calculations. Our calculated optical band gap shows anisotropy with an absorption edge of 1.22 eV for out-of-plane polarisation and 1.25 eV for in-plane polarisation. These values lie within the experimentally reported range, confirming that $\text{CH}_3\text{NH}_3\text{SnI}_3$ has potential as a solar cell absorber.

1. Introduction

Hybrid halide perovskites have recently emerged as potential new materials for solar cell applications leading to a new class of hybrid semiconductor photovoltaic cells [1, 2]. It is exemplified by the remarkable increase in power conversion efficiency from 3.8% by Miyasaka [3] to over 20% by Korea Research Institute of Chemical Technology (KRICT) [4] using low cost production methods. This performance is due to the exceptional properties of hybrid halide perovskites displaying high absorption coefficients, high carrier mobility, direct and tunable band gaps [5] and long charge carrier diffusion lengths [6, 7, 8]. Progress in efficiency, however, is hindered by many challenges such as the instability of many perovskite phases [9] and the toxicity of Pb in lead halide perovskites, the absorber in the prototypical high efficiency perovskite based solar cells [10]. Therefore, it is necessary to find an alternative material that does not contain toxic lead. A possible candidate is tin organic-inorganic halide perovskite, $\text{CH}_3\text{NH}_3\text{SnX}_3$ ($\text{X} =$

Cl, Br or I), which has been reported to have a band gap of 1.21 eV and 1.35 eV depending on the preparation method [11]. Depending on temperature, $\text{CH}_3\text{NH}_3\text{SnX}_3$ (X= Cl, Br or I) reveals a very rich phase diagram; i.e., the crystal structure of tin halide perovskite goes from cubic, tetragonal, orthorhombic and monoclinic to triclinic phase by cooling [12]. At room temperature, $\text{CH}_3\text{NH}_3\text{SnI}_3$ structure presents a cubic phase, and it changes to tetragonal at 275 K and to orthorhombic at 110 K [13, 14], but there is no clearly define temperature range in the literature for the triclinic phase.

The first lead-free solar cell made of tin halide perovskite was demonstrated by the Noel et al. group [10] and the Hao et al. group [15] in 2014. Hao et al. investigated the photovoltaic properties of the tetragonal phase of $\text{CH}_3\text{NH}_3\text{SnI}_3$ and found that it has a direct-gap with an energy gap of 1.3 eV, which is significantly redshifted compared with $\text{CH}_3\text{NH}_3\text{PbI}_3$, whose band gap is 1.55 eV [16, 17]. Recent studies reported that $\text{CH}_3\text{NH}_3\text{SnI}_3$ could serve as a lead-free light absorbing material, and solar cell power conversion efficiencies (PCE) in the range of 5-6% have been obtained, however the stability of $\text{CH}_3\text{NH}_3\text{SnI}_3$ remains a challenge [10, 15]. Sn-based perovskites in particular, have shown excellent mobilities in transistors [18]. Theoretical studies were carried out by Paolo Umari et al. [19] using GW (where G is the Green's function and W is the screened Coulomb interaction) calculations including spin orbit coupling of $\text{CH}_3\text{NH}_3\text{XI}_3$ (X = Pb, Sn) in the tetragonal phase. Their calculations gave band gaps of 1.67 eV and 1.10 eV for $\text{CH}_3\text{NH}_3\text{PbI}_3$ and $\text{CH}_3\text{NH}_3\text{SnI}_3$ respectively. They showed $\text{CH}_3\text{NH}_3\text{SnI}_3$ to be a better candidate for electron transport than $\text{CH}_3\text{NH}_3\text{PbI}_3$.

In this work, we perform density functional theory (DFT) calculations of the electronic and optical properties focusing on the triclinic phase of the $\text{CH}_3\text{NH}_3\text{SnI}_3$. To the best of our knowledge, the electronic and optical properties of the triclinic phase of $\text{CH}_3\text{NH}_3\text{SnI}_3$ have not been investigated extensively. We hope that the present investigation will contribute to a better theoretical understanding of the properties of this material, especially its potential in low band gap solar cell applications.

2. Methodology

The crystal structure of the triclinic phase of the hybrid halide perovskite ($\text{CH}_3\text{NH}_3\text{SnI}_3$) is shown in Figure 1. The unit cell of $\text{CH}_3\text{NH}_3\text{SnI}_3$ contains 24 H atoms, 4 Pb atoms, 4 C atoms, 12 I atoms, and 4 N atoms, with $a = 9.06 \text{ \AA}$, $b = 9.06 \text{ \AA}$ and $c = 12.56 \text{ \AA}$ (Material Project ID: mp-995238). In this work, the investigation of the electronic structure properties was performed

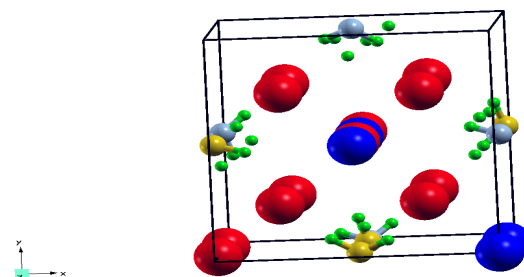


Figure 1. (Color online) The crystal structure of the triclinic phase of $\text{CH}_3\text{NH}_3\text{SnI}_3$ (green: hydrogen; grey: nitrogen; yellow: carbon; red: iodine; blue: tin).

using the Vienna Ab-initio Simulation Package (VASP) [20, 21] based on Density Functional Theory (DFT) [22, 23]. The Projector-Augmented Wave (PAW) [24] method was employed to

treat the electron-ion interactions. To describe the electrons exchange and correlation effects, we used the Generalized Gradient Approximation (GGA) as parametrized by Perdew, Burke and Ernzerhof (PBE) [25], the modified Becke-Johnson (MBJ) [26] and the hybrid functional HSE06 [27], where the Hartree-Fock screening parameter μ is set at 0.2 \AA^{-1} . $4 \times 4 \times 4$ Monkhorst-Pack meshes were used in sampling the Brillouin zone (BZ) with an energy cut-off of 520 eV. These parameters were found to be sufficient for energy convergence. The BZ sampling was chosen in such a way that the convergence of free energy is less than 1 meV/atom. The convergence threshold for self-consistent field iteration was set at 10^{-6} eV. In order to study the optical properties, we performed non-selfconsistent G_0W_0 [28] calculations with 4008 bands and with an energy plane wave cut-off of 300 eV and a cut-off of 150 eV for the plane wave basis of the response function expansion. Optical spectra were calculated at the Bethe-Salpeter Equation (BSE) [29] level of approximation with input from a G_0W_0 calculations.

3. Results and Discussions

3.1. Electronic Properties

The Kohn-Sham band structure of the studied material was calculated using the PBE functional. The calculated electronic band structure and its corresponding total and partial density of states (TDOS and PDOS) are displayed in Figure 2. The electronic band structure calculations demonstrate that this phase has a DFT direct band gap at the gamma point. We note from the PDOS that the valence band edge is dominated by I orbitals and the conduction band edge by Sn orbitals. The organic cation CH_3NH_3^+ do not have any significant contribution around the band edge. Our calculated approximate DFT and many body perturbation theory at the G_0W_0 level of approximation fundamental band gaps for the triclinic perovskite $\text{CH}_3\text{NH}_3\text{SnI}_3$ are listed in Table 1. The only available experimental data is that reported by Stoumpos et al. [11], where, depending on the preparation method, they reported that the experimental band gap of tin based hybrid halide perovskites to be 1.21 eV and 1.35 eV. Our results are consistent with these results.

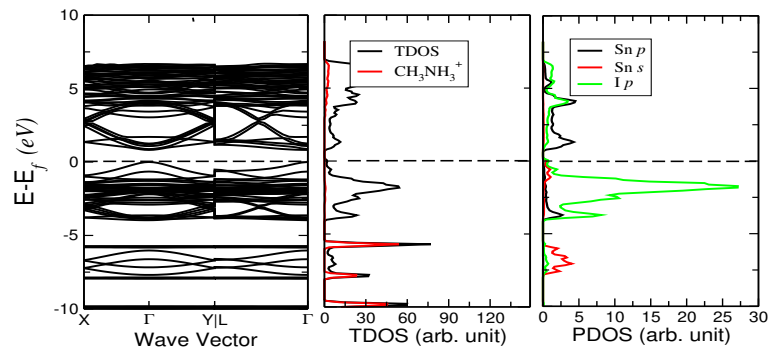


Figure 2. DFT calculated electronic structure of the triclinic phase of $\text{CH}_3\text{NH}_3\text{SnI}_3$ using PBE: band structure (left), total density of states (TDOS) and the partial density of states (PDOS) due to CH_3NH_3^+ (middle); and PDOS due to Sn and I (right).

3.2. Optical Properties

The optical properties can be calculated from the complex dielectric tensor, $\varepsilon(\omega) = \varepsilon_1(\omega) + i\varepsilon_2(\omega)$ which describes the polarization response of a material to an externally applied electric field \mathbf{E} . Using the real part $\varepsilon_1(\omega)$ and the imaginary part $\varepsilon_2(\omega)$ of the dielectric tensor $\varepsilon(\omega)$, we compute

Table 1. Our calculated and the experimental band gap of triclinic $\text{CH}_3\text{NH}_3\text{SnI}_3$.

Functional	PBE	MBJ	HSE06	GW	Exp.[11]
Band gap (eV)	0.82	1.25	1.32	1.54	1.21 and 1.35

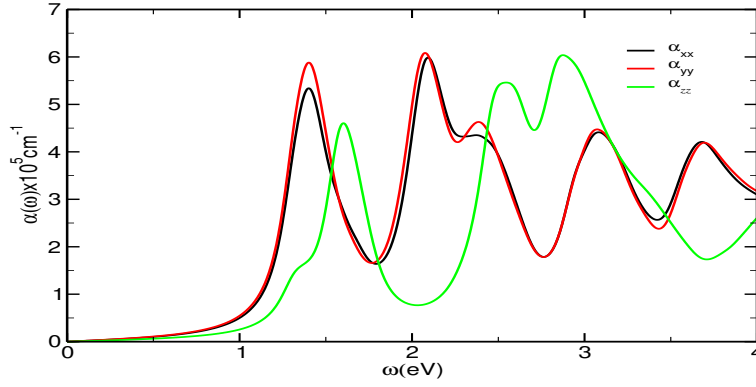


Figure 3. The optical absorption coefficient spectra of triclinic $\text{CH}_3\text{NH}_3\text{SnI}_3$.

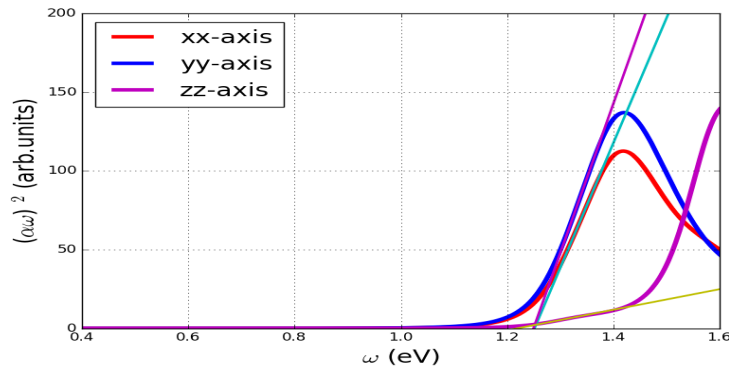


Figure 4. Tauc plot of the absorption coefficient, showing the polarization-dependent onsets.

the optical absorption coefficient spectra using the following equation.

$$\alpha(\omega) = \sqrt{2}\omega \left([\varepsilon_{\text{re}}^2(\omega) + \varepsilon_{\text{im}}^2(\omega)]^{\frac{1}{2}} - \varepsilon_{\text{re}}(\omega) \right)^{\frac{1}{2}}. \quad (1)$$

The results in Figure 3 show that the highest absorption peak in the region (1.0-2.5) eV of $\alpha_{yy}(\omega)$ component is higher than that of $\alpha_{xx}(\omega)$ and $\alpha_{zz}(\omega)$. Figure 4 shows the absorption coefficient $\alpha(\omega)$ for triclinic $\text{CH}_3\text{NH}_3\text{SnI}_3$ plotted in Tauc formalism. From Figure 4 we can see there are featured edges as a function of polarization. Due to the structural anisotropy we observed variation of band edge in the different polarizations. For in plane polarisation the onset is at 1.25 eV and for out of plane polarisation the onset is at 1.22 eV within the experimentally reported values (1.21 and 1.35) eV.

4. Conclusions

The electronic and optical properties of the triclinic $\text{CH}_3\text{NH}_3\text{SnI}_3$ have been calculated using first-principles methods. The material was found to be a direct band gap semiconductor. Depending on the method used, our calculated band gaps are 0.82 eV (PBE), 1.25 eV (MBJ), 1.32 eV (HSE06) and 1.54 eV (G_0W_0). Obtained values agree well with the experimental results (1.21 eV and 1.35 eV). Moreover, the BSE absorption edges using the Tauc form are found to be 1.22 eV for out-of-plane polarisation and 1.25 eV for in-plane polarisation. This anisotropy seen in the BSE absorption edges may be related to the experimental result 1.21 and 1.35 eV. Inspection of the obtained band structure, PDOS and TDOS reveals that the organic cation CH_3NH_3^+ does not have significant contribution around the band edges as I and Sn. Our results confirm that the triclinic phase of $\text{CH}_3\text{NH}_3\text{SnI}_3$ has potential as a solar cell absorber. Finally, with the help of the real part $\varepsilon_{\text{re}}(\omega)$ and the imaginary part $\varepsilon_{\text{im}}(\omega)$ of the dielectric tensor $\varepsilon(\omega)$ we derive all the desired frequency dependent optical spectra such as absorption coefficient at BSE level of approximation, which show a significant optical anisotropy.

5. Acknowledgement

IOAA would like to acknowledge the support he received from NRF-TWAS for funding, and Sudan University of Science and Technology (SUST). We also wish to acknowledge the Centre for High Performance Computing (CHPC), South Africa, for providing us with computing facilities.

References

- [1] Green M A and Ho-Baillie A 2017 *ACS Energy Letters* **2** 822–830
- [2] Park N G 2013 *The Journal of Physical Chemistry Letters* **4** 2423–2429
- [3] Kojima A, Teshima K, Shirai Y and Miyasaka T 2009 *Journal of the American Chemical Society* **131** 6050–6051
- [4] Yang W S, Noh J H, Jeon N J, Kim Y C, Ryu S, Seo J and Seok S I 2015 *Science* **348** 1234–1237
- [5] Noh J H, Im S H, Heo J H, Mandal T N and Seok S I 2013 *Nano Letters* **13** 1764–1769
- [6] Stranks S D, Eperon G E, Grancini G, Menelaou C, Alcocer M J, Leijtens T, Herz L M, Petrozza A and Snaith H J 2013 *Science* **342** 341–344
- [7] Dong Q, Fang Y, Shao Y, Mulligan P, Qiu J, Cao L and Huang J 2015 *Science* **347** 967–970
- [8] Shi D, Adinolfi V, Comin R, Yuan M, Alarousu E, Buin A, Chen Y, Hoogland S, Rothenberger A, Katsiev K *et al.* 2015 *Science* **347** 519–522
- [9] Zhang Y Y, Chen S, Xu P, Xiang H, Gong X G, Walsh A and Wei S H 2018 *Chinese Physics Letters* **35** 036104
- [10] Noel N K, Stranks S D, Abate A, Wehrenfennig C, Guarnera S, Haghighirad A A, Sadhanala A, Eperon G E, Pathak S K, Johnston M B *et al.* 2014 *Energy & Environmental Science* **7** 3061–3068
- [11] Stoumpos C C, Malliakas C D and Kanatzidis M G 2013 *Inorganic Chemistry* **52** 9019–9038
- [12] Feng J and Xiao B 2014 *The Journal of Physical Chemistry C* **118** 19655–19660
- [13] Parrott E S, Milot R L, Stergiopoulos T, Snaith H J, Johnston M B and Herz L M 2016 *The Journal of Physical Chemistry Letters* **7** 1321–1326
- [14] Takahashi Y, Obara R, Lin Z Z, Takahashi Y, Naito T, Inabe T, Ishibashi S and Terakura K 2011 *Dalton Transactions* **40** 5563–5568
- [15] Hao F, Stoumpos C C, Cao D H, Chang R P and Kanatzidis M G 2014 *Nature Photonics* **8** 489

- [16] Eperon G E, Stranks S D, Menelaou C, Johnston M B, Herz L M and Snaith H J 2014 *Energy & Environmental Science* **7** 982–988
- [17] Ali I O A, Joubert D P and Suleiman M S H 2018 *Materials Today: Proceedings* **5** 10570–10576
- [18] Kagan C, Mitzi D and Dimitrakopoulos C 1999 *Science* **286** 945–947
- [19] Umari P, Mosconi E and De Angelis F 2014 *Scientific Reports* **4** 4467
- [20] Kresse G and Hafner J 1993 *Physical Review B* **47** 558
- [21] Kresse G and Hafner J 1994 *Physical Review B* **49** 14251
- [22] Hohenberg P and Kohn W 1964 *Physical Review* **136** B864
- [23] Kohn W and Sham L J 1965 *Physical Review* **140** A1133
- [24] Kresse G and Joubert D 1999 *Physical Review B* **59** 1758
- [25] Perdew J P, Burke K and Ernzerhof M 1996 *Physical Review Letters* **77** 3865
- [26] Becke A D and Johnson E R 2006 *The Journal of Chemical Physics* **124** 221101
- [27] Krukau A V, Vydrov O A, Izmaylov A F and Scuseria G E 2006 *The Journal of Chemical Physics* **125** 224106
- [28] Hedin L 1965 *Physical Review* **139** A796
- [29] Salpeter E E and Bethe H A 1951 *Physical Review* **84** 1232

Structural, elastic and electronic properties of binary titanium-based shape memory alloys

M E Baloyi¹, R Modiba², P E Ngoepe¹ and H R Chauke¹

¹Materials Modelling Centre, University of Limpopo, Private Bag X1106, Sovenga, South Africa

²Materials Science and Manufacturing, CSIR, PO Box 395, Pretoria, 0001, South Africa

Email: mphamela.baloyi@ul.ac.za

Abstract. Ab initio density functional theory approach was employed to investigate the structural properties, elastic constant and phonon dispersion of B2 binary TiPt, TiNi and TiCo shape memory alloys. We employed the plane-wave pseudopotential method within generalized gradient approximation parameterized by Perdew, Burke and Enzerhof using VASP code. These alloys have the ability to remember their shapes after deformation, and this is due to their shape memory effect and super elasticity properties. We found that the lattice parameters are in good agreement with the experimental results. Furthermore, the TiPt structure is thermodynamically stable displaying lowest heats of formation. Their calculated elastic constant indicated that TiPt has higher transformation temperature. The Pugh's ratio clearly indicates that all titanium-based binary alloys are ductile ($B/G > 1.75$). Phonon dispersion curves shows that TiCo is vibrational stable and there are acoustic modes observed at the gamma directions while TiPt is not due to the existence of imaginary frequencies observed along M high symmetry direction, in agreement with calculated elastic constants.

1. Introduction

Shape memory alloys (SMAs) have the ability to recover their original shapes after being deformed when heated above certain temperature [1]. They exhibit two interesting properties, shape memory effect and superelasticity. Titanium-based SMAs have attracted significant attention due to its distinctive properties for extensive applications such as actuators and sensors, which are displayed in martensitic transformations [2]. It is well known that most Ti-based alloys have an ordered B2 phase at high temperatures and transform to low temperature martensitic phase (B19/19') when temperature decreases [3]. TiNi exhibits significant shape memory effect (SME) and Nitinol became the most commonly used SMAs [4]. The development of SMAs which can operate at high temperature is important to improve shape memory properties [5]. An increase of the martensitic transformation of SMAs allows for extending their application range to high temperatures. These alloys possess higher martensitic transformation temperature above 373 K [6]. In addition, elevated temperature SMAs such as Ti(Pt, Pd) are of potential technological interest for elevated temperature SMA applications [5].

Furthermore, B2 TiNi and TiCo have martensitic transformation temperature of 320 K and 40 K, respectively [7, 8, 9]. Platinum have higher temperature of 2041 K which leads to TiPt having the highest martensitic transformation of about 1300 K and exhibit B2 to B19 transformation [10]. In this paper, we

investigate the phase stability of TiPt, TiNi and TiCo alloys at 50:50 equiatomic composition using the heats of formation, elastic properties, electronic properties (density of states) and phonon dispersion curves of B2 structures. We found that B2 TiPt is unstable at low temperature, in agreement with experimental findings. Our results also show that B2 TiCo is stable with no soft modes observed. However, TiCo has shown potential for alloy development, being elastically and vibrationally stable.

The structures of TiPt is shown in figure 1 below. It is a cubic B2 structure also known as a high temperature beta phase with the space group of Pm-3m. Its experimental equilibrium lattice parameter is 3.192 Å [11]. The lattice parameter of the cubic B2 TiNi and TiCo are reported to be 3.015 Å [12] and 2.988 Å [9], respectively. All the structures have a B2 CsCl prototype structure.

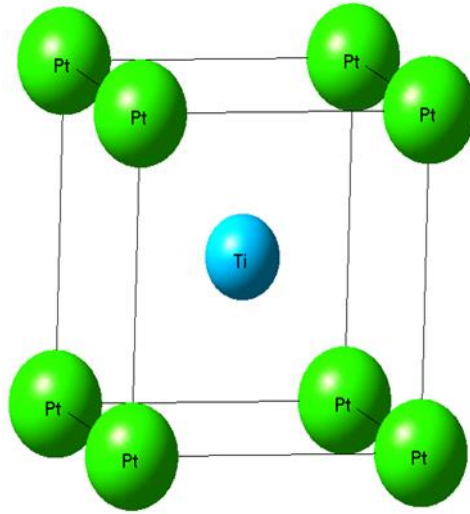


Figure 1. The cubic phase TiPt binary alloys at 50:50 equiatomic composition.

2. Methodology

The calculations were carried out using ab initio density functional theory (DFT) [13] formalism with the projector augmented wave (PAW) [24], as implemented in VASP code [14]. An energy cutoff of 500 eV was used, to achieve a good convergence of the parameters. For exchange-correlation functional, the generalized gradient approximation of Perdew, Burke and Enzerhof (GGA-PBE) [15] was chosen. Interactions in the Brillouin zone were performed with special k-spacing of 0.2 with accordance to Monkhorst and Parck scheme [16]. The phonon dispersion spectra were evaluated using PHONON code [17] as implemented in Materials Design within MedeA software of VASP code [14].

3. Results and discussion

3.1. Equilibrium lattice parameter

In Table 1; calculated equilibrium lattice parameters and heats of formation for the B2 Ti-based binary alloys are shown. The equilibrium lattice parameter results are in good agreement with the experimental findings. Heats of formation is used to predict the stability of alloys and in constructing their phase diagrams [18]. The equation for determining heats of formation (ΔH_f) is given by [23]:

$$\Delta H_f^{Ti-M} = \frac{1}{n} E^{Ti-M} - [(1-x)E^{Ti} + xE^M] \quad (1)$$

where E^{Ti-M} is the total energy of alloy, E^{Ti} is the total energy of Ti, E^M is the total energy of element M=Pt, Co, Ni, n is the total number of atoms and x is the fractional concentration of the constituent element. The lowest and highest heats of formation show the most and least stable material, respectively.

TiPt is found to be more stable with the lowest heats of formation of -0.821 eV/atom while that of TiNi was found to be the least stable with the highest value of -0.403 eV/atom.

Table 1. Equilibrium lattice parameters (Å) and heats of formation ΔH_f (eV/atom) of B2 TiPt, TiNi and TiCo.

Structures	a	ΔH_f
TiPt	3.180 (3.192) ^a	-0.821
TiCo	2.994 (2.988) ^b	-0.527
TiNi	3.011 (3.015) ^c	-0.403

^a reference [11]

^b reference [9]

^c reference [12]

3.2. Elastic constants

We have also calculated the elastic constants C_{ij} , Anisotropy (A) and Pugh's ratio (B/G) for cubic phases as shown in Table 2. For us to understand the martensitic transformation of these alloys, we investigate their elastic properties [7]. The stability criterion for the cubic system to be mechanically stable are as follows [19];

$$C_{44} > 0, C_{11} + 2C_{12} > 0, \text{ and } C_{11} > |C_{12}|. \quad (2)$$

The elastic moduli are then calculated based on the three independent elastic constants in equation (2) above:

$$C' = \frac{C_{11} - C_{12}}{2} \text{ and } A = \frac{C_{44}}{C'}, \quad (3)$$

where C' is shear modulus and A is the anisotropy factor [20]. TiPt fails to satisfy the criterion shown in equation (2), $C_{11} < C_{12}$ leading to a negative C' of -32 GPa. Hence, B2 TiPt is mechanically unstable at 0 K. B2 TiCo and TiNi satisfy all the cubic stability criterion and these alloys are considered to be mechanically stable. Lower C_{44} value of 44.07 GPa of TiCo signals that the C_{44} shear resistance becomes comparable to the C' shear resistance, resulting in low anisotropy value of 1.72 which give rise to monoclinic B19' martensite [7]. Therefore, TiCo undergoes the B2 to B19' martensitic transformation due to its lower A . These results are consistent with the experimental findings [3]. Higher A indicates the higher transformation temperature, B2 to B19 transformation. Calculated A of TiNi with a value of 2.52 agrees with the experimental value of 2.4 [12]. In addition, A of TiCo agrees to within 3% the experimental with value 1.72 (1.84) [21]. The bulk (B) and shear (G) moduli are calculated to investigate ductility of these alloys. The investigated binary alloys are found to be ductile since $B/G > 1.75$ [22].

Table 2. Lattice parameters (Å), elastic constants (GPa) and heats of formation (eV/atom) of TiPt, TiNi and TiCo binary alloys.

Structures	C_{11}	C_{12}	C_{44}	C'	A	B/G
TiPt ^d	145	210	45	-32		2.20
TiCo	266.89	215.73	44.07	25.58	1.72 (1.84) ^e	3.35
TiNi	190.32	143.97	58.36	23.18	2.52 (2.40) ^f	5.57

^d reference [19]

^e reference [21]

^f reference [12]

3.3. Phonon dispersions

We have performed the phonon dispersions calculations on structures and the plots are shown in figure 2. Soft modes are observed at the M and R high symmetry direction indicating the instability of TiPt. Phonon density of states (PDOS) suggest that the soft modes observed are due to high vibration of Pt atom. In addition, our phonon dispersion calculations show TiNi to be unstable since there are soft modes observed in the phonon curves. These soft modes are observed along M directions and this could be attributed to high vibration of Ni atoms as shown on the phonon DOS. TiCo is found to be vibrationally stable with no soft modes observed, in agreement with predicted elastic constants where we observed a lower A as compared to the other structures.

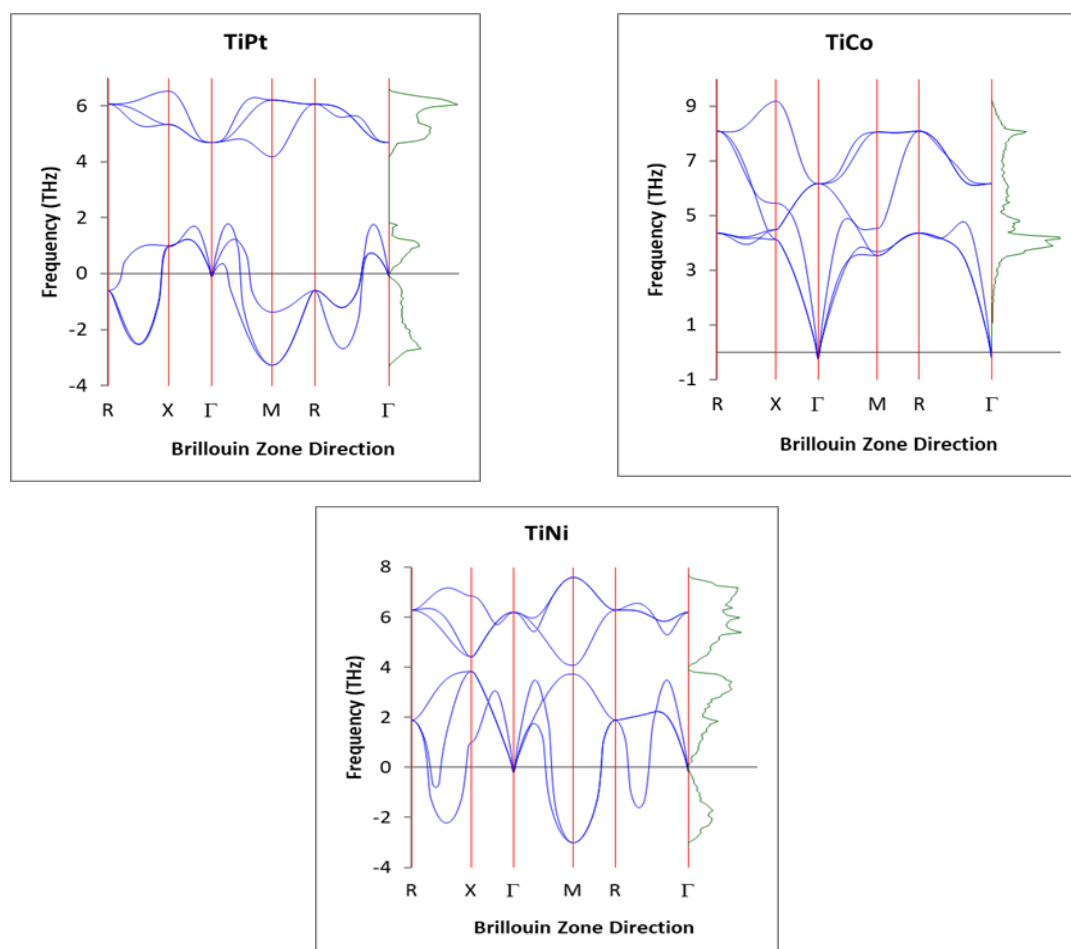


Figure 2. Phonon dispersion curves and Phonon density of states of TiPt, TiNi and TiCo binary alloys.

3.4. Electronic density of states

In figure 3, the total (tDOS) and partial density of states (PDOS) of TiPt, TiNi and TiCo binary alloys are shown. DOS of the alloys indicates the stability with respect to their behavior at the Fermi level E_f . The structure with highest and lowest DOS at the E_f is considered least and most stable, respectively. Shapes of all tDOS curves are similar comprising of two set of peaks separated by a pseudo-gap. The lower tDOS peaks are occupied by Pt for TiPt, Co for TiCo and Ni for TiNi, and the higher tDOS peaks are mainly due to the d state of Ti atoms. TiCo has the lowest Ti d DOS value of 1 states per eV at the E_f , indicating the stability of these alloys. In addition, TiPt is the least stable alloy due to its higher Ti d

DOS value of 1.6 eV at the E_f . Our DOS results agree with our calculated elastic constant, showing that TiCo is the most stable structure.

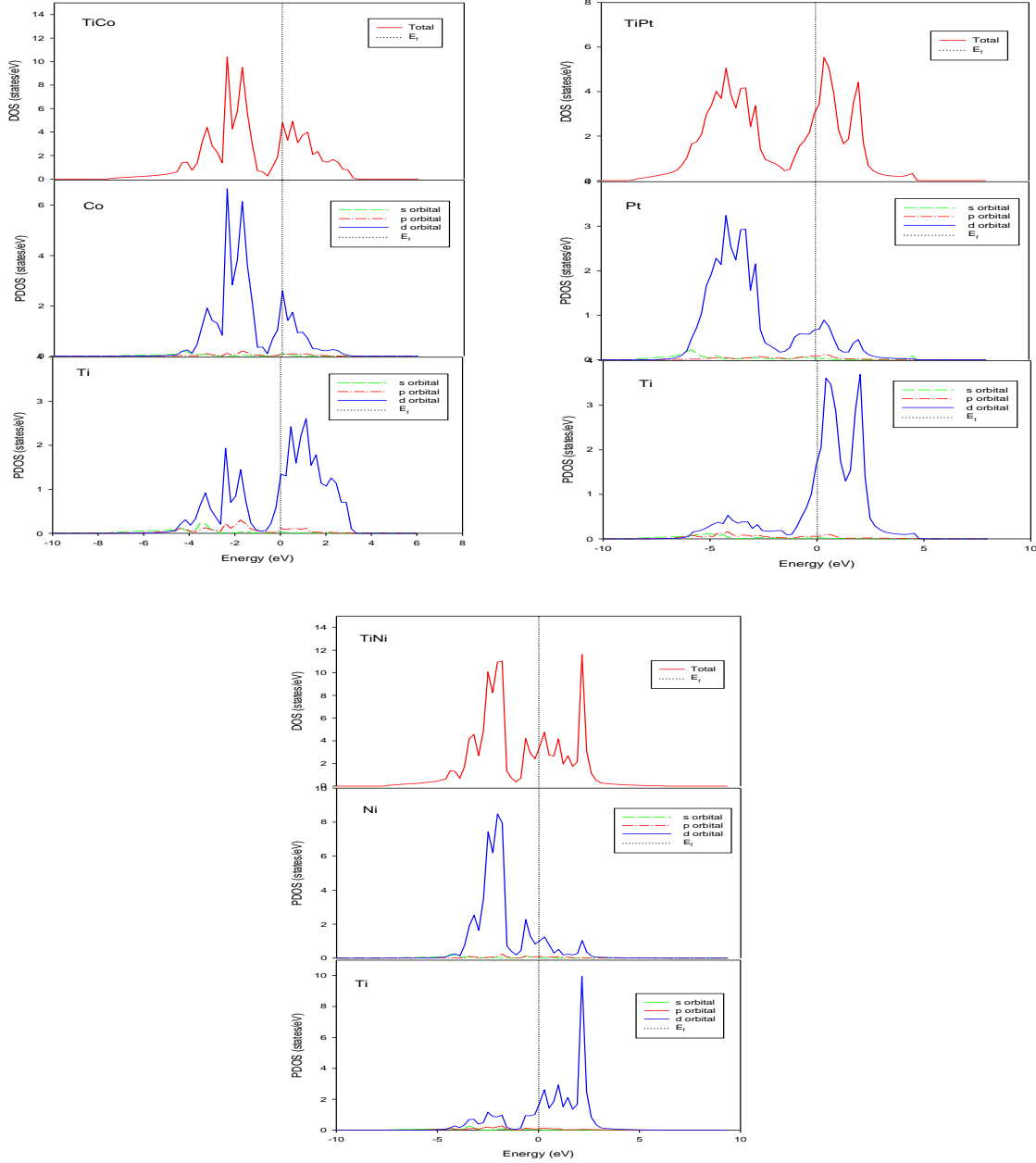


Figure 3. Total and partial density of states of TiCo, TiPt and TiNi binary alloys. The Fermi level is at the value of 0 eV.

4. Summary and conclusion

The equilibrium lattice parameters, heats of formation, elastic properties and electronic properties of equiatomic B2 TiCo, TiNi and TiPt were determined using the first principle calculations. Our results are in agreement with the experimental findings within 3 %. We note that the predicted heats of formation confirm the stability of binary alloys investigated. Calculated elastic constants show that TiPt

is mechanically unstable at low temperature whereas TiCo and TiNi are mechanically stable. It is interesting to note that TiCo is vibrationally stable with no soft modes observed, in agreement with the predicted heats of formation and elastic constants. Only TiCo is energetically, mechanically and dynamically stable according to the calculations, performed at zero temperature and pressure.

Acknowledgements

I would like to thank NRF and CSIR for the financial support. The work was carried at the Materials Modelling Centre, University of Limpopo and the Centre for High performance computing (CHPC) in South Africa. The support of the Department of Science and Technology, DST is highly recognised.

References

- [1] Mahlangu R, Chauke H R and Ngoepe P E 2014 *Advanced Material Science* **1019** 385-390
- [2] Lagoudas D C and Hartl D J 2007 *J. Aerospace Engineering* **221** 535-549
- [3] Chang-Long T, Wei C and Jing-Chuan Z 2006 *Chin. Phys. Lett.* **23** 2863-2866
- [4] Strittmatter J and Gumpel P 2009 *Australian J. Mech. Eng.* **7** 99-109
- [5] Yamabe-Mitarai Y and Wadood A 2014 *Mater. Sci. Eng. A* **601** 106-110
- [6] Yamabe-Mitarai Y, Arockiakumar R, Wadood A, Suresh K S, Kitashima T, Hara T, Shimojo M, Tasaki W, Takalashi M, Takalashi S and Hosoda H 2015 *Materials Today* **2S** 517-522
- [7] Biggs T, Cornish L A, Witcomb M J and Cortie M B 2004 *J. of Alloys and Compounds* **375** 120-127
- [8] Xu K, Huang X M, Lu J, Lui H S, Cai G and Jin Z P 2018 *Calphad* **60** 191-199
- [9] Wadood A, Takalashi M, Takalashi S, Hosoda H and Yamabe-Mitarai 2013
- [10] Miyazaki S and Ishida A 1999 *Mater. Sci. Eng. A* **273-275** 106-133
- [11] Kresse G and Hafner J 1994 *Phys. Rev. B* **49** 251-269
- [12] Nishida M, Matsuda M, Yasumoto Y, Yano S, Yamabe-Mitarai Y and Hara T 2013 *Mater. Sci. Tech.* **24** 884-889
- [13] Tan C L, Tian X H, Ji G J, Gui T L and Cai W 2008 *Solid State Communications* **147** 8-10
- [14] Kresse G and Hafner J 1993 *Phys. Rev. B* **47** 558561
- [15] Perdew J P, Burke K and Enzerhof M 1996 *Phys. Rev. Lett.* **77** 88-92
- [16] Monkhorst H J and Pack J D 1976 *Phys. Rev. B* **13** 88-92
- [17] Parlinski K, Li Z Q and Kawazoe Y 1997 *Phys. Rev. Lett.* **78** 4063-4066
- [18] Hennig R G, Carlsson A E, Kelton K F and Henley C L 2005 *Phys. Rev. B* **71** 100-103
- [19] Mahlangu R, Phasha M J, Chauke H R and Ngoepe P E 2013 *Intermetallics* **33** 27-32
- [20] Phasha M J, Ngoepe P E, Chauke H R, Pettifor D G and Nguyen-Mann D 2010 *Intermetallics* **18** 2083-2089
- [21] Lin Y S, Cak M, Paidar V and Vitek V 2012 *Acta Mater.* **60** 881-888
- [22] Pugh S F 1954 *J. Sci.* **45** 823-843
- [23] Fernando G W, Watson R E and Weinert M 1992 *Phys. Rev. B* **45** 15 8233
- [24] Blöchl P E 1992 *Phys. Rev. B* **50** 17953-17979

First principles investigation of structural, elastic, electronic and optical properties of Barium seleno-germanate, Ba_2GeSe_4

Abdu Barde^{1,2} and Daniel P Joubert¹

¹ The National Institute for Theoretical Physics, School of Physics and Mandelstam Institute for Theoretical Physics, University of the Witwatersrand, Johannesburg, Wits 2050, South Africa.

² College of Science and Technology, Jigawa state Polytechnic, Dutse - Jigawa state, Nigeria.

E-mail: abdubarde@gmail.com

Abstract. Ternary and quaternary chalcogen-germanates and stannates have a rich structural chemistry. Experimental studies of their non-linear optical properties have been reported, but there are few published computational studies on their structural, elastic, electronic and optical properties. In this work, we investigate the structural, elastic, electronic and optical properties of Ba_2GeSe_4 using Density Functional Theory (DFT) and post-DFT many body perturbation theory. The ground state energy and properties, including equilibrium lattice parameters, bulk modulus and band gap were calculated at the DFT level of approximation. The fundamental gap was determined at the post-DFT G_0W_0 level of approximation while optical absorption was determined with the Bethe-Salpeter Equation approximation. The ground state energy and mechanical results show that Ba_2GeSe_4 is a stable compound while the calculated optical absorption results and estimated optical band gap show that it is a wide band gap material that is well-situated for photon absorption in the high energy visible range with potential application in multi-junction solar cells.

1. Introduction

The ternary and quaternary compounds containing metal chalcogenides, chalcogen-germanates and thiostannates have received considerable attention due to their structural chemistry [1, 2], important physical and chemical properties for potential applications in non-linear optics (NLO) [3, 4], thin film for solar cell [5] and visible light response photocatalysts [6, 7]. Among the family of chalcogen-germanates is seleno-germanate earth alkali metal barium seleno-germanate Ba_2GeSe_4 . The experimental synthesis of Ba_2GeSe_4 has been reported and the compound is found to crystallize in a monoclinic structure with space group $p12/m$ [8]. The thio/seleno-germanate and stannate compounds exhibit interesting physical properties due their isolated tetrahedral ortho-anion $[\text{MQ}_4]^{4-}$ corner shearing, where $[\text{M} = \text{Ge, Sn; Q} = \text{S, Se}]$. The compounds are well known to have a structure of type A_2MQ_4 [4]. Little has been reported on the structural, elastic, electronic and optical properties of Ba_2GeSe_4 . We are only aware of the study of Assoud and Soheilnia [8], where the authors reported experimental data on the structure and lattice constants and theoretically investigated the electronic properties using density functional theory with the local density approximation (LDA). However, the authors did not measure the optical band

gap of this compound, but predicted it to lie within 2.6 - 3.0 eV. LDA is well known to give a less accurate description of electronic and optical properties of materials due to the omission of the contribution from quasiparticle renormalization of electronic band gaps and excitonic effect in the linear and non-linear optical absorption [9]. In view of this and the rich range of properties of the seleno-germanate family of compounds with potential practical applications, it is worthy here to investigate the structural, elastic, electronic and optical properties of Ba_2GeSe_4 . We use two DFT exchange-correlation approximations, the Perdew-Burke-Ernzerhof generalised gradient approximation (PBE) [10] and PBEsol [11] to determine the ground state energy and lattice structure. DFT band structure calculations were performed using two hybrid functionals, the modified Johnson Becke (MBJ) [12] and Heyd-Scuseria-Ernzerhof (HSE) [13], two approximations that normally improve on the band gap underestimation by local and semi-local DFT approximations. A Green's function (GW) calculation was used to determine the fundamental gap while optical absorption properties were determined within the Bethe-Salpeter Equation (BSE) approximation, which is effective in reproducing the experimental band gap for semiconductors.

2. Computational details

The investigation of structural, elastic, electronic and optical properties of Ba_2GeSe_4 were carried out within the framework of density functional theory (DFT) as implemented in the Vienna Ab initio simulation package (VASP) [14, 15]. A projected-augmented-wave (PAW) [16] formulation was used for the description of electron-ion interactions. The groundstate energy was calculated within the Perdew-Burke-Ernzerhof generalised gradient approximation (PBE) [10] and PBEsol [11] for the electron exchange correlation relations. Equilibrium structure optimization was performed on the primitive cell of the structure with cut-off energy of 520 eV and a $6 \times 6 \times 4$ Monkhorst-pack mesh for sampling the Brillouin zone. The k-point mesh sampling was chosen to achieve convergence energies within less than 1 meV/atom. The elastic tensor was calculated for the fully relaxed equilibrium geometry with PBE and PBEsol. DFT band structure calculations were performed for the PBEsol optimized structure using PBEsol and the modified Johnson-Becke potential (MBJ) [12]. The band gap was also estimated with the hybrid Heyd-Scuseria-Ernzerhof (HSE) [13] approximation. The MBJ and HSE approximations normally give a better estimate of the band gap at the DFT level when compared to conventional DFT calculations with local or semi-local exchange-correlation functions. Moreover, in this study we performed a post-DFT many-body Green's function G_0W_0 , [17, 18] calculation to obtain an estimate of the quasi-particle excitations. We used a 180 eV energy cut-off for the response functions to determine the fundamental gap. Finally, the optical absorption spectrum was obtained by including excitonic effects using the $G_0W_0 + \text{BSE}$ approximation [19, 20, 21]. From the optical absorption spectra, the optical band gap was determined using a Tauc plot [22].

3. Result and discussion

3.1. Structural properties

X-ray powder diffractogram structural studies reveal that at room temperature the layered ternary Ba_2GeSe_4 compound contains isolated tetrahedral GeSe_4 that form the structure type of K_2ZnBr_4 . The compound crystallises in a monoclinic structure, space group $\text{p}2_1/\text{m}$ [8], with a conventional unit cell made which contains two Ba_2GeSe_4 formula per unit cell. Figure 1 shows the Ba_2GeSe_4 super cell showing the tetrahedral GeSe_4 arrangements.

Energy versus volume calculations for Ba_2GeSe_4 were performed with the PBE and PBEsol approximations. A 3rd order Murnaghan equation of state (EOS) function [23] was fitted to the calculated values and is shown in Fig.2(b). The results show that the PBEsol equilibrium volume is closer to the experimental value than the PBE value. Calculated equilibrium structural parameters and the available experimental data are given in Table.1. Compared to the

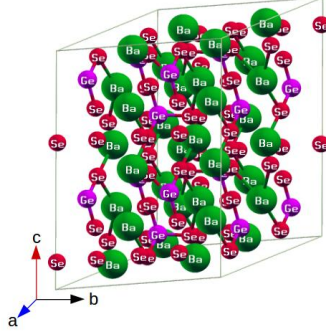


Figure 1. Craystal structure of Ba_2GeSe_4 .

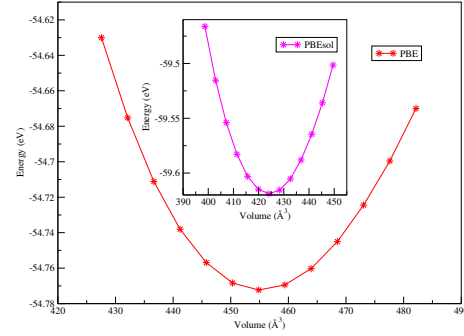


Figure 2. Variation of total energy as a function of volume.

experimental data one can clearly see that the calculated lattice parameters (a, b and c), β , the angle between cell length a, b , and one of factors that defines the lattice plane spacing, and volume of the unit cell obtained by PBEsol, are very close to the experimentally measured values. The percentage difference of calculated lattice parameter and angle values from experimental values do not exceed 1.54%. Based on the consistent performance of the calculated PBEsol structural parameters, this approximation was used to determine DFT electronic and optical properties and the orresponding calcaulted structure was used for the GW and BSE calculations.

Table 1. Calculated and experimental structural parameters for Ba_2GeSe_4 . Lattice parameters a, b and c in Å. The angle between a and b , β , in degrees. Volume V , in Å³. E_{coh} , cohesive energy per atom, in eV.

	a	b	c	V	β	E_{coh}
PBE	7.204	7.240	9.292	454.96	108.52	-3.61
PBEsol	7.022	6.986	9.150	424.20	109.078	-3.95
Exp.[8]	6.9958	7.0938	9.1738	430.11	109.153	-

3.2. Elastic Properties

The elastic properties of a material provides important information about structural stability, binding characteristic, the anisotropy character, the link between mechanical and dynamical properties of a crystal. There are 13 independent elastic constants elastic stiffness constants C_{ij} for Ba_2GeSe_4 , a monoclinic system. The calculated values of the elastic constants, for PBE and PBEsol, satisfy the stability criteria for monoclinic systems [24]. In Table 2 the bulk modulus B , the shear modulus G , Young's E modulus calcaulted from the C_{ij} values using the Voigt-Reuss-Hill (VRH) approximation[25, 26] and the ratio B/G , A^U , the universal measure of anisotropy of a material, and the Poisson ratio ν of Ba_2GeSe_4 are shown. The bulk modulus is a measure of resistance to volume change in response to an applied pressure, while the shear modulus G is a measure of resistance to reversible deformation due to shear stress. Young's modulus is a measure of resistance to linear stress. Pugh [27] suggested the critical value of 1.75, for $B/G > 1.75$ the

material behaves in ductile manner otherwise it is brittle. The Voigt and Reuss methods are known to define the upper and lower limits, respectively, of the mechanical parameters. We therefore, use Hill's value which is an arithmetic average of Voigt and Reuss[28] for calculating the values of B/G and ν . The determined value of B/G from both PBE and PBEsol indicating that Ba₂GeSe₄ is ductile material. Similarly, ν provides an information of nature in bonding forces and volume compressibility of solid materials, ν takes values between $-1 < \nu < 0.5$ [29]. The determined ν for both PBE and PBEsol indicated that Ba₂GeSe₄ is of good plasticity and have central inter-atomic forces. The calculated bulk modulus at zero pressure, B₀, from EOS fit, Table 2 and B from VRH approximation are in good agreement demonstrating the reliability of this calculation. The relatively small value of the bulk modulus in Table 2 is evidence that Ba₂GeSe₄ is not very resistant to volume change with applied pressure. Similarly the values of Young's E is greater than bulk B modulus demonstrating that the title compound is soft material. The departure of A^U from zero defines the extent of single crystal anisotropy [30]. A^U and the Poisson ratio ν were calculated using equations from Ref.[24, 30] which are depicted in Table 2.

Table 2. Calculated mechanical parameters. Bulk modulus B₀ and its derivative B'_0 from EOS fitting, bulk B_V, shear G_H and Young's E_H from VRH-approximations modulus in GPa, universal anisotropy A^U , Poisson's ratio ν and ratio B/G of Ba₂GeSe₄

	B ₀	B'_0	B _H	G _H	E _H	A^U	ν	B/G
PBE	23.49	6.08	24.44	11.87	30.64	0.939	0.29	2.06
PBEsol	28.01	5.16	26.05	13.29	34.08	1.963	0.28	1.96

3.3. Electronic Properties

In Figure 3 and 4 the band structure along the high symmetry directions in the Brillouin zone are shown for PBEsol and the modified Becker Johnson potential (MBJ). MBJ normally gives a better estimation of the gap for large band gap semiconductors. From the band structures for PBEsol and MBJ, Figure 3 and 4 Ba₂GeSe₄ has a direct band gap of 1.46 eV and 2.26 eV located at Γ , respectively. It is also observed that from the projected density of states (PDOS) that the dominant contributions to the lower conduction band (CB) come from the hybridizations of Se(p), Ge(s) and Ba(d) orbitals, while the upper valency band (VB) is dominated by contributions from Se(p) with a limited contribution from Ba(d) orbitals. Band gaps calculated with PBE, PBEsol, MBJ, HSE and the fundamental gap at the G₀W₀ level of approximation, are listed in Table 3. The PBE and PBEsol gaps are smaller than the experimental gap, while the MBJ and HSE gaps are closer to the experimental range. The G₀W₀ estimate of the fundamental gap is smaller than the experimental gap, which is surprising since this estimate is frequently larger than the experimental optical gap.

3.4. Optical properties

The study of optical properties gives a better understanding of electronic structure and possible applications of a materials. The frequency dependent dielectric function $\varepsilon(\omega) = \varepsilon_1(\omega) + i\varepsilon_2(\omega)$ fully described the optical properties of a materials [31]. The imaginary part $\varepsilon_2(\omega)$ is obtained from the momentum matrix element between the occupied electronic states relations, while the real part $\varepsilon_1(\omega)$ is determined from the imaginary part through the Kramers-Kronig relations using equations from Ref. [31]. From the calculated structural parameter $A^U = 1.963$, Ba₂GeSe₄ is anisotropic in nature. This is confirmed by the anisotropic nature of its optical properties

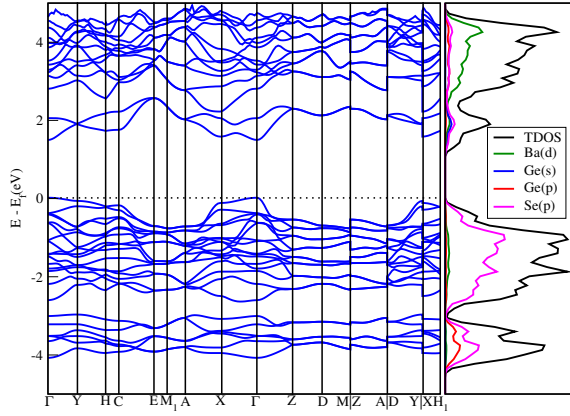


Figure 3. PBEsol Electronic bands structure along high symmetry directions

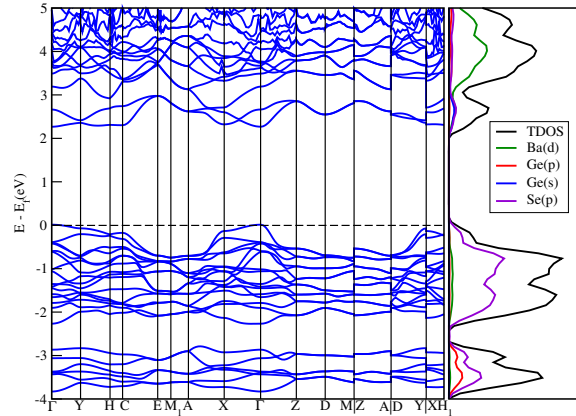


Figure 4. MBJ Electronic bands structure along high symmetry directions

Table 3. Calculated and experimental band gaps, E_g , of Ba_2GeSe_4 .

	PBE	PBEsol	MBJ	HSE	G_0W_0	Others (LDA)	Exp.
$E_g(\text{eV})$	1.38	1.46	2.26	2.66	2.53	1.70[8]	2.6 - 3.0 [8]

determined using the $G_0W_0 + BSE$ calculations. The resolved optical spectra correspond to electric vector polarizations along the x, y and parallel to z directions, respectively. The imaginary part of the dielectric matrix, the optical absorption spectrum and corresponding Tauc plots in the x, y, z directions, are show in Figure 5 and 6. The optical band gap are estimated from Tauc plots with the onset of yy is at 2.05 eV, xx at 2.38 eV and zz at 2.58 eV, which agrees well with the experimental range of 2.6-3.0 eV.

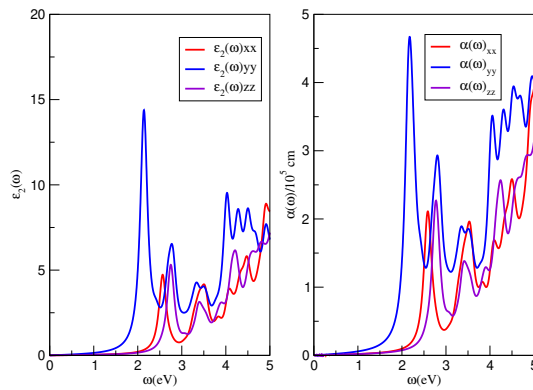


Figure 5. The calculated optical functions from left, the imaginary part of the dielectric function, the optical absorption spectra at G_0W_0+BSE level

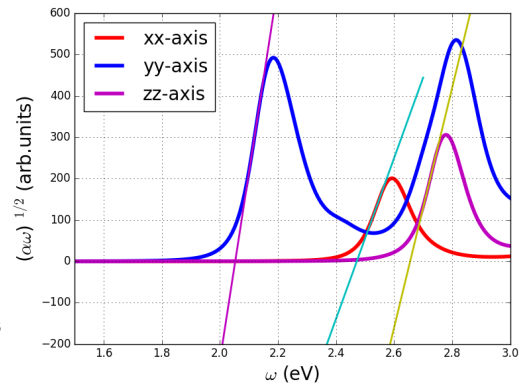


Figure 6. The Tauc plot of optical absorption spectra versus photon energy at G_0W_0+BSE level

3.5. Conclusion

Using first principle calculations, we investigate the structural, elastic, electronic and optical properties of the barium seleno-germanate Ba_2GeSe_4 compound. The calculated lattice parameters are in reasonable agreement with available experimental data. The electronic band structure calculations from MBJ which provide accurate band structure for most large band gap semiconductors shows an 2.26 eV direct band gap at $\Gamma - \Gamma$ points other energy gap calculation from HSE and G_0W_0 are within the predicted value. The significant hybridization of Ba(d), Ge(s) and Se(p) was observed from the PDOS analysis of conduction band indicating covalent character in addition to ionic character. The calculated optical properties shows anisotropy. The optical gap are in energetic order of $yy < xx < zz$, the onset of yy is at 2.05 eV, xx at 2.38 eV and zz at 2.58 eV, which agreed well with predicted value of 2.6-3.0 eV [8]. Our result shows that Ba_2GeSe_4 potential as wide band gap material [32] with potential applications in multi-junction solar cells. [33].

3.6. Acknowledgments

The support of Tertiary education trust fund (TET-fund), Nigeria toward this research is here by acknowledged. We highly acknowledged the centre for high performing computing, South-Africa for providing us with computing facilities.

References

- [1] Wachhold M and Kanatzidis M G 1999 *Inorg. Chem.* **38** 4178–4180
- [2] Sheldrick W S and Wachhold M 1998 *Coord. Chem. Rev.* **176** 211–322
- [3] Mei D, Yin W, Feng K, Lin Z, Bai L, Yao J and Wu Y 2011 *Inorg. Chem.* **51** 1035–1040
- [4] Wu K, Su X, Yang Z and Pan S 2015 *Dalton Trans.* **44** 19856–19864
- [5] Scragg J J et al 2013 *Chem. Mater.* **25** 3162–3171
- [6] Regulacio M D and Han M Y 2016 *Acc. Chem. Res.* **49** 511–519
- [7] Zhou M, Xiao K, Jiang J, Huang H, Lin Z, Yao J and Wu Y 2016 *Inorg. Chem.* **55** 12783–12790
- [8] Assoud A, Soheilnia N and Kleinke H 2004 *Zeitschrift für Naturforschung B* **59** 975–979
- [9] Yakovkin I and Dowben P A 2007 *Surf. Rev. Lett.* **14** 481–487
- [10] Perdew J P, Burke K and Ernzerhof M 1996 *Phys. Rev. Lett.* **77** 3865
- [11] Perdew J P et al 2008 *Phys. Rev. Lett.* **100** 136406
- [12] Tran F and Blaha P 2009 *Phys. Rev. Lett.* **102** 226401
- [13] Heyd J, Scuseria G E and Ernzerhof M 2003 *J. Chem. Phys.* **118** 8207–8215.
- [14] Kresse G and Hafner J 1993 *Phys. Rev. B* **47** 558
- [15] Kresse G and Furthmüller J 1996 *Comput. Mater. Sci.* **6** 15–50
- [16] Kresse G and Joubert D 1999 *Phys. Rev. B* **59** 1758
- [17] Hedin L 1965 *Phys. Rev.* **139** A796
- [18] Hybertsen M S and Louie S G 1986 *Phys. Rev. B* **34** 5390
- [19] Onida G, Reining L and Rubio A 2002 *Rev. Mod. Phys.* **74** 601
- [20] Hanke W and Sham L J 1980 *Phys. Rev. B* **21** 4656
- [21] Salpeter E E and Bethe H A 1951 *Phys. Rev.* **84** 1232
- [22] Tauc J, Grigorovici R and Vancu A 1966 *phys. Stat. Sol. b* **30** 244–247
- [23] Murnaghan F D 1944 *Proc. Natl. Acad. Sci.* **30** 244–247
- [24] Wu Z, Zhao E, Xiang H, Hao X, Liu X and Meng J 2007 *Phys. Rev. B* **76** 054115
- [25] Reuss A 1929 *J. Appl. Math. Mech.* **9** 49–58
- [26] Hill R 1952 *Proc. Phys. Soc. Sec. A* **65** 349
- [27] Pugh S F 1954 *Phil. Mag.* **45** 823–843
- [28] Hirsekorn S 1990 *Text. Stress, Micro.* **12** 1–14
- [29] Boucetta S 2014 *J. Mag. Allo.* **2** 59–63
- [30] Ranganathan S I and Ostojia-Starzewski M 2008 *Phys. Rev. Lett.* **101** 055504
- [31] Saha S, Sinha T P and Mookerjee A 2000 *Phys. Rev. B* **62** 8828
- [32] Yoshikawa A, Matsunami H and Nanishi Y 2007 *Wide Bandgap Semiconductors* (Berlin: Springer)
- [33] Green M A 2003 *Third generation concepts for photovoltaics* (IEEE: 3rd World Conference on Photovoltaic Energy Conversion, Proceedings of)

Growth and structural characterization of germanium on Pt(111)

C Dansou, G B Geetha, E Carleschi, B P Doyle

Department of Physics, University of Johannesburg, PO Box 524, 2006 Auckland Park, Johannesburg, South Africa

E-mail: carmel@aims.edu.gh, bpdoyle@uj.ac.za

Abstract. We explore the possible growth of germanene on Pt(111) with low energy electron diffraction and X-ray photoemission spectroscopy. Our results suggest that the growth structure of Ge on Pt(111) is substrate- and annealing-temperature dependent. Below one monolayer (0.42 ML) we found that Ge forms a $(\sqrt{7} \times \sqrt{7})$ structure on Pt(111) held at 400°C. Upon annealing to 750°C, Ge diffuses into Pt bulk with a change to $(\sqrt{19} \times \sqrt{19})$ structure with respect to Pt(111). From our analysis, these structures likely fit with a 2D surface alloy made of Ge₃Pt tetramers with a subsurface Ge atom.

1. Introduction

Recently germanene, the germanium monolayer counterpart of graphene, has attracted much attention because of its properties for technological application as well as for fundamental use [1, 2]. Germanene has a very high carrier mobility and has been predicted to be a room temperature 2D quantum Hall insulator, hence potentially usable in spintronics and topological quantum computing [3, 4]. Also, its compatibility with existent silicon-based electronics makes it a promising candidate to be easily incorporated into today's electronics industry [5]. Unlike graphene, freestanding germanene does not exist: it must be grown on a substrate. So far, several substrates from metal to insulator have been used to synthesize germanene [6-11]. As Pt is a fairly unreactive substrate, we expect the Dirac cones in the electronic structure of germanene to be preserved. This has been predicted by a density functional theory study [12]. On Pt(111), germanene has been claimed to form a $(\sqrt{19} \times \sqrt{19})$ superstructure by Li et al. [10]. However, Svec et al. suggested that this structure is a 2D surface alloy [13]. They studied the Si/Pt system with a variety of experimental techniques complemented by theoretical calculations and claimed that their findings could be extended to Ge/Pt. In their model, Ge is embedded in the Pt surface [13]. The real structure of Ge on Pt(111) is therefore still controversial.

2. Experimental details

The Pt(111) surface was cleaned by several cycles of argon ion sputtering (E=1 keV, I=6 mA, 1.4×10^{-5} mbar) and annealing at 750°C until a sharp surface exhibiting the hexagonal symmetry of the Pt(111) surface is seen by low energy electron diffraction (LEED). X-ray photoemission spectroscopy (XPS) showed no sign of carbon or oxygen contamination. Ge was deposited onto the clean Pt(111) surface held at 400°C by resistively heating an ingot of pure Ge contained in a boron nitride crucible within a low temperature effusion cell. We degassed properly the

evaporator, LEED and ion gun before every set of experiments. The base pressure of both the preparation and analysis chambers was less than 2×10^{-10} mbar. The pressure in the preparation chamber was less than 3×10^{-9} mbar during evaporation. LEED was used to characterize the symmetry of the superstructure and XPS to study the dynamics of the interaction between Ge and Pt atoms. It thus also gives information on the nature of the formed superstructure.

3. Results and discussion

3.1. LEED results and analysis

The LEED pattern of the clean Pt(111) is shown in figure 1(a). This is the well-known (1×1) structure of the Pt(111) surface. After Ge deposition, the LEED shows extra spots in addition to those from Pt. It is displayed in figure 1(c). We have made schematic diagrams of the patterns for better understanding. In figure 1(d) it can be seen that the pattern is composed of two symmetrically equivalent domains with the lattice vectors rotated with respect to those of Pt(111). This structure is the same as the one reported by Meng et al. for buckled silicene on Ir(111) [14]. Thus we identified it as a $(\sqrt{7} \times \sqrt{7})$ structure with respect to Pt(111). For brevity it will be called $\sqrt{7}$ throughout this paper.

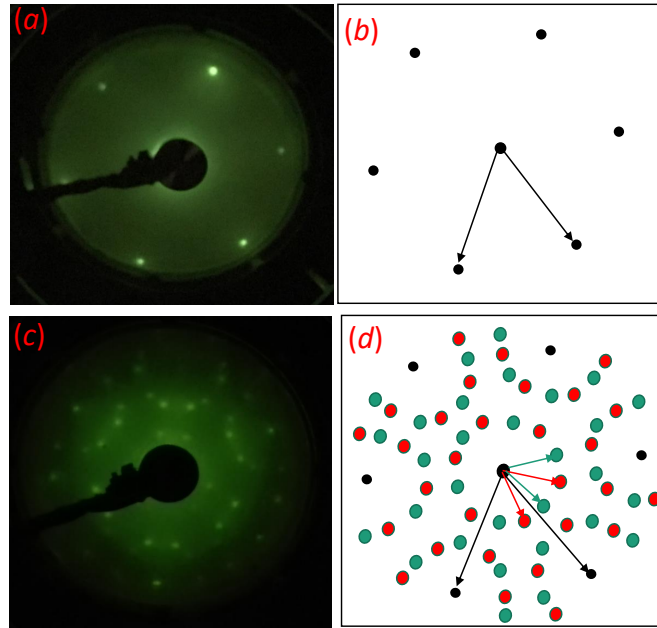


Figure 1. (a) LEED image taken at 73 eV of clean Pt(111). (b) Schematic diagram of the pattern shown in (a). The black arrows are the unit vectors of Pt. (c) LEED image taken at 65 eV of Ge/Pt(111). (d) Schematic diagram of the LEED pattern of Ge/Pt(111). The red and green arrows are the unit vectors of the two domains formed by Ge.

Upon annealing to 750°C, the structure changed to a new structure displayed in figure 2a. It was composed of two symmetrically equivalent domains with rotated lattice vectors with respect to Pt(111). This is the previously reported $(\sqrt{19} \times \sqrt{19})$ reconstruction formed by Ge on Pt(111) by Li et al., that they ascribed to germanene [10]. We call this structure $\sqrt{19}$ for brevity.

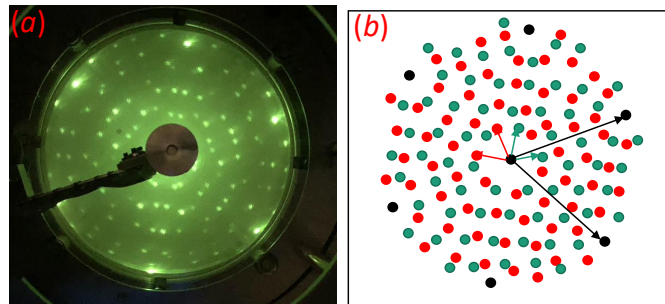


Figure 2. (a) LEED image taken at 65 eV of Ge/Pt(111) annealed at 750°C. (b) Schematic diagram of the Ge/Pt(111) LEED pattern.

3.2. XPS analysis

Detailed XPS measurements were carried out before and after Ge deposition and annealing on Pt(111). Figure 3 shows the spectra of Pt 4f and Ge 3d. It can be seen from figure 3a that

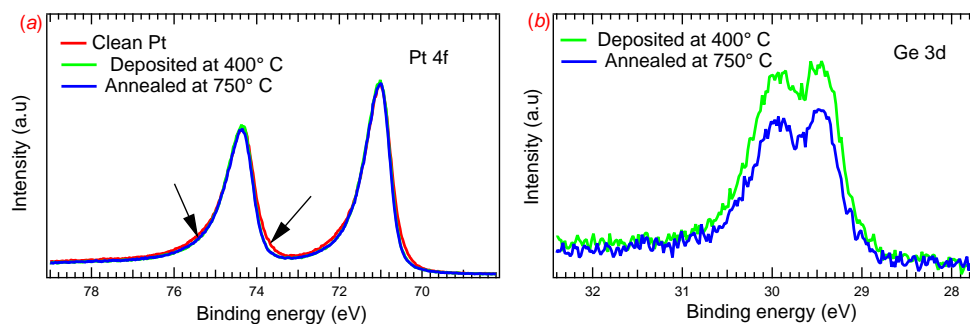


Figure 3. (a) Pt 4f XPS spectra for the clean Pt (red), Ge deposited at 400°C (green) and after annealing at 750°C (blue). The arrows show the reduction in the line-width after annealing. (b) Ge 3d spectra after deposition at 400°C (green) and after annealing at 750°C (blue).

the positions of the Pt 4f core level peaks remained constant upon Ge deposition, even after annealing to 750°C. However, the width of the peaks decreased after Ge deposition. Generally a decrease in line-width means either a more ordered surface (less chemical environments for the Pt atoms) or an increase in the lifetime of the core-hole produced during the photoemission process. The Pt(111) surface is already very well ordered and it is unlikely that Ge deposition would somehow increase this order. This suggests an increase of the core-hole lifetime. This would most likely result from a reduction in the metallic behaviour of Pt. The absence of a core level shift means that Ge atoms do not affect the state of Pt atoms at the surface. There are two possible explanations for this. The first is that we were in the presence of a GePt surface alloy where the Ge-Pt interaction strength is the same as that of Pt-Pt. This is possible because of the relatively close electronegativity of Pt and Ge (2.28 for Pt and 2.01 for Ge) [15, 16]. Ge-Pt can therefore form a nonpolar covalent bond with electrons localized between the two atomic nuclei. The second explanation is that we had a 2D layer of Ge atoms (germanene) interacting weakly with the Pt surface. In this case, the structure is probably buckled as reported by Li et al [10].

The intensity from the Pt 4f core levels was used to evaluate the thickness of the deposited Ge using the formula $A = A_0 e^{-t/\lambda}$ where A_0 and A are respectively the areas of the clean Pt 4f curve and after Ge deposition, t the Ge thickness and λ the inelastic mean free path of Pt 4f electrons in Ge. This resulted in 0.42 ML just after the deposition, upon annealing it reduced to 0.30 ML. Ge has therefore diffused into the Pt bulk or desorbed into the vacuum of the preparation chamber. Over several experiments we noticed that annealing Pt that has been cleaned by sputtering would result in the appearance of Ge on the surface. Hence Ge atoms diffused into the Pt bulk during the original annealing after Ge deposition. In addition, 750°C is well below the sublimation temperature of Ge in a vacuum. The conversion of the $\sqrt{7}$ structure into the $\sqrt{19}$ structure is therefore driven by a diffusion process.

To gain more insight the Ge 3d core level spectra have been fitted. For both structures, the Ge 3d spectra could be fitted with the same two components (figure 4). This indicated that Ge

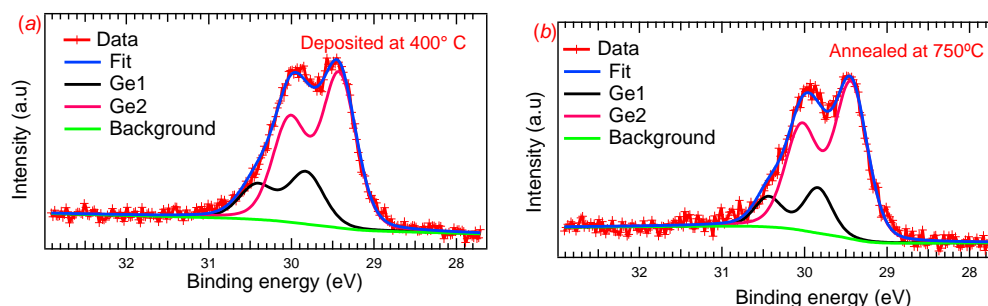


Figure 4. Fits of Ge 3d spectra (a) deposited at 400°C and (b) after annealing at 750°C. The background shown in both panel is a Shirley-type background.

was in the same two different chemical environments. The two components appeared at 29.8 eV (Ge1) and 29.4 eV (Ge2). Their widths were 0.5 eV (Ge1) and 0.48 eV (Ge2). Upon annealing to 750°C, these components did not shift in energy. In contrast their widths decreased upon annealing to 0.47 eV (Ge1) and 0.40 eV (Ge2).

The ratio of the areas of the two components in the Ge 3d spectra was 1:3 for the $\sqrt{7}$ and 1:4 for the $\sqrt{19}$ structure. This rules out unbuckled germanene as in it all the Ge atoms occupy identical sites. Buckled germanene has been reported to either have a 1:1 ratio between the two sites [5], or a 1:5 ratio [10]. In order to better understand the origin of the two sites we looked at the Ge 2p_{3/2} core level for the Ge deposited at 400°C, shown in figure 5. The Ge 2p core levels are at a much higher binding energy than the Ge 3d, which means that the 2p photoelectron emitted from the Ge has a much lower kinetic energy. This in turn means that it is substantially more surface sensitive than the 3d levels. Figure 5 clearly shows that the component at higher binding energy was significantly smaller in the surface sensitive regime. In other words, it originated from the bulk, and the component at lower binding energy originated from the surface. The existence of a bulk component is not surprising, given our experience of the diffusion of Ge in Pt. All our evidence pointed towards a Ge-Pt surface alloy. If we look more carefully at the model proposed by Švec et al., we see that the $\sqrt{7}$ structure has more Ge atoms per unit surface area than the $\sqrt{19}$. This agrees with the decrease in surface coverage that we saw with annealing. It suggests that diffusion into the bulk and the resultant lower surface coverage have favoured the formation of the $\sqrt{19}$ structure. The bulk component indicates the existence of a subsurface Ge atom underneath the first layer, possibly below each tetramer. We note that Švec et al. did not see a bulk component in their XPS measurements. This could well be explained by the photon energy that they used, 150 eV, which resulted in an exceptionally

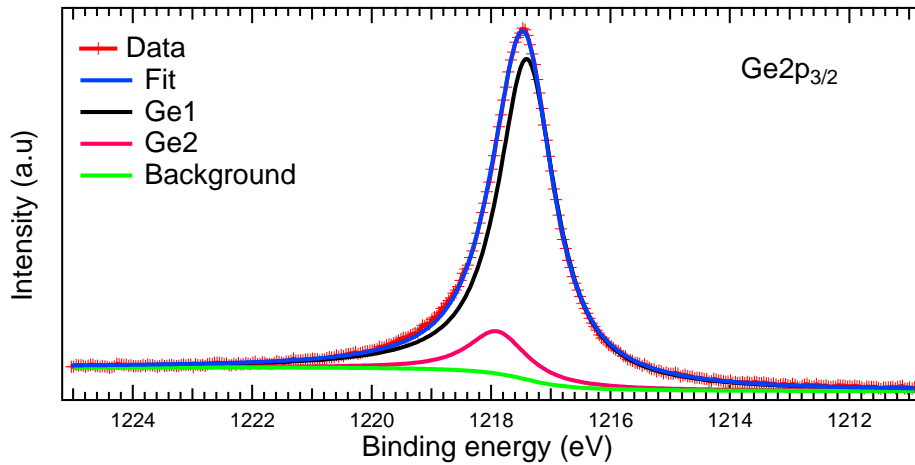


Figure 5. Ge 2p_{3/2} spectrum for Ge deposited at 400°C.

surface sensitive measurement.

4. Conclusion

We report that Ge can form a $\sqrt{7}$ or $\sqrt{19}$ structure on Pt(111) depending on the substrate- and annealing-temperatures. This is the first time that Ge with a $\sqrt{7}$ structure has been found experimentally on Pt(111). In both structures the Ge atoms are found to interact weakly with the Pt atoms. From our LEED and XPS analysis, these structures match the Ge₃Pt tetramer model put forth by Švec et al. In addition we found evidence for a subsurface Ge atom. Both the $\sqrt{19}$ structure and the subsurface Ge resulted from the diffusion of Ge into the Pt crystal.

References

- [1] Cahangirov S, Topsakal M, Aktürk E, Sahin H and Ciraci S 2009 *Phys. Rev. Lett.* **102** 236804
- [2] Dávila M, Xian L, Cahangirov S, Rubio A and LeLay G 2014 *New J. Phys.* **16** 095002
- [3] Ye X S, Shao Z G, Zhao H, Yang L and Wang C L 2014 *R.S.C. Adv.* **4** 21216
- [4] Liu C, Feng W and Yao Y 2011 *Phys. Rev. Lett.* **107** 76802
- [5] Acun A et al. 2015 *J. Phys. Condens. Matter.* **27** 443002
- [6] Derivaz M, Dentel D, Stephan R, Hanf M C, Mehdaoui A, Sonnet P and Pirri C 2015 *Nano. Lett.* **15** 2510
- [7] Golias E, Xenogiannopoulou E, Tsoutsou D, Tsipas P, Giamini S and Dimoulas A 2013 *Phys. Rev. B* **88** 075403
- [8] Bampoulis P, Zhang L, Safaei A, Van Gastel R, Poelsema B and Zandvliet H 2014 *J. Phys. Condens. Matter.* **26** 442001
- [9] Qin Z, Pan J, Lu S, Shao Y, Wang Y, Du S, Gao H and Cao G 2017 *Adv. Mat.* **29** 1606064
- [10] Li L, Lu S, Pan J, Qin Z, Wang Y, Cao G, Du S and Gao H 2014 *Adv. Mat.* **26** 4820
- [11] Zhang L, Bampoulis P, Van Houselt A and Zandvliet H 2015 *Appl. Phys. Lett.* **107** 111605
- [12] Wang Y, Li J, Xiong J, Pan Y, Ye M, Guo Y, Zhang H, Quhe R and Lu J 2016 *Phys. Chem. Chem. Phys.* **18** 19451
- [13] Švec M et al. 2014 *Phys. Rev. B* **89** 201412
- [14] Meng L, Wang Y -L, Zhang L -Z, Du S -X and Gao H -J 2015 *Chin. Phys. B* **24** 086803
- [15] Allen L C 1989 *J. Am. Chem. Soc.* **111** 9003
- [16] Mann J B, Meek T L, Knight E T, Capitani J F and Allen L C 2000 *J. Am. Chem. Soc.* **122** 5132

A numerical study of heterogeneous annealing in a finite one-dimensional geometry

Jeremiah Lethoba¹, Pavel M Bokov² and Pavel A Selyshchev¹

¹Department of Physics, University of Pretoria Private bag X20 Hatfield 0028 South Africa

² The South African Nuclear Energy Corporation (Necsa), Building 1900, P.O. Box 582, Pretoria 0001, South Africa

E-mail: lethoba77@gmail.com, pavel.bokov@necsa.co.za, selyshchev@gmail.com

Abstract. In this paper, a numerical investigation of initiation of thermal annealing of radiation-induced defects in a sample with finite dimensions is performed. The annealing is initiated by means of a thermal pulse that heats the sample to a specific temperature and set depth from its surface. The dependence of the annealing time on the initial defect density and on the parameters of the thermal pulse is studied.

1. Introduction

The irradiation of a material with high-energy particles causes the formation of different types of defects in its crystalline lattice. At any temperature above absolute zero, the defects anneal spontaneously and the rate of annealing increases with temperature. Therefore, in order to anneal crystal defects, the sample must be heated. Usually, the temperature is increased on the surface of the sample and is kept constant for some time [1]. For small samples, transient processes (heating) can be neglected and the temperature distribution can be assumed to be uniform over the sample. For large samples, on the contrary, transient processes can not be neglected and achieving a homogeneous temperature distribution can require considerable time and energy. However, in order to anneal defects throughout the volume of the sample, it is not always necessary to heat the entire sample. It is known that under certain circumstances it is possible to develop a self-propagating annealing similar to an autowave [2, 3]. Its initiation requires significantly less energy, and the annealing occurs in a much shorter time. In this case, the annealing actually takes place near the wave front, in the so-called *annealing zone* (Fig. 1). The annealing zone separates regions of the sample with and without defects and moves into the latter at a constant velocity. In the coordinate system that moves with this velocity, the temperature and defect distributions remain constant over the sample (Fig. 2). The density of defects in the annealing zone falls from its initial value ahead of the wave front to practically zero value behind the wave front. The width of the annealing region and the speed of its propagation depend on the characteristics of the sample and on the defect density.

However, in pure form, an autowave of annealing is realized only in an infinite sample, which is at absolute zero temperature, when spontaneous thermal annealing is completely “frozen”. Besides, it is assumed that the autowave is initiated infinitely far from the place of observation.

When a sample of finite size is annealed, the autowave regime can be realized as a part of inhomogeneously developing annealing, since transient processes, related to the initiation of an

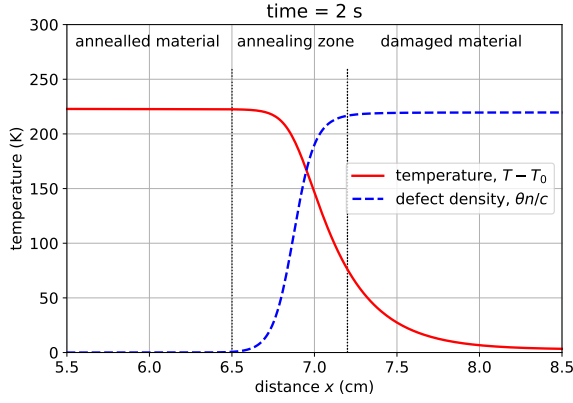


Figure 1. Schematic of the annealing wave front, propagating from the annealed material to the damaged material. Annealing predominantly takes place in the area indicated as “annealing zone”.

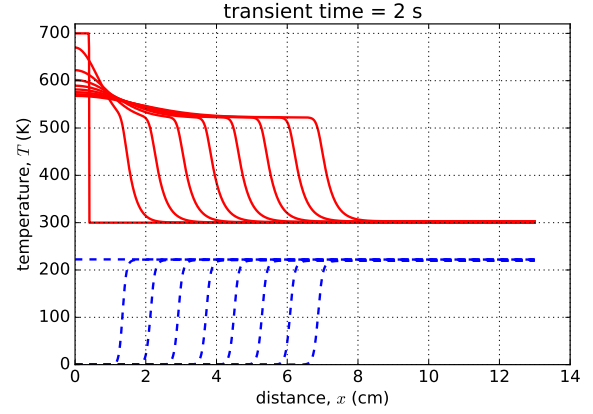


Figure 2. Annealing propagation fronts at 0.2 s time intervals for temperature (top) and defect density (bottom) in a sample of length $L = 13$ cm. Parameters of initial heating are $\Delta T = 400$ K and $\Delta x = 4$ mm.

autowave, or the influence of boundaries (sample surfaces), are always present in this case. It is therefore important to compare the sizes of the sample with the characteristic sizes of the annealing regions, of the wave initiation, and of the influence of the boundary regions. This comparison is especially indispensable at sample temperatures other than absolute zero, when the annealing wave is damped as a result of spontaneous annealing, which occurs throughout the sample volume: the defect density decreases, the influence of the thermo-concentration feedback weakens (reduces), and the criterion for the development of the autowave regime ceases to be satisfied. Thus, minimizing the annealing time of defects of a finite sample with given sizes at a nonzero initial temperature becomes nontrivial and requires the use of numerical methods.

2. Formulation of the problem and basic equations

Consider a sample having the form of a slab of thickness L , which is located in the region $0 < x < L$ and assumed to be infinite in lateral directions (one-dimensional problem). The initial distribution of defects over the volume of the sample is homogeneous and has a density n_0 . The initial temperature of the sample is T_0 everywhere except for a subsurface layer at $x = 0$ with a depth $\Delta x < L$, where the temperature is higher by an amount of ΔT .

Following [4], we take into account that when annealing each defect, an energy, which is approximately equal to the energies of formation of this defect, is released. The released energy is converted into heat and causes an increase in the temperature of the sample. Due to the increase in temperature, the annealing rate also increases. This forms a nonlinear feedback between the temperature and the density of the defects. Due to this feedback and the thermal conductivity of the sample, a self-propagating self-sustaining annealing mode can develop [2].

With this connection in mind, equations for the evolution of the defect density and temperature distributions take the following form

$$\begin{aligned} \frac{\partial n}{\partial t} &= -\frac{n}{\tau}, \\ c \frac{\partial T}{\partial t} &= \kappa \frac{\partial^2 T}{\partial x^2} + \theta \frac{n}{\tau}. \end{aligned} \quad (1)$$

Here c is the volumetric heat capacity and κ is the thermal conductivity of the material; θ is

the energy released as a result of annealing of one defect. The characteristic lifetime of defects, τ , depends, as a rule, on the temperature according to the Arrhenius law:

$$\tau^{-1} = \tau_0^{-1} \exp(-E_a/k_B T), \quad (2)$$

where E_a is the activation energy of annealing, k_B is the Boltzmann constant and τ_0 is a constant depending on material properties. Equations (1) are similar to the governing equations for combustion waves in a premixed solid fuel in a one-dimensional configuration [5].

The problem (1)–(2) is solved subject to the zero-flux boundary conditions:

$$\left. \frac{\partial n}{\partial x} \right|_{x=0} = \left. \frac{\partial n}{\partial x} \right|_{x=L} = 0, \quad \left. \frac{\partial T}{\partial x} \right|_{x=0} = \left. \frac{\partial T}{\partial x} \right|_{x=L} = 0, \quad (3)$$

and initial distributions of defect density and temperature (initial conditions):

$$\begin{aligned} n(t=0, x) &= n_0, & 0 < x < L; \\ T(t=0, x) &= \begin{cases} T_0 + \Delta T, & 0 < x < \Delta x; \\ T_0, & \Delta x < x < L. \end{cases} \end{aligned} \quad (4)$$

The problem (1)–(4) was solved numerically with a Python program, developed and implemented as a part of the research project. In the algorithm employed by the program, a finite difference discretization was performed in space thus yielding a system of coupled nonlinear ordinary differential equations [6], which then were numerically integrated with the `odeint` submodule of the Python's `Scipy` package [7]. The implemented solution method was verified by comparing results obtained by varying the spatial mesh size and by using different temporal integration algorithms. Additionally, for the homogeneous problem (see discussion in the next section) the results of numerical calculations were verified against analytical solutions.

For the sake of comparison with results presented in [3, 8], values of the model parameters, corresponding to aluminium, were used in our calculations, i.e. $E_a = 0.55$ eV, $\theta = 5.4$ eV, $\tau_0 = 10^{-7}$ s, $c = 2.57 \times 10^6$ J/K m³ and $\kappa = 2.2 \times 10^2$ W/m K.

3. Results and discussion

In this work we define the *annealing time*, t^a , as the time at which the total number of defects in the sample becomes less than 1% of its initial value. We investigate the dependence of the annealing time for different annealing initiation temperatures (ΔT) and at various heating depths (Δx), including (for comparison) case $\Delta T = 0$, in which annealing occurs spontaneously. In this case, due to the symmetry of the problem, the annealing occurs *homogeneously* and the annealing time does not depend on the sample dimensions.

In the case of homogeneous spontaneous annealing, as shown in [8], the defect density decreases and the temperature increases as:

$$\frac{t}{\tau_0} = \text{Ei}\left(\frac{T_a}{T}\right) - \text{Ei}\left(\frac{T_a}{T_0}\right) + \exp\left(\frac{T_a}{T_{\text{tot}}}\right) \left[\text{Ei}\left(\frac{T_a}{T_0} - \frac{T_a}{T_{\text{tot}}}\right) - \text{Ei}\left(\frac{T_a}{T} - \frac{T_a}{T_{\text{tot}}}\right) \right], \quad (5)$$

where $T_a = E_a/k_B$ is the activation energy in kelvin, $T_{\text{tot}} = T_0 + \Theta$ (here $\Theta = \theta n/c$ is a temperature increase due to annealing of defects and $\Theta_0 = \theta n_0/c$) and $\text{Ei}(\cdot)$ is the exponential integral function, definition of which can be found, e.g., in [9]. Formula (5) provides an implicit dependence of temperature on time. A similar dependence for the defect density can be obtained by taking energy conservation into account. Indeed, in the process of homogeneous annealing in a thermally isolated system the energy stored in defects is converted to heat, hence $T = T_{\text{tot}} - \Theta$, and (5) can be rewritten as an implicit dependence of defect density on time:

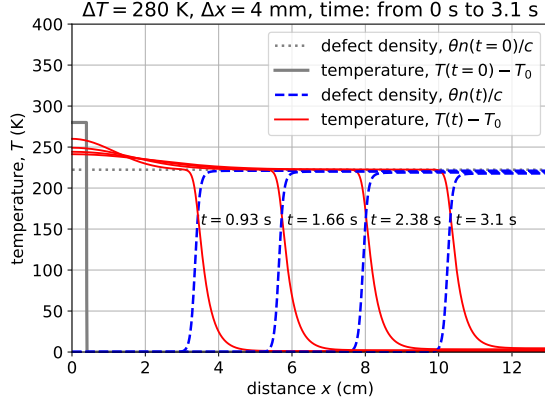


Figure 3. Schematic of annealing wave fronts propagating from the annealed material to the damaged material in the autowave regime.

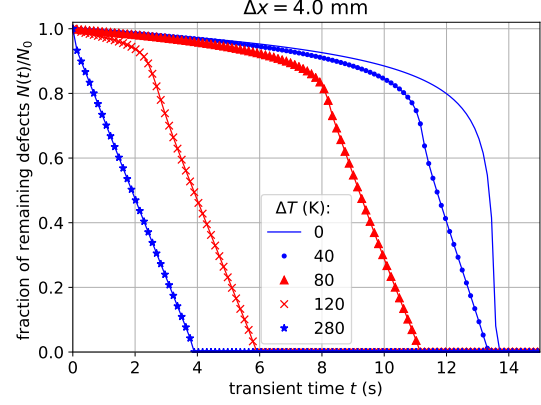


Figure 4. The time evolution of the fraction of remaining defects for different initiating energies.

$$\frac{t}{\tau_0} = \text{Ei} \left(\frac{T_a}{T_{\text{tot}} - \Theta} \right) - \text{Ei} \left(\frac{T_a}{T_0} \right) + \exp \left(\frac{T_a}{T_{\text{tot}}} \right) \left[\text{Ei} \left(\frac{T_a}{T_0} - \frac{T_a}{T_{\text{tot}}} \right) - \text{Ei} \left(\frac{T_a}{T_{\text{tot}} - \Theta} - \frac{T_a}{T_{\text{tot}}} \right) \right]. \quad (6)$$

The annealing time, t^a , can be determined analytically by substituting $\Theta = \Theta_0 \times 1\%$ into formula (6). It follows from (6) that the annealing time decreases with increasing initial temperature and initial defect density. It also decreases with increasing energy released in the process of annealing of one defect, θ . For homogeneous initial distributions of temperature and defect density $T_0 = 300$ K and $n_0 = 6.63 \times 10^{26} \text{ m}^{-3}$, respectively, and for the energy released per one annealed defect $\theta = 5.4$ eV, the annealing time is $t^a = 13.63$ s. This value of the annealing time coincides with the value that was determined numerically in this study using the finite difference method. Since the autowave moves at a constant speed, the annealing rate of the total number of defects per unit area, defined as $R = -dN/dt$, is a constant. This allows us to diagnose the establishment of the autowave regime and determine the propagation velocity of the annealing front using the rate of change of the fraction of the total number of defects, $F = N/N_0$, in time

$$v = -\frac{d}{dt} \int_0^L \frac{n(t, x)}{n_0} dx \approx -L \frac{\Delta F}{\Delta t}. \quad (7)$$

In Fig. 3 we show the evolution of the annealing front in a sample of length $L = 13$ cm with the initial defect density is $n_0 = 6.63 \times 10^{26} \text{ m}^{-3}$. One may observe that, in the autowave regime, defects in the sample anneal at a constant rate. The corresponding time evolution of the fraction of defects remaining in the sample is shown in Fig. 4 for different initiating energies. By using (7) we determined that the speed the annealing front is of $v = 3.18$ cm/s.

The annealing front speed in the autowave regime can also be determined by observing the time required for the front to move through the sample. If we neglect the development time of the autowave regime and the influence of boundaries, then the annealing time in this regime is approximately $t^a = (L - \Delta x)/v$, where v is the annealing propagation speed. Our calculations show that for a localized initial heat distribution at the left boundary of $\Delta T = 280$ K for $\Delta x = 4$ mm, initial defect density $n_0 = 6.63 \times 10^{26} \text{ m}^{-3}$ and $L = 13$ cm, the annealing time is $t^a = 3.85$ s and the annealing propagation speed is $v = 3.27$ cm/s. The results of annealing time calculations for this set of parameters are presented in Figs. 5 and 6.

Alternatively, the annealing propagation speed in the autowave regime can be obtained from

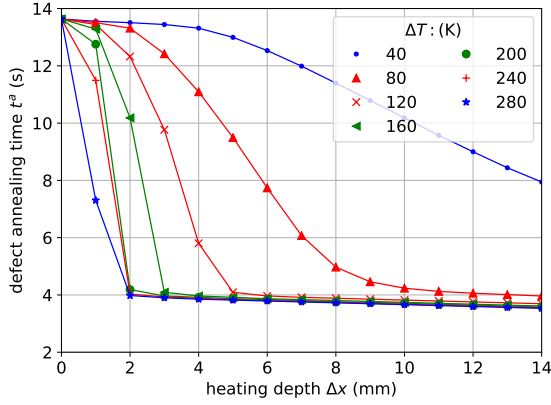


Figure 5. The defect annealing times for different initiating energies.

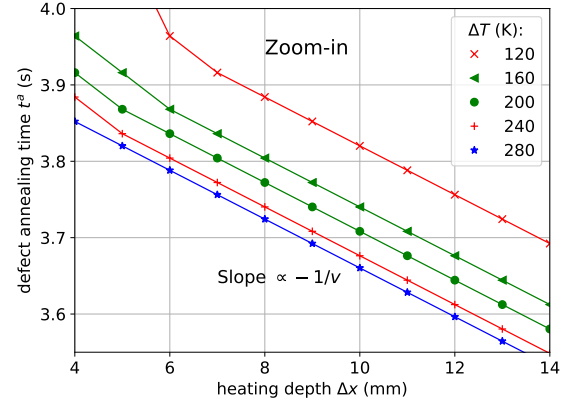


Figure 6. Zoom-in at Δx from 4 mm to 14 mm of Figure 5.

the dependence of the annealing time, t^a , on the heating depth, Δx . Thus, for two different heating depths, Δx_1 and Δx_2 and a fixed ΔT , the propagation speed can be estimated from two corresponding annealing times with the formula, $v = -(\Delta x_2 - \Delta x_1)/(t_2^a - t_1^a)$, where t_2^a and t_1^a are annealing times corresponding to Δx_2 and Δx_1 , respectively. For $\Delta x_1 = 4$ mm and $\Delta x_2 = 14$ mm the annealing times are $t_1^a = 3.85$ s and $t_2^a = 3.28$ s, respectively, for an initiation temperature of $\Delta T = 280$ K. For this configuration, we calculated $v = 3.12$ cm/s.

Therefore, by taking all three estimated values of the annealing propagation speed (v) into account, we find an average value of 3.19 ± 0.08 cm/s (i.e. the spread of speed values in terms of relative standard deviation is within 2.4%).

When annealing is initiated by heating the left boundary of the sample, the annealing occurs in-homogeneously: heat flows from the left boundary to the right and the annealing follows the heat flow. At higher initiation temperatures the defects are annealed faster and for some combinations of parameters the self-propagating annealing wave develops (Figs. 5 and 6).

With the increase in the initiation energy (defined, per unit of surface, as $Q = c\Delta x\Delta T$), the duration and length of the transition regime decreases and tends to zero, an autowave regime appears and displaces the transient mode (Fig. 5). The autowave regime is realized at an earlier time and covers a larger and larger part of the sample. As the autowave regime develops, the annealing time decreases (first quickly and then slowly) and tends to its limit, which corresponds to the time which the autowave initiated at infinity passes the interval $L - \Delta x$ (Figs. 5 and 6).

Furthermore, according to Fig. 5, the influence of the increase in the initiation temperature ΔT is more prominent than the increase in the heating depth Δx . Indeed, at constant initiation energy Q_0 , it is the rise in the initiation temperature and the reduction in the heating depth (rather than the converse) that leads to a decrease in the annealing time. This is due to the fact that the rate of annealing and the accompanying heat release are functions (exponential) of the temperature.

The initiation temperature affects the most strongly the modes in which the autowave formation occurs at the length of the sample. When annealing is realized in a mode close to a hybrid of homogeneous and autowave modes, the autowave regime does not have time to develop or it develops very rapidly. So an increase of Δt at constant energy of initiation does not lead to a decrease in neither the annealing time nor its speed. Conversely, in the autowave regime, there is a slight increase in the annealing time with growth of ΔT .

An increase in the initial defect density leads to a decrease in the annealing time (Fig. 7). This dependence arises from a nonlinear feedback between the temperature and the annealing rate

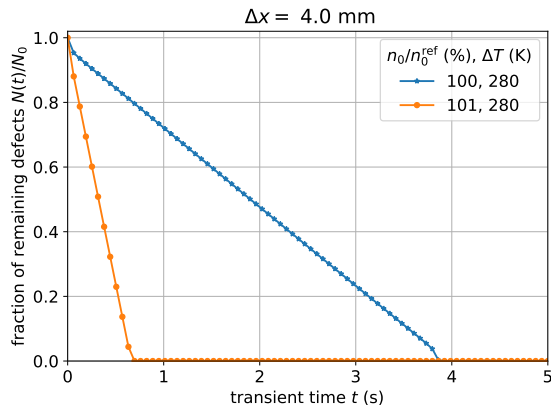


Figure 7. The evolution of the fraction of remaining defects in time for different initial defect densities. Here $n_0^{\text{ref}} = 6.63 \times 10^{26} \text{ m}^{-3}$.

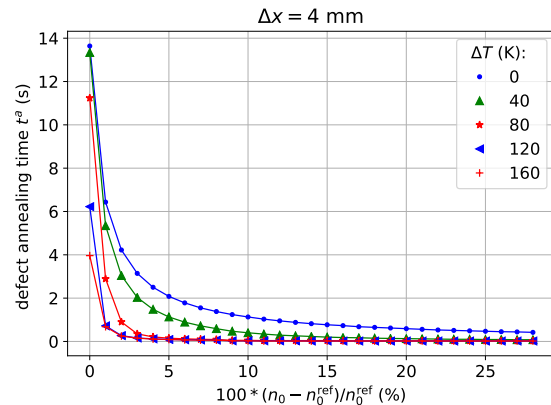


Figure 8. The defect annealing times for different initial defect densities. The reference value is $n_0^{\text{ref}} = 6.63 \times 10^{26} \text{ m}^{-3}$.

of the defects: one can demonstrate that for uniform *isothermal* annealing, this time does not depend on the initial density of the defects. With the dominance of self-propagating annealing, an increase in the initial defect density leads to an increase of the speed of its propagation, as is clearly seen in Fig. 7, as well as to a change in the annealing time. When the initial defect density was increased by one percent, we observed an increase in the annealing speed to $v = 19.08 \text{ cm/s}$. Initiation by a stronger heating pulse intensifies the annealing process and reduces the annealing time even further (Fig. 8).

4. Conclusion

Our calculations have shown that for a sample of a given size (13 cm) and for the parameters used, the annealing time decreases both with an increase in the initiation energy and with an increase in the initial defect density. We have found out that the speed of annealing propagation in the autowave regime is constant, and the time of homogeneous annealing does not depend on the size of the sample. Estimations of the speed of the autowave, performed in three different ways, show a good agreement (the relative standard deviation is within 2.4%).

References

- [1] Bondarenko G G 2016 *Radiation physics, structure and strength of solids* (Moscow: BKL Publishers) (in Russian)
- [2] Selyshchev P A 2014 *Proceedings of the XXIV International Conference Radiation Physics of Solids* ed Bondarenko G G (Moscow: GNU NII PMT) pp 589–594 (in Russian)
- [3] Bokov P M and Selyshchev P A 2016 *IOP Conference Series: Materials Science and Engineering* **110** 012055
- [4] Selyshchev P A 2008 *Self-organization in radiation physics* (Moscow, Izhevsk: R&C Dynamics) (in Russian)
- [5] Weber R O, Mercer G N, Sidhu H S and Gray B F 1997 *Proceedings of the Royal Society of London A: Mathematical, Physical and Engineering Sciences* **453** 1105–1118
- [6] Bokov P M 2017 Finite-difference method for modelling the self-sustained annealing of radiation defects Tech. Rep. RRT-FMR-REP-17001 Necsa
- [7] Jones E, Oliphant T, Peterson P *et al.* 2001– SciPy: Open source scientific tools for Python [Online; accessed 2018-06-09] URL <http://www.scipy.org/>
- [8] Selyshchev P A and Bokov P M 2018 *Nonlinear Systems, Vol. 2: Nonlinear Phenomena in Biology, Optics and Condensed Matter* ed Archilla J F R, Palmero F, Lemos M C, Sánchez-Rey B and Casado-Pascual J (Cham: Springer International Publishing) pp 283–314 ISBN 978-3-319-72218-4
- [9] Press W H, Teukolsky S A, Vetterling W T and Flannery B P 1992 *Numerical Recipes in C (2nd Ed.): The Art of Scientific Computing* (New York, NY, USA: Cambridge University Press) ISBN 0-521-43108-5

ZnO nanoparticles doped with cobalt and indium mechano-chemically for methane gas sensing application

M F Manamela¹, T E Mosuang^{1,*}, and B W Mwakikunga²

¹Department of Physics, University of Limpopo, Private Bag x1106, Sovenga, 0727, South Africa

²DST/CSIR National Centre for Nano-Structured Materials, P O Box 395, Pretoria 0001, South Africa

Email: manamela.mf@gmail.com, thuto.mosuang@ul.ac.za, bmwakikunga@csir.co.za

Abstract. Mechano-chemical technique was utilised to synthesise the undoped ZnO, 5% cobalt and indium single doped and Co-In double doped ZnO nanoparticles. The kenosistec station equipment was employed to probe the prepared samples for gas sensing application. Methane (CH₄) gas is being investigated in the present work. Current versus time curves show good response and recovery at 200 °C. Sensitivity against concentration curves reflect good sensitivity of (Co-In)-ZnO nanoparticles at 200 °C and good sensitivity of Co-ZnO nanoparticles at 350 °C. The Co-ZnO nanoparticles show great sensitivity to methane gas at the concentration of 40 ppm. In-ZnO nanoparticles have the fastest response and recovery times for the methane gas.

1. Introduction

Methane (CH₄) gas is a naturally occurring hydrocarbon, which forms whenever plant and animal matter decays. It is extremely flammable and dangerous because it is lighter than air, odorless, colorless, and tasteless, which makes it difficult to sense [1]. This gas has been reported to have a significantly higher global warming potentials than carbon dioxide [2, 3]. In so speaking, there is a great need for monitoring concentrations of CH₄ gas in the atmosphere. Hence, some techniques such as the infrared absorptions spectroscopy, optical interferometry, catalytic combustion, and semiconductor based modus are used to detect methane (CH₄) gas in the atmosphere [4, 5]. In this article semiconductor metal oxide based gas sensor applications are being discussed. This is because such gas sensors have been found to be cost effective and easy to develop as compared to the other form of sensors. CH₄ is also a useful gas for domestic purposes; it is used for cooking and heating. In industry, methane is used to refine petrochemicals and in power stations to drive turbines for generating electricity. Food processors and other companies that work with clay, stone and glass, make use of the energy released during extraction of CH₄ gas [6, 7]. This helps in maintaining healthy working and living environment, to avoid risk of accidental explosion and public safety in general [4]. It is in this regard that the development of pocket size, portable CH₄ and related gases detector is of crucial importance for human and environmental safety.

Various literature studies confirm that metal oxides have been identified as good candidates for gas sensors due to their ability to react with various elements [8]. To be precise, the development of these oxides at nanoscale level seem to be the ideal breaker for the optimum performance of gas sensors. Further on, one and two dimensional nanostructures pave the way in the design and development of high performing gas sensors [9]. In this article, ZnO doped nanoparticles are being discussed. Specifically, single against dual doped ZnO nanoparticles are being explored for the detection of CH₄ gas. ZnO

* To whom any correspondence should be addressed.

nanoparticles are n-type semiconducting, non-toxic, physically and chemically stable with rich defect chemistry [10 -12]. Schmidt-Mende et. al [10] further reported that the ZnO nanostructures have high surface area and their electronic processes are strongly influenced by surface morphology. The crystal defects of ZnO nanostructure surface such as oxygen vacancies [13], or shallow donors [14] play a major role as absorption sites for gas molecules. This feature assist in determining the gas sensing property of the nanostructures. Thus, ZnO nanostructures have a high sensitivity to a variety of chemical environments. To enhance their sensitivity and selectivity more, introduction of transition metal dopants into the ZnO matrix has been considered [15]. The In-doped ZnO nanofibers show high sensitivity to acetone than ethanol at 275 °C with minimum concentraton of 37.5 ppm [16]. Moosavi et al. [17] further reported good performance of Co-doped ZnO thin films to volatile organic compounds despite a notable increase in the crystallite size. In order to overcome the increasing crystallite size with some dopants but not compromising the sensitivity and selectivity of the system, a dual doping with indium (In) and cobalt (Co) is proposed. Studies by Shah et al. [18] suggested that double doping ZnO nanostructures by Al and Cr enhance its properties. Even Wang et al. [12] in 2010 illustrated that the gas sensing performance significantly increases with the decreasing crystallite size. In this approach, synthesis of nanoparticles by varying their morphology as well as reducing their crystallite sizes anticipates improving sensing towards CH₄ and other gases.

In this paper, the undoped ZnO, (Co or In) single and (Co, In) dual doped ZnO nanoparticles are subjected to CH₄ gas to check their sensitivity and selectivity. The gas sensing ability of the nanostructures to CH₄ gas is analysed with reference to their response to ammonia (NH₃) gas [19]. The operating temperature has an effect on how the nanostucture react with the CH₄ gas molecules for an appropriate selectivity and response. The results obtained suggest that the undoped and dual doped ZnO nanoparticles exhibits good sensitivity and response at a temperatue of 200 °C.

2. Procedure

The mechano-chemical technique was utilised to prepare the undoped ZnO nanoparticles, 5wt.% Co-ZnO, In-ZnO and (Co-In)-ZnO nanoparticles samples. The KENOSISTEC station equipment was used to characterise the prepared samples for CH₄ gas sensing at various temperatures (200-350°C) and concentrations (5-100 ppm). In the process, all the samples which were in powder form were sonicated in ethanol for 5 minutes before being coated on the surface of the aluminium substrate. The latter was placed between two Pt electrodes and a heater. The substrates, coated with undoped ZnO, Co, In and Co-In double doped ZnO nanoparticles, were inserted in a chamber within the KENOSISTEC station machine. All the samples were subjected to concentrations of 5, 10, 20, 40, 60, 100 ppm of CH₄ gas. The station was maintained at constant voltage of 5 V. The gas flow in and out of the station was maintained at 5 minutes intervals.

3. Results and discussion

3.1 Gas sensing applications

The undoped, Co and In single doped and (Co-In) double doped ZnO nanoparticles samples were all examined in the CH₄ gas environment for gas sensing application. In resemblance to the earlier ammonia (NH₃) gas testing [19], four distinct temperatures: 200, 250, 300 and 350 °C, were adopted for CH₄ gas testing. The response curves in CH₄ gas environment are plotted for the said temperatures as shown in Figure 1. All in all, it can be observed that a good response occurs at 200 °C. When the temperature is elevated to 250 °C and above, a poor response even with low CH₄ gas concentrations is observed. The indication is that the various ZnO nanoparticles samples operate very well at lower temperatures for CH₄ gas. Stolper et al. [20] reported that the thermogenic gases get produced in the temperature range of 157° to 221 °C. This further suggest that the nanoparticles reported in this paper could only sense methane gas at 200 °C.

In Figure 2, the undoped ZnO nanoparticles shows poor sensitivity to CH₄ gas throughout all the tested temperatures. The double doped ZnO nanoparticles also reflect an ascending order in sensitivity as the concentration is increasing in the operating temperature of 200 °C. At 350 °C, all the single doped

samples reflect enhanced sensitivity in all the concentrations. On the other hand, Co doped ZnO nanoparticles sensitivity to CH_4 gas reflects an ascending order with increasing concentration in the 250 and 300 °C operating temperatures. In the same manner, the opposite is observed for the sensitivity of Co doped ZnO nanoparticles to NH_3 gas between 200 – 300 °C [19]. The In doped ZnO nanoparticles sensitivity is typically low at 250 and 300 °C operating temperatures with a maximum sensitivity of 5 at 350 °C in all the gas concentrations except 5 ppm. An overall observation is that Co-ZnO nanoparticles is the most sensitive to CH_4 gas at concentrations greater than 40 ppm and high temperatures [21]. Motaung et al. [21] also observed similar results for ZnO nanostructures which were exposed to CH_4 gas of different concentrations at 300 °C for 24 hours. In Table 1, the double doped ZnO nanoparticles show constant response and recovery time to methane gas, while In-ZnO nanoparticles have the fastest response time. The undoped ZnO nanoparticles demonstrate the fastest recovery time.

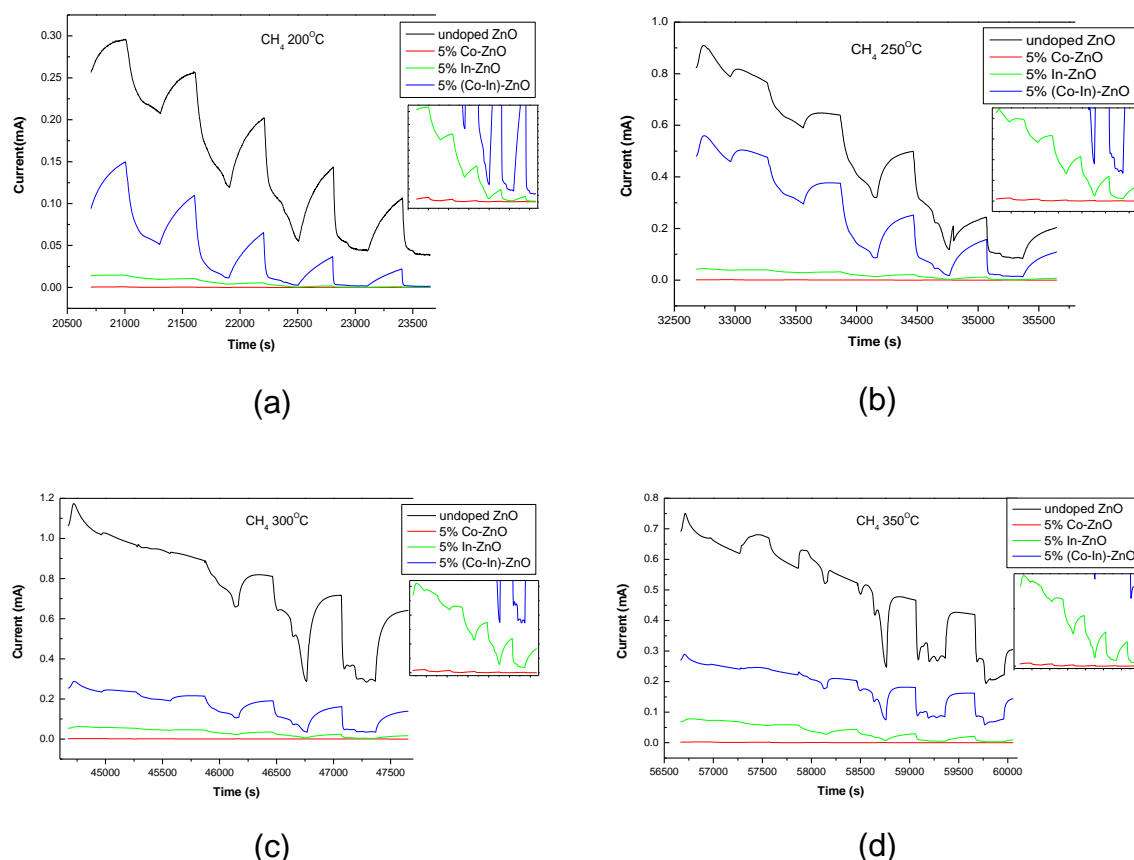


Figure 1: The graphs of current against time for the doped and undoped ZnO nanoparticles at various temperatures for concentrations range 5-100 ppm.

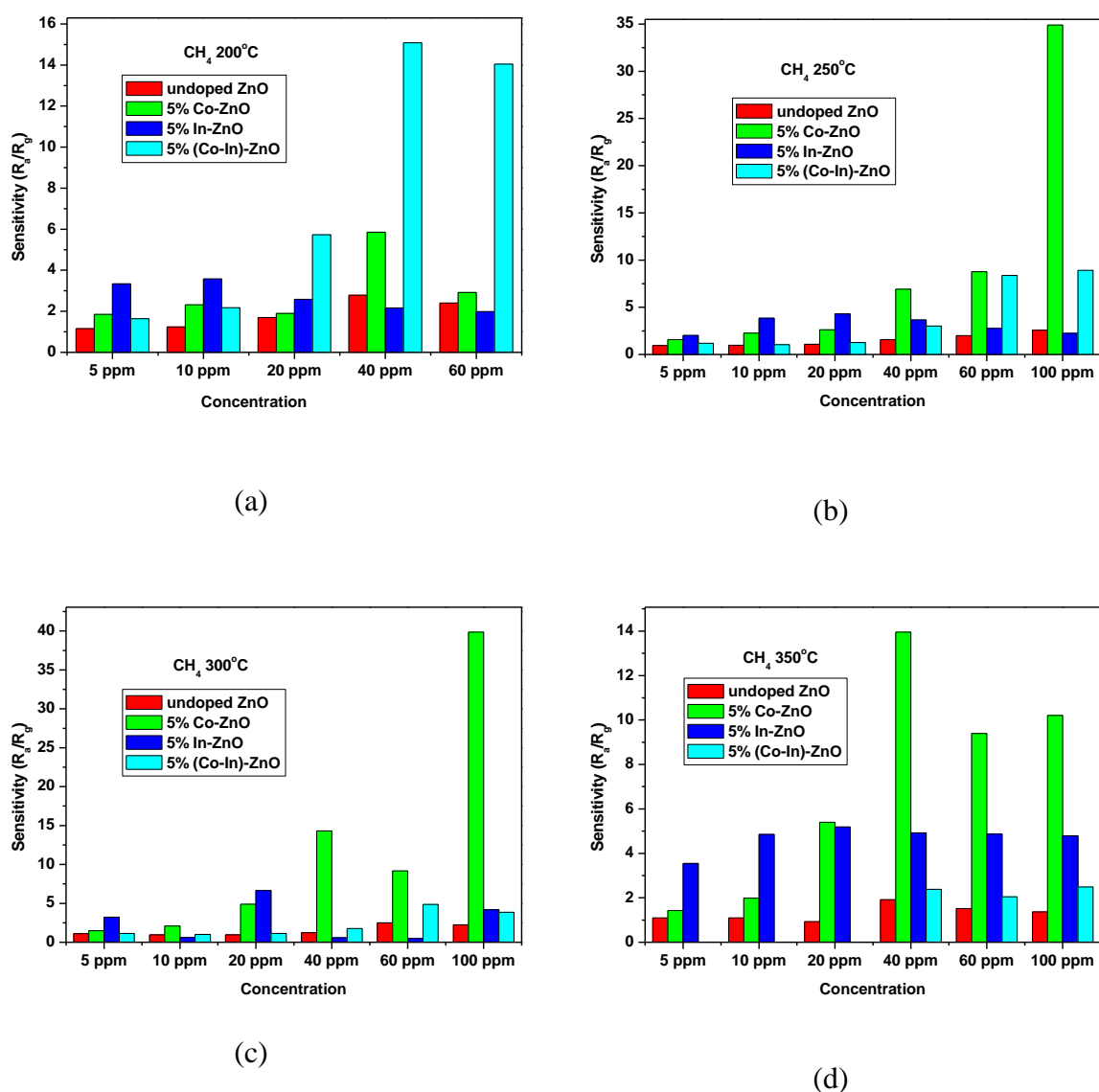


Figure 2: The sensitivity versus CH_4 gas concentration plot for the doped and undoped ZnO nanoparticles at various temperatures.

Table 1: The CH_4 gas response and recovery for the doped and undoped ZnO nanoparticles at 10 ppm.

Sample	Response time (s)	Recovery time (s)
Undoped ZnO	300	289
Co-ZnO	299	300
In-ZnO	298	297
(Co-In)-ZnO	299	299

4. Summary

The doped and undoped ZnO nanoparticles were successfully synthesised mechano-chemically. The current versus time curves show good response and recovery for undoped and double doped samples at 200 °C. The undoped and (Co-In) doped ZnO nanoparticles are more favoured compared to the Co and In single doped ZnO nanoparticles samples. The sensitivity of the Co doped ZnO nanoparticles is more dominant at 350 °C. On the contrary, the (Co-In) doped ZnO nanoparticles is only sensitive at 200 °C. The Co-ZnO nanoparticles reflect an ascending response magnitude with increasing concentration of CH₄ gas at all temperatures. The undoped ZnO nanoparticles reflect poor sensitivity in all operating temperatures. The In doped ZnO nanoparticles possess the shortest response time.

Acknowledgements

The authors acknowledge the financial support from UL, NRF and IBSA. The Council for Scientific and Industrial Research (CSIR) branch of National Centre for Nano-structured Materials is thanked for characterisation facilities.

References

- [1] Pachauri R K, Allen M, Barros V, Broome J, Cramer W, Christ R, Church J, Clarke L, Dahe Q and Dasgupta P, "Climate change 2014 synthesis report. contribution of Working Groups I, II and III to the Fifth Assessment Report of the Intergovernmental Panel on Climate Change," *IPCC*, 151, 2014.
- [2] Pierre-Alexandre G, Thomas J and Beth P, "Cyclic-Voltammetry-Based Solid-State Gas Sensor for Methane and Other VOC Detection," *Analytical Chemistry*, **90**, 6102-6108, 2018.
- [3] Viswanathan S, Eria L, Diunugala N, Johnson J and McClean C, "An analysis of effects of San Diego wildfire on ambient air quality," *Journal of Air & Waste Management Association*, **56**, 55-67, 2016.
- [4] Hui-fang L, Qi-xin H, Chuan-tao Z and Yi-ding W, "Development of a portable mid-infrared methane detection device," *Optoelectronics letters*, **13**, 0100 - 0103, 2017.
- [5] Dinh T-V, Choi I-Y, Son Y-S and Kim J-C, "A review on non-dispersive infrared gas sensors: Improvement of sensor detection limit and interference correction," *Sensors and Actuators B*, **231**, 529-538, 2016.
- [6] Bull S, "Methane General information," *Health protection agency, CRCE HQ, HPA, Version 1*, 2-4, 2010.
- [7] Pugh D C, Luthra V, Singh A and Parkin I, "Enhanced gas sensing performance of indium doped zinc oxide nanopowders," *The Royal Society of Chemistry Advances*, **5**, 85767-74, 2015.
- [8] Galstyan V, Poli N and Comini E, "Highly sensitive and selective H₂S chemical sensor based on ZnO nanomaterial," *Applied Science*, **9**, 1167(1-10), 2019.
- [9] Spencer M J S, "Gas sensing applications of 1d-nanostructured zinc oxide: Insights from density functional theory calculations," *Proress in Material Science*, **57**, 437- 486, 2012.
- [10] Schmidt-Mende L and MacManus-Driscoll J L, "ZnO- nanoparticles, defects, and devices," *Materials today*, **10**, 40-48, 2007.
- [11] Soitah T N, Chunhui Y and Liang S, "Effect of Fe doping on structural and electrical properties of nanocrystalline ZnO thin films prepared by sol-gel dip coating technique," *Science of Advanced Materials*, **2**, 534-538, 2010.
- [12] Wang C, Yin L, Zhang L, Xiang D and Gao R, "Metal Oxide Gas Sensors: Sensitivity and Influencing Factors," *Sensors*, **10**, 2088-2106, 2010.

- [13] Ahn M -W, Park K -S, Heo J -H, Park J -G, Kim D -W, Choi K J, Lee J -H and Hong S -H, “Gas sensing properties of defect-controlled ZnO-nanowire gas sensor,” *Applied Physics Letters*, **93**, 263103, 2009.
- [14] Han N, Wu X, Chai L, Liu H and Chen Y, “Counterintuitive sensing mechanism of ZnO nanoparticle based gas sensors,” *Sensors and Actuators B: Chemical*, **150**, 230–238, 2010.
- [15] Xu X, Fan H, Lui Y, Wang L and Zhang T , “Au-loaded In₂O₃ nanofibers-based ethanol micro gas sensor with low power consumption,” *Sensors and Actuators B: Chemical*, **160**, 713-719, 2011.
- [16] Qi J, Zhang H, Lu S, Li X, Xu M and Zhang Y, “High performance indium-doped ZnO gas sensor,” *Journal of Nanomaterials*, **2015**, 1-6, 2014.
- [17] Moosavi F, Bahrololoom M E, Kamjou R, Mirzaei A, Leonardi S G and Neri G, “Hydrogen sensing properties of Co doped ZnO nanoparticles,” *Chemosensors*, **6**, 61(1-11), 2018.
- [18] Shah A H, Ahamed M B, Neena D, Mohamed F and Iqbal A, “Investigations of optical, structural, and antibacterial properties of Al-Cr dual doped ZnO nanostructures,” *Journal of Alloys and Compounds*, **606**, 164-170, 2014.
- [19] Manamela M F, Mosuang T E and Mwakikunga B W, “The structural and sensing properties of cobalt and indium doped zinc oxide nanopowders synthesised through high energy ball milling technique,” in *SAIP2017 Conference Proceedings*, 66-70, Western Cape, Stellenbosch, 2018.
- [20] Stolper D A, Lawson M, Davis C L, Ferreira A A, Santos-Neto E V, Ellis G S, Lewan M D, Martini A M, Tang Y, Schoell M, Sessions A L and Eiler J M, “Gas formation. Formation temperatures of thermogenic and biogenic methane,” *Science*, **344**, 1500-1503, 2014.
- [21] Motaung D E, Makgwane P R and Ray S S, “Induced ferromagnetic and gas sensing properties in ZnO-nanostructures by altering defect concentration of oxygen and zinc vacancies,” *Materials Letters*, **139**, 475-479, 2015.

First principle studies of palladium nanoparticles on titanium dioxide surfaces for catalytic application

A F Mazibuko, R G Diale, H R Chauke and P E Ngoepe

Materials Modelling Centre, University of Limpopo, Private bag x1106, Sovenga, 0727, South Africa

E-mail: andile.mazibuko@ul.ac.za

Abstract. Palladium-based catalysts are being developed as an alternative to the commonly used high cost platinum catalyst due to similar electronic configurations and lattice constants. Pd catalysts are cheaper than platinum with a high methanol-tolerance. In this study, first principle density functional theory was used to study the catalytic properties of Pd/TiO₂, the interaction and the electronic behavior of palladium nano-clusters on a stable titanium dioxide surface using the plane-wave pseudo-potential method. Titanium dioxide is used as a metal support to develop the palladium catalyst and is the most important transition metal oxide since its photo-catalytic activity was discovered. This transition metal oxide is used in many catalytic processes in the industries such as metal catalysts, which include the platinum group metals such as Pd, Pt, and Rh. These metals are involved in processes such as fuel cells, methane oxidation, catalysis, and in emission control technology. Firstly, the stability of titanium dioxide polymorphs was deduced from elastic properties and are in good agreement with the experimental values to within 3%. The observation made was based on the shear modulus of rutile being higher and positive compared to that of the other polymorphs suggesting that rutile is more stable. The order of surface stabilities is given as (110) > (100) > (101) > (001) > (111), and in good agreement with previous work. Adsorption of water on the stable (110) surface showed that the (110) surface was more exothermic. Secondly, the interaction of palladium clusters with titanium dioxide surface showed that Pd₁₃ prefers the top adsorption site due to the least negative adsorption energy. The findings of this work suggest that palladium-based catalysts may play a significant role in future developments and applications in emission control technologies.

1. Introduction

Palladium is found as a free metal that forms part of the platinum group metals (PGMs) but it is more reactive than the heavier platinum [1]. Pd nanoparticles are ideal for use in catalytic reactions because of their increased surface area compared to that of the bulk material and as such are an important material component in hydrogen storage and gas sensing applications [1]. The most important attribute of Pd is its high hydrogen adsorption capacity which is greater than for any other metal.

Titanium dioxide (TiO₂) is a semiconducting transition metal oxide that is alternatively used as a support material in catalysis because of its useful physical properties and applications in various technologies [1]. Metal nanoparticles supported on metal oxides are used in various industrial catalytic processes [2]. The most used catalysts are Pt and Pt-based catalysts. Recently, Pd-based catalysts are being developed since they have similar electronic configurations and lattice constants as Pt but cheaper [3]. Pd is used as an electrode material in fuel cell applications where a highly pure hydrogen production

is important and gaseous hydrogen is the only gas that can pass this metal. Car exhaust fumes might be made less toxic by using Pd as a catalyst in the catalytic convertors of cars [3, 4].

The oxide supported metal catalysts are necessary to enhance catalytic activity and durability of catalysts during methane oxidation, photocatalysis and CO oxidation [5]. There has been a variety of experimental studies on supported palladium catalysts that raised an interest to this field of research [6,7]. However, the challenge is understanding the interaction between catalytic metals and the support materials. In recent studies, density functional theory (DFT) has been used to investigate surface properties and interactions of many systems including oxide supported metals [8,9].

In this paper, we use density functional theory to investigate the TiO₂ surface interaction with water and Pd nanoclusters on (110) TiO₂ surface and to study the catalytic properties of Pd/TiO₂. The Pd-based catalyst play a significant role in emission control technology, particularly as an automotive exhaust catalyst. The surface energies and effect on hydrated surfaces is important to establish the dominant surface of titanium. Firstly, TiO₂ surface and adsorption energies of H₂O/TiO₂ and Pd₁₃/TiO₂ were calculated. Secondly, a systematic investigation on the stability of Pd_n clusters (n=3-19) will be drawn from the binding energy and second order difference energy (D₂E). It will be established that the Pd₁₃ nanocluster is more stable and may have a great potential for enhancing catalytic properties. Finally, the rest of the paper is arranged in the following manner: section 2 provides computational details; section 3 is the results and discussions on the two interacting Pd clusters and Pd/TiO₂ systems; and, lastly the conclusion.

2. Computational details

First principle density functional theory (DFT) calculations were performed using the generalized gradient approximation (GGA) refined by Perdew, Burke and Ernzerhof (PBE) [10] as implemented in the CASTEP [11] and VASP codes [12]. The plane wave cut-off energy of 500 eV was used for all structures and the Brillouin zone sampling scheme of Monkhorst-Pack [13] with 6x6x1 k-point mesh for all TiO₂ surfaces and 3x3x1 for the palladium nanoclusters. All surface calculations were performed within a (2X2) supercell, using a 12-layer slab with the vacuum slab of 15 Å to avoid an interaction of the adsorbate with the repeating upper slab. The palladium nanoclusters (n=3-19) were constructed using KLMC and optimized using CASTEP. Convergence was achieved when the maximum component of the residual forces was less than 0.01 eV/Å. After adsorption, the 6 bottom layers were frozen while the top layers could interact with the palladium cluster. Density functional tight binding theory (DFTB⁺) was used to parametrize TiO₂ at different radii and to derive the potentials for Ti-O, O-O, O-Ti, Ti-Ti interactions. The surface stabilities for different terminations are determined by their surface energy, calculated as:

$$E_{\text{surface}} = \left(\frac{1}{2A}\right) [E_{\text{slab}} - (n_{\text{slab}})(E_{\text{bulk}})] \quad (1)$$

where E_{slab} is the total energy of the cell containing the surface slab, n_{slab} is the number of atoms in the slab, E_{bulk} is the total energy per atom of the bulk and A is the surface area. A low positive value of E_{surface} indicates stability of the surface termination. The strength of the interaction of the surface with the adsorbate is shown by the adsorption energy, as:

$$E_{\text{adsorption}} = [E_{\text{system}} - (E_{\text{slab}} + E_{\text{palladium}})] \quad (2)$$

where E_{system} is the energy of the surface slab with collector, E_{slab} is the energy of the surface slab (Equation 1), n is the number of adsorbates adsorbed on the surface and $E_{\text{palladium}}$ is the energy of the isolated palladium clusters. A negative value reveals a strong interaction between the adsorbate and the surface, whereas a positive value reveals the opposite.

3. Results and discussion

3.1. Structural properties of TiO₂.

It was observed from the parameterization of TiO₂, that the lattice parameters and bond lengths obtained are in good agreement with that of the standard DFT and experimental data. In Table 1, the calculated

lattice parameters and bond lengths for TiO₂ are presented. The Slater-Koster files for TiO₂ were refined by varying the radius and the best fit was obtained with lattice parameters (a=4.566, c=3.168) which compare very well with experimental values (a=4.567, c=2.932).

Table 1. Lattice parameters and bond lengths for TiO₂.

Structure	Atom	Lattice parameters			Bond length (Å)
		a (Å)	b (Å)	c (Å)	
	Exp. [14]	4.567	4.567	2.932	2.025
TiO ₂	Calc.	4.566±0.12	4.566±0.12	3.168±0.08	2.055±0.11

3.1.1. Mechanical properties of the TiO₂ polymorphs.

The elastic properties provide an estimate of the mechanical stability, strength and indirectly the melting temperature. We observe that all three TiO₂ polymorphs (rutile, anatase and brookite) are mechanically stable since they display positive shear modulus ($C' > 0$). The shear modulus is higher for rutile compared to the other polymorphs which implies that rutile is the most stable. The calculated (Calc.) values accord well with experimental (Exp.) data. Furthermore, the ratio of brittleness/ductility (B/G) as proposed by Pugh [15], reveal that the polymorphs are ductile (since B/G > 1.75).

Table 2. Elastic constants C_{ij} , bulk B (GPa), shear G (GPa), Young moduli E (GPa) and ratio of brittleness/ductility (B/G) of TiO₂.

Structure	Rutile		Anatase		Brookite
	Calc.	Exp. [16]	Calc.	Exp. [16]	Calc.
C_{11}	260.237	268	354.339		287.658
C_{12}	160.323	175	116.550		148.716
C_{13}	150.253	147	136.398		148.610
C_{21}	160.323	-	116.550		148.716
C_{22}	260.237	-	354.339		296.769
C_{23}	150.253	-	136.398		125.080
C_{31}	150.253	-	136.398		148.610
C_{32}	150.253	-	136.398		125.080
C_{33}	467.803	484	207.011		291.593
C_{44}	120.806	124	81.435		95.083
C_{55}	120.806	-	81.435		90.681
C_{66}	211.497	190	60.354		77.682
C'	49.957	-	118.895		69.471

Structure	Rutile		Anatase		Brookite
	Calc.	Exp. [16]	Calc.	Exp. [16]	
Bulk modulus	206.476	212	182.943	178	191.943
Shear modulus	113.194	113	76.805	-	82.272
Young modulus	287.114	-	201.379	-	215.845
B/G	1.82	-	2.4	-	2.3

3.1.2. Surface energies of rutile.

The TiO₂ surfaces and energies of the rutile surfaces are shown in Figure 1. The surfaces were cleaved from the optimized bulk rutile with spacegroup P4₂/mm. The surface with the smallest surface energy is considered stable [17]. The slab models in Figure 1 show the order of stability of the surfaces taken before relaxation. We note that the most stable surface is the (110) surface with a surface energy of 0.083 eV/Å², 12 layers and 24 atoms.

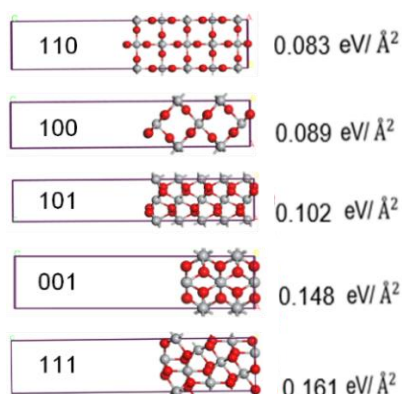


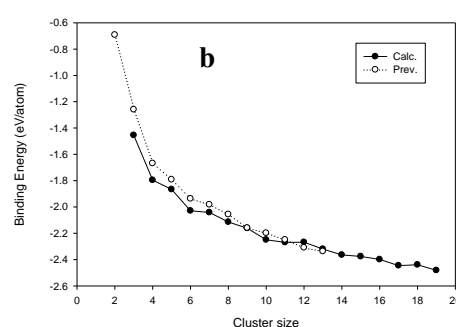
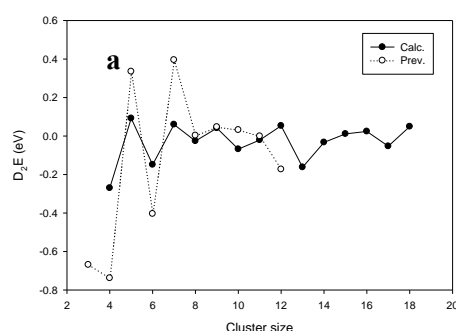
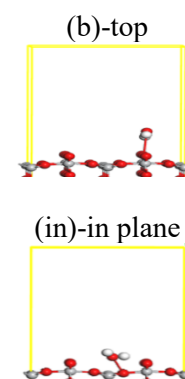
Figure 1. Rutile (TiO₂) surfaces in the order of stability (110) > (100) > (101) > (001) > (111).

3.1.3. Adsorption of water onto rutile surfaces.

Table 3 lists the adsorption energies of the five surfaces and their adsorption sites ((b)-top and (in)-in plane as indicated on the right of Table 3). We found that the (110) TiO₂ surface is stable as shown by a more negative E_{ads} value. This suggests that the surface is more exothermic, and the reaction is spontaneous. These results accord well with the surface energies (Figure 1). We also found that the more negative value is on the oxygen adsorption site which is in the plane.

Table 3. The calculated adsorption energies of H₂O molecule adsorbed on different adsorption sites on the five stable TiO₂ surfaces. The adsorption sites are indicated on the right.

Surface	Adsorption site	E_{ads} (eV)
100	H ₂ O on O site	-1.765
100	H ₂ O on Ti site	-1.934
101	H ₂ O on O(in)site	-4.309
101	H ₂ O on O(b) site	-4.242
101	H ₂ O on Ti site	-5.028
110	H ₂ O on O(b) site	-9.592
110	H ₂ O on O(in)site	-10.562
110	H ₂ O on Ti site	-10.426
001	H ₂ O on O site	-3.748
001	H ₂ O on Ti site	-4.904
111	H ₂ O on O(b) site	6.282
111	H ₂ O on Ti(in)site	6.073
111	H ₂ O on O(in)site	-3.212
111	H ₂ O on Ti(b) site	6.930



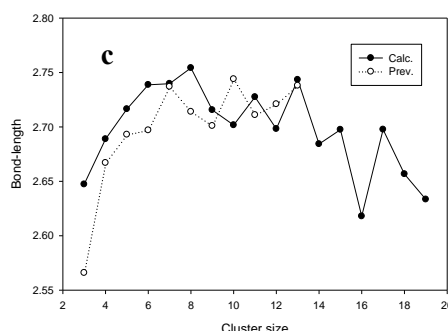


Figure 2. (a) Second order energy difference, D_2E , (b) Binding energy and (c) Bond length with respect to cluster size for Pd_n nanoclusters ($n=3-19$). The current work (Calc.) is compared with previous theoretical (Prev.) findings [18].

3.2. Palladium nanoparticles

The second order difference energy (D_2E) is a stability function and stable structures can be identified from the lowest peaks as shown in Figure 2a. We note from Figure 2a that $n=4, 6, 8, 10, 13$ and 17 are in local minima. These structures are referred to as the stable clusters or magic clusters. The predicted magic number clusters assigned $n=4, 6$ and 13 are most preferred and agrees with previous theoretical studies [18], while cluster 10 was only found in the current work. The magic clusters behavior was also investigated using the binding energies and are plotted in Figure 2b.

We obtained that the binding energies and the D_2E energy agree well with experimental and theoretical data. It was observed from the binding energy results that the clusters are far from converging, which can only be achieved when clusters are increased to larger sizes. Furthermore, the Pd_{13} cluster is used for further adsorption calculations since it has an enhanced stability for large clusters under consideration. It was observed from Figure 2c that the bond lengths of the palladium nanoclusters used are in good agreement with the experimental values to within 3%. It was noted that the cluster size increases as the binding energy per atom decreases and this is a common behavior for all metal clusters in this paper.

3.3. Pd adsorption on (110) TiO_2

The effect of Pd/TiO_2 is determined by examining the adsorption energies and bond lengths of Pd on (110) TiO_2 . In this work Pd_{13} was adsorbed on various sites of (110) TiO_2 surface and optimized (relaxing top layers and fixed 6 bottom layers) as shown in Figure 3. The preferred adsorption sites, adsorption energies and bond lengths are listed in Table 4. The Pd_{13} is adsorbed at a distance of 2.053 from the (110) surface as shown in Figure 3(a) and we note that Pd_{13} is likely to adsorb on the top oxygen as shown on Figure 3(b).

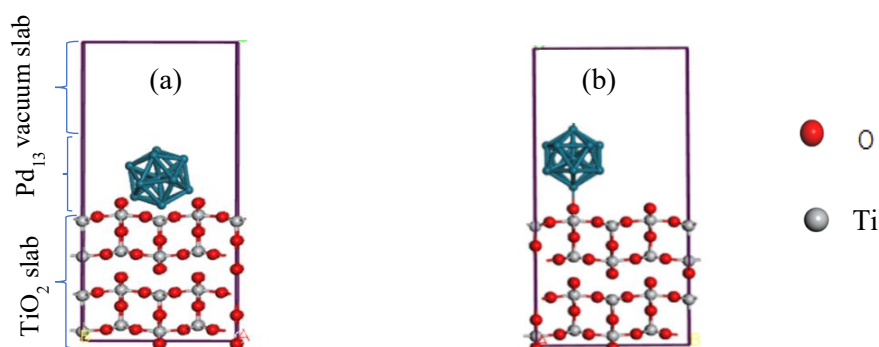


Figure 3. The geometries of Pd_{13} adsorption on a (110) TiO_2 surface: (a) Pd_{13}/TiO_2 and (b) $Pd_{13}-O/TiO_2$.

We observe from Table 4 that in terms of relaxed bond lengths, the preferred adsorption site is the one with the lowest Pd-O bond length which is where Pd₁₃ is bonded to three top oxygen (3b) atoms, with a Pd-O bond length of 2.054 Å. The adsorption strength of the interaction of Pd₁₃ with (110) TiO₂ was calculated using Equation 2.

Table 4. The calculated Pd-O bond length and adsorption energies of the Pd₁₃/TiO₂ (110) system.

Adsorption site	Pd-O bond length (Å)		E _{ads} (eV)
	Calc.	Exp. [19]	
O(b)	2.063	2.036	-1.746
Ti(in)	2.278	2.264	-1.438
O(in)	2.109	2.096	-2.259
O(2b)	2.083	-	-2.842
O(3b)	2.054	-	-1.815

Interestingly, compared to the bond lengths, the adsorption energies show that the preferred adsorption site is the Pd bonded to two top oxygens (2b) with an adsorption energy of -2.842 eV. This suggests that the reaction is spontaneous and exothermic.

4. Conclusion

Calculations on the lattice parameters of TiO₂ polymorphs were performed using first principles method and the results were found to be in good agreement with the available experimental data. The mechanical properties suggested that rutile is the most stable polymorph. The surface energies for the five crystallographic planes showed the (110) surface as the most stable surface with the smallest surface energy of 0.083 eV/Å². The interaction between water and the surfaces of rutile (TiO₂) was investigated, it was found that the (110) surface with water adsorbed on the oxygen site because of the most negative adsorption energy. Furthermore, the order of stability accords well with previous surface work done [17]. We have also calculated the binding energies and second difference energy of the palladium clusters and found good agreement with the experimental data [18].

The Pd₁₃/TiO₂ (110) interactions were determined by adsorbing palladium (Pd₁₃) at different adsorption sites and we observed the effect on the bond lengths and adsorption energies of the system. The adsorption energy for the Pd₁₃/TiO₂(110) suggested that the reaction is spontaneous (negative, E_{ads}<0). Furthermore, the Pd-Ti bond distances are comparable before and after adsorption with a slight increase from 2.057 Å to 2.278 Å. This may suggest a good catalytic reactivity of the Pd₁₃/TiO₂(110). The findings of this research may suggest that the interactions of Pd₁₃/TiO₂(110) are favorable and may be used in catalytic convertors.

Acknowledgements

The work was carried out at the Materials Modelling Centre (MMC), University of Limpopo. We acknowledge the Centre for High Performance Computing (CHPC) for computing resources and the National Research Foundation for financial assistance. The authors also wish to recognize the support of the South African Research Chair initiative of the Department of Science and Technology.

References

- [1] Wang M, Guo D and Li H 2005 *J. Solid State Chem.* **178** 1996
- [2] Chen J, Arandiyá H, Gao X and Li J 2015 *Catal. Surv. Asia* **19** 140
- [3] Zhang C and He H 2007 *Catal. Today* **126** 345
- [4] Youngku S 2010 *Appl. Surf. Sci.* **257** 1692
- [5] Shao Y, Liu J, Wang Y and Lin Y 2009 *J. Mater. Chem.* **19** 46
- [6] Rao C R K and Trivedi D C 2005 *Coord. Chem. Rev.* **249** 613
- [7] Yui T, Kan A, Saitoh C, Koike K, Ibusuki T and Ishitani O 2011 *ACS Appl. Mater. Interfaces* **3** 2594

- [8] Wanbayor R and Ruangpornvisuti 2012 *Appl. Surf. Sci.* **258** 3298
- [9] Dianat A, Seriani N , Ciacchi L C, Pompe W, Cuniberti G and Bobeth M " 2009 *J. Phys. Chem. C* **113** 21097
- [10] Perdew J P, Burke K and Ernzerhof M 1996 *Phys. Rev. Lett.* **77** 38
- [11] Segall M D, Lindan P J D, Probert M J, Pickard C J, Hasnip P J, Clark S J and Payne M C 2002 *J. Phys. Cond. Matter.* **14** 2717
- [12] Kresse G and Furthmüller J 1996 *Phys. Rev.* **154** 11169
- [13] Monkhorst H F and Park J D 1976 *Phys. Rev. B* **13** 5188
- [14] Rezaee M, Khoie S M and Liu K H 2011 *Cryst. Eng. Com.* **13** 5055
- [15] Pugh S F 1954 *Philos. Mag.* **45** 823
- [16] Isaak D G, Carnes J D, Anderson O L, Cynn H and Hake E 1998 *Phys. Chem. Miner.* **26** 31
- [17] Mellan T A and Grau-Crespo 2012 *J. Chem. Phys.* **137** 154706
- [18] Chattaraj D, Parida S C, Dash S and Majumder C 2014 *Eur. Phys. J. D.* **68** 302
- [19] Sanz J F and Ma´rquez A 2007 *J. Phys. Chem. C* **111** 3949

Effect of temperature on the structure and dynamic properties of metal sulphide nanostructures via molecular dynamics simulation

M A Mehlape, T G Mametja, T E Letsoalo and P E Ngoepe

Materials Modelling Centre, School of Physical and Mineral Sciences, University of Limpopo, South Africa, Private Bag, X1106, SOVENGA, 0727

Email:mofuti.mehlape@ul.ac.za

Abstract. Metal sulphide nanostructures via molecular dynamics (MD) simulations at different temperatures are presented and discussed in order to understand their structure and dynamic properties. Nanostructured metal sulphides have attracted the attention of researchers in the fields of materials science, physics and chemistry. They have enhanced structure and dynamic properties due to their large surface-to-volume ratio; hence making them desirable to a wide range of industries. They are promising materials for catalysis, batteries and photovoltaic, however the understanding on the structure and dynamic conditions of large-scale nanostructures are still to be explored more. Computational modelling technique, MD was performed to provide atomic or molecular level insights of the structure and dynamic properties of nanostructured metal sulphides. The effect of temperature on different sizes of nanostructures are analysed in a form of structure and dynamic properties; namely radial distribution functions, potential energy and diffusion coefficient. The results showed that temperature associated with the melting transition and stability increased with an increase in the nanostructure size.

1. Introduction

Nanoscience and nanotechnology collectively represent one of the fastest growing interdisciplinary scientific areas, spanning interests from physics, through chemistry and geoscience, to biology [1]. Nanostructures have been identified worldwide as the key to unlocking a new generation of devices with revolutionary properties and functionalities [2]. Nanostructures have many interesting properties (for example structural and dynamic properties), as they bridge the gap between bulk materials and atomic or molecular structures [3]. Nanostructures offer the advantages of high surface-to-volume ratios, favourable transport properties [4]. Herein, we report the effect of temperature on the structure and dynamic properties of metal sulphide, FeS₂ pyrite nanostructures. Pyrite, also known as Fool's Gold, is a very attractive next-generation photovoltaic (PV) material that is abundant in nature and nontoxic [5]. Various FeS₂ pyrite nanostructures such as nanostructures [6], nanocrystals [7], nanotubes [8] and nanowires [9] to name but a few, have been studied experimentally. However, experimental difficulties in studying nanostructures arise from their small size, which limits the use of traditional techniques for measuring other properties and conditions (such as physical, structural and dynamic properties, pressure and temperature) [10]. Hence, computational simulation is used to access those conditions that are sometimes difficult to obtain experimentally and simulation is also useful for planning experiments that require complicated setups [11]. Computational simulation technique, molecular dynamics (MD) is used to investigate the effect of temperature on the structure and dynamic properties of FeS₂ nanostructures.

1.1. Pyrite, FeS_2 structure

Cubic pyrite, FeS_2 belongs to the space group $\text{Pa}\bar{3}$ [12]. FeS_2 has a NaCl-type cubic structure with the $(\text{S}_2)^{2-}$ groups situated at the cube centre and midpoints of the cube edges, and the low-spin Fe^{2+} atoms located at the corners and face centres [13]. Cubic FeS_2 structure together with the nanostructure are shown in Figure 1.

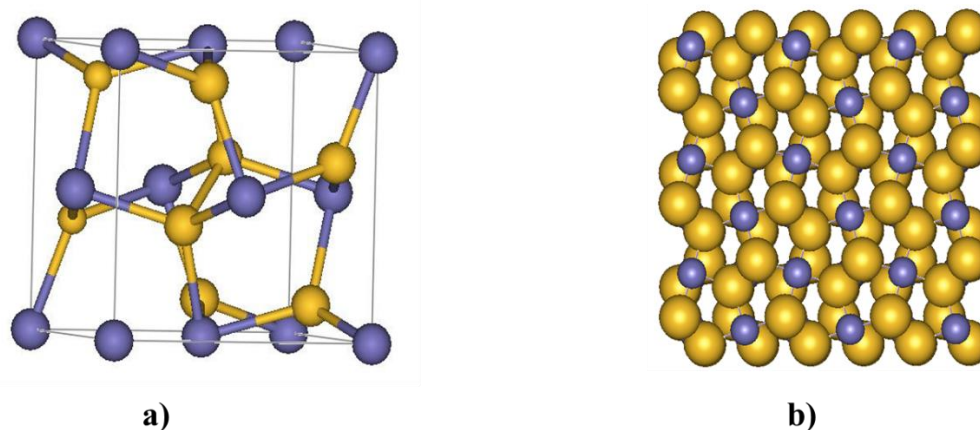


Figure 1: Snapshots of a) cubic bulk structure of pyrite, FeS_2 , and b) Initial FeS_2 nanostructure, where purple atoms represent iron (Fe) and yellow atoms represent sulphur (S).

2. Computational Details

2.1. Creation of nanostructures and methodology

Initial configuration of FeS_2 nanostructures was constructed using METADISE code [14], which uses Wulff constructions [15] to predict the morphology. This approach follows the theory of Gibbs to generate the lowest total surface energy morphology from facets that may each have different surface energies. The stable $\{100\}$ surface [16] was used to create its cubic nanostructures. MD simulations of nanostructures were performed with DLPOLY_2.20 code [17]. The MD simulation of the nanostructures were carried out in an ensemble approximating the canonical with constant number of atoms N and volume V . Temperature is controlled by a Nose-Hoover thermostat [18], in order to avoid steady energy drifts caused by the accumulation of numerical errors during MD simulations [19]. The equations of motion were integrated using the Verlet Leapfrog algorithm [20] with a time step of 1 fs. The constant temperature and volume simulations were performed over the temperature range of 300 K to 2000 K with 100 K increments at zero pressure for the nanostructures of between 1 nm and 4.5 nm in diameter. The sizes of the nanostructures of FeS_2 used in this study, and the corresponding number of FeS_2 units are given in Table 1. MD simulations were performed under non-periodic boundary conditions to make sure that the results are not affected by boundary conditions.

Table 1: Size of nanostructures (in diameter) and the corresponding number of FeS_2 units used for nanostructures.

Particle Dimension (nm)	Number of Atoms
1.0	96
1.5	324
2.9	1997
3.4	3295
4.5	7369

2.2. Representation of interatomic potentials

The Born ionic model [21] was used and parameters were derived for short range interactions represented by the Buckingham potential, harmonic function and three body terms:

2.2.1. Buckingham Potential

In the Buckingham potential, the repulsive term is replaced by an exponential term and potential takes the form

$$U(r_{ij}) = A_{ij} * \exp^{-r_{ij}/\rho_{ij}} - \frac{C_{ij}}{r_{ij}} \quad (1)$$

where A_{ij} and ρ_{ij} are parameters that represent the ion size and hardness, respectively, while C_{ij} describe the attractive interaction and r_{ij} is the distance between ion i and ion j . The first term is known as the Born-Mayer potential and the attraction term (second term) was later added to form the Buckingham potential. Very often, for the cation-anion interactions, the attractive term is ignored due to the very small contribution of this term to the short-range potential, or, alternatively, the interaction is subsumed into the A and ρ parameters.

2.2.2. Harmonic Potential

The interaction between the sulphur atoms of the S-S pair were described by a simple bond harmonic function:

$$U(r_{ij}) = \frac{1}{2} k_{ij} (r_{ij} - r_0)^2 \quad (2)$$

where k_{ij} is the bond force constant, r_{ij} the interionic separation and r_0 the separation at equilibrium.

2.2.3. Three-Body Potential

A further component of the interactions of covalent species is the bond-bending term, which is added to take into account the energy penalty for deviations from the equilibrium value. Hence, this potential describes the directionality of the bonds and has a simple harmonic form:

$$U(\theta_{ijk}) = \frac{1}{2} k_{ijk} (\theta_{ijk} - \theta_0)^2 \quad (3)$$

where k_{ijk} is the three-body force constant, θ_0 is equilibrium angle and θ_{ijk} is the angle between two interatomic vectors $i-j$ and $i-k$. The potential parameters for the nanostructures of FeS₂ was previously successfully used for the investigation of bulk and surfaces of FeS₂ [16, 22].

3. Results and Discussions

3.1. Dynamic properties

Thermodynamically, the melting of bulk crystalline solids is characterized by a sudden increase in the free energy [23]. The curves of potential energy versus temperature for FeS₂ nanostructures were obtained. Figure 2 shows the potential energy variation with temperature for nanostructures with different number of atoms, i.e., 96, 324, 1997, 3295 and 7369 atoms, which corresponds to 1 nm, 1.5 nm, 2.9 nm, 3.4 nm and 4.5 nm in diameter, respectively. The phase transition from solid to liquid phase can be identified by a jump in the energy curve. The melting point of the FeS₂ nanostructures can be estimated from the change in slope of the temperature dependence of the energy. The variation of potential energy per atom of the system, with temperature for different nanostructure sizes is shown in Figure 2. The observation is that there is an increase in potential energy with temperature for all sizes. However the sudden steep increase in the rate of change of potential energy at a particular temperature, which is associated with the melting transition, is more apparent in the case of a nanostructure of 4.5 nm. This implies that as the size of the nanostructure increase, the temperature associated with melting transition is more apparent.

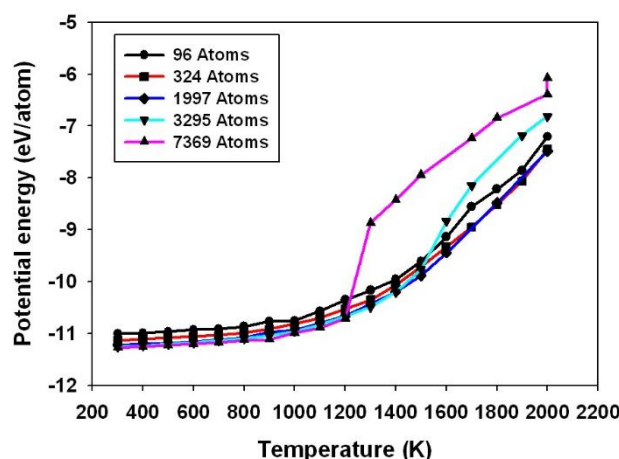


Figure 2: The potential energy per atom as a function of temperature for nanostructures with different number of atoms. Number of atoms corresponds to the diameters depicted on Table 1.

3.2. Structural properties

Radial distribution functions (RDFs) for FeS_2 nanostructures of 324 and 7369 atoms are shown in Figure 3 for Fe–Fe, Fe–S and S–S pairs at temperatures between 300 and 1500 K. RDFs describe the local coordination around a specific atom and represent the internal structure of a material [24]. The RDFs change from well-ordered to molten configuration for increasing temperature. The well-ordered configuration is characterised by a profile which manifests a greater number of narrower peaks with increasing radius. The molten configuration is characterised by a profile with both fewer and broader peaks. It can be observed that the RDFs show structural changes at different temperatures for different sizes of nanostructures. The nanostructure with 324 atoms, in Figure 3(a), has a crystalline and well-ordered structure, as observed by many peaks of the RDFs, from 300 to 500 K. The height of the peaks is also reduced as the temperature increases. The significant peak height reduction for the Fe–Fe, Fe–S and S–S pairs is observed at 1000 K; whereby the peaks become smoother, indicative of a liquid phase of the nanostructure with 324 atoms. The nanostructures with 7369 atoms at the temperatures leading to the melting are shown in Figure 3(b). It can be deduced from the many peaks of the RDFs that from 300 to 1000 K, the nanostructures has a crystalline and well-ordered structure. At 1000 K the peaks start to broaden and the height has decreased substantially as compared to those at lower temperatures; however at 1500 K the peaks are broadened and smoother, indicative of the liquid phase of the nanostructure with 7369 atoms.

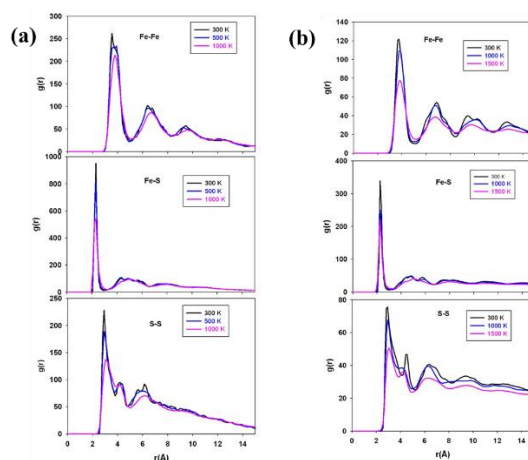


Figure 3: The radial distribution functions (RDFs) of FeS_2 nanostructures at various temperatures with different number of atoms. (a) 324 atoms and (b) 7369 atoms.

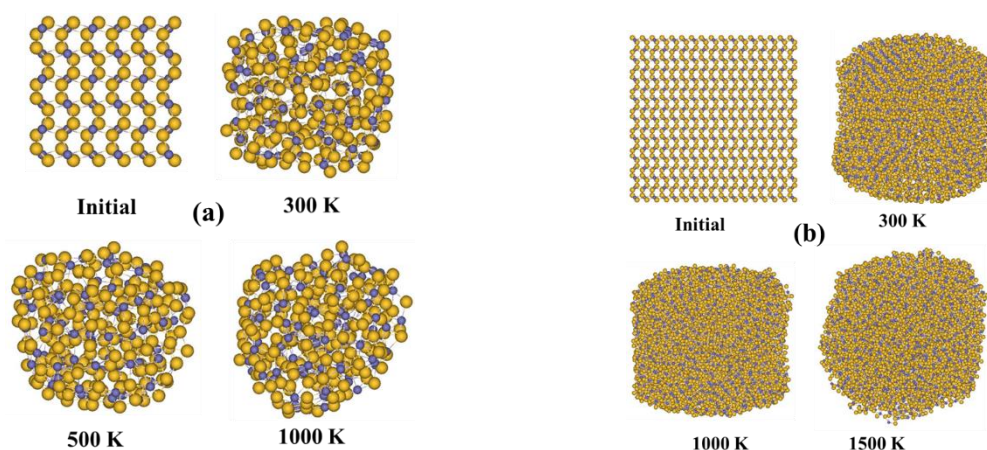


Figure 4: Structural changes of FeS₂ nanostructures with a) 324 atoms and b) 7369 atoms before and after MD simulation at different temperatures.

Figure 4 show the initial configuration structures and the structural changes of FeS₂ nanostructures (with 324 and 7369 atoms) at elevated temperatures. It can be seen that the nanostructures retain their cubic shapes more below the transition temperature as the particle size increases. For a nanostructure with 324 atoms the cubic structure is maintained at the temperature of 300 K, however at the elevated temperatures (from 500 K), the atomic arrangement disappear. In the case of a nanostructure with 7369 atoms the cubic shape is maintained up to the temperature of 1000 K, and disordering is observed at a higher temperature of 1500 K. This implies that the structural stability of the nanostructure is retain at higher temperature as the particle size increases.

4. Conclusion

Molecular dynamics simulations were performed with the aim of investigating the dynamic and structural properties of pyrite FeS₂ nanostructures. It was observed that the temperature of melting transition increased with an increase in particle size. The melting of nanostructures was observed through the variation of energy as a function of temperature, whereby there is a sudden change of slope at a certain temperature, indicative of phase transition. At low temperatures the RDFs have many and sharp peaks, however, at higher temperatures the RDFs curve are relatively smooth and does not exhibit any defined peaks, indicative of structural change from solid to liquid phase. The height of the peaks are also reduced as the temperature increases. The structural snapshots suggest that the nanostructure with less number of atoms maintain their cubic shape up to 500 K and for the nanostructures with large number of atoms maintain their cubic form up to 1000 K. This implies that the stability of the nanostructure increase as the particle size increases. We further observed that the change in energy gradient associated with the melting transition occurred at almost similar temperatures associated with the stretching and broadening of the RDFs. Molecular dynamic simulations of FeS₂ nanostructures provided in this study will give more understanding in the prediction of their structural and dynamic properties for developing new applications, especially in the next-generation of photovoltaic. Furthermore, the properties presented in this study could form as a basis for future studies.

Acknowledgements

The computations were performed at the Materials Modelling Centre (MMC), University of Limpopo and at the Centre for High Performance Computing (CHPC), Cape Town. We also acknowledge the National Research Foundation (NRF) for funding.

References

- [1] Spagnoli D and Gale J G 2012 *Nanoscale* **4** 1051.
- [2] Akbarzadeh H, Abroshan H and Parsafar G A, 2010 *Solid State Commun.* **150**, 254.
- [3] Heikkilä E, Martinez-Seara A A, Hakkinen H, Vattulainen I and Akola J 2012 *J. Phys. Chem.* **166**, 9805.
- [4] Rui X, Tan H and Yan Q 2014 *Nanoscale* **6** 9889.

- [5] Bi Y, Exstrom C L, Darveau S A and Huang I 2012 *Nano Lett.* **11**, 4953.
- [6] Chin P P, Ding J, Yi J B and Liu B H 2005 *J. Alloys. Compd.* **390** 255.
- [7] Trinh T K, Pham V T H, Truong N T N, Kim C D and Park C 2017 *J. Cryst. Growth.* **461** 53.
- [8] Macpherson H and Stoldt C R 2012 *ACS Nano* **6**, 8940.
- [9] Caban-Acevedo M, Faber M S., Tan Y, Hamers R J and Jin S 2012 *Nano Lett.* **12** 1977.
- [10] Suh Y J, Prikhodko S V and Friedlander S K *Microsc. Microanal.* 2002 **8** 497.
- [11] Rodrigues A M, Rino J P, Pizani P S and Zannotto E D 2016 *J. Phys. D: Appl. Phys.* **49** 1.
- [12] Liu S, Li Y, Yang J, Tian H, Zhu B and Shi Y 2014 *Phys. Chem. Miner.* **41** 189.
- [13] Huang S-Y, Sodano D, Leonard T, Luiso S and Fedkiw P S 2017 *J. Electrochem. Soc.* **164** F276.
- [14] Watson G W, Kelsey E T, de Leeuw N H, Harris D J and Parker S C 1996 *J. Chem. Soc. Faraday Trans* **92** 433.
- [15] Wulff G Z 1901 *Krystallogr. Minera.* **34** 449.
- [16] Mehlae M A, Parker S C and Ngoepe P E 2015 in *Proceedings of the 60th Annual Conference of the South African Institute of Physics* edited by M. Chithambo and A. Venter, (SAIP2015, Richard's Bay, South Africa,) 67.
- [17] Smith W and Forester T R 1996 *J. Mol. Graphics* **14** 136.
- [18] Nosé S 1990 *J. Phys.:Condens. Matter* **2** 115.
- [19] Rühle V 2008 *Berendsen and Nose-Hoover thermostats*
<http://www2.mpipmainz.mpg.de/~andrienk/journal club/thermostats.pdf>, (University of Mainz, Journal Club) Accessed 02 May 2019.
- [20] Verlet L 1967 *Phys. Rev.* **159** 98.
- [21] Born M and Huang K 1954 *Dynamical Theory of Crystal Lattices*, 1st ed. (University Press, Oxford).
- [22] de Leeuw N H, Parker S C, Sithole H M and Ngoepe P E 2000 *J. Phys. Chem. B* **104** 7969.
- [23] Adnan A and Sun C T 2008 *Nanotechnology* **19** 1.
- [24] Okeke G, Antony S J, Hammond R B and Ahmed K 2017 *J. Nanopart. Res.* **19** 237.

Lattice thermal conductivity of bulk PtTe₂ and PtSe₂

Hamza A H Mohammed^{1,2*}, Daniel P Joubert¹ and G M Dongho Nguimdo³

¹The National Institute for Theoretical Physics, School of Physics and Mandelstam Institute for Theoretical Physics, University of the Witwatersrand, Johannesburg, Wits 2050, South Africa.

²Department of Physics, Shendi University, Shendi, Sudan

³College of Graduate Studies, University of South Africa, Pretoria, Unisa 0003, South Africa

E-mail: hamzad00@gmail.com

Abstract. Thermoelectric devices can play a role in efficiently using available energy by converting heat produced by a wide range of devices into electricity. Low lattice thermal conductivity is a requirement for efficient thermoelectric devices and layered materials offer potential in reducing the lattice thermal conductivity perpendicular to the layers. We present density functional theory calculations of the structural and lattice thermal properties of layered platinum dichalcogenides PtTe₂ and PtSe₂ compounds in the CdI₂ structure, space group $P\bar{3}m1$. Phonon and elastic constants calculations confirm that the compounds are dynamically and mechanically stable. Lattice thermal conductivities were calculated within the single-mode relaxation-time approximation of the linearized phonon Boltzmann equation. We found that at the room temperature, the in-plane lattice thermal conductivities for PtTe₂ and PtSe₂ are 6.54 and 9.33 Wm⁻¹K⁻¹, while perpendicular to the plane they are 1.8 and 2.06 Wm⁻¹K⁻¹, respectively. The out-of-plane thermal conductivities confirm that further investigation of PtTe₂ and PtSe₂ as thermoelectric materials is necessary.

1. Introduction

Thermoelectricity is the simplest technology applicable for direct thermal-electrical energy conversion. Thermoelectric (TE) devices can directly convert heat to clean electricity or work in "reverse" as a heat pump, without any noise, hazardous liquids, or greenhouse-gas emissions [1]. To evaluate thermoelectric performance, the dimensionless figure of merit $ZT = \frac{S^2\sigma}{\kappa}T$ is often used. Here S is the Seebeck coefficient, σ is the electrical conductivity, κ is the total thermal conductivity which is a sum of lattice contribution (κ_L) and electronic contribution (κ_e), and T is the temperature. It is rare to have a large Seebeck coefficient and metallic conductivity simultaneously. The discovery of NaCo₂O₄, which is a metallic transition-metal oxide, had a great impact on the search for thermoelectric materials since it has both a relatively high conductivity and a large Seebeck coefficient [3]. Transition-metal dichalcogenides (MX₂, M = transition metal, X = chalcogen) with CdI₂ trigonal structure and space group $P\bar{3}m1$ (No. 164) have layers that are weakly bound by long range van der Waals forces. Intercalation of many molecular and atomic species has been achieved in these materials, and the impact on their structural, magnetic, and electronic properties have been characterized [4] and a few MX₂ compounds have been the focus of thermoelectric studies [5]. Transition metal dichalcogenides (TMDs) have attracted a lot of attention in recent years due to their various applications,

including electrocatalysis, optoelectronics, supercapacitors and batteries [6].

Recently, PtTe₂ was reported to be a Lorentz violating type-II Dirac semimetal [7]. Its sister compound PtSe₂ has also been predicted to be a type-II Dirac semimetal. So far experimental research in bulk PtSe₂ crystals has been limited due to the lack of high quality single crystals [8]. In this work we investigated the lattice thermal conductivity of PtTe₂ and PtSe₂ and found that they have promising thermoelectric properties because of their relatively small lattice thermal conductivity.

2. Computational details

All calculations in this work were performed using Density Functional Theory (DFT) with the projector-augmented wave (PAW) pseudopotential [9] approach as implemented in the VASP package [10]. The generalized gradient approximation (GGA) of Perdew, Burke and Ernzerhof (PBE) [11] and its modified form for solid materials, PBEsol [12], were used as exchange correlation approximations. We performed calculations using an energy cut-off of 520 eV which leads to a total energy tolerance of about 0.1 meV. For the integration over the BZ, a Γ -centered Monkhorst-pack grid [13] of $8 \times 8 \times 6$ was found to be sufficient. Long range interactions important in TMD compounds are not accounted for in the PBE and PBEsol approximations. Since they are often approximated by van der Waals corrections, we examined the effects of vdW-D2 [14], vdW-D3 [15] and vdW-TS [16] van der Waals corrections in conjunction with a PBE exchange-correlation approximation in this study. A $3 \times 3 \times 3$ supercell was used for displacive phonon calculations [17] and for solving the linearized lattice Boltzmann transport equation in the single mode relaxation time approximation [19] using the phonopy [18] and phono3py [19] packages, respectively. In the thermal conductivity calculation 1057 unique triplet displacements were included in the calculation of the scattering terms [19].

3. Results and discussion

3.1. Structural parameters

We first present the calculated total binding energy against the cell volume for the studied PtTe₂ and PtSe₂ under the PBEsol, vdW-D3, vdW-D2 and vdW-TS approximations in Figure 1 and Figure 2 respectively. The solid line shows a third order Murnaghan equation of state [20] fit to the calculated data. The fully optimized equilibrium lattice constants of PtTe₂ and PtSe₂ for different approximations compared with experimental data are listed in Table 2. We observe that the formation and cohesive energies are negative, indicating that the reaction leading to the formation of the PtTe₂ and PtSe₂ structures is exothermic, suggesting that structures can be formed from their constituent atoms [21]. The a and b lattice parameters, the in-layer structural parameters, show the least variation across the different approximations. The interlayer spacing, defined by the c lattice parameter, show the most variation. We note that PBEsol gives the best equilibrium structural parameters for the PtTe₂ and PtSe₂, when compared to experiment. This is surprising, since for other layered transition metal dichalcogenides, for example MoX₂ compounds [22], van der Waals corrections are important in the simulated search for reasonable interlayer spacings.

3.2. Elastic stability

Elastic constants of PtTe₂ and PtSe₂ were calculated in order to check the mechanical stability. PtTe₂ and PtSe₂ in the trigonal $P\bar{3}m1$ symmetry has eight independent elastic constants, shown in Table 2. The elastic constants in Table 2, satisfy all the Born stability criteria [25], which indicate that PtTe₂ and PtSe₂ compounds are mechanically stable. Voigt (V) and Reuss (R) approximations [26] tend to give upper and lower limits of the mechanical and thermodynamic properties of a material, respectively. It was shown by Hill that the Reuss moduli are always less than the Voigt moduli, and the true values are expected to lie between the two approximations

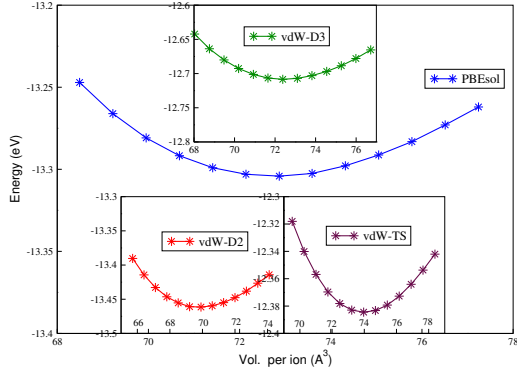


Figure 1. Calculated total binding energy versus cell volume, of PtTe₂ using PBEsol, vdW-D2, vdW-D3 and vdW-TS approximations.

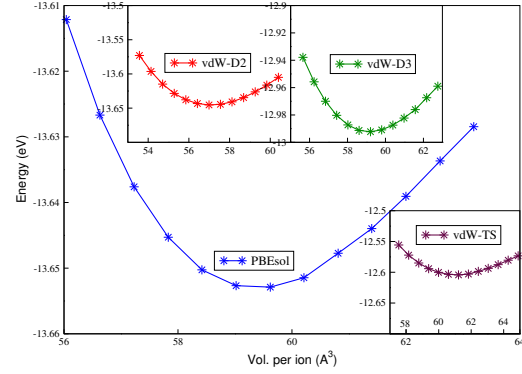


Figure 2. Calculated total binding energy versus cell volume, of PtSe₂ using PBEsol, vdW-D2, vdW-D3 and vdW-TS approximations.

Table 1. Calculated equilibrium lattice parameters, cohesive energy (E_{coh}) per atom and formation energy (E_{form}) per atom, bulk modulus B_0 (GPa), together with the experimental structural values of PtTe₂ and PtSe₂.

		$a = b(\text{\AA})$	$c(\text{\AA})$	$V_o(\text{\AA}^3)$	$E_{coh}(\text{eV})$	$E_{form}(\text{eV})$	$B_0(\text{GPa})$
PtTe ₂	PBEsol	4.049	5.114	72.04	-4.43	-0.40	60
	vdW-D2	4.012	5.019	70.01	-4.48	-0.19	74
	vdW-D3	4.072	5.042	72.44	-4.23	-0.36	65
	vdW-TS	4.095	5.087	73.89	-4.13	-0.37	64
	Exp.[24]	4.010	5.201	72.43	—	—	—
PtSe ₂	PBEsol	3.765	4.976	61.11	-4.55	-0.43	50
	vdW-D2	3.771	4.622	56.94	-4.55	-0.23	84
	vdW-D3	3.794	4.743	59.14	-4.33	-0.40	64
	vdW-TS	3.809	4.871	61.24	-4.20	-0.38	57
	Exp.[23]	3.727	5.081	61.15	—	—	—

[27]. Therefore, in this work, we consider the Hill method to derive the bulk modulus, elastic modulus and crystal elastic constant, as an average of the Voigt and Reuss values. Young's modulus (E) is the tendency of an object to deform along an axis when opposing forces are applied along that axis. Bulk moduli (B), describe the volumetric elastic tendency of an object to deform in all directions when uniformly loaded. We can loosely express it as an extension of Young's modulus in 3D. Shear moduli (G), describes the tendency of an object to shear (the deformation of shape at a constant volume) when acted upon by opposing forces. Poisson's ratio (ν), is associated with the nature of the atomic bonding. The values of bulk moduli obtained by the Birch equation of state shown in Table 2, is lower than that which are obtained by Hill approach shown in Table 2. The Young's moduli are higher than the bulk moduli and are similar to the Young's moduli of Silicon (Si) which is in range 133 - 188 GPa [28]. As stated before, Poisson's ratio (ν) provides information on bonding nature. Poisson's ratio for ionic bonding is

equal to or greater than $\nu = 0.25$ [29]. The calculated results of $\nu = 0.25 \sim 0.24$ for PtTe₂ and PtSe₂ suggest marginal ionic bonding.

Table 2. Elastic constants C_{ij} (GPa), elastic bulk moduli B_V (GPa), shear moduli G (GPa), Young's moduli E (GPa), Poisson's ratio and for of PtTe₂ and PtSe₂.

		C_{11}	C_{12}	C_{13}	C_{22}	C_{33}	C_{44}	C_{55}	C_{66}	B_V	E	G	ν
PtTe ₂	PBEsol	170	53	42	170	67	45	45	58	68	105	42	0.24
	vdW-D2	200	62	55	200	83	65	65	68	84	129	52	0.24
	vdW-D3	175	52	48	175	77	49	49	61	74	111	44	0.25
	vdW-TS	169	52	42	169	69	42	42	58	68	103	41	0.24
PtSe ₂	PBEsol	197	67	41	197	51	40	40	64	66	102	41	0.24
	vdW-D2	262	83	62	262	94	69	69	89	101	157	63	0.24
	vdW-D3	202	63	41	202	61	43	43	69	71	111	45	0.24
	vdW-TS	183	59	41	183	62	38	38	61	68	102	40	0.25

3.3. Dynamical stability

In order to test the dynamic stability of the PtTe₂ and PtSe₂, their underlying phonon dispersion relations were calculated. Since PBEsol gave the best lattice parameters, it was used in the computations of the phonon structure. The phonon band structure and density of states for PtTe₂ and PtSe₂ are presented in Figure 3 and Figure 4 respectively. The phonon frequencies are in the range of 0 – 6 THz for PtTe₂ and 0 – 7 THz for PtSe₂. The reduction in the range can be attributed to the relative atomic weights of Te and Se. All the phonon frequencies are positive, which indicates that the structure of PtTe₂ and PtSe₂ are dynamically stable, thereby satisfying one of the necessary conditions for crystal stability.

The primitive cell of PtTe₂ and PtSe₂ contains three atoms and therefore there are nine phonon modes for each wave vector, three acoustic modes and six optical modes. The highest frequencies of the acoustic modes, defined here as the acoustic cutoff, are approximately 3.44 THz and 4.58 THz for PtTe₂ and PtSe₂, respectively.

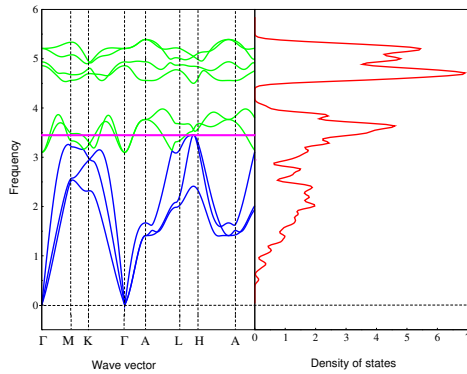


Figure 3. Phonon dispersion and DOS for PtTe₂.

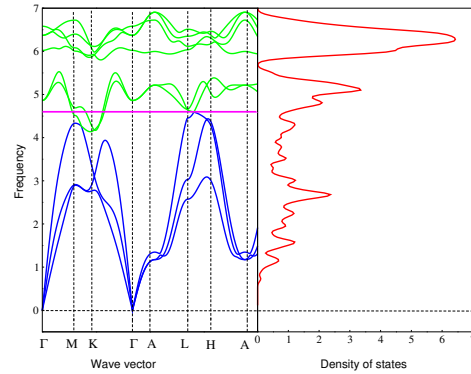


Figure 4. Phonon dispersion and DOS for PtSe₂.

3.4. Lattice thermal conductivity

The lattice thermal conductivity of PtTe₂ and PtSe₂ was calculated using the single-mode relaxation-time approximation to the linearized phonon Boltzmann equation [19]. The calculated lattice thermal conductivities of PtTe₂ and PtSe₂ in the range 0 to 1000 K are shown in Figure 5 and Figure 6 respectively, while the average of the cumulative thermal conductivities, as function of frequency at 300 K, are shown in Figure 7 and Figure 8 respectively. We note that the lattice thermal conductivity is highly anisotropic, with the thermal conductivity in the plane of the layers much higher than in the cross-plane direction.

Using Mattheissens rule [30] the average lattice thermal conductivity of PtTe₂ and PtSe₂ is 3.49, and 4.28 Wm⁻¹K⁻¹ respectively. The lattice thermal conductivities of these compounds is therefore small, which makes these compounds potential good thermoelectric materials.

We also estimated the contribution to the thermal conductivity from the acoustic modes at 300 K. We found that the in-plane acoustic mode contribution is 88.36% and 87.63% and cross-plane 71.34% and 68.00% for PtTe₂ and PtSe₂ respectively. This is in clear contrast to the conventional understanding, especially in the cross-plane direction, that the acoustic modes dominate thermal conductivity [30].

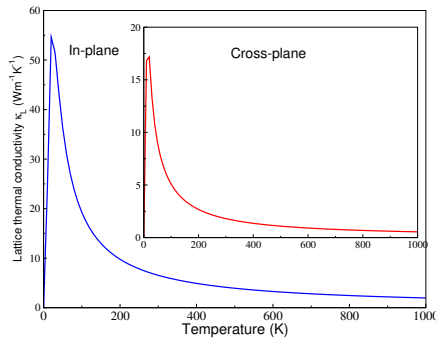


Figure 5. Lattice thermal conductivity Wm⁻¹ K⁻¹ $\kappa_L(T)$ for PtTe₂.

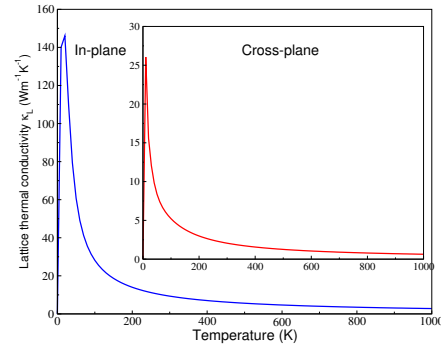


Figure 6. Lattice thermal conductivity Wm⁻¹ K⁻¹ $\kappa_L(T)$ for PtSe₂.

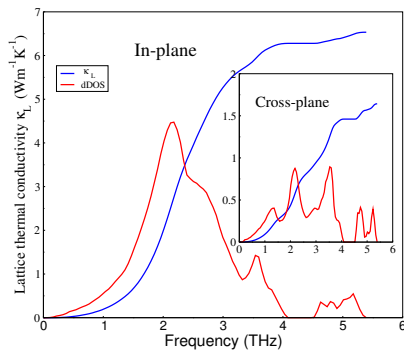


Figure 7. Average cumulative lattice thermal conductivity and derivative density $\kappa_L(\omega)$ for PtTe₂.

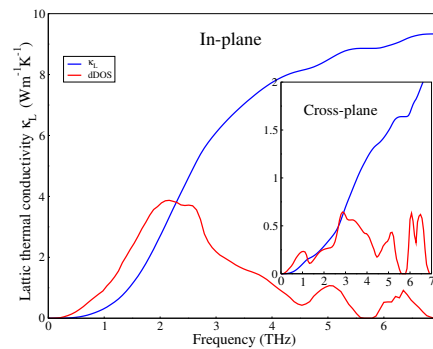


Figure 8. Average cumulative lattice thermal conductivity and derivative density $\kappa_L(\omega)$ for PtSe₂.

4. Conclusion

We have investigated the structural, mechanical and dynamical properties as well as the lattice thermal conductivity of bulk PtTe₂ and PtSe₂ from a first principles Density Functional Theory approach. Furthermore, we showed that the thermal conductivity of bulk PtTe₂ and PtSe₂ is highly anisotropic with the in-plane thermal conductivity much higher than the cross-plane thermal conductivity. The low value of the lattice thermal conductivity in the out-of-plane direction for both structures suggests that these materials are good candidates for thermoelectric applications.

Acknowledgements

We would like to acknowledge the financial support received from Shendi University, Shendi, Sudan. We also wish to acknowledge the Center for High Performance Computing (CHPC), Cape Town, South Africa, for providing us with computing facilities.

References

- [1] Holgate T C, *et al* 2013 *J. Elec. Mater.* **42** 1751–1755.
- [2] Mahan G D 1979 *Solid State Phys.* **51** 81–157.
- [3] Terasaki I, Sasago Y and Uchinokura K 1997 *Phys. Rev. B.* **56** R12685.
- [4] Yoffe A D 1983 *Solid State Ion.* **9** 59–69.
- [5] Hor S and Cava J 2009 *Mater. Res. Bull.* **44** 1375–1378.
- [6] Chen X, Wang M, Mo C and Lyu S 2015 *J. Phys. Chem. C* **119** 26706–26711.
- [7] Yan M, *et al* 2017 *Nat. Commun.* **8** 257.
- [8] Zhang K, *et al* 2017 *Phys. Rev. B* **96** 125102.
- [9] Kresse G and Joubert D 1999 *Phys. Rev. B* **59** 1758.
- [10] Kresse G and Furthmüller J 1996 *Comput. Mater. Sci.* **6** 15–50.
- [11] Perdew P, Burke K and Ernzerhof M 1996 *Phys. Rev. Lett.* **77** 3865.
- [12] Ruzsinsky A, Csonka G I and Vydrov O A 2008 *Phys. Rev. Lett.* **100** 136406.
- [13] Monkhorst J and Pack D 1976 *Phys. Rev. B* **13** 5188.
- [14] Bucko T, Hafner J, Lebegue S and Ángyán J G 2010 *J. Phys. Chem. A* **114** 11814–11824.
- [15] Moellmann J and Grimme S 2014 *J. Phys. Chem. C* **118** 7615–7621.
- [16] Bučko T, Lebegue S, Ángyán J G and Hafner J 2014 *J. chem. phys.* **141** 034114.
- [17] Togo A, Chaput L and Tanaka I 2015 *Phys. Rev. B* **91** 094306.
- [18] Togo A, and Tanaka I 2015 <http://phonopy.sourceforge.net>.
- [19] Togo A and Tanaka I 2015 *Scr. Mater.* **108** 1–5.
- [20] Murnaghan D 1944 *Proc. Natl. Acad. Sci.* **30** 244–247.
- [21] Lamfers J, Meetsma A, Wieggers A and De Boer L 1996 *J. Alloys Compd.* **241** 34–39.
- [22] Zappa D 2017 *Materials.* **10** 1418.
- [23] Furuseth S, Selte K and Kjekshus A 1965 *Acta Chem. Scand.* **19** 257.
- [24] Thomassen L 1929 *J. Phys. Chem.* **2** 349–379.
- [25] Mouhat F and Coudert X 2014 *Phys. Rev. B.* **90** 224104.
- [26] Luo J and Stevens R 1996 *J. Appl. Phys.* **79** 9057–9063.
- [27] Hill R 1952 *J. Proc. Phys. Soc.* **65** 349.
- [28] Hopcroft M A, Nix W D and Kenny T W 2010 *J. Microelectromech. S* **19** 229–238.
- [29] Bouhemadou A, *et al* 2009 *Comput. Mater. Sci.* **45** 474–479.
- [30] Kittel C 2005 *Introduction to solid state physics* (USA: John Wiley and Sons, Inc).

Magnetic and physical properties of new hexagonal compounds PrPt_4X ($X = \text{Ag}, \text{Au}$)

Michael O Ogunbunmi and André M Strydom

Highly Correlated Matter Research Group, Physics Department, University of Johannesburg,
P. O. Box 524, Auckland Park 2006, South Africa.

E-mail: mogunbunmi@uj.ac.za, moogunbunmi@gmail.com

Abstract. We have synthesized PrPt_4Ag and PrPt_4Au compounds for the first time and report their crystal structure, as well as magnetic and physical properties in the temperature range of 1.9 K to 300 K. Both compounds are derived from the substitution of Pt with Ag and Au, respectively in the parent compound PrPt_5 which crystallizes in the hexagonal CaCu_5 -type structure. Here we observed the preservation of the hexagonal CaCu_5 -type structure under such substitutions, which is in contrast to the observations in PrCu_4Ag and PrCu_4Au adopting the cubic MgCu_4Sn -type structure upon substitution on parent hexagonal PrCu_5 . The temperature dependences of specific heat $C_p(T)$, and electrical resistivity $\rho(T)$ of PrPt_4Ag show an anomaly at 7.6 K. This is absent in the magnetic susceptibility $\chi(T)$, thus suggesting a possible multipolar ordering of the Pr^{3+} moment. PrPt_4Au on the other hand does not show any anomaly but an upturn in $C_p(T)/T$ below about 10 K and attains $1.23 \text{ J}/(\text{mol K}^2)$ at 1.9 K. In addition, $\rho(T) \sim T$ for nearly a decade in temperature. These observations for PrPt_4Au are the hallmark of a non-Fermi liquid (nFL) behavior and is characteristic of a system near a quantum critical point. The analyses of the low-temperature $C_p(T)$ for PrPt_4Ag and PrPt_4Au give values of the Sommerfeld coefficient, $\gamma = 728.5 \text{ mJ}/(\text{mol K}^2)$ and $509.1 \text{ mJ}/(\text{mol K}^2)$, respectively, indicating a significant enhancement of the quasiparticle mass in the two compounds.

1. Introduction

PrPt_5 is a Van-Vleck paramagnet that has been studied mostly for nuclear cooling by adiabatic demagnetization [1]. This technique profits from the high nuclear spin ($I = 5/2$) of the only known stable ^{141}Pr isotope. It crystallizes in the hexagonal CaCu_5 -type structure with space group $P6/mmm$ (No. 191) [2]. It has been observed that the lack of magnetic ordering in PrPt_5 is associated with its weak exchange interaction [3]. In addition, magnetization studies have revealed a nuclear spontaneous ferromagnetic Weiss temperature, $\theta_p = 2 \text{ mK}$, which is attributed to nuclear hyperfine enhancement in the system [4]. In a substitution study by Malik *et al.* [5], the RPt_4In ($R = \text{La-Tm}$) compounds, which represent a doping of 20% on the Pt site, were reported to adopt the cubic MgCu_4Sn -type structure with the exception of TmPt_4In which forms in the Cu_3Au -type structure. Also, ErPt_4In and HoPt_4In were observed to possess a mixture of MgCu_4Sn and Cu_3Au phases as evidenced from the X-ray diffraction patterns. PrPt_4In was reported to remain paramagnetic down to 4.2 K [5]. Here we report the synthesis, as well as the magnetic and physical properties of the new compounds PrPt_4Ag and PrPt_4Au . Interestingly, it was found that both compounds crystallize in the same hexagonal CaCu_5 parent structure. This is in contrast with the observations in PrCu_4Ag and PrCu_4Au [6, 7] which adopt

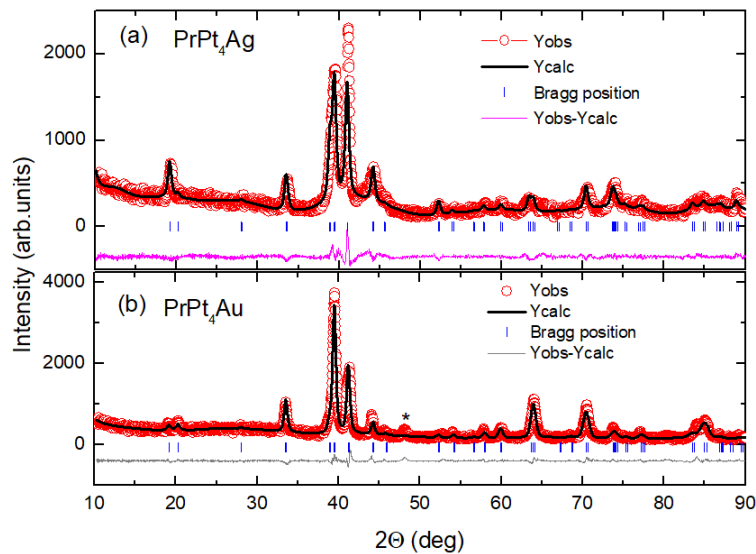


Figure 1. Powder X-ray diffraction patterns of PrPt_4Ag and PrPt_4Au shown in (a) and (b) with Rietveld refinements (black lines) based on the $P6/mmm$ space group. The vertical bars are the Bragg peak positions, while the difference between the experimental and calculated intensities are shown as pink and gray lines, respectively. The peak in the PrPt_4Au spectrum marked with an asterisk does not belong to the major phase as discussed in the text.

the cubic MgCu_4Sn -type structure similar to those of RPt_4In compounds reported by Malik *et al.* [5].

2. Experimental methods

Polycrystalline samples of PrPt_4Ag and PrPt_4Au were prepared by arc melting stoichiometric amounts of high-purity elements (wt.% ≥ 99.9) on a water-cooled Cu plate under a purified static argon atmosphere in an Edmund Buehler arc furnace. The weight losses for both compounds were $\sim 0.09\%$. The arc-melted pellets were then wrapped in Ta foil, placed in an evacuated quartz tube and annealed at 800°C for 14 days so as to improve the quality of the samples. Room temperature powder X-ray diffraction (XRD) patterns were recorded on pulverized samples using a Rigaku diffractometer employing $\text{Cu-K}\alpha$ radiation. The XRD patterns with the Rietveld refinements [8] employing the FullProf suite of programs [9] are shown in Fig. 1. The lattice parameters obtained from the Rietveld refinements are presented in Table 1. For both compounds, the XRD results confirm phase formation of the desired compounds. For the case of PrPt_4Au , a spurious peak, barely resolved above the background noise was detected at $2\theta = 48^\circ$. It was verified that this peak does not have its origin in any of the elements Pr, Pt or Au thus the origin of this peak remains unknown.

Magnetic properties were measured using the Magnetic Property Measurement System (Quantum Design Inc., San Diego) between 1.8 K and 300 K with an external magnetic field up to 7 T. The four-probe DC electrical resistivity, specific heat and thermal transport between 1.9 K and 300 K were measured using the Physical Property Measurement System also from Quantum Design.

3. Magnetic properties

The temperature dependences of magnetic susceptibility $\chi(T)$ of both compounds in an external field of 0.1 T are shown in Fig. 2 (a) and (b). From the plots, $\chi(T)$ of both compounds are

Table 1. Lattice parameters of PrPt₄Ag and PrPt₄Au obtained from the Rietveld refinements of their XRD patterns.

Compound	<i>a</i> (Å)	<i>c</i> (Å)	<i>V</i> (Å ³)	<i>R_p</i> (%)	<i>R_{wp}</i> (%)	χ ²
PrPt ₄ Ag	5.344(2)	4.399(2)	108.8(9)	9.597	12.25	4.596
PrPt ₄ Au	5.343(3)	4.378(5)	108.3(8)	8.957	11.89	4.875

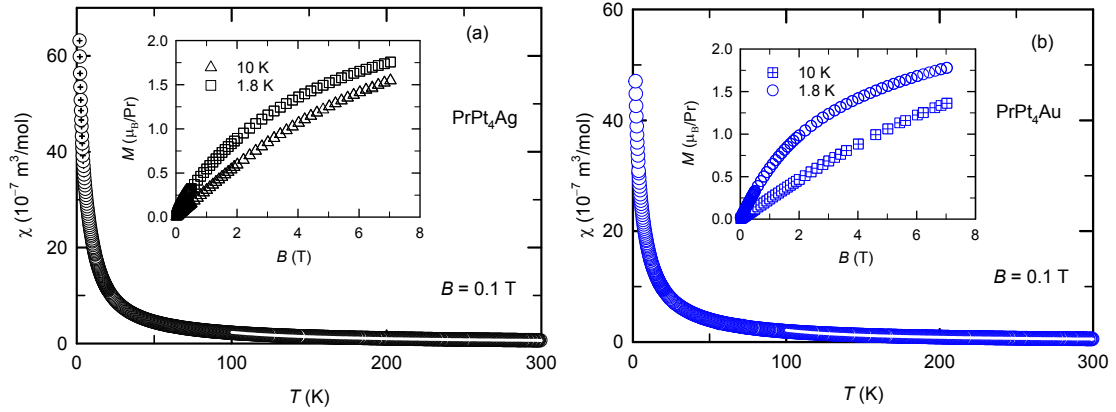


Figure 2. (a) Temperature dependence of magnetic susceptibility $\chi(T)$ of PrPt₄Ag in an external field of 0.1 T with a Curie-Weiss fit shown as a white line. Inset: Isothermal magnetization of PrPt₄Ag at 1.8 K and 10 K. (b) Plot of χ against T for PrPt₄Au with a Curie-Weiss fit represented by the white line. Inset: Isothermal magnetization of PrPt₄Au at 1.8 K and 10 K.

qualitatively similar and show no visible anomaly down to 1.9 K. For temperatures above 100 K, $\chi(T)$ for both compounds follow a Curie-Weiss behavior based on the expression: $\chi(T) = N_A \mu_{\text{eff}}^2 / (3k_B(T - \theta_p))$, where μ_{eff} is the effective magnetic moment, θ_p is the Weiss temperature, N_A is the Avogadro number and k_B is the Boltzmann constant. From the least-square fits shown as white lines in Fig. 2 (a) and (b), values of $\mu_{\text{eff}} = 3.30 \mu_B/\text{Pr}$, $\theta_P = 95.10$ K and $\mu_{\text{eff}} = 3.15 \mu_B/\text{Pr}$, $\theta_P = 99.16$ K for PrPt₄Ag and PrPt₄Au, respectively are obtained. These values of μ_{eff} are slightly reduced in comparison to the value of $3.58 \mu_B/\text{Pr}$ calculated for a free Pr³⁺ ion. Such reduction in μ_{eff} can be attributed to the crystalline electric field (CEF) effect on the Pr³⁺ moment. The isothermal magnetization for both compounds measured at temperatures of 1.8 K and 10 K are shown in the insets to Fig. 2 (a) and (b). The magnetization trend shows a little curvature at 10 K which becomes more pronounced at 1.8 K for both compounds. PrPt₄Ag and PrPt₄Au attain magnetization of $\approx 1.8 \mu_B/\text{Pr}$ at 7 T, which is about 50% reduced compared to the value of $3.2 \mu_B/\text{Pr}$ expected for a free Pr³⁺ ion. Assuming that at a temperature of 1.8 K no higher-lying levels of the $J = 4$ multiplet of Pr are occupied, we attribute this deficiency in the extracted magnetization to the effects of magneto-crystalline anisotropy in both compounds.

4. Specific heat

The temperature dependence of the specific heat $C_p(T)$ between 1.9 K and 300 K for PrPt₄Ag and PrPt₄Au are shown in Fig. 3 (a) and (b). Values of ≈ 150 J/(mol K) are observed at room temperature for both compounds, which correspond to the Dulong-Petit value. In inset (i) of Fig. 3 (a), the low- T plot of C_p/T against T for PrPt₄Ag is shown. At 7.6 K an anomaly with a broad feature is observed. The electrical resistivity results to be presented in Section 5 also

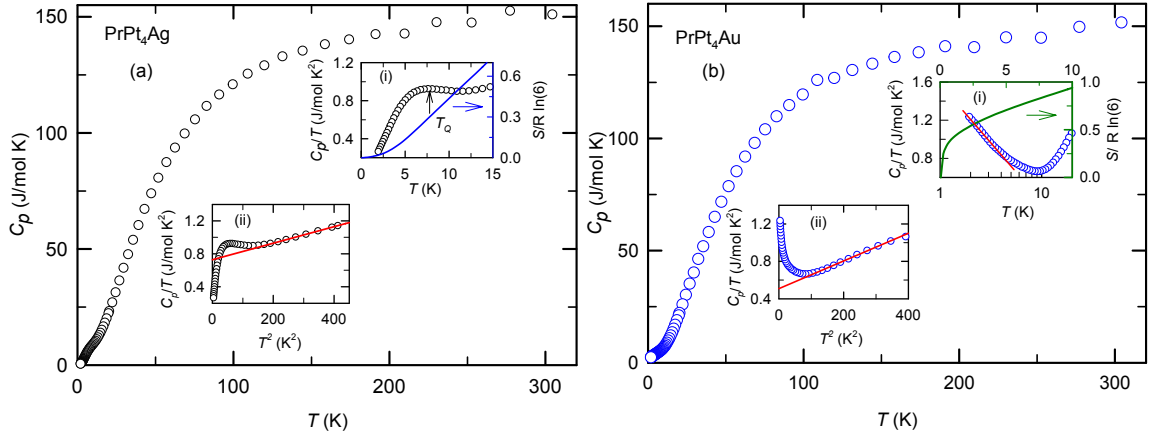


Figure 3. (a) Temperature dependence of specific heat $C_p(T)$ of PrPt₄Ag. Inset (i): Low- T plot of C_p/T against T with the arrow indicating the phase transition at T_Q . Also shown is the calculated entropy (blue line) with axis on the right. Inset (ii): Plot of C_p/T against T^2 for PrPt₄Ag together with a linear fit (red line) to extract the Sommerfeld coefficient. (b) Plot of C_p against T for PrPt₄Au. Inset (i): Plot of C_p/T against T on a semi-log axis. The red line is a guide to the eye indicating a logarithmic divergence of $C_p(T)/T$. The calculated entropy (green line) is also shown with axis on the right. Inset (ii): Plot of C_p/T against T^2 for PrPt₄Au together with a linear fit (red line) to extract the Sommerfeld coefficient.

reveal an anomaly around the same temperature. No such an anomaly is however observed in $\chi(T)$ presented in the previous section, thus suggesting a possible multipolar ordering of the Pr³⁺ moment in PrPt₄Ag. This is supported by the Van-Vleck paramagnetism observed in $\chi(T)$ indicating that spins or dipolar order do not play a detectable role in the anomaly. In the absence of a long-range magnetic order in Pr systems, the 4*f*-electrons orbitals are the only effective degrees of freedom and multipolar ordering of the Pr³⁺ moment can be realized [10, 11]. Also shown is the plot of the calculated entropy. At T_Q only an amount of $0.3R\ln(6)$ is released which is only about one third of the total entropy expected. The plot of C_p/T against T on a semi-log scale for PrPt₄Au shown in inset (i) of Fig. 3 (b) shows an upturn below 10 K reaching a value of 1.23 J/(mol K²) at 1.9 K. We have also observed a linear-in- T behavior of $\rho(T)$ which is discussed in Section 5. These observations in PrPt₄Au are the hallmark of a non-Fermi liquid (nFL) behavior. Among many other reasons, proximity to a quantum critical point or possible spin/elemental disorder such as in doped systems could be responsible for such behavior [12]. The calculated entropy is also presented in the same plot. At 8 K, the recovered entropy is about $0.9R\ln(6)$ which is close to the full entropy expected.

We further analyzed the low- T behavior by plotting of C_p/T against T^2 for both compounds as shown in inset (ii) of Fig. 3 (a) and inset (ii) of Fig. 3 (b). Least-square fits to both sets of data (represented as red lines) based on the expressions: $C_p/T = \gamma + \beta T^2$ and $\beta = 12\pi^4 nR/(5\theta_D^3)$, where n and R are the number of atoms per formula unit and universal gas constant, respectively, γ is the Sommerfeld coefficient and θ_D is the Debye temperature are shown. From the fits, $\gamma = 728.50$ J/(mol K²) and 509.10 J/(mol K²) are obtained for PrPt₄Ag and PrPt₄Au, respectively. The observed γ values for these two compounds are more than two orders of magnitude greater than what is expected for an ordinary metal and qualitatively similar to those of the heavy fermion (HF) systems, where significant enhancement of the quasiparticles mass have been observed [13].

Table 2. A collection of estimated characteristic HF parameters of PrPt₄Ag and PrPt₄Au.

Compound	γ (mJ/(mol _{Pr} K ²))	A ($\mu\Omega\text{cm}/\text{K}^2$)	A/γ^2 ($\times 10^{-5}\mu\Omega\text{cm}(\text{mol}_{\text{Pr}} \text{K}/\text{mJ})^2$)	R_w
PrPt ₄ Ag	728.50	0.010	0.00188	1.38
PrPt ₄ Au	509.10	0.117	0.0449	1.62

5. Electrical transport

The temperature dependence of the electrical resistivity $\rho(T)$ for PrPt₄Ag and PrPt₄Au investigated between 1.9 K and 300 K are presented in Fig. 4 (a) and (b), respectively. The observed values of residual resistivity are ≈ 6 and ≈ 3 for PrPt₄Ag and PrPt₄Au, respectively. Both compounds show typical metallic behavior down to low temperatures. A broad curvature is observed at intermediate temperatures in PrPt₄Ag, which is common to rare-earth intermetallic systems; possibly associated to thermal de-population of the crystal field levels as temperature is lowered. A plot of $\rho(T)$ against T^2 presented in the inset of Fig. 4 (a) indicates a power law behavior based on the expression: $\rho(T) = \rho_0 + AT^2$. A fit of the expression to the data is shown as the red line. The residual resistivity, $\rho_0 = 10.46 \mu\Omega\text{cm}$ and the coefficient of the quadratic term, $A = 0.010 \mu\Omega\text{cm}/\text{K}^2$ are obtained. The Kadowaki-Woods ratio (KWR) [14], $A/\gamma^2 = 1.88 \times 10^{-8} \mu\Omega\text{cm}(\text{mol K}/\text{mJ})^2$ is obtained by using $\gamma = 728.5 \text{ mJ}/(\text{mol K}^2)$ obtained from $C_p(T)$ analysis. The relationship between $\chi(T)$ and γ is also evaluated using the Wilson ratio [15] given as: $R_w = \pi^2 k_B^2 \chi(T \rightarrow 0)/(\mu_{\text{eff}}^2 \gamma)$. Using the observed low- T values of $\chi(T \rightarrow 0) = 0.5025 \text{ emu/mol}$, $\gamma = 728.5 \text{ mJ}/(\text{mol K}^2)$ and $\mu_{\text{eff}} = 3.30 \mu_B/\text{Pr}$ yields $R_w = 1.38$ which is comparable to a value of unity expected for HF systems. Also, a little anomaly is noticeable in the low- T plot at $\sim 7.6 \text{ K}$ which coincides with the anomaly observed in $C_p(T)$ around the same temperature.

PrPt₄Au on the other hand is quasi-linear in nature down to low temperatures. In the inset of Fig. 4 (b), the low- T behavior of PrPt₄Ag is shown together with a fit (shown as red line) using the expression; $\rho(T) = \rho_0 + AT^n$. From the fit, the residual resistivity, $\rho_0 = 14.58 \mu\Omega\text{cm}$, $n = 1$ and $A = 0.117 \mu\Omega\text{cm}/\text{K}$ are obtained. Such a temperature dependence of $\rho(T)$ deviates from the Fermi-liquid behavior expected at low temperatures for normal metals. Results from $C_p(T)$ of PrPt₄Au discussed in Section 4 have also shown a temperature dependence that deviates from those of ordinary metals. Using the values of $A = 0.117 \mu\Omega\text{cm}/\text{K}^2$ and $509.10 \text{ mJ}/(\text{mol K}^2)$, yields $\text{KWR} = 4.49 \times 10^{-7} \mu\Omega\text{cm}(\text{mol K}/\text{mJ})^2$. Also, using the values of $\chi(T \rightarrow 0) = 0.3743 \text{ emu/mol}$, $\gamma = 509.10 \text{ mJ}/(\text{mol K}^2)$ and $\mu_{\text{eff}} = 3.15 \mu_B/\text{Pr}$ yields $R_w = 1.62$. The parameters observed in PrPt₄Ag and PrPt₄Au reveal both compounds as new HF systems.

6. Discussion and conclusion

The existence of the hexagonal PrPt₄Ag and PrPt₄Au compounds are reported together with their physical and magnetic properties. PrPt₄Ag shows a putative multipolar ordering at $T_Q = 7.6 \text{ K}$. From the crystal field levels permitted for the $J = 4$ multiplet in a D_{6h} local symmetry, one would expect to have 3 Γ_3 non-Kramers doublets and another 3 Γ_1 singlets. However, the observation of such an anomaly at T_Q makes Γ_3 the likely ground state in PrPt₄Ag. In contrast, the low- T region of PrPt₄Au shows a logarithmic divergence of $C_p(T)/T$, and a linear-in- T behavior of $\rho(T)$ below 10 K which is typical of a non-Fermi liquid behavior. These behaviors are likely associated with spin scatterings observed for a system in the proximity of a quantum critical point. Further analyses of $C_p(T)$ of both compounds reveal $\gamma = 728.50 \text{ J}/(\text{mol K}^2)$ and $509.10 \text{ J}/(\text{mol K}^2)$ for PrPt₄Ag and PrPt₄Au, respectively. In Table 2, a collection of characteristic HF parameters are presented for easy comparison with the observations in this work. The observation of enhanced γ value in systems with a Γ_3 non-Kramers ground state are often associated to the quadrupolar Kondo effect [10, 11]. Future studies will focus on

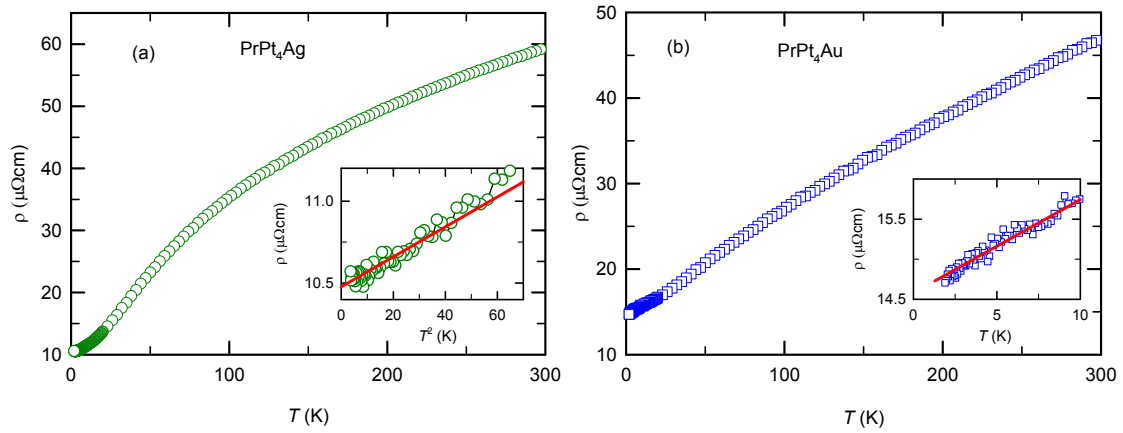


Figure 4. (a) Temperature dependence of electrical resistivity, $\rho(T)$, of PrPt_4Ag . Inset: Low- T plot of ρ against T^2 together with a fit (red line) described in the text. (b) Plot of $\rho(T)$ against T of PrPt_4Au . Inset: Low- T plot of ρ and the red line is a fit described in the text.

experiments below 2 K in order to further unravel the physics involved in the ground state of these two non-Kramers-ion systems.

Acknowledgment

MOO acknowledges the UJ-URC bursary for doctoral studies in the Faculty of Science. AMS thanks the SA-NRF (93549) and UJ-URC for financial support.

References

- [1] Andres K and Bucher E 1970 *Phys. Rev. Lett.* **24** 1181
- [2] Buschow K H J 1972 *J. Less Common Met.* **29** 283
- [3] Narasimhan K S V L, Rao V U S and Butera R A 1973 *AIP Conf. Proc.* **10** 1081
- [4] Karaki Y, Yotsui K, Kubota M and Ishimoto H 2000 *Physica B* **284-288** 1688
- [5] Malik S K, Vijayaraghavan R, Adroja D T, Padalia B D and Edelstein A S 1990 *J. Magn. Magn. Mater.* **92** 80
- [6] Zhang S, Mizushima T, Kuwai T and Isikawa Y 2009 *J. Phys. Condens. Matter* **21** 205601
- [7] Zhang S, Isikawa Y, Tayama T, Kuwai T, Mizushima T, Akatsu M, Nemoto Y and Goto T 2010 *J. Phys. Soc. Jpn.* **79** 114707
- [8] Thompson P, Cox D E and Hastings J B 1987 *J. Appl. Crystallogr.* **20** 79
- [9] Rodríguez-Carvajal J 1993 *Physica B* **192** 55
- [10] Suzuki O, S Suzuki H, Kitazawa H, Kido G, Ueno T, Yamaguchi T, Nemoto Y and Goto T 2005 *J. Phys. Soc. Jpn.* **75** 013704
- [11] Tanida H, S Suzuki H, Takagi S, Onodera H and Tanigaki K 2006 *J. Phys. Soc. Jpn.* **75** 073705
- [12] Schofield A J 1999 *Contemp. Phys.* **40** 95
- [13] Stewart G R 1984 *Rev. Mod. Phys.* **56** 755
- [14] Kadowaki K and Woods S B 1986 *Solid State Commun.* **58** 507
- [15] Wilson K G 1975 *Rev. Mod. Phys.* **47** 773

Crystal structure and thermodynamic properties of the non-centrosymmetric PrRu_4Sn_6 caged compound

Michael O Ogunbunmi and André M Strydom

Highly Correlated Matter Research Group, Physics Department, University of Johannesburg,
P. O. Box 524, Auckland Park 2006, South Africa.

E-mail: moogunbunmi@gmail.com, mogunbunmi@uj.ac.za

Abstract. PrRu_4Sn_6 is a tetragonal, non-centrosymmetric structure compound. It is isostructural to the extensively studied Kondo insulator CeRu_4Sn_6 which crystallizes in the YRu_4Sn_6 -type structure with space group $I\bar{4}2m$. In this structure, the Pr atom fills the void formed by the octahedral Ru_4Sn_6 units which results in a tetragonal body-centred arrangement. Here we present reports on the physical and magnetic properties of PrRu_4Sn_6 . The temperature dependences of specific heat, $C_p(T)$, electrical resistivity, $\rho(T)$, and magnetic susceptibility, $\chi(T)$, reveal the absence of a long-range magnetic ordering down to 2 K. $\chi(T)$ follows a Curie-Weiss behaviour above 100 K with an effective magnetic moment, $\mu_{\text{eff}} = 3.34 \mu_B/\text{Pr}$ and paramagnetic Weiss temperature, $\theta_p = -19.47$ K indicating a dominant antiferromagnetic interaction. The magnetization at 2 K is quasi-linear in nature and attains a value of $0.86 \mu_B/\text{Pr}$ at 7 T which is well reduced compared to the calculated value of $3.32 \mu_B/\text{Pr}$ expected for a free Pr^{3+} ion. This is attributed to possible magneto-crystalline anisotropy in the system. $C_p(T)$ indicates the presence of an optical-phonon mode which is supported by a glass-like thermal conductivity above ~ 45 K. This observation is associated with caged structured compounds where the low-frequency optical-phonon mode of the guest atom interacts with the host lattice, resulting in the scattering of heat-carrying quasiparticles.

1. Introduction

The RRu_4Sn_6 ($R = \text{Y, La-Nd, Sm, Gd-Ho}$) series are intermetallic compounds which crystallize in the tetragonal YRu_4Sn_6 -type structure with a non-centrosymmetric space group $I\bar{4}2m$ (No. 121) [1]. The structure was first reported by Venturini *et al* [2]. The crystal structure is made up of an octahedral Ru_4Sn_6 unit enclosing the guest R atom. Crystal structures of this nature have generated much interest lately especially in the search for new superconductors [3, 4]. Also, the non-centrosymmetric nature of the space group is characteristic of certain superconductors where the mixing of the spin-singlet and spin-triplet Cooper pairing channels have been found to give rise to a two-component order parameter [5–7]. CeRu_4Sn_6 is a Kondo insulator, and it is the most extensively studied member of the series [8–11]. Other studies by Koch and Strydom reveal a magnetic ordering for the isostructural compounds of RRu_4Sn_6 , with $R = \text{Sm, Gd}$ and Dy compounds at low temperatures while those of Nd, Tb and Ho compounds are paramagnetic down to 2 K [12].

As part of our search for Pr-based systems exhibiting novel ground states, we have synthesized a polycrystalline sample of PrRu_4Sn_6 and investigated its physical and magnetic properties. It is noted that the existence of PrRu_4Sn_6 was first reported by Zundick and Pöttgen [1] but no

physical or magnetic properties have been reported thereafter. The Pr atom in this structure has a tetragonal site symmetry of D_{2d} similar to those of the $\text{Pr}_3\text{T}_4\text{X}_{13}$ compounds, resulting in the crystal electric field splitting of the $J = 4$ multiplet into seven levels consisting of five singlets and two non-Kramers doublets.

2. Experimental methods

A polycrystalline sample of PrRu_4Sn_6 was prepared by arc melting stoichiometric amounts of high-purity elements (wt.% ≥ 99.9) on a water-cooled Cu plate under a purified static argon atmosphere in an Edmund Buehler arc furnace. The weight loss after melting was $\sim 0.05\%$. The arc-melted pellet was wrapped in Ta foil, placed in an evacuated quartz tube and annealed at 900°C for 21 days. A powder X-ray diffraction (XRD) pattern was recorded on a pulverized sample using a Rigaku diffractometer employing $\text{Cu-K}\alpha$ radiation. The obtained powder XRD pattern was refined using the Rietveld method [13] employing the FullProf suite of programs [14]. We found that the compound was phase-pure within the limits of the resolution of the instrument. In Table 1, the atomic positions and lattice parameters obtained from the refinement are presented and are comparable with a previous report [1]. The refined XRD pattern and the crystal structure are shown in Fig. 1.

Magnetic properties were measured using the Magnetic Property Measurement System (Quantum Design Inc., San Diego) between 2 K and 300 K with an external magnetic field up to 7 T. The four-probe DC electrical resistivity, specific heat and thermal transport measurements between 2 K and 300 K were measured using the Physical Property Measurement System also from Quantum Design.

Table 1. The atomic positions and lattice parameters of PrRu_4Sn_6 obtained from a Rietveld refinement of the XRD pattern.

Site notation	Atom	Wyckoff site	Point symmetry	x	y	z
Sn(1)	Sn	$8i$	m	0.17635	0.17635	0.28771
Ru	Ru	$8i$	m	0.32788	0.32788	0.08126
Sn(2)	Sn	$4c$	222	0	$1/2$	0
Pr	Pr	$2a$	$-42m$	0	0	0
a (Å)	c (Å)	V (Å ³)	formula units (Z)	R_{wp} (%)	R_p (%)	χ^2
6.870(3)	9.761(2)	461.5(9)	2	8.588	7.295	5.210

3. Magnetic properties

The temperature dependence of magnetic susceptibility, $\chi(T)$, of PrRu_4Sn_6 in an external field of 0.1 T and in the temperature range of 2 K to 300 K is presented in Fig. 2. $\chi(T)$ shows a paramagnetic behaviour down to low temperatures with no indication of a long-range magnetic ordering observed. The white-solid line is a Curie-Weiss fit based on the expression: $\chi(T) = N_A\mu_{\text{eff}}^2/(3k_B(T - \theta_p))$ for data above 100 K with values of effective magnetic moment, $\mu_{\text{eff}} = 3.34 \mu_B/\text{Pr}$ and Weiss temperature, $\theta_p = -19.47$ K. The observed μ_{eff} is close to the calculated value of $3.58 \mu_B/\text{Pr}$ expected for a free Pr^{3+} ion. At low temperatures, a Van-Vleck paramagnetic behaviour in $\chi(T)$ suggests a nonmagnetic ground state in PrRu_4Sn_6 . The isothermal magnetization at 2 K is presented in the inset (b) of Fig. 2. The magnetization follows a quasi-linear behaviour up to 7 T and attains a value of $0.86 \mu_B/\text{Pr}$ at 7 T which is well reduced compared to the saturation moment of $3.32 \mu_B/\text{Pr}$ expected for a free Pr^{3+} ion implying a possible magneto-crystalline anisotropy in the compound.

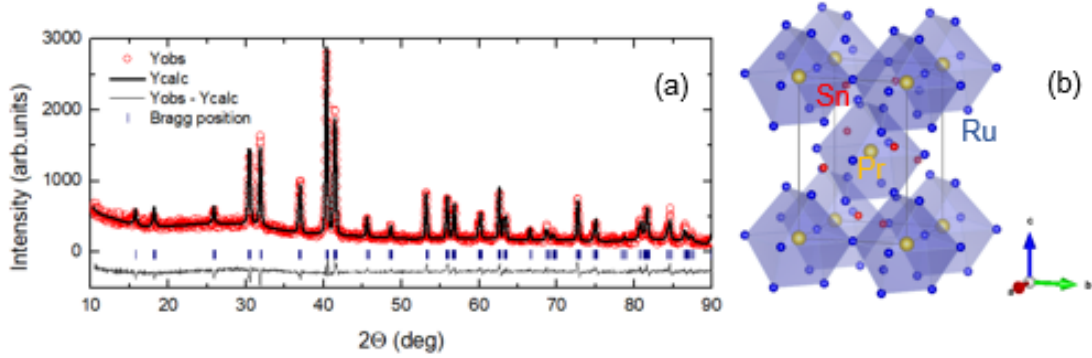


Figure 1. (a): Powder X-ray diffraction pattern of PrRu_4Sn_6 (red circles) with a Rietveld refinement (black line) based on the $I\bar{4}2m$ space group (No. 121). The vertical bars are the Bragg peak positions while the grey line represents the difference between the experimental and calculated intensities. (b): Crystal structure of PrRu_4Sn_6 showing Pr atom being enclosed by the Ru_4Sn_6 octahedral unit.

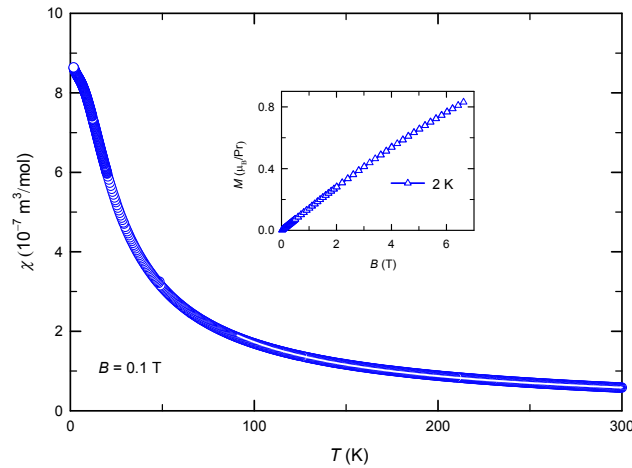


Figure 2. Temperature dependence of magnetic susceptibility, $\chi(T)$, of PrRu_4Sn_6 measured in a field of 0.1 T. The white-solid line is a Curie-Weiss fit described in the text. Inset (b): Isothermal magnetization of PrRu_4Sn_6 at 2 K.

4. Specific heat

The temperature dependence of specific heat, $C_p(T)$, of PrRu_4Sn_6 studied between 2 K and 300 K is presented in Fig. 3. Inset (a) of Fig. 3 shows a plot of C_p/T^3 against T . Such a plot is important in determining the possible presence of low-frequency Einstein modes in $C_p(T)$ through the occurrence of a local maximum in C_p/T^3 . A local minimum is observed in the plot as indicated by the arrow at $T_{\text{max}} = 6$ K which confirms the presence of low-frequency Einstein modes in PrRu_4Sn_6 . T_{max} is the temperature below which the Einstein modes are frozen out. By using a model incorporating both the Debye and Einstein terms, the experimental specific heat is fitted as shown by the red line in Fig. 3. The Debye-Einstein model is given by:

$$C_p(T) = mD\left(\frac{\theta_D}{T}\right) + nE\left(\frac{\theta_E}{T}\right), \quad (1)$$

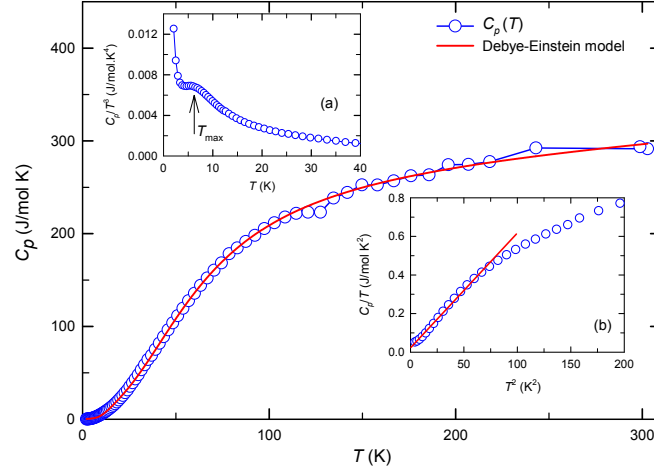


Figure 3. Temperature dependence of specific heat, $C_p(T)$, of PrRu_4Sn_6 . Inset (a): Low-temperature plot of C_p/T^3 against T . Inset (b): Plot of C_p/T against T^2 along with a linear fit indicated by the red-solid line to extract the Sommerfeld coefficient.

$$D\left(\frac{\theta_D}{T}\right) = 9R\left(\frac{T}{\theta_D}\right)^3 \int_0^{\theta_D/T} \frac{x^4 \exp(x)}{(\exp(x) - 1)^2} dx, \quad (2)$$

$$E\left(\frac{\theta_E}{T}\right) = 3R\left(\frac{\theta_E}{T}\right)^2 \cdot \frac{\exp(\theta_E/T)}{(\exp(\theta_E/T) - 1)^2}, \quad (3)$$

where θ_D and θ_E are the Debye and Einstein temperatures with values of 241.73(9) K and 32.431(3) K, respectively. It is observed that $T_{max} \simeq 0.2\theta_E$ which is in agreement with the observation in $\text{Ce}_3\text{Rh}_4\text{Sn}_{13}$ [15]. In Inset (b), a plot of C_p/T against T^2 is shown together with a least-square fit (red line) based on the expression: $C_p/T = \gamma + \beta T^2$ and $\beta = 12\pi^4 nR/(5\theta_D^3)$, where n and R are the number of atoms per formula unit and universal gas constant, respectively, γ is the Sommerfeld coefficient and θ_D is the Debye temperature. Values obtained from the fit are: $\gamma = 38.60 \text{ mJ}/(\text{K}^2 \text{ mol})$ and $\theta_D = 154.50 \text{ K}$. The γ observed for PrRu_4Sn_6 is about 10 times the values found in ordinary metals.

5. Transport properties

To further understand the physical properties of PrRu_4Sn_6 , a thermal transport measurement was carried out between 2 K and 300 K. The temperature dependences of thermoelectric power, $S(T)$, and thermal conductivity, $\kappa(T)$, were measured simultaneously on a bar-shaped sample. As shown in Fig. 4 (a), $S(T)$ is positive throughout the temperature range investigated and attains a value of $18.81 \mu\text{V/K}$ at room temperature. The red and black-dashed lines suggest two areas of linear-in- T behaviour on either side of $\sim 135 \text{ K}$. At 2 K, $S(T)$ has a value of $\sim 1 \mu\text{V/K}$ indicating a significant drop in the carrier concentration between room temperature and 2 K. The change in slope of $S(T)$ at about 145 K is consistent with the anomaly observed in $C_p(T)$ around the same temperature. The origin of such an observation is not immediately clear and further measurements are needed to resolve the physics at play. A plot of $S(T)/T$ is shown in the inset of Fig. 4 (a). For $T \leq 100 \text{ K}$ the slope of $S(T)/T$ is $\sim 0.7 \mu\text{V/K}^2$ which is slightly above those of ordinary metals. The general feature of $S(T)$ suggests a hole-type charge carriers near the Fermi level.

The total thermal conductivity, $\kappa_T(T)$, of PrRu_4Sn_6 is presented in Fig. 4 (b) on a log-log

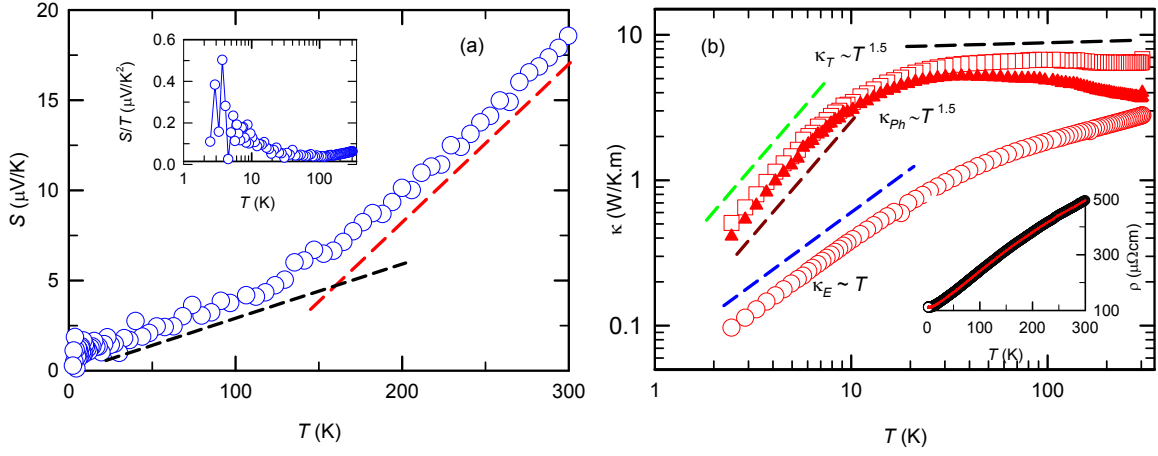


Figure 4. (a) Temperature dependence of thermoelectric power, $S(T)$, of PrRu_4Sn_6 . The red and black-dashed lines are guides to the eye, indicating a change in slope of $S(T)$ at ~ 145 K. Inset: Plot of S/T against T on a semi-log axis. (b) Temperature dependences of total thermal conductivity, $\kappa_T(T)$, phonon thermal conductivity, $\kappa_{Ph}(T)$ and electronic thermal conductivity, $\kappa_E(T)$. The green, brown and blue dashed-lines represent the power-law behaviours of $\kappa_T(T)$, $\kappa_{Ph}(T)$ and $\kappa_E(T)$, respectively while the black-dashed line is a guide to the eye described in the text. Inset: Temperature dependence of electrical resistivity with a BG fit (red line) described in the text.

axes. $\kappa_T(T)$ is nearly temperature independent from room temperature down to about 45 K (as shown by the black-dashed line) which is characteristic of a glassy behaviour in thermal conductivity. The observation of a glass-like thermal conductivity in a crystalline compound is often associated with caged systems. The low-frequency optical-phonon mode of the guest atom scatters heat-carrying quasiparticles thus leading to a reduction in lattice thermal conductivity. Using the Wiedemann-Franz relation [16] given as: $\kappa = L_0 T / \rho(T)$, where L_0 is the Lorentz number given by: $L_0 = \pi^2 k_B^2 / 3e^2 = 2.45 \times 10^{-8} \text{ W}\Omega/\text{K}^2$, the electronic contribution to the thermal conductivity, $\kappa_E(T)$ is extracted and it is also presented in Fig. 4 (b). Also shown in the plot is $\kappa_{Ph}(T)$ obtained by subtracting $\kappa_E(T)$ from $\kappa_T(T)$. Below about 10 K, $\kappa_T(T)$ and $\kappa_{Ph}(T)$ show power-law behaviour of $T^{1.5}$ while $\kappa_E(T)$ is linear-in- T as indicated by the green, brown and blue-dashed lines. This indicates a good metallic behaviour. $\kappa_{Ph}(T) > \kappa_E(T)$ in the whole temperature range studied revealed that the heat transport is not charge-carrier dominated.

The temperature dependence of electrical resistivity, $\rho(T)$, of PrRu_4Sn_6 is presented in the inset of Fig. 4 (b) between 2 K and 300 K. $\rho(T)$ follows a typical metallic behaviour down to low temperature with residual resistivity ratio ≈ 5 which indicates a good crystalline quality. No signature of long-range magnetic or any type of ordering is observed in the temperature range studied in support of the observations in $\chi(T)$ and $C_p(T)$. To further understand the electrical transport properties of PrRu_4Sn_6 , the Bloch-Grüneisen (BG) expression [17] was fitted to the data in the whole temperature range (shown as a red line). The BG expression is given as:

$$\rho(T) = \rho_0 + \frac{4K}{\Theta_R} \left(\frac{T}{\Theta_R} \right)^5 \int_0^{\Theta_R/T} \frac{x^5 dx}{(e^x - 1)(1 - e^{-x})}, \quad (4)$$

where ρ_0 is the residual resistivity due to defect scattering in the crystal lattice, K is the electron-phonon coupling constant and Θ_R is the resistivity Debye temperature. Values of $\rho_0 =$

102.8(2) $\mu\Omega$ cm, $K = 90.19(1)$ $\mu\Omega$ cm K, and $\Theta_R = 39.20(1)$ K are obtained from the least-square fit. This observation here further supports a metallic behaviour of PrRu_4Sn_6 .

6. Conclusion

We have studied the physical and magnetic properties of the non-centrosymmetric PrRu_4Sn_6 compound. A paramagnetic ground state is inferred from the magnetic susceptibility results down to 2 K. The presence of low-frequency Einstein modes are observed in $C_p(T)$. This observation is further supported by the glass-like thermal conductivity for temperatures above 45 K. $S(T)$ undergoes a change in slope at ~ 145 K, which is around the same temperature an anomaly in $C_p(T)$ is observed. Further measurements are expected to help clarify the origin of the observations in $C_p(T)$ and $S(T)$.

Acknowledgement

MOO acknowledges the UJ-URC bursary for doctoral studies in the Faculty of Science. AMS thanks the SA-NRF (93549) and UJ-URC for financial support.

References

- [1] Zumdick M F and Pöttgen R 1999 *Z. Naturforsch. B* **54** 863
- [2] Venturini G, El Idrissi B C, Maréché J F and Malaman B 1990 *Mater. Res. Bull.* **25** 1541
- [3] Yamada A, Higashinaka R, Matsuda T D and Aoki Y 2018 *J. Phys. Soc. Jpn.* **87** 033707
- [4] Winiarski M J, Wiendlocha B, Sternik M, Wiśniewski P, O'Brien J R, Kaczorowski D and Klimczuk T 2016 *Phys. Rev. B* **93** 134507
- [5] Bauer E, Hilscher G, Michor H, Paul C, Scheidt E W, Griбанov A, Seropegin Y, Noël H, Sigrist M and Rogl P 2004 *Phys. Rev. Lett.* **92** 027003
- [6] Bauer E, Khan R T, Michor H, Royanian E, Grytsiv A, Melnychenko-Koblyuk N, Rogl P, Reith D, Podloucky R, Scheidt E W, Wolf W and Marsman M 2009 *Phys. Rev. B* **80** 064504
- [7] Okuda Y, Miyauchi Y, Ida Y, Takeda Y, Tonohiro C, Oduchi Y, Yamada T, Duc Dung N, D Matsuda T and Haga Y 2007 *J. Phys. Soc. Jpn.* **76** 044708
- [8] Strydom A M, Guo Z, Paschen S, Viennois R and Steglich F 2005 *Physica B* **359-361** 293
- [9] Brüning E M, Baenitz M, Gippius A A, Paschen S, Strydom A M and Steglich F 2006 *Physica B* **378-380** 839
- [10] Brüning E M, Brando M, Baenitz M, Bontien A, Strydom A M, Walstedt R E and Steglich F 2010 *Phys. Rev. B* **82** 125115
- [11] Sundermann M, Strigari F, Willers T, Winkler H, Prokofiev A, Ablett J M, Rueff J P, Schmitz D, Weschke E, Sala M M and Severing A 2015 *Sci. Rep.* **5** 17937
- [12] Koch N E and Strydom A M 2008 *J. Magn. Magn. Mater.* **320** 128
- [13] Thompson P, Cox D E and Hastings J B 1987 *J. Appl. Crystallogr.* **20** 79
- [14] Rodriguez-Carvajal J 1993 *Physica B* **192** 55
- [15] Köhler U, Pikul A P, Oeschler N, Westerkamp T, Strydom A M and Steglich F 2007 *J. Phys. Condens. Matter* **19** 386207
- [16] Kittel C 2004 *Introduction to Solid State Physics* 8th ed (Wiley, New York)
- [17] Mott N F and Jones H 1958 *The Theory of the Properties of Metals and Alloys* (Dover publications, Inc., Oxford, England)

Thermoelectric properties of CdGa_2O_4 spinel

Elkana Rugut^{1,2}, Daniel Joubert¹ and Glenn Jones²

¹ The National Institute for Theoretical Physics, School of Physics and Mandelstam Institute for Theoretical Physics, University of the Witwatersrand, Johannesburg, Wits 2050, South Africa

² Johnson Matthey Research (PTY) Limited, Scientia, CSIR Campus, Meiring Naude Road, Brummeria, Pretoria, South Africa

E-mail: elkanatawich@gmail.com

Abstract. Thermoelectric materials can convert heat into electricity and thermoelectric devices can play an important role in the efficient use of energy. In this study, we investigate the thermoelectric properties of the hard glassy spinel mineral CdGa_2O_4 . The potential of a material to be a candidate as the active component of a thermoelectric device is given by the figure of merit (denoted by ZT), which includes information on the lattice and electronic transport properties. Given the difficulties of directly measuring ZT experimentally, we computed its value within density functional theory using linearised Boltzmann transport equations in a relaxation time approximation. From the determined ZT values, we find that CdGa_2O_4 is promising as a high temperature thermoelectric material.

1. Introduction

The world continues face a grand challenge in discovering sustainable and alternative energy sources. To help meet this challenge a significant scientific effort is needed in basic science related to clean energy generation, conservation and utilization. To this end we present results from ab-initio calculations on thermoelectric materials that show promise for application in this technological and societally valuable field. Thermoelectric materials can generate electricity from waste heat or be used as solid state Peltier coolers which in turn play a crucial role in finding a global sustainable energy solution. Although a number of materials have been studied as well as applied in thermoelectric applications such as Bi_2Te_3 [1], PbTe [2] and MgIn_2X_4 ($\text{X}=\text{S}, \text{Se}$) [3] just to mention a few; the attainable efficiency at the moment is very low for practical large scale energy production. In this study, we explore CdGa_2O_4 as a candidate for thermoelectric applications based on first principles study. CdGa_2O_4 belongs to a group of compounds called spinels. Generally, a spinel is a hard glassy mineral that occur either as octahedral or tetrahedral crystals of variable colour consisting mainly of magnesium and aluminium oxides having a general formula AB_2O_4 [4]. CdGa_2O_4 belong to space group $\text{Fd}\bar{3}\text{m}$ consisting of 8 formula units having a closed packed face-centered-cubic structure hence highly symmetric. To review what has been done on this compound, first principle studies on structural, electronic, optical and mechanical properties of CdGa_2O_4 has been reported by Bouhemadou *et al.* [5]. As per Nguyen and Koffyberg [6], this compound has a wide indirect experimental band gap of 3.07 eV. In addition, it has been explored as a sensor [7] as well as a phosphor when combined with ZnGa_2O_4 [8]. To the best of author's knowledge, lattice thermal conductivity, transport and thermoelectric

properties of CdGa₂O₄ spinel has never been reported before, which forms the basis of the present study.

2. Methodology

We report a computational study on the structural, vibrational, energetic, mechanical, electronic, thermal, transport and thermoelectric properties of CdGa₂O₄ done using density functional theory as implemented in Vienna *ab initio* simulation package (VASP) [9]. In order to test the reliability of our results, structural, energetic and mechanical studies were carried out using three functionals namely: local density approximation (LDA), generalized gradient approximation (GGA-PBE) as well as PBEsol (a functional intended for solid state and surface systems). The energy cut-off for the plane wave expansion was fixed at 520 eV. The atomic forces and energies were converged within 10⁻⁴ eV/Å and 10⁻⁸ eV respectively for structural calculations. For elastic constant calculations, stress-strain technique proposed by Shang *et al.* was applied [10]. Vibrational studies were carried out following the finite displacement approach as implemented in Phonopy [11] with a 2×2×2 supercell of the primitive unit cell consisting of 112 atoms with a Monkhorst-Pack grid of size 3×3×3 used to sample the Brillouin zone in order to obtain the second and third order force constants from Phonopy and Phono3py [12] respectively. We computed the intrinsic lattice thermal conductivity of CdGa₂O₄ by solving Boltzmann transport equations based on first principle studies under the mode dependent relaxation time approximation. A mesh size of 20×20×20 was found sufficient for computing lattice thermal conductivity. All triplet displacements in the supercell were included.

3. Results and discussion

3.1. Structural and energetic properties

From Table 1, LDA functional is capable of reproducing the structural properties of CdGa₂O₄ better than PBE and PBEsol in comparison with the existing experimental information. Hence further in-depth study on phonon, electronic, thermal and transport properties of CdGa₂O₄ was conducted using LDA functional. Moreover, negative values of formation and cohesive energies obtained indicates that this material is energetically stable [13].

Table 1. Structural and energetic parameters.

	a (Å)	V_0 (Å ³)	E_{coh} (eV/atom)	E_{form} (eV/atom)
PBE	8.783	677.52	-4.078	-1.630
PBEsol	8.666	650.80	-4.535	-1.683
LDA	8.583	632.29	-4.974	-1.796
Expt.[14]	8.590	633.84	-	-

3.2. Mechanical properties

Table 2 gives a summary of the bulk (B), shear (G) and Young's modulus (E) as well as the independent elastic coefficients of cubic CdGa₂O₄. Its Zener anisotropy factor (A) and Fratserich's ratio (G/B) computed using three functionals in comparison with existing theoretical values. From the elastic coefficient values obtained, $C_{44} > 0$; $C_{11} > |C_{12}|$ and $(C_{11} + 2C_{12})C_{33} > 2C_{13}^2$ fulfilling the requirement of mechanical stability in cubic crystals [15]. Computed values of Zener anisotropy factor is non-unity for all functionals, suggesting that CdGa₂O₄ possess mechanical anisotropy. Fratserich's ratio (G/B) [16] is less than 0.571 for all the three functionals used, indicating that CdGa₂O₄ is ductile in nature.

Table 2. Mechanical properties of CdGa₂O₄ spinel oxide.

	B (GPa)	G (GPa)	E (GPa)	C ₁₁ (GPa)	C ₁₂ (GPa)	C ₄₄ (GPa)	A	G/B
LDA	182.21	61.45	165.71	229.38	158.63	88.92	2.51	0.34
PBEsol	166.49	56.85	153.13	208.45	145.51	84.42	2.68	0.34
PBE	149.08	56.05	149.43	190.00	128.62	83.83	2.73	0.38
Theory [17]	154.00	-	102.00	203.00	130.00	91.00	-	-

3.3. Dynamical and electronic properties

Phonon dispersion curves had no soft phonon modes as provided in Figure 1 which indicates dynamical stability in CdGa₂O₄. The acoustic cut-off frequency which marks the maxima of acoustic phonon modes was determined to be 3.9 THz. From the partial phonon density of states, the primary element contributing to the acoustic phonon modes is Cadmium. To overcome the shortcoming of band gap underestimation at DFT level, we applied the scissor correction technique [18] to open the indirect band gap of CdGa₂O₄ from its 1.805 eV DFT value to its reported experimental gap of 3.07 eV [6] as shown in Figure 2. This was attained by upshifting the conduction band energies. The resultant energies were then used as input for BoltzTrap code [19] in order to explore transport properties of CdGa₂O₄. In addition, our computed DFT value of the indirect band gap (1.805 eV) is comparable to that reported by Bouhemadou *et al.* [5] (1.899 eV) along the K-Γ point in the Brillouin zone.

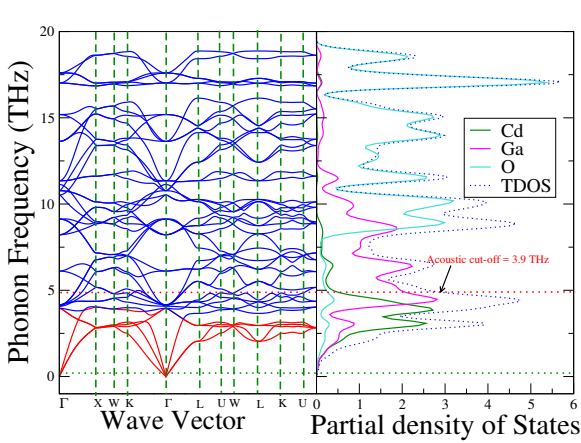


Figure 1. Phonon dispersion.

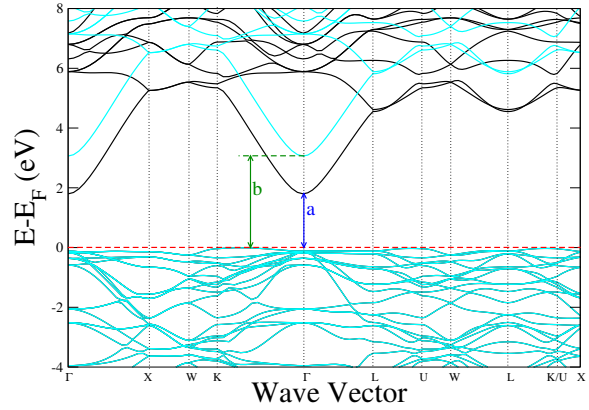


Figure 2. Electronic bands with (cyan) and without (black) scissor correction at DFT level.

3.4. Thermal properties

Atoms constituting a crystal vibrate about their mean positions generating thermal energy arising from the vibrational motion. This thermal energy increases with an increase in temperature and dictates the thermal properties of a given material. For CdGa₂O₄, specific heat capacity at a constant volume (C_v), approaches constant value of about 340 J(mol K)⁻¹ at high temperature. This value is known as Dulong-Petit limit [20]. From Figure 3, we predict that at 300 K, entropy, Helmholtz free energy and specific heat capacity of CdGa₂O₄ are 50.3 kJmol⁻¹, 274.4 J(mol K)⁻¹ and 271.7 J(mol K)⁻¹ respectively. It is evident that the degree of

disorderness (entropy), increases with an increase in temperature whereas the reverse is true for free energy. CdGa_2O_4 shows isotropic thermal properties in that its lattice thermal conductivity is similar in all the directions. This could be attributed to the fact that this compound is highly symmetric having a cubic structure. At 300 K, the predicted K_l value is 9.38 W/mK as indicated in the inset plot of Figure 4. In addition, the cumulative lattice thermal conductivity (Cum K_l) and its derivative (dK_l) attest that the dominant contributor to K_l is acoustic phonon modes. This is reinforced by the fact that below 3.9 THz which is the acoustic cut-off limit (dotted), there is a sizable increase in Cum K_l and dK_l with an increase in frequency.

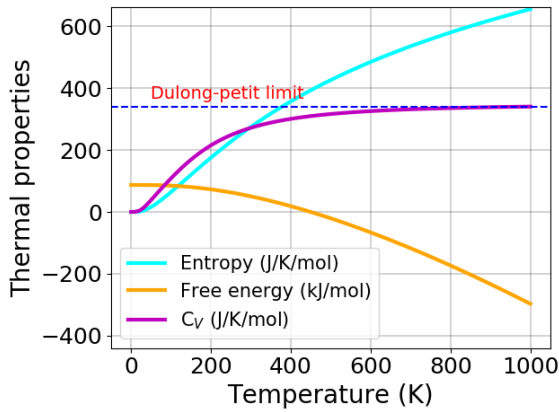


Figure 3. Calculated temperature dependence of free energy, entropy and C_v .

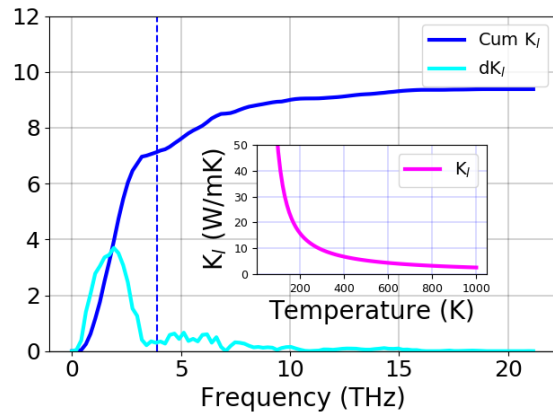


Figure 4. Calculated K_l , its cumulative and derivative.

3.5. Transport properties

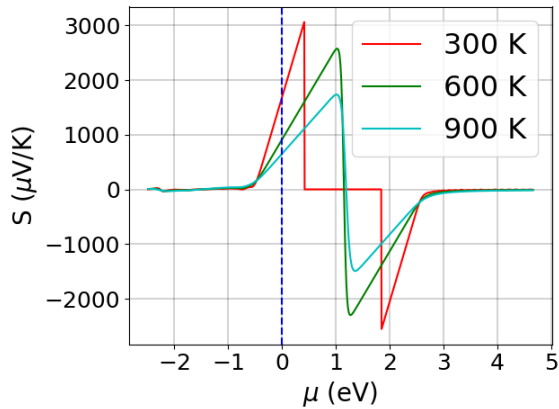


Figure 5. Seebeck coefficient vs chemical potential (μ).

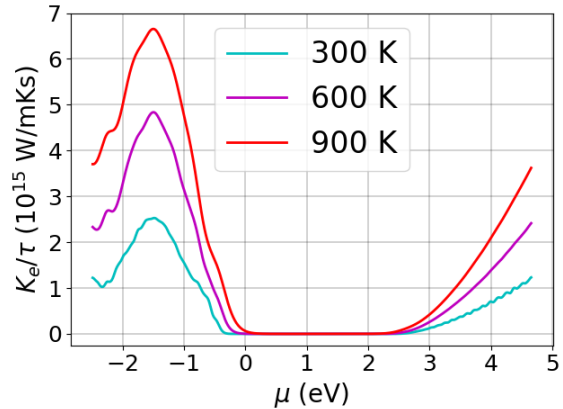


Figure 6. Electronic contribution to total thermal conductivity.

From Figure 5, it is visible that when $\mu = 0$ eV the value of Seebeck coefficient (S) is positive which indicates prior doping, CdGa_2O_4 is an intrinsic p-type semiconductor with a value of about $1700 \mu\text{V/K}$ at 300 K. Moreover, the magnitude of S increases with an increase in temperature at a constant μ value whereas the inverse is true for K_e/τ as substantiated by Figure 5 and 6.

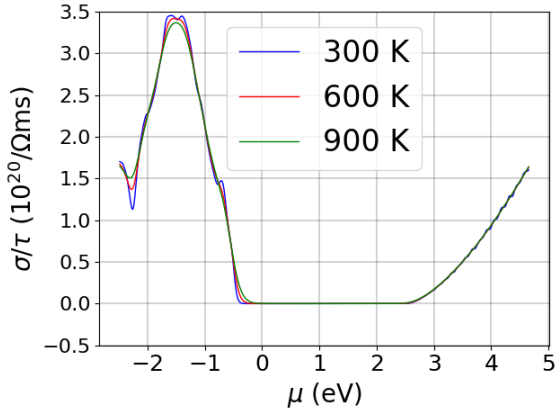


Figure 7. Electrical conductivity.

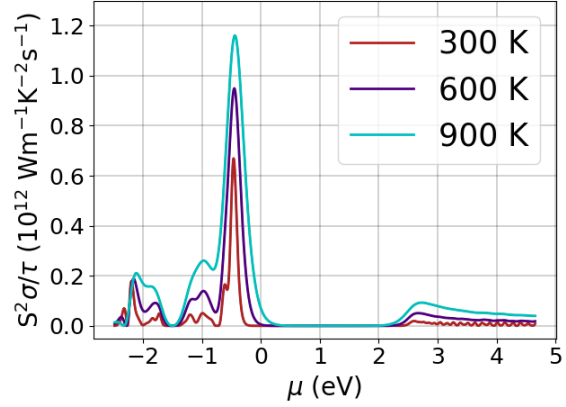


Figure 8. Power factor.

Within the rigid band-shift model, the chemical potential determines the carrier concentration of a compound. For p-type (n-type) doping, the Fermi-level shifts down (up) corresponding to a negative (positive) chemical potential [21]. The intensity of the peaks for σ/τ , K_e/τ and power factor are higher for p-type than n-type indicating that CdGa_2O_4 is more efficient when majority charge carriers are holes than electrons as backed by Figure 7 and 8. This is further verified by the magnitudes of ZT with respect to temperature at various doping levels as presented in Figure 9.

3.6. Thermoelectric properties

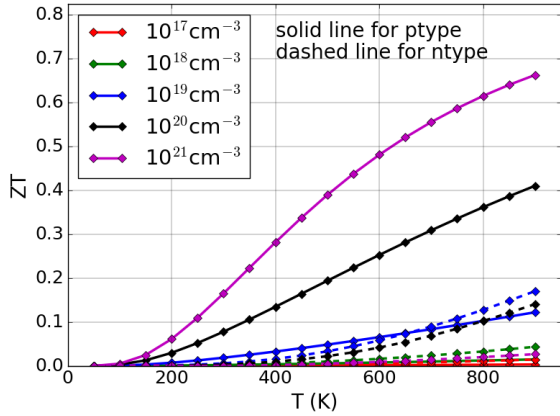


Figure 9. ZT for both holes and electrons.

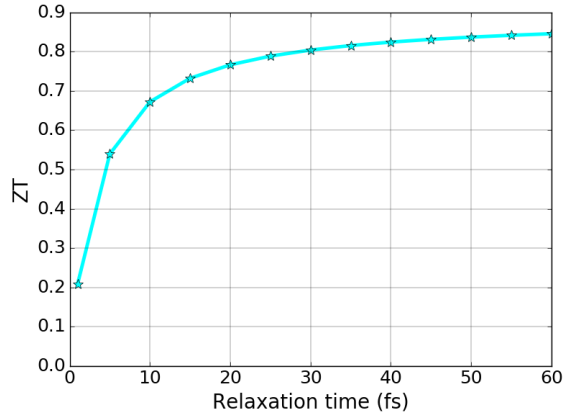


Figure 10. Variation of ZT with τ .

All the above transport and thermoelectric analysis was done at the constant relaxation time (τ) value of 10 fs as implemented in Boltztrap code. To further check the behaviour of ZT upon varying τ during data analysis, we performed ZT convergence with respect to τ as exhibited in Figure 10. Above 45 fs, the value of ZT becomes less dependent on τ . When τ is 45 fs, the optimum value of ZT attained at high temp of 900 K with hole concentration of 10^{21} cm^{-3} is 0.82 which is slightly higher than 0.66 attained when relaxation time is kept at its default value of 10 fs.

4. Summary and conclusion

We have computed structural, vibrational, energetic, mechanical, electronic, thermal, transport and thermoelectric properties of CdGa₂O₄ based on density functional theory. Besides being stable, CdGa₂O₄ is a promising high temperature thermoelectric material. The highest ZT value is attained when majority charge carriers are holes with a concentration of 10²¹ cm⁻³ at 900 K having an estimated ZT value of 0.66 and 0.82 when the constant relaxation time is 10 fs and 45 fs respectively.

Acknowledgments

This work was supported by the Johnson Matthey Technology Centre (Pretoria) under contract number JM6473. We thank Centre for High Computing, Cape Town for computational resources.

References

- [1] Saleemi M, Toprak M S, Li S, Johnsson M and Muhammed M 2012 *J. Mater. Chem.* **22** 725-730
- [2] Pei Y, LaLonde A, Iwanaga S, Snyder G J 2011 *Energy Environ. Sci.* **4** 2085-2089
- [3] Mahmood Q *et al.* 2019 *J. Mol. Graph. Model.* **88** 168-173
- [4] Garcia P 1984 *J. Solid State Chem* **52** 187-193
- [5] Bouhemadou A, Khenata R, Rached D, Zerarga F and Maamache M 2007 *EPJ AP* **38** 203-210
- [6] Nguyen S and Koffyberg F 1990 *Solid State Commun.* **76** 1243-1245
- [7] Xiangfeng C and Jun 2002 *Electrochem. Solid State Lett* **5** H4-H6
- [8] Choi S K, Moon H S, Mho S I, Kim T W and Park H L 1998 *Materials Research Bulletin.* **33** 693-696
- [9] Kresse G and Hafner J 1993 *Phys. Rev. B* **47** 558
- [10] Shang S, Wang Y and Zi-Kui L 2007 *Appl. Phys. Lett* **90** 101909
- [11] Togo A and Tanaka I 2015 *Scr. Mater* **108** 1-5
- [12] Togo A, Chaput L and Tanaka I 2015 *Phys. Rev. B* **91** 094306
- [13] Zhou J, Zhimei S, Xuan C and Ying Z 2009 *Intermetallics* **17** 995-999.
- [14] Huber M 1960 *J. Chim. Phys.* **57** 202-227
- [15] Wu Z, Zhao E, Xiang H, Hao X, Liu X and Meng J 2007 *Phys. Rev. B* **76** 054115
- [16] Tariq S, Ahmed A, Saad S and Tariq S 2015 *AIP Adv.* **5** 077111
- [17] Bouhemadou A, Khenata R and Zerarga F 2007 *Comput. Mater. Sci* **39** 709-712
- [18] Levine Z 1989 *Phys. Rev. Lett.* **63** 1719
- [19] Madsen Georg and Singh D 2006 *Comput. Phys. Commun* **175** 67-71
- [20] Laing M and Laing M 2006 *J. Chem. Educ* **83** 1499
- [21] Wang L, Mao L, Wang Z, Wei W, Xiong R, Liu H, Shi J and Tang X 2009 *J. Appl. Phys* **105** 013709

The structural, electronic, and optical properties of $\text{CH}_3\text{NH}_3\text{PbI}_3$

Aya S A Sidahmed^{1,2} and Daniel P Joubert¹

¹ The National Institute for Theoretical Physics, School of Physics and Mandelstam Institute for Theoretical Physics, University of the Witwatersrand, Johannesburg, Wits 2050, South Africa.

² Department of Physics, Sudan University, Khartoum, Sudan.

E-mail: ayasedig@gmail.com

Abstract.

Organic-inorganic halide perovskites are promising candidates for low cost, high-efficiency solar cells. We examined the structural, electronic, and optical properties of the low temperature tetragonal phase of the halide perovskites $\text{CH}_3\text{NH}_3\text{PbI}_3$ using Density Functional Theory (DFT). Our numerically predicted structure is in agreement with existing experimental data. DFT electronic structure calculations show that relativistic effects are important for the heavy lead atom and spin-orbit coupling has to be included for accurate results. The experimental band gap of 1.63 to 1.66 eV is similar in magnitude to the DFT direct gap of 1.72 eV, which suggests that many-body and relativistic effects cancel in this compound. Our calculated fundamental gap, at the G_0W_0 level of approximation, is 2.48 eV. Optical anisotropy of tetragonal $\text{CH}_3\text{NH}_3\text{PbI}_3$ was investigated by including many-body effects at the time dependent Hartree Fock and the Bethe-Salpeter equation level of approximation, with input data from a range separated Heyd-Scuseria-Ernzerhof DFT functional calculation. The optical edge for radiation polarized parallel to the *a*- and *b*-axes differ by about 0.15 eV and for polarization parallel to the *b*- and *c*-axes the difference is about 0.05 eV.

1. Introduction

Since the high power conversion efficiency of 16% to 21% [1, 2, 3, 4] was reported for mixed perovskites based solar cell (PSCs) from 2012 to 2015, metal halide perovskites have attracted the interest of researchers in the materials science community due to their excellent photovoltaic properties [5]. A prototypical example is $\text{CH}_3\text{NH}_3\text{PbI}_3$, which is readily available and inexpensive, easy to manufacture, has a very high diffusion length and high absorption coefficient, making it a promising material for commercialization. At low temperatures $\text{CH}_3\text{NH}_3\text{PbI}_3$ crystallises in an orthorhombic structure [6]. It undergoes a phase transition at 330.4 K to the room temperature tetragonal phase and above 330.4 K it has a cubic structure [7]. The objective of this work was to investigate the structural, electronic and optical properties of the room temperature tetragonal phase of $\text{CH}_3\text{NH}_3\text{PbI}_3$ using density functional theory (DFT) and post-DFT many-body perturbation theory.

2. Computational details

All simulations were performed with the Vienna *Ab-initio* simulation package (VASP) [8]. Structural properties were investigated using the Generalized Gradient Approximation (GGA) for the exchange-correlation energy as parametrized by Perdew-Burke-Ernzerhof (PBE) [9]. Atoms were relaxed till all forces were less than 10^{-3} eV/atom. These parameters were sufficient to produce converged results. The electronic structure was investigated at the DFT level using PBE and the Heyd-Scuseria-Ernzerhof (HSE) functional [10, 11] to describe electron exchange and correlation effects. In order to obtain the optical spectra of $\text{CH}_3\text{NH}_3\text{PbI}_3$, we used two different approaches. First, we solved the Bethe-Salpeter-equation (BSE) for electron-hole excitations [12, 13, 14, 15], using the PBE-GW results as input [16, 17]. Second, we used time-dependent hybrid functional calculations (TD-HSE) to include exciton effects, which depend on the exchange-tuned hybrid HSE functional. In this approach the exciton effects are approximately described by replacing the electron-hole ladder diagrams with the screened exchange [18].

3. Results and discussion

3.1. Structural parameters

The lattice parameters of the $\text{CH}_3\text{NH}_3\text{PbI}_3$ tetragonal phase, space group P_1 , were fully optimized using the PBE exchange-correlation approximation. The calculated structural parameters are listed in Table 1, together with the results from representative previous calculations [19] and experimental values [20, 21, 22, 23]. From the results shown in Table 1, we can see that our PBE calculation gives a volume within 0.1% of the experimental volume. This is better than the volume reported in similar previous calculations [19, 24]. We do not have an explanation for the difference, apart from possible different convergence criteria used.

Table 1. Calculated equilibrium lattice constants and cohesive energy for $\text{CH}_3\text{NH}_3\text{PbI}_3$, together with the previously calculated and experimental values.

	a (Å)	c (Å)	V (Å ³)	E_{coh} (eV/atom)
This work (PBE)	8.800	12.685	982.33	-3.06
Previous [19]	8.887	13.020	1028.33	–
Previous [24]	8.940	12.980	1037.40	–
Exp. [20, 21].	8.855	12.659	992.60	–
Exp. [22, 23].	8.80	12.685	982.33	–

3.2. Electronic properties

We investigated the electronic structure of $\text{CH}_3\text{NH}_3\text{PbI}_3$ at the DFT level using PBE with spin-orbit coupling (PBE-SOC) and without spin-orbit coupling (PBE). The presence of the heavy Pb element introduces significant relativistic effects as can be seen in Figure 1. Our calculations confirm that tetragonal $\text{CH}_3\text{NH}_3\text{PbI}_3$ has a direct band gap at the Γ point. The PBE and PBE-SOC bands have similar structures, but the dispersion of the low lying PBE-SOC conduction bands show larger dispersion. Band gaps calculated using different approaches are shown in Table 2. Non-relativistic local and semi-local exchange-correlation Kohn-Sham (KS) approximations tend to under estimate band gaps while hybrid- and meta-GGA approximations in generalized Kohn-Sham calculations tend to improve band gap approximations [9]. Contrary to the general trend, both the KS PBE and generalized KS HSE gaps are larger than the experimental gap. Inclusion of spin-orbit coupling (SOC) reduces the KS-PBE gap from 1.72 eV

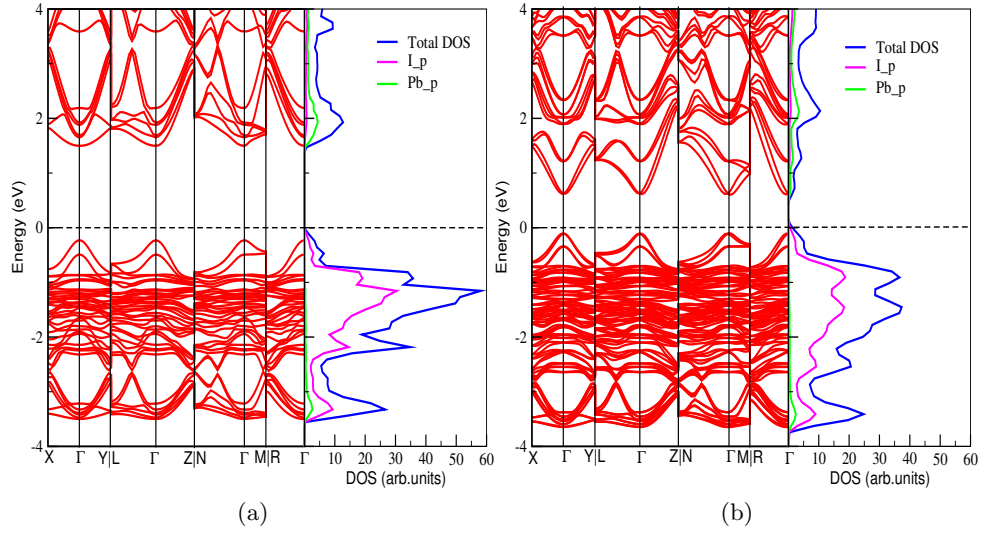


Figure 1. Band structure, total density of states, and partial density of states for $\text{CH}_3\text{NH}_3\text{PbI}_3$ using PBE (a) without SOC (b) with SOC.

to 0.71 eV, a change of 1.01 eV, which is of the same order of magnitude as the experimental gap. The generalized KS HSE gap is reduce by 1.34 eV when SOC is included and the resulting gap under estimates the experimental value. This clearly shows that relativistic effect are important for calculating electronic properties of $\text{CH}_3\text{NH}_3\text{PbI}_3$.

Table 2. Calculated band gap of $\text{CH}_3\text{NH}_3\text{PbI}_3$, together with the previously calculated and experimental values.

Method	Band gap (eV)
PBE	1.72
PBE-SOC	0.71
HSE	2.39
HSE-SOC	1.05
GW	2.48
Theory [19]	1.89
Theory [25]	1.33
Theory (PBE+Soc) [25]	0.09
Exp.[20, 21].	1.63
Exp.[22, 23].	1.66

3.3. Optical properties

We investigated optical properties for the room temperature tetragonal phase of $\text{CH}_3\text{NH}_3\text{PbI}_3$ in the TD-HSE and HSE-GW-BSE approximations without spin-orbit coupling by calculating the real part $\epsilon_{re}(\omega)$ and imaginary part $\epsilon_{im}(\omega)$ of the dielectric tensor, the absorption coefficient $\alpha(\omega)$ and the refractive index $n(\omega)$. In Table 3 we list the real part of the static dielectric constant $\epsilon(0)$ and static limit of the refractive indices. It is clear from the table that tetragonal

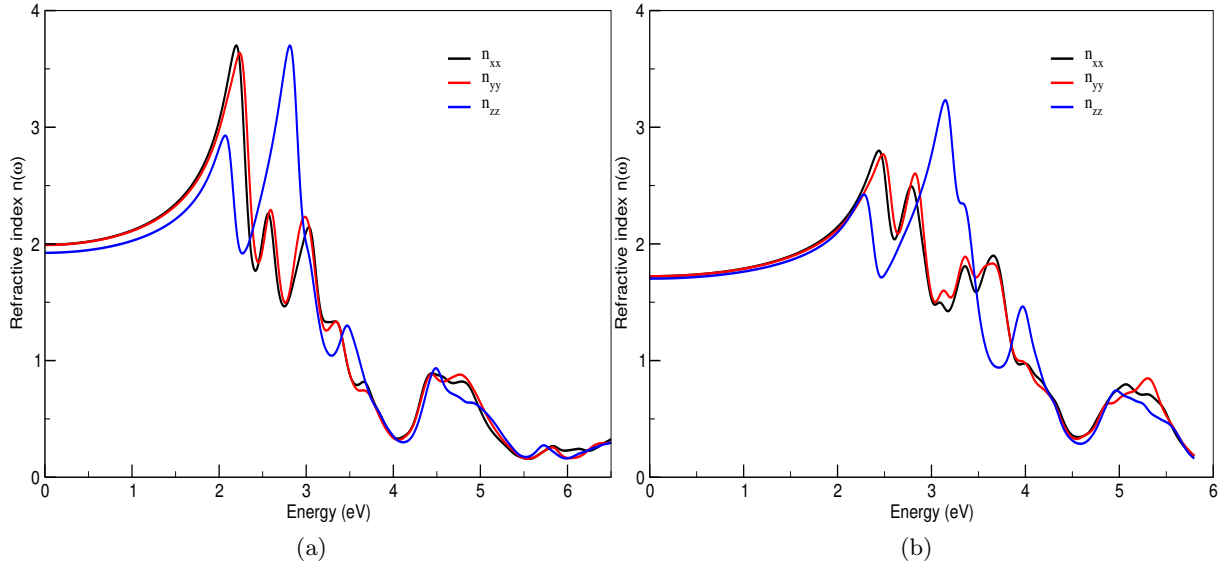


Figure 2. (a) The refractive indices obtained by (a) HSE-GW-BSE and (b) hybrid TD-HSE for $\text{CH}_3\text{NH}_3\text{PbI}_3$.

$\text{CH}_3\text{NH}_3\text{PbI}_3$ is optically anisotropic. Reflection for radiation polarized in the x - or (y -) plane differs from the reflection of radiation polarized in the z -plane where the x, y and z directions coincide with the a, b and c axes of the tetragonal system. Unfortunately the HSE-GW-BSE and TD-HSE approximations do not agree on the polarization for maximum static reflection. The energy dependent refractive index $n(\omega)$ is shown in Figure 2. The highest refractive index was found for polarization in the z -plane around 3.7 eV and 3.22 eV by using BSE and TD-HSE respectively, which is located in the ultraviolet range. The sharp peaks in the refractive index spectrum result from exciton transitions.

Table 3. The static dielectric constant $\varepsilon(0)$ and static refractive indices $n(0)$ obtained with HSE-GW-BSE and TD-HSE.

METHOD	$\varepsilon_1(0)$	$\varepsilon_{1xx}(0)$	$\varepsilon_{1yy}(0)$	$\varepsilon_{1zz}(0)$	$n(0)$	$n_{xx}(0)$	$n_{yy}(0)$	$n_{zz}(0)$
GW(BSE)	3.75	3.91	3.91	3.60	1.95	1.99	1.99	1.91
TD-HSE	2.91	2.97	2.97	2.85	1.70	1.69	1.69	1.71

In Figure 4 we also see from the different energy dependence of the absorption coefficient components that the optical absorption is anisotropic. The optical band gap (E_g) was estimated using the Tauc approach [26] by plotting $(\alpha E) = A(E - E_g)^{1/2}$ as a function of energy. The gap is estimated by extrapolating the best linear fit to the x -axis ($\alpha E = 0$) as shown in Figure 3.

The absorption coefficient is an important optical constant $\alpha(\omega)$, and is a measure of the amount of light absorbed by given medium. In Figure 4 the main peaks in α_{zz} is higher than those for α_{xx} and α_{yy} which means that absorption polarization in the z -plane is greater than for polarization in x - or y -planes. The exciton binding energy E_b , defined as the difference between the GW band gap and the optical absorption edge at the BSE level of approximation. The lowest exciton binding energy for our calculations is $E_b = 0.38$ eV.

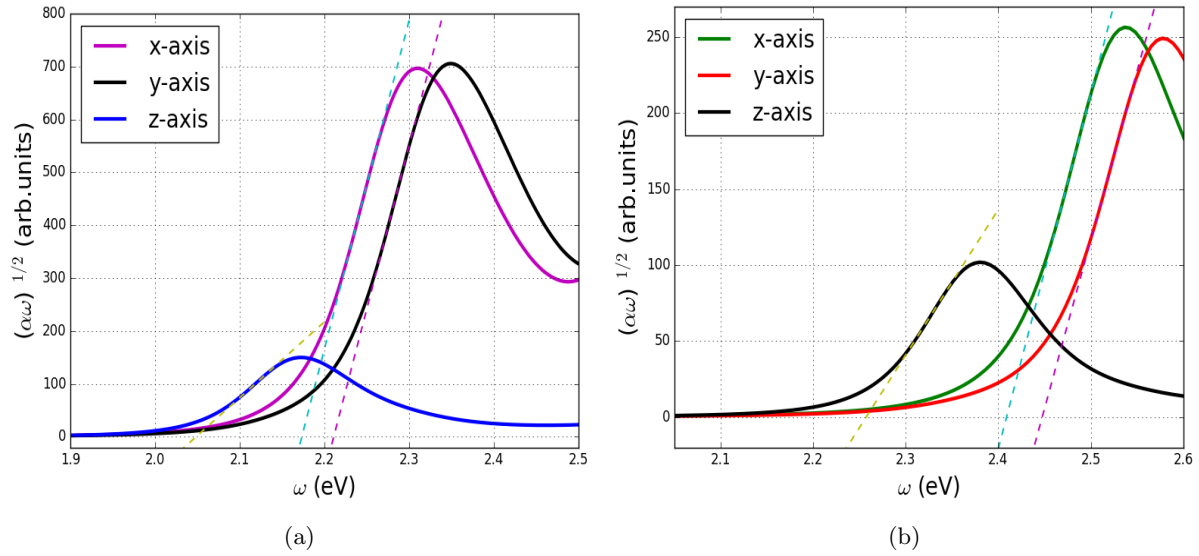


Figure 3. Optical band gaps obtained by Tauc plots for (a) HSE-GW-BSE and (b) hybrid TD-HSE calculations for $\text{CH}_3\text{NH}_3\text{PbI}_3$.

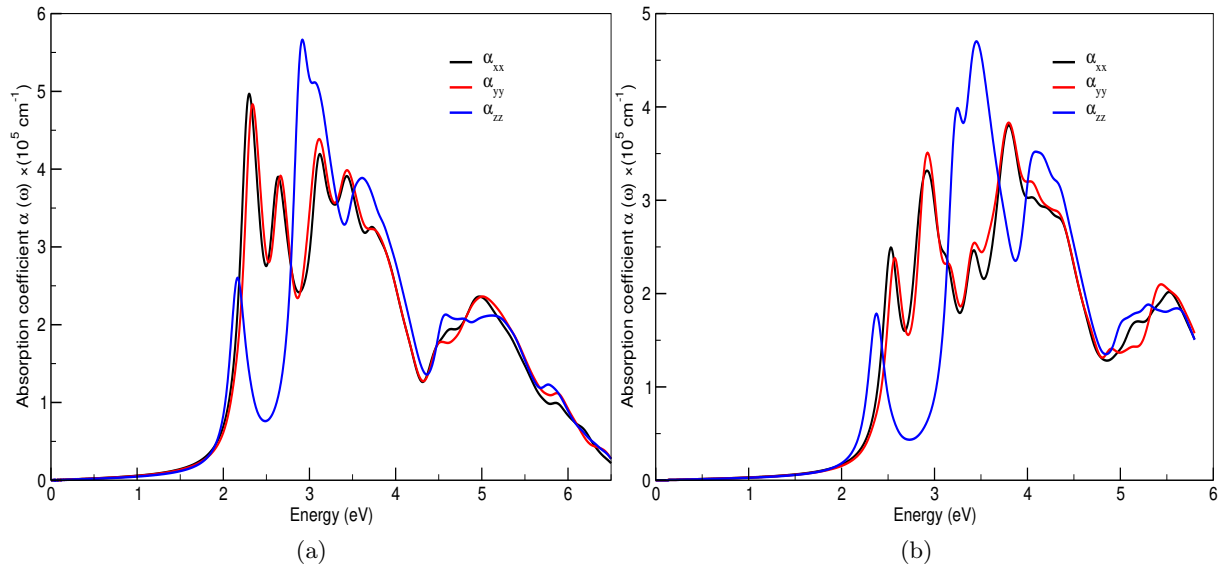


Figure 4. (a) The absorption coefficient obtained by HSE-GW-BSE and (b) hybrid TD-HSE.

3.4. Conclusion

In summary, structural, electronic and optical properties of the organic-inorganic halide perovskites were investigated using Density Functional Theory. The PBE predicted structural lattice parameters and volume are in good agreement with experimental values. Electronic properties were studied by calculating the band structure, with and without SOC. The results show that tetragonal $\text{CH}_3\text{NH}_3\text{PbI}_3$ is a direct band gap semiconductor with at gap at Γ . Relativistic effects are important due the the presence of heavy Pb atoms. Optical properties

show anisotropy with peak absorption strength for polarization parallel to the *c*-axis.

References

- [1] Lee M M, Teuscher J, Miyasaka T, Murakami T N and Snaith H J 2012 *Science* **10** 1228604.
- [2] Green M A, Ho-Baillie A and Snaith H J 2014 *Nat. Photonics* **8** 506–514.
- [3] Chen Q, et al. 2015 *Nano. Today* **10** 355–396.
- [4] Park NG 2015 *Mater. Today* **18** 65–72.
- [5] Umari P, Mosconi E and De Angelis F 2014 *Sci. Rep.* **4** 4467.
- [6] Stoumpos C C, Malliakas C D and Kanatzidis M G. 2013 *Inorg. Chem.* **52** 9019–9038.
- [7] Baikie T, et al. 2013 *J. Mater. Chem. A* **1** 5628–5641.
- [8] Kresse G and Joubert D 1999 *Phys. Rev. B* **59** 1758.
- [9] Perdew JP, Burke K and Ernzerhof M 1996 *Phys. Rev. Lett.* **18** 3865.
- [10] Heyd J, Scuseria G E and Ernzerhof M 2003 *J. Chem. Phys.* **118** 8207–821.
- [11] Heyd J, Scuseria G E and Ernzerhof M 2006 *J. Chem. Phys.* **124** 219906.
- [12] Onida G, Lucia R and Angel R 2002 *Rev. Modern Phys.* **74** 601
- [13] Strinati G 1984 *Phys. Rev. B* **29** 5718.
- [14] Hybertsen M S and Louie S G 1986 *Phys. Rev. B* **34** 5390.
- [15] Albrecht A, Onida G and Reining L 1997 *Phys. Rev. B* **55** 10297.
- [16] Hedin L 1965 *Phys. Rev.* **139** A796.
- [17] Broido M M and Taylor J G 1969 *J. Math. Phys.* **10** 184–209.
- [18] Paier J, Marsman M and Kresse G 2008 *Phys. Rev.* **78** 121201.
- [19] Feng J and Xiao B 2014 *J. Phys. Chem. Lett.* **5** 1278–1282.
- [20] Kawamura Y, Mashiyama H and Hasebe K 2002 *J. Phys. Soc. of Japan* **71** 1694–1697.
- [21] Maalej A, Abid Y, Kallel A, Daoud A, Lautie A and Romain F 1997 *Solid State Commun.* **103** 279284.
- [22] Poglitsch A and Weber 1997 *J. Chem. Phys.* **87** 6373–6378.
- [23] Umebayashi T, Asai K, Kondo T and Nakao A 2003 *Phys. Rev. B.* **67** 155405.
- [24] Wei G, et al 2014 *J. Phys. Chem. C* **118** 119565–19571.
- [25] Edoardo M Paolo U and Filippo D A 2016 *Phys. Chem. Chem. Phys.* **18** 27158–27164.
- [26] Stenzel O 2005 *The physics of thin film optical spectra* (Springer-Verlag Berlin Heidelberg).

Structural and optical properties of spin coated graphene oxide films

B C Tladi, R E Kroon and H C Swart

Department of Physics, University of the Free State, Bloemfontein, South Africa

Email: Tladibc@ufs.ac.za, KroonRE@ufs.ac.za, SwartHC@ufs.ac.za

Abstract. Graphene oxide (GO) is a derivative of graphene, consisting of an atomic layer of carbon bonded to oxygen functional groups such as hydroxyl and epoxide, which make it insulating and hydrophilic. This novel material has attracted much research recently, although there is varying information in the literature, because the properties may depend on the synthesis technique and form (powder, film, solution). An investigation of the structural and optical properties of spin coated GO films was made. GO powder was purchased from Sigma Aldrich (15-20 sheets, 4-10% edge-oxidized) and used to prepare a GO suspension in distilled water (1 mg/ml), which was ultrasonicated and centrifuged. The supernatant black solution was spin coated on silicon substrates to produce films. The solution was characterized using photoluminescence (PL) and UV-vis absorption measurements, while the GO powder and films were assessed using X-ray diffraction (XRD). A broad absorption band was observed at 273 nm, although subsequent PL measurements showed that this was not an efficient excitation wavelength. Instead, the weak blue luminescence observed at 444 nm could be excited at 325 nm. Blue luminescence has been attributed to thoroughly exfoliated GO suspensions, while red emission (not observed here) to poorly dispersed suspensions. The Raman peak of water was observed on the short wavelength side of this emission. The XRD pattern for the commercial GO powder had a peak near $2\theta = 13.3^\circ$. This low angle, compared to the corresponding peak of graphite (26°), indicated much wider spaced interplanar layers as a result of oxidation, but showed that the GO was stacked in multiple layers. A weak band near 30° suggested that the powder probably also contained a small amount of graphite. This was absent for the film since it was likely removed by centrifuging. The XRD peak of the film was shifted to $2\theta = 13.8^\circ$, indicating a small reduction in the interplanar spacing. Although the XRD data corresponded to stacked GO, the optical properties suggest that significant reduction was present in the commercial powder.

1. Introduction

Nanoscience and technology are at the forefront of modern research which deals with the exploration and exploitation of nanomaterials. Since its discovery in 2004, graphene – one of the most promising nanomaterials, has increased research interest in graphene-based nanomaterials [1-2]. Graphene oxide (GO) is of great interest due to its low cost, easily scalable and widespread ability to convert to graphene i.e. chemically modified graphene. GO is a derivative of graphene which consists of an atomic layer of carbon bonded to oxygen functional groups such as hydroxyls and epoxides on the top and bottom surfaces and edges of each sheet. GO is produced from the oxidation of graphite using principle methods developed by Hummers [2]. GO has unique properties which

depend on the method of synthesis, the material form as well as the level of oxidization in the compound [3]. GO can be reduced using chemical and physical treatments. The reduction of GO partly restores the structure and properties of pristine graphene. Different reduction processes results in different properties of reduced GO (rGO). These properties of GO and rGO makes them potential candidates for the coatings as transparent electrodes for light-emitting diodes (LEDs) [4] and solar cell devices [5]. For this work we investigated the structural and optical properties of spin coated GO films. These GO films will be used to form coatings over phosphors thin films i.e. ZnO:Zn and $\text{La}_2\text{O}_2\text{S:Eu}^{3+}$, which can provide protection from environmental degradation and its effect on the optical properties.

2. Experimental

GO powder (15-20 sheets, 4-10% edge oxidized) was purchased from Sigma Aldrich and used as received. 100 mg of GO powder was suspended in 100 ml of de-ionized water under ultrasonication for 30 min. Then the black solution was centrifuged at 4000 rpm for 30 min to separate large particles from the exfoliated GO sheets. 40 μL of the supernatant solution was dropped onto a cleaned silicon (100) wafer and spin coated at 3000, 4000, 6000, or 8000 rpm for 30 s. The coated samples were dried on a hot-plate at 100 $^{\circ}\text{C}$ in air for 10 min to evaporate the solvent. The coating process was repeated 5 times Structural and optical properties of the films were then assessed. X-ray diffraction (XRD) using a Bruker D8 Advance instrument was used to analyze the crystal structure of the powder and films. The scans were measured in the conventional theta-2theta configurations in the range 5-80 $^{\circ}$ in a step of 0.01 $^{\circ}$ while the X-ray generator was set at 40 kV and 40 mA. Scanning electron microscopy (SEM) performed with a JEOL JSM-7800F instrument was used to assess the surface morphology and uniformity of the films. Atomic force microscopy (AFM) was performed using a Shimadzu SPM-9600 system to analyze the surface topography. The optical properties were analyzed using UV-vis spectroscopy (PerkinElmer Lambda 950) to measure the absorbance of the solution, while photoluminescence (PL) of the solution was recorded using an Edinburgh Instruments FLS980 system with xenon lamp (325 nm excitation wavelength) and PL of the film was excited using a Kimmon IK series He-Cd 325 nm laser and recorded with a Hamamatsu R942 photomultiplier tube attached to an Horiba iHR320 spectrometer.

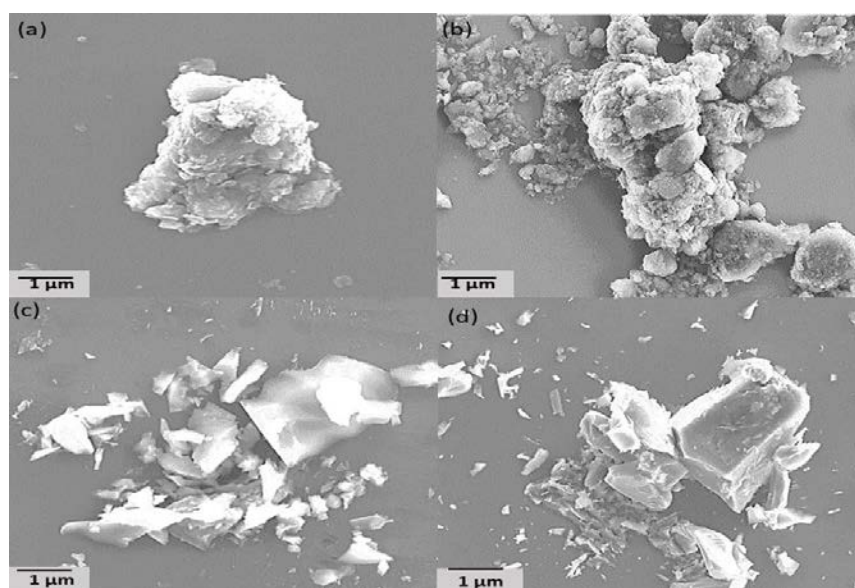


Figure 1. SEM images of GO films spun at (a) 3000, (b) 4000, (c) 6000 and (d) 8000

3. Results and discussion

3.1. Surface morphology

The morphology and uniformity of all films were observed using SEM images recorded at an accelerating voltage of 10 kV and higher magnification and are shown in Figure 1. The GO films are not uniform all over the substrate. Instead, the GO sheets look clustered, heavily wrinkled and scattered on the surface of the wafer, which results in less coverage of the silicon surface. This could have resulted due to minimum adhesion of the solution onto the surface of the wafer during spin coating and the Van der Waals attraction between the sheets. The film spun at 4000 rpm has greater coverage of the GO sheets on the substrate surface compared to others and therefore was used for further evaluation. The surface topography of this film was examined using AFM as shown in Figure 2, where the height of GO clusters was estimated to be about 100 nm.

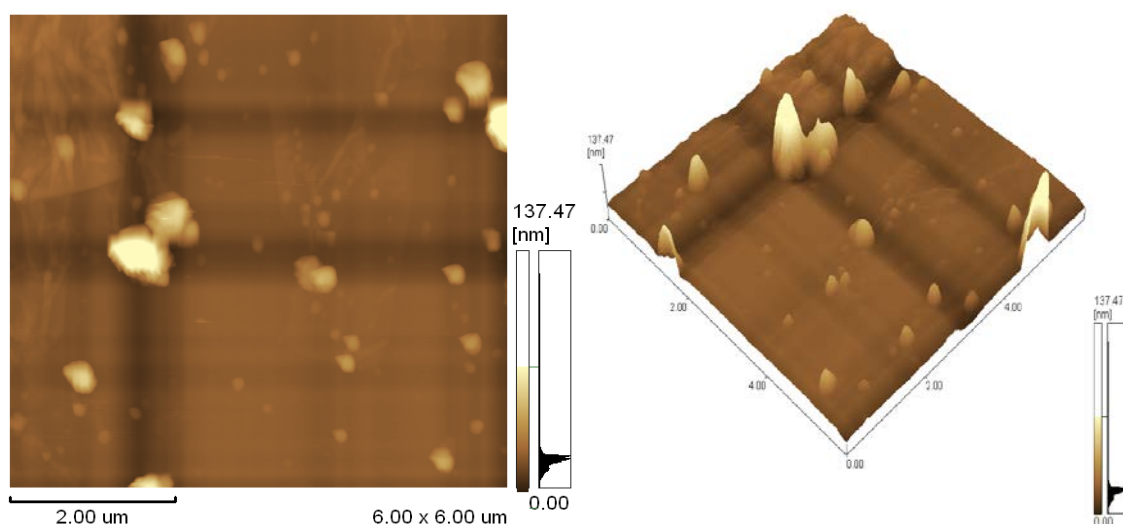


Figure 2. 2D and 3D AFM images of 4000 rpm spun sample. The dark bands intersecting at the particles are image processing artifacts due to the line-by-line background leveling algorithm.

3.2 X-ray diffraction analysis

XRD patterns of the GO powder and film are presented in Figure 2. The (001) XRD peak of the GO commercial powder was found at $2\theta = 13.3^\circ$, corresponding to an interplanar spacing of 0.665 nm (i.e. significantly expanded compared to 0.335 nm between the sheets of graphite). Diffraction corresponding to the c -axis interplanar spacing is only possible for multiple layers, which indicated that the GO was not thoroughly exfoliated into single sheets and may thus be visualized as multilayered graphite oxide. A weak peak near $2\theta = 30^\circ$ corresponding to the (002) plane is due to incomplete oxidation as the commercial powder is only 4-10% edge oxidized. The XRD pattern of the film only shows the characteristic peak at $2\theta = 13.8^\circ$ with interplanar spacing of 0.641 nm. Peaks from the silicon substrate were avoided by not rotating the sample, which was placed at a slight mis-orientation perpendicular to the diffractometer rotation axis. Most of the unoxidized graphite layers were probably removed during centrifugation. Based on literature, the XRD peak of graphite occurs near $2\theta = 26^\circ$ and when it has been oxidized the intensity of this peak sharply decreases and forms a new peak at around $2\theta = 15^\circ$ [6]. When graphite oxide is thoroughly exfoliated to form single or few layers of GO, the XRD peak shifts to lower angles at $2\theta \sim 10^\circ$ due to further expansion of the interlayer distance [7]. The XRD results of the GO samples are therefore in good agreement with published reports available in the literature.

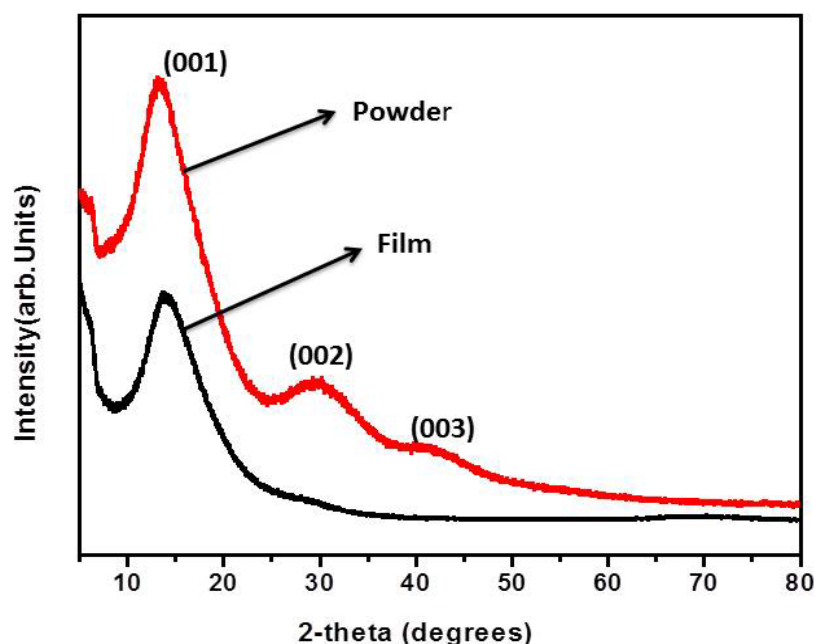


Figure 3. XRD patterns of GO powder and film.

3.3 Optical and photoluminescence studies

The absorption spectrum of the GO suspension in the range 200-800 nm is shown in Figure 4. The maximum absorbance of the commercial powder was found at 273 nm. The same peak was observed by Uran et al. [8] for different graphite materials (powder and rod) and assigned to graphene. In support that it could be the graphene peak, Thema et al. [9] and Eda et al. [10] have reported a red shift from 230 nm to ~270 nm for rGO which is most likely due to a decrease in the concentration of the carbonyl groups because GO sheets with less oxygen functional groups bonded to the carbon atoms have more sp² hybridized C-C bond similar to pristine graphene which its referred to as rGO. The optical absorbance of GO is reported to have two characteristics peaks i.e. the main peak at 230 nm due to π - π^* transitions of the C=C bonds and a shoulder peak at ~320 nm is attributed to the n- π^* transitions of the C=O bonds, which were not observed.

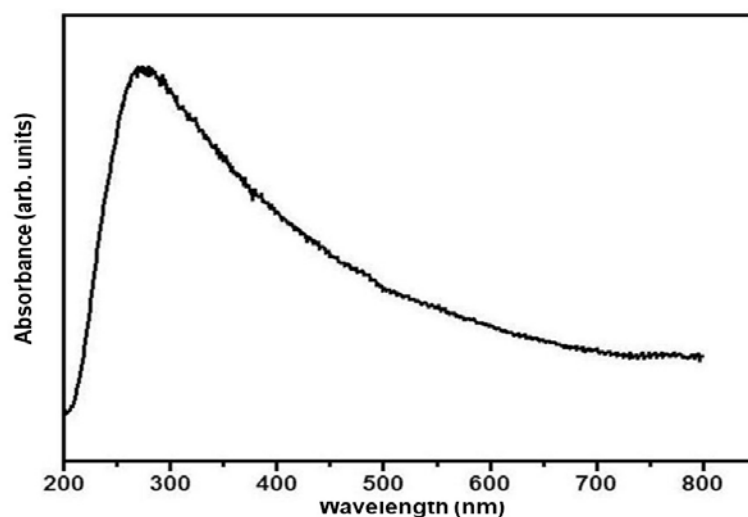


Figure 4. The absorbance spectrum of the GO suspension.

The PL spectra of the GO suspension and film are shown in Figure 5. Since the commercial powder is partially oxidized, a weak luminescence in the blue region at 444 nm was observed when excited at 325 nm for the suspensions and at 420 nm for the film. Due to the non-uniformity of the film, the luminescence of the film was very weak compared to the suspension. In agreement with the present results, Du *et al.* [11] reported a blue PL band of GO when excited at 320 nm and Eda *et al.* [10] reported similar results for highly exfoliated GO suspensions when excited at 320 nm. In contrast to our results, Chien *et al.* [12] reported a long wavelength (red) band when excited at 325 nm which Eda *et al.* [10] identified as emission from poorly exfoliated suspensions. Based on literature, GO is reported to have two main PL bands i.e. one in the blue band and another in the long wavelength band due to the opening of the band gaps caused by oxygen functionalities from oxidation. Only the blue emission was observed from our samples.

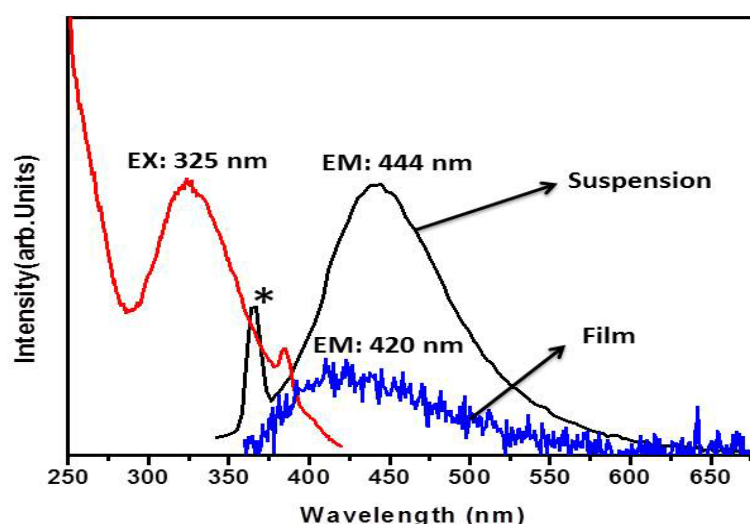


Figure 5. PL spectra of GO suspension and film. The peak labelled * is the Raman peak of water.

4. Conclusion

The commercial GO powder was partially oxidized (4-10%) and thus behaved as reduced, which was observed by the black colour compared to a yellow brown colour reported for well oxidized GO. The GO films were deposited on silicon substrates using spin coating technique. The SEM images revealed that the film spun at 4000 rpm had better surface coverage of the GO sheets. The XRD and UV-vis revealed that the powder still contained unoxidized graphite layers at $2\theta = 26^\circ$ which was supported by the shift in UV absorbance from 230 nm to 273 nm assigned to reduced GO. XRD of the film showed that the deposited GO was better exfoliated than in the original commercial powder, which is attributed to removal of the larger particles by centrifuging. PL measurements of the suspension and film showed a blue luminescence, which has been reported for highly exfoliated GO. Due to the poor uniformity of the GO films spin-coated over the substrate, alternate ways of producing such films will also be investigated in future work.

5. Acknowledgements

This work was financially supported by the South African National Nanoscience Postgraduate Teaching and Training Platform (NNPTTP) of the Department of Science and Technology (DST). This research is supported by the South African Research Chairs Initiative of the Department of Science and Technology and the National Research Foundation of South Africa (84415). This work is based on the research supported in part by the National Research Foundation of South Africa (R.E. Kroon, Grant Number 93214).

References

- [1] Perumbilavil S, Sankar P, Priya Rose T and Philip R 2015 *Appl. Phys. Lett.* **107** 051104
- [2] Hummers Jr W S, Offeman R E 1958 *J. Am. Chem. Soc.* **80** 1339
- [3] Jeong H, Lee Y P, Lahaye R J W E *et al.* 2008 *J. Am. Chem. Soc.* **130** 1362
- [4] Matyba P, Yamaguchi H, Eda G *et al.* 2010 *ACS Nano* **4** 637
- [5] Li S, Tu K, Lin C *et al.* 2010 *ACS Nano* **4** 3169
- [6] Zhang K, Zhang Y and Wang S 2013 *Sci. Rep.* **3** 3448
- [7] Wang X and Liu T 2011 *J. Macromol. Sci. B* **50** 1098.
- [8] Uran S, Alhani A and Silva C 2017 *AIP Advances* **7** 035323.
- [9] Thema F, Moloto M, Dikio E *et al.* 2013 *J. Chem.* **2013** 150536
- [10] Eda G, Lin Y, Mattevi C, *et al.* 2009 *Adv. Mater.* **21** 505
- [11] Du D, Song H, Nie Y, *et al.* 2015 *J. Phys. Chem C* **119** 20085
- [12] Chien C, Li S, Lai W *et al.* 2012 *Chemie Int. Ed.* **51** 6766

DIVISION B

Division for Nuclear, Particle and Radiation Physics

A comparative study of the high fluence neutron radiation effects on the properties of plastic scintillator UPS-923A for the TileCal of the ATLAS detector

V Baranov^a, Yu I Davydov^a, R Erasmus^{b,c}, C O Kureba^d, J E Mdhluli^e, B Mellado^{e,f}, G Mokgatitswane^{d,1}, E Sideras-Haddad^{e,c}, I Vasilyev^a, P N Zhmurin^g

^aJoint Institute for Nuclear Research, Dubna, Russia, 141980

^bSchool of Physics, University of the Witwatersrand, Johannesburg 2050, South Africa

^cDST-NRF Centre of Excellence in Strong Materials, University of the Witwatersrand, Johannesburg 2050, South Africa

^dDepartment of Physics and Astronomy, Botswana International University of Science and Technology, Private Bag 16, Palapye, Botswana

^eSchool of Physics and Institute for Collider Particle Physics, University of the Witwatersrand, Johannesburg, Wits 2050, South Africa

^fiThemba LABS, National Research Foundation, PO Box 722, Somerset West 7129, South Africa

^gInstitute for Scintillation Materials, Kharkov, Ukraine

E-mail: ¹gmokgatitswane@gmail.com

Abstract. The Ukrainian Polystyrene-based Scintillator (UPS-923A) doped with PTP and POPOP has been irradiated with a beam of neutrons. The neutron beams were provided by the IBR-2 pulsed reactor at the Frank Laboratory of Neutron Physics at the Joint Institute for Nuclear Research in Dubna, Russia. The neutron fluence ranged approximately between 10^{13} – 10^{16} neutrons/cm². A yellowish to brownish coloration in the plastic scintillator samples was observed after irradiation. The radiation effects on the mechanical and scintillation properties were investigated by conducting Raman spectroscopy and fluorescence yield measurements. The results obtained show a substantial drop in scintillation intensity, of 65% loss after neutron bombardment. This effect is attributed to radiation-induced absorption of the fluorescence light by the damaged polystyrene base. A slight change in the Raman intensity of aromatic structures was also observed.

1. Introduction

Plastic scintillators are organic hydrocarbon compounds that are capable of emitting light when they interact with ionizing radiation [1]. They have many advantages such as fast rise and decay time, high optical transmission for enabling efficient data acquisition, as well as the fact that the manufacturing process is straightforward. On the other hand, inorganic crystals are more difficult to fabricate. Plastic scintillators are more cost effective when covering the typically large detector areas. For these reasons, plastic scintillators are widely used around the world for radiation detection in the scientific and industrial fields. The calibre of radiation detector depends primarily on the quality of the plastic scintillator employed.

The radiation detector systems used in high energy physics experiments such as the ATLAS detector of the Large Hadron Collider at CERN drives the need for use of plastic scintillators that can withstand the harsh radiation environment. This dire need directs attention to study radiation hardness of currently

available plastic scintillators, to aid with the selection criteria of suitable fluorescence materials and ultimately develop radiation-hard scintillators for the future.

The plastic scintillator under investigation consists primarily of polystyrene base doped with 2% p-terphenyl (PTP) and 0.03% diphenyloxazolyl- benzene (POPOP) organic fluors [2]. The polystyrene base is a synthetic of aromatic benzene-ring structures that influence the scintillation properties of plastics. The chemical bonds present in a benzene ring are made up of σ -bonds which are in-plane and π -bonds which are out-of-plane of the benzene ring and overlap, as illustrated in Fig. 1. The π -bonds give rise to a delocalized electron clouds above and below the molecular plane as shown.

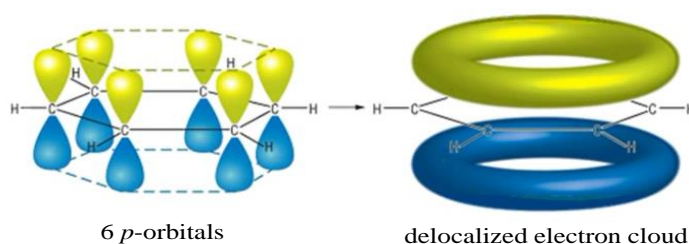


Figure 1: Representation of chemical bonding in a benzene molecule.

The π -electron structure plays a key role in the scintillation mechanism of plastic scintillators during interaction with energetic particles. Incident radiation causes electronic excitations within the benzene molecule. The de-excitation of π -electrons to the ground state through fluorescence results in the emission of photons within the visible light spectrum [1]. The neutron radiation damage of plastic scintillators has been studied and reported in Refs. [3, 4, 5]. This study forms a comparative investigation effort in understanding radiation hardness of plastic scintillators at high neutron fluences.

2. Experimental details

The structural properties of radiation damaged polystyrene-based scintillator UPS-923A were investigated. The samples were cut and polished to dimensions of 14.4 x 7.2 cm with 6 mm thickness at the Institute for Scintillation Materials (ISMA, Kharkov, Ukraine). The irradiation of samples was performed at the Frank Laboratory of Neutron Physics (FLNP) at the Joint Institute for Nuclear Physics (JINR) in Dubna, Russia using the IBR-2 pulsed reactor [6, 7].

The samples were bombarded with a beam of neutrons provided by the IBR-2 reactor operated at an average power of 1875 kW. In order to achieve varying target neutron fluences, the samples were placed at different positions away from the reactor core and water moderator. In addition, during the irradiation only neutrons with energy $E > 1$ MeV were monitored since they are the ones which provided high neutron fluences. The neutron fluence ranged approximately between 10^{13} – 10^{16} neutrons/cm². After irradiation, coloration of the samples was observed as neutron fluence increased. Figure 2 shows a photograph of the samples after irradiation.

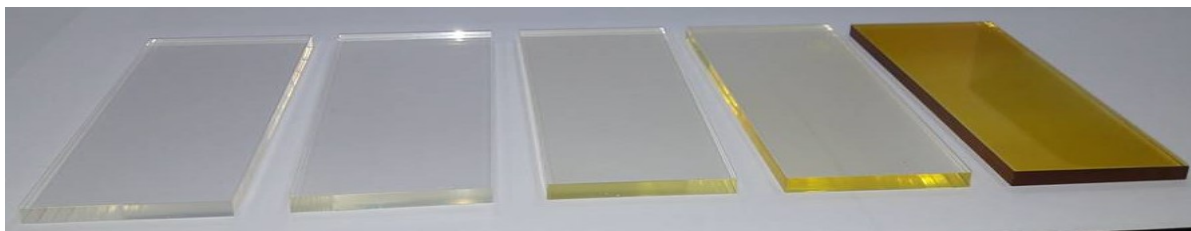


Figure 2: Neutron irradiated UPS-923A scintillators. From the left to right: non-irradiated, 10^{13} , 10^{14} , 10^{15} and 10^{16} neutrons/cm².

The assessment of structural disorder in samples after irradiation was performed by conducting Raman spectroscopy measurements. Raman spectroscopy is perhaps the most valuable method because it provides readily distinguishable structural signatures of carbon species present in the material. It is based on the Raman effect which is the result of inelastic scattering of light. The incident laser light interacts with lattice phonons leading to virtual excitations which then de-excite by releasing a photon of wavelength corresponding to a specific virtual mode. These Raman active modes are characteristic of certain bonding structures in the material. Raman spectra for the non-irradiated control samples as well as the irradiated samples were obtained using Horiba LabRAM HR Raman spectrometer. A 785 nm diode laser was used to excite the Raman modes and the spectrograph was calibrated via the zeroth order reflection of a white light source from the grating.

The scintillation efficiencies of irradiated samples were measured using the Horiba LabRAM HR Raman spectrometer. A laser excitation wavelength (λ_{ex}) of 244 nm, with a power of ~ 20 mW at the source spot size of $0.7 \mu\text{m}$ was used to excite light emission through luminescence, and a laser spot size of $0.7 \mu\text{m}$ provided energy that allowed molecular excitations to occur. A grid of 11×11 points (121 acquisition spots) was mapped across a surface area of $200 \times 200 \mu\text{m}$ using a motorised X-Y stage. This allowed for an average representative spectrum to be determined largely free from local variations introduced by surface features such as scratches.

3. Raman Spectroscopy Results and Analysis

Raman spectroscopy measurements were performed for non-irradiated control samples and irradiated samples. Figure 3 shows selected regions of Raman spectra containing aromatic structures. These structures are labeled as peak number 1 to 4 as shown in the figure. The peaks were assigned to their characteristic vibrational groups [8, 9].

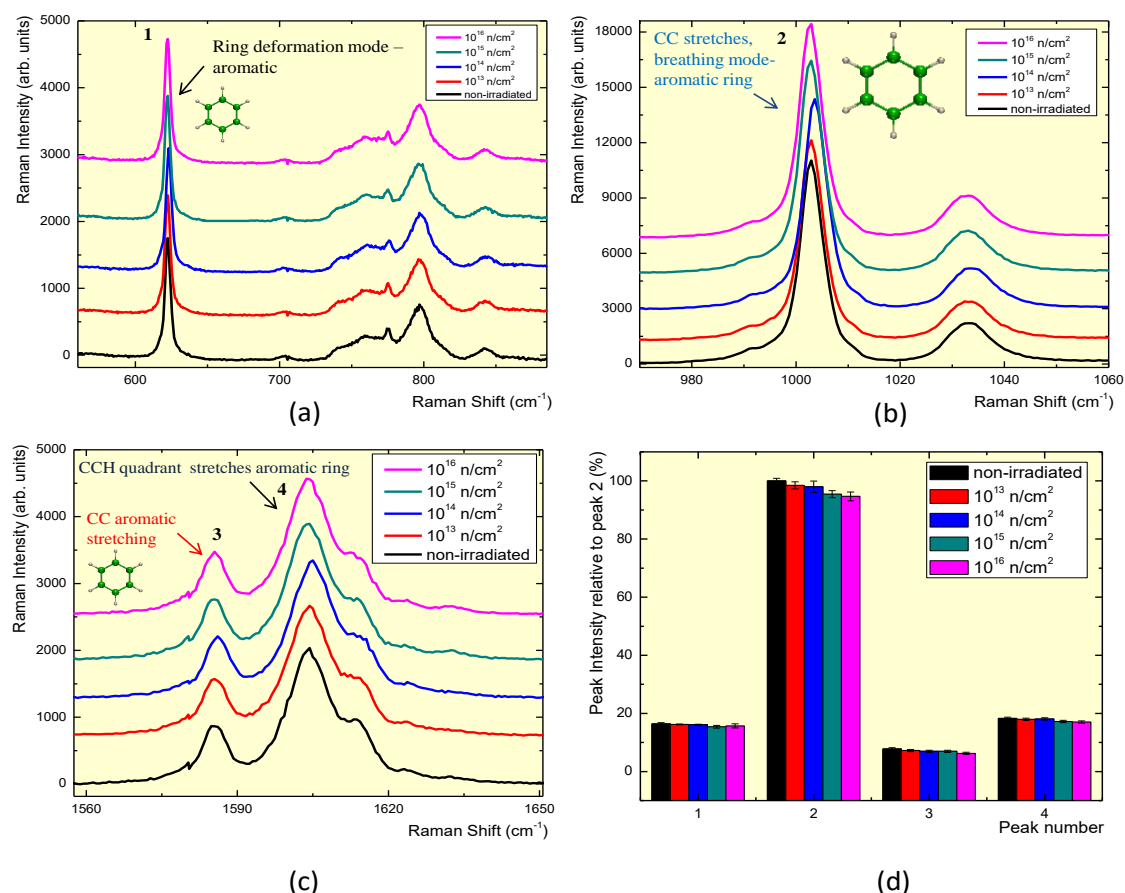


Figure 3: (a), (b) and (c)-Selected regions of background subtracted Raman spectra containing aromatic structures and (d)-Plot of intensities of peaks relative to peak 2 (non-irradiated) representing C-C breathing mode. NB: The Raman spectra have been vertically offset for better visual presentation.

The aromatic structures were assessed for radiation damage. The intensities of peaks were plotted relative to peak 2 (non-irradiated) in order to gauge change in the concentrations. Peak 2 corresponds to the breathing mode of the benzene ring. This is the most intense peak that largely influences the scintillation properties of plastics. With reference to Fig. 3(d), it can be observed that the intensities of peaks 1, 3 and 4 remain almost the same after irradiation. However, peak 2 becomes less intense as the neutron fluence increases. Torris, 2002 [10] ascribes this effect to a strong dehydrogenation due to the weak C-H bond breakage in the benzene ring and an emission of different C_xH_y groups with the absorbed neutron fluence. This reduces the concentration of species present in the material.

4. Fluorescence Spectroscopy Results and Analysis

Figure 4(a) shows the fluorescence spectra of non-irradiated and irradiated UPS-923A samples over a wavelength region of 300–505 nm. Several peaks are observed in the emission spectra. The wavelength regions at 300–375 nm and 375–505 nm correlate with fluorescence of the polystyrene base and organic fluor dopants, respectively. After irradiation of samples, a significant intensity drop is observed over the base region in comparison with fluor dopants region. There is competition for light absorption between the radiation-induced free radicals and fluor dopants [11].

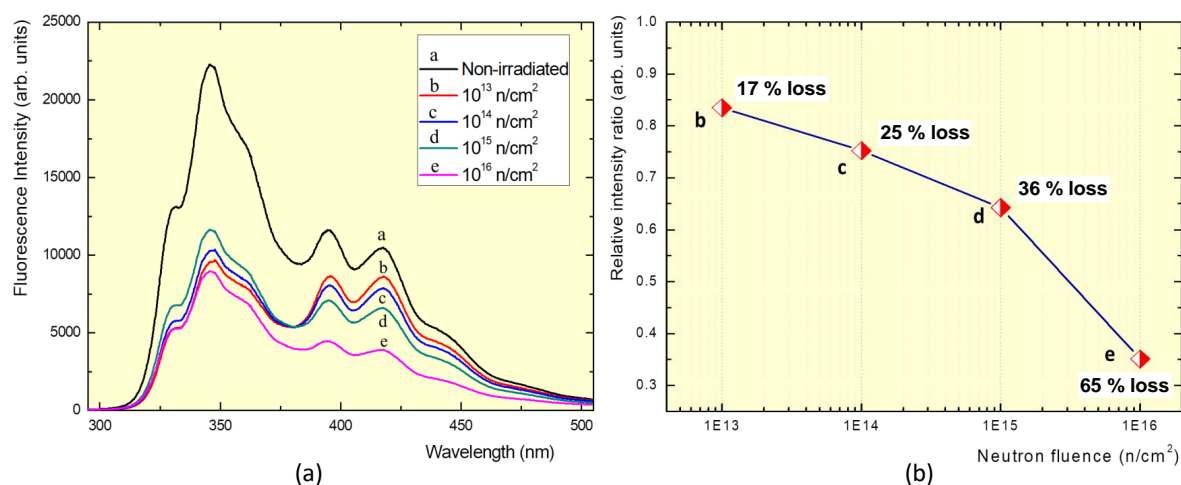


Figure 4: (a)-Fluorescence spectra and (b)-Relative intensity ratio as a function of neutron fluence measured at 430 nm wavelength, for UPS-923A samples.

Figure 4(b) shows relative intensity losses as a function of neutron fluence. This was measured at a wavelength of 430 nm since it correlates with the peak absorption wavelength of the wavelength shifting optical (WLS) fibers. An intensity loss of 65% is observed at higher neutron fluence of 10^{16} neutrons/cm², compared with much lesser percentage losses at lower fluences.

5. Conclusion

The structural and scintillation properties of Ukrainian polystyrene-based UPS-923A scintillator irradiated with a beam of neutrons were investigated. All the irradiated scintillator samples reveal evidence of radiation damage. A yellowish to brownish coloration in the plastic scintillator samples was observed after irradiation with higher neutron fluence. When a plastic scintillator is bombarded with high energy particles, weak C–H chemical bonds within the material are broken and form free radicals. The free radicals initiate chemical reactions and form absorption color centers which could account for the observed coloration [10].

The aromatic benzene structures present in the scintillator material were identified and assessed through Raman spectroscopy. These species play a very important role in the scintillation mechanism since they give rise to delocalized electron clouds responsible for fluorescing upon excitation by incident ionising radiation. Amongst the four aromatic structures identified (peak 1 to 4), a noticeable slight intensity decrease was only observed in peak 2. This peak largely contributes to the scintillation yield of plastics, it typically represents C–C ring breathing mode. The decrease in the intensity is ascribed to breakage of chemical bonds after irradiation.

From the fluorescence results obtained, it is evident that neutron bombardment affects the luminescence properties of plastic scintillators. A significant drop in the fluorescence yield is observed. At higher neutron fluences, radiation induced free radicals absorb the fluorescence light that could have been detected. The damage to the π -electron structure within the polymer matrix also accounts for the fluorescence yield losses.

6. Acknowledgement

We would like to express our gratitude to staff of the Institute for Scintillation Materials in Kharkov, Ukraine for providing plastic scintillators for this study, the staff of Frank Laboratory of Neutron Physics at the Joint Institute for Nuclear Research in Dubna, Russia for making the IBR-2 reactor available for

irradiation, as well as the University of the Witwatersrand for providing equipment for analysis. This project was funded by BIUST, SA-CERN consortium, NRF-SA and SA-JINR.

References

- [1] Knoll G F 2010 *Radiation Detection and Measurement, Fourth Edition* (New York: John Wiley & Sons Inc.) 223–224
- [2] Artikov A, Budagov J, Chirikov-Zorin I, Chokheli D, Lyablin M, Bellettini G, Menzione A, Tokar S, Giokaris N and Manousakis-Katsikakis A 2005 *Nucl. Instr. Meth. Phys. Res. A* **555** 125–131
- [3] Mdhululi J E, Davydov Yu I, Baranov V, Mthembu S, Erasmus R, Jivan H, Khanye N, Tlou H, Tjale B, Starchenko J, Solovyanov O, Mellado B and Sideras-Haddad E 2017 *J. Phys.: Conf. Series* **889** 012009
- [4] Mdhululi J E, Jivan H, Erasmus R, Davydov Yu I, Baranov V, Mthembu S, Mellado B, Sideras-Haddad E, Solovyanov O, Sandrock C, Peter G, Tlou S, Khanye N, Tjale B 2017 *J. Phys.: Conf. Series* **878** 012008
- [5] Mthembu S, Davydov Yu I, Baranov V, Mellado B, Mdhululi J and Sideras-Haddad E 2017 *J. Phys.: Conf. Series* **889** 012019
- [6] Bulavin M, Cheplakov A, Kukhtin V, Kulagin E, Kulikov S, Shabalin E and Verkhoglyadov A 2015 *Nucl. Instr. Meth. Phys. Res. B* **343** 26–29
- [7] Shabalin E P, Verkhoglyadov A E, Bulavin M V, Rogov A D, Kulagin E N and Kulikov S A 2015 *Nucl. Instr. Meth. Phys. Res. B* **12** 336–343
- [8] Holder J M, Wynn-Williams D D and Rull Perez F 2000 *New Phytol.* **145** 271–280
- [9] Menezes D B, Reyer A, Marletta A and Musso M 2017 *Mater. Res. Express* **4** 015–303
- [10] Torrisi L 2002 *Radiat. Phys. Chem.* **63** 89–92
- [11] Busjan W, Wick K and Zoufal T 1991 *Nucl. Instr. Meth. Phys. Res. B* **152** 89–104

AdS/CFT predictions for correlations, suppression, and flow of heavy flavours at RHIC and LHC

R Hambrock and WA Horowitz

Department of Physics, University of Cape Town, Private Bag X3, Rondebosch 7701, South Africa

E-mail: roberthambrock@gmail.com, wa.horowitz@uct.ac.za

Abstract. We use two AdS/CFT based energy loss models to compute the suppression, flow, and azimuthal correlations of heavy quarks in heavy ion collisions at RHIC and LHC. The model with a velocity independent diffusion coefficient is in good agreement with **B** and **D** meson suppression data up to high transverse momentum. The partonic azimuthal correlations are compared with those from perturbative QCD based simulations, Ref. [1]. When restricted to leading order production processes, we find that the strongly coupled correlations of high transverse momentum pairs (> 4 GeV) are broadened less efficiently than the corresponding weak coupling based correlations, while low transverse momentum pairs ($1 - 4$ GeV) are broadened with similar efficiency, but with an order of magnitude more particles ending up in this momentum class. We thus propose heavy flavour momentum correlations as a distinguishing observable of weakly- and strongly-coupled energy loss mechanisms.

1. Introduction

The quark gluon plasma is of great interest since it represents our first case study of the emergent physics of the non-abelian gauge theory QCD. A key step in understanding this state of matter is identifying its relevant coupling strength. The perturbative techniques of QCD are only adequate in a weakly coupled plasma, with calculations for strongly coupled plasmas constrained to methods like AdS/CFT-based approaches or Resonance Scattering [2]. Both weak and strong coupling based approaches have had their respective successes in the past. For instance, measurements of the nuclear modification factor of pions, R_{AA}^π , show surprisingly consistent agreement with predictions from pQCD based models [3], while AdS/CFT based calculations have fared strongly by predicting a global lower bound on the shear-viscosity-to-entropy ratio of QGP-like systems of, in natural units, $\frac{\eta}{s} \sim 0.1$ [4], which is in line with hydrodynamic inferences from collider data from LHC and RHIC [5].

Both frameworks show qualitative agreement with measurements of the nuclear modification factor of **D**-mesons, R_{AA}^D [3], suggesting they have attained sufficient maturity to investigate more differential observables.

In [1], the azimuthal correlations of heavy $q\bar{q}$ pairs in a weakly coupled plasma in Pb+Pb collisions (center-of-mass energy $\sqrt{s} = 2.76\text{TeV}$) were studied, both for a model using purely collisional energy loss and one additionally incorporating radiative corrections. These weak coupling based azimuthal correlations provide a secondary indicator for the momentum correlations of heavy quarks. We will compare these correlations with two different AdS/CFT based energy loss models, one having a velocity-*dependent* diffusion coefficient [6], and the other

having a diffusion coefficient that is *independent* of the heavy quark's velocity [7]. Furthermore, we will probe the spectrum of their possible predictions (translated back to QCD) with two plausible [8] 't Hooft coupling constants ($\lambda_1 = 5.5$ and $\lambda_2 = 12\pi\alpha_s \approx 11.3$ with strong coupling $\alpha_s = 0.3$) where for λ_1 , we also equate the QCD and $\mathcal{N} = 4$ super Yang-Mills (which is dual to the AdS_5 setting our calculations are performed in) temperatures, while λ_2 has the QCD temperature equated with the $\mathcal{N} = 4$ super Yang-Mills energy density instead.

The calculations will be performed at leading order for the same transverse momentum classes as in [1]. Additionally, we will consider momentum correlations that take initial momentum correlations into account. These correlations provide evidence that heavy quarks traversing a strongly coupled plasma are more likely to stay correlated in momentum than they would if inside a weakly coupled plasma, and we thus argue that heavy flavour momentum correlations constitute a promising differentiator between weakly and strongly coupled plasmas.

Finally, we will compare our results with heavy flavour measurements from LHC and provide predictions for RHIC.

2. Energy Loss Model

2.1. Overview

The following will outline our computational procedure and its background. Subsequent to initializing the momenta of heavy quark pairs either to leading order with FONLL [9] or to next-to-leading order with aMC@NLO [10] using Herwig++ [11] for the showering, the production points of the heavy quarks are weighted by the Glauber binary distribution [6]. The particles are propagated through the plasma via the energy loss mechanism described in 2.2, either until the temperature in their local fluid cell drops below a critical threshold where hadronization is presumed to occur, or until the maximum time the VISHNU background [5] is calculated for has passed. If next-to-leading order initialization has been used, the heavy quarks are now hadronized. Finally, the heavy quarks are binned pairwise according to their relative azimuthal angle and each particle's final three-momentum.

2.2. Langevin Energy Loss

The stochastic equation of motion for a heavy quark in the fluid's rest frame is [12]

$$\frac{dp_i}{dt} = -\mu p_i + F_i^L + F_i^T \quad (1)$$

where F_i^L and F_i^T are longitudinal and transverse momentum kicks with respect to the quark's direction of propagation and μ is the drag loss coefficient, given by $\mu = \pi\sqrt{\lambda}T^2/2M_Q$ [13] where M_Q is the mass of a heavy quark in a plasma of temperature T with 't Hooft coupling constant λ . The correlations of momentum kicks at time t_1 and t_2 are given by

$$\langle F_i^T(t_1)F_j^T(t_2) \rangle = \kappa_T(\delta_{ij} - \frac{\vec{p}_i\vec{p}_j}{|\vec{p}|^2})g(t_2 - t_1) \quad (2) \quad \langle F_i^L(t_1)F_j^L(t_2) \rangle = \kappa_L \frac{p_i p_j}{|\vec{p}|^2} g(t_2 - t_1) \quad (3)$$

where the function g is only known numerically [6] and with

$$\kappa_T = \pi\sqrt{\lambda}T^3\gamma^{1/2} \quad (4) \quad \kappa_L = \gamma^2\kappa_T = \pi\sqrt{\lambda}T^3\gamma^{5/2} \quad (5)$$

$$\hat{q} = \langle p_\perp(t)^2 \rangle \lambda \approx \kappa_T t / \lambda = \gamma(2\pi T^3 \sqrt{\lambda}) / v \quad (6)$$

where γ is the speed of the quark. It should be noted that this construction does not obey the fluctuation-dissipation theorem [6]. The computations based on this model will be labeled $D(p)$.

2.3. Development on energy loss model

The problem with the energy loss mechanism described in 2.2 is that, since the longitudinal momentum fluctuations grow as $\gamma^{\frac{5}{2}}$, our setup breaks down for high momenta, where in a

perturbative QCD setting, Brehmstrahlung would restrict the momentum growth of the quark. Via a novel calculation presented in [7, 14, 15], we instead consider a stationary string in AdS_d hanging into a black hole horizon and calculate $s^2(t, a, d)$, the average transverse distance squared travelled by the string's free endpoint, where t is the time, d the dimension of the setup, and a parametrizes between a heavy quark for $a = 0$ and a light quark for $a = 1$. Crucially, $s^2(t, a, d = 3)$ can be determined analytically for small string lengths, which is identical to the asymptotically late time behavior of a string with arbitrary initial length. We thus find the asymptotically late time behavior of a string in d dimensions by

$$\begin{aligned} s^2(t \gg \beta, a, d) &= s_{\text{small}}^2(t \gg \beta, a, d) \\ &= \left(\frac{d-1}{2}\right)^2 s_{\text{small}}^2(t \gg \beta, a, d = 3) = \frac{(d-1)^2}{8\pi\sqrt{\lambda}} \beta \left(1 - \frac{a}{2}\right) \end{aligned} \quad (7)$$

where $\beta = T^{-1}$. At late times, the motion is diffusive, thus we can extract the diffusion coefficient

$$D(a, d) \sim \frac{1}{2} s^2(t \gg \beta, a, d) \quad (8)$$

which in AdS_5 for a heavy quark reads $2\beta/\pi\sqrt{\lambda}$. From this, we obtain

$$\kappa_T = 2T^2/D = \pi\sqrt{\lambda}T^2/\beta = \pi\sqrt{\lambda}T^3 \quad (9)$$

$$\hat{q} = \langle p_{\perp}(t)^2 \rangle \lambda \approx \kappa_T t / \lambda = (2\pi T^3 \sqrt{\lambda}) / v \quad (10)$$

Requiring these fluctuations to obey the fluctuation-dissipation theorem (which the construction in 2.2 could not), we attain $\mu = \pi\sqrt{\lambda}T^2/2E$. The computations based on this model will be labeled $D=const$.

3. Leading Order Correlations

3.1. 2D correlations

In Fig. 1 and Fig. 2, the $\frac{d^2N}{d\phi dp_T}$ correlations in Pb+Pb collisions $\sqrt{s_{NN}} = 2.76$ TeV at 40 – 50% centrality¹, are depicted for representative sections of the respective transverse momentum p_T . We observe that, for low p_T , we attain very efficient broadening of the angular correlations. For mid p_T , the angular correlations are much tighter, however with greater broadening of the momentum correlations, at least in absolute terms. For $\lambda_2 = 11.3$, both angular and momentum correlations are much weaker than for $\lambda_1 = 5.5$, given the larger consequent drag coefficient of the former.

3.2. Azimuthal correlations

In [1], at leading order, the weak coupling based computations exhibited very efficient broadening of initial azimuthal correlations for low p_T $b\bar{b}$ pairs ([4 – 10] GeV), which were washed out once NLO production processes were taken into consideration.

Both for mid- and high- p_T ([4–10] GeV and [10–20] GeV respectively), the initial correlations survive to a large degree, both at leading order and at next-to-leading order, suggesting that they may still be observable in an experimental context.

We compare our strong coupling azimuthal correlations to the weak coupling ones in Fig. 3. For [10 – 20] GeV, our correlations are significantly more peaked at their initial back-to-back correspondence. At [4 – 10] GeV, this observation still holds for the upper bound of our

¹ In Monte Carlo simulations of heavy ion collisions, the centrality quantifies the percentage of collisions that have a smaller impact parameter than the considered collision. In experimental heavy ion collisions, an estimator of the impact parameter has to be used, such as the charged particle multiplicity or the transverse energy of the collision (both inversely correlated with the impact parameter). For a detailed discussion, see [16].

$$\lambda_1 = 5.5$$

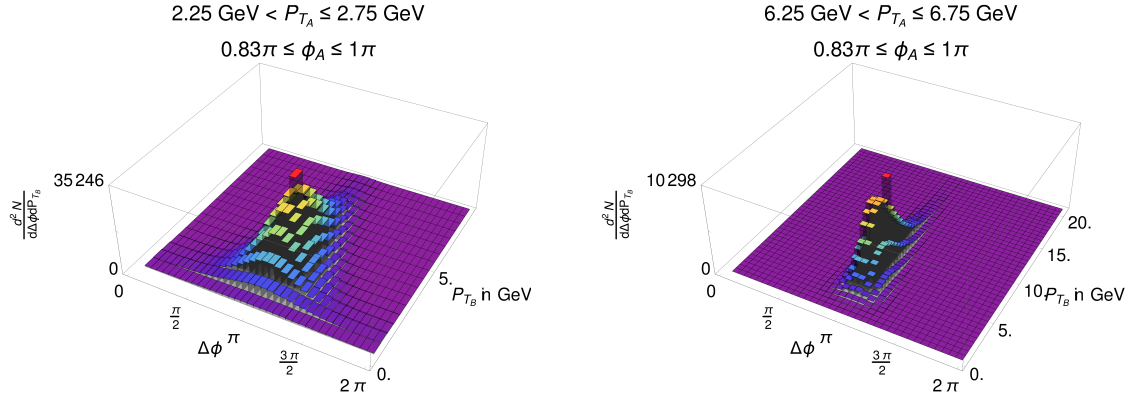


Figure 1: $\frac{d^2 N}{d\phi dp_T}$ of $b\bar{b}$ pairs for $p_A = \{2.5, 6.5\}$ GeV in the $D(p)$ model

$$\lambda_2 = 11.3$$

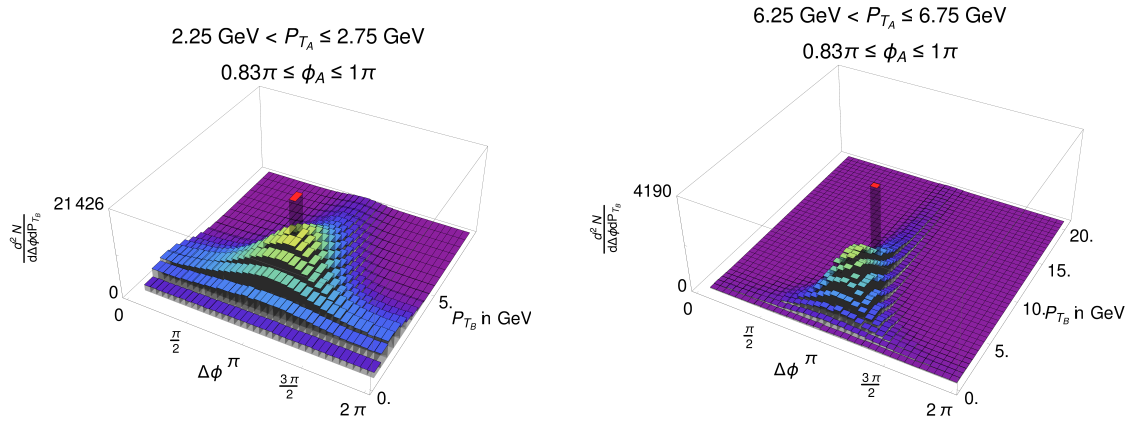


Figure 2: $\frac{d^2 N}{d\phi dp_T}$ correlations of $b\bar{b}$ pairs for $p_A = \{2.5, 6.5\}$ GeV in the $D(p)$ model

parameters with $\lambda_1 = 5.5$, while the $\lambda_2 = 11.3$ bounded result is of similar magnitude, but with looser angular correlation than either the collisional or the collisional + Bremsstrahlung based results. In the $[1 - 4]$ GeV range, the azimuthal correlations are almost entirely washed out for $\lambda_2 = 11.3$, while for $\lambda_1 = 5.5$, they are broadened with similar efficiency to the weak coupling results.

Of particular interest is the difference in momentum correlations the $[1 - 4]$ GeV range exhibits. At about an order of magnitude, this difference promises a distinguishing observable of weak- and strong-coupling energy loss in the medium, and should be investigated experimentally.

4. R_{AA} and v_2

We compare bottom and charm suppression predictions with data from CMS and ALICE (Fig. 4). While the agreement with CMS data for **B** meson suppression is comparable between the $D(p)$ and $D=const$ models, the comparison with ALICE data for **D** mesons shows the limited validity range of the $D(p)$ model, whereas the $D=const$ model remains consistent with data even for high- p_T . More fundamentally, for the $D(p)$ model, the AdS/CFT picture naturally breaks down at $p_T \sim 100$ GeV [6]. For the $D=const$ model, there is no such natural breakdown. Only

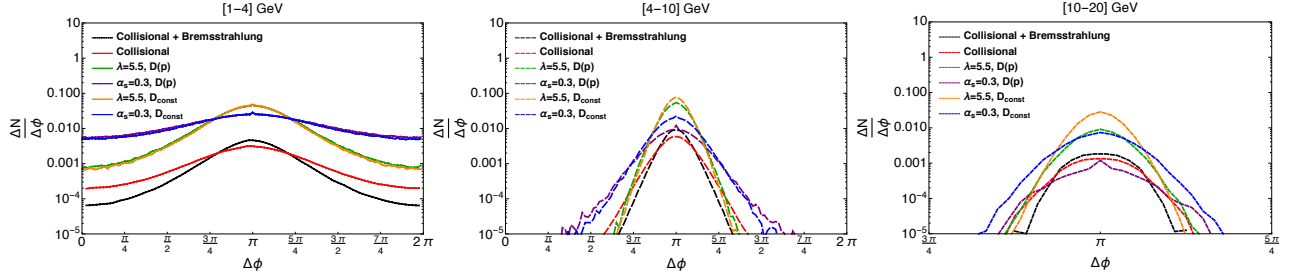


Figure 3: $\frac{dN}{d\phi}$ correlations for the specified classes.

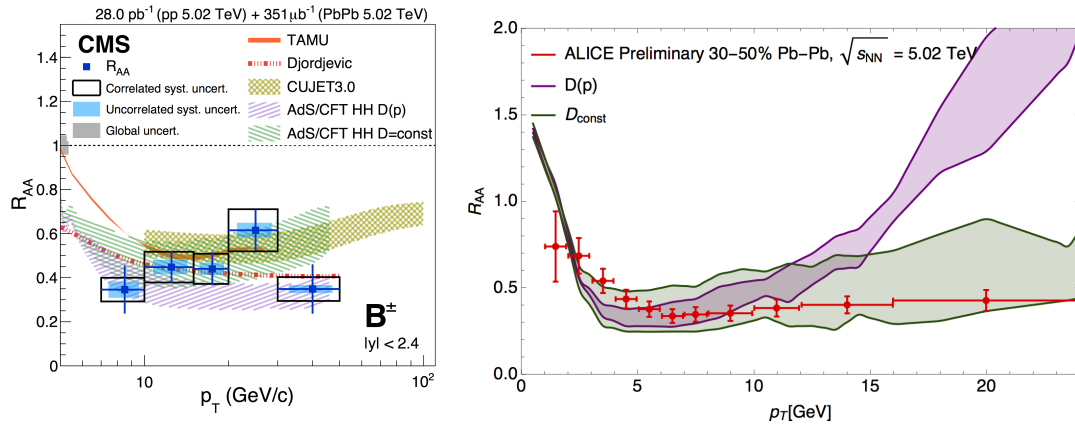


Figure 4: (Left) Comparison with R_{AA}^B data from CMS [17] with $\sqrt{s_{NN}} = 5.02$ TeV, $|y| < 2.4$. (Right) Comparison with R_{AA}^D data from ALICE [18] with $\sqrt{s_{NN}} = 5.02$ TeV, $|y| < 0.5$. The bands range from $\lambda = 5.5$ to $\lambda = 11.3$.

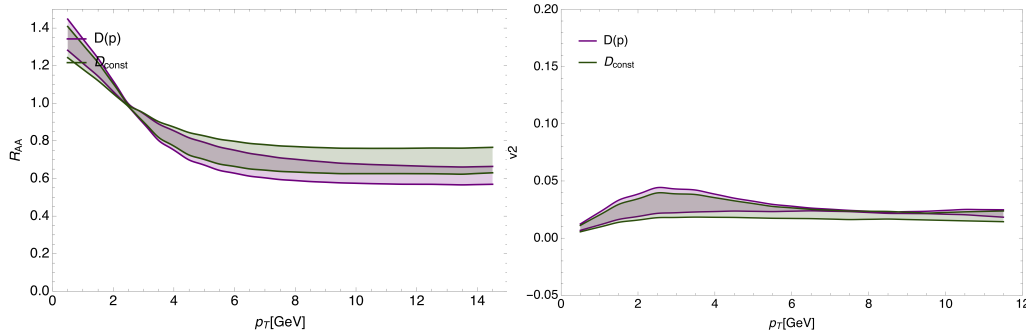


Figure 5: (Left) R_{AA}^B and (Right) v_2^B with $\sqrt{s_{NN}} = 200$ GeV, $|y| < 1.0$ and 10–40% centrality for future RHIC measurements. The bands range from $\lambda = 5.5$ to $\lambda = 11.3$.

for asymptotically large p_T and T is one guaranteed that the physics is perturbative.

In Fig. 5, we show our predictions for suppression and flow of **B** mesons at RHIC. **B** mesons are noticeably less suppressed than at the LHC, due to the substantially cooler medium in heavy collisions at RHIC.

The bands of our predictions range from $\lambda = 5.5$ to $\lambda = 11.3$ and account for statistical uncertainties. We note that, in particular for the high- p_T range of the **B** meson predictions in

Fig. 4 (left), our results' uncertainty is significant for high- p_T . This is due to the production spectrum of heavy quarks dropping as $\sim p_T^{-4}$. The aMC@NLO framework, at the time of writing, does not allow event generation weighted by p_T . In future work, we will use POWHEG's weighted event generation [19] to explore high- p_T phase space of our observables.

5. Conclusion & Outlook

We have compared the azimuthal correlations predicted by pQCD and AdS/CFT based computations and found that, while the azimuthal correlations are qualitatively similar, the momentum correlations tell a different tale. In particular, the surprise of our findings is the large dissimilarity in low momentum correlations of the pQCD and AdS/CFT based simulations; see Fig. 3 (left). Thus, bottom quark momentum correlations present an opportunity to distinguish between the energy loss mechanisms of the two frameworks.

Whether this order of magnitude difference in predictions for low p_T correlations of heavy quarks exposes weaknesses in either or both of the frameworks cannot be declared until experimental data of bottom quark momentum correlations emerge. Strong coupling based approaches have fared better in the low momentum domain, where pQCD is restrained by uncertainties in the running coupling.

While the agreement with CMS data for **B** meson suppression is comparable between the $D(p)$ and $D=const$ models, the comparison with ALICE data for **D** mesons shows the limited validity range of the $D(p)$ model. In contradistinction, the $D=const$ model remains consistent with data even for high- p_T . The RHIC data exhibits decreased suppression compared with the LHC data, which can be understood from the lower temperatures of the medium at RHIC.

The high- p_T reach of recent results from the LHC Fig.4, particularly CMS Fig.4 (left), exposes the limited statistics of our simulations for high- p_T . In future calculations, we will migrate from aMC@NLO to POWHEG [19] to facilitate weighted event generation, which mitigate the issue of limited statistics at high- p_T .

6. Acknowledgements

The authors wish to thank the NRF and SA-CERN for their generous financial support.

References

- [1] Nahrgang M, Aichelin J, Gossiaux P B and Werner K 2014 *Phys. Rev.* **C90** 024907 (*Preprint* 1305.3823)
- [2] Casalderrey-Solana J, Liu H, Mateos D, Rajagopal K and Wiedemann U A 2011 *Gauge/String Duality, Hot QCD and Heavy Ion Collisions* (*Preprint* 1101.0618)
- [3] Horowitz W A 2013 *Nucl. Phys.* **A904-905** 186c–193c (*Preprint* 1210.8330)
- [4] Gubser S S, Klebanov I R and Peet A W 1996 *Phys. Rev.* **D54** 3915–3919 (*Preprint* hep-th/9602135)
- [5] Shen C, Heinz U, Huovinen P and Song H 2011 *Phys. Rev.* **C84** 044903 (*Preprint* 1105.3226)
- [6] Horowitz W A 2015 *Phys. Rev.* **D91** 085019 (*Preprint* 1501.04693)
- [7] Moerman R W and Horowitz W A 2016 (*Preprint* 1605.09285)
- [8] Gubser S S 2008 *Nucl. Phys.* **B790** 175–199 (*Preprint* hep-th/0612143)
- [9] Cacciari M, Frixione S, Houdeau N, Mangano M L, Nason P and Ridolfi G 2012 *JHEP* **10** 137 (*Preprint* 1205.6344)
- [10] Alwall J, Frederix R, Frixione S, Hirschi V, Maltoni F, Mattelaer O, Shao H S, Stelzer T, Torrielli P and Zaro M 2014 *JHEP* **07** 079 (*Preprint* 1405.0301)
- [11] Bahr M *et al.* 2008 *Eur. Phys. J.* **C58** 639–707 (*Preprint* 0803.0883)
- [12] Moore G D and Teaney D 2005 *Phys. Rev.* **C71** 064904 (*Preprint* hep-ph/0412346)
- [13] Herzog C P, Karch A, Kovtun P, Kozcaz C and Yaffe L G 2006 *JHEP* **07** 013 (*Preprint* hep-th/0605158)
- [14] Hambrock R and Horowitz W 2017 *J. Phys. Conf. Ser.* **889** 012015
- [15] Hambrock R and Horowitz W A 2017 *Nucl. Part. Phys. Proc.* **289-290** 233–236 (*Preprint* 1703.05845)
- [16] Das S J, Giacalone G, Monard P A and Ollitrault J Y 2018 *Phys. Rev.* **C97** 014905 (*Preprint* 1708.00081)
- [17] Sirunyan A M *et al.* (CMS) 2017 *Phys. Rev. Lett.* **119** 152301 (*Preprint* 1705.04727)
- [18] ALICE Collaboration 2017 (*Preprint* ALI-PREL-128542)
- [19] Alioli S, Hamilton K, Nason P, Oleari C and Re E 2011 *JHEP* **04** 081 (*Preprint* 1012.3380)

Performance of missing transverse energy reconstruction in pp collisions at 13 TeV in the diphoton channel with ATLAS

S. Liao, B. Mellado and X. Ruan on behalf of the ATLAS Collaboration

School of Physics, University of the Witwatersrand, 1 Jan Smuts Avenue, Braamfontein, Johannesburg, 2000, South Africa

E-mail: shell-may.liao@cern.ch

Abstract. A good measurement of missing transverse energy is pre-eminent for many searches for new physics carried out by the ATLAS experiment at the LHC. The measurement of missing transverse energy in the ATLAS detector makes use of the full event reconstruction and a calibration based on reconstructed physics objects. The performance of MET reconstruction is evaluated using data collected in proton-proton collisions at a centre-of-mass energy of 13 TeV in Run 2 of data taking in the diphoton channel. Regrettably, these high luminosities achieved lead to undesirable backgrounds due to additional proton-proton collisions occurring at the same bunch crossing as the collision of interest (pile-up). As a result of this downside, several methods have been implemented in an effort to alleviate the effects of pile-up on the reconstruction and performance of MET. Some of these methods and the consequent performance of MET reconstruction at ATLAS in events with two photons are deliberated.

1. Introduction

A particle consistent with the Standard Model (SM) Higgs boson (h) was observed by the ATLAS [1] and CMS [2] collaborations back in 2012. Since then, more efforts have been directed towards performing Higgs boson measurements in order to better understand its properties. At the Large Hadron Collider (LHC), missing transverse energy (MET) plays an important role in Higgs boson measurements and various Beyond the Standard Model (BSM) physics searches. In proton-proton collisions most of the SM particles leave tracks or deposit energy inside the detector compartments as they traverse it, however, this is not the case for undetectable particles such as neutrinos and other possible BSM particles. The initial momentum of the colliding particles is almost zero in the transverse plane such that the presence of these undetectable particles can be inferred by the resultant momentum imbalance in this plane. This momentum imbalance is referred to as MET and is essentially enforced by energy-momentum conservation.

The high luminosity in Run 2 of data taking results in an increase in the additional proton-proton collisions which are superimposed on the hard physics processes. These additional interactions are referred to as pile-up interactions. MET measurement is significantly affected by these pile-up interactions and various techniques have been developed by ATLAS to suppress such effects. A high pile-up environment enhances the number of fake tracks thus increasing

the probability of misreconstruction. The performance of the reconstruction of this MET is therefore essential in evaluating these fake MET suppression efforts.

The diphoton channel ($h \rightarrow \gamma\gamma$) is important for searches for BSM physics, since new high-mass states decaying to two photons are predicted in many classes of extensions of the SM. The $h \rightarrow \gamma\gamma$ decay channel provides a very clean final-state topology with an invariant mass peak that is reconstructed with great precision. Final states in proton-proton collisions containing photons and significant MET emerge from a variety of new physics scenarios such as the search for dark matter (DM) in association with MET [3]. A hypothesized heavy scalar H is considered whereby $H \rightarrow h\chi\chi$, a search driven largely by MET such that $h(\rightarrow \gamma\gamma)+\text{MET}$. MET performance studies are essential for the search as well as other analyses in progress containing photons and MET signatures. This paper discusses MET performance studies in accordance with diphoton searches with MET signatures based on data recorded in 2015, 2016 and 2017 at a center-of-mass energy of 13 TeV. Altogether the data corresponds to 43.8 fb^{-1} of integrated luminosity.

2. The ATLAS detector

ATLAS is a multi-purpose particle detector with a forward-backward symmetric cylindrical geometry and a near 4π coverage in solid angle. It uses a right-handed coordinate system with the origin at the interaction point (IP) in the centre of the detector. The z -axis is along the beam pipe, the x -axis points from the IP to the centre of the LHC ring and the y -axis points upwards towards the earth's surface. In the transverse plane, cylindrical (r, ϕ) coordinates are used, where r is a radial dimension measuring the distance from the beam line and ϕ is the azimuthal angle around the beam pipe. The polar angle θ is the angle measured from the beam axis and the pseudorapidity is defined in terms of this angle as $\eta = -\ln[\tan(\theta/2)]$. The pseudorapidity is used as an angular coordinate in place of θ and the angular separation between objects is defined as $\Delta R = \sqrt{\Delta\eta^2 + \Delta\phi^2}$. The transverse momentum, transverse energy and missing transverse momentum are all defined in the x - y plane.

ATLAS is made up of the following sub-systems: the inner detector (ID), the magnetic system, calorimeters and the Muon spectrometer (MS). The ID is surrounded by a 2 T superconducting solenoid which bends charged particles to enable particle momentum measurements. The ID tracks charged particles allowing particle identification and vertex measurements. This sub-system covers a pseudorapidity range of $|\eta| < 2.5$ [4]. The electromagnetic calorimeter (EMCAL) surrounds the ID and absorbs energy from particles which interact electromagnetically as they move through the detector. The EMCAL covers $|\eta| < 3.2$. The Hadronic calorimeter (HCAL) surrounds the EM calorimeter and is made up of steel plates and plastic scintillator plates which absorb energy from hadrons. These HCAL constituents provide a hadronic coverage of $|\eta| < 1.7$ and LAr technology is also used for the HCAL end-cap region. The entire HCAL covers a pseudorapidity range of $|\eta| < 4.9$. The outermost part of the detector is made up of the MS which consists of three large superconducting toroid systems which provide exceptional muon momentum measurements through accurate tracking.

3. MET reconstruction at ATLAS

MET is referred to as the energy which is not detected in a particle detector but is expected due to the laws of energy-momentum conservation. That is, the momentum in the transverse plane is expected to be zero implying that any vector momentum imbalance in the transverse plane goes into the MET calculation. MET is basically obtained from the negative vector sum of the momenta of all particles detected, these include: electrons, photons, hadronically decaying τ -leptons, jets and muons.

The electrons are reconstructed from energy deposits in the EMCAL, associated with tracks reconstructed in the ID. Those with $p_T > 10 \text{ GeV}$ and $|\eta| < 2.47$ are selected [5]. The photons

are reconstructed from energy clusters in the EMCAL and required to have $p_T > 25 \text{ GeV}$ and be within a region of $|\eta| < 2.3$. A *tight* photon identification requirement is applied to the photon candidates in order to reduce misidentification [6]. Hadronically decaying tau-leptons are required to have $p_T > 20 \text{ GeV}$ and be within $|\eta| < 2.5$ and those falling between $1.37 < |\eta| < 1.52$ are not considered. Muons are reconstructed from tracks in the ID and the MS and those with $p_T > 10 \text{ GeV}$ and $|\eta| < 2.7$ are selected. Muons in the region $|\eta| < 2.5$ must be matched to ID tracks. Jets are reconstructed from energy deposits in EMCAL and HCAL using the anti-kt algorithm [7]. They are required to have $p_T > 20 \text{ GeV}$ and be within $|\eta| < 4.5$. The jets with $|\eta| < 2.4$ and $p_T < 60 \text{ GeV}$ must pass the jet vertex tagger selection (JVT) [8]. This JVT technique separates hard scatter jets from pile-up jets in the central region of the detector, a very useful pile-up suppression method.

These physics objects are essentially the ingredients of the MET calculation which is done as follows [9, 10]:

$$E_{x(y)}^{miss} = E_{x(y)}^{miss,e} + E_{x(y)}^{miss,\gamma} + E_{x(y)}^{miss,\tau} + E_{x(y)}^{miss,jets} + E_{x(y)}^{miss,\mu} + E_{x(y)}^{miss,SoftTerm}, \quad (1)$$

where each term is calculated from the negative vectorial sum of momenta of the calibrated cell energies corresponding to objects as follows:

$$E_x^{miss,term} = - \sum_{i=1}^{N_{cell}^{term}} E_i \sin \theta_i \cos \phi_i \quad (2)$$

$$E_y^{miss,term} = - \sum_{i=1}^{N_{cell}^{term}} E_i \sin \theta_i \sin \phi_i \quad (3)$$

The actual value of MET (E_T^{miss}) and its azimuthal coordinate are calculated as follows:

$$E_T^{miss} = \sqrt{(E_x^{miss})^2 + (E_y^{miss})^2} \quad (4)$$

$$\phi^{miss} = \arctan(E_y^{miss}/E_x^{miss}) \quad (5)$$

Remaining calorimeter deposits not associated to the reconstructed objects are summed together in what is referred to as the *Soft Term* of equation 1. Several methods can be used to reconstruct the *Soft Term*, all of which affect the MET performance. At ATLAS the favourable method used to reconstruct the *Soft Term* is the track-based (TST) *Soft Term*.

ATLAS measures the momenta of charged particles using the ID and the series of hits in the ID which are efficiently reconstructed as tracks. Collisions which produce multiple tracks are reconstructed into vertices and these vertices give the position of the proton-proton collisions. Each vertex is required to have at least three tracks with $p_T > 0.4 \text{ GeV}$. The primary vertex (PV) in each event is selected as the vertex with the largest value of $\sum (p_T)^2$, where the scalar sum is taken over all the tracks associated to that particular vertex. The TST *Soft Term* is constructed from tracks passing these discussed selections with $p_T > 0.5 \text{ GeV}$ and not associated to any of the hard physics objects. This method allows excellent vertex association of the *Soft Term* used in the MET reconstruction.

4. MET performance

This section shows some basic MET distributions after the diphoton selection. In the $h \rightarrow \gamma\gamma$ final state at least two photon candidates are required such that the leading photon has $p_T > 35 \text{ GeV}$ and the sub-leading has $p_T > 25 \text{ GeV}$. Following this, in order to maintain good data quality, the events passing this selection pass through additional selection criteria. As

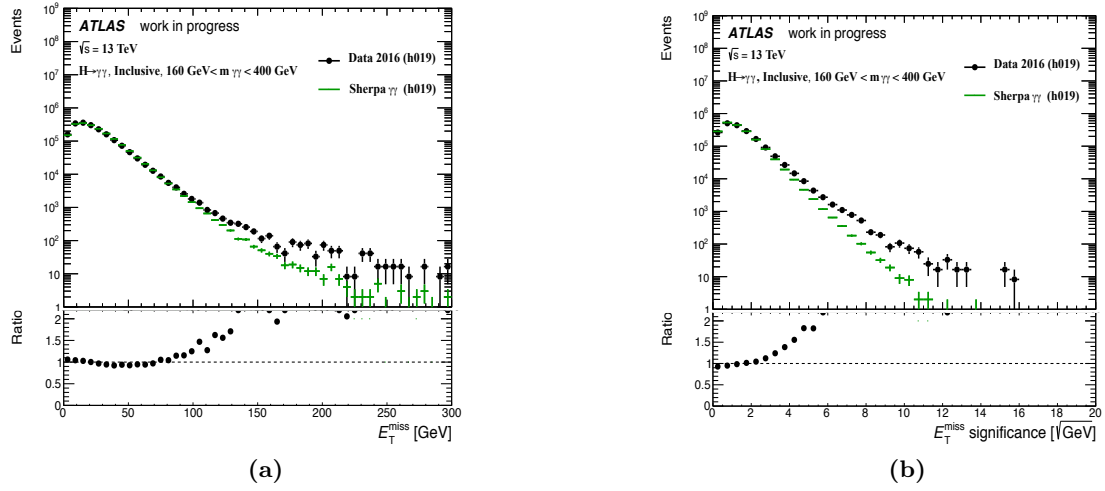


Figure 1: MET TST distributions comparing 2015+2016 data corresponding to 36.1 fb^{-1} and Sherpa $\gamma\gamma$ MC, where (a) is the MET distribution and (b) is the MET significance distribution. The MC has been normalized to the total number of events in the inclusive sample of the data [11].

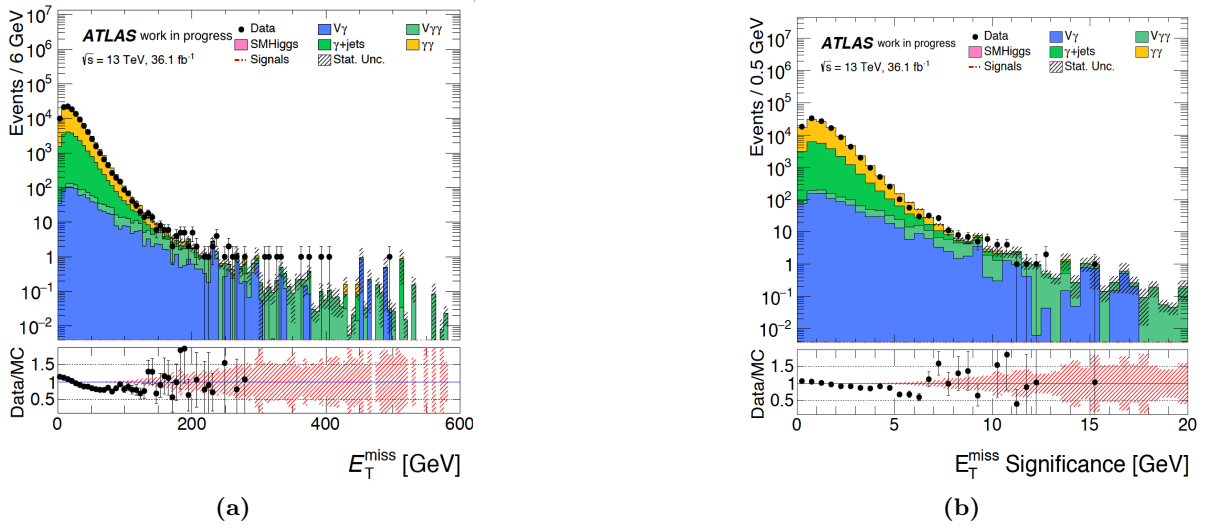


Figure 2: MET TST distributions comparing 2015+2016 data corresponding to 36.1 fb^{-1} and additional processes, where (a) is the MET distribution and (b) is the MET significance distribution. The MC have been normalized to the total number of events in the inclusive sample of the data [11].

discussed in Section 3, the photon candidates must satisfy *tight* ID criteria and satisfy the following relative p_T cuts: leading must satisfy $p_{T\gamma 1}/m_{\gamma\gamma} > 0.35$ and sub-leading must satisfy $p_{T\gamma 2}/m_{\gamma\gamma} > 0.25$. Lastly, the events are required to have $160 \text{ GeV} < m_{\gamma\gamma} < 400 \text{ GeV}$ where the diphoton mass is calculated assuming that the photons originate from the diphoton primary vertex. The diphoton primary vertex position is obtained by combining the trajectories of both photon candidates.

The performance checks are done using 2015+2016 data corresponding to 36.1 fb^{-1} and 2015+2016+2017 data corresponding to 43.8 fb^{-1} , respectively. The Higgs boson signal Monte Carlo (MC) comprises the ggF , VBF , Wh , Zh and $t\bar{t}h$ production modes. The signals produced via ggF and VBF are generated with PowHeg [12]. The Wh and Zh are generated with

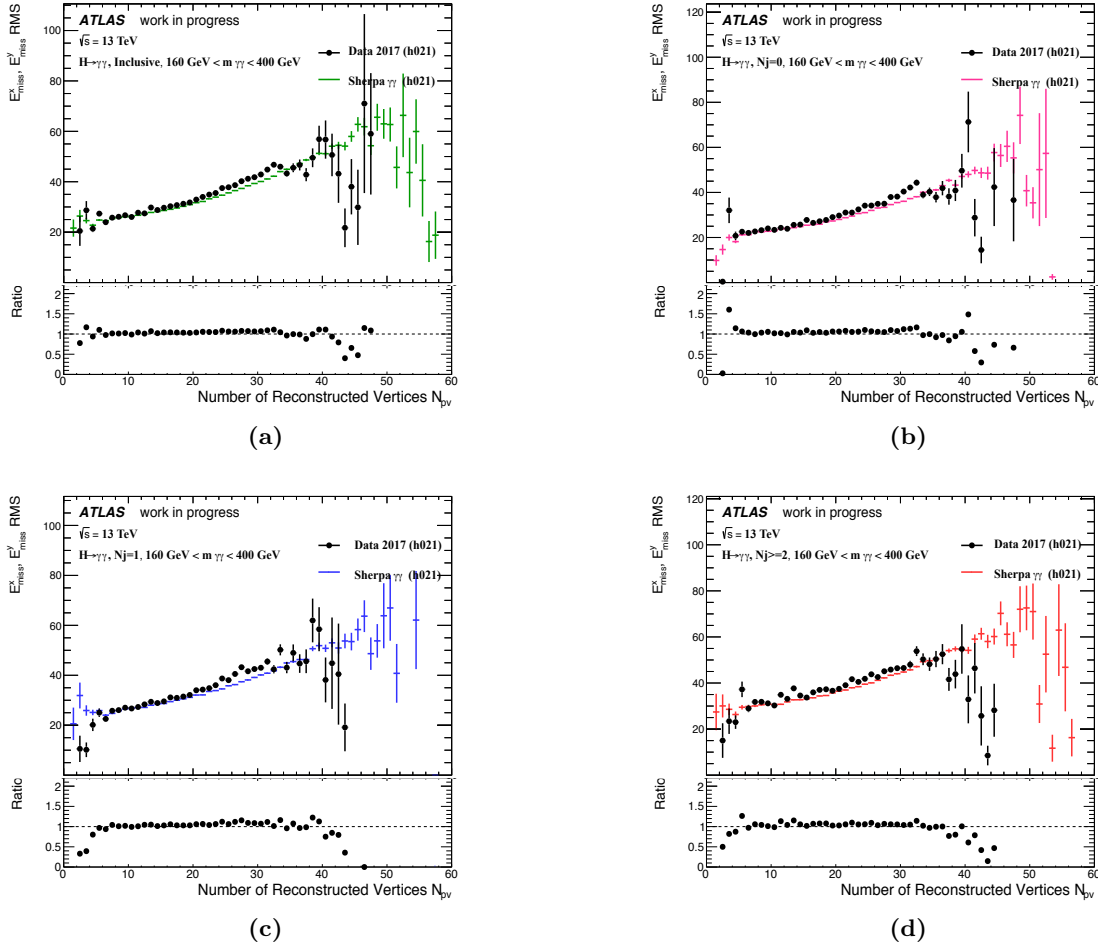


Figure 3: E_T^{miss} resolution distributions showing the x and y components of the E_T^{miss} as a function of N_{pv} . The comparisons are between 2015+2016+2017 data corresponding to 43.8 fb^{-1} and Sherpa $\gamma\gamma$ MC. The distributions are split into (a) inclusive case, (b) 0-jet case, (c) 1-jet case and (d) ≥ 2 -jet case [11].

Pythia8 [13] and the $t\bar{t}h$ signal is generated with MadGraph5 aMC@NLO [14]. For the direct comparison checks, the Sherpa $\gamma\gamma$ MC is used as this is the most dominant background. The Sherpa $\gamma\gamma$ events are simulated using the SHERPA version 2.1 event generator [15] with up to two additional partons in the final state with the CT10 PDF. SHERPA is also used to generate $V\gamma$ and $V\gamma\gamma$ backgrounds which are also contributors. The γ +jets background sample is represented by data, whereby only one of the two photons in the selection is required to pass the reverse photon isolation criteria.

Figure 1 shows the data versus Sherpa $\gamma\gamma$ MC while Figure 2 shows the data versus additional MC [11]. Figure 1(a) represents the MET TST distribution and Figure 1(b) shows MET TST significance distribution and in both cases MC has been normalized to the total number of events in the inclusive sample of the data. Some discrepancies are observed in the tails of these distributions. These are reduced by the addition of other processes with real MET as can be seen in Figure 2. Good agreement is then observed between data and MC with the addition of other processes.

In order to study the degradation of the MET performance the MET resolution distributions

are of great importance. The resolution distributions shown are done using 2015+2016+2017 blinded data corresponding to 43.8 fb^{-1} of integrated luminosity. The root-mean-square (RMS) of the superimposed x and y components of the E_T^{miss} is used to estimate the resolution. Figure 3 shows the MET resolution as a function of the number of primary vertices (N_{pv}) for the Figure 3(a) inclusive case, Figure 3(b) 0-jet case, Figure 3(c) 1-jet case and Figure 3(d) ≥ 2 -jet case. Good agreements are observed. The most stable performance is observed in the case where no jets (0-jet) are required as it has the least slope. In fact, all the jet binning cases perform better than the inclusive case which has the highest slope. This shows that an increased number of jets degrades the MET resolution.

5. Conclusion

The measurement of MET is an important attribute of numerous interesting physics analyses at the LHC. The ATLAS calorimeter provides commendable energy resolution but is highly sensitive to pile-up. The reconstruction and performance of MET based on various recent datasets and MC has been presented. The reconstructed MET is validated using Run 2 ATLAS data showing a good agreement with Monte Carlo simulation. MET resolution distributions have been studied by binning in jet multiplicity in order to observe the effects of the presence of jets on the MET performance. Looking at the jet binning cases it is clear that the degradation in resolution originates mostly from the jet multiplicity and thus the amount of overall activity within the detector. In fact, the resolution in the inclusive case has a slightly larger slope than the jet binning cases, which implies that the higher slope comes from an increased number of jets at larger N_{pv} .

Acknowledgements

I would like to thank the SA-CERN program for providing the research opportunity to visit CERN. The National Research Foundation (NRF) of South Africa for the bursary they provided. I would also like to thank the School of Physics, the Faculty of Science and the Research Office at the University of the Witwatersrand.

References

- [1] Aad G *et al.* (ATLAS) 2012 *Physics Letters B* **716** 1–29 ISSN 03702693 (*Preprint* 1207.7214)
- [2] Khachatryan V *et al.* (CMS) 2012 *Physics Letters B* **716** 30–61 ISSN 03702693 (*Preprint* 1207.7235)
- [3] Aad G *et al.* (ATLAS) 2017 *Phys. Rev. Lett.* **119** 181804 (*Preprint* 1707.01302)
- [4] Aad G *et al.* (ATLAS) 2012 *The European Physical Journal C* **72** 1844 ISSN 1434-6044 (*Preprint* 1108.5602)
- [5] Aad G *et al.* (ATLAS) 2014 *Eur. Phys. J.* **C74** 3071 (*Preprint* 1407.5063)
- [6] Aad G *et al.* (ATLAS) 2016 *Eur. Phys. J.* **C76** 666 (*Preprint* 1606.01813)
- [7] Cacciari M, Salam G P and Soyez G 2008 *JHEP* **04** 063 (*Preprint* 0802.1189)
- [8] Aad G *et al.* (ATLAS) 2014 Tagging and suppression of pileup jets with the ATLAS detector Tech. Rep. ATLAS-CONF-2014-018 Geneva URL <https://cds.cern.ch/record/1700870>
- [9] Aad G *et al.* (ATLAS) 2012 *Eur. Phys. J.* **C72** 1844 (*Preprint* 1108.5602)
- [10] Aad G *et al.* 2015 Performance of missing transverse momentum reconstruction for the ATLAS detector in the first proton-proton collisions at $\sqrt{s} = 13 \text{ TeV}$ Tech. Rep. ATL-PHYS-PUB-2015-027 CERN Geneva URL <https://cds.cern.ch/record/2037904>
- [11] Ruan X *et al.* 2018 Supporting note: Search for a new resonance in the di-photon decay in association with missing transverse energy in pp collisions at $\sqrt{s} = 13 \text{ TeV}$ with the ATLAS detector Tech. Rep. ATL-COM-PHYS-2018-970 CERN Geneva URL <https://cds.cern.ch/record/2628349>
- [12] Nason P and Oleari C 2010 *JHEP* **02** 037 (*Preprint* 0911.5299)
- [13] Sjostrand T, Mrenna S and Skands P Z 2008 *Comput. Phys. Commun.* **178** 852–867 (*Preprint* 0710.3820)
- [14] Alwall J, Frederix R, Frixione S, Hirschi V, Maltoni F, Mattelaer O, Shao H S, Stelzer T, Torrielli P and Zaro M 2014 *JHEP* **07** 079 (*Preprint* 1405.0301)
- [15] Gleisberg T, Hoeche S, Krauss F, Schonherr M, Schumann S, Siegert F and Winter J 2009 *JHEP* **02** 007 (*Preprint* 0811.4622)

Background estimation for multilepton and b -jets analysis at ATLAS at the LHC

Jeremiah Monnakgotla¹, Lebohang Mokoena¹, Lehumo Mashishi¹,
Yesenia Hernández Jiménez¹, and Bruce Mellado^{1,2}

¹ School of Physics and Institute for Collider Particle Physics, University of the Witwatersrand, Johannesburg, Wits 2050, South Africa

² iThemba LABS, National Research Foundation, PO Box 722, Somerset West 7129, South Africa

E-mail: jeremiah.kgomotso.monnakgotla@cern.ch

Abstract. Background estimation is one of the most important aspects for all the analysis at the Large Hadron Collider. This proceeding presents the background estimation for the $A \rightarrow ZH$ search with the heavy scalar H decaying into a pair of Higgs, or Higgs-like Scalar bosons. The final state for this search is formed by three leptons, at least two b -tagged jets and low jet multiplicity. The $t\bar{t}Z$ process is the dominant background contribution for this analysis. The second important background is the WZ for which a control region is defined to check the modeling and the normalization of this process.

1. Introduction

This work performs a background estimation for the Madala hypothesis [3] in the multi-lepton and b -jets production at the LHC. This hypothesis considers a production of a CP-odd scalar A which decays to H and the Z bosons leaving a final state of three leptons and at least two b -tagged jets and low jet multiplicity [4]. A wide range of analysis have been performed by ATLAS and CMS collaborations observe discrepancies between data and Monte Carlo (MC) which can be explained by the Madala hypothesis. Firstly in CMS, a supersymmetry search with the production of $t\bar{t}Z$ decay with three lepton and b -tagged jets was used as one of the control regions (CRs) for background normalization [1]. Secondly, the measurement of the $t\bar{t}Z$ cross section observe a discrepancy at low jet multiplicity [2]. Furthermore, the observed discrepancies between data and MC has opened a window for searches Beyond Standard Model (BSM). It is clear that the LHC data is not well understood. With that in view this proceeding describes the background estimation for the $A \rightarrow ZH$ search. In Addition, the technique of control region (CR) is implemented by inverting one of requirements in the signal region (SR).

2. Signal Model

In the model depicted in Figure 1, a new heavy scalar boson decays into the heavy scalar (H) which subsequently decays into a pair of Higgs, or Higgs-like scalar (S) bosons leaving a final state of three leptons and at least two b -jets. Therefore the S and the h decay to WW bosons (decay semi-leptonically) and two b -tagged jets. The Z boson decays to a pair of leptons and h is the standard model (SM) Higgs boson with the mass of 125 GeV. The masses of the H and

S are assumed to be 250 GeV and 145 GeV respectively as discussed in ref [[3, 4]]. The mass of CP odd-Higgs A is expected to be greater than sum of the masses of H and Z boson.

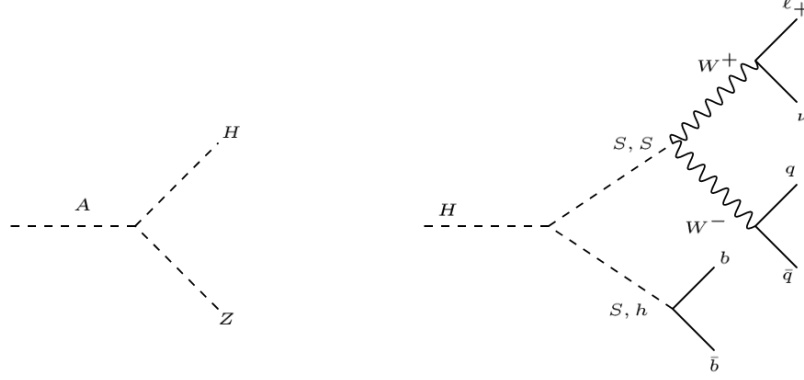


Figure 1. The Feynman diagram of the $A \rightarrow ZH$ production (left) and of Higgs and Higgs-like scalar bosons.

3. Signal Region Definitions

In this analysis two different SRs are defined to be $3l - Z - 2b2j$ and $3l - Z - 2b3j$. The final state is characterized by events containing exactly three leptons with the same flavour lepton pair closest to the Z mass, at least at least two b -tagged jets and two or three jets. it can be clearly seen that the signal sensitivity for $A \rightarrow ZH$ is high for events having exactly two or three jets [4]. Events should contain at least one pair of leptons with same-flavor and opposite sign (SFOS). In addition, the invariant mass of the SFOS pair ($m_{l_{\pm}l_{\mp}}$) must be compatible with the Z boson mass (m_Z) in a window of 20 GeV. The leading lepton is required to have a transverse momentum (P_T) above 27 GeV while for other two leptons this threshold is lowered to 20 GeV. The three leptons have a total charge of ± 1 . The exact signal definitions and event selection are summarized in Table 1

Table 1. Summary of the event selection in the signal region.

Variable	signal region	
	$3l - Z - 2b2j$	$3l - Z - 2b3j$
Number of Leptons	3	
Leading Lepton P_T	> 27 GeV	
Second and Third Lepton P_T	> 20 GeV	
Lepton Total Charge	± 1	
One SFOS Lepton Pair	required	
Z-like SFOS Pair	$ m_{l_{\pm}l_{\mp}} - m_Z < 10$ GeV	
$N_{b\text{-tagged jets}}$	≥ 2	≥ 2
N_{jets}	$= 2$	$= 3$

4. Analysis Strategy

The background estimation is evaluated by defining CRs to be orthogonal to the SRs. The SRs are set to be characterized by events with low jet multiplicity, therefore the CRs will be expected to contain events with high jet multiplicity. The jet multiplicity distribution in Figure 2 with events containing at least two b -tagged jets, clearly illustrates the SR and the CR.

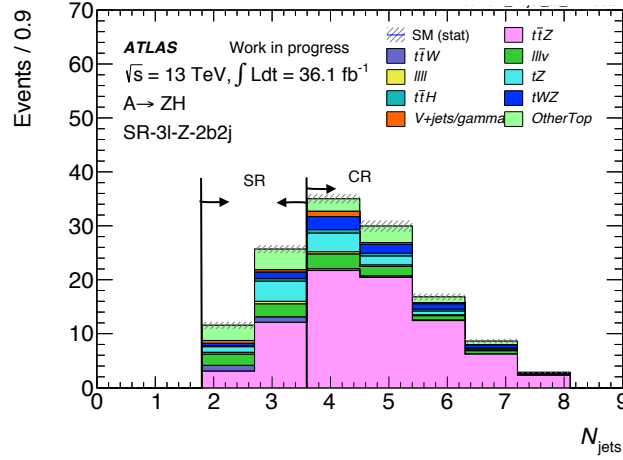


Figure 2. Jet multiplicity distribution after the selection of at least two b -tagged jets.

5. Background Estimation

In the three leptons final state the SM background arises from $t\bar{t}Z$, WZ and other top ($t\bar{t}$) processes. These SM backgrounds are predicted using MC simulation which are commonly known as the irreducible background. A strategy is developed to estimate these background processes which involve the construction of CRs which depends on the requirement of the SR. Henceforth four CRs are constructed to evaluate the dominant background processes and to observe events which are topologically similar to the signal events. The first three CRs required SFOS pair whose mass is closest to the Z boson mass.

5.1. Control region for the $t\bar{t}Z$

The $t\bar{t}Z$ background is particularly important in the three leptons analysis, and it is estimated by the use of two CRs which are labeled as: $3l - Z - 1b4j$ and $3l - Z - 2b4j$. The former requires at least four jets with exactly one b -tagged jet. The later requires at least four jets with at least two b -tagged jets. With these requirement the $t\bar{t}Z$ process contribute 70 % and 40 % with respect to each CR. The distributions of the invariant mass of the lepton pair are shown in Figure 3 and Figure 4.

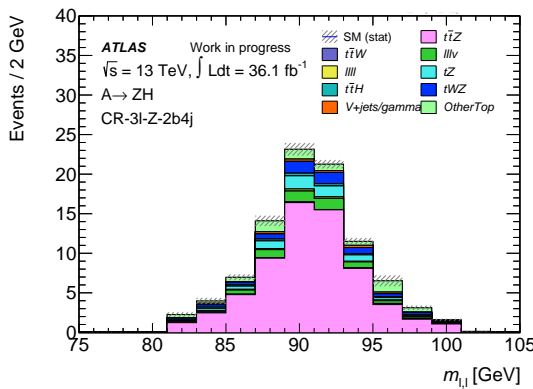


Figure 3. Invariant mass of Z -like lepton pair after the selection of at least four jets with at least two b -tagged jets.

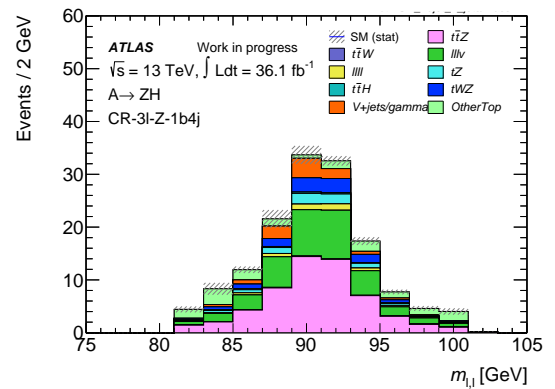


Figure 4. Invariant mass of Z -like lepton pair after the selection of at least four jets with exactly 1 b -tagged jet.

5.2. Control Region for the WZ

The third CR which is sensitive to the WZ process is labeled as: $3l - WZ$. This CR select events with at least three jets and zero b -tagged jets. In addition, missing transverse momentum is required to be greater than 40 GeV. With these requirement the WZ contribution is roughly 80.1% of the total background. A very small percentage arise from the V +jets/ γ and ZZ processes as shown in Figure 5 and Figure 6.

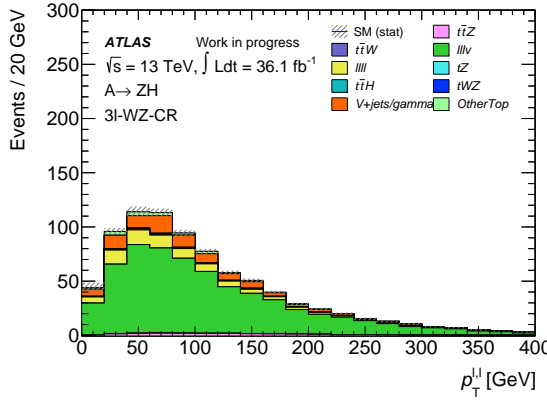


Figure 5. P_T of Z -like lepton pair after selecting at least three jet with zero b -tagged jet.

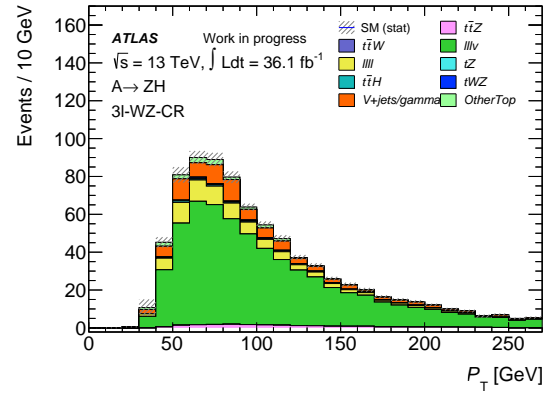


Figure 6. P_T leading lepton after selecting at least three jet with zero b -tagged jet.

5.3. Control Region for the Z mass veto

The $3l - noZ - 2b4j$ region select events with exactly three leptons, at least four jets, at least two b -tagged jets and veto events containing Z -like lepton pair. In Figure 7 the leading lepton P_T illustrates that the other top process dominates, the contribution of $t\bar{t}Z$ is highly reduced since the events associated with Z boson decaying leptonically are rejected. With these requirements the other top ($t\bar{t}$) contribute roughly 50.2% of the total background, where other top ($t\bar{t}$) is the combination of $t\bar{t}$, $3top$ and $4top$ SM processes but dominated by $t\bar{t}$ process. The $t\bar{t}Z$ background contribute approximately 24.8% of the total background. Table 2 show the expected numbers of events in the CRs.

Table 2. The expected event yields in the CRs for an integrated luminosity of 36.1 fb^{-1} . Uncertainties are statistical only.

	$3l - Z - 1b4j$	$3l - Z - 2b4j$	$3l - Z - 0b3j$	$3l - noZ - 2b4j$
$t\bar{t}Z$	57.32 ± 0.57	64.13 ± 0.61	20.83 ± 0.33	13.44 ± 0.29
$t\bar{t}W$	0.80 ± 0.08	0.75 ± 0.09	0.47 ± 0.06	4.60 ± 0.21
WZ	36.99 ± 1.25	6.01 ± 0.44	616.42 ± 5.28	0.82 ± 0.15
ZZ	4.57 ± 0.21	0.91 ± 0.10	81.84 ± 0.95	0.35 ± 0.09
tZ	7.66 ± 0.20	6.09 ± 0.18	6.03 ± 0.17	0.54 ± 0.05
$t\bar{t}H$	1.63 ± 0.10	1.80 ± 0.10	0.51 ± 0.05	5.46 ± 0.19
tWZ	10.91 ± 0.51	5.92 ± 0.40	6.83 ± 0.39	0.76 ± 0.13
V +jets/ γ	10.32 ± 2.18	1.67 ± 0.33	94.55 ± 8.39	0.53 ± 0.14
$OtherTop$	16.11 ± 1.66	7.22 ± 1.24	19.14 ± 1.39	25.92 ± 1.85
Total Background	146.30 ± 3.13	94.51 ± 1.56	846.62 ± 10.06	52.41 ± 1.91

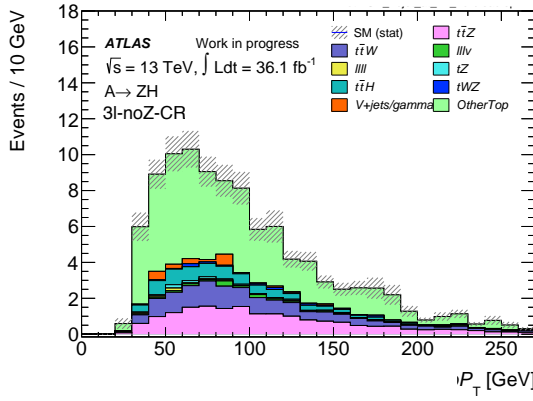


Figure 7. Leading lepton P_T after the selection of at least four jets with at least two b -tagged jets.

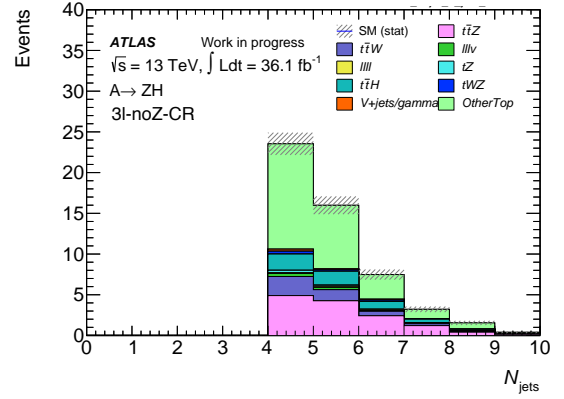


Figure 8. Jet multiplicity distribution after the selection of at least four jets with at least two b -tagged jets.

6. Conclusion

The proceeding presents the background estimation for the $A \rightarrow ZH$ search, which is performed by constructing four CRs with their requirements orthogonal to the SRs. The main background processes are the $t\bar{t}Z$, WZ and "other top" ($t\bar{t}$). The analysis will be performed with the full Run 2 data set. The next step is to check the performance of the MC for different SM processes and extrapolate their contributions to the SR.

7. References

- [1] Sirunyan AM 2018 *Phys. Rev. D* **97** 9 Phys. Rev. D 97, 032009 (2018) [hep-ex]
- [2] Sirunyan AM 2018 *JHEP* **08** 9 JHEP 08 (2018) 011 [hep-ex]
- [3] von Buddenbrock S Chakrabarty N Cornell AS et al 2015 5 arXiv:1506.00612 [hep-ph]
- [4] von Buddenbrock S Chakrabarty N Cornell AS et al 2016 *Eur. Phys. J. C* **76** 16 Eur. Phys. J. C (2016) 76: 580

Studying the effects of pileup on the leptonic properties in the $H \rightarrow ZZ \rightarrow 4\ell$ channel using the ATLAS detector

Onesimo Mtintsilana¹ and Theodota Lagouri¹

¹ School of Physics and Institute for Collider Particle Physics, University of the Witwatersrand, Johannesburg, Wits 2050, South Africa

E-mail: ¹onesimo.mtintsilana@cern.ch

Abstract. The background composition and shapes are studied in spectral control regions which are constructed by inverting selections or lepton identification requirements. Here we show the effect of pileup for the $H \rightarrow ZZ \rightarrow 4\ell$ channel with weighted histograms, normalized to the expected luminosity. The background considered is the $qq \rightarrow ZZ$ irreducible background which is from a dominant quark-antiquark initial state. We present on the event yields between mc16a and mc16d samples and the overall difference is approximately 3.77%. Comparisons between the two samples on the effect of pileup are also presented which show no effect of pileup between 2015 to 2017 data.

1. Introduction

Since the discovery of the Higgs boson at a mass of 125 GeV at the Large Hadron Collider (LHC) at CERN, one important question is whether the newly discovered particle is part of an extended scalar sector as postulated by various extensions to the Standard Model (SM) [1]. These extensions predict additional Higgs-like bosons, motivating searches in an extended range of mass. This paper reports on searches for a heavy resonance decaying to a pair of Z bosons encompassing a final state of charged leptons (electrons or muons), $ZZ \rightarrow \ell^+\ell^-\ell^+\ell^-$ as shown in Figure 1. Events with four muons (four electrons) associated to the two Z bosons are called 4μ ($4e$) events. In cases where the leading Z boson is formed from muons (electrons) and the subleading from electrons (muons) then the events are labelled as $2\mu 2e$ ($2e 2\mu$).

We study the effect of pileup for the $H \rightarrow ZZ \rightarrow 4\ell$ channel for both 2015 + 2016 (mc16a) and 2017 (mc16d) datasets. Furthermore, the pile-up profile is reweighed to a luminosity weighted combination of the pileup conditions for the two years. This analysis focuses on the intermediate mass ranges (100 - 800) GeV for the heavy scalar

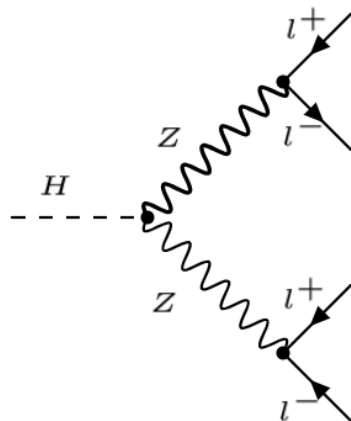


Figure 1: Illustration of the $H \rightarrow ZZ \rightarrow 4\ell$ channel.

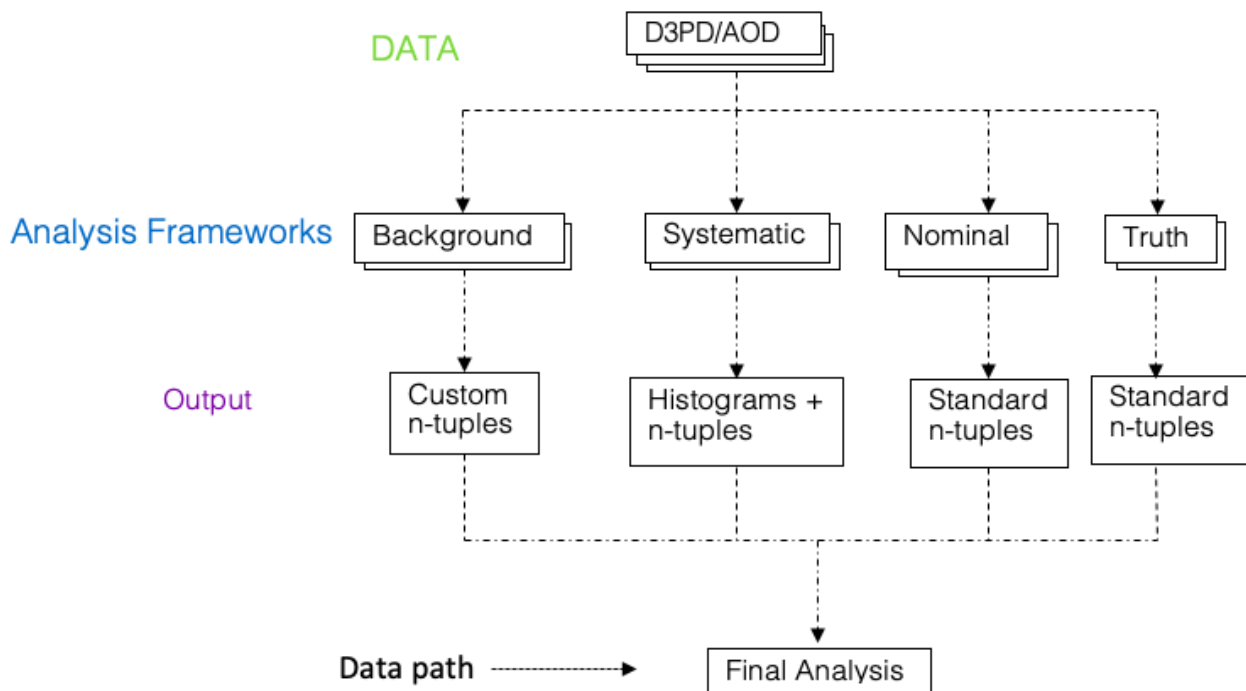


Figure 2: Designed $H4\ell$ Run2 analysis framework model.

boson and the events generated are fully simulated using the ATLAS detector simulation within the $H4\ell$ framework (detailed in the next section) as displayed in Figure 2. Monte Carlo (MC) simulation is used to model the detector response for the background process. The main background contribution to this decay channel comes from the ZZ irreducible background, which is from a dominant quark-antiquark initial state and

Event Pre-selection
Veto
Veto any event where detector is not working properly
Triggers
Single electron, single muon, di-electron, di-muon and electron-muon triggers
Electrons
Caliberated Loose Like quality electrons with $E_T > 7$ GeV and $ \eta < 2.47$
Muons
Smeared combined or segment-tagged muons with $p_T > 6$ GeV and $ \eta < 2.7$,
Maximum one calo-tagged or standalone muon in the quadruplet,
Smeared calo-tagged muons with $p_T > 15$ GeV and $ \eta < 0.1$,
Smeared stand-alone muons with $p_T > 6$ GeV, $2.5 < \eta < 2.7$ and $\Delta R > 0.2$ from closest segment-tagged
Jets
Calibrated R= 0.4 Anti kT jets with $p_T > 25$ GeV and $ \eta < 2.4$ or $p_T > 30$ and $2.4 < \eta < 4.5$
Overlap removal
Remove overlap between different physics objects

Table 1: Summary of the nominal $H4\ell$ event selection requirements.

was modelled using Sherpa 2.2.2 event generator [1]. Other important background contributions come from $t\bar{t}$ and Z +jets which contribute to the reducible background. These are usually caused by fake leptons from jets, top quark and bottom quark. Additionally, carefully selected impact parameter cuts and isolation cuts on the events will suppress this background contribution [2].

2. $H4\ell$ Framework

The analysis framework is important as it used to reduce AODs/D3PDs/xAODs to a manageable size and format that we use for producing final results and plots. This is accomplished by imposing specific analysis cuts and vetoing events that do not pass the full selection requirements. Table 1 summarizes the cuts used by the $H4\ell$ group for its nominal analysis. These cuts match the kinematic distributions from the HZZ decay channel and also reduce background events, where the jets may have been misidentified as leptons [3]. To estimate the backgrounds, control regions are created by inverting and relaxing isolation requirements on electrons or selecting the quadruplets with different flavor composition and charges [1].

Electron clusters are reconstructed using a sliding window algorithm, which searches for small-radius energy deposits contained in the Electromagnetic (EM) calorimeter. Furthermore, to improve reconstruction for electrons (which undergo energy loss due to bremsstrahlung) the track associated with a cluster which passes the loose shower shape requirement, is refitted using a Gaussian-Sum Filter [3]. Additionally, muon track reconstruction is first performed independently in the Inner Detector (ID) and the Muon Spectrometer (MS). Hit information from the individual subdetectors is then used in a combined muon reconstruction, which includes information from the calorimeters.

Samples	4μ	$4e$	$2\mu 2e$	Overall
mc16a	249.92	157.76	398.38	805.76
mc16d	240.28	152.44	383.77	776.49
mc16a/mc16d	1.04	1.03	1.03	1.03
Rel. diff in %	4.01	3.52	3.81	3.77

Table 2: Summary of the yield calculations for 2015-2017 in the four decay channels after the event selection, in the mass range $140 \text{ GeV} < m_{4\ell} < 130 \text{ GeV}$.

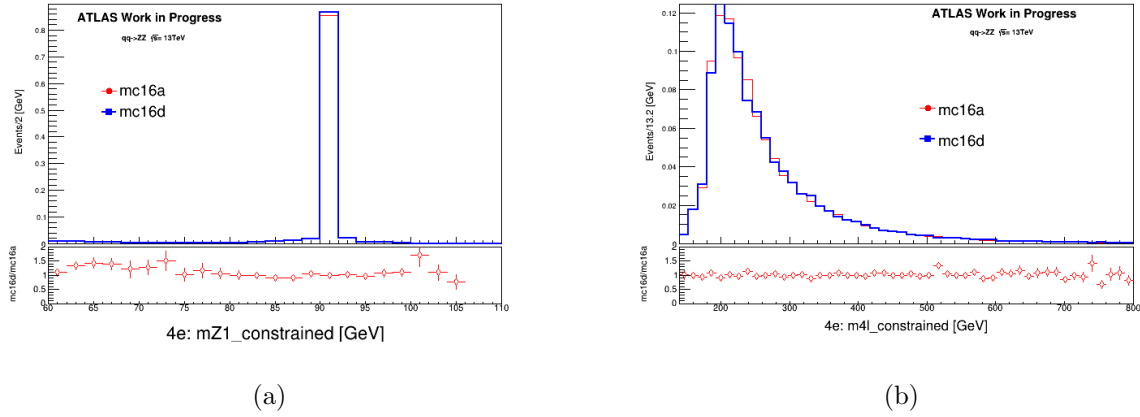


Figure 3: Shape comparisons between mc16a and mc16d for m_{Z_1} and $m_{4\ell}$ for only the $4e$ final state.

Once the events have been selected, variables important to the final analysis are calculated and stored in minitrees. For the MC events, weight variables for which the overall normalization and truth matched information is considered, are calculated and saved in the final output.

3. Results

3.1. Yield Events

A summary of the yield events is shown in Table 2 in the $ZZ \rightarrow 4\ell$ channel in the region $140 \leq m_{4\ell} \leq 800 \text{ GeV}$. The event yields are computed after the aforementioned standard selection criteria are applied, which corresponds to a total integrated luminosity of up to 50.0 fb^{-1} for the 2015 - 2017 datasets [1]. They are calculated per decay channel (4μ , $4e$ and $2\mu 2e$) and for all the channels combined. The background yields are either obtained from MC for the ZZ continuum, or using data driven techniques for the reducible contributions, as described previously. However, in the high mass region, we select $2e2\mu$ or $2\mu 2e$ by taking the pair closest to the Z - mass ($\approx 91 \text{ GeV}$). Additionally, with both pairs on-shell, it is only the measurement resolution that tends to decide which

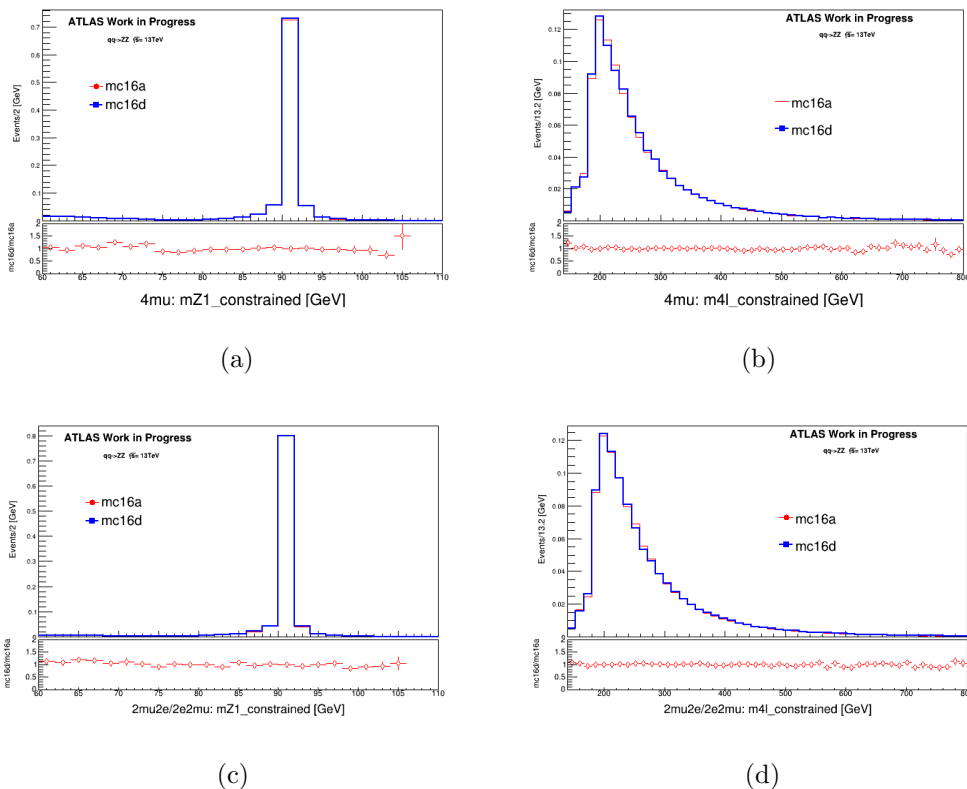


Figure 4: Shape comparisons between mc16a and mc16d for m_{Z_1} and m_{4l} for the 4μ and $2\mu 2e$ final states.

way the pairing goes. As expected, the 4μ final state has the highest efficiency and the $4e$ final state has the lowest efficiency since muon kinematic cuts are looser for electrons.

We then compared the MC data between 2015 to 2017. Figure 3 shows shape comparisons for only the $4e$ final state for m_{Z_1} and m_{4l} distribution for the $qqZZ$ background in the $60 < m_{Z_1} < 110$ GeV region [3]. Leptons are paired to leading and subleading Z bosons, the leading pair (m_{Z_1}) is taken as the Z -pair closest to Z mass and the pair that is next-to-closest to the Z mass in the range $12 < m_{ll} < 115$ GeV is taken as the subleading Z -pair. The invariant mass of the four leptons is known as m_{4l} [3]. We also show shape comparisons for 4μ and $2\mu 2e$ final states in Figure 4. No significant differences between the two MC samples can be observed for all the final states.

4. Conclusion

Our results for the yield events were as expected, with 4μ final state having the highest efficiency. The event yields are higher for mc16a than mc16d, however the overall difference was 3.77%.

For the shape comparisons, between mc16a and mc16d, their ratio was found around 1 and only a few statistical fluctuations were observed. Therefore, no significant effect of pileup was observed on the mass resolution, energy/momentum scale.

References

- [1] Aaboud M *et al.* (ATLAS) 2018 *Eur. Phys. J.* **C78** 293 (*Preprint* 1712.06386)
- [2] Aad G *et al.* (ATLAS) 2016 *Eur. Phys. J.* **C76** 45 (*Preprint* 1507.05930)
- [3] Aaboud M *et al.* (ATLAS) 2018 *Phys. Lett.* **B784** 345–366 (*Preprint* 1806.00242)

Mitigating the effect of fake missing energy using Machine learning technique in the ATLAS experiment

K G Tomiwa^{1*} Xifeng Ruan¹ Bruce Mellado¹

¹ School of Physics and Institute for Collider Particle Physics, University of the Witwatersrand, Johannesburg, Wits 2050, South Africa.

E-mail: kehinde.gbenga.tomiwa@cern.ch

Abstract.

The missing transverse momentum in the ATLAS experiment is the momentum imbalance in the plane transverse to the beam axis. That is the resultant of the negative vectorial sum of the momenta of all particles that are involved in the proton-proton collision. A precise measurement of the missing transverse energy is essential for many physics studies at the LHC, such as Higgs boson measurements and dark matter search. The result presented in this study are from the implementation of Boosted Decision Tree (BDT) based on vertex variables and fake/real missing samples. The preliminary results show the BDT classifiers can improve signal purity to about 50% as compared to the nominal selection.

1. Introduction

The Standard Model (SM) of particle physics has been very successful in the predictability of new particles that have been confirmed by many experiments. Despite its success, the SM is not perfect because the theory holds many unexplained phenomena like its inability to explain gravity, the reason for the mass of neutrinos, dark matter, and dark energy. A number of theoretical efforts to explain some of these phenomena have been published in terms of physics beyond the standard model. One of these theories is the heavy scalar model, developed by the high energy physics group of the University of the Witwatersrand [1].

The heavy scalar model resulted from the explanation of the discrepancies seen in the ATLAS and CMS observed data and the standard model prediction, Ref [2] gives a detailed list of excess used for the postulation. The model postulated a heavy scalar particle with the mass range within twice the mass of Higgs boson and top quark ($2m_h < m_H < 2m_t$, where H is the heavy scalar particle and h is the Higgs boson). Ref [1] gives a comprehensive list of decay modes of the heavy scalar particle, one of which is the associated production of Higgs boson and a scalar mediator ($H \rightarrow hS$), the mediator scalar mostly decays to dark matter particle. This gives the possibilities of searching for the heavy scalar particle in a various Higgs final state with an additional requirement of missing transverse energy (E_T^{miss}).

The heavy scalar particle was first searched in the Higgs to di-photon and missing transverse energy [3]. Since the analysis is heavily based on the reconstruction of missing transverse energy, a considerable effort was put into studying real and fake missing transverse energy with the ATLAS experiment. In Run 2, it was discovered that the jet vertex tagger algorithm

used by the analysis has the potential of introducing fake missing transverse energy and in turn contaminating the signal of the heavy scalar particle. The JVT variable was developed to reject pileup jets in the central region of the ATLAS detector, it was discovered that the JVT variable can fail due to misidentification of some physics object (see the right figure in Figure 1a). When this happens, the E_T^{miss} reconstruction algorithm reconstructs a fake E_T^{miss} due rejection of physics objects, this E_T^{miss} is called the fake E_T^{miss} , while the real E_T^{miss} arises from non-interacting particles like the dark matter particles and the neutrinos.

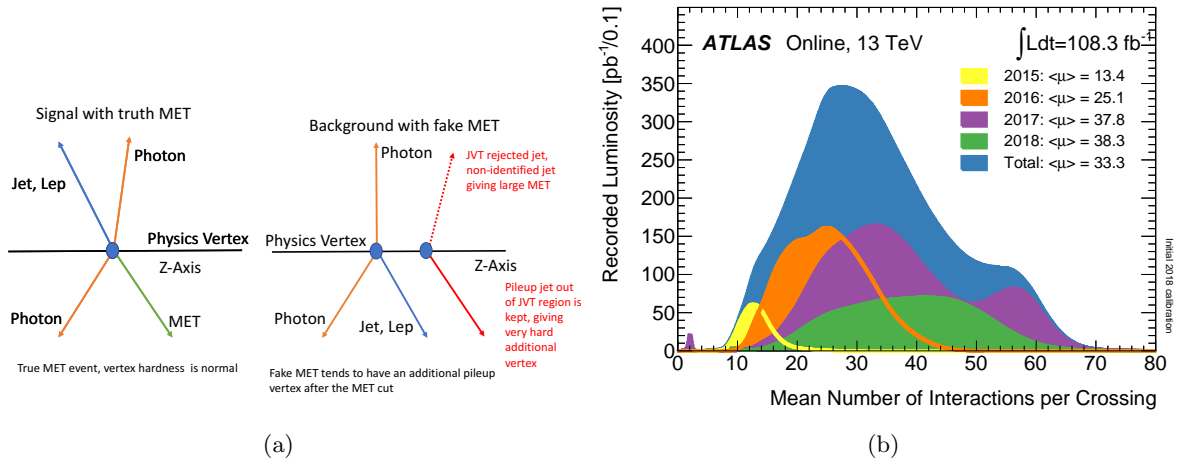


Figure 1: (a) Real and fake missing transverse energy in ATLAS experiment. (b) Number of interaction per crossing in the 13 TeV data from 2015 to 2018.

An improved result was presented in Ref. [4], the event selection categories were re-optimized with the introduction of the Same Vertex method (SV). The SV method was introduced to suppress fake E_T^{miss} by requiring the sum squared of momentum of tracks from the interesting physics primary vertex ($\sum (p_T^{track})^2(Physics)$) minus the sum squared of momentum of tracks from pileup vertex $\sum (p_T^{track})^2(Pile-up)$ to be larger than 0. This method has about 60% background rejection efficiency, this performance is expected to get worse in Phase 2 of Run 2 data taking, due to the increase in average collision interaction per crossing (Figure 1b). The Multivariate analysis (MVA) techniques were introduced to improve the suppression of fake missing energy.

2. Multivariate Analysis Technique

The Boosted Decision Tree (BDT) is the multivariate analysis technique used in this research. A decision tree uses more than one variable to solve a classification or regression problem. The boosting method tried to improve a single decision tree by training several decision trees (forest of trees) and using the aggregation over the many trees as the final decision tree. The boosted method generally increases the robustness of a single decision against data outliers and statistical fluctuation. In this analysis, BDT classifiers are trained to distinguish events with real E_T^{miss} from fake E_T^{miss} . BDT (Figure 2a) is a structured cut (similar to the nominal physics cut-based analysis) organized into the node to form a tree. It aims to learn cut structure that maps a set of features ($x = x_1, \dots, x_d$) to a target labels (y , for this analysis the target labels are binary label, where 1 represents signal sample with real E_T^{miss} events and 0 represents background sample with fake E_T^{miss} events).

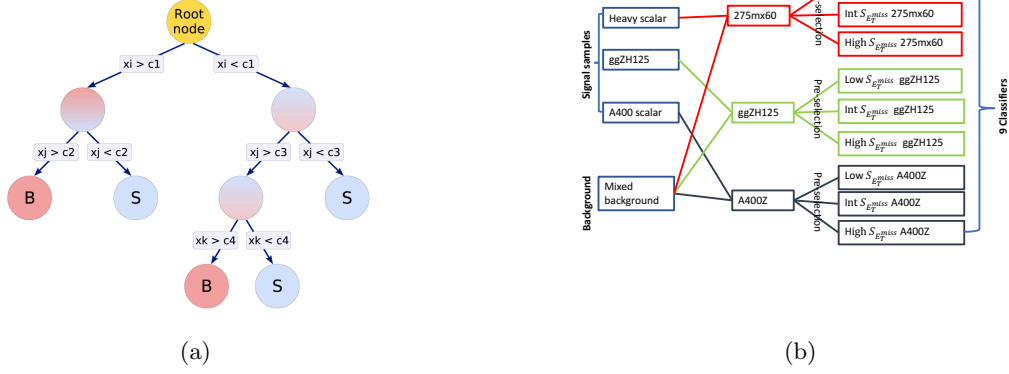


Figure 2: (a) Schematic view of a decision tree. (b) BDT classifiers by categories

Table 1: Signal and Background dataset used for MVA training

Acronym	Description
275mx60	Heavy scalar decaying to one Higgs boson in association with dark matter (Real E_T^{miss} from dark matter candidate).
ggZH125	Z boson produced from gluon-gluon fusion (Real E_T^{miss} from neutrinos produced by Z decay).
A400Z	heavy pseudo-scalar particle decaying to Z boson and heavy scalar (Real E_T^{miss} from neutrinos produced by Z decay and dark matter candidate produced heavy scalar decay).
Mixed background	$\gamma\gamma$, $\gamma - Jet$ and W/Z background sample

3. BDT samples and Categorization

Table 1 gives the acronyms and description of signal and background samples used for this analysis. All the signal samples are normalized to their corresponding cross-section and each samples of the combined background sample is scaled so that they can describe the Higgs side-band.

Classifiers are formed from the combination of the mixed background sample with each of the signal sample. Each combination of samples are categorized by the preselection in Table 2, this results in nine different classifiers, Figure 2b is a schematic description of how the classifiers are formed. The events are binned by missing transverse energy significance ($S_{E_T^{miss}}$) and the number of central jets, $S_{E_T^{miss}}$ is defined as the ratio of E_T^{miss} and square sum of transverse energy of all particle detected.

3.1. BDT Training and hyper-parameters

The entire dataset is divided into test-set and train-set in 50 to 50 ratio. The trainset is used to model development and training while the test-set is used for evaluation and BDT performance measurement. The following BDT hyper-parameters are used to configure decision trees:

Number of trees (NTrees): Number of trees in the forest (T). It represents the total number of aggregation in the boosted decision tree. NTrees is set to 800 for this study.

Table 2: Table showing BDT categories.

BDT cat	Pre-Selection
Low $S_{E_T^{miss}}$	$S_{E_T^{miss}} > 2.5 \ \&\& \ S_{E_T^{miss}} < 3.5 \ \sqrt{GeV} \ \&\& \ N_{jet} \geq 1$
Int $S_{E_T^{miss}}$	$S_{E_T^{miss}} > 3.5 \ \&\& \ S_{E_T^{miss}} < 5.5 \ \sqrt{GeV} \ \&\& \ N_{jet} \geq 1$
High $S_{E_T^{miss}}$	$S_{E_T^{miss}} > 5.5 \ \sqrt{GeV} \ \&\& \ N_{jet} \geq 1$

Minimum node size: The minimum percentage of training event required in a leaf node. This is one of the stop criteria of a decision tree.

Shrinkage: The learning rate (g), see above description for more details, g is set to 0.06.

Number of cuts: The number of grid points in a variable range used in finding the optimal cut in node splitting.

Maximum depth: The maximum tree depth allowed, Tree depth is defined as the length of the longest path from the tree root to a leaf. the root node is considered to have a depth of 0.

3.2. Variables

The variables below are used for this MVA study, they include photon and jet kinematics and the number of interaction per bunch crossing.

- **Photon pointing Vertex $\sum p_T^2$:** Photon pointing vertex sum p_T squared.
- **Pile-up Vertex $\sum p_T^2$:** Pile-up vertex sum p_T squared.
- μ : Number interaction per crossing.
- $\Delta\phi(\gamma\gamma, jet_1)$: Angular distance between diphoton system and leading jet (jet_1).
- $\Delta\phi(jet, E_T^{miss})$: Angular distance between jets system and missing transverse energy.
- $\sum p_T^2 (\sum p_{T(ph)}^2 - \sum p_{T(PU)}^2)$: difference between photon pointing and pile-up vertex p_T .
- **Corrected jet vertex tagger (JVT_{corr}):** Corrected jet vertex fraction is the ratio of track p_T and p_T of jets in the calorimeter.
- $R_{p_T}^{jet}$: Scalar sum of jet primary vertex track and jet track p_T associated with the diphoton system.
- $\Delta\phi(\gamma\gamma, E_T^{miss})$: Angular difference between diphoton system and missing transverse energy.
- $\Delta\phi(\gamma\gamma 1, \gamma 2)$: Angular difference between leading and sub-leading photon.
- $\Delta\phi(softjet, E_T^{miss})$: Angular difference between soft jets (jets with p_T less than 30 GeV) and missing energy.
- $\Delta\phi(Fjet, E_T^{miss})$: Angular difference between forward jets (jets outside the central region of the detector, $\eta \leq 2.4$)
- **Difference of ref jets and p_T^{jj} :** Scalar difference of ref jets and the p_T of two leading jets.

3.3. Results

The performance of the BDT classifiers is measured in terms of background rejection efficiency against the signal acceptance efficiency, in the Receiver Operating Curve (ROC). By definition, the top right-most point on the ROC distribution gives the best trade-off point between signal acceptance and background rejection. Figure 3a, 3b and 3c show the performance of the classifiers, an additional benchmark distribution of no improvement spectrum is added. The no

improvement spectrum represents the minimum signal to background significance. The region below the distribution is the no improvement region and the region above the distribution is the region with maximum improvement.

The ROC curve of the intermediate $S_{E_T^{miss}}$ classifiers shows that we can attain up to 64%, 80%, and 33% improvement insignificance if we cut on 0.9 for A400Z, ggZH125 and 275mx60 classifiers respectively. Another way of checking the performance of the BDT classifiers is to evaluate the trained information on a new dataset. Figures 4a, 4b and 4c show the evaluation performance on data side-band, mixed background, pseudoscalar signal, heavy scalar signal and standard model Higgs production samples. The performance of all the classifiers give a background like a shape on the data side-band and the shape of the data side-band distribution is similar to background shape.

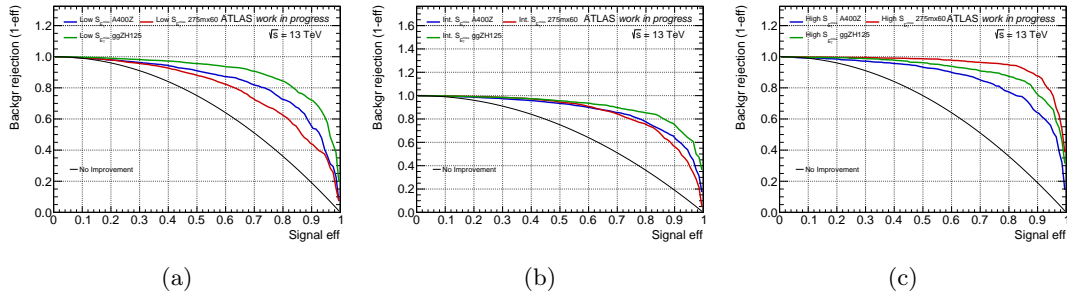


Figure 3: ROC for (a)Low $S_{E_T^{miss}}$ region (b) intermediate $S_{E_T^{miss}}$ region (c) High $S_{E_T^{miss}}$ region

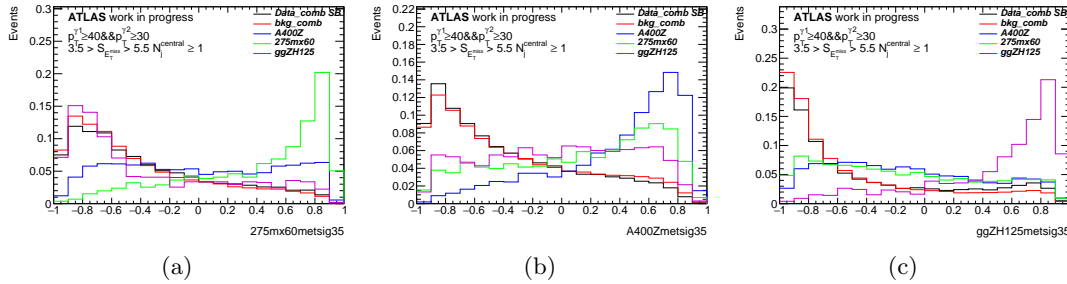


Figure 4: Evaluation of classifier in the intermediate $S_{E_T^{miss}}$ category for (a) 275mx60 (b) A400Z (c) ggZH125 samples

The performance results suggest we can define a new set of BDT categories, by choosing BDT 0.4 as a working point in the intermediate category. Table 3 gives a summary of the new categories. The lower region represents the background region and the high region represent the BDT signal region.

4. Conclusion

The search for dark matter particle with missing transfer energy signature is very important to most beyond the standard model and in particular the heavy scalar model. The clean signatures of missing transverse energy are mostly contaminated by fake missing energy arising from pileup interactions. The purity of this search region depends heavily on the correct reconstruction primary vertex of interaction. The photon pointing method is developed for correctly identifying

Table 3: Table showing BDT categories.

BDT classifier	BDT High	BDT Low
A400Met35	A400BDT > 0.4	A400BDT < 0.4
ggZh125Met35	ggZh125BDT > 0.4	ggZh125BDT < 0.4
275mx60Met35	275mx60BDT > 0.4	275mx60BDT < 0.4

the vertex of interaction. The diphoton analysis has developed a number of techniques to reject pileup objects. The jet vertex tagger and the forward jet tagger to suppress pile up jets in the forward region and outside the forward region of the detector respectively.

It was observed that the JVT suppression method sometimes causes fake missing energy by removing non-identified physics objects. The same vertex method was developed to reduce fake missing transverse energy caused by JVT. The same vertex variable ensures that the diphoton system is from the actual vertex of interaction and not the pileup vertex. The same vertex method attends over 50% performance of suppressing fake missing transverse energy. The ATLAS detector has seen an increase in average interaction per bunch and increase in pileup interaction. A multivariate analysis technique is developed to further suppress the fake missing energy due to an increase in pileup interaction. The MVA method uses photon and jet kinematics and $\langle \mu \rangle$ to develop classifiers. The classifiers have about 80% performance for fake missing transverse energy rejection.

References

- [1] von Buddenbrock S, Chakrabarty N, Cornell A S, Kar D, Kumar M, Mandal T, Mellado B, Mukhopadhyaya B, Reed R G and Ruan X 2016 *Eur. Phys. J.* **C76** 580 (*Preprint* 1606.01674)
- [2] von Buddenbrock S, Chakrabarty N, Cornell A S, Kar D, Kumar M, Mandal T, Mellado B, Mukhopadhyaya B and Reed R G 2015 (*Preprint* 1506.00612)
- [3] Aad G, Abbott B and Abdallah J (ATLAS Collaboration) 2015 *Phys. Rev. Lett.* **115** 131801. 19 p URL <https://cds.cern.ch/record/2021099>
- [4] Aaboud M *et al.* (ATLAS) 2017 *Phys. Rev.* **D96** 112004 (*Preprint* 1706.03948)

DIVISION C

Division for Photonics

Measurements of phase distortions through pulse characterization

GO Dwapanyin, GW Bosman, PH Neethling and EG Rohwer

Laser Research Institute, Physics Department, Stellenbosch University, Private bag X1, Matieland, 7602, South Africa

E-mail: 19724020@sun.ac.za

Abstract. The interaction of light with any material with refractive index, n , affects not only the amplitude of the transmitted light but also its phase. Accurate determination of the spectral phase of a laser pulse is paramount in various spectroscopic applications. There are many phase measurement techniques such as direct interferometric approaches including Frequency Resolved Optical Gating (FROG) and Spectral Phase Interferometry for Direct Electric-field Reconstruction (SPIDER) as well as indirect techniques such as ptychography. This work discusses an alternative approach of measuring phase distortions through the use of a Multiphoton Intrapulse Interference Phase Scan (MIIPS) and investigates the possibility of using MIIPS as a new complimentary phase contrast imaging technique. The principle of the technique as well as the determination of the group delay dispersion (GDD) of the generated signal is analysed and it's potential use in phase contrast imaging has also been identified.

1. Introduction

The propagation of a broadband ultrashort laser pulse through a dielectric medium results in the dispersion of the spectral components of the pulse due to the wavelength dependence of the refractive index n of the medium. The spectral components therefore travel with different speeds which may result in temporal pulse broadening and compression. More precisely, each of the spectral components of the pulse, propagating through a dispersive medium of length L will acquire a phase shift given by,

$$\phi(\omega) = k(\omega)L \quad (1)$$

here $k(\omega) = n(\omega)\omega/c$ is the frequency dependant propagation function, $n(\omega)$ the refractive index and c the speed of light. The functional dependence of phase shift, or rather the relative phase shift between the spectral components contained in the pulse, provides insight into how the pulse profile changes as it propagates through the medium. For the propagation of an ultrashort pulse through a dispersive medium, the velocity at which the pulse envelope propagates is of key importance. This velocity, known as the group velocity v_g , is defined as the inverse derivative of the propagation constant with respect to the angular frequency:

$$\frac{1}{v_g} = \frac{dk}{d\omega} = \frac{n}{c} + \frac{\partial n}{\partial \omega} \frac{\omega}{c} \quad (2)$$

For a dispersive medium where $\frac{\partial n}{\partial \omega} \neq 0$, the v_g therefore varies as the pulse propagates through the medium. To illustrate the influence this has on pulse propagation, it is customary to compute

the Taylor expansion of $k(\omega)$ about a central frequency ω_0 of the pulse

$$k = k_0 + k'(\omega - \omega_0) + \frac{k''}{2!}(\omega - \omega_0)^2 + \frac{k'''}{3!}(\omega - \omega_0)^3 + \dots \quad (3)$$

where (...) corresponds to higher order expansion terms. Substituting eqn.3 into eqn.1 gives a polynomial function of the order $\phi = \phi_0 + \phi' + \phi'' + \dots$ where it can be shown that $\phi_0 = k(\omega_0)L$ is related to the phase velocity of the pulse, $\phi' = k'(\omega - \omega_0)L$ relates to the group velocity of the pulse, $\phi'' = k''(\omega - \omega_0)^2L$ is the phase dispersion term where its coefficient, $k'' = \partial^2 k / \partial \omega^2$, is the group velocity dispersion (GVD), whilst the GVD per unit length is the group delay dispersion (GDD). Note that the GVD is a purely medium dependent parameter. Furthermore, the GVD (or GDD) under specific circumstances is responsible for the temporal pulse broadening and compression [1].

There are many techniques to measure [1–3] and compensate for the phase shift between the spectral components of an ultrashort laser pulse. Compensation techniques includes the use of chirped mirrors [4], rotating cylindrical lens [5] and temporal pulse compression algorithms [6]. The phase distortion (dispersion) of a pulse can also be measured and corrected using an algorithm that combines both spectral phase characterization and compensation with temporal pulse compression in a single technique. This technique is Multiphoton Intrapulse Interference Phase Scan (MIIPS) [7].

2. Theory of MIIPS

MIIPS is a technique that permits the simultaneous measurement and shaping of femtosecond laser pulses. Unlike conventional pulse measurement techniques such as FROG [1], SPIDER [2] and background-free autocorrelation which measure only pulse characteristics, MIIPS can measure the characteristics as well as compress the pulse to a transform limited pulse. It entails the use of a $4f$ -shaper setup along with an iterative algorithm to measure the group delay dispersion (GDD) and to compensate for this measured phase distortion [8]. This is the fundamental advantage of MIIPS over FROG and SPIDER [9]. MIIPS works by introducing a guess phase as a reference phase function onto the 1D spatial light modulator that is in the $4f$ -shaper. This reference phase reduces or cancels phase distortions along the spectrum in order to determine the unknown phase of the pulse.

For every spectral component in the pulse the accompanying generated second harmonic electric field is

$$E(2\omega) = \int |E(\omega + \Omega)| |E(\omega - \Omega)| e^{i[\phi(\omega + \Omega) + \phi(\omega - \Omega)]} d\Omega \quad (4)$$

with SHG intensity is given by $|E(2\omega)|^2$ and the total spectral phase can be written as $\phi(\omega) = \psi(\omega) + f(\omega)$, where $\psi(\omega)$ and $f(\omega)$ represent the unknown input laser phase and reference phase functions respectively. The reference function is chosen as $f(\omega) = \alpha \cos(\gamma\omega - \delta)$ where α is the amplitude, γ is the temporal duration and δ is the scanning parameter ensuring that reference function samples all the frequencies in the bandwidth [10]. A Taylor expansion of the phase term and neglecting third and higher order terms gives:

$$E(2\omega) \approx e^{2i\phi(\omega)} \int |E(\omega + \Omega)| |E(\omega - \Omega)| e^{i[\frac{\partial^2 \phi(\omega)}{\partial \omega^2}]} d\Omega \quad (5)$$

with the GDD = $\frac{\partial^2 \phi(\omega)}{\partial \omega^2}$. The SHG is maximised when the GDD is zero, which leads to the condition to find spectral phase.

$$\frac{\partial^2 \phi(\omega)}{\partial \omega^2} = \psi''(\omega) + f''(\omega) = 0 \quad (6)$$

$$\psi''(\omega) = -f''(\omega) = -\alpha\gamma^2 \cos(\gamma\omega - \delta) \quad (7)$$

From equation 7, the unknown phase which is the GDD can be determined. The MIIPS process is summarized in figure 1.

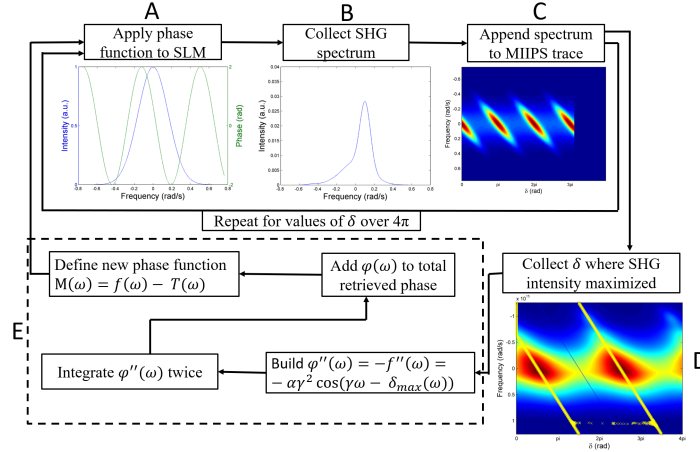


Figure 1: Schematic diagram of the MIIPS process. This include the definition and application of reference phase function onto the SLM (A), scanning over the laser pulse to measure the SHG for each spectral phase (B). The SHG spectrum is recorded (C) and the region where the scanning parameter δ is maximised is recorded (D). The process of retrieving the phase is summarized in section E.

3. Experimental setup

Figure 2 shows the setup used. A Ti:Sapphire femtosecond laser (Tsunami: Spectra-Physics) delivering pulses centred at 800 nm with a pulse duration of 90 fs and delivering energies of around 12 nJ was coupled into a highly nonlinear polarization maintaining all normal dispersion photonic crystal fiber (ANDi PCF) (NL-1050-NE PM, NKT Photonics) of approximately 14 cm in length. An ANDi PCF was used as a result of preliminary studies carried out in this type of fiber which showed that a coherent and flat-top spectra spanning over more than one octave can be generated over a wide range of pump pulse parameters. This earlier studies also showed the independence of coherence properties, spectral bandwidth and temporal compressibility on input pulse duration with the use of ANDi PCF [11, 12]. It is also established that the high peak power propagating in the micron sized PCF induces nonlinear effects. The two dominant processes are self phase modulation (SPM) and stimulated Raman scattering (SRS) within the fiber resulting in spectral broadening and the creation of a broadband supercontinuum light source [13].

Chirped mirrors were used in pre-compression before going into a pulse shaper consisting of two diffraction gratings (Thorlabs GR13-0608), two plano cylindrical lenses ($f = 250$ mm) and a 1-D computer addressable spatial light modulator (SLM)(Jenoptik S640d). The components were arranged in a $4f$ configuration similar to that outlined by Weiner et al [14]. A $100 \mu\text{m}$ β -barium borate (BBO) and recrystallized urea crystals were used to generate SH signals which were collected by a spectrometer (Avantes) after passing through a band pass emission filter (Thorlabs BG39) used to block the illumination light. Scanning was carried out using computer controlled piezo stages (Newport Agilis 25) with a discrete step size of $1.5 \mu\text{m}$ while detection was carried out in the transmission geometry. The generated supercontinuum is focused tightly onto the sample with a high NA objective (0.9). A z-scan MIIPS was also performed to determine the effect of the focal position in the sample on the MIIPS process.

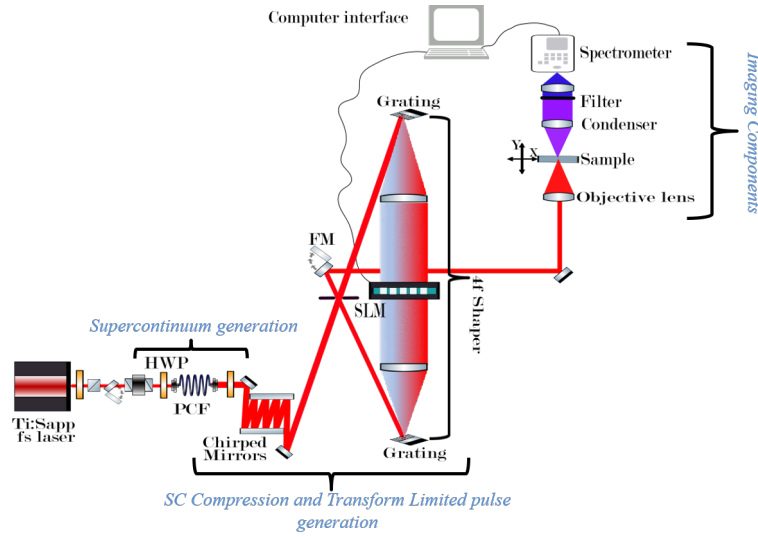


Figure 2: Schematic diagram of the experimental setup showing the region of supercontinuum generation, pulse characterization and compression as well as imaging configuration.

4. Results and discussion

From MIIPS theory, SHG is maximized when the quadratic phase of a laser pulse is zero (refer to equation 6). This implies for a compressed pulse, the total phase of the pulse within the SC region must be approximately zero. As seen from figure 3(a), the total phase (red line) is approximately flat within the SC spectrum (blue line) in accordance with MIIPS phases previously recorded [10, 15]. The phase is compensated to within 0.001 rad over the entire pulse bandwidth indicating that distortions introduced by the high-NA objective are well compensated [10]. This implies there is negligible phase difference between the spectral components. The GDD obtained from the retrieved phase, in frequency space, (black data points) is measured at a wavelength corresponding to the central excitation wavelength using a polynomial (from equation 3)(green line).

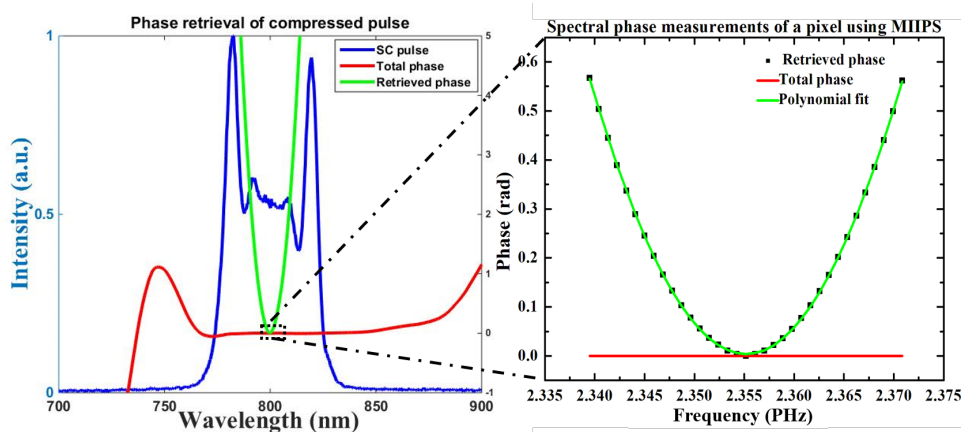


Figure 3: Spectral phase information obtained after MIIPS procedure.

The polynomial parameters for figure 3 are summarized in the table 1 below.

The GDD value determined in this instance is $2.36 \times 10^{-3} \text{ rad.ps}^2$. Coefficients of third and higher order terms are insignificant because MIIPS is only limited to the measurement of second

Table 1: Polynomial fit parameters.

Parameter	Value	Error	Interpretation
k_0 (rad)	0.0039	± 0.0004	Envelope of phase propagation.
k' (rad.ps)	-0.00116	± 0.00005	Temporal shift of propagating pulse.
k'' (rad.ps ²)	0.00236	± 0.00001	Group delay dispersion (GDD).

order polynomial coefficient [8]. Variation of GDD with scan position across recrystallized urea salt are shown in figure 4a. The GDD variation is as a result of the different urea thickness formed during recrystallization resulting in different optical path lengths.

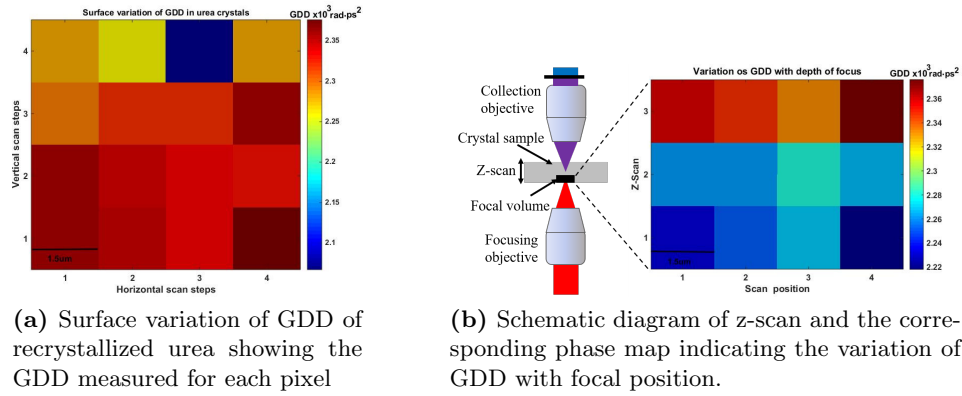


Figure 4: Phase contrast maps of recrystallized urea and BBO.

As depicted in figure 4b, the focal position affects the GDD. This shows that unlike other techniques that permitted the measurement across the entire thickness of the sample [16, 17], the signal response from MIIPS depends on the focal position within the sample. The closer to the first surface the focus is, the smaller the GDD recorded which implies the pulse traverses a shorter distance thereby reducing the impact of GDD.

MIIPS phase contrast imaging: A potential application for this phase measurement technique is the possibility of implementing it in GDD (phase) contrast microscopy. Preliminary contrast imaging was conducted on recrystallized urea crystals and the $100\mu\text{m}$ β -barium borate (BBO) with camera images shown in figure 5. Phase contrast mapping generated via scanning a 5×5 grid in $1.5 \mu\text{m}$ steps is shown in figure 6 (a) and (b) respectively.

The GDD map of BBO shows an expected nearly constant GDD across the scan. In contrast to that of the BBO, the map of urea shows greater variation with a range from 1.5 to above $3.5 \times 10^{-3} \text{ rad.ps}^2$ implying that for a non uniform sample, the extracted phase acquired thorough the MIIPS process is sensitive to position. These results indicate that MIIPS can offer a new complimentary technique to phase contrast microscopy.

5. Conclusion

We have demonstrated the working principle of MIIPS as a temporal pulse characterization technique and its potential use as a complimentary phase contrast imaging technique. Variation of GDD with depth of focus indicates compression using MIIPS is carried out in the focal volume

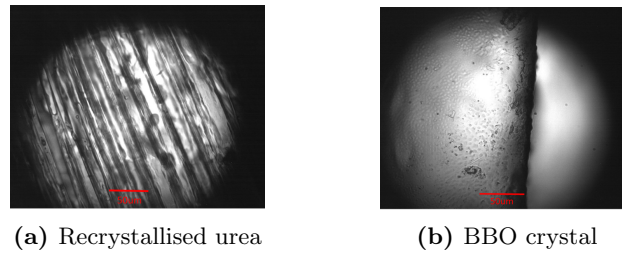


Figure 5: Bright-field micrograph of recrystallized urea and BBO

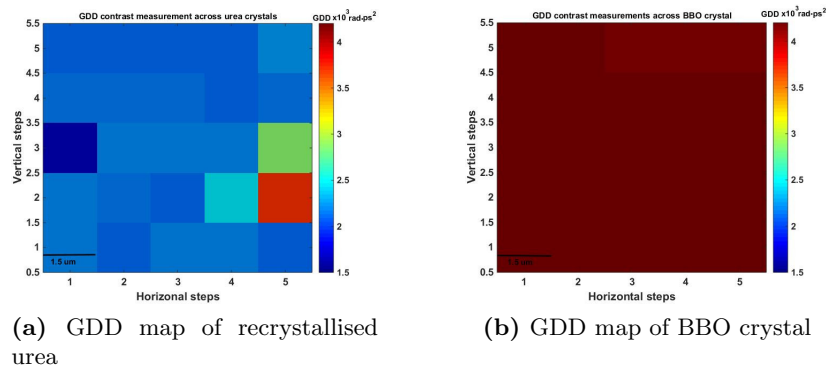


Figure 6: Phase contrast maps of recrystallized urea and BBO

of the focusing objective. This makes it possible to extract information from a specific area and depth within a given material. We have also seen that for a non uniform sample, the extracted phase acquired thorough the MIIPS process is sensitive to position, and therefore suggests phase contrast imaging is possible.

References

- [1] Trebino R 2000 *Frequency-Resolved Optical Gating: The Measurement of Ultrashort Laser Pulses* **Ed.1** (Springer US) ISBN 978-1-4613-5432-1
- [2] Iaconis C and Walmsley IA, 1998 *OPTICS LETTERS* **23** pp 792-794
- [3] Spangenberg D, Rohwer E, Brüggemann MH, and Feurer T 2015 *OPTICS LETTERS* **40** pp 1002-1005
- [4] Sukhoivanov I, Iakushev S, Shulika O and Lysak V 2007 *9th International Conf. on Transparent Optical Networks* Rome pp 128-131
- [5] Durst M, Kobat D and Xu C 2009 *Optics Express* **34** pp 1195-1197
- [6] Mak K, Travers J, Joly N, Abdolvand A and Russell P 2013 *Optics Express* **38** pp 1195-1197
- [7] Lozovoy V, Pastirk I and Dantus M 2004 *Optics Letters* **29** pp 775-777
- [8] Comin A, Ciesielski R, Piredda G, Donkers K and Hartschuh A 2014 *Journal of the Optical Society of America B* **31** pp 1118-1125
- [9] Tu H, Liu Y, Lægsgaard J, Turchinovich D, Siegel M, Kopf D, Li H, Gunaratne T and Boppart SA 2012 *Applied Physics B: Lasers and Optics* **106** pp 379-384
- [10] Xu B, Gunn J, Cruz J, Lozovoy V and Dantus M 2006 *Journal of the Optical Society of America B* **23** pp 750-759
- [11] Heidt A 2010 *Journal of the Optical Society of America B* **27** pp 550-559
- [12] Heidt A, Rothhardt J, Bartelt H, Rohwer E, Limpert J and Tünnermann A 2011 *Optics Express* **19** pp 13873-13879
- [13] Dudley J M, Genty G and Coen S 2006 *Reviews of Modern Physics* **78** pp 1135-1184
- [14] Weiner A M, 2000 *Review of Scientific Instruments* **71** pp 1929-1960
- [15] Comin A, Ciesielski R, Coca-López N and Hartschuh A 2016 *Optics Express* **24** pp 2505-2512
- [16] Rosker M J, Cheng K and Tang C L 1985 *IEEE Journal of Quantum Electronics* **21** pp 1600-1606
- [17] Tamošauskas G, Beresnevičius G, Gadonas D and Dubietis A 2018 *Opt. Mater. Express* **8** pp 1410-1418

Using optical tweezers to measure the forces exerted by molecular motors in onion cells

A Erasmus, GW Bosman, PH Neethling and EG Rohwer

Laser Research Institute, Physics Department, Stellenbosch University, Private bag X1, Matieland, 7602, South Africa

E-mail: 16529138@sun.ac.za

Abstract. Optical tweezers enable the application of piconewton forces on a microscopic particle inside living cells. This allows for a particle to be spatially manipulated in three dimensions. In this study, the optical tweezers are used to investigate the forces needed to stall the motion of vesicle-carrying molecular motors in onion (*Allium cepa*) cells. The optical tweezers were constructed and the trap strength was calibrated. An integrated microscopy imaging setup was used to see and trap vesicles transported by molecular motors in the cells. The force calibration was then used to determine the intracellular forces of the molecular motors.

1. Introduction

Optical tweezers have been well established in biological and biophysical laboratories [1]. The optical trapping and tweezing of particles is possible due to the fact that light can apply radiation pressure on particles [2]. In this work a stable, single beam optical trap is constructed and used to trap particles with a higher refractive index than their surrounding medium.

For particles that are much larger than the wavelength of the trapping light, geometric ray optics can be used to describe the optical trapping. As light propagates through the particle refraction occurs and the light exiting the particle will have a different direction and thus momentum (Δp_{light} - see figure 1). The change of momentum of the light is away from the optical axis because the particle has a higher refractive index than the surrounding medium ($n_1 > n_2$). Due to conservation of momentum, the particle will experience a change of momentum and a force towards the optical axis ($\Delta p_{particle}$).

Light incident onto the particle will also scatter off the particle and induce a scattering force in the forward direction of the beam. The particle will therefore travel along the beam path. To overcome the scattering force and create a stable trap to keep the particle stationary along the optical axis, the trapping force must be increased sufficiently. This is achieved by arranging the rays in a converging manner, which translates to using a focused beam in an experimental setup. This is equivalent to creating an electric field with a steeper gradient thus producing a larger trapping force.

In this work an optical tweezers was constructed to measure the stall forces of molecular motors in onion (*Allium cepa*) cells. In the cell, molecular motors transport vesicles along the cytoskeleton (microtubules or actin filaments). Vesicles are spherical structures, encased by a lipid bi-layer, that hold proteins, nutrients, etc. Molecular motors assist with the efficient delivery of the above mentioned products in the cell by ‘walking’ along the cytoskeleton [3].

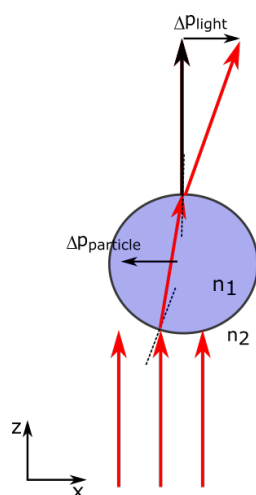


Figure 1. A particle in a laser beam will experience a force towards the optical axis ($\Delta p_{particle}$) due to the refraction of the transmitted light.

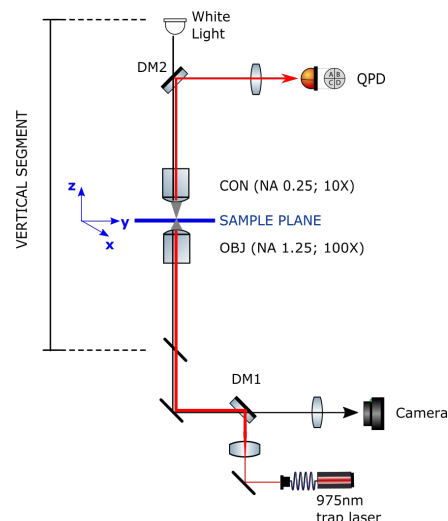


Figure 2. The optical tweezers setup is shown schematically here. The trap is created by focusing a 975 nm diode laser using a high numerical aperture microscope objective (NA of 1.25). A white light LED is used for wide field imaging.

The vesicles have a higher refractive index than the cytosol and it is therefore possible to trap them using the optical tweezers. Vesicles transported by molecular motors are identified by observing vesicles moving along a linear path, assumed to be the cytoskeleton, at a near constant speed. The force needed to trap the vesicle gives a measure of the force with which the molecular motor transports the vesicle.

In order to determine the force needed to stall the motion of a vesicle carried by molecular motors, the force that the optical tweezers exert on a trapped particle must be determined. This is done by trapping silica beads of similar size to that of the vesicles and using the power spectrum method [4].

Power spectrum method A particle in the optical trap can be modeled as a driven damped harmonic oscillator where the motion of the particle is driven by its Brownian motion in the medium it is suspended in. The restoring force that the particle in the trap experiences for a displacement x can be approximated by $F = -kx$. Here k is the trap stiffness constant which can be determined using the power spectrum of the variance of the displacement of the particle's position in the trap, which is measured on a position sensitive detector. From the power spectrum the corner frequency $f_c = \frac{k}{2\pi\gamma}$ can be determined (where $\gamma = 6\pi\eta r$ is the viscous drag coefficient), and so too the trap stiffness constant. Here η is the viscosity of the water (1.012 mPa.s) and r is the radius of the trapped particle. Figure 3 shows the signal from the position sensitive detector for the x coordinate, for a 1 μm bead's position in the trap, as well as the corresponding power spectrum. The corner frequency is indicated on the figure.

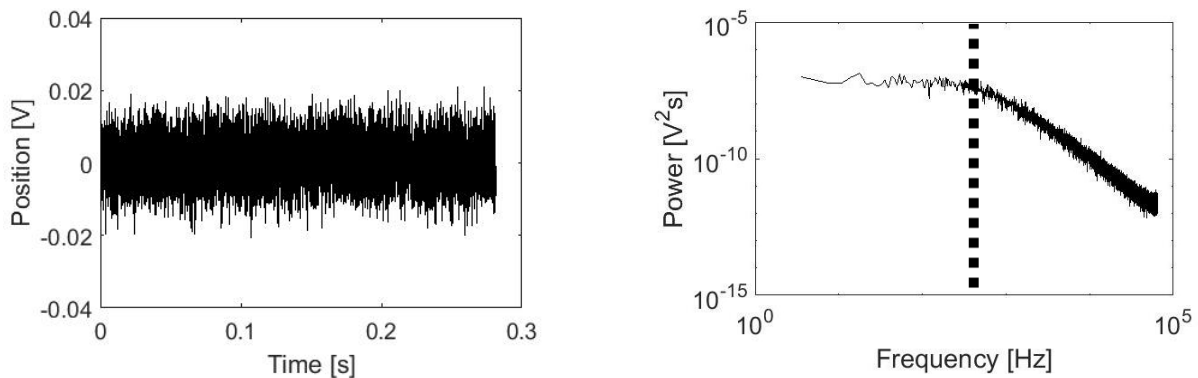


Figure 3. On the left, the position sensitive detector’s signal for the x coordinate shows the displacement of a $1\ \mu\text{m}$ bead’s position in the trap due to Brownian motion. The corresponding power spectrum is shown on the right with the corner frequency, that can be calculated, indicated by a dotted line.

2. Experimental setup

Figure 2 shows a brief schematic of the optical tweezers setup used in this work. A narrow bandwidth near-infrared laser (wavelength of 975 nm) is used since this wavelength reduces local heating as the samples are predominantly transparent in the near infrared region.

The laser light is coupled into a single mode optical fiber and expanded to ensure optimal filling of the back aperture of a high numerical aperture (NA of 1.25) 100X oil immersion microscope objective. The sample is placed on a cover slide and its position is controlled with a computer controlled 3-axis piezo translation stage with 5 nm step resolution.

The transmitted trapping beam is collected by a condenser lens (10X, NA 0.25). The trapping light is reflected by a dichroic mirror (DM2) and imaged onto a quadrant position detector (QPD).

The movement of a trapped bead relative to the trap center is measured on the quadrant position detector. The temperature of the sample is monitored and measurements are conducted under constant temperature conditions to ensure that the viscosity of the fluid remains constant.

The optically trapped particle in the sample is imaged onto a CMOS camera using a white light LED as a light source and a 150 mm focal length bi-convex tube lens.

For force calibration measurements, dielectric silica beads of average diameter $1.01\ \mu\text{m} \pm 0.09\ \mu\text{m}$ was used. These beads were suspended in distilled water at a low concentration to avoid trapping multiple beads simultaneously.

Onion cell samples are prepared by removing a single layer of cells from the membranous outer layer of the onion, and fixing this layer on a microscope cover slide. The sample is placed at the focus of the objective and the vesicles are observed by imaging them on the camera.

The power in the trap was measured before the light enters the objective and it is assumed that the light lost through the objective is negligible. By measuring the force exerted by the optical tweezers at various incident powers, a force calibration curve of the trap strength versus incident laser power can be determined. This is used to determine the stall forces of vesicle-carrying molecular motors.

3. Results and discussion

Using the optical tweezers setup described above, silica beads of $1\ \mu\text{m}$ in diameter were trapped. Figure 4 shows frames of a video of the trapped bead held stationary while freely diffusing beads

in its surrounding are moved towards the left with respect to the trapped bead.



Figure 4. This figure shows the movement of a trapped 1 μm bead (circled in white) relative to the other freely diffusing 1 μm beads (circled in black). This is achieved by moving the sample to the left while the trap position remains stationary.

The force calibration was completed as described above and the results are shown in figure 5. The trap constant, k , is shown to increase linearly along the x and y axes of the trap as the power in the trap increases. The parabolic approximation of the trap potential holds for a displacement equal to the length of the radius of the particle [5]. Therefore, for a 1 μm diameter particle typical forces are determined for a 0.5 μm displacement of the particle from the trap center. The trap exerts forces in the piconewton range on the particle (using $F = -kx$). For example, a 1 μm silica bead displaced 0.5 μm from the trap center experiences a restoring force towards the trap of 29 pN ($k = 5.8 \times 10^{-5}$ N/m) along the y axis of the trap when the trap power is 0.1 W, which is in good agreement with literature [6]. The difference in trap stiffness along the x and y axes is due to astigmatism of the focus.

The optical tweezers was then used to trap vesicles in onion cells and to determine the stall forces of molecular motors in the cell. It was assumed that the viscosity of the cytosol is similar to that of water [7]. The diameter of the vesicles were measured to be between 0.42 μm to 1.12 μm . This is of the same size as the beads used to calibrate the trap. The refractive index of the vesicles is assumed to be similar to that of the silica beads [8]. The force calibration, depicted in figure 5, can therefore be used to determine the stall forces of the molecular motors transporting the vesicles in the onion cells.

The onion sample is placed in the focus of the optical tweezers setup. The optical resolution of the imaging setup only allows for the imaging of the vesicles and not the cytoskeleton or the molecular motors (figure 6). By observing the movement of the vesicles it can be seen that some vesicles follow linear paths across large distances (many microns) at a near constant speed. It is assumed that molecular motors are transporting these vesicles along the cytoskeleton. In figure 6 two such paths are indicated with the superimposed black lines.

The trap is positioned along the path of the motors and vesicles. The trapping laser's power is increased until a vesicle is trapped, thus stalling the motion of the motor. The results of the stalling forces required is presented in table 1. The y component of the force calibration in figure 5 is used. It is used because it yields a higher trap stiffness value k , and therefore gives an upper bound for the force of the molecular motor.

Again a displacement of 0.5 μm is selected to calculate the stall force from a given laser power and trap stiffness. The average force required to trap a vesicle attached to a molecular motor was measured as 16.8 pN. This is therefore the force required to stall a molecular motor transporting the vesicle. This force is significantly larger than the force required to trap a freely moving vesicle that is not transported along a linear path in the cell (not attached to a motor), 3.39 pN. For vesicles attached to a motor, the trap must overcome the pulling force of the motor

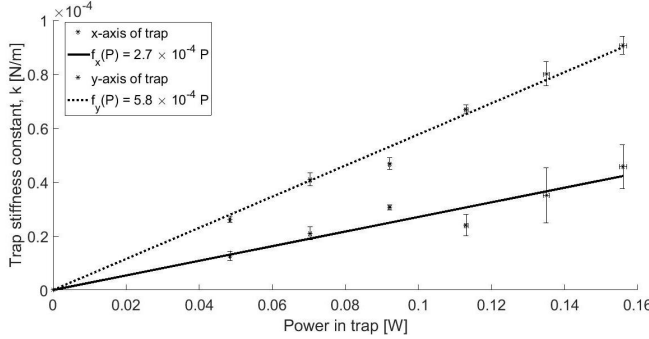


Figure 5. Results of the force calibration for $1 \mu\text{m}$ beads are shown here. The linear fits as a function of the power (P) in the trap for the x and y axes of the trap are $f_x(P) = 2.7 \times 10^{-4}P$ ($R_x^2 = 0.93$) and $f_y(P) = 5.8 \times 10^{-4}P$ ($R_y^2 = 0.99$).

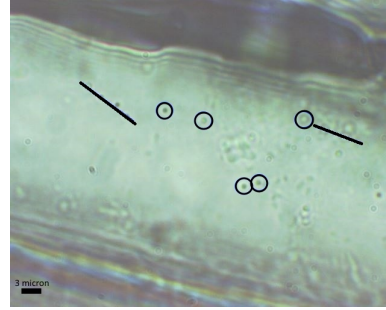


Figure 6. In the still image of an onion cell, examples of vesicles are circled in black and the black superimposed lines indicate paths where vesicles are transported along the cytoskeleton by molecular motors. These are identified, because multiple vesicles follow the same path at near constant speeds.

Table 1. The stall force (component along the y axis of the trap) for vesicles transported by molecular motors is shown for displacements of $0.5 \mu\text{m}$ from the trap center. The force at which the molecular motor recovers and removes the vesicle from the trap is also shown. The average over multiple measurements, using various onion cells, is indicated and the standard deviation is indicated for these force measurements.

	Trapping of vesicles attached to molecular motors (50 measurements)	Trapping of free diffusing vesicles (22 measurements)	Releasing the vesicles from the trap (34 measurements)
Average force [pN]	16.8	3.39	2.66
Standard deviation [pN]	2.57	0.756	1.94
Minimum [pN]	10.0	2.20	1.04
Maximum [pN]	21.9	4.52	6.84

transporting it along its path, whereas for a freely diffusing vesicle not transported along a path, the trap must only overcome the stochastic forces causing diffusion of the vesicle in the cell.

Subsequent to measuring the stall force of the molecular motor, the trap strength is decreased sufficiently such that the motor can move the vesicle out of the trap, and continue on its previous path. This highlights the nondestructive nature of the optical tweezers in that the vesicle is not detached from the molecular motor. It also confirms that it is the motion of the motor that is stalled. The average force at which the vesicle can escape the trap is 2.66 pN . The standard deviation in the results of the stall forces shown in table 1 can be attributed to size variation of the vesicles as well as the number of molecular motors attached to individual vesicles. The relatively large standard deviation can also be attributed to variation of the local viscosity within the cytoplasm since it is non-Newtonian [9], and the viscosity varies locally from that of

water [10, 11] to values a hundred times greater than that of water [12, 13]. This variation in viscosity, in addition to the dense and complex structure of the cytoplasm [14, 15], affects the force required to trap and release a vesicle in the cell and can explain the variation in the results.

4. Conclusion

In this work an optical tweezers setup was constructed and used to investigate the stall forces of molecular motors in onion cells. The forces exerted by the optical tweezers were calibrated using silica beads of 1 μm in diameter suspended in water. Using the power spectrum of the variance of the displacement of the bead in the trap due to Brownian motion, the trap stiffness constant was determined for various trapping laser powers.

Due to the piconewton range of forces that the optical tweezers applies, it is a useful tool to study biological samples. There is a large interest in the biological sciences into the mechanisms and dynamics of molecular motors that transport cellular cargo [1]. In this study, vesicles transported by molecular motors along the cytoskeleton of the cell were trapped *in vivo*. The nondestructive nature of the technique is demonstrated in the release of the trapped vesicle and further movement of the molecular motor that followed. Using the force calibration of the optical tweezers, the force required to stall the molecular motor's motion was found to be in the order of piconewtons which is in agreement with literature [16].

References

- [1] Moffitt J R, Chemla Y R, Smith S B and Bustamante C 2008 *Annual Review of Biochemistry* **77** 205-28
- [2] Ashkin A 1970 *Physical Review Letters* **24** 156-9
- [3] Lodish H, Berk A, Zipursky S L, Matsudaira P, Baltimore D and Darnell J 1999 *Molecular Cell Biology* (New York, NY: W H Freeman and Company) 809
- [4] Visscher K, Gross S P, Block S M 1996 *IEEE Journal on Selected Topics in Quantum Electronics* **2** 1066-76
- [5] Jones PH, Marag OM and Volpe G 2015 *Optical tweezers: principles and applications* (United Kingdom: Cambridge University Press) 34
- [6] Lee W M, Reece P J, Marchington R F, Metzger N K and Dholakia K 2007 *Nature Protocols* **2** 3226-38
- [7] Verkman A S 2002 *Trends Biochemical Science* **27** 2733
- [8] Chandler W L, Yeung W and Tait J F 2011 *Journal of Thrombosis and Haemostasis* **9** 1216-24
- [9] Wayne R 2009 *Plant cell biology: From Astronomy to zoology* (USA: Elsevier) 147
- [10] Kao H P, Abney J R, and Verkman A S 1993 *The Journal of Cell Biology* **120** 175-84
- [11] Bicknese S, Periasamy N, Shohet S B and Verkman A S 1993 *Biophysical Journal* **65** 1272-82
- [12] Keith A D and Snipes W 1974 *Science* **183** 666-8
- [13] Scherp P and Hasenstein K H 2007 *American Journal of Botany* **94** 1930-4
- [14] Fushimi K and Verkman A S 1991 *The Journal of Cell Biology* **112** 719-25
- [15] Jünger F, Kohler F, Meinel A, Meyer T, Nitschke R, Erhard B and Rohrbach A 2015 *Biophysical Journal* **109** 869-82
- [16] Lodish H, Berk A, Zipursky S L, Matsudaira P, Baltimore D and Darnell J 1999 *Molecular Cell Biology* (New York, NY: W H Freeman and Company) 771

The effect of photobiomodulation at 660 nm on the differentiation of diabetic wounded WS1 human fibroblasts into myofibroblasts

D R Mokoena, N N Houreld, S S Dhilip Kumar and H Abrahamse

Laser Research Centre, Faculty of Health Sciences, University of Johannesburg, P.O. Box: 17011, Johannesburg 2028, South Africa

Email: nhoureld@uj.ac.za

Abstract. Diabetes is associated with complicated wound healing and rapid wound progression which may be due to cells that fail to proliferate and differentiate, thus leading to ulcers and possible limb amputation. The administration of photobiomodulation (PBM) has been associated with increased cellular proliferation, a decrease in wound repair duration and an increase in wound flexibility. Most studies performed on PBM and myofibroblasts dwell mostly on fibrosis, and a minority of studies have investigated fibroblast differentiation for use in diabetic wound healing. This study aimed to determine the effect of PBM at 660 nm with 5 J/cm² on the differentiation of diabetic wounded human fibroblasts 48 h post-irradiation. This was achieved by measuring the expression of the fibroblast surface marker Thy-1 (CD90), proto-myofibroblast marker EDA fibronectin (EDA-FN), and the myofibroblast marker alpha smooth muscle actin (α -SMA) by immunofluorescence and flow cytometry. Post-PBM, there was a significant decrease in Thy-1, and an increase in EDA-FN and α -SMA, indicating the transformation of fibroblasts during wound healing. Photobiomodulation at 660 nm with 5 J/cm² stimulates cellular differentiation of diabetic wounded fibroblast cells into myofibroblasts, which contributes to the increased rate of wound healing.

1. Introduction

Diabetes Mellitus (DM) is a common metabolic disorder resulting from the lack of or resistance to insulin by cells [1]. As a result, blood glucose levels are high, which leads to a number of complications such as inflammation, nephropathy, retinopathy, neuropathy and cardiovascular disease [2], as well as delayed wound healing. Globally, DM is a growing problem and poses an economic burden to all countries [3]. In Africa alone, the number of cases of DM is expected to increase by 162.5% from 2017 to 2045. Individuals are at risk of limb amputations in their productive years due to impaired wound healing, resulting in an increased economic burden, as well as reduced quality of life. It is estimated that a lower limb or part of the lower limb is lost in every 30 seconds worldwide [2].

The normal wound healing process is characterized by three overlapping phases namely: inflammation, proliferation and remodeling. In diabetic or chronic wounds, the wound healing process remains trapped in the inflammation phase and cells do not differentiate to aid in wound closure. Fibroblasts are one of the cells that play a major role in wound healing. They infiltrate the wound site and differentiate into myofibroblasts which are liable for wound contraction. They also produce most of the extracellular matrix (ECM), collagens, matrix metalloproteinase (MMPs), tissue inhibitors of the

matrix metalloproteinase (TIMPs) and glycosaminoglycans (GAGs) [4]. Fibroblasts express the cell surface marker CD90 or Thy-1. During wound healing they differentiate into extra domain-A fibronectin (EDA-FN) expressing proto-myofibroblasts, which finally differentiate into alpha smooth muscle actin (α -SMA) expressing myofibroblasts via the Smad pathway [5]. The presence of EDA-FN aids in the complete differentiation into myofibroblasts [6]. It is believed that in diabetic wounds this differentiation does not occur as the wound healing process remains stagnant in the inflammatory phase [7].

Photobiomodulation (PBM) is a non-invasive, non-thermal therapy which involves the application of red or near-infrared (NIR) light to stimulate, regenerate, protect and heal injured or degenerating tissues [8]. Its exact mechanism is not fully understood. However, it is known that PBM activates photoreactive proteins such as cytochrome C oxidase in the mitochondrion's respiratory sequence, thus increasing the presence of adenosine triphosphate (ATP) in the cells [9]. This increase has been found to normalize cellular functions, decrease pain and activate the healing process. Most studies performed on PBM and myofibroblasts dwell mostly on fibrosis, and a minority of studies have investigated fibroblast differentiation for use in diabetic wound healing. The aim of this study was to investigate the effect of PBM on the differentiation of fibroblasts into myofibroblasts in diabetic induced wound healing *in vitro* using a 660 nm diode laser.

2. Materials and methods

Human skin fibroblast cells (WS1, ATCC® CRL-1502™) were grown according to standard techniques. Cells were continuously grown in minimal essential media (MEM) containing 10% foetal bovine serum (FBS), 0.1 mM non-essential amino acids (NEAA), 1 mM sodium pyruvate, 1% amphotericin B, 1% penicillin-streptomycin, 2 mM L-glutamine, and to diabetic cultures 17 mMol/L D-glucose was added to achieve a diabetic model [10, 11]. Cells (6×10^5 for immunofluorescence, and 1×10^6 for flow cytometry) were seeded into 3.4 cm² culture plates. A wound model was created via the scratch assay, in which a confluent monolayer of cells was scrapped with a sterile 1 mL pipette. Cells were irradiated with a 660 nm diode laser at a fluence of 5 J/cm² in the dark from above with the culture dish lid off. Laser parameters are shown in Table 1. This was followed by incubation for 48 h. Non-irradiated cells were used as controls (0 J/cm²). Immunofluorescence and flow cytometry techniques were performed.

For flow cytometry, harvested cells were pelleted and fixed with 0.5 mL cold flow cytometry fixation buffer (FC004, R&D Systems, Whitehead Scientific, South Africa) and incubated at room temperature (22°C) for 10 min. Following two washes with phosphate buffered saline (PBS), pelleted cells were re-suspended in 150 μ L flow cytometry permeabilization /wash buffer I (FC005, R&D Systems, Whitehead Scientific, South Africa) and incubated for 30 min at room temperature (22°C) in 10 μ L phycoerythrin (PE)-conjugated antibody (mouse, anti-Human CD90/Thy1, FAB2067P; mouse, anti-Human α -smooth muscle actin, IC1420p; R&D Systems, Whitehead Scientific, South Africa). Cells were washed twice with flow cytometry permeabilization /wash buffer I and re-suspended in 300 μ L PBS for flow cytometric analysis on the BD Accuri C6.

For immunofluorescence, cells were fixed on a coverslip with 4% paraformaldehyde for 15 min at room temperature, permeabilized with 0.5% triton X-100 in PBS, and blocked with 1% bovine serum albumin (BSA) in PBS to prevent any non-specific binding. Cells were first labelled with primary antibody (sheep, anti-human CD90/Thy1, AF2067; mouse, anti-human alpha-Smooth Muscle Actin, MAB1420; R&D Systems, Whitehead Scientific, South Africa; and rabbit, anti-human EDA, HPA037972; Sigma-Aldrich, South Africa). After washing, cells were labelled with a fluorescently conjugated secondary antibody (557-conjugated Anti-Sheep IgG Secondary Antibody NL010; or 557conjugated Anti-Mouse IgG Secondary Antibody, NL007; R&D Systems, Whitehead Scientific, South Africa; or FITC-conjugated Anti-Rabbit IgG antibody, D2706, Santa Cruz, Anatech Instruments (Pty) Ltd, South Africa; respectively). After washing, nuclei were counter stained with 1 μ g/mL 4,6diamidino-2phenyindole (DAPI). The coverslip was mounted onto a slide and viewed on the Carl Zeiss Axio Z1 Observer using AxioVision software.

Statistical analysis was achieved on three repeats of each sample. The t-test was used to determine statistical differences using Sigma Plot version 13.0 (Systat Software Inc., San Jose, California) and was considered significant when $P < 0.05$.

Table 1. Laser parameters.

Variables	Diode laser
Wavelength (nm)	660
Light source	Diode laser
Wave emission	Continuous wave
Spot Size (cm ²)	9.1
Power output (mW)	100
Power density (mW/cm ²)	11
Irradiation time	7 min 34 s
Energy density (J/cm ²)	5

3. Results and discussion

Post-irradiation, Thy-1 immunofluorescence results revealed a decrease in signal for the irradiated diabetic wounded model (DW5J) as compared to the non-irradiated diabetic wounded model (DW0J) (figure 1). The flow cytometry results showed and confirmed this significant decrease ($P < 0.001$) in Thy-1 in DW5J cells (1.2% of cells stained positive for Thy-1) as compared to their control DW0J (3.2% of cells stained positive for Thy-1) (figure 2). There was an increase in the proto-myofibroblast marker EDA-FN, as well as the myofibroblast marker α -SMA, in the DW5J model compared to the control DW0J 48 h post-irradiation (figure 1). A significant increase in α -SMA was confirmed in the DW5J model by flow cytometry ($P < 0.001$), with 14.2% of the population staining positive for α -SMA as compared to only 4.8% in the DW0J model (figure 2).

During normal wound healing, fibroblasts migrate into the wound site and secrete cytokines, growth factors and the ECM [5, 12]. Once activated they differentiate into myofibroblasts which also participate in ECM secretion and wound size reduction through contraction [5, 13]. In DM there is little production and quick removal of collagen, which is the main content of the ECM. This leads to debilitated wound healing and cells remaining senescent in the inflammation phase. Maione et al observed that in diabetic wound healing, fibronectin (FN) content is increased and the ECM deposited is thinner in comparison to normal wound healing, they then concluded that the increased FN hindered the secretion of a more mature ECM which is excreted by myofibroblasts [14]. This suggests that in diabetic wound healing differentiation of fibroblasts does not occur, and if it does occur it remains in the proto-myofibroblast phenotype, hence the increased FN. Modern day treatments of diabetic and chronic wounds are associated with failure and relapse which increases the expense of wound care [7].

PBM has been proven to stimulate cellular processes without any harmful effects. It works by stimulating cytochrome C oxidase leading to increased ATP production, cellular regeneration, and enhanced survival and proliferation. Increased ATP is evidenced by the activation of cellular pathways associated with wound healing, cell differentiation and proliferation [8, 15]. A study done on dermal wounded and immunosuppressed rats irradiated at 810 nm showed a reduction in the pro-inflammatory cytokine tumour necrosis factor- α (TNF- α), and an increase in the expression of fibroblast growth factor receptor (FGFR-1) and FN, which enhances the protein expression of α -SMA. This showed that PBM results in an increase in cellular motility and contractility, which is linked to an increased expression of α -SMA [16].

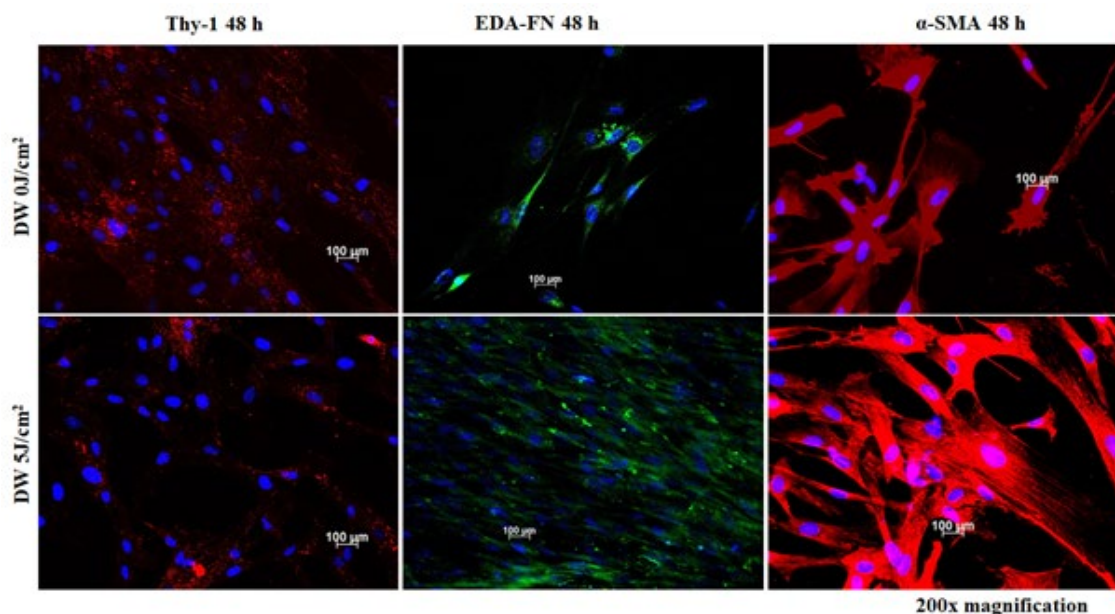


Figure 1. Diabetic Wounded (DW) fibroblasts irradiated with 660 nm at a fluence of 5 J/cm² (DW 5 Jcm²) and control cells (non-irradiated 0J/cm²; DW 0J/cm²). Cells were incubated for 48 h and stained for the Thy-1 marker with NL557-conjugated anti-sheep IgG antibody (red); EDA-FN was stained with FITC-conjugated Anti-Rabbit IgG antibody (green); and α-SMA was stained with NL557-conjugated anti-Mouse antibody (red). Nuclei were counterstained with DAPI (blue).

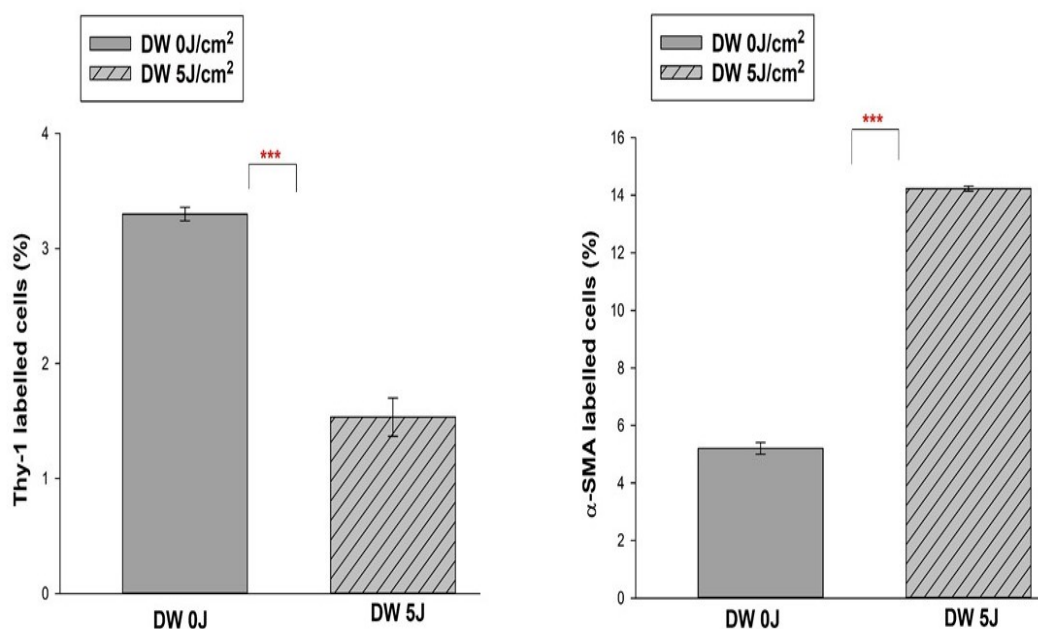


Figure 2. Flow cytometry analysis of Thy-1 and α-SMA in irradiated (5 J/cm²) and non-irradiated (0 J/cm²) diabetic wounded (DW) cells incubated for 48 h. Statistical significance is shown as *** $p < 0.001$ (SEM) in comparison to non-irradiated cells (0 J/cm²).

Studies have shown that laser irradiation at 660 nm and a fluence of 5 J/cm² has the ability to stimulate wound healing, increase cellular proliferation and enhance cellular viability [17; 18]. Naderi and colleagues have also shown that higher fluences do not have any effect compared to their respective non-irradiated controls [18]. This brings us back to the biphasic dose response phenomenon, which denotes the “Arndt-Schulz Law”, in which low doses can result in insignificant effects, while too much light delivery can result in inhibition [19]. In this study, PBM at 660 nm with 5 J/cm² has proved to stimulate the transition of fibroblasts into myofibroblasts by decreasing Thy-1, and increasing EDA-FN and α -SMA in irradiated diabetic wounded fibroblasts, which is vital for proper and successful wound healing.

4. Conclusion

The aim of this study was to determine the effect of PBM at 660 nm with 5 J/cm² on the differentiation of diabetic wounded fibroblasts into myofibroblasts 48 h post-irradiation. The results obtained indicated that PBM had a positive effect on irradiated diabetic wounded fibroblast cells (DW5J), and therefore resulted in a significantly increased rate of differentiation of fibroblasts into myofibroblasts in comparison with the non-irradiated model (DW0J). Hence, the evident decrease in Thy-1, and increase in EDA-FN and α -SMA expression at 48 h in irradiated cells (DW5J). This transition is important since myofibroblasts play a major role in wound contraction and ECM deposition to achieve successful wound healing. This contributes to the knowledge that PBM has therapeutic properties which enable it to stimulate wound healing in diabetic wounded cells *in vitro*, thus increasing the chances of its application and acceptance as one of the therapeutic modalities in chronic and diabetic wound care.

Acknowledgments

This work is based on the research supported by the South African Research Chairs Initiative of the Department of Science and Technology and National Research Foundation of South Africa (Grant No 98337). The authors also thank the University of Johannesburg, the National Laser Centre and the National Research Foundation of South Africa for their financial grant support.

References

- [1] Hameed I, Masoodi S R, Mir S A, Nabi M, Ghazanfar K and Ganai B A 2015 *World J. Diabetes* **6** 598-612.
- [2] International Diabetes Federation, IDF 2017 *Diabetes Atlas*, 8th edition, Available from www.diabetesatlas.org, Accessed on 11/04/18.
- [3] Bommer C, Sagalova V, Heesemann E, Manne-Goehler J, Atun R, Bärnighausen T, Davies J and Vollmer S 2018 *Diabetes Care* **41** 963-70.
- [4] Matsuzaki S, Hiratsuka T, Taniguchi M, Shingaki K, Kubo T, Kiya K, Fujiwara T, Kanazawa S, Kanematsu R, Maeda T, Takamura H, Yamada K, Miyoshi K, Hosokawa K, Tohyama M and Katayama T 2015 *PLoS One* **10** 1-11.
- [5] Darby I A, Leverdet B, Bonté F and Desmouliere A 2014 *Clin. Cosmet. Investig. Dermatol.* **7** 301-311.
- [6] Thiruvoth F M, Mohapatra D P, Sivukumar D K, Chittoria R K and Nandhagopal V 2015 *Plast. Aesthet. Res.* **2** 250-6.
- [7] Frykberg F G, and Banks J 2015 *Adv. Wound Care* **4** 560-82.
- [8] Hamblin M R 2016 *BBA Clin.* **6** 113-24.
- [9] Góralczyk K, Szyma J, Szot K, Fisz J and Roś D 2016 *Lasers Med. Sci.* **31** 825-31.
- [10] Ayuk S, Houreld N and Abrahamse H 2014 *Int. J. Photoenergy* **2014** 1-34.
- [11] Houreld N and Abrahamse H 2007 *Photomed. Laser Surg.* **25** 78-84.
- [12] Tracy L E, Minasian R A and Caterson E J 2016 *Adv. Wound Care* **5** 119-36.

- [13] Hinz B 2007 *J. Invest. Dermatol.* **127** 526–37.
- [14] Maione A G, Smith A, Kashpur O, Yanez V, Knight E, Mooney D J, Veves A, Tomic-Canic M and Garlick J A 2016 *Wound Repair Regen.* **24** 630-43
- [15] De Freitas L F and Hamblin M R 2016 *IEEE J. Sel. Top Quantum Electron* **22** 1– 37
- [16] Keshri G K, Gupta A, Yadav A, Sharma S K and Singh S B 2016 *PLoS One* **11** doi:10.1371/journal.pone.0166705.
- [17] Jere S W, Houreld N N and Abrahamse H 2018 *J. Photochem. Photobiol. B* **179** 74–83.
- [18] Naderi M S, Razzaghi M, Esmaeeli Djavid G and Hajebrahimi Z 2017 *J Lasers Med Sci* **8** S46–50.
- [19] Huang Y-Y, Chen A C -H, Carroll J D, Hamblin M R 2009 *Dose-Response* **7** 358–83.

Investigation of a specifically targeted photosynthetic nanoparticle drug delivery system for enhanced photodynamic therapy treatment of metastatic melanoma

C Naidoo, C A Kruger and H Abrahamse

Laser Research Centre, Faculty of Health Sciences, University of Johannesburg, P.O. Box: 17011, Johannesburg 2028, South Africa

Email: habrahamse@uj.ac.za

Abstract. Metastatic melanoma (MM) is the 6th most common cancer diagnosed worldwide, with approximately 100, 000 annual related deaths. Photodynamic therapy (PDT) is a photochemotherapeutic cancer treatment that utilizes a photosensitizer (PS) drug that, when activated by laser light at a specific wavelength, yields reactive oxygen species (ROS), which in turn induces cell death. However, due to the passive diffusion of PSs, normal surrounding cells are sometimes affected and their targeted concentrations in cancer cells tends to be minimal, thus limiting the effectiveness of this treatment. Therefore, a multicomponent drug targeting strategy is often applied to improve PS specific delivery and concentration in cancer cells only, which in turn can improve the effectiveness of PDT. Thus, the intention of this study was to improve the photosynthetic drug delivery of Zinc Phthalocyanine Tetrasulfonic acid (ZnPcS₄) in MM cells, by enhancing its chemical structure. ZnPcS₄ was successfully conjugated to pegylated gold nanoparticles (AuNP) to maximize its solubility and stability, as well as bound to active tumour-associated antibody-antigens (Anti-MIA Ab) to aid in specific targeted PS delivery. Within *in vitro* cultured MM (A375) cells, the final molecular drug conjugate proved to have enhanced subcellular uptake in cells, when compared to ZnPcS₄ PS drug delivery alone. Moreover, after conducting *in vitro* PDT experiments a significant amount of 76% cytotoxicity was noted in cells which were treated with final molecular conjugate, versus 48% cytotoxicity when ZnPcS₄ PS drug was administered alone. Suggesting, that overall the final molecular drug conjugation combination of ZnPcS₄ with AuNP and anti-MIA Ab, proved to enhance the treatment capabilities of PDT for MM through improved PS drug delivery via active targeting mechanisms.

1. Introduction

Cancer is the rapid abnormal proliferation of cells to produce either benign or malignant tumours.^[1] Malignant tumours often spread to surrounding tissues and move throughout the body using circulatory or lymphatic systems, causing metastasis.^[2] Melanoma is extremely invasive and due to this it is considered one of the deadliest skin cancers at present.^[3] MM is the 6th most common cancer diagnosed worldwide, with approximately 100, 000 annual related deaths.^[4] Melanoma originates in the deepest regions of the epidermis and in the beginning of the dermis, where melanocytes which produce the melanin pigment are located.^[5, 6] MM is Stage IV of skin cancer and occurs when cancerous cells have metastasized and developed in other organs that are located far from the primary site of occurrence.^[5] In the last 50 years the incidence rate of MM has increased more significantly when compared to other types of cancer.^[6] It is crucial to detect melanoma in the early stages, as once it metastasized it is difficult

to locate where it originated, and so plays a major role in patient survival rates as surgery is no longer an option due to multiple secondary sites and thus makes it more difficult to treat.^[6]

PDT is an unconventional treatment used to treat cancer, which has been investigated for the past 3 decades.^[7] It utilizes a PS which is a light sensitive drug that when activated at a specific wavelength causes excitation.^[8] This excitation process causes the PS to produce ROS, which induce damage to the cells through photo-cytotoxicity caused by oxidative stress which renders the cells inactive.^[9] This is a less invasive form of cancer treatment as the cancerous tumour region is targeted and produces localized destruction with limited side effects when compared to conventional treatments like chemotherapy and radiation.^[10]

The PS Zinc Phthalocyanine Tetrasulfonic acid (ZnPcS₄) is a second generation metallated phthalocyanine sensitizer that can be used in phototherapeutic applications, with minimal dark toxicity.^[11] It contains a zinc diamagnetic central atom, which determines not only the high triplet state quantum yields of ROS, but also the prolonged lifespan of the molecule once excited.^[11] The PS also contains various sulfonated thiol groups which makes it hydrophilic and so increases its solubility in terms of cellular uptake.^[12] Studies reported post-irradiation that when 5 μ M of ZnPcS₄ was applied to in vitro cultured human MM cells and PDT light induced at a wavelength of 680nm with a fluence of 10 J/cm², more than 50% growth inhibition and apoptotic cell death cytotoxic side-effects were noted.^[13]

Passive targeting strategies are often accomplished when the PS that is bound to the nanoparticle (NP) accumulates within the tumour cells, this passive diffusion is due to the characteristics that the NPs have.^[14] For effective PDT, functionalized NP platforms need to be used to enhance PS drug delivery and each type has their own individual advantages, whether it may be passively or actively absorbed by tumour cells.^[15] The characteristics which NP exhibit are that they have a large surface-area-to-volume ratio; they have simple surface chemistry with the possibility of engineering and functionalization; small dimensions so they can easily accumulate in cells due to the enhanced permeability and retention (EPR) effect; and NPs go undetected by the immune system barriers as they mimic biological molecules and can combine to other molecules such as PSs which improves and enhances drug delivery.^[16] AuNPs have been extensively investigated in PDT induced cancer treatments as they have tuneable optics and photothermal properties, which allows for the conversion of laser light into heat improving targeted cellular destruction.^[17] NPs can be further functionalized into active targeting molecules through the attachment of molecules which are specifically compatible to targeted receptor tumour sites on the surface of the cancer cell.^[16]

Active targeting strategies have been used by incorporating cell-targeting peptides or antibodies (Ab) onto a NP surface is highly desirable in PDT therapeutic applications, as it allows for selective cell tumour cell targeting.^[17] The protein Melanoma Inhibitory Activity (MIA) was identified as a key component that was involved in the progression and metastasis of MM.^[18] Studies noted that MM cells tend to over express MIA, as it is a melanoma-cell specific antigen, which plays a vital role in carcinogenesis and is not expressed in melanocytes. Thus, MIA has been utilized as a biomarker for diagnosis and detection of MM as it is highly specific and a sensitive marker for MM.^[18]

2. Methodology

2.1. Chemical Synthesis of Multicomponent Nanoparticle Drug Based System

Equal ratios of HS Pegylated 500 amine functionalized AuNP (Sigma 765309) were added to 500 μ M ZnPcS₄ (w/v in 0.001M PBS) (CAS 61586-86-5) and vortexed overnight at room temperature, with 15000rpm rotation speed to promote spontaneous ligand exchange and absorption. The mixture was then purified by centrifugation at room temperature (15000rpm for 1hr) and the pellet was re-suspended in 1ml 0.001M PBS. To conjugate the Anti-MIA Ab (ab166932) to the previous AUNP-ZnPcS₄ molecular suspension, an amide bond was achieved through EDC N-(3-Dimethylaminopropyl)-N'-ethyl carbodiimide hydrochloride and NHS (N-Hydroxysulfosuccinimide sodium salt), through a two-step coupling activation of the carboxylic terminus of the Anti-MIA Ab, which was then purified by

ultrafiltration centrifugation. 200 µg/ml of activated Anti-MIA was then added to 1ml of conjugated AuNP-ZnPcS₄ and vortexed overnight. This allowed the activated carboxylic moiety succinimidyl ester of the Ab to react with the amine functionalized group on AuNP and so stable amide bond was induced. Characterization and photostability of the final molecular conjugate were performed using UV-visible spectroscopy.

2.2. Cell Culture

MM cancer (A375) cells were cultured in Dulbecco's modified Eagle's media, 15% foetal bovine serum, 0.1% penicillin-streptomycin and 0.1% amphotericin-B, with incubation at 37°C, 5% CO₂ and 85% humidity. Cells (2.5 X 10⁵/ml) were seeded into various experimental and control culture dishes. Dose response studies were conducted to determine the lowest concentration to induce 50% cytotoxicity (ICD50), which is required when administering ZnPcS₄ alone, to regulate and compare the effective PDT concentration that was needed within final molecular conjugate PDT experiments which displayed enhanced cellular targeting abilities. The PDT results are not shown; however, it was noted that 2.5µM ZnPcS₄ was the most effective in inducing ICD50, in MM cells, thus within final molecular conjugate experiments MM cells received 2.5µM ZnPcS₄ + AUNP + Anti-MIA Ab. Laser photo-irradiation experiments were conducted using a continuous semiconductor diode laser (Oriel Corporation) emitting at a wavelength of 673 nm with a fluence of 10J/cm². All control and experimental groups after treatment were then additionally incubated for 24 hrs in fresh, drug-free media before cytotoxicity biochemical responses were determined.

2.3. Sub Cellular Localization of Multicomponent Nanoparticle Drug Based System

Immunofluorescent staining was used to determine the successful uptake of ZnPcS₄. A375 cells were grown on glass coverslips in culture dishes. An hour prior to observation, cells were stained with ICAM-1 mouse monoclonal IgG, goat anti-mouse IgG-FITC human absorbed fluorescein13, to enhance membrane matrix proteins for observation, and then fixed with paraformaldehyde for nuclei counterstaining with 40-6-Diamidino-2-phenylindole (DAPI). Slides were examined using the Carl Zeiss Axio Z1 immunofluorescent microscope, to observe blue DAPI counter stained nuclei and green FITC ICAM-1 membrane proteins in cells, while the Cy5 auto fluorescent signal of ZnPcS₄ was noted to detect enhanced cellular uptake of the final conjugate in cells.

2.4. Cytotoxicity Biochemical Assays

The non-radioactive CytoTox96® assay (Promega G1780) was used to measure lactate dehydrogenase (LDH) supernatant released from cells cytosol upon cellular membrane damage before and after treatment in 96 micro well plates. Absorbance was read using a Victor³ microplate reader (Perkin-Elmer) at 490nm and results interpreted quantitatively.

3. Results and Discussion

3.1. Characterization of Multicomponent Nanoparticle Drug Based System

The final molecular conjugate was found to be photostable over its period of experimental utilization. With reference to Figure 1, the AuNPPEG-CSH-NH and ZnPcS₄ visible absorption spectrum peaks were not affected after conjugation and remained prominent, however lowered in absorption and so a final conjugate concentration of 227µM ZnPcS₄ was found to be bound to 0.89 X 10¹⁵ AuNP particles/ml, which could effectively be diluted to 2.5µM ZnPcS₄ in relation to ICD50 dose response assays. Moreover, the ZnPcS₄ absorption spectrum peak at 673nm remained present after final conjugation, suggesting the PS properties were preserved for PDT effective ROS and singlet oxygen yield production. Lastly, the peaks of the final molecular conjugate did slightly broaden, however remained smooth, suggesting an increase in molecular size due to bonding with additional components with minimal

aggregation and the slight shift in resonance peak position of AuNP after conjugation indicated the Ab and PS had been successfully conjugated to its surface.

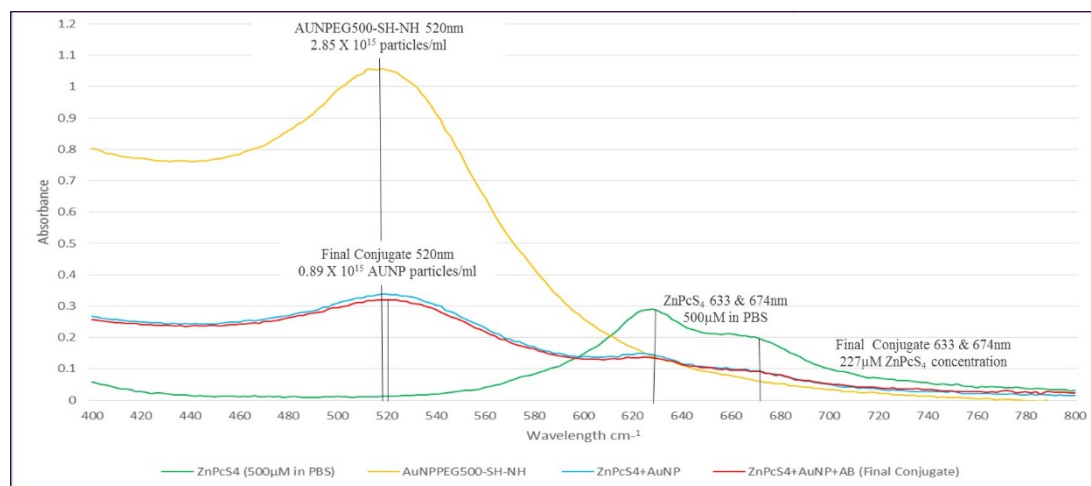


Figure 1: UV-visible spectrophotometry absorption and fluorescence spectra of final molecular conjugate and controls.

3.2. Sub Cellular Localization of Multicomponent Nanoparticle Drug Based System

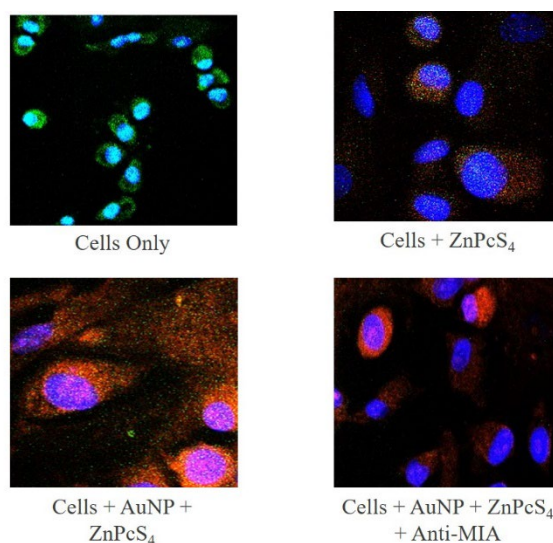


Figure 2: Immunofluorescent Staining of final molecular conjugate and controls.

Live cell imaging immunofluorescent staining was used to determine subcellular localization and uptake of the PS (ZnPCs_4) alone versus the final molecular conjugate ($\text{AUNPPEG500-SH-NH} + \text{ZnPCs}_4 + \text{Anti-MIA Ab}$) within in vitro cultured MM cells (Figure 2). MM cells showed poor uptake of ZnPCs_4 PS drug alone, however when conjugated to the AuNP and Anti-MIA Ab, improved and concentrated PS drug uptake was observed in cellular cytoplasm and nuclei. These findings suggest that the targeting affinity of the PS drug conjugate in relation to Anti-MIA Ab biomarker specify for MM A375 cells was functional, and so improved the subcellular localization and concentration uptake within these cells.

3.3. Cytotoxicity Biochemical Assays

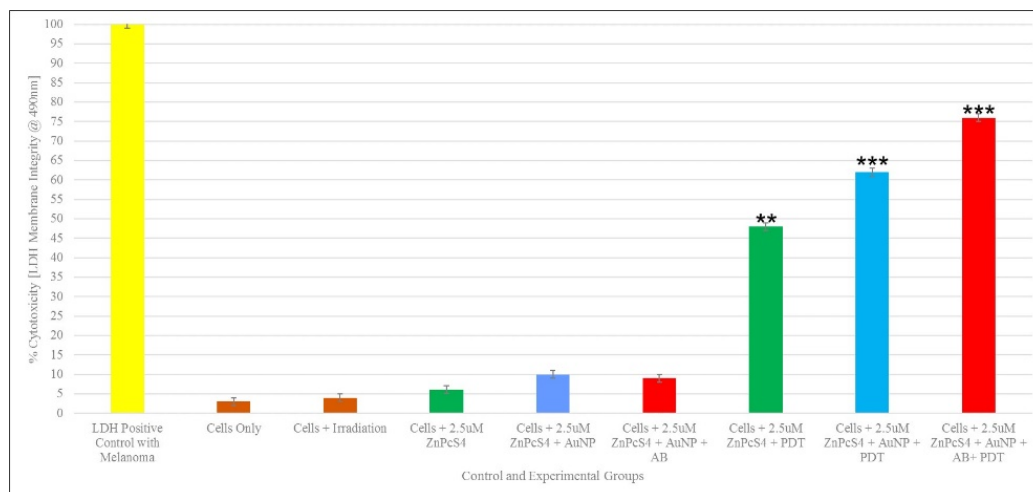


Figure 3: Cellular Cytotoxicity of Final Molecular Conjugate before and after PDT

With reference to Figure 3, the LDH positive control represents 100 % cellular cytotoxicity in MM cells, due to cell lysis and so was used as a standard reference to calculate percentage cytotoxicity in all control and experimental groups. The control group of cells only, was used as a standard reference for viable MM cells, which obviously reflect no cellular cytotoxicity, for statistical comparison in all other control and experimental groups. In control groups, which received laser irradiation only, no significant increase in cellular cytotoxicity was noted. This indicates that laser irradiation at 673 nm with a fluency of 10 J/cm² has no phototoxic side effect on cultured MM cells. Within control groups which received 2.5 μM of ZnPcS₄ PS drug only, no significant cytotoxicity was noted. These results suggest that the administration of PS drug to MM cells in the absence of light has no dark toxic side effects. Additionally, there was no significant cellular cytotoxicity observed in MM control groups, which received control 2.5 μM ZnPcS₄ – AuNP-PEG5000-SH-NH₂ or experimental 2.5 μM ZnPcS₄ – AuNP-PEG5000-SH-NH₂ – Anti-MIA Ab final molecular PS drug conjugate administration alone. These findings indicate that even when the ZnPcS₄ PS drug was bound to either AuNP-PEG5000-SH-NH₂, as well as Anti-MIA Ab, it remained stable pre-PDT and had no cytotoxic effects on cells. The results from these control groups were used as a reference so that the findings from the final molecular conjugate PDT experimental groups could be compared to these control references, making it possible to identify significant increases in cellular cytotoxicity ($P < 0.05^*$) ($P < 0.01^{**}$) ($P < 0.001^{***}$).

All PDT treated experimental groups showed a highly significant cellular cytotoxicity values when compared to the control of MM cells only, however these significant increases percentage values varied over the different groups. Within PDT experimental groups which received 2.5 μM ZnPcS₄ PS drug only and 10 J/cm² laser irradiation, a significant increase of 45 % (***) cellular cytotoxicity was noted. Whereas, within PDT experimental groups which received 2.5 μM ZnPcS₄ – AuNP-PEG5000-SH-NH₂ and 10 J/cm² laser irradiation an even higher significant increase of 59 % (***) was found. These findings suggest that the binding of ZnPcS₄ PS drug to AuNP-PEG5000-SH-NH₂ promoted its passive uptake in cultured MM cells and so when subjected to laser irradiation their PDT induced cytotoxicity significantly increased. However, the most significant increase of 76 % (***) in cellular cytotoxicity was found in PDT experimental groups, which received 2.5 μM ZnPcS₄ – AuNP-PEG5000-SH-NH₂ – Anti-MIA Ab. Overall, the final molecular ZnPcS₄ PS drug conjugate induced far more significant cytotoxicity (76%) in MM cells after PDT treatment, when compared to PS drug alone PDT treatment

(48%) at the same PS concentration. These findings suggest that the conjugation of Anti-MIA Ab to ZnPcS₄ – AuNP-PEG5000-SH-NH₂, within the final molecular conjugate actively, as well as specifically enhanced PS drug uptake in MM cancer cells and so improved PDT cytotoxic treatment outcomes enormously.

4. Conclusion

ZnPcS₄ PS was successfully conjugated to PEG500-SH-NH₂, to maximize its solubility and stability, as well as bound to active tumour-associated antibody-antigens (anti-MIA Ab) to aid in specific targeted PS delivery. Within in vitro cultured MM (A375) cells, this final molecular drug conjugate proved to have far more enhanced and concentrated cellular uptake of ZnPcS₄ PS, than when just administered without drug delivery modification. Moreover, the final molecular ZnPcS₄ PS drug conjugate induced far more significant cytotoxicity (76%) in MM cells after PDT treatment when compared to PS drug alone PDT treatment (48%) and the same PS concentration was applied.

This suggests that the multicomponent AuNP PS drug-based system did have specific MIA antigenic targeting abilities for the active and far more concentrated photosynthetic drug delivery of ZnPcS₄ in MM cancer cells. Thus, the final molecular conjugate did in fact enhance PDT treatment in MM cells, though increased theranostics, as well as far more specific and targeted PS drug delivery, improving cellular uptake and overall cytotoxicity cell death induction. In relation to this studies increased specificity of PDT treatment, future investigative approaches will include the use of another normal cell line in order to be able to compare efficiency result outcomes.

5. Acknowledgements

This work is based on the research supported by the South African Research Chairs Initiative of the Department of Science and Technology and National Research Foundation of South Africa (Grant No 98337).

References

- [1] Martin TA, Ye L, Sanders AJ, Lane J, Jiang WG 2013 *Madame Curie Bioscience Database*.
- [2] Alderton GK 2015 *Nature Reviews Cancer* **15** 255.
- [3] Mayer JE, Swetter SM, Fu T, Geller AC 2014 *Journal of the American Academy of Dermatology* **71** 599.
- [4] American Cancer Society 2018 *American Cancer Society*.
- [5] Swavey S, Tran M 2013 *InTech*. doi: 10.5772/54940.
- [6] Matthews NH, Li WQ, Qureshi AA, et al. 2017 *Cutaneous Melanoma: Etiology and Therapy* doi: 10.15586/codon.cutaneousmelanoma.2017.ch1.
- [7] Van Straten D, Mashayekhi V, de Bruijn HS, Oliveira S, Robinson DJ 2017 *Current Clinical Status and Future Directions* **9** 19 doi:10.3390/cancers9020019.
- [8] Agostinis P, Berg K, Cengel KA, et al. 2011 *CA: a cancer journal for clinicians* **61** 250 doi:10.3322/caac.20114.
- [9] Allison RR, Moghissi K 2013 *Clinical Endoscopy* **46** 24.
- [10] Cheng-Yi T, Yong-hui L, Guo-Sheng T, Xiao-Ming W, Gui-Hua L, Yong-Hua Y 2015 *RSC Advances* **5** 50572.
- [11] Manoto SL, Sekhejane PR, Houreld NN, Abrahamse H 2012 *Photodiagnosis and photodynamic therapy* **9** 52.
- [12] Nombona N, Maduray K, Antunes E, Karsten A, Nyokong T 2012 *Journal of Photochemistry and Photobiology B: Biology* **107** 35.
- [13] Robertson CA, Abrahamse H 2010 *Lasers in surgery and medicine* **42** 926.
- [14] Pelloso DS, De Jesus PD, Tedesco AC 2017 *Expert Opinion on Drug Delivery* **2**.
- [15] Jabir NR, Tabrez S, Ashraf GM, Shakil S, Damanhoury GA, Kamal MA 2012 *International Journal of Nanomedicine* **7** 4391 doi:10.2147/IJN.S33838.
- [16] Nicolas J, Mura S, Brambilla D, Mackiewicz N, Couvreur P 2013 *Chemical Society Reviews* **42** 1147.
- [17] Babu A, Templeton AK, Munshi A, Ramesh R 2013 *Journal of Nanomaterials* **1** 14.
- [18] Pleshkan VV, Zinov'yeva MV, Sverdlov ED 2011 *Molecular Biology* **45** 375.

Simulation of time-domain terahertz ellipsometry measurements towards data extraction

Shane Smith, Pieter Neethling, Erich Rohwer

Department of Physics, Stellenbosch University, Stellenbosch, South Africa

E-mail: srsmith@sun.ac.za

Abstract. Terahertz time-domain transmission spectroscopy is a powerful tool for performing non-destructive spectroscopy on many materials. One known limitation of this spectroscopy technique is that it is not well suited for use with optically dense materials, such as aqueous solutions. One method to circumvent this limitation is by working in reflection, as opposed to transmission. In order to avoid alignment complications introduced by changing between a reference mirror and sample, as is required for standard specular reflection spectroscopy, ellipsometry can also be implemented which avoids the need for a reference. In our lab we have constructed a terahertz time-domain ellipsometer. In order to test data extraction techniques for the constructed setup, simulated measurements were generated to test the constraints of the setup. These simulated measurements can be used to construct data extraction algorithms for future measurements. It is found that the simulated data matches the experimental data, and thus the simulated data can be used for testing data extraction techniques developed for our setup.

1. Introduction

Terahertz (THz) radiation is a powerful tool for performing non-destructive spectroscopy on many materials. Most commercial and reported systems operate in transmission [1–3], but this does not allow for the examination of optically dense materials, such as aqueous solutions [4]. One method for circumventing such limitations is to work in reflection. This can be problematic, since it introduces alignment errors, due to changes between the sample and a reference mirror being required [5]. The alignment tolerance between the sample and mirror is experimentally challenging ($< 1 \mu\text{m}$ positional accuracy) [5]. In our lab we have implemented ellipsometry to avoid the need for a reference, since this technique compares the s- and p-polarized light reflected from a sample in order to obtain information about the sample [6]. A custom designed time-domain THz ellipsometer has been constructed in our laboratory and is operational. In order to test the validity of the measurements as well as the extracted material parameters, experimental measurements are simulated. Material parameters can then be extracted from the simulated data, thereby testing the extraction model for accuracy.

Several steps are required to generate the expected THz time-domain electric field. This process is depicted by the flow diagram in figure 1. First an initial THz time-domain electric field, E_0 , is generated. This field is then transformed to the frequency domain via a Fast Fourier Transform (FFT). The dielectric medium is represented by frequency domain transfer functions for both the p- and s-polarizations. These transfer functions contain the material properties of interest namely the frequency dependent refractive index and extinction coefficient.

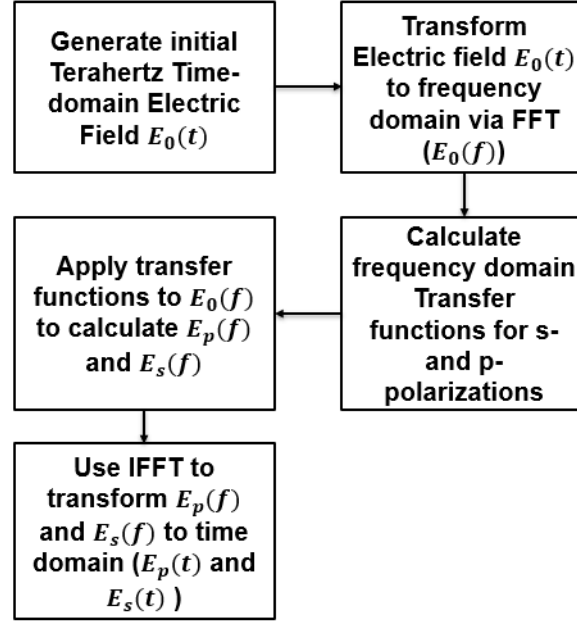


Figure 1. Flow diagram of the simulation process illustrating that all calculations occur in the frequency domain and measurements in the time domain.

Multiplication of the incident electric field with the transfer functions yields the expected detected signals (p and s) in the frequency domain. These two signals are then Fourier transformed to the time-domain, in order to represent the measured signals.

2. Incident THz time-domain electric field

In our setup we make use of photo-conductive antennae to generate THz radiation. Photo-conductive antennae are dipole antennae that are printed on photo-conductive substrates with short excitation lifetimes. Femtosecond laser pulses are used to optically trigger these antennae. When triggered, these antennae allow for a single electric current oscillation, which leads to the generation of THz electric fields. The electric field generated by the photo-conductive antenna can be described by the following equation [7]:

$$E(r, t) = \frac{l_e}{4\pi\epsilon_0 c^2 r} \frac{\partial J(t)}{\partial t} \sin \theta \quad (1)$$

$$J(t) = \frac{e\tau_s}{m} E_{DC} I_{opt}^0 \int_0^\infty e^{-(t-t')^2/\tau_p^2 - t'/\tau_c} [1 - e^{-t'/\tau_s}] dt' \quad (2)$$

where $J(t)$ is the current in the dipole, l_e the effective length of the dipole, r is the distance between the emitting and receiving antennae and θ the polar observation angle for the dipole. For the purposes of this simulation, θ is taken to be 90° , since the optical path is perpendicular to the emitter. The carrier lifetime of the substrate is represented by τ_c , τ_s is the momentum relaxation time of the substrate, m is the effective mass of the charge carriers, e is the charge of an electron and E_{DC} is the applied bias field. A Gaussian pump pulse with a temporal width, FWHM, τ_p and intensity of I_{opt}^0 is used [7].

Our pump pulse has a width (FWHM) of 90 fs, the substrate on which the antennae are printed has an excitation lifetime of 300 fs (in our setup we use low temperature grown GaAs as

the substrate), the momentum relaxation time is 25 fs, l_e is 20 μm and r is 45 mm (the distance between the emitter and the first collimation optic in our setup). The electric field represented by figure 2 is generated via equation 1.

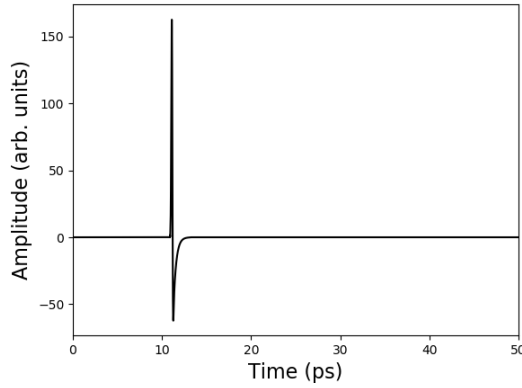


Figure 2. Time-domain electric field generated via equation 1 for a 20 μm antenna on low temperature grown GaAs.

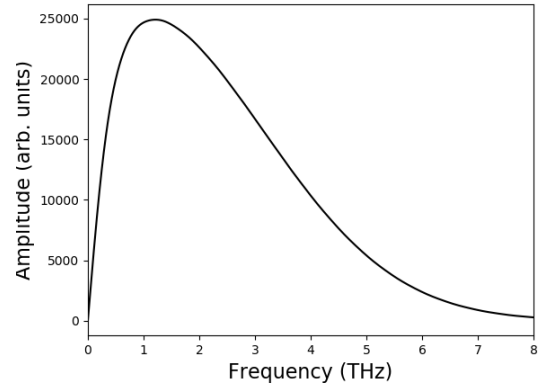


Figure 3. Frequency-domain electric field generated by performing an FFT on the electric field displayed in figure 2.

These values were chosen, since they correspond to the system in our laboratory [7].

It is easier to calculate the transfer functions for a sample in the frequency domain. In order to transform the THz electric field to the frequency domain a FFT is used. The FFT amplitude data for figure 2 is represented by figure 3.

3. Material transfer functions

In our simulation we will consider a single layer dielectric medium. According to the Fresnel equations, at the interface between two media with different refractive indexes, part of an incident electric field will be reflected and part will be transmitted.

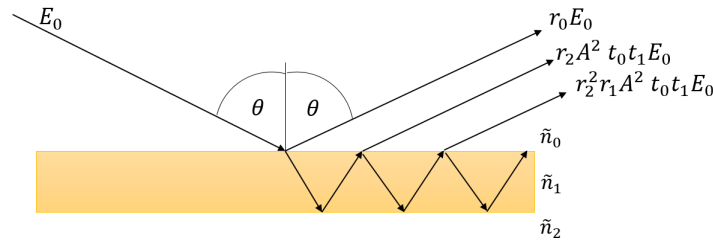


Figure 4. A diagram depicting the light-matter interaction for a single-layered dielectric sample.

Using Snell's laws the angle of transmission can be calculated and it is known that the angle of reflection is the same as the angle of incidence. According to the Lorentz model, as light travels through a medium, it undergoes both absorption and retardation [8]. In the case of a single layer dielectric medium, both external and internal reflections occur in the medium. A

depiction of this process can be seen in figure 4. Considering a material with refractive index $n(f)$, extinction coefficient $k(f)$ and thickness d_0 , we can calculate the expected reflected s- and p-polarized electric fields as follows:

$$E_s(t) = r_{s0}E_{s0}(t) + t_{s0}r_{s2}t_{s1}X^2E_{s0}(t - 2\tau) + t_{s0}r_{s2}^2r_{s1}t_{s1}X^4E_{s0}(t - 4\tau) + \dots \quad (3)$$

$$= r_{s0}E_{s0}(t) + t_{s0}r_{s2}t_{s1} \sum_{j=0}^{\infty} (r_{s1}r_{s2}X^2)^j E_{s0}(t - (j+1)2\tau) \quad (4)$$

$$E_p(t) = r_{p0}E_{p0}(t) + t_{p0}r_{p2}t_{p1}X^2E_{p0}(t - 2\tau) + t_{p0}r_{p2}^2r_{p1}t_{p1}X^4E_{p0}(t - 4\tau) + \dots \quad (5)$$

$$= r_{p0}E_{p0}(t) + t_{p0}r_{p2}t_{p1} \sum_{j=0}^{\infty} (r_{p1}r_{p2}X^2)^j E_{p0}(t - (j+1)2\tau) \quad (6)$$

$$\tau = \frac{dn}{c} \quad (7)$$

$$X = e^{\frac{-2\pi fkd}{c}} \quad (8)$$

$$d = \frac{d_0}{\cos \theta_1} \quad (9)$$

$$\theta_1 = \sin^{-1} \left(\frac{\tilde{n}_0}{\tilde{n}_1} \sin \theta_0 \right) \quad (10)$$

where t_{s0} , t_{p0} , r_{s0} , r_{p0} are the transmission and reflection coefficients for the interface between the initial medium and the sample. The transmission and reflection coefficients for the interface between the sample and the initial medium are represented by t_{s1} , t_{p1} , r_{s1} , r_{p1} and t_{s2} , t_{p2} , r_{s2} , r_{p2} represent the transmission and reflection coefficients for the interface between the sample and the medium following the sample. These coefficients are calculated using the Fresnel equations. The attenuation and retardation coefficients, X and τ , are as described by the Lorentz model [8]. The distance that the electric field travels through the medium is represented by d . The complex refractive indexes of the initial medium, the sample and the medium following the sample are represented by \tilde{n}_0 , \tilde{n}_1 and \tilde{n}_2 .

Due to the complex refractive index being frequency dependent, it is preferable to work in the frequency domain. Working in the frequency domain also allows for the transfer function associated with the medium to be separated from the electric field. To achieve this, a Fourier transform is performed on the electric fields

$$E_s(f) = (r_{s0}(f) + t_{s0}r_{s2}t_{s1}A \sum_{j=0}^{\infty} (r_{s1}r_{s2}A^2)^j) E_{s0}(f) \quad (11)$$

$$E_p(f) = (r_{p0}(f) + t_{p0}r_{p2}t_{p1}A \sum_{j=0}^{\infty} (r_{p1}r_{p2}A^2)^j) E_{p0}(f) \quad (12)$$

$$A = e^{\frac{-2\pi fkd}{c}} e^{\frac{-2i\pi fnd}{c}} = e^{\frac{-2i\pi f\tilde{n}d}{c}} \quad (13)$$

4. Simulated THz electric field

Using equation 11 and 12 it is now possible to simulate a THz electric field for a dielectric sample. As an example, if we take a sample that has a flat real refractive index of 3.4177, a flat absorption coefficient of 0.03 cm^{-1} and a thickness of $500 \mu\text{m}$, that is surrounded by air, the following electric fields in the frequency domain are generated

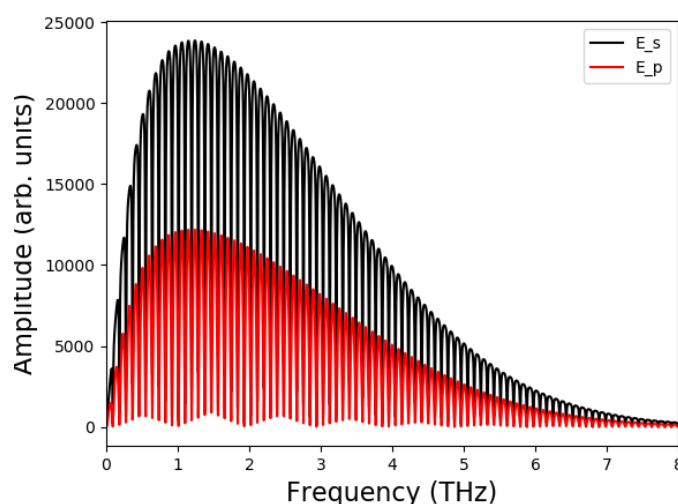


Figure 5. Frequency-domain electric fields generated by equations and for a sample with real refractive index 3.4177, absorption coefficient 0.03 cm^{-1} and thickness $500 \mu\text{m}$.

These values are based on the characteristics of high resistivity silicon [9, 10].

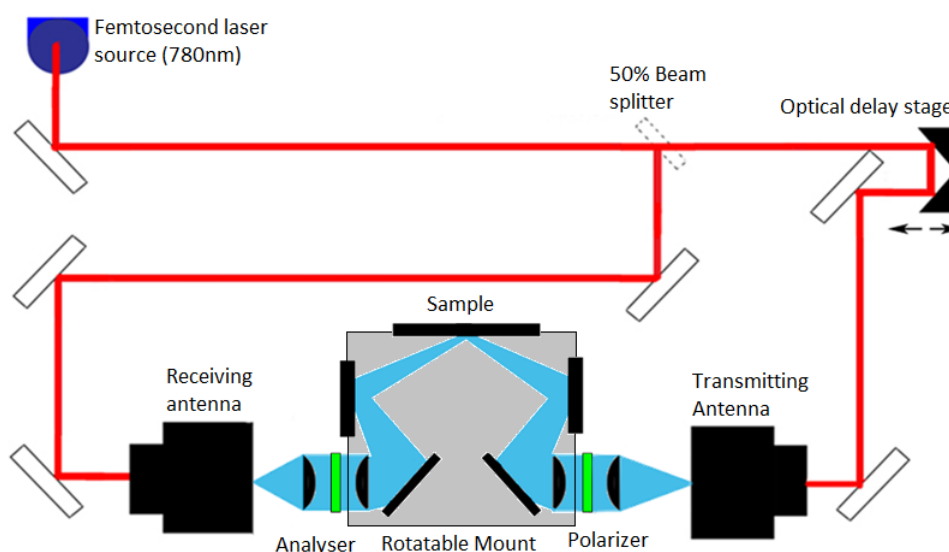


Figure 6. A diagrammatic representation of the experimental setup used by our lab.

By using an IFFT the electric fields can be transformed back to the time-domain. Experimental data for this sample was measured using a setup with a layout as depicted in figure 6. Since the experimental setup performs its measurements in the time-domain, it is convenient to compare the simulated data and experimental data in the time-domain.

By comparing figure 7 and 8, it is found that the simulated data correlates with the experimental data. The time delay between successive pulses correspond and, the phase shifts in pulses are as expected in both the simulated and experimental data (seen in pulses

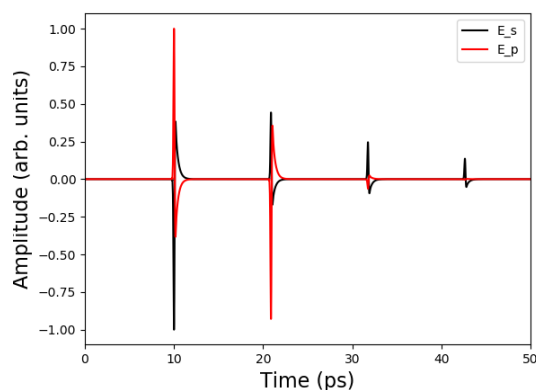


Figure 7. Normalized time-domain electric fields generated by taking an IFFT of electric fields presented in figure 5.

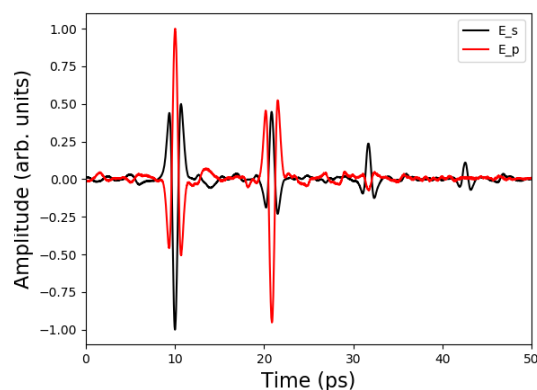


Figure 8. Normalized time-domain electric fields measured in our lab for a high resistivity silicon sample.

flipping when a π phase-shift occurs). Finally, the decrease in amplitude between successive pulses is also well matched.

5. Conclusion

The applicability of time-domain THz ellipsometry relies heavily on the quality of the material parameters that can be extracted from experimental data. In order to verify extracted material parameters, we have successfully simulated real time-domain THz ellipsometry measurements on high resistivity single crystalline Silicon, and compared these simulations to experimental measurements. The simulations and measurements agreed in shape and structure, which lends credibility to the simulated data. This simulated data will in future be used to test our material parameter extraction algorithms, in order to verify their accuracy. This verification is crucial in validating material parameters extracted from our experimental measurements of unknown or complex samples

References

- [1] Pedersen J and Keiding S 1992 *IEEE Journal of Quantum Electronics* **28** 2518–2522
- [2] He M, Azad A K, Ye S and Zhang W 2006 *Optics Communications* **259** 389 – 392
- [3] Lenz M, Matheisen C, Nagel M and Knoch J 2017 *Applied Physics Letters* **110** 072103
- [4] Wu Y 2018 *Proc.SPIE* **10616** 10616 – 10616 – 9
- [5] Nagashima T and Hangyo M 2001 *Applied Physics Letters* **74** 3917–3919
- [6] Tompkins H and Irene E 2005 *Handbook of Ellipsometry* (William Andrew Publishing)
- [7] Sakai K 2005 *Terahertz Optoelectronics* 1st ed (Springer-Verlag New York, LLC, 233 Spring Street, New York, NY 10013, USA: Springer-Verlag)
- [8] Born M and Wolf E 1975 *Principles of Optics* 5th ed (Pergamon Press)
- [9] Li J and Li J 2008 *Microwave and Optical Technology Letters* **50** 1143–1146
- [10] Jepsen P 2007 *Optics Express* **15** 14717 – 14737

DIVISION D1

Division for Astrophysics

Dark matter gets DAMPE

Geoff Beck and Sergio Colafrancesco

School of Physics, University of the Witwatersrand, Private Bag 3, WITS-2050, Johannesburg, South Africa

E-mail: geoffrey.beck@wits.ac.za; sergio.colafrancesco@wits.ac.za

Abstract. The DArk Matter Particle Explorer (DAMPE) recently reported an excess of electrons/positrons above expected background fluxes even when a double power-law background spectrum is assumed. Several dark matter models that involve TeV-scale leptophilic WIMPs have been suggested in the literature to account for this excess. All of these models are associated with the presence of a nearby dark matter clump/over-density.

In this work we set out to explore how current constraints from observational data impact the suggested parameter space for a dark matter explanation of the DAMPE excess, as well as make projections of the capacity of LOFAR and the up-coming SKA to observe indirect radio emissions from the nearby dark matter over-density.

We show that LOFAR is incapable of probing the parameter space for DAMPE excess models, unless the dark matter clump is in the form of an ultra-compact mini halo. Fermi-LAT limits on dark matter annihilation are unable to probe these models in all cases. Limits derived from diffuse Coma cluster radio emission can probe a substantial portion of the parameter space and muon neutrino limits inferred from galactic centre gamma-ray fluxes heavily restrict muon coupling for the proposed WIMPs. The SKA is shown to be able to fully probe the parameter space of all the studied models using indirect emissions from the local dark matter over-density.

1. Introduction

The DArk Matter Particle Explorer (DAMPE) has reported the direct detection of a break in cosmic ray electron spectrum at an energy ~ 1 TeV [1]. This corresponds to an excess in the electron/positron flux around 1.4 TeV. Many recent works have proposed Dark Matter (DM) models to account for this excess via the annihilation of WIMPs and subsequent decay of a leptophilic mediator [2, 3, 4]. A common element of all these models is that they contain leptophilic WIMPs of TeV mass and require the presence of an over-dense clump of DM within a radius < 1 kpc of the solar system in order for the DM models to also satisfy DM cosmological abundance constraints on the annihilation cross-section.

In this work we will explore the effects of current data on the parameter space for all the cases presented in [2, 3, 4]. We agree with the arguments in [2, 3, 4] that current gamma-ray limits from Fermi-LAT [5] don't have any substantial impact on constraining the proposed DAMPE excess DM models. However, we show that radio limits from the Coma cluster derived in [6], and limits from muon neutrino fluxes inferred from gamma-ray fluxes from the galactic centre [7] can make some impact on the allowed parameter space. We then explore the discovery potential for the necessary DM clumps with Low Frequency ARray (LOFAR) and the Square Kilometre Array (SKA) in radio. In so doing we show that only the SKA has the potential to completely rule out DAMPE models by hunting for radio emissions from the necessary local DM clump.

This paper is structured as follows: in section 2 we discuss the candidate models in more detail, in sections 3 and 4 we detail the DM annihilation formalism and the subsequent radio emissions. In sections 5 and 6 we provide information on the current constraints on DM we employ and the telescope sensitivities respectively. Finally, in sections 7 and 8 we display and discuss our results.

2. Dark Matter Models for the DAMPE Excess

The DM models considered are heavy leptophilic WIMPs ψ that couple to the Standard Model particles via a heavy mediator that is too large to allow for the decay of the WIMP [2, 3]. Hence only annihilation will be considered here. We will consider the following ranges from the models listed above: ψ couples to muons and electrons and spans a mass range around 1.4 to 1.7 TeV with cross-sections ranging from 3×10^{-26} to $5 \times 10^{-24} \text{ cm}^3 \text{ s}^{-1}$ in accordance with [2]. The emissions stem from a DM clump of mass $10^6 M_\odot$ within a distance of 0.1 kpc [2] or a Ultra-Compact Mini-Halo (UCMH) of mass $\sim 3 M_\odot$ within a distance of 0.3 kpc [4]. For details of the UCMH formalism we refer the reader to [8, 9].

The second set of models considered has $\langle \sigma V \rangle = 3 \times 10^{-26} \text{ cm}^3 \text{ s}^{-1}$ with the electron only coupling (e^+e^-) and three lepton democratic coupling ($3l$) cases. For the $3l$ case we will work in the scenario of a DM clump situated at 0.3 kpc with a mass of $2 \times 10^8 M_\odot$. For the case of coupling to electrons only we use a halo with mass $8.0 \times 10^7 M_\odot$ within a distance 0.3 kpc.

The distance and mass choices are representative of the models as a whole, as the distance and mass must co-vary to maintain the same flux in accounting for the excess observed by DAMPE. Non-UCMH clumps are considered to have NFW [10] density profiles with concentration parameters calculated according to [11].

3. Dark Matter Annihilation

The source function annihilation of WIMPs ψ into final-state electrons with energy E at halo position r is given by

$$Q_i(r, E) = \frac{1}{2} \langle \sigma V \rangle \sum_f \frac{dN_e^f}{dE} B_f \left(\frac{\rho_\psi(r)}{m_\psi} \right)^2, \quad (1)$$

where $\langle \sigma V \rangle$ is the non-relativistic velocity-averaged annihilation cross-section at 0 K, B_f is the branching fraction for intermediate state f , $\frac{dN_e^f}{dE}$ is the differential electron yield of the f channel, and $\left(\frac{\rho_\psi(r)}{m_\psi} \right)^2$ is the WIMP pair number density.

The functions $\frac{dN_e^f}{dE}$ will be sourced from [12, 13]. We will follow the standard practice of studying each annihilation channel f independently, assuming $B_f = 1$ for each separate case (an exception is the $3l$ case where we weight each lepton channel equally). The studied channels will all be leptonic: τ leptons, muons, and electrons/positrons in accordance with [2, 3, 4].

4. Dark Matter Emissions

The emission of interest in this work is synchrotron radiation produced by electrons sourced from DM annihilation and the subsequent decay of heavier products (if electrons are not directly produced). The average power of the synchrotron radiation at observed frequency ν emitted by an electron with energy E in a magnetic field with amplitude B is given by [14]

$$P_{synch}(\nu, E, r, z) = \int_0^\pi d\theta \frac{\sin^2 \theta}{2} 2\pi \sqrt{3} r_e m_e c \nu_g F_{synch} \left(\frac{\kappa}{\sin \theta} \right), \quad (2)$$

where m_e is the electron mass, $\nu_g = \frac{eB}{2\pi m_e c}$ is the non-relativistic gyro-frequency, $r_e = \frac{e^2}{m_e c^2}$ is the classical electron radius, and the quantities κ and F_{synch} are defined as

$$\kappa = \frac{2\nu(1+z)}{3\nu_g\gamma^2} \left[1 + \left(\frac{\gamma\nu_p}{\nu(1+z)} \right)^2 \right]^{\frac{3}{2}}, \quad (3)$$

where $\nu_p \propto \sqrt{n_e}$ with n_e being the density of the local thermal electron population, and

$$F_{synch}(x) = x \int_x^\infty dy K_{5/3}(y) \simeq 1.25x^{\frac{1}{3}} e^{-x} (648 + x^2)^{\frac{1}{12}}. \quad (4)$$

The magnetic field producing the synchrotron radiation will be taken to be that of the Milky-Way which hosts the DM clump producing the DAMPE excess. The field strength is thus taken to be the value in the solar neighbourhood $B = 1.5 \mu\text{G}$ [15] and the thermal plasma density is given by $n_e = 0.03 \text{ cm}^{-3}$ [16], these will be assumed constant over the volume of the DM clump or UCMH due to its small size. The Milky-Way magnetic field will be assumed to exhibit Kolmogorov-type turbulence with 1 kpc coherence length.

The local emissivity for synchrotron emission can then be found as a function of the DM-produced electron and positron equilibrium distributions as well as the synchrotron power

$$j_{synch}(\nu, r, z) = \int_{m_e}^{M_\psi} dE \left(\frac{dn_{e^-}}{dE} + \frac{dn_{e^+}}{dE} \right) P_{synch}(\nu, E, r, z), \quad (5)$$

where $\frac{dn_{e^-}}{dE}$ is the equilibrium electron distribution from DM annihilation (see below). The flux density spectrum within a radius r is then written as

$$S_i(\nu, z) = \int_0^r d^3r' \frac{j_{synch}(\nu, r', z)}{4\pi D_L^2}, \quad (6)$$

where D_L is the luminosity distance to the halo.

In electron-dependent emissions there are two processes of importance, namely energy-loss and diffusion. Diffusion is typically only significant within small structures [17, 18], thus must be accounted for within the environment of the DM clumps of interest for the DAMPE excess. The equilibrium electron distribution is found as a stationary solution to the equation

$$\frac{\partial}{\partial t} \frac{dn_e}{dE} = \nabla \cdot \left(D(E, \mathbf{r}) \nabla \frac{dn_e}{dE} \right) + \frac{\partial}{\partial E} \left(b(E, \mathbf{r}) \frac{dn_e}{dE} \right) + Q_e(E, \mathbf{r}), \quad (7)$$

where $D(E, \mathbf{r})$ is the diffusion coefficient, $b(E, \mathbf{r})$ is the energy loss function, and $Q_e(E, \mathbf{r})$ is the electron source function from DM annihilation. In this case, we will work under the simplifying assumption that D and b lack a spatial dependence and thus we will include only average values for magnetic field and thermal electron densities. For details of the solution see [17].

We thus define the functions as follows [19]

$$D(E) = \frac{1}{3} c r_L(E) \frac{\overline{B}^2}{\int_{k_L}^\infty dk P(k)}, \quad (8)$$

where \overline{B} is the average magnetic field, r_L is the Larmour radius of a relativistic particle with energy E and charge e and $k_L = \frac{1}{r_L}$. This combined with the requirement that

$$\int_{k_0}^\infty dk P(k) = \overline{B}^2, \quad (9)$$

where $k_0 = \frac{1}{d_0}$, with d_0 being the smallest scale on which the magnetic field is homogeneous, yields the final form

$$D(E) = D_0 d_0^{\frac{2}{3}} \left(\frac{\overline{B}}{1\mu\text{G}} \right)^{-\frac{1}{3}} \left(\frac{E}{1\text{GeV}} \right)^{\frac{1}{3}}, \quad (10)$$

where $D_0 = 3.1 \times 10^{28} \text{ cm}^2 \text{ s}^{-1}$. We assume that $d_0 = 1 \text{ kpc}$ in order to make a conservative estimate of synchrotron emissions as the d_0 in the Milky-Way may be expected to be between 1 pc and 1 kpc [20, 21].

The energy loss function is defined by

$$\begin{aligned} b(E) = & b_{IC} E^2 (1+z)^4 + b_{synch} E^2 \overline{B}^2 \\ & + b_{col} \overline{n} (1+z)^3 \left(1 + \frac{1}{75} \log \left(\frac{\gamma}{\overline{n} (1+z)^3} \right) \right) \\ & + b_{brem} \overline{n} (1+z)^3 \left(\log \left(\frac{\gamma}{\overline{n} (1+z)^3} \right) + 0.36 \right), \end{aligned} \quad (11)$$

where \overline{n} is the average thermal electron density in the UCMH and is given in cm^{-3} , while b_{IC} , b_{synch} , b_{col} , and b_{brem} are the inverse Compton, synchrotron, Coulomb and bremsstrahlung energy loss factors, taken to be 0.25, 0.0254, 6.13, and 1.51 respectively in units of $10^{-16} \text{ GeV s}^{-1}$. Here E is the energy in GeV and the B-field is in μG .

5. Existing DM Limits

We make use of the Fermi-LAT dwarf spheroidal galaxy limits on the annihilation cross-section [5], as well as those derived from the diffuse radio emissions of the Coma cluster of galaxies [6].

We also make use of the observed spectrum of the galactic centre in gamma-rays [22] and infer from it a muon neutrino flux following [7]. This flux is then used to derive upper limits on the DM annihilation cross-section through comparison to predicted fluxes from the galactic centre using the same galactic halo parameters as used in [22].

6. Telescope Sensitivities

We compare sensitivity projections for the SKA [23] and LOFAR¹ to determine the smallest value of $\langle \sigma V \rangle$ that would be detectable at a confidence level of 5σ .

In the case of the clumps with NFW profiles we must account for flux loss by these interferometers due to the minimum baseline effect (UCMHs are too compact to suffer from this). To this effect we use the fact that the Westerbork Synthesis Radio Telescope (WSRT) was found to capture only 0.16 of the radio flux emitted by the nearby M33 object [24]. Thus, we will make use of an ansatz that the flux captured by radio interferometry can be estimated as

$$f_{cap} = 0.16 \frac{\theta_{M33}}{\theta_{halo}} \frac{l_{WSRT}}{l_{obs}}, \quad (12)$$

where θ_{M33} and θ_{halo} are the angular sizes of M33 and the angular radius containing 99% of the flux from the DM clump (with a steeply peaked spatial profile reflecting that of an NFW density distribution squared), l_{WSRT} and l_{obs} are the minimum baseline lengths of WSRT and either the SKA or LOFAR. Using this calculation we find that $f_{cap} \sim 10^{-3}$ for clumps with NFW profiles at the distances given in Section 2.

¹ <http://www.astron.nl/radio-observatory/astronomers/lofar-imaging-capabilities-sensitivity/sensitivity-lofar-array/sensiti>

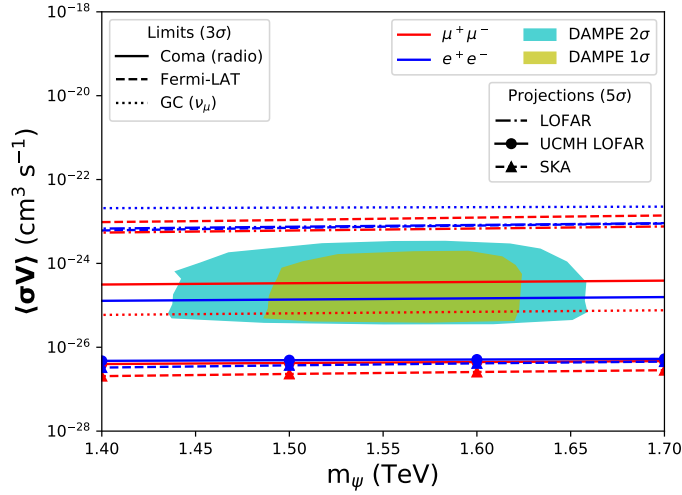


Figure 1. Cross-section upper limits on DAMPE excess models from [2, 4]. GC (ν_μ) refers to inferred galactic centre neutrino flux limits.

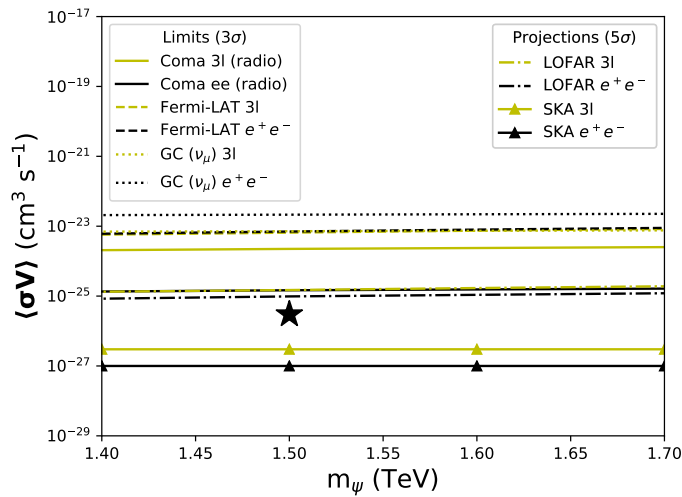


Figure 2. Cross-section upper limits on DAMPE excess models from [3], the model parameter space is given by the star. GC (ν_μ) refers to inferred galactic centre neutrino flux limits. Note the Fermi-LAT lines lie nearly atop each other.

7. Results

In fig. 7 we display the results for the models from [2, 4], particularly upper-limits on $\langle\sigma V\rangle$ either compatible with known constraints on WIMPs or projections derived from potential non-observation of radio emissions from the local DM clump with a given instrument. We can see that the existing Fermi-LAT limits do not restrict the parameter space at all, as claimed by the authors of [2]. However, some constraint is possible with the Coma limits from [6] and with the inferred neutrino flux from the galactic centre [22, 7] for the case of the muon coupling only. LOFAR is unable to detect the extended clumps but is suggested to be able to probe the complete parameter space for the UCMH objects. The strongest possibility comes from the SKA, where it can find the radio emissions from annihilation the DM clumps for the entire parameter space.

In fig. 7 we see the results for [3]. In both the electrons only and the 3l model only the SKA can reach below the thermal relic cross-section specified by the DM model and still detect the emissions of the DM clump. However, LOFAR gets close to the thermal relic cross-section for both cases and the Coma limits are similar for the e^+e^- only case.

8. Conclusions

In conclusion we can see that new limits on the DM models conjectured to explain the DAMPE excess are possible with existing results from the Coma cluster and from inferred muon neutrino fluxes from the galactic centre. In particular, the inferred neutrino constraints provide little room for any muon coupling in the model of [2]. However, Fermi-LAT is unable to observe gamma-ray emissions from the DM clumps that form part of these models. LOFAR can only detect the UCMH type clump from [4] due to flux loss over large extended sources. The SKA will be capable of probing the full parameter space for all the studied DAMPE excess models and would be able to rule them out in its phase 1 configuration by hunting for the radio emissions from the nearby DM clump that is necessary for all the studied models.

Acknowledgments

This work is based on the research supported by the South African Research Chairs Initiative of the Department of Science and Technology and National Research Foundation of South Africa (Grant No 77948).

References

- [1] Ambrosi G *et al.* 2017 *Nature* **552** 63
- [2] Fan Y, Huang W, Spinrath M, Tsai Y S and Yuan Q 2017 *Preprint* arXiv: 1711.10995
- [3] Yuan Q *et al.* 2017 *Preprint* arXiv: 1711.10989
- [4] Yang F, Su M and Zhao Y 2017 *Preprint* arXiv: 1712.01724
- [5] Drlica-Wagner A *et al.* 2015 *Astrophys. J.* **809** L4
- [6] Beck G and Colafrancesco S 2016 *JCAP* **05** 013
- [7] Celli S, Palladino A and Vissani F 2017 *Eur. Phys. J.* **C77** 66
- [8] Ricotti M and Gould A 2009 *Astrophys. J.* **707** 979
- [9] Bringmann T, Scott P and Akrami Y 2012 *Phys. Rev.* **D85** 125027
- [10] Navarro J F, Frenk C S and White S D M 1996 *Astrophys. J.* **462** 563
- [11] Prada F, Klypin A A, Cuesta A J, Betancort-Rijo J E and Primack J 2012 *MNRAS* **423** 3018
- [12] Cirelli M *et al.* 2011 *JCAP* **1103** 051
- [13] Ciafaloni P *et al.* 2011 *JCAP* **1103** 019
- [14] Longair M S 1994 *High Energy Astrophysics* (Cambridge University Press)
- [15] Haverkorn M 2015 *Magnetic Fields in Diffuse Media. Astrophysics and Space Science Library vol 407* ed Lazarian A, de Gouveia Dal Pino E and Melioli C (Springer, Berlin, Heidelberg)
- [16] Cordes J M and Lazio T J W 2002 *Preprint* arXiv: astro-ph/0207156
- [17] Colafrancesco S, Profumo S and Ullio P 2007 *Phys. Rev.* **D75** 023513
- [18] Colafrancesco S, Marchegiani P and Beck G 2015 *JCAP* **02** 032C
- [19] Colafrancesco S and Blasi S 1998 *Astropart. Phys.* **9** 227
- [20] Jansson R and Farrar G R 2012 *The Astrophysical Journal* **757** 14
- [21] Jansson R and Farrar G R 2012 *The Astrophysical Journal* **761** L11
- [22] Ajello M *et al.* 2016 *Astrophys. J.* **819** 44
- [23] Dewdney P, Turner W, Millenaar R, McCool R, Lazio J and Cornwell T 2012 *SKA baseline design document* http://www.skatelescope.org/wp-content/uploads/2012/07/SKA-TEL-SKO-DD-001-1_BaselineDesign1.pdf
- [24] Viallefond F, Goss W M, van der Hulst J M and Crane P C 1986 *A&A Suppl. Ser.* **64** 237

Probing the intergalactic magnetic field through observations of high-energy gamma rays produced by electromagnetic cascades

B Bisschof, B van Soelen and P J Meintjes

Department of Physics, University of the Free State, Bloemfontein, South Africa

E-mail: bisschoffb@ufs.ac.za

Abstract. Currently there is limited knowledge related to the origin of the intergalactic magnetic fields (IGMF) that permeate the space between galaxies, galaxy clusters and cosmic voids. Understanding the origin of the IGMF is a crucial component in models of galaxies and galaxy cluster formation. This magnetic field can be probed indirectly by its effect on electromagnetic cascades initiated by gamma-gamma absorption of very-high-energy (VHE) gamma rays, produced in blazars, due to its interaction with the extragalactic background light (EBL). The electron-positron pairs produced via this process interact with the intergalactic magnetic field (IGMF) and can be deviated from their original path. These pairs can then Compton-scatter off the cosmic microwave background (CMB) to produce high-energy (HE) gamma rays that may be detected by, e.g., *Fermi*-LAT. The strength of this signal strongly depends on the IGMF strength (B) and the coherence length (λ_B). This secondary gamma-ray emission would be superimposed on the blazars' intrinsic gamma-ray spectrum. A selection of bright blazars will be re-analysed using the upgraded Pass 8 analysis pipeline, to search for this secondary component. This will be used to place constraints on the IGMF strength. The initial results from this project, namely the *Fermi*-LAT analysis of a selection of candidate blazars for this study are presented. The results showed that the light curves and the spectral shape of the SEDs showed negligible variability and that the spectral parameters and fluxes values overlapped within one standard deviation within the results from Finke et al. [12]. This indicates that these are appropriate sources to use for further modelling.

1. Introduction

For a variety of astrophysical objects, like galaxies and galaxy clusters, magnetic fields play a very important role. Observations of Faraday rotation and Zeeman splitting of atomic lines in the radio band and the observations of the polarization of starlight in the optical band, established the existence of galactic magnetic fields with strengths of $1 - 10 \mu\text{G}$ [1, 2]. The cores of galaxy clusters also have magnetic fields of similar strengths [3]. Recently magnetic fields of $10^{-8} - 10^{-7}\text{G}$ have also been discovered outside galaxies and galaxy clusters in the intergalactic space [4, 5].

The galactic magnetic fields, in galaxies and galaxy clusters, are assumed to be caused by the amplification of the weak seed fields that are of cosmological origin. The mechanism of the amplification, nature and origin of these weak seed fields are currently still unknown. By making measurements of these initial seed fields, this process can be constrained. This intergalactic magnetic field (IGMF) can be indirectly measured with gamma-ray telescopes based on its

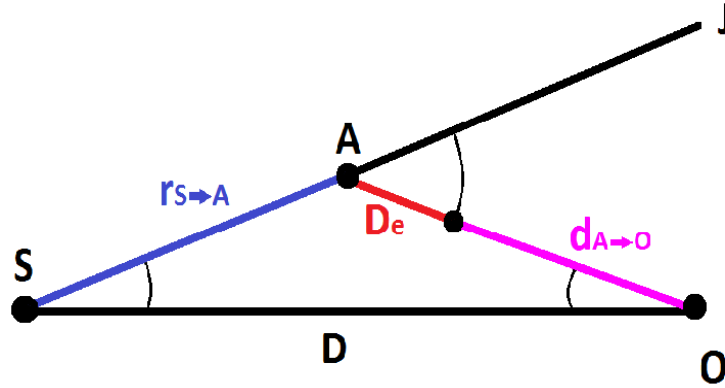


Figure 1. The electromagnetic cascade process occurs close to the blazar jet situated at point S and separated by the distance D from the observer on Earth at the point O . The line $r_{S \rightarrow A}$ represents the distance the VHE photons, originating from the blazar, travel before interacting with the EBL at point A to form electron-positron pairs. D_e is the electron cooling distance which the electron/positron travel, while being deviated from the original path by an angle δ , before interacting with a CMB photon and upscattering these photons to high-energies. The HE photons then travel a distance $d_{A \rightarrow O}$ before finally reaching the observer at point O .

effect on the emission originating from electromagnetic cascades from extragalactic sources such as Blazars [6, 7, 8, 9, 10].

The range of the IGMF parameters, such as the strength (B) and the coherence length (λ_B), can be found, based on the knowledge of the sensitivity of existing and future gamma-ray telescopes, with two available measurement techniques (timing [6, 8] or imaging [7, 9, 10] of the gamma-ray cascade signal). The timing method measures the effect of the IGMF on the arrival times of gamma rays from extragalactic sources. The imaging method measures the effect of the IGMF on the angular profile of the extended emission coming from blazars. In the imaging method the sources need to be non-variable in flux because the modelling requires a stable emission output from the blazar source. The timing analysis becomes uncertain for determining magnetic field strengths larger than 10^{-18} G when the delay times of the secondary spectrum becomes large, up to a 100 years for magnetic field strengths $>10^{-16}$ G [11]. Thus its much more practical to measure the angular extend of a source than to measure the time delays in flaring events.

For this analysis, stable sources are required, so the SEDs are not complicated by flaring or variability events. As the first step in this project we have investigated the stability of three potential sources for this analysis. In section 2 we discuss the pencil beam model (model for non-variable sources) for the electromagnetic cascade process that occurs in the blazar jets and how these cascade signals are influenced by the IGMF. Then in section 3 to we explain how FermiPy was used to reduce and analyze the data from three different blazar sources. In section 4 the spectral index and flux variability of these three sources were determined and then compared to the results of Finke et al. [12]. Finally we discuss our obtained results and the following steps that will be taken to model and put constraints on the IGMF parameters (B) and (λ_B).

2. Theory

Consider a blazar positioned at a point S as shown in figure 1. The AGN emits a narrow beam of very-high-energy (VHE) gamma rays along SJ that is misaligned with the line of sight SO . The VHE photons are absorbed, after traveling a distance $r_{S \rightarrow A}$, at point A through gamma-

Table 1. SED model fitting results obtained from Finke et al. [12] for the three different blazar sources: 1ES 1218+304, 1ES 0414+009 and 1ES 1101-232.

Source Name	Redshift	TS	Flux[$10^{-9}.\text{cm}^{-2}.\text{s}^{-1}$]	Spectral Index	Variability Index
1ES 1218+304	0.182	1690	15.6 ± 1.5	1.68 ± 0.03	92
1ES 0414+009	0.287	127	3.10 ± 0.99	1.74 ± 0.10	56
1ES 1101-232	0.186	75.6	1.57 ± 0.67	1.63 ± 0.14	37

gamma absorption, due to interaction with lower-energy extragalactic background light (EBL) photons, and electron-positron pairs are created [6, 7]. These pairs then traverse a distance D_e , in the direction of O , in the presence of the intergalactic magnetic field (IGMF) before colliding with a lower energy cosmic microwave background (CMB) photon. The two charged particles can deviated from their original path by an angle δ while traversing space in the presence of the IGMF. The deflection angle δ strongly depends on the strength and spacial structure of the magnetic field. If the magnetic field lines are tangled up in a region smaller than the electron cooling distance D_e , then the charged particles will follow a random walk process rather than a circular deviation path in the presence of the IGMF. This spacial structure of the IGMF is described by the coherence length of the IGMF which is defined as the average distance in which the magnetic field changes its orientation by 90 degrees. After this CMB photons are up-scattered to high-energy photons by the electron-positron pairs. This will result in an attenuation and energy shift of the original gamma-ray emission profile.

The power of the Inverse Compton (IC) emission from the electron-positron pairs is given by [13],

$$\frac{dP_{IC}}{dr} = \frac{E_{\gamma 0} N_0}{D_{\gamma 0}} e^{-\frac{r}{D_{\gamma 0}}}, \quad (1)$$

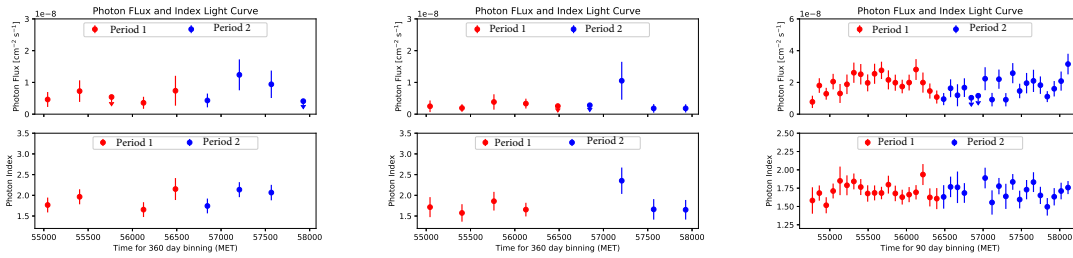
where N_0 , $E_{\gamma 0}$ and $D_{\gamma 0}$ are the number of photons, energy and the mean free path of the primary gamma rays emitted from the blazar jet and r is the distance from point S to point A . The angle of deflection, caused by the interaction of the positron-electron pairs with the IGMF, for the secondary photon cascade for two different regimes is [14],

$$\delta(x) = \begin{cases} \frac{D_e}{R_L} \cong 3 \times 10^{-6} (1 + z_{\gamma\gamma})^{-4} \left(\frac{B'}{10^{-18}\text{G}}\right) \left(\frac{E'_e}{10\text{TeV}}\right)^{-2}, & D_e \ll \lambda'_B \\ \frac{\sqrt{\lambda_B D_e}}{R_L} \cong 5 \times 10^{-7} (1 + z_{\gamma\gamma})^{-2} \left(\frac{B'}{10^{-18}\text{G}}\right) \left(\frac{E'_e}{10\text{TeV}}\right)^{-\frac{3}{2}} \left(\frac{\lambda'_B}{1\text{kpc}}\right)^{\frac{1}{2}}, & D_e \gg \lambda'_B, \end{cases} \quad (2)$$

where D_e is the electron cooling distance, R_L is the Larmor radius, $z_{\gamma\gamma}$ is the redshift at point A , B' and λ'_B are the IGMF strength and coherence length and E'_e is the redshift dependent electron energy.

Table 2. Spectral parameter results obtained with FermiPy for the blazar sources: 1ES 1218+304, 1ES 0414+009 and 1ES 1101-232.

Source Name	Redshift	TS	Flux[$10^{-9} \cdot \text{cm}^{-2} \cdot \text{s}^{-1}$]	Spectral Index
1ES 1218+304	0.182	3464.24	16.72 ± 0.87	1.71 ± 0.02
1ES 0414+009	0.287	257.11	5.04 ± 0.94	1.91 ± 0.07
1ES 1101-232	0.186	202.58	2.33 ± 0.54	1.72 ± 0.08



(a) Light curve for the source 1ES 0414+009 for the Period 1 (2008/08/04 to 2013/07/12) and Period 2 (2014/07/08 to 2018/01/01) time periods. (b) Light curve for the source 1ES 1101-232 for the Period 1 (2008/08/04 to 2013/04/13) and Period 2 (2013/07/12 to 2018/01/01) time periods. (c) Light curve for the source 1ES 1218+304 for the Period 1 (2008/08/04 to 2013/04/13) and Period 2 (2013/07/12 to 2018/01/01) time periods.

Figure 2. Lights curves for the sources a) 1ES 0414+009, b) 1ES 1101-232 and c) 1ES 1218+304. The data for two different time periods (Period 1, Period 2) are represented by red and blue data points in the figures above.

The IGMF strength and coherence length evolve with time as follows:

$$B'(z) \sim B_0(1 + z_{\gamma\gamma}^2)$$

$$\lambda'_B = \lambda_{B0}(1 + z_{\gamma\gamma})^{-1}$$

3. Data Reduction and Analysis

An investigation of this effect, of the IGMF suppressing some of the high-energy inverse compton spectrum coming from blazar sources, was previously undertaken by Finke et al. [12], however, their analysis was undertaken using Pass 7. As a first step in this project we have re-analysed three of the same sources using the newer Pass 8 analysis method (Table 1).

The high-energy photon data and spacecraft files for the sources 1ES 1218+304, 1ES 0414+009 and 1ES 1101-232 were extracted from the *Fermi* website. The high-energy data (0.1 – 300GeV) were extracted from 2008-08-04 00:00:00 to 2018-01-01 00:00:00 within a region of interest (ROI) radius of 30 degrees.

FermiPy (with *Fermi* Science Tools package version: v11r5p3, and Python package version: 2.7.8) was then used to reduce and analyze the gamma-ray photon data. Fermipy was also used to perform the likelihood analysis on the three sources for different spectrum models. The normalization parameters of all the sources within a radius of 10 degrees from the center of the ROI were allowed to be free.

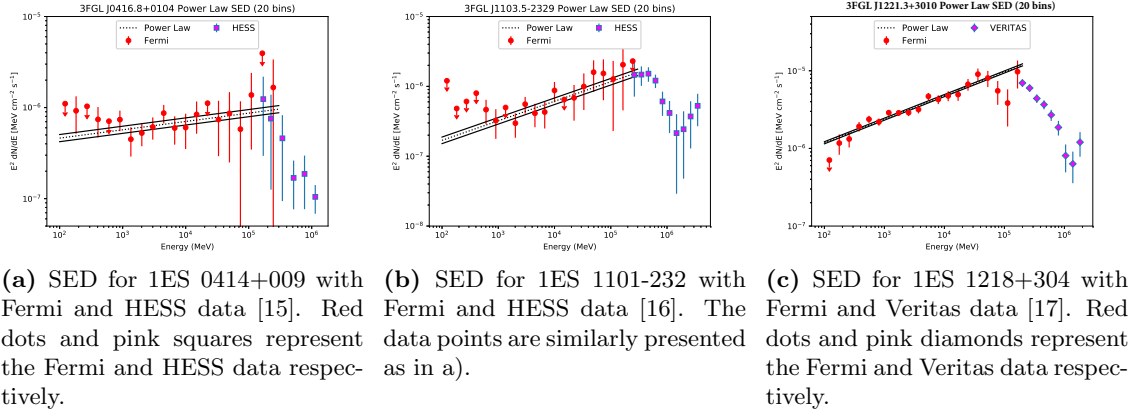


Figure 3. SEDs for the sources a) 1ES 0414+009, b) 1ES 1101-232 and c) 1ES 1218+304. The black dotted line represents the power-law model fit and the black filled lines represent the power-law model fit with one standard deviation from the dotted line fit.

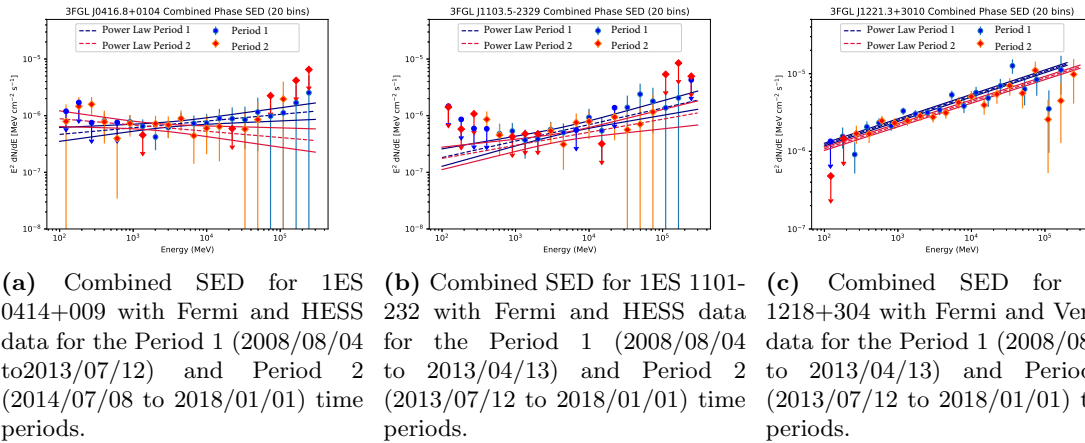


Figure 4. Combined SEDs for different time periods (Period 1 and Period 2) represented in the figures (blue dots and red diamonds) for the sources a) 1ES 0414+009, b) 1ES 1101-232 and c) 1ES 1218+304. Both time period periods (Period 1 and Period 2) are fitted with a power-law model, with one standard deviation, represented by the dotted and filled lines respectively (navy and maroon).

4. Results

The variability of each source has been investigated by producing light curves shown in figure 2. SEDs were also constructed during periods of higher and lower activity to compare whether the SEDs remained sufficiently stable and are shown in figure 3 for each source. A power-law, power-law with a super exponential cut off, log parabola, broken power-law and the smooth broken power-law spectrum models were tested for goodness-of-fit. The power-law spectrum model had the overall best Log Likelihood and test statistics (TS) values and also a better fit to the high-energy data points. For each blazar source a light curve, spectral index plot, SED plot and a combined SED plot for different time periods (Period 1 and Period 2) of the light curves, were produced (figure 4). These two time periods were chosen such that Period 1 and Period 2 had a maximum difference in there average spectral index values. All the SED and light curve plots showed little variability in the spectral index value, and the slopes of the spectrum

Power law models in the SED plots, and flux values. Thus all the investigated sources can be considered sufficiently non-variable for the future modelling. The spectral values obtained from all the sources are also consistent with those obtained by Finke et al. [12].

5. Conclusion

The results from all the sources above, for the test statistic (TS) value integrated flux and the spectral index, are all within one standard deviation in agreement with the results obtained from the Finke et al. [12] paper. The errors we have obtained are smaller because of the much higher TS values. This is because we have used approximately 9.5 years of data with Pass 8 where as Finke et al. [12] used approximately 6 years of data with Pass 7. The spectral shape of the sources during different variable time periods (Period 1 and Period 2) in figure 2, showed little variability and the difference in spectral index between the two time periods lies within one standard deviation of one another and the spectral index for the full SED in figure 3. Thus our three sources are stable enough to model the IGMF affecting the VHE cascade spectra of these sources and place constraints on the IGMF strength and coherence length. Data analysis for an additional sample of sources is currently in progress. After this is completed a model based on the work of Arlen et al. (2014) will be developed with the use of the Monte Carlo code from Kachelrieß et al. (2012) to compare to the Fermi data. We will use this to place constraints on the IGMF.

References

- [1] Kuksrud R M and Zweibel E G 2008 *Rept. Prog. Phys.* **71** 0046091
- [2] Beck R 2009 *AIP Conf. Proc.* **1085** 83
- [3] Carilli C L and Taylor G B 2002 *Ann. Rev. Astron. Astrophys.* **40** 319
- [4] Xu Y, Kronberg P P, Habib S and Dufton Q W 2006 *Astrophys. J.* **637** 19
- [5] Kronberg P P, Kothes R, Salter C J and Perillat P 2007 *Astrophys. J.* **659** 267
- [6] Plaga R 1995 *Nature* **374** 430
- [7] Neronov A and Semikoz D V 2007 *JETP Lett.* **85** 473
- [8] Murase K, Takahashi K, Inoue S, Ichiki K and Nagataki S 2008 *Astrophys. J.* **686** L67
- [9] Elyiv A, Neronov A and Semikoz D V 2009 *Phys. Rev. D* **80** 023010
- [10] Dolag K, Kachelriess M, Ostapchenko S and Tomas R 2009 *Astrophys. J.* **703** 1078
- [11] Dolag K, Kachelriess M, Ostapchenko S and Tomas R 2010 *Astrophys. J.* **727** L4
- [12] Finke J D and Reyes L C 2015 *Astrophys. J.* **814** 20
- [13] Neronov A, Taylor A M, Tchernin C and Vovk I 2013 *Astronomy and Astrophysics* **554** 5
- [14] Neronov A and Semikoz D V 2009 *Phys. Rev. D* **80** 123012
- [15] Abramowski A, Acero F, and Aharonian F 2012 *Astronomy and Astrophysics* **538** A103
- [16] Aharonian F, Akhperjanian A G and Bazer-Bachi A R *Astronomy and Astrophysics* **470** 475
- [17] Acciari V A, Aliu E and Arlen T 2009 *Astrophys. J.* **695** 2
- [18] Arlen T C, Vassilev V V and Weisgarber T 2014 *ApJ* **796** 18
- [19] Kachelrieß M, Ostapchenko S and Toms R 2012 *Computer Physics Communications* **183** 1036

Gamma-Gamma Absorption in γ -ray Binaries

DC du Plooy and B van Soelen

Department of Physics, University of the Free State, 9300 Bloemfontein, South Africa

DuPlooyDC@ufs.ac.za, VanSoelenB@ufs.ac.za

Abstract. Gamma-ray binaries are a class of high-mass binary systems, which are distinguished by having spectral energy distributions which peak above 1 MeV. Gamma-ray binaries consist of a compact object, either a neutron star or black hole, orbiting a massive O or B-type star. While there is some debate around how the gamma rays are produced, in two systems, PSR B1259-63 and PSR J2032+4127, the compact object is known to be a pulsar, and the gamma ray production is due to particle acceleration in the shock that forms between the pulsar and stellar winds. It has been suggested by some studies that there may be different sites of particle acceleration in these systems, with the GeV and TeV emission being produced in different locations. Gamma-gamma absorption of the TeV emission could significantly modify the observed emission. This may provide a mechanism to constrain the location of the production of TeV gamma rays. We plan to model the effect of gamma-gamma absorption in six of the seven known gamma-ray binary systems, in order to investigate how this will modify the observed spectrum. This may be used to place constraints on the production location when combined with the observations of the TeV emission. We will investigate this for the upcoming Cherenkov Telescope Array (CTA). We present the initial results from this project.

1. Introduction

Gamma-ray binaries are high-mass binary systems which consist of a compact object, either a neutron star or a black hole, in orbit around a massive O or B type star. Gamma-ray binaries are differentiated from X-ray binary systems by their spectral energy distributions (SED) which peak above 1 MeV. The recently discovered γ -ray binary LMC P3 is the first γ -ray binary discovered outside of our own galaxy, found in the Large Magellanic Cloud (LMC) [1]. To date there are only seven known γ -ray binary systems, the newest is PSR J2032+4127 [2]. Out of all of these systems, in only two, PSR B1259-63/LS 2883 and the newly discovered PSR J2032+4127, is the nature of the compact objects known to be pulsars [3, 4]. Although all of these systems consist of the same or similar components the nature of their orbital parameters can differ substantially. While the underlying emission mechanism is likely the same, differences in the orbital parameters, pulsar spin down luminosities, and the presence or absence of a discretion disc around the companion star, will modify the observed emission.

In the two aforementioned binary systems the most probable mechanism that produces γ -rays is the interaction between the stellar wind and the pulsar wind. However, the possibility of a microquasar scenario cannot be ruled out for the other systems. In this case γ -rays can be produced via Compton scattering close to the base of the relativistic jets.

There is still an open question of whether the GeV and TeV emission arises at the same location. Measuring the γ - γ absorption in γ -ray binaries can lead to a method of constraining the location of the GeV and TeV emission. The γ - γ absorption is dependent on the binary parameters, the stellar

temperature and the viewing angle of the observer. In general, more absorption occurs when the compact object, or γ -ray emission region, is behind the companion star, which leads to a denser photon field for the γ -ray to travel through to reach an observer. The position of the γ -ray emission region is not necessarily located at the position of the pulsar but also at the shock front, which forms between the pulsar and the companion star.

2. Theory

A γ -ray photon with energy E_γ emitted at a certain location travelling in the direction \vec{e}_γ will come into contact with a stellar photon with a certain energy ϵ travelling in the direction \vec{e}_* after a certain path length l . If the energy of the stellar photon exceeds the threshold energy for γ - γ absorption (ϵ_{\min}) then the γ -ray photon will undergo γ - γ absorption, or e^-e^+ pair-production, where both photons are eliminated and in the process an electron-positron pair will be produced.

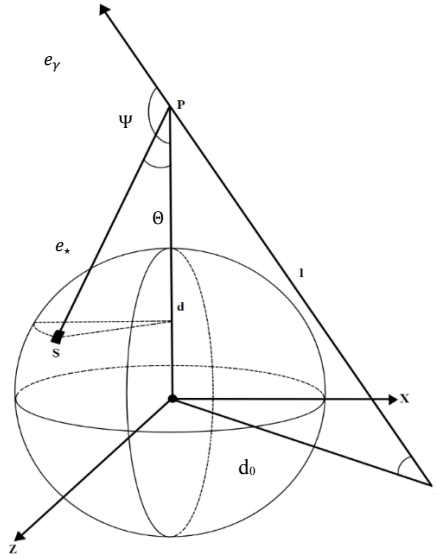


Figure 1. Geometry for γ - γ absorption due to e^-e^+ pair-production at a position P between a γ -ray emitted at E and a stellar photon emitted at S. The γ -ray is emitted at an angle Ψ_0 , relative to the stellar centre and the line PE, and travels a distance l towards an interaction point P. The distances d_0 and d describe the distances from the stellar centre towards the emission region and interaction position respectively. The vector motion of the stellar photon and γ -ray photon are described by \vec{e}_* and \vec{e}_γ respectively.

The differential optical depth is given by [5]

$$d\tau_{\gamma\gamma} = (1 - \vec{e}_\gamma \cdot \vec{e}_*) n_\epsilon \sigma_{\gamma\gamma} d\epsilon d\Omega dl, \quad (1)$$

where n_ϵ is the photon number density and $\sigma_{\gamma\gamma}$ is the γ - γ cross-section. If the companion star is assumed to be a perfect blackbody emitter, then the stellar photon number density is given by

$$n_\epsilon = \frac{2\epsilon^2}{h^3 c^3} \frac{1}{\exp(\epsilon/kT_*) - 1} \text{ ph cm}^{-3} \text{ erg}^{-1} \text{ sr}^{-1}, \quad (2)$$

where ϵ is the photon energy, c the speed of light, h the Planck constant, k the Boltzmann constant, and T_* is the stellar surface temperature. The γ - γ cross-section is given by [6]

$$\sigma_{\gamma\gamma}(\beta) = \frac{3}{16} \sigma_T (1 - \beta^2) \left[(3 - \beta^4) \ln \left(\frac{1+\beta}{1-\beta} \right) - 2\beta(2 - \beta^2) \right], \quad (3)$$

where σ_T is the Thomson cross-section and β is given by

$$\beta = \sqrt{1 - \frac{2m_e^2 c^4}{\epsilon E_\gamma (1 - \vec{e}_\gamma \cdot \vec{e}_*)}}. \quad (4)$$

where m_e is the electron mass. In general, the opacity can be calculated using a quadruple integral which is dependent on l , θ , ϕ , and ϵ , and is given by

$$\tau_{\gamma\gamma} = \int_{l_{\min}}^{l_{\max}} \int_{\mu_{\min}}^1 \int_0^{2\pi} \int_{\epsilon_{\min}}^{\epsilon_{\max}} n_e \sigma_{\gamma\gamma} (1 - \vec{e}_\gamma \cdot \vec{e}_*) d\epsilon d\phi d\mu dl \quad (5)$$

where $\mu_{\min} = (1 - R_*/d^2)^{1/2}$, $\mu = \cos \theta$, l is the path length the γ -ray travels, θ is the colatitude, ϕ is the longitude, and \vec{e}_γ and \vec{e}_* are unit vectors depicting the directions of propagation of the gamma-ray photon and stellar photon respectively. In a point source approximation, the stellar photons are no longer emitted from various regions across the surface of a star but rather all of them are emitted from a single point located at the centre of the star. The γ - γ absorption in a point source approximation is [7]

$$\tau_{\gamma\gamma} = \int_{l_{\min}}^{l_{\max}} \int_{\epsilon_{\min}}^{\epsilon_{\max}} \pi \left(\frac{R_*}{d} \right)^2 n_e \sigma_{\gamma\gamma} (1 - \vec{e}_\gamma \cdot \vec{e}_*) d\epsilon dl, \quad (6)$$

where d is the binary separation and R_* is the radius of the companion star. For each binary the opacity was calculated assuming the γ -rays are emitted at the centre of the compact object, except for PSR B1259-63 where the shock front location was also considered. The absorption at each orbital phase is calculated by determining the initial binary separation and interaction angle, and then integrating over the opacity function over the path length l and the photon energy ϵ . The point-source approximation is accurate to $\leq 2\%$ for the binary systems considered here.

3. Results

The results presented in this paper show the behavior of the γ - γ absorption for various orbital parameters and γ -ray photon energies. The binary parameters used for modelling the γ -ray binary systems are given in table 1. The binary separation of these systems has been calculated for both a neutron star and black hole compact object.

Table 1. Parameters used for modelling the γ -ray binary systems.

	HESS J0632+057 ^a	PSR B1259-63 ^b	LS I+61°303 ^c	1FGL J1018.6-5856 ^d	LS 5039 ^e
P_{orb} (days)	315(5)	1236.72432(2)	29.496(3)	16.544	3.90603(8)
e	0.83(8)	0.8698872(9)	0.54(3)	0.31±0.16	0.35(3)
ω (°)	129(17)	138.6659(1)	41(6)	89±30	226
i (°)	47&80	19&31	10&60	33&41	20&60
T_* (K)	30000	33500	22500	38900	39000
R_* (R_\odot)	8.0	9.2	10.0	10.1	9.3
M_* (M_\odot)	16.0	31.0	12.0	20.0&26.4	23.0
M_{compact} (M_\odot)	2.0&4.0	1.4	1.4&4.0	2.0	1.4&4.5
$\phi_{\text{periastron}}$	0.967	0	0.23	0.974	0

^a [8, 9, 10], ^b [11, 12, 13], ^c [14, 15, 16, 17, 18], ^d [19, 20, 21], ^e [22, 23, 24]

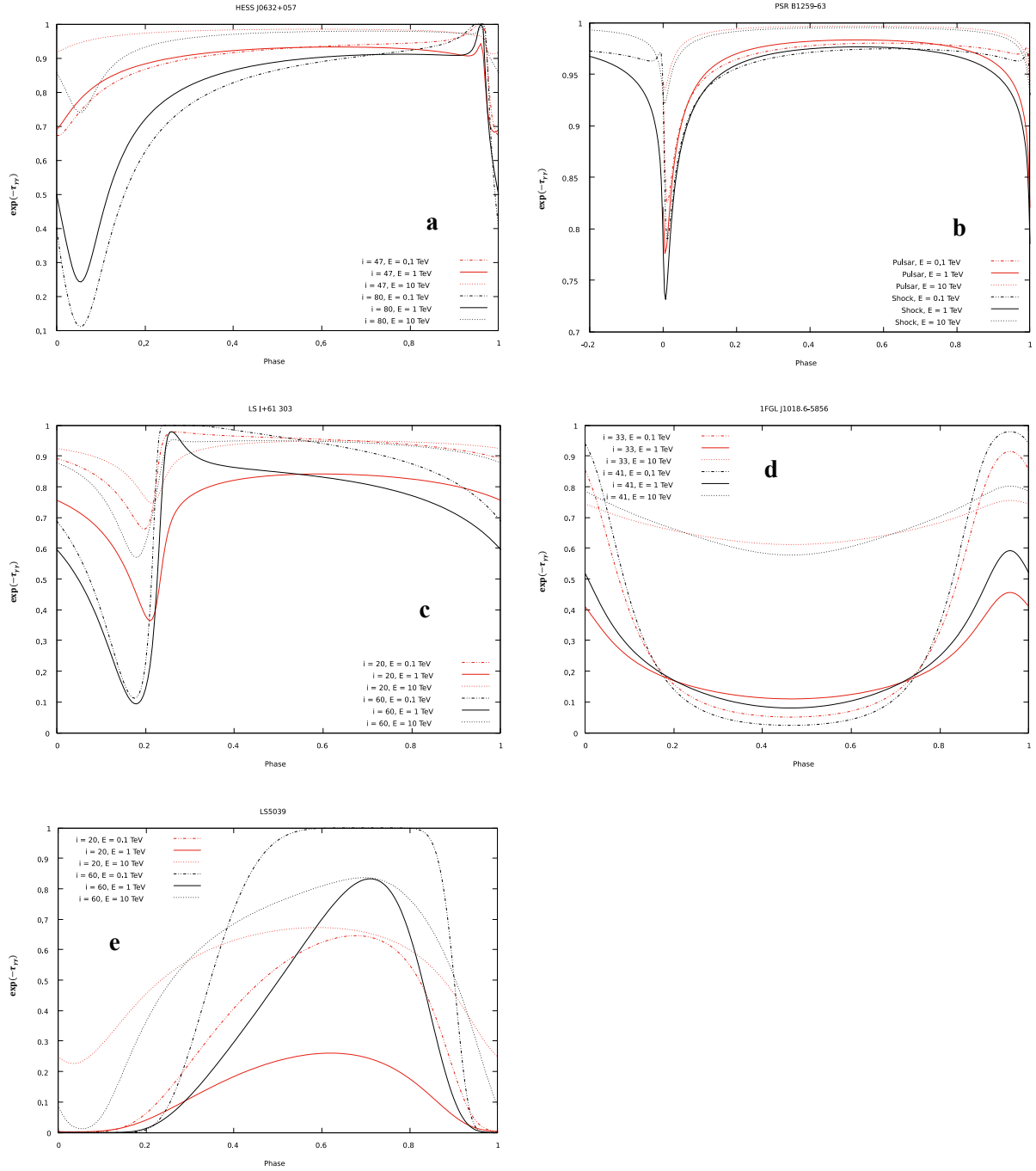


Figure 2. The $\gamma\gamma$ absorption HESS J0632+057 (a), PSR B1259-63 (b), LS I+61°303 (c), 1FGL J1018.6-5856 (d), LS5039 (e), plotted as $\exp(-\tau_{\gamma\gamma})$ vs. orbital phase. The lines denote the behaviour of the $\gamma\gamma$ absorption vs. phase for γ -ray energies of 0.1 TeV (dot-dashed line), 1 TeV (solid line), and 10 TeV (dotted line). The inclination for each system is given in the key with their respective line colours, where the red line represents the case where the compact object is a neutron star and the black line the case of a black hole. For PSR B1259-63/LS 2883 the red line represents the $\gamma\gamma$ absorption when the γ -ray emitting region is assumed to be at the pulsar location and the black line when it is assumed to be at the shock-front location.

For PSR B1259-63 the γ - γ absorption was calculated assuming two different locations of the γ -ray emission region, one being at the position of the pulsar and the other at the shock-front between the pulsar and the companion star. The distance between the pulsar and the apex of the shock-front can be estimated using [25]

$$r_p = d \frac{\sqrt{\eta}}{(1+\sqrt{\eta})}, \quad (7)$$

where η is the ratio of the ram pressure of the stellar and pulsar wind which was set as $\eta = 0.05$. The resulting γ - γ absorption calculations are shown in figure 1. For the “neutron star or black hole” case, two different compact object masses were chosen where each has its own corresponding inclination angle. For 1FGL J1018.6-5856 the exact mass of the companion star is unknown but the compact object mass is believed to be approximately $2.0 M_\odot$. Therefore the companion star mass was chosen to vary and the γ - γ absorption was calculated for a companion star mass of $20 M_\odot$ and $26.4 M_\odot$.

The results presented here for all systems show a similar trend where maximum absorption occurs close to superior conjunction. However, the magnitude of the absorption is most likely slightly underestimated by the point source approximation due to fact that it does not consider the effects of the angles described by θ and ϕ , which close to the companion star slightly underestimates the stellar photon density. However, the underestimation effect of the point source approximation at large distances becomes less (see Dubus 2006).

4. Discussion & Conclusion

In γ -ray binaries the maximum GeV and TeV emission should occur at or near superior conjunction because of the high angular dependence of inverse Compton scattering. However, at superior conjunction the energy of the very high energy (VHE) photons may exceed the energy threshold for γ - γ absorption which also leads to a maximum absorption of the TeV emission at superior conjunction. Hence, what may be observed, is that the maximum GeV emission occurs at or near superior conjunction and the maximum TeV emission occurs at or near inferior conjunction. This effect has been proposed for γ -ray binaries previously [6]. In particular, it has been suggested as a mechanism to explain the difference in the GeV and TeV light curves for LS 5039 and LMC P3 [6, 26, 27]. It has also been suggested as a mechanism to explain the local minimum seen in the TeV light curve of PSR B1259-63/LS 2883 [28]. For closely separated binaries the absorption period would occur throughout a much larger timeframe since the absorption is not only dependent on the angle of interaction but also on the separation distance and hence the energy density of the optical photons. For LS 5039 a relative amount of absorption will still occur even if the interaction angle is not optimal since the separation distance between the γ -ray emission region and the companion star is small. For highly eccentric binary systems such as PSR B1259-63/LS 2883 the absorption timeframe is very short and occurs only close to periastron. In future work we will now expand the modelling to investigate in what regions the TeV emission can and cannot originate from by means of absorption maps where regions around the binary system are also considered, and investigate how γ - γ absorption will modify the observed spectrum. This will be used to make predictions for future CTA observations.

References

- [1] Corbet R. H. D, et al 2016 *Asrophys. J.* **826** 105C
- [2] Ho W C G, Ng C -Y, Lyne A G, Strappers B W, Coe M J, Halpern J P, Johnson T J and Steele I A 2017 *Mthly. Notices of the Royal Astron. Soc.* **464** 1211
- [3] Johnston S, Lyne A G and Manchester R N et al. 1992 *Mthly. Notices of the Royal Astron. Soc.* **255** 401
- [4] Johnston S, Manchester R N and Lyne A G et al. 1992 *Astrophys. J. Letters*, **387**, L37
- [5] Gould R J and Schröder G P 1967 *Phys. Rev.* **155** 1404
- [6] Jauch J M and Rohrlich F 1976 *Texts and Monographs in Physics 2nd ed* (New York: Springer)

- [7] Dubus G 2006 *Astron. & Astrophys.* **451** 9
- [8] Aragona C, McSwain M V and De Becker M 2010 *Astrophys. J.* **724** 306
- [9] Casares J, Ribó M and Ribas I. et al. 2012 *Mthly. Notices of the Royal Astron. Soc.* **421** 1103
- [10] Bordas P and Maier G 2012 in American Inst. of Phys. Conf. Proc. vol 1505 Proc. of Gamma 2012 (Germany: Heidelberg) July 2012 ed F A Aharonian, W Hofmann and F M Rieger 366-369
- [11] Wang N, Johnston S and Manchester R N 2004 *Mthly. Notices of the Royal Astron. Soc.* **351** 599
- [12] Moldón J, Johnston S, Ribó M, Paredes J M and Deller A T 2011a *Astrophys. J.* **732** L10
- [13] Negueruela I, Ribó M and Herrero A et al. 2011 *Astrophys. J.* **732** L11
- [14] Howarth I D 1983 *Mthly. Notices of the Royal Astron. Soc.* **203** 801
- [15] Frail D A and Hjellming R M 1991, *Astron. J.* **101** 2126
- [16] Martí J and Paredes J M 1995 *Astron. & Astrophys.* **298** 151
- [17] Gregory P C 2002 *Astrophys. J.* **575** 427
- [18] Aragona C, McWain M V and Grundstrom E D et al. 2009, *Astrophys. J.* **698** 514
- [19] Monageng I M, McBride V A, Townsend L J, Kniazev A Y, Mohamed A, Böttcher M 2017 *Astrophys. J.* **847** 68
- [20] Fermi/LAT collaboration, Ackermann M and Ajello M et al. 2012 *Science* **335** 189
- [21] Napoli V J, McSwain M V, Boyer A N M and Roettenbacher R M 2011 *Publ. of the Astron. Soc. of the Pac.* **123** 1262
- [22] McSwain M V, Gies D R and Huang W et al. 2004 *Astrophys. J.* **600** 927
- [23] Casares J, Ribó M and Ribas I et al. 2005 *Mthly. Notices of the Royal Astron. Soc.* **364** 899
- [24] Casares J, Corral-Santana J M and Herrero A et al. 2011 in High-Energy Emiss. from Pulsars and their Sys.: Proc. of the First Sess. of the Sant Cugat Forum on Astrophys., Astrophys. and Space Sci. Proc. ed D F Torres and N Rea (Berlin: Springer-Verlag) 559
- [25] Eichler D and Usov V 1993 *Astrophys. J.* **402** 271
- [26] Böttcher M and Dermer C D 2005 *Astrophys. J.* **634** L81
- [27] H.E.S.S Collaboration et al. 2018 *Astron. & Astrophys.* **610** L17
- [28] Sushch I, van Soelen B 2017 *Astrophys. J.* **837** 175

H α images of nearby galaxy groups NGC193 and NGC940

S Hattingh¹, S I Loubser¹, A Babul², E O'Sullivan³

¹ Centre for Space Research, North-West University, Potchefstroom, South Africa

² University of Victoria, Canada

³ Harvard-Smithsonian Centre for Astrophysics, USA

E-mail: sumarihatt@gmail.com

Abstract. A significant fraction of the baryons in galaxy groups and clusters is not locked up in stars and the interstellar medium (ISM), but exists in the form of extended multi-phase gas. The advantage of nearby galaxy groups is that this multi-phase gas can be studied via X-ray observations probing the hot gas ($\approx 10^7 K$), and optical emission line observations (e.g. H α filaments) probing the ionised warm gas. Another advantage is that the effects of the galaxies' heating process of their surrounding gas (e.g. feedback from AGN) are more visible due to lower density and mass, and because groups contain fewer galaxies than rich clusters. Interaction between the different phases is important for galaxy formation and evolution due to the fact that at least 50% of galaxies can be found in groups and clusters.

The Complete Local-Volume Groups Sample (CLOGS) is an optically selected sample of 53 groups within 80 Mpc of which the X-ray observations (*Chandra* / *XMM-Newton*) have already been done and can be used to infer important physical properties, such as gas temperature and X-ray luminosity. In this project the H α images, observed using the WIYN 0.9m telescope on Kitt Peak, are analysed with the aim to compare the H α filaments to the X-ray emission images. Here we present preliminary results and a multi-wavelength comparison for two rich galaxy groups: NGC193 and NGC940. Despite their differences, we detect H α in the central members of both galaxy groups.

1. Introduction

In this study, we investigate the dominant early-type galaxy and surrounding members of two galaxy groups, NGC193, a galaxy group with its main member an X-ray bright radio galaxy with a powerful central jet, and the other group NGC940, with its main member an X-ray faint galaxy with only a weak radio point source. The two groups are part of the high-richness subsample of the Complete Local-volume Groups Sample (CLOGS). CLOGS is an optically-selected and statistically-complete sample of groups in the nearby Universe. Probing the luminous intra-group medium (IGM), CLOGS is specifically chosen and studied with optical observations for this project, since radio and X-ray bands [1] are already available. Important physical properties of the IGM are gas temperature and the total X-ray luminosity, both probing the environment in which the group members are located [2]. Together, the CLOGS observations can be used to investigate the role of active galactic nuclei (AGNs) in maintaining the thermal balance of the IGM, to name one example. The CLOGS galaxy groups were observed using the Giant Metrewave Radio Telescope (GMRT) in dual-frequency 235/610 MHz mode [1], with *Chandra* / *XMM-Newton*, and now also in H α with the WIYN 0.9m telescope.

The brightest, dominant early-type galaxies of groups are known for their typically high luminosity, and are old galaxies located near the centres of the group. These brightest group galaxies often reveal activity in their nuclei by radio emission & jets; depositing their energy back to the IGM. If conditions are favourable, the gas surrounding the brightest group member can cool down to form stars and feed the black hole. The latter results in AGN heating, which can heat the gas and cause the cycle to continue.

In this article, we study two of the 53 groups, and we give a brief overview of their properties below.

NGC0193¹

This central dominant, jet-dominated, early-type galaxy, at the centre of the group NGC193, is a currently-active large-scale jet system located at a right ascension of 00h39m18.6s and a declination of +03d19m52s. Its jet components extend several tens of kpc away from the host galaxy, and are seen as very bright, straight jets. These radio jets contribute to the heating of the IGM by balancing the radiative energy losses and also maintaining the long-term thermal equilibrium [3].

The radio jets, known for their large cavities or “cocoon”-like structures, cause disturbances in the X-ray emitting gas [1]. These two bright, straight jets are revealed by the radio contours (see the right image of figure 2) and are in a low-surface brightness “cocoon”, extending perpendicular to the jet axis, out to a projected distance of ~ 30 kpc from the centre - beyond the possible central cavity - and show very little correlation with the substructures detected in the X-ray image. Opposed to this, a correlation is observed between the outer border of the “cocoon” and the bright X-ray rim of the cavity in the northern region [4]. This may suggest that the cavity is possibly filled by the radio plasma in the diffuse “cocoon”. The X-ray bright rim represents a shell of gas, brightened on its edge, leaving little cool gas in the galaxy core.

In addition, this central member has X-ray emission-shells that surround its radio-lobes. The *Chandra* image (see the left image of figure 2), shows a bright ring with radius ~ 20 kpc around the nucleus of the central X-ray peak. This bright ring is either the outer shell of a large single X-ray cavity projected towards the group centre, or the result of the superposition of two cavities along the line of sight [4].

NGC0940²

This central dominant early-type galaxy in the centre of the group, NGC940, located at a right ascension of 02h29m27.5s and declination of +31d38m27.3s, shows vastly different properties to NGC0193. The radio emission shows a point source presenting a greater flux density at 610 MHz than at 235 MHz. No hot gas halo is detected in the X-rays [5].

The *XMM-Newton* image (see the left image of figure 5) shows a ~ 4 kpc radius bright ring around the nucleus of the central X-ray peak, with the contours indicated in black.

Figure 5 (see the image on the right) shows the 610 MHz contours (indicated with green colours), overlaid on the smoothed optical Digital Sky Survey (DSS) image.

2. Observations

$H\alpha$ is a strong spectral line visible in the red part of the optical electromagnetic spectrum, which makes it easily traceable. This spectral line has a rest wavelength of 6562.8\AA and is emitted when a hydrogen atom falls from its third ($n = 3$) to second ($n = 2$) lowest energy level.

In this project, the wide-field $H\alpha$ -images used for both galaxy groups contain group members of different morphological types. One example of this is a spiral galaxy (refer to figure 3). This type is known for its spiral structure from its centre into the galactic disc and this morphological type makes up approximately 60% [6] of the local galaxy population in the current Universe. These galaxies contain more young, massive and bright stars in the spiral arms and therefore appear very bright.

Another type of galaxy is an elliptical galaxy, which has an elliptical shape with almost no features but a much more concentrated / compact structure. Such an example is shown in figure 3, the NGC0193 galaxy. The stars found in elliptical galaxies are older than the young bright stars found in the spiral arms of a spiral galaxy, and are known to be low-mass stars (opposed to the massive stars in spiral arms).

The $H\alpha$ -filter, $I_{H\alpha}$, used to observe both galaxy groups for this project had a bandwidth of 81.33\AA ($k_{H\alpha}$) and a transmission rate of 90.58% ($\tau_{H\alpha}$), whereas the r-band, I_r , had a bandwidth of 1475.17\AA (k_r) and a transmission rate of 92.83% (τ_r). To see the ionised gasses clearly, the r-band images must be used to subtract the continuum (i.e. stellar emission).

These images were scaled by using the formula [7]:

$$I_{[H\alpha]} = \frac{I_{H\alpha} \cdot k_r - I_r \cdot k_{H\alpha}}{\tau_{H\alpha} \cdot k_r - \tau_r \cdot k_{H\alpha}} \quad (1)$$

¹ Since the galaxy groups are named after their brightest early-type members, we denote the galaxy as NGC0193, and the group as NGC193.

² Similarly, we denote the other brightest early-type member as NGC0940, and the group as NGC940.

where the intensity I is in counts/sec.

This method then effectively shows the ionised hydrogen gasses very clearly, with prominent clumps of stars visible, especially in the spiral galaxy members of both galaxy groups. Such an example can be seen in figure 6 where the clumps of stars are clearly visible.

3. Discussion

3.1. NGC193

Radio jets are known for its large cavities, heating the surrounding gas, which are often used to look at the power output of these jets [2]. The size of cavities are defined by matching an ellipse to their apparent shape. This is a very compact group since it has a higher density of galaxies in the centre (see Figure 1).

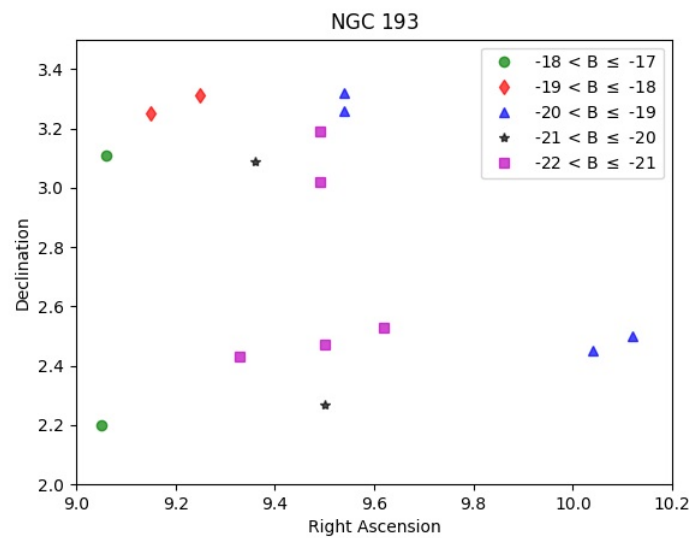


Figure 1. 15 Members of galaxy group NGC193 plotted according to their projected location in the group, colour-coded by brightness. The range in which each galaxy's magnitude lies, is indicated by the letter B.

Figure 1 corresponds to the coordinates of the members on the $H\alpha$ image taken on the WIYN 0.9m telescope on Kitt Peak and the members were colour-coded according to their magnitudes where we show members with B-magnitude values between -18 and -21. Figure 1 shows that the main member, NGC0193 (number 7) is surrounded by five other bright members (purple indicated squares) of this galaxy group.

X-ray and radio data for this group's main member, NGC0193, indicate full- and low-resolution contours on the Chandra and optical image, respectively (see Figure 2). The two very bright jet components are revealed by radio contours.

For three members of this group, NGC0193, NGC0198 and NGC0200, the r-band was subtracted from the continuum and scaled (see Figure 3) by a formula [7] discussed in the previous section. The ionised hydrogen gasses are shown very clearly for these three members with prominent clumps of stars for NGC0198 and NGC0200 (images on the right).

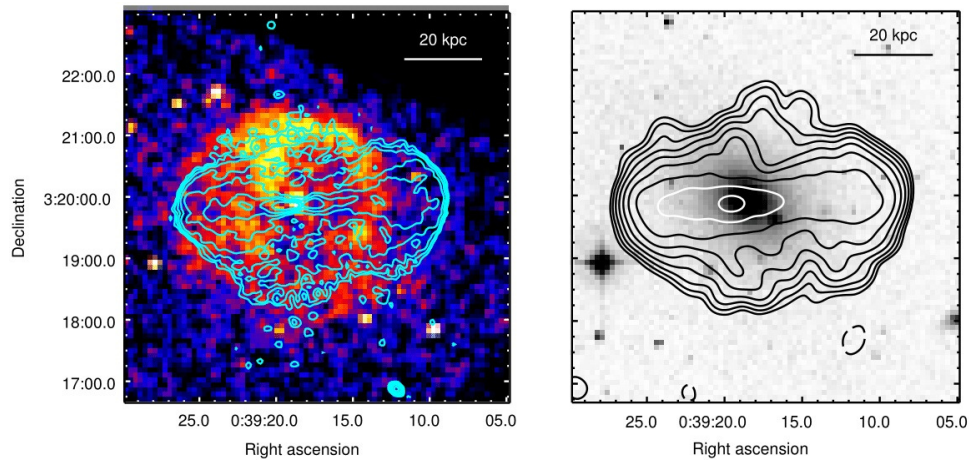


Figure 2. X-ray and radio data for group NGC193. *Left:* GMRT 610 MHz full-resolution contours overlaid on the smoothed, 0.3-2.0 keV Chandra image. *Right:* GMRT 235 MHz low-resolution contours on the optical image. Both images' radio contours are spaced by a factor of 2 [4]

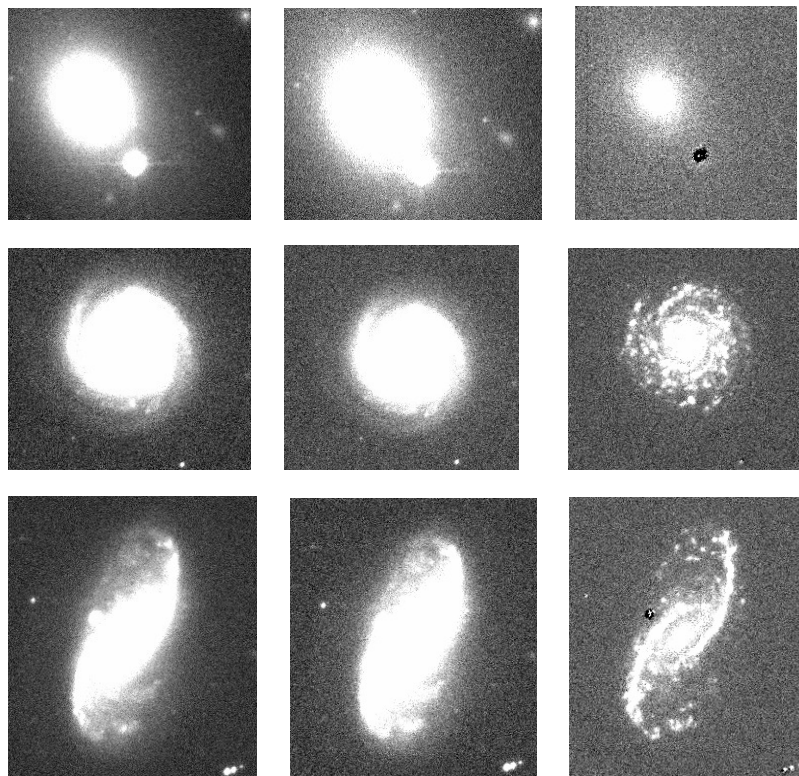


Figure 3. Three bright members NGC0193, NGC0198 and NGC0200 (in order from top to bottom) of the galaxy group NGC193. H α filter images (left), r-band images (middle) and the r-band subtracted from the H α (right).

3.2. NGC940

For this galaxy group, no diffuse hot halo has been detected in X-ray observations, but rather a point-source. This galaxy group is much less compact in terms of galaxies, since it only has nine members with the main member (see Figure 6) one of the brightest galaxies in this group, which was expected.

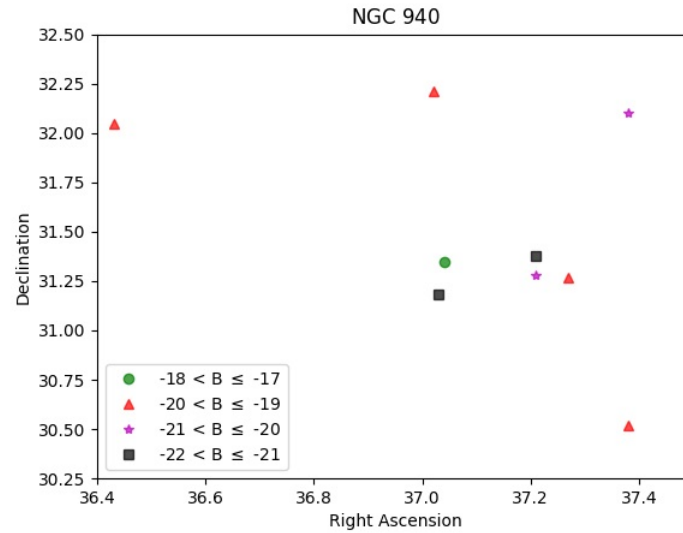


Figure 4. Nine members of galaxy group NGC940 plotted according to their projected location in the group, colour-coded by brightness. The range in which each galaxy's magnitude lies, is indicated by the letter B.

Figure 4 indicates that the main member, NGC0940 (number 5) is surrounded by one other bright member (purple indicated squares) of this galaxy group. The members were colour-coded according to their B-magnitude values between -18 and -21.

X-ray and radio data for main member NGC0940 reveal low- and full-resolution contours on the *XMM-Newton* and optical DSS image, respectively (see Figure 5). The contours overlaid on both images indicates no jet components, since this main member does not have a hot halo but is rather detected as a point source.

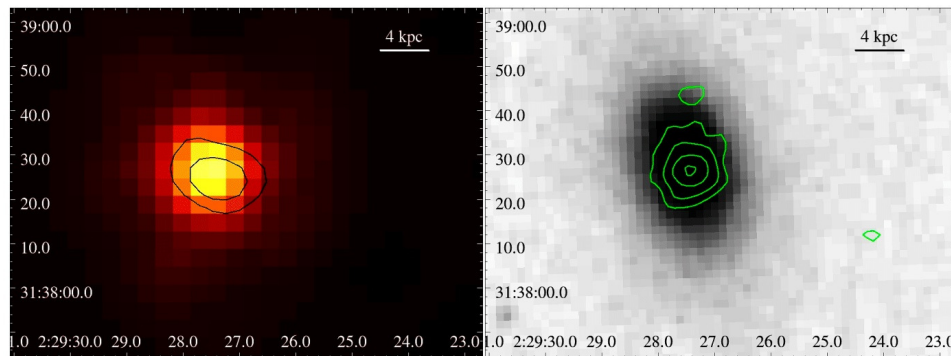


Figure 5. X-ray and radio data for group NGC940. *Left:* GMRT 235 MHz low-resolution contours in black overlaid on the adaptively smoothed, 0.3-2.0 KeV of *XMM-Newton* image. *Right:* GMRT 610 MHz full-resolution contours in green overlaid on the optical DSS image. [1]

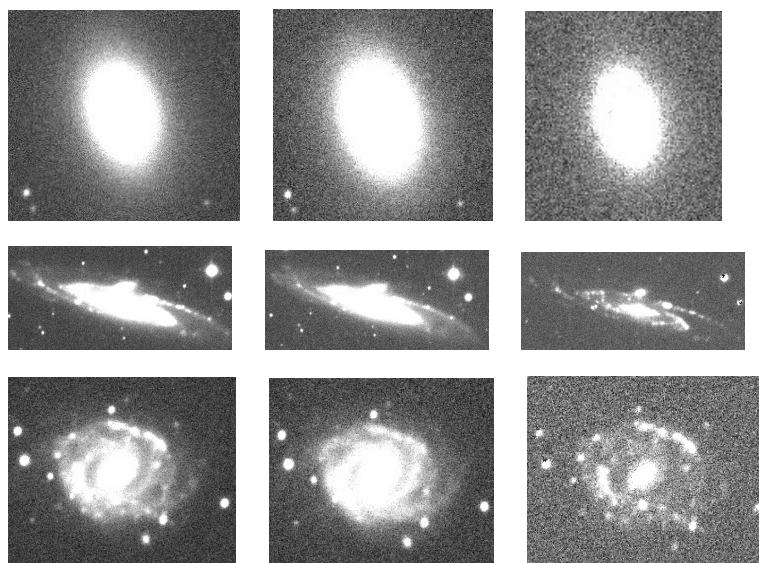


Figure 6. Three bright members, NGC0940, NGC0931 and UGC01963 (in order from top to bottom) of the galaxy group NGC940. $H\alpha$ filter images (left), r-band images (middle) and the r-band subtracted from the continuum (right).

Figure 6 shows that three bright members were scaled by making use of the formula [7] as discussed in the previous section. After the r-band of each member was subtracted from the continuum (images on the right), the ionised hydrogen gasses were clearly visible, showing the prominent clumps of stars in members NGC0931 and UGC01963.

4. Conclusions

In this study we have investigated surrounding members of two rich galaxy groups, NGC193 and NGC940 which are part of the CLoGS sample and can be used to investigate the role of AGNs to maintain the thermal balance of the IGM. Here we present preliminary results for both galaxy groups, detecting $H\alpha$ in their central members - despite of the two galaxies' different properties from X-ray and radio observations (e.g. jet-dominated vs point-source). Therefore, the environment and the IGM surrounding their dominant central galaxies are very diverse. Yet, intriguingly, $H\alpha$ -emission is detected in both dominant galaxies, and the physical connection between the different phases (e.g. hot gas, and warm ionised gas) is not obvious. It will be interesting to now investigate the other members of the galaxy groups (surrounding the dominant member), as well as extend the study to include more CLoGS groups to thoroughly explain the origin of the ionised $H\alpha$ gas.

Acknowledgments

Acknowledgements SH is supported by the National Astrophysics and Space Science Program (NASSP). SIL is aided by a Henri Chrétien International Research Grant administered by the American Astronomical Society and the National Research Foundation (NRF).

References

- [1] Kolokythas K et al 2018 The complete local-volume groups sample-ii: a study of the central radio galaxies in the high-richness sub-sample *MNRAS* **481** 1550
- [2] O'Sullivan E et al 2017 The complete local volume groups sample-i: sample selection and X-ray properties of the high-richness subsample *MNRAS* **472** 1482
- [3] Babul A et al 2002 Physical implications of the X-ray properties of galaxy groups and clusters *MNRAS* **330** 329
- [4] Giacintucci S et al 2011 A combined low-radio frequency / X-ray study of galaxy groups i: giant metrowave radio telescope observations at 253 MHz and 610 MHz *ApJ* **732** 95
- [5] Tully R B 2015 Galaxy groups: a 2-mass catalog *ApJ* **1499** 171
- [6] Loveday J 1996 The APM bright galaxy catalogue *MNRAS* **278** 1025
- [7] Terlevich R, Melnick J, Masegosa J, Moles M, Copetti M V F 1991 Spectrophotometric catalogue of HII galaxies *A&AS* **91** 285

Star formation histories of Brightest Group Galaxies in CLoGS

O C Havenga¹, S I Loubser¹, E O'Sullivan², A Babul³ and A Ratsimbazafy¹

¹ Centre for Space Research, North-West University, Potchefstroom, 2520, South Africa

² Harvard-Smithsonian Centre for Astrophysics, 60 Garden Street, Cambridge, MA 02138

³ Department of Physics and Astronomy, University of Victoria, Victoria, BC V8P 1A1, Canada

E-mail: 24909629@nwu.ac.za

Abstract. An important component of galaxy formation and evolution studies, is to accurately constrain the star formation histories (SFHs) of galaxies. While the SFHs of most massive early-type galaxies can be described using a single passively-evolving stellar component (Single Stellar Population [SSP]), there is a fraction of massive early-type galaxies in the centres of galaxy groups and galaxy clusters where recent star formation is observed and are better described by two or more stellar components (Composite Stellar Population [CSP]). In this project we identify and constrain possible recent star formation episodes in a sample of 23 BGGs (Brightest Group Galaxies), which is a sub-sample of the Complete Local-Volume Groups Sample (CLoGS). Most of these BGGs are in the centres of X-ray rich groups and all are closer than 80Mpc. We use archival spatially-resolved long-slit spectroscopy from the Hobby-Eberly Telescope (HET) at the McDonald Observatory, and determine whether the BGGs are better described by an SSP or a CSP using ULYSS. For this, stellar population models were fit to each of the 23 galaxies. The results showed that 11 of the BGGs were better described by a CSP while 12 of the BGGs were better described by an SSP. These results must be compared to the existing X-ray and radio observations of the groups.

1. Introduction

Galaxy groups are some of the best environments for studying the impact of galaxies on the surrounding Intergalactic Medium, as is done in [1].

The CLoGS sample is an optically selected sample of 53 galaxy groups within 80 Mpc. The sample selection is described in detail in [2]. X-ray, radio and sub-mm data have been collected for the entire sample [2]. In addition, [3] have analysed spatially-resolved long-slit spectroscopy from the 10m Hobby-Eberly Telescope (HET at the McDonald Observatory observed in September 2010 [4]) for a sub-sample of 23 BGGs. This project is a continuation, and uses the same sub-sample and data to derive star formation histories for the 23 BGGs. The aim is to study various properties of BGGs that serve as signatures of their evolutionary paths and also interpret the influence of the environment. The central galaxies (or BGGs) are in the centres of the groups' massive dark matter haloes and are thus ideal probes of galaxy evolution.

Table 1 gives information about the galaxies in this sub-sample. The sample was divided into two categories: a high-richness category and a low-richness category. [2] defined a richness parameter (R) as the number of galaxies within that group (within 1 Mpc from the centre and 3σ

in velocity of the BGG) with the luminosity constraint: $\log L_B \geq 10.2$. Groups with $4 \leq R \leq 8$ were classified as High-richness groups and groups with $R = 2-3$ were classified as Low-richness groups.

Table 1. The basic information of the BGGs that are studied in this project.

Galaxy information				
High-richness				
Galaxy	Redshift	RA	DEC	Velocity (km/s)
NGC0410	0.0177	01h10m58.9s	+33d09m07s	5294
NGC0584	0.0060	01h31m20.7s	−06d52m05s	1802
NGC0777	0.0167	02h00m14.9s	+31d25m46s	5015
NGC0924	0.0149	02h26m46.8s	+20d29m51s	4461
NGC1060	0.0173	02h43m15.0s	+32d25m30s	5190
NGC1453	0.0130	03h46m27.2s	−03d58m08s	3886
NGC1587	0.0123	04h30m39.9s	+00d39m42s	3694
NGC2563	0.0149	08h20m35.7s	+21d04m04s	4480
NGC4261	0.0074	12h19m23.2s	+05d49m31s	2212
NGC5353	0.0078	13h53m26.7s	+40d16m59s	2325
NGC5846	0.0057	15h06m29.3s	+01d36m20s	1712
NGC5982	0.0101	15h38m39.8s	+59d21m21s	3017
NGC6658	0.0142	18h33m55.6s	+22d53m18s	4270
NGC7619	0.0125	23h20m14.5s	+08d12m22s	3762
Low-richness				
Galaxy	Redshift	RA	DEC	Velocity (km/s)
NGC0315	0.0165	00h57m48.9s	+30d21m09s	4942
NGC0524	0.0080	01h24m47.7s	+09d32m20s	2403
NGC1779	0.0111	05h05m18.1s	−09d08m50s	3313
NGC2768	0.0045	09h11m37.5s	+60d02m14s	1353
NGC3613	0.0068	11h18m36.1s	+58d00m00s	2051
NGC3665	0.0069	11h24m43.7s	+38d45m46s	2069
NGC5127	0.0162	13h23m45.0s	+31d33m57s	4862
NGC5490	0.0162	14h09m57.3s	+17d32m44s	4855
NGC5629	0.0150	14h28m16.4s	+25d50m56s	4498

[5] did a complimentary study on Brightest **Cluster** Galaxies (BCGs), generally more massive and in denser environments than BGGs. It was found that there are two thresholds in the host clusters that determine whether star formation is allowed in the BCG. The two thresholds are the central entropy and the ratio of cooling-time (t_{cool}) to free-fall time (t_{ff}). We are interested in whether these or similar thresholds exist in X-ray rich groups.

The aim in this research is to constrain the SFH of BGGs. This can be done by classifying the galaxies as better described by a single stellar population (SSP) or a composite stellar population (CSP). According to [5] the convention is that most giant elliptical galaxies, such as the BGGs that is considered here, are passively evolving. Whether this holds true for BGGs, can be revealed by the SFH of the galaxies.

2. Method

2.1. Reduction

Since the data in the HET archive was not sky-subtracted, the first step was to do sky-subtraction. The data was then spatially binned into two bins - an inner bin (from 0 - 1 kpc) and an outer bin (from 1 - 2 kpc). This is done for each of the individual galaxies observed. This binning refers to binning along the spatial direction of the 2D spectra. This was done to ensure a high enough signal-to-noise ratio to have acceptable errors on the derived ages and metallicities.

2.2. ULySS

For the analysis, the stellar population code ULySS (University of Lyon Spectroscopic analysis Software) was used. The main routine in ULySS was used to compare the spectrum of a galaxy to the Vazdekis-MILES models [6] using all 985 stars.

The next step was to test the degree of the multiplicative polynomial. The multiplicative polynomial is used to subtract the continuum and dust as well as to account for any possible flux calibration differences between the galaxy and stellar template spectra. For this an SSP-fit was run for all 23 BGGs and for all MDs (Multiplicative Polynomial Degrees) between 1 and 30. After this, the resulting metallicity and age were plot against the different MDs. The optimal choice, where the solution converged, was a degree of 16.

Although the majority of stars inside the BGGs are believed to be old, we want to identify recent star formation episodes, by running both an SSP and a CSP fit for all 23 galaxies. This method is described in full in [5]. Thus, to accurately determine whether there is recent star formation in a galaxy, a CSP with two very different age components was chosen: a young component and an old component, even though no age or metallicity restrictions were placed on the two components.

The best way to do stellar population fitting is with a wide range of wavelengths, to break the age-metallicity degeneracy [7]. Due to some atmospheric features at the red-end of the spectrum (as can be seen in figure 1 and figure 2), the spectrum was truncated at 6200 Å, yielding a wavelength range of 4600-6200 Å, which is still wide enough for spectral fitting.

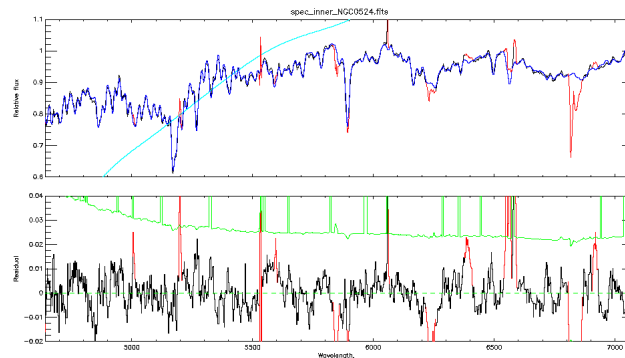


Figure 1. The spectrum of NGC0524 for the full observed wavelength-range. The black line indicates the observed spectrum, the blue line is the stellar population model of the best fit and the red is deviations that are masked during the fitting process. The light blue line shows the multiplicative polynomial that is used to normalize the continuum. The residuals are shown in the lower panel, where the green lines indicate the residuals as allowed by the error spectra (i.e. residuals larger than the green lines indicate deviations from the model as opposed to fluctuations caused by the noise in the spectrum).

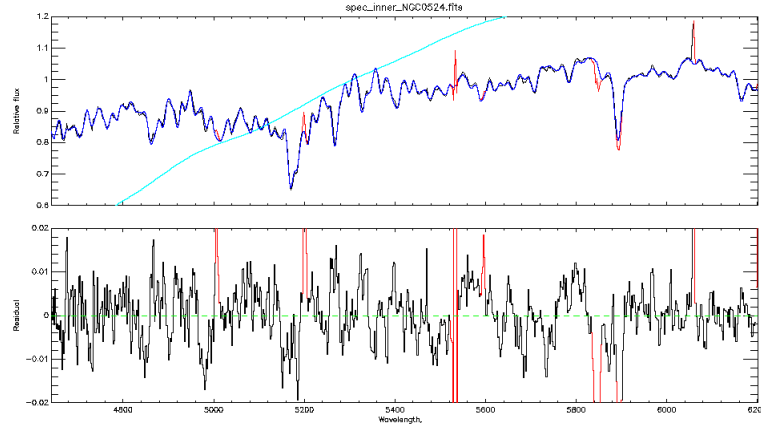


Figure 2. The same spectrum of NGC0524 as shown in figure 1, but now truncated at 4600-6200 Å. Thus, the atmospheric features are excluded.

3. Results and discussion

3.1. Classification

Table 2 gives a summary of the results obtained for both bins of all 23 galaxies.

Table 2. The results of the BGGs by using ULySS, indicating whether the bin was best fit by using a single or composite stellar population.

High-richness					
Galaxy	Inner	Outer	Low-richness		
NGC0410	SSP	SSP	Galaxy	Inner	Outer
NGC0584	CSP	CSP	NGC0315	SSP	SSP
NGC0777	SSP	SSP	NGC0524	CSP	SSP
NGC0924	CSP	SSP	NGC1779	CSP	CSP
NGC1060	SSP	SSP	NGC2768	SSP	SSP
NGC1453	SSP	SSP	NGC3613	SSP	CSP
NGC1587	SSP	SSP	NGC3665	SSP	SSP
NGC2563	CSP	CSP	NGC5127	SSP	CSP
NGC4261	SSP	CSP	NGC5490	SSP	SSP
NGC5353	SSP	SSP	NGC5629	CSP	SSP
NGC5846	SSP	SSP			
NGC5982	CSP	SSP			
NGC6658	CSP	SSP			
NGC7619	SSP	SSP			

In table 2 it is evident that some of the galaxies' inner bins are better described by a CSP while the outer bins are better described using an SSP. This is to be expected as the older stellar components mostly lie on the outskirts of the galaxy and the star formation mostly takes place in the central part of the galaxy (as is the case in NGC0924, NGC5982, NGC6658, NGC0524 and NGC5629). But, as is evident in NGC4261, NGC3613 and NGC5127, the inverse may also be possible (as described by [8] and [9]). For these three galaxies, it was found that the

inner bin was best fit by a single population, while the outer bin was best fit by a composite population. Naively, one might expect recent star formation to occur in the central parts of the BGGs. However, it is possible that processes such as galaxy mergers or infalling satellites can lead to younger stars in the outer parts. Whether this is indeed the case here, needs to be further investigated by also looking at the X-ray and radio observations.

3.2. NaD

Figure 3 clearly shows a feature that is not well fitted by the model (around 5900 Å). The absorption line is that of NaD, which may be sensitive for the initial mass function (IMF), according to [10]. According to [11] this phenomenon can also be seen in dwarf galaxies. This remarkable discrepancy occurs in 14 BGGs and must be investigated further.

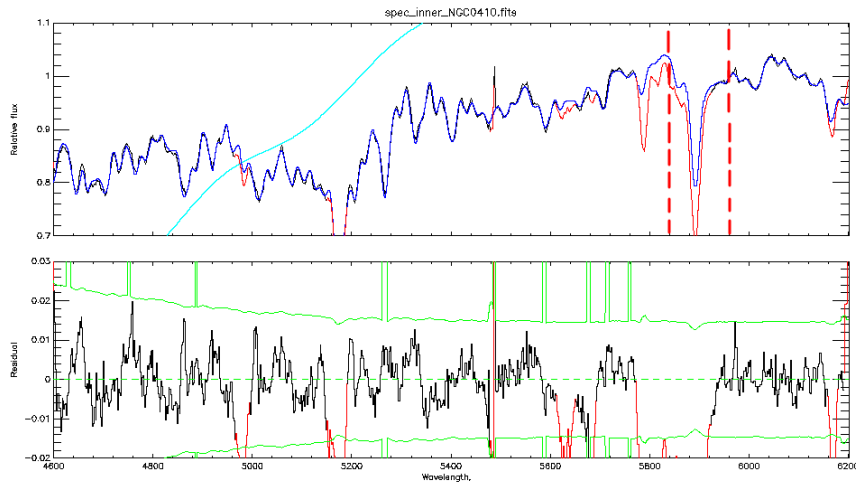


Figure 3. This is the spectrum of NGC0410. The NaD feature can be seen at 5900 Å (between the red dashed lines). The colours have the same meaning as in figure 1.

3.3. Brightest Cluster Galaxies

The same method was used in [5] for 32 BCGs to identify recent star formation episodes. Figure 4 (taken from [3], their figure 2a) shows the combined sample of 55 BGGs and BCGs. From this figure, it can be seen that the two populations, BGGs and BCGs, deviate in their Faber-Jackson relations. Now that we have star formation histories for all 55 central galaxies, these derived properties can be used to look for possible correlations between the galaxy and host group/cluster properties.

4. Conclusion and future work

The results obtained from the stellar population fitting now needs to be compared to data from other wavelengths (X-rays, radio, sub-millimetre, etc.). It is very important to verify why the galaxies which are better described by a CSP, had recent star formation episodes. The results can also be compared with the kinematic signatures of the galaxy groups [3]. After careful interpretation of the preliminary results presented here, we should be able to answer questions such as possible X-ray property thresholds for star formation in groups. Another important line of inquiry is to find out why there is a NaD overabundance as this may disclose some information of the IMF of the galaxies.

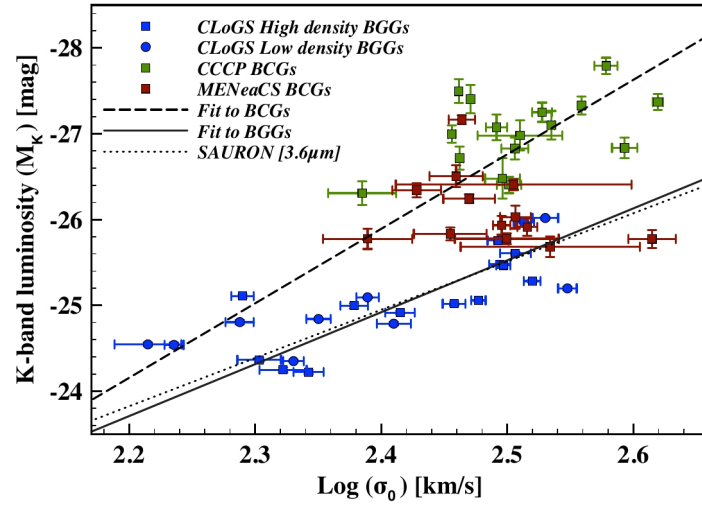


Figure 4. The BGGs are plotted in blue, while the BCGs are plotted in green and red. Note the two different Faber-Jackson relations (FJR) for the two classes. Figure from [3].

Acknowledgments

OCH is aided by the National Astrophysics and Space Science Programme (NASSP) and the National Research Foundation (NRF). SIL is aided by a Henri Chrétien International Research Grant administered by the American Astronomical Society and the NRF.

References

- [1] Ponman T, Sanderson A J R and Finoguenov A 2003 The Birmingham–CFA cluster scaling project – iii. Entropy and similarity in galaxy systems *MNRAS* **343** 331–42
- [2] O’Sullivan E, et al. 2017 The Complete Local Volume Groups Sample - i. Sample selection and X-ray properties of the high-richness subsample *MNRAS* **472**(2) 1482–505
- [3] Loubser S, Hoekstra H, Babul A, and O’Sullivan E 2018 Diversity in the stellar velocity dispersion profiles of a large sample of brightest cluster galaxies $z \leq 0.3$ *MNRAS* **477** 335–58
- [4] van den Bosch R C E, Gebhardt K, Gltekin K, Yıldırım A, and Walsh J L, 2015, Hunting for supermassive black holes in nearby galaxies with the Hobby-Eberly Telescope *ApJS* **218** 10
- [5] Loubser S I, Babul A, Hoekstra H, Mahdavi A, Donahue M, Bildfell C, and Voit G M 2016 The regulation of star formation in cool-core clusters: Imprints on the stellar populations of Brightest Cluster Galaxies *MNRAS* **456** 1565–78
- [6] Vazdekis A, Sánchez-Blázquez P, Falcón-Barroso J, Cenarro A J, Beasley M A, Cardiel N, Gorgas J, and Peletier R F 2010 Evolutionary stellar population synthesis with MILES i. The base models and a new line index system *MNRAS* **404** 1639–71
- [7] Worthey G 1999 The age-metallicity degeneracy in spectrophotometric dating of stars and galaxies *ASPCs* **192** 283
- [8] O’Sullivan E, Combes F, Hamer S, Salomé P, Babul A, and Raychaudhury S 2015 Cold gas in group dominant elliptical galaxies *A&A* **573** A111
- [9] Davis D S, Mushotzky R F, Mulchaey J S, Worrall D M, Birkinshaw M, and Burstein D 1995 Diffuse hot gas in the NGC 4261 group of galaxies *ApJ*, **444**, 582–9
- [10] Spiniello C, Trager S C, Koopmans L V E, and Chen Y P 2012 Evidence for a mild steepening and bottom-heavy initial mass function in massive galaxies from sodium and titanium-oxide indicators *ApJL* **753** L32
- [11] Schwartz C M, and Martin C L 2004 A KECK/HIRES study of kinematics of the cold interstellar medium in dwarf starburst galaxies *ApJ* **610** 201–12

Search for Gamma-ray emission in the White Dwarf pulsar of AR Scorpii

Q. Kaplan, H.J. van Heerden, P.J. Meintjes, A. Odendaal and R. Britto

Department of Physics, University of the Free State, Bloemfontein

E-mail: kaplanq@ufs.ac.za

Abstract. Detailed multi-frequency studies of the white dwarf pulsar AR Scorpii (AR Sco) revealed a Spectral Energy Distribution (SED) which predominantly shows features of non-thermal emission between the Radio and X-ray energies. This implies that AR Sco is a site of particle acceleration, which makes AR Sco an interesting source to investigate for possible gamma-ray emission in Fermi-LAT data (100 MeV-500 GeV). The focus of this paper was to do a preliminary analysis of the total Fermi-LAT dataset (2008-2018) by utilizing the upgraded Fermi-LAT Pass 8 data analysis pipeline to search for possible γ -ray emission in AR Sco. The detection of gamma-rays from AR Sco will be a strong motivation for possible CTA and H.E.S.S. follow-up studies. A positive detection will also be invaluable to the field of gamma-ray astronomy, establishing close binaries containing fast rotating, highly magnetic white dwarfs as a new class of γ -ray source.

1. Introduction

AR Scorpii (henceforth AR Sco) is a newly discovered close binary system consisting of a highly magnetic white dwarf pulsar and a M5 spectral type red dwarf orbiting around their Center of Mass (COM) every 3.56 h^[1]. This suggest some relation to other close binary systems called Cataclysmic Variables (CV) stars. A certain subclass of CVs known as Intermediate Polars (IP), also consist of white dwarfs with strong magnetic fields ranging between 1-10 MG, which is similar to that of AR Sco. White dwarfs (WDs) are very dense stars in their final evolutionary state, supported by electron degeneracy pressure. Some of these WDs spin rapidly about their central axis, possibly due to mass transfer from their companion star. They thus mimic the properties of neutron star pulsars due to their fast rotational velocities and large magnetic fields^[2]. Recently it was discovered that the rotating WD in AR Sco, with a spin period of $P_s = 117$ s, shows strong brightness variations across most of the electromagnetic spectrum^[1], i.e. the emission predominantly modulated at the orbital ($P_o = 3.56$ h) and its beat period ($P_b = 118$ s) with spin period $P_s = 117$ s.

It has been shown that this close binary system is unique, since there is no evidence of mass transfer, mass accretion, or magnetospheric propelling of the mass transfer stream from the binary system^[4]. It was suggested by Marsh et al.^[1] that AR Sco is in the evolutionary stage of an IP, but AR Sco's optical pulsations (70%) far exceeds that of the brightest IP detected thus far, namely FO Aquarii with optical pulsations of 25%. The lack of substantial accretion is inferred from the fact that the X-ray luminosity of AR Sco is less than 1% that of a typical IP^[1]. Therefore, there is no clear evidence to support the notion that AR Sco is an IP.

It was also suggested by Buckley et al.^[4] that the Spectral Energy Distribution (SED) is dominated by non-thermal emission^[4]. One of the most dominant emission features occurs in the radio regime, where strong modulations were found in the radio flux on the orbital period and the beat period^[3] suggesting the emission originates on the M5 secondary star. Possibly in the pumped magnetospheric field of the secondary star as the WD's magnetic field sweeps across it every rotation cycle. It is also proposed that the highly magnetic WD pulsar (order of 10 MG) has the potential to accelerate charged particles like electrons and protons to high Lorentz factors ($\gamma \approx 10^6$) within the light cylinder of the rotating white dwarf^[4]. This provides a vehicle to produce gamma-rays with energies above 1 TeV through e.g. inverse Compton scattering between the relativistic electrons and the photons from the secondary star^[2]. However, it was also recently shown that very high energy gamma-ray production through a hadronic channel like π^0 -decay is also possible^[5].

The aim of the study presented in this paper is to do a complete analysis of the total Fermi-LAT dataset (2008-2018) utilizing the upgraded Fermi-LAT Pass 8 data analysis pipeline to search for a gamma-ray excess from AR Sco. By using the upgraded Pass 8 data pipeline, better constraints can be put on the level of the emission above 100 MeV, which will allow the determination of a high energy SED above this threshold^[6]. This will have important implications for follow-up studies with H.E.S.S. and the future CTA. This study will have a very significant impact in the field of multi-wavelength astrophysics of high energy compact sources, as well as the field of gamma-ray astronomy. The discovery of gamma-rays in AR Sco will lead to a new class of gamma-ray source and the multi-wavelength properties will result in the source being considered as a unique laboratory to study magnetospheric processes that can accelerate charged particles to very high energies.

2. Observations and Analyses

A Fermi-LAT dataset from the past decade (2008-2018) was extracted from the Fermi Science Support Center (FSSC) in the energy range between 100 MeV and 500 GeV. By using the Pass 8 data analysis pipeline, which provides a better determination of the diffuse galactic gamma-ray emission and also a significant improvement in terms of energy resolution from previous Fermi-LAT pipelines, it was possible to do a standard Binned Likelihood Analysis on the Fermi-LAT dataset^[7]. The analysis was performed using Fermipy packages where a number of models were experimented with to fit and produce high energy SEDs for AR Sco. The event files, i.e. the photon and spacecraft files that were extracted from the FSSC site, were chosen to have a Region of Interest (ROI) of 30° , while a 15° ROI was chosen to extract the high energy photons of the target for analysis. All the point sources in the third Fermi-LAT catalog (3FGL) located within the ROI were modelled in the spectral fits, including the isotropic background and galactic diffuse emission. Since AR Sco is not listed in the 3FGL catalog, the source (3FGL J1616.8-2300) closest to the ROI centre (0.01° from ROI centre) was chosen to perform the event selection and create the source maps with Fermipy. AR Sco was added using its coordinates, (RA: $16^h21^m47.28^s$, Dec: $-22^\circ53'10.39''$, J2000) to the source maps and selection files with the help of Fermipy commands so that likelihood analysis could be done. The spectral shape parameters of AR Sco was set to vary during optimization and fitting. The spectral shapes used to model the spectral fit for the extracted data are as follows, namely 1.) a Power Law:

$$dN(E)/dE = N_0(E/E_0)^\Gamma, \quad (1)$$

with N_0 is the normalization factor and where a pivot energy (E_0) of 1 GeV was chosen to fit the model, and 2.) a Log Parabola

$$dN(E)/dE = N_0(E/E_b)^{\alpha-\beta \log(E/E_b)}, \quad (2)$$

where E_b is the break value that should be set near the lower energy range of the spectrum. Here E_b was chosen to be 1 GeV.

Table 1. List of all the model parameters used during optimization to fit the Fermi-LAT data. Where the Test Statistic (TS) value is used to distinguish between flux values ($TS \geq 25$) and 2σ upper limits.

Spectral model	TS	α	β	Γ
Power Law	7.71	N/A	N/A	2.44 ± 0.05
Log Parabola	16.17	2.29 ± 0.2	0.28 ± 0.001	N/A

3. Results and Discussion

The spectral models that were used to model the SED, as mentioned in Section 2, are the power law and log parabola functions. These models were used to determine the emission spectrum that best describes the emission properties from AR Sco. A residual model fit, see Figure 1, was also created to visually indicate how well the model has been fitted to the high energy data.

The upper limits and detected flux values were determined by using the Test Statistic (TS) values generated by the likelihood analysis. These TS values help to determine the probability of detecting emission from the source within each bin. Based on the parameters and overall test statistics (see Table 1) and taking in account how both the power law and log parabola fits the flux values and upper limit within the butterfly plot, see Figure 2 and 3, the best proposed significant fit for AR Sco is represented by the power law model, see Figure 2. Also, from the residual and counts fit (Figure 1), along with the produced SEDs (Figures 2 and 3), it is observed that the most of these detected flux values are within the lower energy regime (up until ~ 10 GeV). TS maps were also generated to show the overall significance of detection from AR Sco within the ROI, see Figure 4 and 5. The bright spot in the ROI, centred at AR Sco, in Figure 6 suggests that there is possible high energy emission from this region. Histograms of significance of all the data points in the ROI also shows the probability of detection within the standard deviation, see Figure 6 and 7. From these figures it is clear that the probability of detection is higher for the power law model as it follows a better Gaussian curve than the log parabola model.

A broadband SED was also created to show how the obtained Fermi-LAT power law spectrum, ranging from 100MeV to 500GeV, can be viewed in relation to previous multi-frequency observations (see Figure 8). The radio to optical data were extracted from the paper published by Marsh et al.^[1] in 2016, whereas the X-ray data was extracted from the paper published by Geng et al.^[3] in 2016.

4. Conclusion

The gamma-ray SED between 100MeV-500GeV seems to be compatible with a power law with $\Gamma=2.4 \pm 0.05$. Our results seem to suggest the possibility of a low-level detection which is compatible with both hadronic and leptonic channels of gamma-ray production. Further analyses are underway to quantify the gamma-ray emission from the selected ROI centred on AR Sco. Unbinned likelihood analyses will also be performed, utilizing all the detected high energy photons, to better determine the gamma-ray excess.

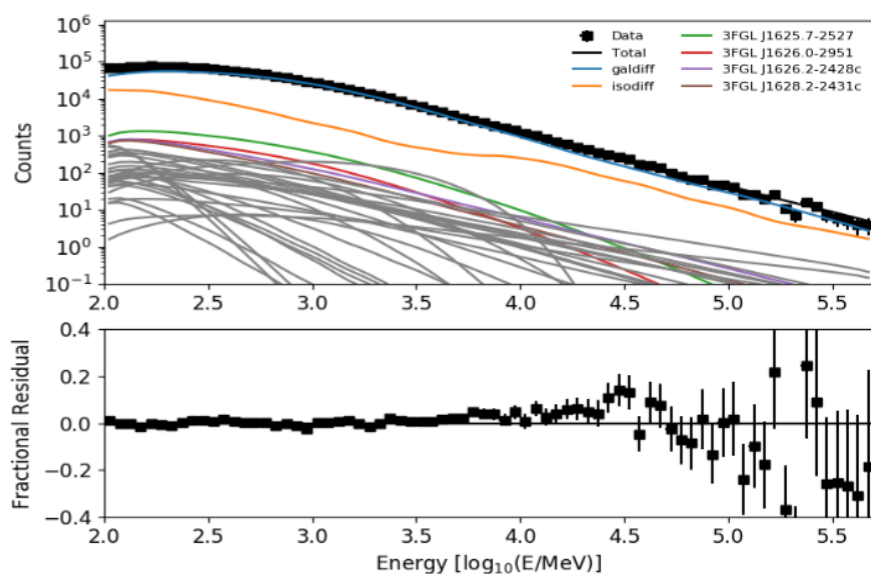


Figure 1. Residual model fit of power law model which best describes the spectral energy distribution.

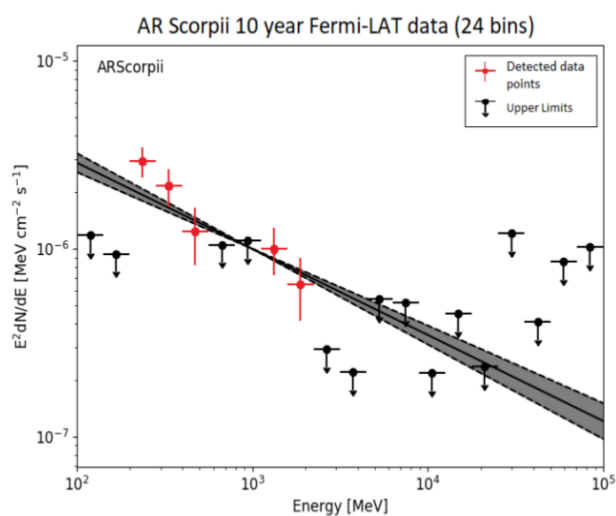


Figure 2. Spectral energy model fit of AR Sco's high energy SED represented by the Power Law function.

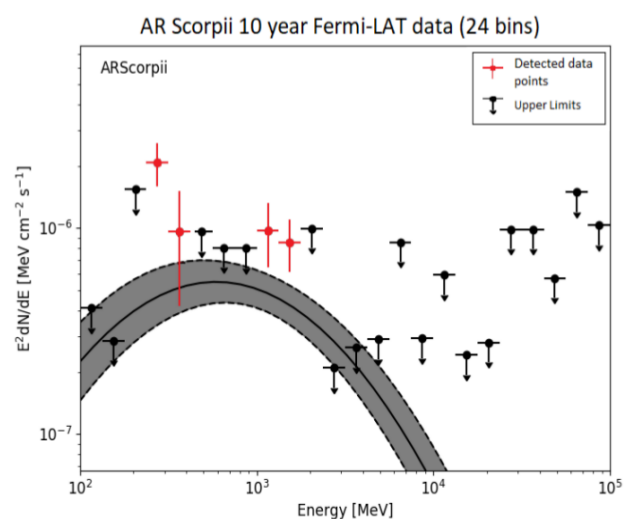


Figure 3. Spectral energy model fit of AR Sco's high energy SED represented by the Log Parabola function.

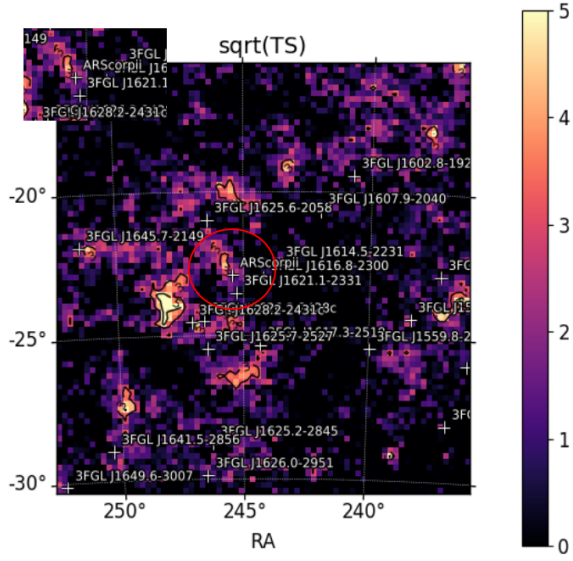


Figure 4. Test Statistic map of the source AR Sco and the galactic diffuse emission. Notice the bright pixels at the ROI centre (red circle).

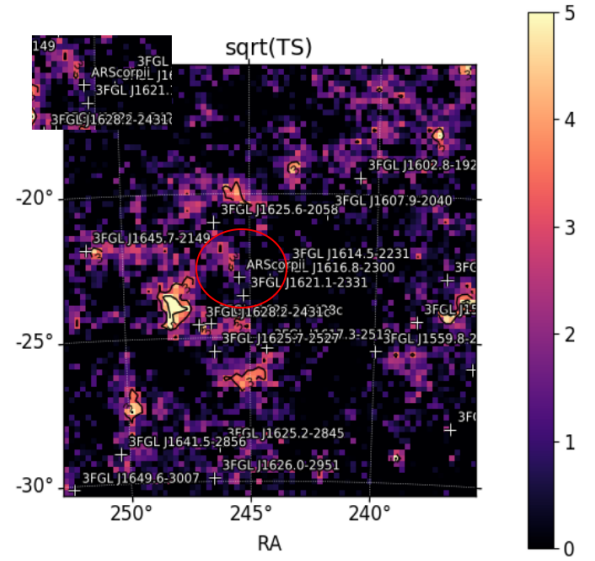


Figure 5. Test Statistic map of just the galactic diffuse emission. Notice the lack of bright pixels at the ROI centre compared to that in Figure 6.

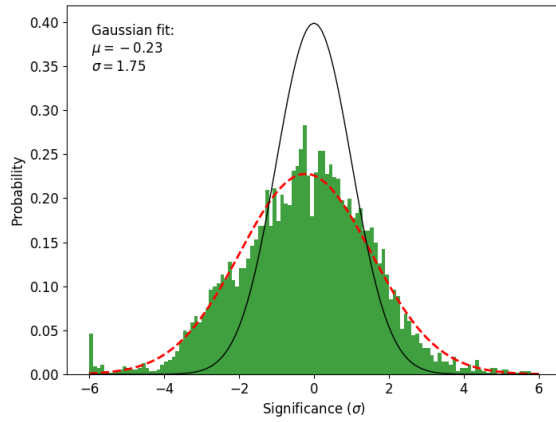


Figure 6. Histogram of significance for all the points on the map, Power Law model.

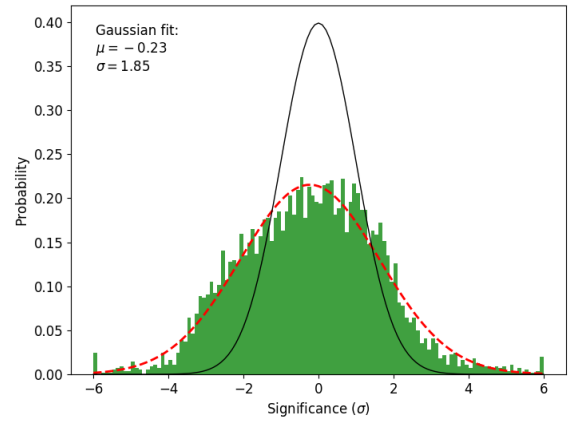


Figure 7. Histogram of significance for all the points on the map, Log Parabola model.

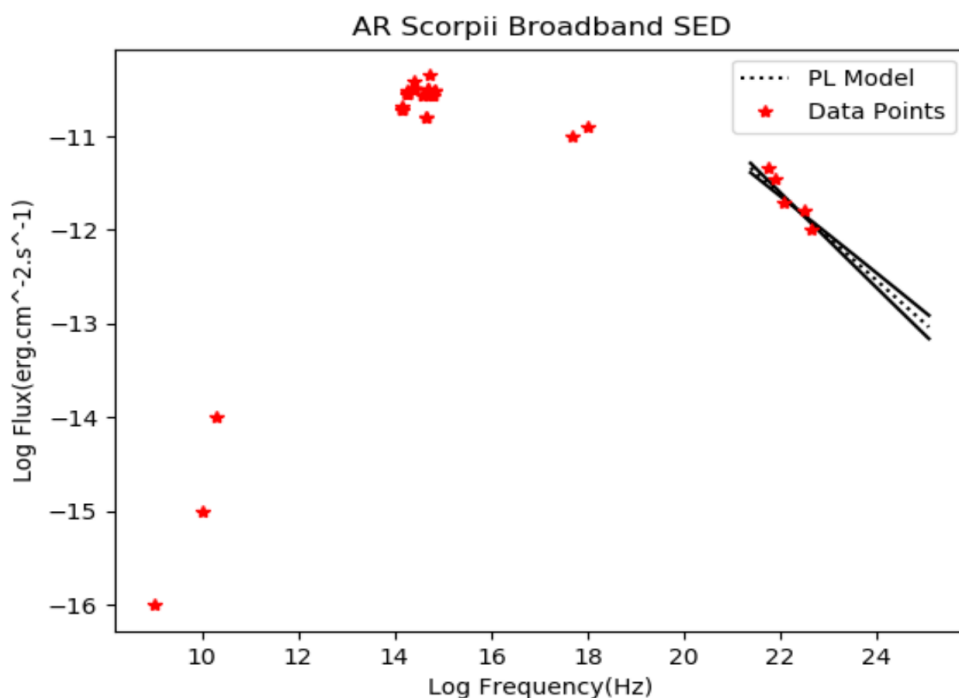


Figure 8. Proposed Broadband SED of AR Sco, ranging from radio to gamma-ray energies. Radio and optical data adapted from Marsh et al.^[1] and Geng et al.^[2]. The dashed and solid lines show the Power Law model butterfly plot produced by the Likelihood Analyses generated in Fermipy.

References

- [1] Marsh T.R. et al. 2016, *A radio pulsating white dwarf binary star*, Nature, 537, 374.
- [2] Geng J. et al. 2016, *A model of white dwarf pulsar in AR Scorpii*, ApJ, 831, L10.
- [3] Stanway E.R. et al. 2018, *VLA radio observations of AR Sco*, Astronomy and Astrophysics, Volume 611, id.A66, 13 pp
- [4] Buckley D.A.H et al. 2017, *Polarimetric evidence of white dwarf pulsar in the binary system AE Scorpii*, Nature Astronomy, 1, 0029.
- [5] Bednarek W. 2018, *Hadronic model fro the non-thermal radiation from the binary system AR Scorpii*, MNRAS, Volume 476, L10-L14.
- [6] Abdo A.A. et al. (*Fermi-LAT collaboration*), 2010, ApJ, 723, 1082
- [7] McEnery J. 2018, *Fermi Science Support Center*, <https://fermi.gsfc.nasa.gov/ssc/>. Date accessed: 18 June 2018

The search for γ -ray emission from AE Aquarii using Fermi-LAT Pass 8 Data pipeline 2008-2018

ST Madzime, HJ van Heerden, PJ Meintjes, A Odendaal, RJ Britto

Department of Physics, University of the Free State, Bloemfontein, South Africa

E-mail: madizimest@ufs.ac.za, VanHeerden@ufs.ac.za, MeintjPJ@ufs.ac.za, winka@ufs.ac.za

Abstract. We present the preliminary results of the search for gamma-ray emission from AE Aquarii (AE Aqr) using the upgraded Fermi-LAT Pass 8 data analysis pipeline. A previous study using the Fermi-LAT Pass 7 data pipeline showed low-level but consistent, pulsed emission at a period of 16.54 seconds, which is the first harmonic of the 33.08 s pulsed emission at the spin period of the white dwarf. This implies possible gamma-ray emission from both polar caps of the spinning white dwarf. A re-analysis with the Pass 8 data pipeline, which uses an improved galactic diffuse gamma-ray emission model as well as more inclusive selection criteria, has resulted in no detection of any gamma-ray emission from AE Aqr according to the Fermi-LAT detection threshold. However, three spectral points with significance just above 2σ were detected according to *fermipy*'s spectral points detection threshold.

1. Introduction

AE Aqr is a cataclysmic variable close binary which consists of a fast rotating magnetized white dwarf orbiting a late-type main sequence companion (K4-5) star, with an orbital period of 9.88 hrs (e.g [1, 2, 3]). The white dwarf is highly magnetic ($\sim 10^6$ Gauss) and rotates with a period of ~ 33 s [4]. AE Aqr exhibits nova-like characteristics in the optical waveband with a visual magnitude varying between $m_v = 10$ and $m_v = 12$ [5].

Initially, the system was erroneously classified as a DQ Her system, based on some similarities with DQ Hercules. However, later studies revealed that the system is significantly different since the white dwarf currently accretes very little material as a result of the magnetospheric propelling of materials from the fast rotating white dwarf magnetosphere, which drives the mass-flow from the secondary star out of the binary system [6, 7].

Non-thermal radio emission from AE Aqr was first detected by Bookbinder & Lamb (1987) [8]. This emission was later shown to be highly transient, showing flaring activity with flux levels varying between 1 and 12 mJy [9] on a continuous basis. In contrast to the initial perception that radio and optical outbursts could be associated with enhancements in the accretion rate onto the white dwarf, Patterson (1979) [10] showed that there was no significant increase in the pulsed fraction of the periodic optical emission during flares. It was shown [11] that a fragmented blobby mass transfer stream from the secondary star ejected by the fast rotating white dwarf (i.e. a magnetospheric propeller) could, in fact, drive the optical flaring, which explains why the pulsed fraction of the 33.08 s rotation period does not increase significantly during the flaring. It has been shown [12] that the white dwarf in AE Aqr could readily accelerate electrons and protons to energies of the order of several TeV ($1 \text{ TeV} = 10^{12} \text{ eV}$), which could provide gamma

rays through leptonic channels (synchrotron, inverse Compton) or a hadronic channel (neutral pion production and decay to gamma rays). These accelerated electrons, continuously pumped by the sweeping white dwarf magnetosphere, also produce non-thermal radio to infrared (IR) flaring emission with the observed van der Laan - type Spectral Energy Distribution (SED) [13].

The transient non-thermal radio flares observed from AE Aquarii, and its similarities with Cyg X-3 (albeit at a lower level), provided the first motivation to embark on a search for TeV emission from this source (see e.g. [14, 15, 16, 17]). Recently a Fermi-LAT search by van Heerden [18], using the Pass 7 pipeline, revealed weak but consistent pulsations at the first harmonic (~ 16.54 s) of the 33.08 s spin period of the white dwarf. In this paper, the preliminary analysis and results in the search for gamma-ray emission from AE Aquarii utilizing Fermi-Pass 8 data will be presented.

2. Data Reduction & Analysis

The archival gamma-ray data from Fermi Large Area Telescope (Fermi-LAT) observed between 4 Aug 2008 to 2 May 2018 were considered. The data comprises of all Fermi-LAT events and spacecraft data. The analysis of the Fermi LAT data were performed using python software *fermipy* (v 0.17.3), which is part of the Fermi Science Tools software packages (v11r0p5). We used the (iso_P8R2_SOURCE_V6_v06.txt) set of response functions and selected corresponding source-class events, events class (evclass=128) and front+back events type (evtype=3). In this analysis, photons were selected from a radius of 10 degrees Region Of Interest (ROI), centered at the optical coordinates of AE Aquarii (RA=310.038, DEC= -0.8708). The zenith angle cut was set at 90 degrees to avoid contamination by photons produced from cosmic-ray interactions with the atmosphere. Binned maximum -log(likelihood) analysis was performed on the energy range 0.1-500 GeV. All sources within 20 degrees of ROI, the instrumental background (iso_P8R2_SOURCE_V6_v06.txt), and the diffuse galactic emission model (gll_iem_v06.fits, [19] as well as the source of interest were used to generate the spectral-spatial model using the python module (make3FGLxml.py). The analysis of AE Aqr was performed utilizing the simplest spectral model for non-thermal emission (i.e a Power Law see equation (1)).

$$\frac{dN}{dE} = N_o \left[\frac{-E}{E_o} \right]^{-\Gamma} \quad (1)$$

The power law model requires three parameters: the power law index (Γ) which controls the hardness of the source, the scale (N_o), this is the normalization factor to scale the observed brightness of the source and the prefactor (E_o), which scales the energy. These parameters and other parameters in the spectral-spatial model were optimized and fitted using the maximum -log(likelihood) technique, [20]. The significance of AE Aqr was assessed using the ratio of -log(likelihood) L . This ratio is known as the test statistics (TS) as shown by equation 2,

$$TS = -2 \log \left(\frac{L_{max,0}}{L_{max,1}} \right) \quad (2)$$

where $L_{max,0}$ is the maximum likelihood value for a model without an additional source (the null hypothesis) and $L_{max,1}$ is the maximum likelihood value for a model with the additional source at a specified location. The term significance in this analysis is defined in σ units, where it is assumed to take the square-root value of TS [20]. Fermi-LAT sources with test statistic less than 25 were removed from the fit, and to get the desired fit status and quality for the model, the parameters of all sources beyond a 5 degrees angular distance from the centre of the ROI were fixed, whereas those of the target source were set free.

Fermipy has several processes and analysis output product that can be used to search for un-modelled sources as well as evaluating the fit quality of the model. These include TS-Map,

TS-Cube, Residual-Map and Source Finding. In this analysis, TS and Residual maps were employed and the Spectral Energy Distribution (SED) was computed.

3. Results

The average TS for AE Aquarii from *fermipy* binned analysis was zero in the energy range 0.1-500 GeV. This value is way below the detection limit which means that the proposed spectral model does not characterize the source correctly, or that the target is not a strong enough emitter to be classified as a gamma-ray source. The left-hand side of Figure 1, shows a counts map of filtered raw data with Good Time Intervals (GTIs') applied and the right-hand side the likelihood model map, which shows all sources that were included in the fit.

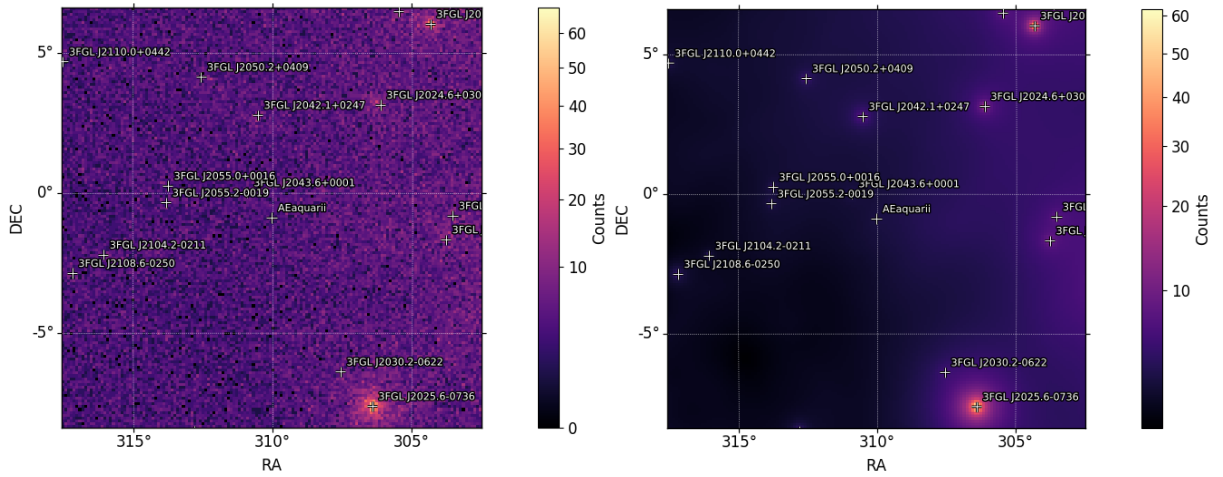


Figure 1: Counts map (left) and model map (right). The counts map is the cumulative data of observed counts at a given grid location. A closer inspection of the counts map generated for ten years of data shows that there are no extremely bright sources in the ROI.

3.1. TS and Residual Maps

TS maps were generated for the entire ROI, using the *gta.tsmaps()* routine which generates a TS map for each source component in the model centered at each spatial bin. TS maps are only sensitive to a positive deviation with respect to the model. The method calculates TS for each bin using equation (2). The TS map on the left-hand side of Figure 2 shows no gamma-ray significance, this corresponds well with the analysis results. On the right-hand side is the residual map generated by the *gta.residmap()* routine, which calculates the residual between the counts' map and model map. The residual map is sensitive to positive and negative deviations. There should be no region with an excess in terms of significance if the model describes the data well.

3.2. Spectral energy distribution (SED)

Additional to TS maps, SED points with 30 energy bins per decade and butterfly plots were generated to see whether the model is in agreement with the data and also to check which energy bins contribute more to the obtained TS. On the left-hand side of Figure 3 is a SED plot fitted with a power law, butterfly plots are also included on the fit and on the right-hand side a broadband SED, with plotted points from this study, archival data, and CTA, and Fermi-LAT sensitivity curves. Further investigations on the energy bins with significance just above 2σ is presented in Fig 4, with energy range between 0.4 and 10 GeV.

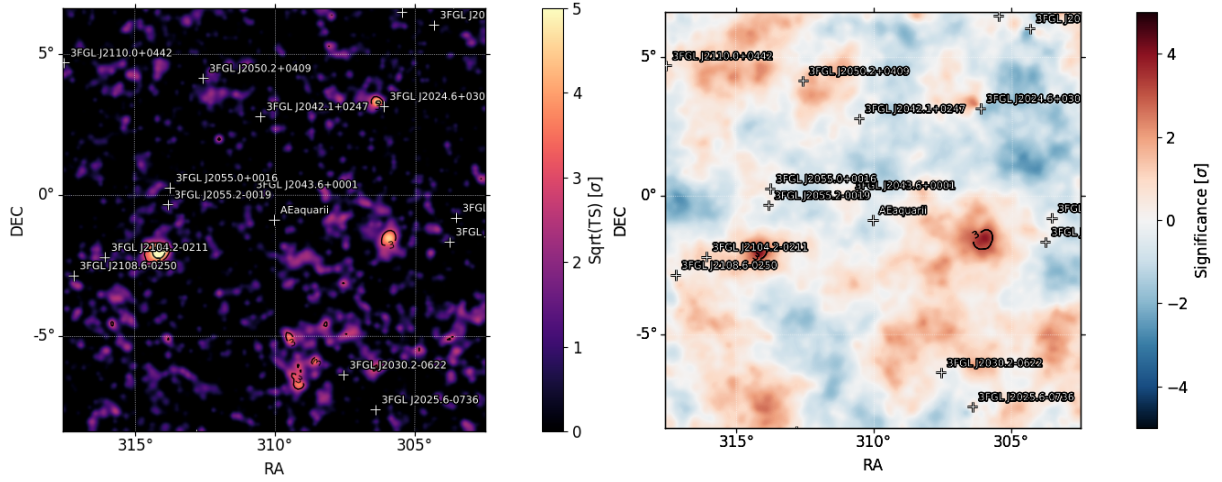


Figure 2: The TS map on the left shows the significance of all sources included in the model, and a residual map is provided on the right.

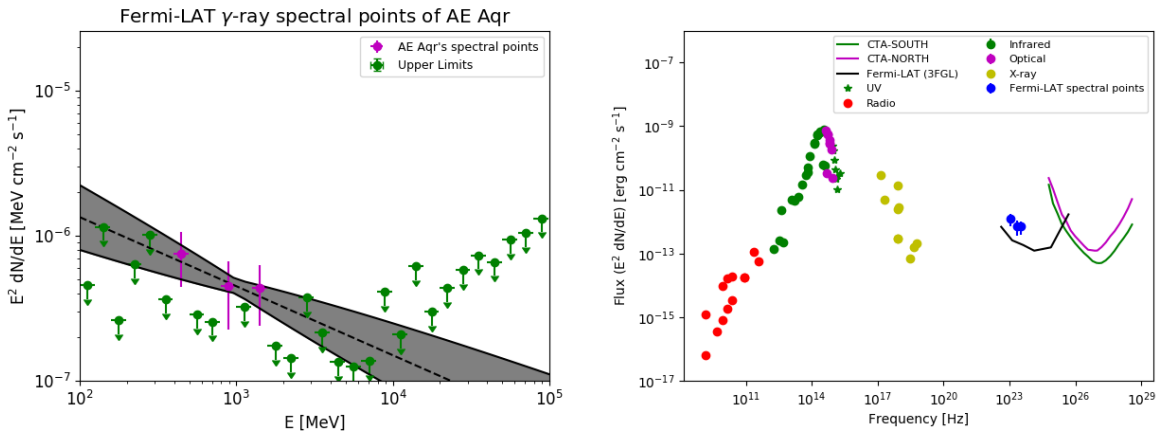


Figure 3: Fermi-LAT spectral points, upper limits, and butterfly plot of AE Aqr (left), and the spectral broad band of AE Aqr from radio to higher energy (right).

4. Discussion & Conclusion

This study resulted in no detection of gamma-ray emission from the region of AE Aqr as per the detection threshold of Fermi-LAT. Van Heerden [18] reported upper limit of 3.47×10^{-7} ph $\text{cm}^{-2}\text{s}^{-1}$ in the energy range 10 - 100 GeV using pass 7 data and Jian [21] reported upper limit of 1.3×10^{-12} erg $\text{cm}^{-2}\text{s}^{-1}$ in the 0.1 - 300 GeV using pass 8 data. These results are consistent with our upper limit results not included in this paper. The significance of the source is negligible over the entire energy range. We, therefore, investigated energy bins that contribute more to the possible emission. Our aim was to check if there is any energy bin with significance values above the Fermi detection threshold. In our results, we saw that in most of the energy bins the source is insignificant except for a few energy bins with significance that barely exceed 2σ . The energy range with 2σ significance is above the energy range that is most affected by the background contamination, therefore if this is a false detection it cannot be attributed to the influence of the background.

The TS and residual maps produced for the full energy range did not confirm any significant increase in gamma-ray emission at the target region as compared to the background (see Figure

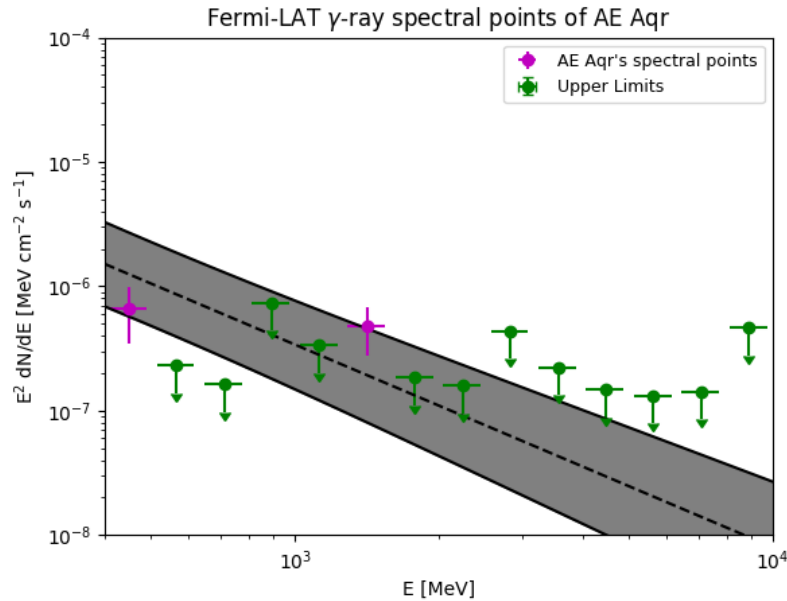


Figure 4: Spectral data points generated on the energy range 0.4-10 GeV, this is the energy range that has the largest significance.

2). The TS map shows that the significance of the target region was less than 2σ significance. This could be because the source is faint due to its proximity to the galactic plane ($b = -0.87$), which causes an increase in the background. Along the latitude of AE Aqr on the left and right of Figure 2, there are two gamma ray sources that are not modelled because they are not in the 3FGL catalog. Since these sources were not modelled they can influence our results. However, the detection of SED points above the *fermipy* threshold shows that there is a possibility of an increase in gamma-ray activity at the region of AE Aqr. Whether this increased activity is just transient or also periodic in nature and could be linked directly to AE Aqr is still to be investigated further.

Most of the gamma ray Fermi-LAT sources in the ROI are hidden in the background. The background in this region is brighter than most sources as seen in the counts map (see, Figure 1). Even the model map shows that the number of predicted counts for each source still results in some sources with negligible counts (see Figure 1). Therefore the new model of the isotropic diffuse background and the diffuse galactic emission model for the 4FGL catalog will likely produce better results.

Acknowledgements

The authors thank the organisers for the opportunity to present this work at the SAIP 2018 conference. They also want to extend their gratitude to the University of the Free State (UFS) postgraduate school and the UFS Department of Physics for assistance. The financial assistance of the National Research Foundation (NRF) towards this research is also acknowledged. Opinions expressed and conclusions arrived at, are those of the author and are not necessarily to be attributed to the NRF.

References

- [1] Joy A H 1954 ApJ **120** 377

- [2] Crawford J A and Kraft R P 1956 ApJ **123** 44
- [3] Chincarini G and Walker M F 1981 A&A **104** 24–32
- [4] Meintjes P J, Odendaal A and van Heerden H J 2015 *Acta Polytechnica CTU Proceedings* **2** 86–89
- [5] Zinner E 1938 *Astronomische Nachrichten* **265** 345–352
- [6] Wynn G A, King A R and Horne K 1997 MNRAS **286** 436–446
- [7] Meintjes P J and Venter L A 2005 MNRAS **360** 573–582
- [8] Bookbinder J A and Lamb D Q 1987 ApJ **323** L131–L135
- [9] Bastian T S, Dulk G A and Chanmugam G 1988 ApJ **324** 431–440
- [10] Patterson J 1979 ApJ **234** 978–992
- [11] Eracleous M and Horne K 1996 ApJ **471** 427
- [12] Oruru B and Meintjes P J 2012 MNRAS **421** 1557–1568
- [13] Venter L A and Meintjes P J 2006 MNRAS **366** 557–565
- [14] Meintjes P J 1989 *M.Sc Thesis (Potchefstroom Univ. for CHE)*
- [15] Meintjes P J 1992 *Thesis (Potchefstroom Univ. for CHE)*
- [16] Meintjes P J, De Jager O C, Raubenheimer B C, Nel H I, North A R, Buckley D A H and Koen C 1994 ApJ **434** 292–305
- [17] Bowden C C G, Bradbury S M, Chadwick P M, Dickinson J E, Dipper N A, Edwards P J, Lincoln E W, McComb T J L, Orford K J, Rayner S M *et al.* 1992 *ASTROPART PHYS* **1** 47–59
- [18] van Heerden H J and Meintjes P J 2015 *Mem. Soc. Astron. Ital.* **86** 111
- [19] Acero F, Ackermann M, Ajello M, Albert A, Baldini L, Ballet J, Barbiellini G, Bastieri D, Bellazzini R, Bissaldi E *et al.* 2016 ApJ **223** 26
- [20] Mattox J R, Bertsch D, Chiang J, Dingus B, Digel S, Esposito J, Fierro J, Hartman R, Hunter S, Kanbach G *et al.* 1996 ApJ **461** 396
- [21] Li J, Torres D F, Rea N, de Ona Wilhelmi E, Papitto A, Hou X and Mauche C W 2016 ApJ **832** 35

Did Dark Matter Kill the Dinosaurs?

Michael Sarkis and Geoff Beck

School of Physics, University of the Witwatersrand, Private Bag 3, WITS-2050, Johannesburg, South Africa

E-mail: michael.sarkis@students.wits.ac.za; geoffrey.beck@wits.ac.za

Abstract. Potential links between astrophysical sources, such as gamma ray bursts and supernovae, and mass extinction events on Earth are of interest in the historical trajectory of life on our planet. There are strong arguments to suggest that these astrophysical sources can have several destructive effects, including depletion of atmospheric ozone and an increase in the radiation dose received by living organisms. Recently, the possibility of galactic dark matter clumps having an affect on life on Earth has been of some interest in the literature. In this work, it is shown that when the Earth passes through clumpy dark matter composed of WIMPs, there will be an increase to the internal heat flow of the Earth of as much as ~ 3706 TW, leading to increased flood-basalt volcanism. There will also be an equivalent dose of ~ 15.9 μSv imparted to organic tissue due to collisions between WIMPs and oxygen nuclei. If WIMPs are found to be a major constituent of dark matter, these effects could provide a supporting explanation for mass extinction events on Earth.

1. Introduction

Throughout the history of life on Earth, there have been periods in which a significant percentage of all living species become extinct. In the past these mass extinction events have been linked with several proposed causes - comet impacts with the Earth, flood-basalt volcanism, and rapid climate change. It has been suggested [1–4] that mass extinction events over the past 250 million years have been periodic, occurring at regular intervals of time. Periods of 26-62 million years have been found to match the extinction record with a high statistical significance, and an explanation for this periodicity could be provided by astrophysical sources, in particular galactic Dark Matter (DM) that resides in the solar system's galactic orbit.

Large scale numerical simulations based on the principles of structure formation in the universe have shown that DM tends to clump together in the form of halos [5–8]. Further, it is believed that substructure is present in these halos, with regions of comparatively high DM density or clumps, interspersed inside the surrounding halo. Several density profiles have been used to model these halos, with more sophisticated simulations leading to more complex profiles. Recently, a proposed halo profile dubbed the UltraCompact MiniHalo (UCMH) [9] has been of interest for its potential to account for microlensing observations of compact objects in the area around our solar system [10–13]. This profile has an extremely steep radial density dependence compared to other halos, and will be used as the model of choice in this work. The DM component of these halos will be considered to be composed of Weakly-Interacting Massive Particles (WIMPs), a generic candidate DM particle.

If the solar system were to interact with a clump of DM, there could be many unfavourable implications for life on our planet, and some of the hypothesised interactions between DM and

the Earth lead to effects that are in agreement with the currently accepted causes of mass extinction events. There has been research conducted into the possibility of a galactic disk of DM gravitationally perturbing the Oort cloud of our solar system, leading to an increase in the number of comets that reach the Earth [14,15]. This corresponds to one of the leading explanations for the extinction event at the Cretaceous-Paleogene boundary ~ 65.5 My ago [16]. There has also been research conducted into the increase in volcanic activity of the Earth due to the heat generated from annihilating DM particles that have been captured in the core of the Earth [17,18], which could correspond to a likely cause of the Permian-Triassic extinction event [19]. There has also been research into the carcinogenic effect of DM particle collisions with organic tissue [20,21], which has obvious harmful implications for life, but could also provide a mechanism for the observed explosions in biodiversity shortly after several mass extinction events. Whether individually or combined, the potential of the above effects to disrupt life on Earth could support the hypothesis that mass extinction events on the Earth have an astrophysical origin.

The structure of this paper will be as follows: in section 2 we present the UCMH model used, in section 3 we discuss the hypothesis of DM capture and the generation of heat in the core of the Earth, and in section 4 we discuss the possibility of carcinogenesis resulting from WIMP collisions with tissue elements. These results are then summarised in section 5.

2. Ultracompact Dark Matter Minihalos

When the existence of UCMHs was proposed by [9], it was largely motivated by the potential for these objects to be observed using microlensing experiments. It is argued that UCMHs could provide a unique probe of the early universe, as they are believed to have formed in a similar way to primordial black holes - seeded by random density perturbations that underwent gravitational collapse and subsequent growth during the radiation and matter dominated epochs. However, the amplitude of the initial density perturbations needed to seed UCMHs would be weaker than those needed to form a black hole, which could make their existence more likely than primordial black holes.

The principles of structure formation and secondary infall predict that halos formed in this way would presently consist of a dense core of DM surrounded by a relatively sparse envelope of accreted dark and baryonic matter. The radial density profile of these objects is then given by

$$\rho_\chi(r) = \frac{3}{16\pi} \frac{\Omega_\chi}{\Omega_m} \frac{M_{\text{UCMH}}}{R_{\text{UCMH}}^{\frac{3}{4}} r^{\frac{9}{4}}}, \quad (1)$$

where Ω_χ/Ω_m are the usual density parameters for dark matter and the total matter content of the universe. R_{UCMH} is the radius of the UCMH at a given redshift, given by

$$R_{\text{UCMH}}(z) = 0.019 \left(\frac{1000}{1+z} \right) \left(\frac{M_{\text{UCMH}}}{M_\odot} \right)^{\frac{1}{3}} \text{ pc}. \quad (2)$$

In this work the redshift is chosen to be $z = 10$, as this corresponds to the redshift at which accretion onto the UCMH ends - effectively setting the present radius of the UCMH. The masses of the UCMHs used follow the relatively conservative estimates adopted in [20]. The profile in (1) breaks down at radii close to the centre of the halo, when the approximation of radial infall is violated. This is remedied by considering the annihilation of WIMPs in the core, which provides an upper limit on the density at the center of the halo. As in [22,23], this is estimated as

$$\rho_{\chi,\text{max}} \equiv \rho_\chi(r_{\text{cut}}) \approx \frac{m_\chi}{\langle \sigma v \rangle (t_0 - t_i)}, \quad (3)$$

where $\langle\sigma v\rangle$ is the WIMP self annihilation cross section, t_0 is the age of the universe and t_i is the time of halo collapse, estimated here as $t_i = t(z_{eq}) \approx 59$ Myr. The density inside the radius r_{cut} is then set to the value of ρ_{max} .

3. Heat Generation and Volcanic Activity

The production of excess heat in the core of the Earth and the subsequent increase in volcanic activity due to DM capture was investigated by Ref. [17, 18], where it was found that DM clumps with high density could generate an extreme amount of heat through WIMP annihilation. According to Ref. [17], the energy produced by collisions between nuclei in the Earth's core and annihilation products of captured WIMPs would dissipate as heat from the core into the lower layers of the mantle, rendering them unstable. Plumes of molten mantle material formed by the breaking up of these layers would then carry the heat upwards through the Earth, creating volcanic rifts and flood basalts when they ultimately reach the surface.

The amount of heat (Q) generated by annihilating WIMPs that have been captured in the Earth's core is calculated as

$$Q = C \cdot m_\chi \cdot e, \quad (4)$$

where C is the capture rate of WIMPs and e represents the fraction of all WIMP annihilations that will lead to energy transfer in the core of the Earth, which is estimated as 0.5.

3.1. WIMP capture rate

The form of the capture rate used in [17, 18] does not consider resonant effects, identified by Ref. [24], which enhance the capture rate when the WIMP mass is similar to the mass of elements found in the Earth's core. A practical form of this improved capture rate equation, when applied to capture by the Earth, is

$$C = 4.0 \times 10^{16} \text{s}^{-1} \left(\frac{\rho_\chi}{0.4 \text{ GeV c}^{-2} \text{ cm}^{-3}} \right) \left(\frac{\mu}{\mu_+^2} Q^2 f \right) \left\langle \hat{\phi} \left(1 - \frac{1 - e^{(-A^2)}}{A^2} \right) \xi_1(A) \right\rangle. \quad (5)$$

In this form, ρ_χ represents the density of WIMPs, the factor $(\mu/\mu_+^2 Q^2 f)$ sets the WIMP-nucleon scattering cross section and the final bracket is a calculation of the suppression/enhancement of capture resulting from differences in mass between WIMPs and nuclei in the Earth (for a detailed explanation of WIMP capture, the reader is referred to [24]). This “resonance” can be clearly seen in Figure 1 by the peaks which occur at WIMP masses that are similar to the most abundant elements in the Earth's core. Further, it should be noted that this equation only considers direct capture of WIMPs, and any WIMPs that don't lose enough energy to be captured but undergo subsequent interactions with the Earth could enhance this capture rate by as much as a factor of 100.

3.2. Updated cross sections from LUX experiment

The WIMP-nuclei cross sections used in [17], when used with the capture rate, lead to large amounts of produced heat when compared to the DM-independent internal heat flow of the Earth, which has been found using terrestrial borehole experiments to be ~ 44.2 TW [25]. The latest (2017) results from the Large Underground Xenon (LUX) experiment [26] suggest significantly lower cross-sections, which leads to a suppression of the overall heat generation. The total heat generated when the Earth passes through an UCMH using Equation 5 and the LUX cross-sections can be seen in Figure 1. Using the values for the heat capacity and mass of the core of the Earth used in [18], this temperature increase can be estimated, and it was found that for the relatively small UCMH mass used in [20], $\Delta T = 0.037$ K. For a UCMH mass of $100 M_\odot$, this value increases to $\Delta T = 3.9$ K. These changes in temperature are much lower than the quoted

values in [18], and small compared to the temperature of the Earth's core without DM effects, believed to be thousands of K [27].

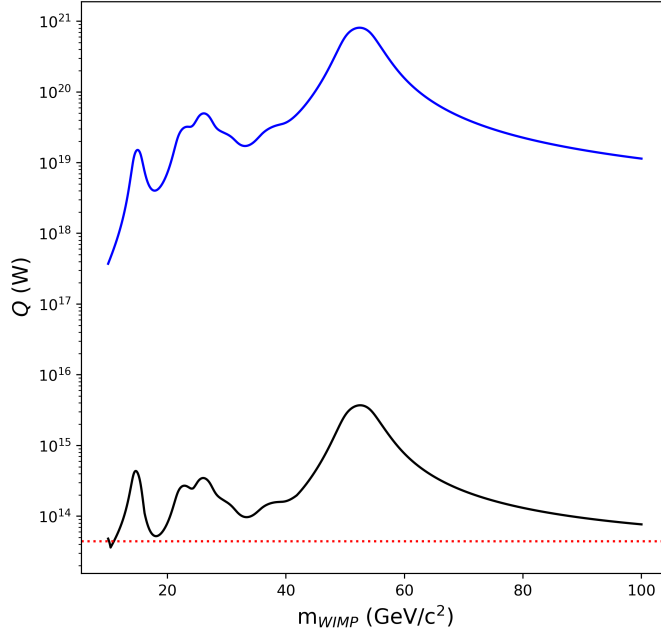


Figure 1. The total amount of heat generated by annihilating WIMPs captured in the core of the Earth during traversal of an UCMH. The blue curve represents the heat generated using previous estimates of the WIMP-nuclei scattering cross sections, and the black curve shows heat generated using the 2017 data on cross-sections from the LUX experiment. The dotted red line at 44.2 TW shows the DM-independent heat flow of the Earth. The largest peak occurs at $m_\chi = m_{56Fe}$, with a maximum value of $Q = 3706$ TW.

4. Carcinogenesis from WIMPs

There is evidence that suggests ionising radiation is a "universal carcinogen", able to form cancers in most of the tissue types of most species, at any age [28]. This could help support claims that mass extinction events have been partly or fully caused by large increases in the radiation levels received by living organisms on Earth. A hypothesis proposed in Ref. [20] tries to estimate the efficacy of carcinogenesis for WIMPs inside a DM clump that pass directly through the Earth. By investigating the deposition of energy into tissue, from direct collisions of WIMPs and secondary recoiled oxygen nuclei, it was proposed that these effects would have a non-negligible impact on life on the planet. This hypothesis was later revisited by Ref. [21], where it was found that this effect would have a much weaker impact than estimated before.

4.1. Estimating the efficacy of carcinogenesis from WIMPs

A measure of the health risk associated with exposure to different radiation types, called the equivalent dose, is defined as

$$\text{equivalent dose (Sv)} = RBE \cdot \text{absorbed dose (Gy)}, \quad (6)$$

where RBE stands for the Relative Biological Effectiveness value, and the absorbed dose represents the amount of energy deposited into a target material by the radiation. The absorbed dose is measured in units of J/kg or Gy (gray) and is independent of the radiation type. The RBE is a number used to scale the effectiveness of different radiation types, and is conventionally defined relative to a specific type, usually X-rays.

The equivalent dose, having units of J/kg but measured specifically in Sv (sievert), represents the stochastic health risk associated with exposure to different radiation types. To find this value, the absorbed dose and RBE values for WIMPs and recoiled nuclei need to be estimated. Since oxygen nuclei constitute the majority of all recoiled tissue nuclei [20, 21], this work only considers the effects of recoiled oxygen nuclei. This approximation produces accurate results for simple tissue compositions, but more detailed tissue compositions would require an analysis

involving all recoiled nuclei. The approximate absorbed dose was calculated by multiplying a scattering rate S by the average recoil energy $\langle T \rangle$ and the duration of a typical clump crossing, for a range of WIMP masses. The scattering rate was calculated as

$$S = \left(\sum_i \frac{f_i(\sigma_N, m_\chi, m_i)}{m_i} \right) \left(\frac{\rho_\chi}{m_\chi} \right) v_{\text{disp}}, \quad (7)$$

where the index i represents each element found in the tissue, f is a total scattering cross section, σ_N is the spin-independent (SI) WIMP-nucleon cross section, and ρ_χ , v_{disp} are the WIMP density and velocity dispersion. The LUX results [26] were used for the WIMP-nucleon cross section.

RBE values for specific types of radiation are usually quantified through experiment. It was found in Ref. [29] that the RBE of several heavy-ions depends both on the absorbed dose and on the Linear Energy Transfer (LET) value, which is a measure of the length scale in which the radiation deposits its energy into the tissue. This dependence showed a peak in the RBE when the LET value was in the range 100-200 keV/ μm , with higher RBE when the dose rate was low. SRIM [30] was used to estimate the LET of oxygen nuclei recoiled from collisions with WIMPs, having an average energy of 25 keV and incident on a representative tissue composition [20]. The results, which show energy deposition via ionisation and the generation of phonons, are shown in Figure 2. Because the LET of WIMP collisions with tissue elements at this time have not been estimated, and under the naive assumption that the RBE of WIMPs is also dependent on the LET value, the RBE and any further effect of direct WIMP collisions has to be neglected.

4.2. Results

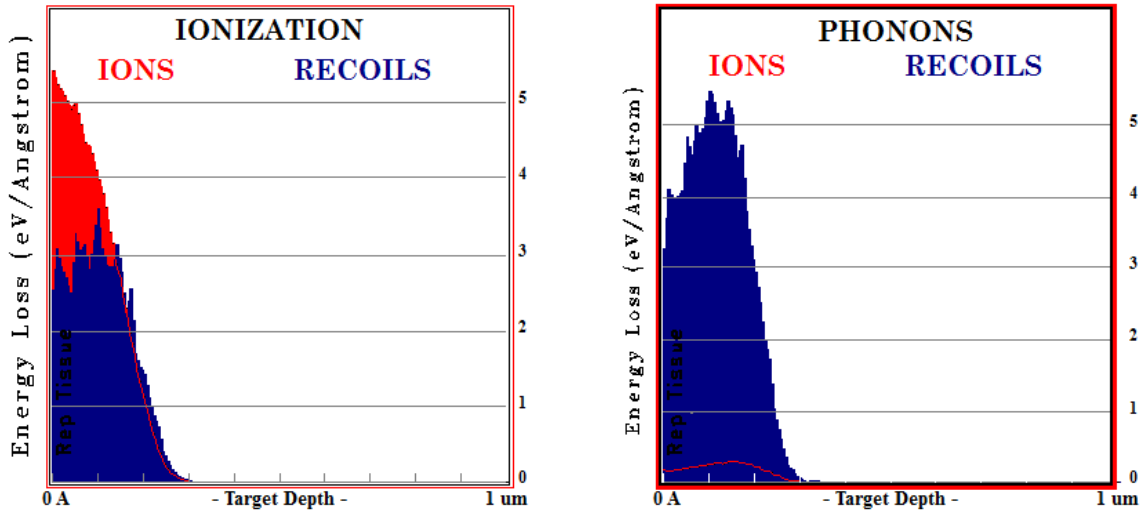


Figure 2. Energy deposition into representative tissue $\text{C}_4\text{H}_{40}\text{O}_{17}\text{N}$ used by Ref. [20] from an oxygen ion of 25 keV, by ionisation of target material and by phonons produced by incident ion. The maximum total LET for oxygen in this tissue type is $\sim 138 \text{ keV}/\mu\text{m}$.

The total LET of recoiled oxygen nuclei in a representative tissue composition was found to be approximately $138 \text{ keV}/\mu\text{m}$. An estimate of the RBE corresponding to this LET value is taken from [31], which set a range of 1.9-3.1 for the RBE of oxygen nuclei incident on human HCC cell lines at an LET of $146 \text{ keV}/\mu\text{m}$. These values, when used together with the typical duration of a clump crossing in the calculation of the equivalent dose for oxygen recoils, yield

a maximum dose of 1.5935×10^{-5} Sv. When compared to the average natural radiation dose rate of 0.4-44 mSv/year [21] protracted over the same period, the risk of this effect having a significant effect on large populations seems unlikely.

5. Conclusion

The possibility of Earth interacting with a dense clump of DM could bring with it disruption to life on Earth. The generation of heat from annihilating WIMPs in the core of the Earth can lead to temperature increases of up to 3.9 K for large UCMHs. Although the instantaneous heat generation is large, the global and long-term effects from the small temperature changes are uncertain. Also, the onset of cancers from recoiled oxygen collisions with tissue elements leads to an equivalent dose of $\sim 15.9 \mu\text{Sv}$, the effect of which could be enhanced if direct WIMP collisions have an LET value that is conducive to DNA damage.

The results from both of these hypotheses are lower than previous estimates, which can be attributed to the new WIMP cross section limits obtained by the LUX experiment. However, when these effects are considered with other potential mechanisms for extinction from DM like gravitational perturbations of the Oort cloud, they could still provide a supporting explanation for mass extinction events on Earth.

Acknowledgments

This work is based on the research that was supported by the South African Research Chairs Initiative of the Department of Science and Technology and National Research Foundation of South Africa (Grant No 77948).

References

- [1] Raup D and Sepkoski Jr J 1984 *Proc. Natl. Acad. Sci. USA* **81** 801-805
- [2] Rampino M and Caldeira K 2015 *MNRAS* **454.4** 3480-3484
- [3] Rohde R and Muller R 2005 *Nature* **434** 208-210
- [4] Lieberman B and Melott A 2007 *PLoS ONE* **2** 1-9
- [5] Navarro J, Frenk C and White S 1997 *ApJ* **490** 493-508
- [6] Stadel J, et al. 2009 *MNRAS* **398** L21-L25
- [7] Burkert A 1995 *ApJ* **447** L25-L28
- [8] Kuhlen M, Vogelsberger M and Angulo R 2012 *Physics of the Dark Universe* **1** 50-93
- [9] Ricotti M and Gould A 2009 *ApJ* **707** 979-987
- [10] Tisserand P, et al. 2007 *A&A* **469** 387
- [11] Alcock C, Allsman R, Alves D, et al. 2000 *ApJ* **542** 281
- [12] Uglesich R, Crotts A, Baltz E, et al. 2004 *ApJ* **612** 877
- [13] Riffeser A, Fliri J, Bender R, et al. 2003 *ApJ* **599** L17
- [14] Randall L and Reese M 2014 *Phys. Rev. Lett.* **112** 161301
- [15] Kramer E and Rowan M 2017 *preprint: arXiv:1610.04239v2* [astro-ph.EP]
- [16] Schulte P, et al. 2010 *Science* **327** 1214-1218
- [17] Abbas S and Abbas A 1998 *Astroparticle Physics* **8** 317-320
- [18] Rampino M 2015 *MNRAS* **448** 1816-1820
- [19] Campbell I, Czamanske G, Fedorenko V, Hill R and Stepanov V 1992 *Science* **258** 1760-1763
- [20] Collar J 1996 *Physics Letters B* **368** 266-269
- [21] Freese K and Savage C 2012 *Physics Letters B* **717** 25-28
- [22] Ullio P, Bergstrm L, Edsj J and Lacey C 2002 *Phys. Rev. D* **66** 123502
- [23] Bringmann T, Scott P and Akrami Y 2012 *Phys. Rev. D* **85** 125027
- [24] Gould A 1987 *ApJ* **321** 571-585
- [25] Mack G, Beacom J and Bertone G 2007 *Phys. Rev. D* **76** 043523
- [26] Akerib D, et al. 2017 *Phys. Rev. Lett.* **118** 021303
- [27] Boehler R 1993 *Nature* **363** 534-536
- [28] Little J 2000 *Carcinogenesis* **21.3** 397-404
- [29] Yang T, Craise L, Mei M and Tobias C 1985 *Radiat. Res., Suppl.* **8** 104 S-177-S-187
- [30] Ziegler J, Ziegler M and Biersack J 2010 *Nucl. Instrum. Methods Phys. Res. B* **268** 1818-1823
- [31] Habermehl D, et al. 2014 *PLoS ONE* **9(12)** e113591

Probing quantum gravity at low energies

Justine Tarrant, Geoff Beck, and Sergio Colafrancesco

School of Physics, University of the Witwatersrand, Private Bag 3, WITS-2050, Johannesburg, South Africa

E-mail: justine.tarrant@wits.ac.za, geoffrey.beck@wits.ac.za,
sergio.colafrancesco@wits.ac.za

Abstract. Planck stars form when a collapsing shell of matter within a black hole reaches the Planck density, roughly equivalent to the mass being compressed into a volumetric size near that of the proton, and rebounds outwards. These Planck stars have been considered as accounting for both non-repeating fast radio bursts and short gamma ray bursts, whilst offering a comparatively low energy perspective onto quantum gravity. The observation of such an event would require black hole masses much smaller than a solar mass, which could be provided by primordial black hole dark matter models. We discuss the low energy isotropic background emissions produced by decaying primordial black holes at all epochs and derive constraints from the spectrum of the extragalactic background light. We find that, in order to avoid exceeding known extragalactic background light emissions, we must restrict the total energy emitted at low frequencies by a Planck star exploding in the present epoch to be less than 10^{13} erg or restrict the primordial black hole population far below any existing limits. This casts doubt on whether exploding Planck stars could actually account for non-repeating fast radio bursts, as they are speculated to in the literature.

1. Introduction

The concept of a “Planck star” has been proposed in the literature [1] as producing both non-singular black hole spacetimes and solving the information-loss problem [2, 3]. It is argued, through loop quantum gravity calculations [4], that the collapsing shell of matter within the event horizon will stop collapsing at a finite density (the Planck density) due to quantum-gravitational pressure [1] and then proceeds to bounce outward in a manner similar to certain collapsing universes in loop quantum cosmology [5]. The now expanding matter within the black hole then tunnels through the horizon producing a white hole [6]. The bounce and tunnelling happen very rapidly in the rest-frame of the black hole [1], but due to time dilation the process takes longer than the lifetime of the universe for black holes above $10^{-7} M_{\odot}$ [7, 6] but remains more rapid than Hawking evaporation [1]. The photon gas, captured during Primordial Black Hole (PBH) formation in the early universe, and then released by the white hole retains a temperature on the order of a TeV [8]. This intriguing possibility has been argued [6] to be able to account for both fast radio bursts [9], with dimensional arguments for emissions around a wavelength equal to the black hole diameter [8], and short gamma-ray bursts provided by the escaping photon gas [8]. Moreover, this scenario offers a comparatively low energy window into the physics of quantum gravity. However, observing such an event requires the presence of black holes with masses considerably below that of the sun.

Fortunately, the possibility of the formation of low-mass PBHs in the very early universe

has a long history in the literature (an early argument can be found in [10]) and have often been put forward as potential candidates for dark matter [11]. Early interest was focussed upon PBHs with masses below that of the sun, but, stringent constraints (see [12] and references therein) prevent PBHs from composing a large fraction of cosmologically relevant dark matter. These constraints, however, assumed the mass distribution of PBHs to be monochromatic and recent work has been able to show that extended mass distributions can either evade [13] or satisfy [14] the constraints that ruled out PBHs as a major component of cosmological dark matter. These works focussed on lognormal differential mass distributions, as these have been shown to approximately model the seeding of PBH density perturbations by many different inflationary scenarios [15, 16, 17]. In particular, the distributions satisfying existing constraints and supplying the bulk of cosmological dark matter have a mean mass around $10 M_\odot$ [14] which has been part of a new interest in more massive PBHs [18, 19, 20] as it correlates with the mass range of black holes observed by LIGO [21].

In this work we will study the possibility of an isotropic radio background produced by exploding Planck stars using lognormal mass distributions that evade the existing constraints (with a mean mass around $10^{-9} M_\odot$ [13]) and those that satisfy constraints [14] (with a mean mass in the LIGO range). This will be done by comparing predicted background spectra to those of known isotropic backgrounds in the same frequency range, known as the Extragalactic Background Light (EBL) with data taken from [22] and references therein. We use this comparison to determine a limit on the maximum fraction of the mass-energy of the PBH that is converted into radio emissions as it decays through the Planck star mechanism. In particular we show that, for both PBH mass distributions studied, the maximal energy in radio emissions is around 10^{13} erg (at a 3σ confidence interval) for a $10^{-7} M_\odot$ PBH exploding in the present epoch. This suggests that such Planck star explosions cannot act as a candidate for fast radio burst emission. These are the first stringent empirical constraints placed on this quantum gravity scenario for black hole decay.

This paper is structured as follows: in section 2 we lay out the formalism for calculating the low-frequency background produced by decaying PBHs up until the present epoch. In section 3 we detail the EBL data used and how we draw constraints from it. Finally, in section 4 and 5 we display and discuss our results.

2. Low-Frequency Emission

The flux of the low-frequency background radiation generated by exploding Planck stars from the time of matter radiation equality will be taken to be

$$\Phi(\lambda) = \int_{z_{eq}}^0 dz \frac{dV}{dz} N_\tau(z) \frac{d\tau}{dz} \frac{c}{2R_{BH}(z)} \frac{\chi(\lambda, z)}{4\pi D_L^2}, \quad (1)$$

where $\frac{dV}{dz}$ is the differential co-moving volume element, $\frac{2R_{BH}(z)}{c}$ is the assumed time taken for emission of the energy of the PBH exploding at z , $N_\tau(z)$ is the differential density of exploding Planck stars per unit time at redshift z , $\chi(\lambda, z)$ is the spectral energy distribution of an individual explosion and D_L is the co-moving distance at redshift z .

N_τ we calculate as follows: take some differential density of primordial black holes per unit mass $N(M)$ and

$$N(M)dM = N(\tau)d\tau. \quad (2)$$

Thus, using the relation for the lifetime τ of the black hole of mass M [1]

$$\tau = \left(\frac{M}{M_{pl}} \right)^2 t_{pl}, \quad (3)$$

we can find the necessary factor of $\frac{dM}{d\tau}$. Here t_{pl} and M_{pl} are the Planck time and mass respectively. The form of $N(M)$ will be taken, following both [14, 13], to be lognormal, as this has been shown to fit a wide range of inflationary formation models for PBHs [15, 16, 17]. $N(M)$ will then be normalised to some fraction f_{pbh} of the total dark matter density being composed of primordial black holes.

At present the functional shape of χ is unknown for low frequencies [7, 8]. However, it is argued in [7, 1, 6] that the majority of low-frequency emission will take place at a wavelength equal to twice the radius of the exploding black hole R_{bh} . Therefore, we will assume the function χ has a thermal shape and peaks at $\lambda = 2R_{bh}$. The energy emitted in radio will then be normalised to some fraction χ_0 of the total mass-energy of the black hole. Additionally, cosmological redshift effects must be taken into account, we do so with the formula [6]

$$\lambda_{obs} \sim \lambda_{em}(1+z) \sqrt{\frac{H_0^{-1}}{6k\Omega_\Lambda^{1/2}} \sinh^{-1} \sqrt{\frac{\Omega_\Lambda}{\Omega_m(1+z)^3}}} , \quad (4)$$

where λ_{obs} and λ_{em} are the observed and emitted wavelengths, H_0 is the Hubble constant from [23], Ω_m and Ω_Λ are the matter and cosmological constant density parameters (also from [23]), and $k = 0.05$ is a pure number originating from loop quantum gravity calculations [4].

3. EBL Data

We source EBL spectral data from [22] and references therein. This will then be compared to the projected low-frequency background emission from Planck star explosions. This comparison will be informative as we should expect the Planck star emissions over all epochs to contribute an extra component to isotropic low-frequency backgrounds. Any value of the free parameter product $f_{pbh}\chi_0$ that allows the Planck star spectrum to exceed the known background by 3σ confidence level or more is then taken as excluded.

4. Results

In figure 1 we see an example where we take a mass function $N(M)$ from [14] with mean $\mu = 10.0 M_\odot$ and deviation $\sigma = 0.25$ (as this can have PBHs constitute almost all dark matter when considering limits from the CMB, micro-lensing, and ultra-faint dwarf galaxies). The minimal χ^2 fitting performed yields a result that $\chi_0 f_{pbh} < 10^{-34}$. Since for this model of the PBH mass function $f \sim 1$ [14], we can see that this yields an extremely stringent limit on the amount of energy emitted in low-frequency by these Planck star explosions. If we take a Planck star, exploding at the present epoch, with mass $\sim 10^{-7} M_\odot$ the total energy yield of the explosion is $\sim 10^{47}$ erg, making it an attractive prospect for explaining non-repeating fast radio bursts [6, 8]. However, with such a severe constraint available we can see that the energy in radio is $\lesssim 10^{13}$ erg. Alternatively we can assume the Planck star supplies a large portion of its energy to radio emission and thus can explain a non-repeating fast radio burst. Then we must conclude that it is f_{pbh} that is extremely tiny and then that very few radio bursts could be the result of Planck star events.

Additionally, we repeated this calculation when $\mu = 10^{-9} M_\odot$ and $\sigma = 0.5$, shown in [13] to be able to constitute $f_{pbh} \sim 1$ by evading any constraints, we still find that $\chi_0 f_{pbh} < 10^{-35}$.

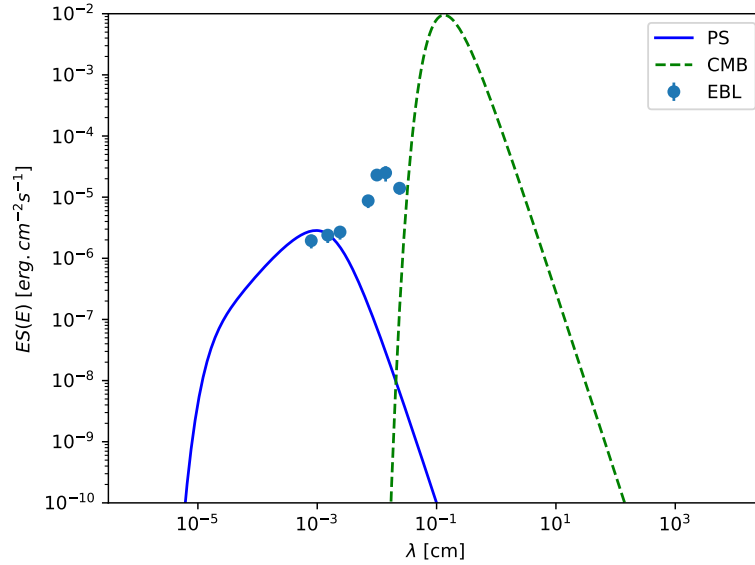


Figure 1. Comparison of low-frequency Planck star background (PS) to EBL data from [22] and the CMB spectrum [23]. Values of $\chi_0 f_{pbh} > 10^{-34}$ are excluded at a 3σ confidence level.

5. Conclusions

We have demonstrated that, using EBL data, we can restrict the total energy emitted at low frequencies by a Planck star object exploding in the present epoch to $\lesssim 10^{13}$ erg, or that only a tiny PBH population is compatible with the Planck star hypothesis. This constraint depends slightly upon the choice of primordial black hole mass distribution. However, we employ a mass distribution model that is shown to approximately describe a wide range of models where the PBH over-densities are seeded by inflation [15, 16, 17]. Despite our two featured mass-function models differing in their mean PBH mass by many orders of magnitude only one order of magnitude separates their limits on the Planck star low frequency emissions. We note that, although the spectral energy distribution of the explosion is unknown at low energies, we employ a simple thermal model due to its steeply peaked nature and thus do not expect the exact nature of the distribution to strongly effect these limits (as the distribution is expected to be steeply peaked anyway [6]). An additional consideration one could take would be whether Planck star emissions are beamed, which would require a revision to our use of an isotropic equivalent flux, and comparison to an isotropic background. To fully consider this point, however, would require a definite mechanism for the low frequency emissions and possibly a careful analysis of the white-hole spacetime produced by the Planck star tunnelling through the event horizon of the PBH. Beaming scenarios are therefore left to future work, with the caveat that our results here assume no beaming takes place.

Thus, the constraints derived here cast doubt upon whether or not exploding Planck stars, described by the model employed here, could account for non-repeating fast radio bursts as speculated by [6, 8], as their low-energy output is shown here to be comparatively small in order for emissions over all epochs to avoid exceeding the known low frequency isotropic backgrounds with both viable PBH distributions used. In addition, even if their energy production is sufficient for a fast radio burst, this would place extremely strong limits on the population of PBHs compatible with the Planck star scenario. This, in turn, could imply such explosion events must be very uncommon and could explain very few fast radio burst events.

Acknowledgments

This work is based on the research supported by the South African Research Chairs Initiative of the Department of Science and Technology and National Research Foundation of South Africa (Grant No 77948).

References

- [1] Rovelli C and Vidotto F 2014 *Int. J. Mod. Phys.* **D23** 1442026 (*Preprint* 1401.6562)
- [2] Hawking S 1975 *Comm. Math. Phys.* **43** 199
- [3] Hawking S 1976 *Phys. Rev. D* **14** 2460
- [4] Haggard H M and Rovelli C 2015 *Phys. Rev.* **D92** 104020
- [5] Ashtekar A, Pawłowski T, Singh P and Vandersloot K 2007 *Phys. Rev.* **D75** 024035 (*Preprint* gr-qc/0612104)
- [6] Barrau A, Rovelli C and Vidotto F 2014 *Phys. Rev.* **D90** 127503 (*Preprint* 1409.4031)
- [7] Barrau A and Rovelli C 2014 *Phys. Lett.* **B739** 405–409 (*Preprint* 1404.5821)
- [8] Rovelli C 2017 *Nat. Astron.* **1** 0065 (*Preprint* 1708.01789)
- [9] Lorimer D R *et al.* 2007 *Science* **318** 777
- [10] Hawking S 1971 *MNRAS* **152** 75
- [11] Hawkins M R S 2011 *MNRAS* **415** 2744
- [12] Capela F, Pshirkov M and Tinyakov P 2013 *Phys. Rev.* **D87** 123524
- [13] Kühnel F and Freese K 2017 *Phys. Rev.* **D95** 083508 (*Preprint* 1701.07223)
- [14] Bellomo N, Bernal J L, Raccanelli A and Verde L 2018 *JCAP* **01** 004
- [15] Dolgov A and Silk J 1993 *Phys. Rev.* **D47** 4244
- [16] Dolgov A D, Kawasaki M and Kevlishvili N 2009 *Nucl. Phys.* **B807** 229
- [17] Blinnikov S, Dolgov A, Porayko N K and Postnov K 2016 *JCAP* **1611** 036
- [18] Clesse S and Garca-Bellido J 2015 *Phys. Rev.* **D92** 023524 (*Preprint* 1501.07565)
- [19] Carr B, Kühnel F and Sandstad M 2016 *Phys. Rev.* **D94** 083504 (*Preprint* 1607.06077)
- [20] Carr B and Silk J 2018 *MNRAS* **478** 3756
- [21] Bird S *et al.* 2016 *Phys. Rev. Lett.* **116** 201301 (*Preprint* 1603.00464)
- [22] Franceschini A and Rodighiero G *A&A* **603** A34
- [23] Ade P *et al.* 2016 *A&A* **594** A13

Implications for gamma-ray production from updated orbital parameters for LMC P3 with SALT/HRS

B van Soelen,¹ N Komin,² D du Plooy,¹ P Väisänen,^{3,4} A Kniazev^{3,4}

¹University of the Free State, 9300, Bloemfontein, South Africa

²University of the Witwatersrand, Johannesburg, South Africa

³South African Astronomical Observatory, PO Box 9, Observatory, 7935, Cape Town, South Africa

⁴Southern African Large Telescope, PO Box 9, Observatory, 7935, Cape Town, South Africa

E-mail: vansoelenb@ufs.ac.za

Abstract. The recently discovered LMC P3 is the most luminous gamma-ray binary detected to date. The source was discovered with *Fermi*-LAT gamma-ray observations which showed a 10.301 ± 0.002 d period. The gamma-ray emission is associated with the previously detected point-like X-ray source CXOU J053600.0-67350, within the supernova remnant DEM L241, and this binary was previously classified as a high mass X-ray binary where the optical companion is a O5III(f) star. The source has also been detected at very high energies with the H.E.S.S. gamma-ray telescope, though in only one phase bin. We have used the High Resolution Spectrograph (HRS) with the Southern African Large Telescope (SALT) to obtain the best binary solution so far for this source, showing that source is slightly eccentric (~ 0.4) and constrained the phases of superior and inferior conjunction. The *Fermi*-LAT and H.E.S.S. results are discussed in relation to the new binary solution.

1. Introduction

Gamma-ray binaries are a rare class of high mass binaries which emit the majority of their radiation in the gamma-ray regime; see e.g. Dubus [1] for a review of these sources. The systems all show orbitally modulated non-thermal emission from radio up to very high energy gamma-rays. So far only seven sources have been discovered, all of which consist of a compact object (in the mass range of a neutron star or black hole) orbiting around an O or Be star. For only two sources, namely PSR B1259-63 and PSR J2032+4127, has the nature of the compact object been confirmed as a neutron star due to the detection of pulsed emission [2, 3]. Assuming all the systems contain a pulsar, the non-thermal emission is produced at the shock that forms between the pulsar and stellar winds, where particle are accelerated and then subsequently cool via synchrotron and inverse Compton scattering. Gamma-ray binaries, therefore, provide a unique case for studying particle acceleration around compact objects.

The gamma-ray binary LMC P3 is the first gamma-ray binary discovered outside of the Milky Way Galaxy [4]. *Fermi*-LAT observations showed a 10.301 ± 0.002 d period and subsequent optical, radio and X-ray observations showed variability on the same period. However, the radio and X-ray light curves are in anti-phase with the *Fermi*-LAT observations. Such an anti-correlation is also seen in, for example, LS 5039 [5, 6, 7]. The source has also been detected

by the H.E.S.S. telescope, though only in one phase bin, which is also in anti-phase with the *Fermi*-LAT observations [8].

The anti-correlation between the GeV and TeV emission could be the result of $\gamma\gamma$ absorption of the photons, see e.g. H.E.S.S. Collaboration [8]. When the pulsar is near to superior conjunction, the observed GeV flux is a maximum, due to the favourable scattering angle for inverse Compton emission. However, this is also the position for maximum $\gamma\gamma$ absorption, and therefore, the TeV emission is a maximum near inferior conjunction.

We have recently undertaken observations of this binary with the Southern African Large Telescope (SALT), and have improved on the orbital parameters. In this paper we briefly discuss the consequences of the updated parameters for gamma-ray production in the system.

2. SALT observations

LMC P3 was observed with the High Resolution Spectrograph (HRS) [9, 10, 11] on SALT [12] between 2016 September 14 and 2017 February 06 in Low Resolution Mode ($R = 14\,000$). The radial velocity was determined using cross-correlation with the IRAF/RVSAO package, against a template created from the observations. The adopted solution shows an eccentricity of $e \approx 0.4$ and places inferior conjunction near phase $\phi \approx 0.24$ and inferior conjunction near $\phi \approx 0.98$, with periastron at $\phi \approx 0.13$ [13]. This confirms that the maximum in the *Fermi*-LAT light curve (at $\phi = 0$) is near superior conjunction, while the maximum in the H.E.S.S. light curve (between $\phi = 0.2 - 0.4$) is near inferior conjunction.

3. Point source modelling

In order to investigate the consequences of this updated orbital parameters, we have modelled the anisotropic inverse Compton and $\gamma\gamma$ absorption from the system, using a point-source approximation, i.e. the optical companion is treated as a point source. The gamma-ray emission is also assumed to originate from a point centred on the pulsar. The binary separation is calculated assuming the mass of the compact object to be $M_X = 1.4 M_\odot$, and the mass of the optical companion $M_{\text{star}} = 33.5 M_\odot$, and the scattering angles are calculated for a binary inclination of $i = 45^\circ$.

The anisotropic inverse Compton emission has been calculated using the analytical approximations presented in Khangulyan et al. [14] as implemented using the NAIMA package [15]. A constant electron spectrum, with an index of $p = 2$ was assumed at all phases, and the target photon energy density was calculated by approximating the star as a black-body emitter with a temperature of $T_{\text{star}} = 39\,400$ K. The $\gamma\gamma$ absorption was calculated using the point-source approximation given in Dubus [16].

In addition, we considered the influence of mild Doppler boosting on the emission, since numerical simulations have suggested the flow at the outer regions of the shock may become mildly relativistic, see e.g. Bogovalov et al. [17].

4. Results

Figure 1 shows the H.E.S.S. light curve compared to the point-source approximation modelling. Since we are initially only investigating the shape of the light curve, the modelled flux has been normalized to the H.E.S.S. measurement. The inverse Compton emission peaks around phase $\phi = 0.1$, slightly after superior conjunction because of the increasing photon energy density nearer to periastron. This is more favourable with the *Fermi*-LAT light curve, but is not consistent with the H.E.S.S. observations. The introduction of $\gamma\gamma$ absorption shifts the peak in the emission closer to phase $\phi \approx 0.2$ which is more consistent with the H.E.S.S. observations. A similar result is obtained for mild Doppler boosting ($\Gamma = 2$), though the rise and fall time of the emission is much faster, an effect that will become stronger for larger values of Γ .

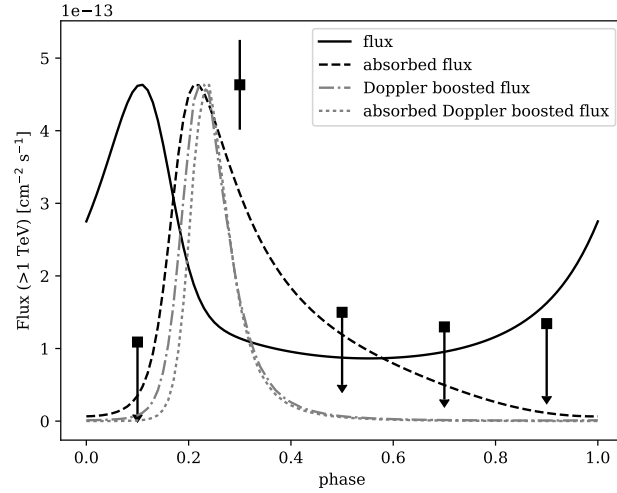


Figure 1. Modelled light curves compared to the H.E.S.S. observations [8]. The inverse Compton flux (solid line) is modified by $\gamma\gamma$ absorption (dashed line), Doppler boosting (dot-dashed line) and both absorption and Doppler boosting (dotted line). In all cases the maximum modelled flux is normalized to the H.E.S.S. measurement.

5. Discussion

The preliminary modelling shows that the updated parameters can shift the peak in the TeV light curve closer to the observed light curve. However, it should be noted that since the source is faint, the peak in the H.E.S.S. light curve is confined to a wide phase bin $\phi = 0.2 - 0.4$. Further observations will help to refine the exactly phase at which the light curve peaks. In addition, a wider range of binary parameters (e.g. inclination angle) as well as particle injection and Doppler boosting should be investigated.

6. Conclusion

The gamma-ray binary LMC P3 has recently been detected in the Large Magellanic Cloud. The multi-wavelength observations show the *Fermi*-LAT light curves are in anti-correlation with the radio, X-ray and TeV gamma-ray light curves, with H.E.S.S. only detecting the source in one phase bin. We have undertaken SALT/HRS observations and have updated the orbital parameters, showing the system is slightly eccentric, with inferior conjunction lying close to the period of maximum TeV emission. We have undertaken preliminary gamma-ray modelling of the system assuming a point source approximation and analytical approximations. We show the combined effect of $\gamma\gamma$ absorption and/or Doppler boosting of the emission can help to explain the H.E.S.S. observations, but that more detailed modelling is required.

References

- [1] Dubus G 2013 *A&ARv* **21** 64
- [2] Johnson S *et al.* 1992 *ApJ* **387** L37
- [3] Abeysekara A U *et al.* 2018 *ApJ* **867** L19
- [4] Corbet R H D *et al.* 2016 *ApJ* **829** 105
- [5] Kishishita T *et al.* 2009 *ApJ* **697** L1
- [6] Fermi/LAT Collaboration 2009 *ApJ* **706** L56
- [7] H.E.S.S. Collaboration 2005 *Science* **309** 746
- [8] H.E.S.S. Collaboration 2018 *A&A* **610** L17

- [9] Bramall D G *et al.* 2010 *Ground-based and Airborne Instrumentation for Astronomy III, Proceedings of SPIE* **vol 7735** p 77354F
- [10] Bramall D G *et al.* 2012 *Ground-based and Airborne Instrumentation for Astronomy IV, Proceedings of SPIE* **vol 8446** p 84460A
- [11] Crause L A *et al.* 2014 *Ground-based and Airborne Instrumentation for Astronomy V, Proceedings of SPIE* **vol 9147** p 91476T
- [12] Buckley D A H *et al.* 2006 *Society of Photo-Optical Instrumentation Engineers (SPIE) Conference Series, Proceedings of SPIE* **vol 6267** p 62670Z
- [13] van Soelen B, Komin N, Kniazev A, Väisänen P 2019 *MNRAS* **484** 4347
- [14] Khangulyan D, Aharonian F A, Kelner S R 2014 *ApJ* **783** 100
- [15] Zabalza V 2015 *Proc. of International Cosmic Ray Conference 2015* p 922
- [16] Dubus G 2006 *A&A* **451** 9
- [17] Bogovalov S V, Khangulyan D, Koldoba A V, Ustyugova G V, Aharonian F A, 2012 *MNRAS* **419** 3426

DIVISION D2

Division for Space Science

dSECS: Including Variometers in Geomagnetic Field Interpolation

MJ Heyns^{1,2}, SI Lotz¹ and CT Gaunt²

¹South African National Space Agency, Space Science Directorate, Hermanus, South Africa

²Department of Electrical Engineering, University of Cape Town, Cape Town, South Africa

E-mail: mheyns@sansa.org.za

Abstract. One of the best tools we have in geophysical modelling is the ability to interpolate the horizontal geomagnetic field at the surface of the Earth. This is especially useful in regions, such as southern Africa, where there is a sparse array of absolute magnetometers available for geomagnetic field measurements. In terms of geomagnetic field interpolation, the spherical elementary current systems (SECS) spatial interpolation scheme has shown to be very successful, and the planar approximation of this method adequate for modelling at mid-latitudes. The SECS interpolation scheme is physics based, making use of the Biot-Savart law and equivalent ionospheric currents to interpolate measured geomagnetic field data. As with most interpolation methods, more data points result in lower error. Therefore, we adapt the SECS method to work with variometers. These instruments measure variations in magnetic field and are more abundant in southern Africa. Merging the two resulting interpolated datasets, the initial absolute geomagnetic field interpolation can be significantly improved. This improved interpolation scheme is not only incredibly useful locally, where a sparse magnetometer array is a challenge, but can also be applied just as effectively in other cases across the globe where there are numerous magnetometers and variometers available.

1. Introduction

In southern Africa, we are lucky enough to have 4 geomagnetic stations which form part of the INTERMAGNET network and measure the absolute geomagnetic field. These stations are located in Hermanus (HER), Hartbeesthoek (HBK), Tsumeb (TSU) and Keetmanshoop (KMH) respectively (see Figure 1). Although this is a very sparse grid, it is in fact typical and many other regions globally have even fewer stations. Partly what makes these stations so difficult to set-up is the cost involved with the equipment and maintenance needed to measure the baseline geomagnetic field accurately. To get around the sparsity of measurement sites, interpolation has to be used. Much more common worldwide are variometers, which do not measure the baseline, but rather the change in the magnetic field. In southern Africa we have a host of these, for example the pulsation magnetometers at Waterberg (WAT) and Sutherland (SUT) and the magnetotelluric station at Kakamas (KMS). Including the additional information from these denser variometers arrays can improve the geomagnetic field interpolation.

1.1. SECS Interpolation

The spherical elementary current systems (SECS) interpolation technique is a physics based interpolation scheme that adds significant robustness when compared to other purely mathematical interpolation schemes such as Fourier, spherical cap or spherical harmonic interpolation schemes [1]. From Helmholtz's theorem, any current flowing on a surface can be broken into a curl-free part (which allows current flow in and out of surface) and a divergence-free part (which allows current flow on surface). When considering real world ionospheric and

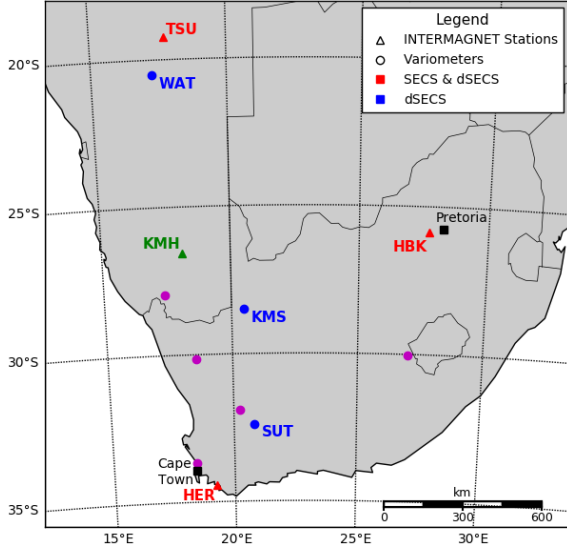


Figure 1. Map of absolute magnetometers and variometers in southern Africa. Magenta circles represent magnetotelluric stations that can possibly be used as variometers as well.

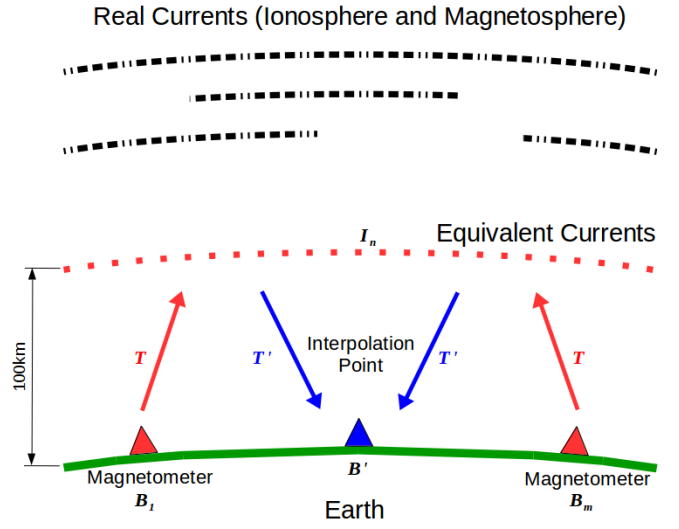


Figure 2. A simple schematic representation of the SECS interpolation scheme and the relevant current systems as described in section 1.1.

magnetospheric currents, it is the divergence-free part that is typically measured by ground-based magnetometers [2]. Furthermore, any real system of currents can be approximated by an equivalent current surface at some arbitrary height. Some studies have used multiple current surfaces to separate the external contribution from the induced current contribution. These studies result in estimations of the actual ionospheric and magnetospheric currents themselves [3–5]. When considering only the horizontal components of the geomagnetic field, it has been shown that a single external equivalent current system suffices [6]. In addition, SECS interpolation has been shown to be particularly accurate given geomagnetically active days and a sparse grid, making it ideal for a southern African context [6].

Assuming Earth-centred spherical coordinates (r, θ, ϕ) , the divergence-free current at a point \vec{r} on the current surface R_{surf} , θ away from a pole at \vec{r}' is,

$$\vec{J}_{df}(\vec{r}) = \frac{I}{4\pi R_{surf}} \cot\left(\frac{\theta}{2}\right) \vec{e}_\phi = \frac{\iint_S \vec{r}' \cdot \vec{\nabla} \times \vec{J}(\vec{r}') dS}{4\pi R_{surf}} \cot\left(\frac{\theta}{2}\right) \vec{e}_\phi. \quad (1)$$

Assuming cylindrical coordinates $(r = \sqrt{x^2 + y^2}, \phi, z)$ [7], with a current element of amplitude of I at height h , the surface current density would be,

$$\vec{J}_{df} = \frac{I}{2\pi r} \vec{e}_\phi. \quad (2)$$

There are a number of factors affecting this planar approximation including an small angle assumption and the resolution of stations. Nevertheless, this approximation of the SECS model has been used effectively for geomagnetic field modelling in a southern African context before [8,9]. Assuming z is downwards and a harmonic time dependence (i.e. $e^{i\omega t}$) [3], the electric field resulting from the element would be,

$$\vec{E} = -\frac{i\omega\mu_0 I}{4\pi} \frac{\sqrt{r^2 + h^2} - h}{r} \vec{e}_\phi. \quad (3)$$

The corresponding magnetic field would then be,

$$\vec{B} = \frac{\mu_0 I}{4\pi r} \left(\left(1 - \frac{h}{\sqrt{r^2 + h^2}}\right) \vec{e}_r + \left(\frac{r}{\sqrt{r^2 + h^2}}\right) \vec{e}_z \right). \quad (4)$$

Given these governing equations for a single current element at a single point in time, a grid of elementary current elements (say n elements) set-up to cover some defined spatial extent. These elements are collected into a vector I . Measured geomagnetic field data from magnetometers (say m stations) is then used to constrain elementary currents, again using the governing equations. As can be expected, $m < n$. These magnetometer stations are collected into a separate vector B . To improve accuracy, as much of the Earth's own magnetic field must be subtracted from the measured magnetic field data to ensure that most of the contribution is from the external current systems. Any remaining offset should largely be absorbed by the equivalent currents. A transfer function matrix T relates the elementary currents and the measured geomagnetic field, such that we have the matrix equation $B = T \cdot I$. Since we are only interested in the horizontal field, only the e_r component of the magnetic field is used. This transfer function is only dependent on the spatial relationship between the elementary current and the magnetometer station. The matrix equation calculation is that performed separately for the x (N-S) and y (E-W) components of I and B respectively, and this process is done for each time step. More specifically,

$$\begin{bmatrix} B_{x,y:1} \\ \vdots \\ B_{x,y:m} \end{bmatrix} = \begin{bmatrix} T_{x,y:11} & \cdots & T_{x,y:1n} \\ \vdots & \ddots & \vdots \\ T_{x,y:m1} & \cdots & T_{x,y:mn} \end{bmatrix} \begin{bmatrix} I_1 \\ \vdots \\ I_n \end{bmatrix} \quad (5)$$

where,

$$T_{x,y:ij} = \frac{\mu_0}{4\pi r} \left(1 - \frac{h}{\sqrt{r_{ij}^2 + h^2}} \right). \quad (6)$$

Since the dimensions of T is $m \times n$ and non-square, I is calculated using the quasi-inverse T^{-1} , i.e. $I = T^{-1} \cdot B$. This quasi inverse T^{-1} is obtained from singular value decomposition. Once the vector I is defined by the measured magnetic field, it can be used interpolate the magnetic field to any other point of of interest, i.e. $B' = T' \cdot I$ (see Figure 2). The physical consistency and adherence to Maxwell's equations makes the SECS interpolation method incredibly robust.

2. dSECS

Although variometers are not absolute, they can very accurately measure the change in the magnetic field, i.e. $\Delta B = B(t_i) - B(t_{i-1})$. Since the SECS method is entirely linear in time, ΔB can be interpolated in the same way as B using the same method (T is purely a spatial constant). The only difference in this case is that I becomes ΔI ,

$$\begin{aligned} B(t_i) - B(t_{i-1}) &= T \cdot I(t_i) - T \cdot I(t_{i-1}) \\ &= T \cdot (I(t_i) - I(t_{i-1})) \\ \Delta B &= T \cdot \Delta I. \end{aligned} \quad (7)$$

With more variometers than absolute magnetometers (magnetometers can act as variometers as well), the confidence in ΔB interpolation is much higher than that for B . ΔB is also what is typically used for geoelectric studies.

3. Merging SECS and dSECS

Using the greater accuracy in the interpolation of ΔB , we can improve the interpolation of B . In order to do this, we consider the two resulting time series of B and ΔB . Let us assume B is of length $N + 1$ and hence ΔB is of length N . Given a set of perturbations ϵ , the two resulting time series can be equated,

$$\begin{aligned} \Delta B_1 &= (B_2 + \epsilon_2) - (B_1 + \epsilon_1) \\ &\dots \\ \Delta B_N &= (B_{N+1} + \epsilon_{N+1}) - (B_N + \epsilon_N). \end{aligned} \quad (8)$$

This can then be rewritten in a matrix equation of the form $A\vec{x} = \vec{b}$,

$$\begin{matrix} & \xrightarrow{N+1} \\ \downarrow N & \begin{bmatrix} -1 & 1 & 0 & \cdots & 0 \\ 0 & -1 & 1 & \cdots & 0 \\ \vdots & \ddots & \ddots & \ddots & \vdots \\ 0 & \cdots & 0 & -1 & 1 \end{bmatrix} \begin{bmatrix} \epsilon_1 \\ \epsilon_2 \\ \vdots \\ \epsilon_{N+1} \end{bmatrix} = \begin{bmatrix} \Delta B_1 + B_1 - B_2 \\ \Delta B_2 + B_2 - B_3 \\ \vdots \\ \Delta B_N + B_N - B_{N+1} \end{bmatrix} \end{matrix} \quad (9)$$

Although the sparse matrix A is non-square, it has a very well behaved quasi-inverse. This quasi-inverse is again used as before to solve for the perturbations \vec{x} , since all the components in \vec{b} are known. Each original interpolated B_i is updated by its corresponding perturbation ϵ_i for each time step, with the resulting interpolation now also constrained by the more accurate interpolated ΔB .

4. Results

In order to validate the method an elementary current grid spanning 34.5-18.5°S and 6.5-28.0°E was used, which is roughly 1 200km in the East-West direction and 1 700km in the North-South direction. This grid had dimensions 13 x 18 in these respective directions, which in turn relates to a grid spacing of roughly 100km in both directions. In preprocessing the data, the Enhanced Magnetic Model (EMM2017) was used to subtract as much of the Earth's magnetic field as possible to allow the dSECS method to focus on the external contributions. Figure 3 shows the resulting interpolated magnetic field and the interpolated change in the magnetic field over the this same elementary current grid.

From the stations described in section 1, KMH was used as the validation point for the dSECS method. For this validation, 4 different geomagnetic storms in 2015 were used. There were some

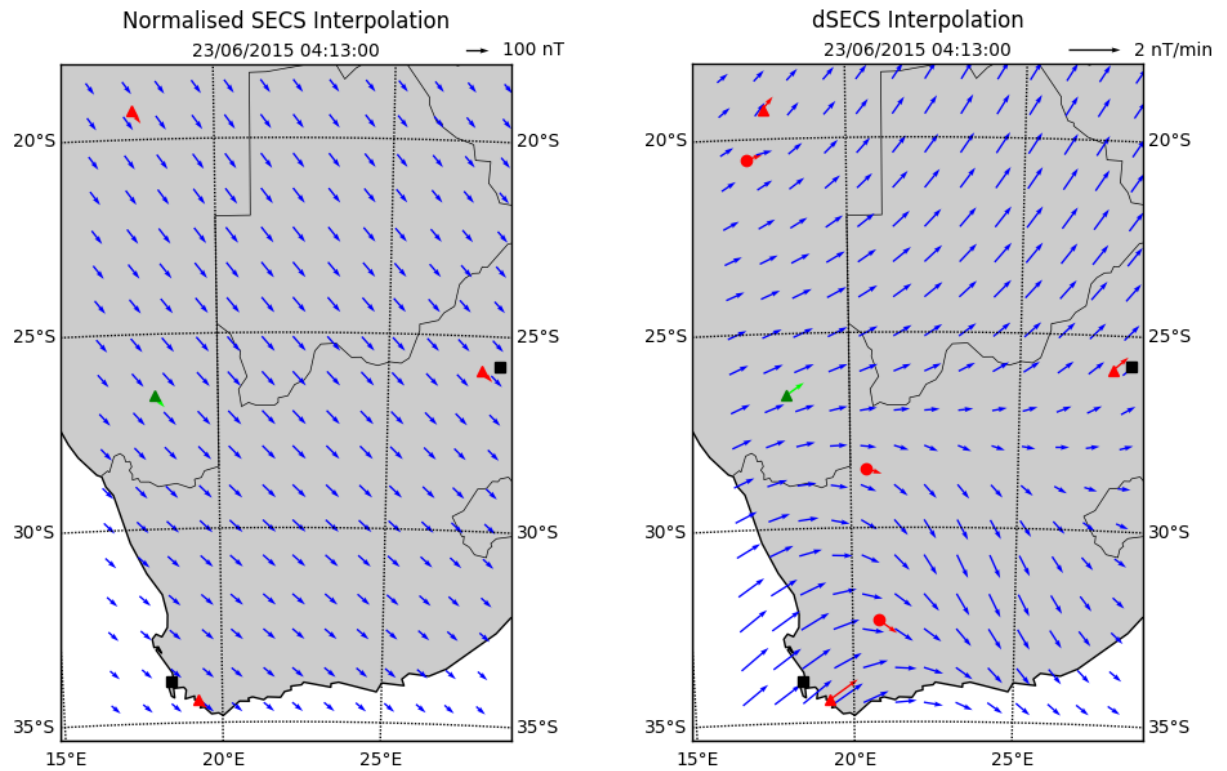


Figure 3. Typical results of SECS and dSECS interpolations over southern Africa. Blue vectors indicate the interpolated field and the red vectors indicate the measured field used to interpolate. The green vector is measured data not included in the interpolation and used for validation.

data gaps as a result of data availability of all the instruments, but the resulting validation set included quiet time, sudden storm commencement, main phase and recovery phase. Figure 4 shows the resulting time series for one of these storms for the B_x component. Also shown is the SYM-H index. This is a global index of the ring current and is indicative of the state of the geomagnetic field. For the period shown, there is a distinct sudden storm commencement after a period of quiet time, which is followed by the main phase of the storm. This period has a complex structure with significant fluctuations in the geomagnetic field (large $|\Delta B|$).

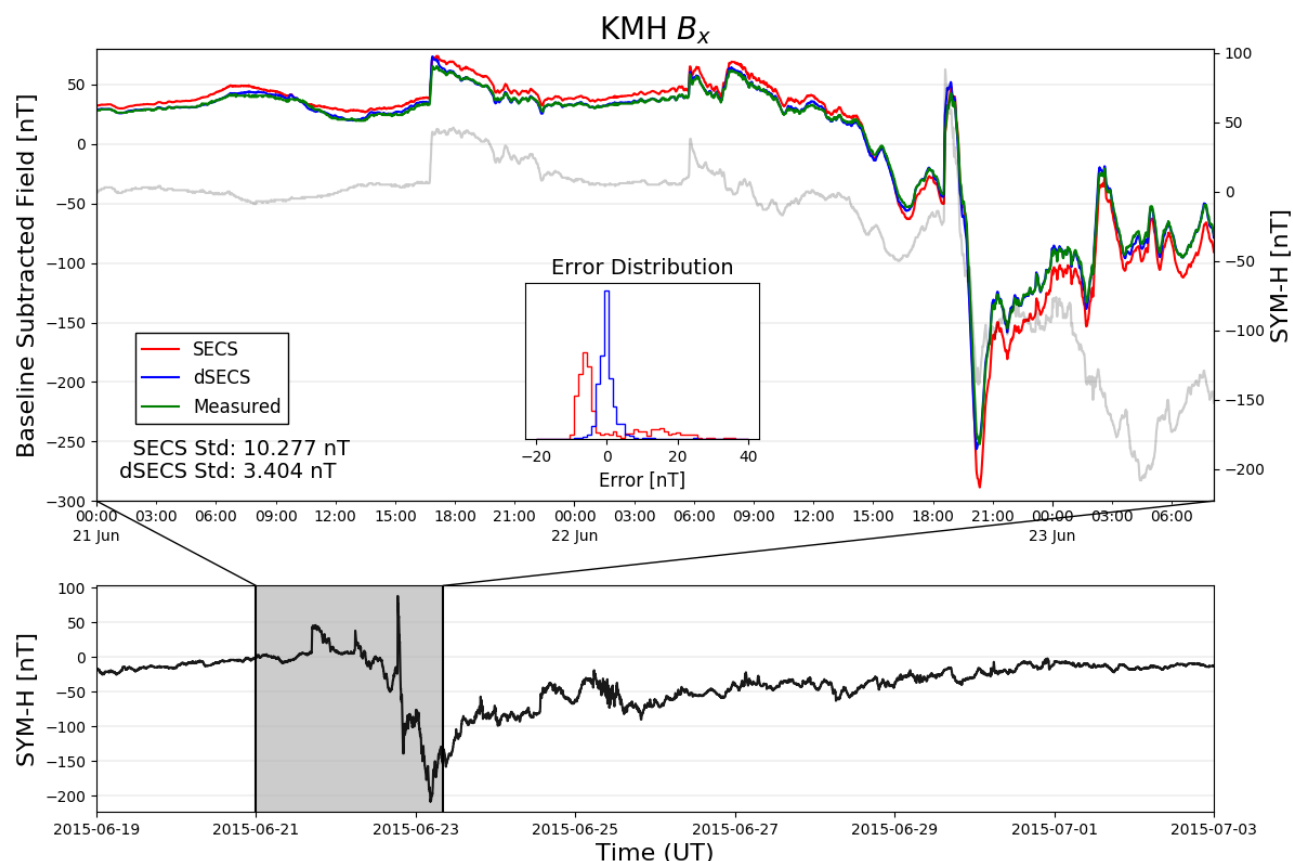


Figure 4. The performance of the different interpolation schemes is shown for the B_x component of the geomagnetic field at Keetmanshoop (KMH) during a geomagnetic storm.

5. Discussion and Conclusion

From the resulting modelling and error distributions, it is evident that including the variometers improves geomagnetic field interpolation. When considering the total error distributions (see Figure 5), in all magnetic field components the standard deviation is significantly smaller for the dSECS method (between 38-52% improvement). All dSECS error distributions also tend more towards Gaussian error distributions when compared to the typical SECS method. This suggests that there is less systematic error and more random or sampling error. For the KMH dataset used, there was a known issue with the decimal point rounding that would be a source of such sampling error. It is interesting to note that the B_y component benefits most from the inclusion of variometers. At midlatitudes, this component is typically associated with induction effects which tend to be more localised. Hence the addition of more local variometers is most likely what drives this improvement. Typically, the B_x component is most affected during storm times which may suggest the slightly less Gaussian error distribution. When considering the total horizontal field error though, we again have a roughly Gaussian error distribution which is significantly improved by including variometers.

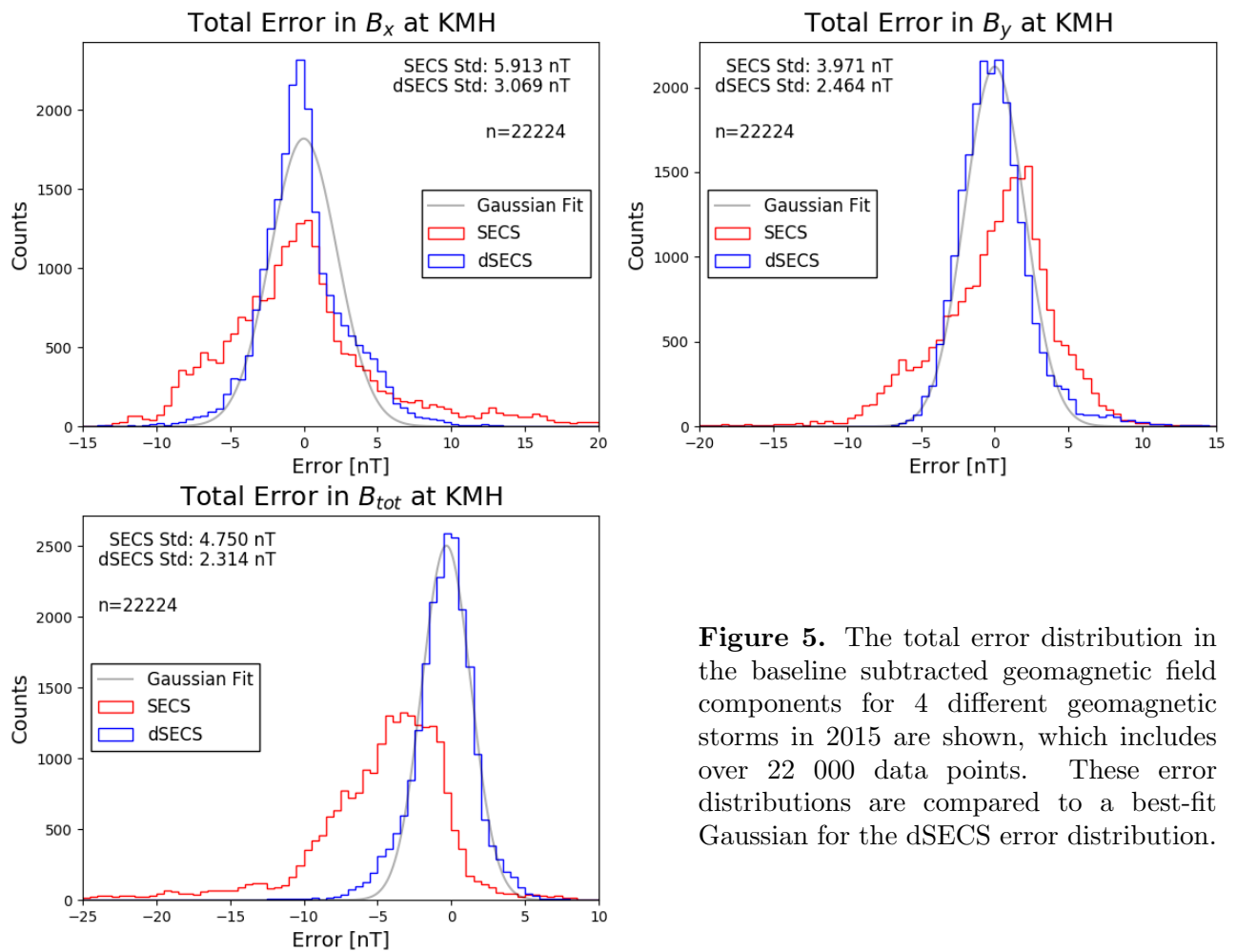


Figure 5. The total error distribution in the baseline subtracted geomagnetic field components for 4 different geomagnetic storms in 2015 are shown, which includes over 22 000 data points. These error distributions are compared to a best-fit Gaussian for the dSECS error distribution.

With the dSECS method validated and showing improvement, the method can be used not only for geomagnetic field interpolation but also geoelectric field studies. Geoelectric field studies require ΔB , and hence only variometers are needed. Variometers are much cheaper than absolute magnetometers and more robust, making them feasible for large array implementations. Ultimately, the larger and more dense the array, the greater the interpolation accuracy.

References

- [1] Amm O and Viljanen A 1999 *Earth, Planets and Space* **51** 431–440
- [2] Amm O 1997 *Journal of Geomagnetism and Geoelectricity* **49** 947–955
- [3] Pulkkinen A, Amm O, Viljanen A, Korja T and BEAR Working Group 2003 *Earth, Planets and Space* **55** 117–129
- [4] Pulkkinen A, Amm O, Viljanen A, Korja T and BEAR Working Group 2003 *Journal of Geophysical Research: Space Physics* **108** 1–9
- [5] Marsal S, Torta J M, Segarra A and Araki T 2017 *Journal of Geophysical Research: Space Physics* **122** 194–211
- [6] McLay S A and Beggan C D 2010 *Annales Geophysicae* **28** 1795–1805
- [7] Viljanen A, Pulkkinen A, Amm O, Pirjola R, Korja T and BEAR Working Group 2004 *Annales Geophysicae* **22** 101–113
- [8] Bernhardt E H, Cilliers P J and Gaunt C T 2008 *South African Journal of Science* **104** 265–272
- [9] Ngwira C M, McKinnell L A, Cilliers P J, Viljanen A and Pirjola R 2009 *Space Weather* **7** 1–5

DIVISION E

Division for Physics Education

The relativistic length transformation: more than a Lorentz contraction

R E Kroon

Department of Physics, University of the Free State, Bloemfontein, South Africa

KroonRE@ufs.ac.za

Abstract. A well known result of special relativity is that an object, moving with constant speed away from an inertial observer, has its proper length along the direction of observation reduced due to the Lorentz contraction. Although some might describe this effect as the relativistic length transformation, a more appropriate use of this term could apply to how the observed length of the object changes as the observer goes from the original inertial frame to a new one. Therefore the relativistic length transformation might yield an elongation or a contraction, depending on the circumstances. The general result for parallel velocities is derived. The important concept of the length transformation does not seem to be presented in this way in introductory texts. As an example of its application, the result is used to substantially simplify the derivation given in a well-known electrodynamics textbook of the relativistic transformation of the electric field, where the physical interpretation of the length transformation is obscured by the mathematics.

1. Introduction

Consider an object which has proper length L_0 , as measured when it is stationary relative to the observer. If it is later moving parallel to its length at speed v , then it appears to instead have the contracted length

$$L_0 \sqrt{1 - \frac{v^2}{c^2}} = \frac{L_0}{\gamma_v} \quad \dots (1)$$

where $\gamma_v = 1/\sqrt{1 - \frac{v^2}{c^2}}$ is the Lorentz factor [1]. This well-known result is of fundamental importance, but does it represent the general relativistic length transformation? The answer depends on what one means by length transformation, but this short paper aims to show that there is more to the relativistic length transformation than just the Lorentz contraction. The important concept of the length transformation does not seem to be presented in this way in introductory texts. Here the result is derived and then applied, as an example, to obtain the relativistic transformation of the electric field. The explicit use of the length transformation in this context provides a derivation which is clear on a physical basis and not obscured by copious mathematics.

2. The relativistic length transformation

Consider an observer in an inertial frame S observing a spaceship travelling with constant speed u towards a distant planet. This observer measures the length of the spaceship as L . This is not the proper length of the spaceship, since the observer is seeing it already Lorentz contracted according to

$$L = \frac{L_0}{\gamma_u} = L_0 \sqrt{1 - \frac{u^2}{c^2}} \quad \dots (2)$$

where $\gamma_u = 1/\sqrt{1 - \frac{u^2}{c^2}}$ is the appropriate Lorentz factor.

For our purposes, we consider the length transformation as the relationship between the original length L as observed in this inertial frame S , and the new length \bar{L} of the spaceship as observed from a new inertial reference frame \bar{S} moving at speed v relative to frame S .

For simplicity we consider the new frame \bar{S} to move at speed v along the direction parallel to the spaceship motion, so that all motions are along the same axis. The velocity of the spaceship relative to frame \bar{S} can be obtained with the Einstein velocity addition rule [1]

$$\bar{u} = \frac{u - v}{1 - uv/c^2}, \quad \dots (3)$$

and it therefore has length

$$\bar{L} = \frac{L_0}{\gamma_{\bar{u}}} = L_0 \sqrt{1 - \frac{\bar{u}^2}{c^2}}. \quad \dots (4)$$

The length transformation is therefore given by

$$\frac{\bar{L}}{L} = \frac{\sqrt{1 - \frac{\bar{u}^2}{c^2}}}{\sqrt{1 - \frac{u^2}{c^2}}} = \frac{\sqrt{1 - \frac{1}{c^2} \left(\frac{u-v}{1-uv/c^2} \right)^2}}{\sqrt{1 - \frac{u^2}{c^2}}}. \quad \dots (5)$$

The part in the square root of the numerator, namely

$$1 - \frac{1}{c^2} \left(\frac{u-v}{1-uv/c^2} \right)^2 = \frac{c^2(1-uv/c^2)^2 - (u-v)^2}{c^2(1-uv/c^2)^2} = \frac{c^2 \left(1 - \frac{2uv}{c^2} + \frac{u^2v^2}{c^4} \right) - (u^2 - 2uv + v^2)}{c^2(1-uv/c^2)^2}$$

can be simplified to

$$\frac{c^2 + \frac{v^2u^2}{c^2} - u^2 - v^2}{c^2(1-uv/c^2)^2} = \frac{(c^2 - v^2) \left(1 - \frac{u^2}{c^2} \right)}{c^2(1-uv/c^2)^2} = \frac{\left(1 - \frac{v^2}{c^2} \right) \left(1 - \frac{u^2}{c^2} \right)}{(1-uv/c^2)^2}.$$

Hence

$$\bar{L} = \frac{\sqrt{\frac{\left(1 - \frac{v^2}{c^2} \right) \left(1 - \frac{u^2}{c^2} \right)}{(1-uv/c^2)^2}}}{\sqrt{1 - \frac{u^2}{c^2}}} L = \frac{L}{\gamma_v(1-uv/c^2)}. \quad \dots (6)$$

The relativistic length transformation therefore consists of the Lorentz contraction factor γ_v together with the additional factor $1 - uv/c^2$. This additional factor plays a key part later in the derivation given for the relativistic transformation of the electric field.

Equation 6 reduces, as it must, to the special case $\bar{L} = \frac{L_0}{\gamma_v}$ when $u = 0$. In the range $0 < v < u$ there is actually an increase in the observed length of the spaceship, until when $v = u$ the observer and spaceship are stationary relative to one another and

$$\bar{L}_{max} = \frac{L}{\gamma_u(1 - u^2/c^2)} = \gamma_u L = L_0. \quad \dots (7)$$

This is illustrated in figure 1.

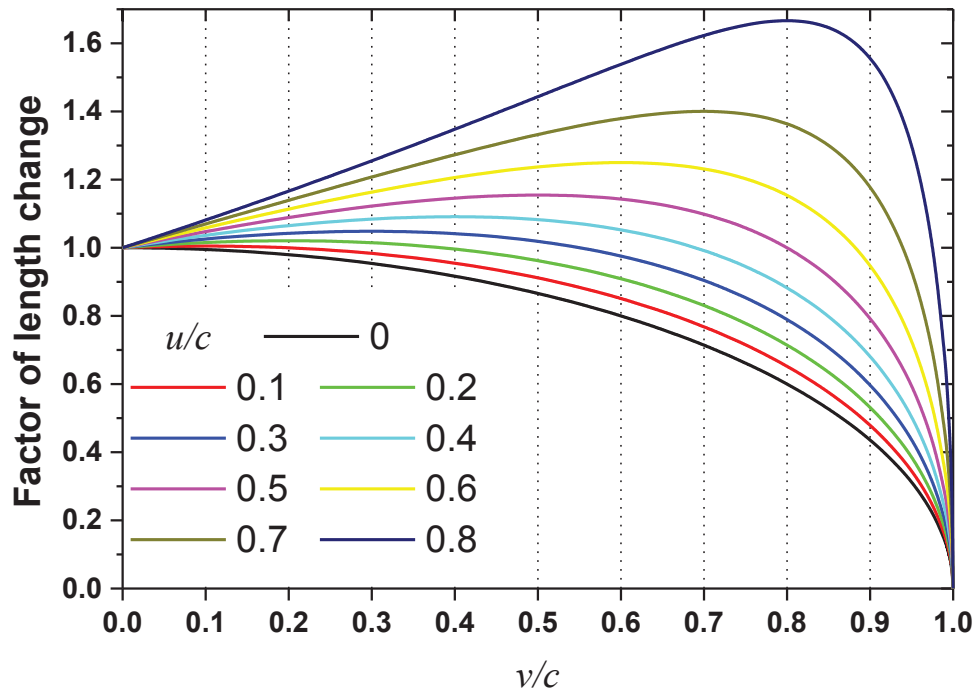


Figure 1. The factor of the length change as a function of the speed (v/c) of the new reference frame \bar{S} , for various speeds u/c of the object in the initial frame S .

For larger speeds a length contraction relative to the proper length L_0 occurs and there is some speed $v > u$ for which $\bar{L} = L$ again, i.e. when there is no change in the observed length despite the change in the observer's inertial reference frame. Some analysis reveals that this occurs when

$$v = \frac{2c^2}{c^2 + u^2} u \quad \dots (8)$$

as may readily be verified by substitution into equation (6). It may be noted that an alternative manner to obtain this result is to simply set $\bar{u} = -u$ in equation 3.

3. Transformation of the electric field considered as a consequence of the length transformation

This general length transformation can, for example, be used to simply derive the transformation of the transverse component of an electric field for a change in reference frame. Consider a parallel plate capacitor with plates of equal but opposite surface densities $\pm\sigma$ lying parallel to the XZ plane and moving with speed u in the X direction. Ignoring edge-effects, this produces an electric field $E_y = \frac{\sigma}{\epsilon_0}$ and a magnetic field $B_z = \mu_0\sigma u$ in the region between the plates [2].

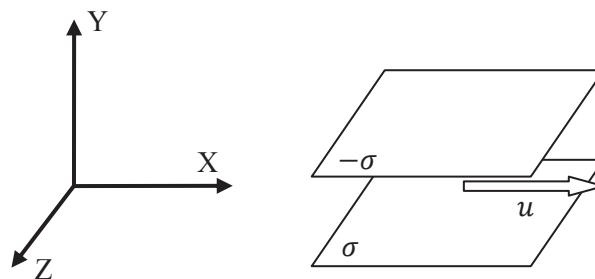


Figure 2. Moving parallel plate capacitor in original reference frame.

If the observer now moves along the X direction at speed v , there is a length transformation in the X direction i.e. contraction by the factor $\gamma_v(1 - uv/c^2)$, while the transverse Y and Z lengths are not affected. This does not affect the general geometry of the system and in the new frame

$$\bar{E}_y = \frac{\bar{\sigma}}{\epsilon_0} = \frac{\sigma\gamma_v(1 - uv/c^2)}{\epsilon_0} \quad \dots (9)$$

where the surface charge density has increased by the factor of the length contraction in the X direction. Therefore $\bar{E}_y = \gamma_v \left[\frac{\sigma}{\epsilon_0} - \frac{\sigma uv}{\epsilon_0 c^2} \right]$. The first term in the bracket is the electric field in the original reference frame. Since $\frac{1}{\epsilon_0 c^2} = \mu_0$ the second term is $\mu_0 \sigma uv$ and so

$$\bar{E}_y = \gamma_v [E_y - vB_z]. \quad \dots (10)$$

The second term in the bracket, involving the magnetic field, is therefore a direct consequence of the additional factor in equation 6 besides the Lorentz contraction for the length transformation. This derivation is given, for example, by Griffiths in his textbook *Introduction to Electrodynamics* [2]. However, the length transformation is not made explicit and the derivation is therefore significantly more complicated than necessary, which detracts from the presentation and obscures the focus on the physical concepts. The length transformation is expected to be a useful concept in many problems involving special relativity.

4. Conclusion

A description of the relativistic length transformation has been provided which is more general than the well known Lorentz contraction, which may be considered as a particular case. From the derived result a change in the observer's inertial reference frame may also result in a length increase or there may be no change in the length despite the change of the observer's inertial reference frame. Use of the relativistic length transformation, where appropriate, can simplify the physics both conceptually and mathematically, which has been illustrated here for a derivation of the transformation of the transverse component of an electric field for a change in reference frame.

References

- [1] Beiser A 2003 *Concepts of Modern Physics* 6th Ed (New York: McGraw-Hill)
- [2] Griffiths D J 2017 *Introduction to Electrodynamics* 4th Ed (Cambridge: Cambridge University Press)

DIVISION F

Division for Applied Physics

Migration behaviour of selenium implanted into polycrystalline-SiC

ZAY Abdalla^{1,*}, TT Hlatshwayo¹, EG Njoroge¹, M Mlambo¹, E Wendler², JB Malherbe¹

¹*Department of Physics, University of Pretoria, Pretoria 0002, South Africa*

²*Institut für Festkörperphysik, Friedrich-Schiller Universität Jena, 07743 Jena, Germany*

E-mail: u17208620@tuks.co.za

Abstract. The migration behaviour of selenium (Se) implanted into polycrystalline SiC was investigated using Rutherford backscattering spectrometry (RBS). Se ions of 200 keV were implanted into polycrystalline SiC samples to a fluence of $1 \times 10^{16} \text{ cm}^{-2}$ at room temperature. Some of the implanted samples were annealed in vacuum at temperatures ranging from 1000 to 1500°C in steps of 100°C for 10 hours. No diffusion was observed at annealing temperatures up to 1300°C. Diffusion of Se was observed after annealing at 1400°C and increased with annealing temperature. This diffusion was accompanied by a peak shift towards the surface and loss of implanted Se. From fitting of the Se profiles, diffusion coefficients of 8.0×10^{-21} and $1.1 \times 10^{-20} \text{ m}^2\text{s}^{-1}$ were estimated at 1400 and 1500°C, respectively.

1. Introduction

Silicon carbide (SiC) is considered as one of the few lightweight covalently bonded ceramics with interesting properties, such as a low thermal expansion coefficient and high thermal conductivity, mechanical strength and hardness [1]. The outstanding properties of SiC, make it suitable for applications in the petrochemical and specifically, for the purpose of this work, the nuclear industries [2]. The safety of modern nuclear reactors depends on the retainment of all the radioactive fission products that may leak into the environment during its operation [3]. In the Pebble Bed Modular Reactor (PBMR) which is one of Very High Temperature Reactors (VHTR), the containment of fission products (FP) within Tristructural-isotropic (TRISO) fuel particles is critical to the successful and safe operation of the reactor. The SiC layer is a very important layer in these particles because it has a number of very crucial functions, such as structural support and acting as the main fission products barrier [4][5].

Selenium (Se) is a non-metallic element with atomic number 34. It has many radioactive isotopes such as ^{72}Se , ^{75}Se , ^{79}Se , ^{80}Se and ^{82}Se . ^{79}Se is a component of spent nuclear fuel, and is found in high-level radioactive wastes resulting from processing spent fuel associated with the operation of nuclear reactors and fuel reprocessing plants. The health hazards of ^{79}Se come from the beta particles emitted during its radioactive decay, and the main concern is associated with the increased likelihood of

*Corresponding author.

Email: u17208620@tuks.co.za

inducing cancer [6]. ^{80}Se is one of the stable isotopes, the most prevalent, comprising about half of natural selenium [6]. It is both naturally occurring and produced by fission [7].

The extremely low diffusivities for impurities in SiC is one of the reasons SiC is used as the fission product barrier in TRISO fuel [8]. The migration behaviour of fission products such as strontium, iodine, cesium and silver in SiC at temperatures above 1000°C have been studied extensively [9]. There is no reported information on the migration behaviour of selenium in SiC which is important in order to ensure the efficiency of SiC layer.

In this study, we investigate the migration behaviour of ^{80}Se implanted into polycrystalline 3C-SiC at room temperature to a fluence of $1 \times 10^{16} \text{ cm}^{-2}$ at temperatures above 900°C.

2. Experimental procedure

Polycrystalline 3C-SiC wafers from Valley Design Corporation were used in this investigation. Se ions with energy of 200 keV were implanted into the wafers to a fluence of $1 \times 10^{16} \text{ cm}^{-2}$ at room temperature. The implantation was performed at the Friedrich-Schiller-University Jena, Germany. Some of the implanted samples were isochronal annealed in vacuum using a computer controlled Webb 77 graphite furnace at temperatures ranging from 1000 to 1500°C in steps of 100°C for 10 hours. Se profiles of the as-implanted and annealed samples were monitored using Rutherford backscattering spectrometry (RBS) of the Van de Graaff accelerator at the University of Pretoria, which uses certain principles of operation [10]. RBS was performed at room temperature using He^+ particles with energy of 1.6 MeV. The beam current was approximately 15 nA. 8 μC was collected per measurement. The RBS spectra were converted to depth in nm using the energy loss data and density of pristine SiC (3.21 g cm^{-3}). The depth profiles were fitted to a Gaussian function to extract the projected ranges (R_p) and stragglings (ΔR_p) for each sample and also to the solution of the Fick diffusion equation for a Gaussian as-implanted profile to extract the diffusion coefficients [11].

3. Results and discussion

In Fig. 1, the Se depth profile of as-implanted sample is compared with that one simulated using TRIM 2012 software [12] assuming a displacement threshold energy (E_d) of 20 eV for C and 35 eV for Si [2]. The experimental projected range (R_p) of 87.7 nm was slightly lower than the theoretical value of 89.6 nm. The value obtained is within the experimental error of the RBS measurements about 2% and the uncertainties of the SRIM simulations. The experimental straggling (ΔR_p) value is about 11% larger than that obtained by theoretical simulation viz. 29.9 and 26.5 nm. This discrepancy in the ΔR_p might be implies to the fact that re-distribution of Se is already taking placed during implantation process. The implanted selenium profile is almost a Gaussian distribution with the kurtosis ($\beta = 2.9$) and skewness ($\gamma = 0.28$). For a true Gaussian distribution ($\beta = 3$) and ($\gamma = 0$). What is also evident in Fig. 1 is that the maximum damage of about 1.3 dpa is at about 70 nm below the surface as compared to the experimental R_p of 87.7 nm. If one assumes that 0.3 dpa amorphises SiC [13], it is quite clear that 125 nm layer of SiC from the surface is amorphized. From these results it is quite clear that the majority of implanted Se is embed in the amorphous SiC.

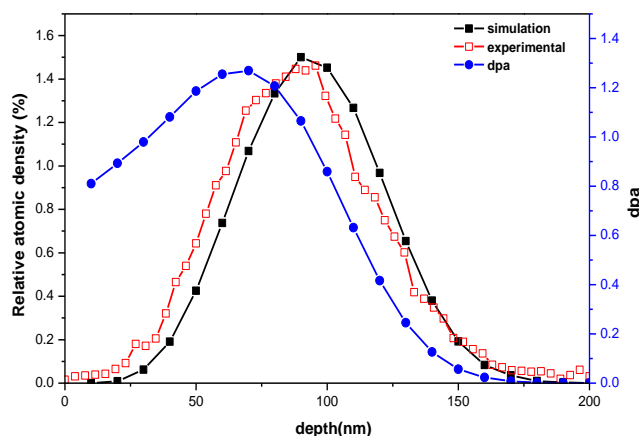


Figure 1. The RBS depth profile of Se implanted into SiC, TRIM2012 simulation and damage profile.

To investigate the migration behaviour of Se in polycrystalline SiC, the implanted samples were subjected to sequential isochronal annealing at temperatures ranging from 1000 to 1500°C in steps of 100°C for 10 hours. The Se depth profiles obtained from RBS before and after annealing are shown in Fig. 2. Neither a change in implanted Se profile nor broadening was observed after annealing at temperatures from 1000 up to 1200°C. These indicated the lack of detectable diffusion after annealing at these temperatures. The RBS profiles for the 1300°C samples indicated a small broadening of the profile and shift of the peak position of the Se profile. However, both were within the experimental error of the depth scale of our RBS measurements. For the 1400°C and 1500°C annealed samples there were measurable (only just for the 1400°C sample) broadening of the profiles and shift of the peak positions towards the surface (see Fig. 3(a) for the latter). Broadening of the profile is an indication of Fickian diffusion of the Se [11]. What was also noticeable was a general decrease in the heights of the profiles. To quantify this, the total integrated counts of the RBS Se signal (counts) were taken. The results are shown in Fig. 3(b). There was also a very slight asymmetry near the surface (i.e. $x = 0$) in the Se profiles at these two temperatures. This is due to evaporation into the vacuum of the Se atoms which diffused to the surface. The boiling point of Se is 685°C is significantly less than the annealing temperatures.

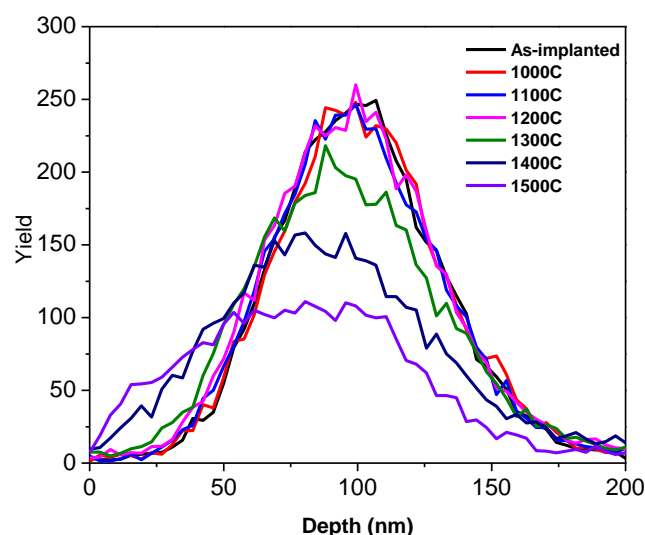


Figure 2. Depth profiles of selenium implanted in 3C-SiC at room temperature and after sequential isochronal annealing from 1000 to 1500 °C for 10 hours.

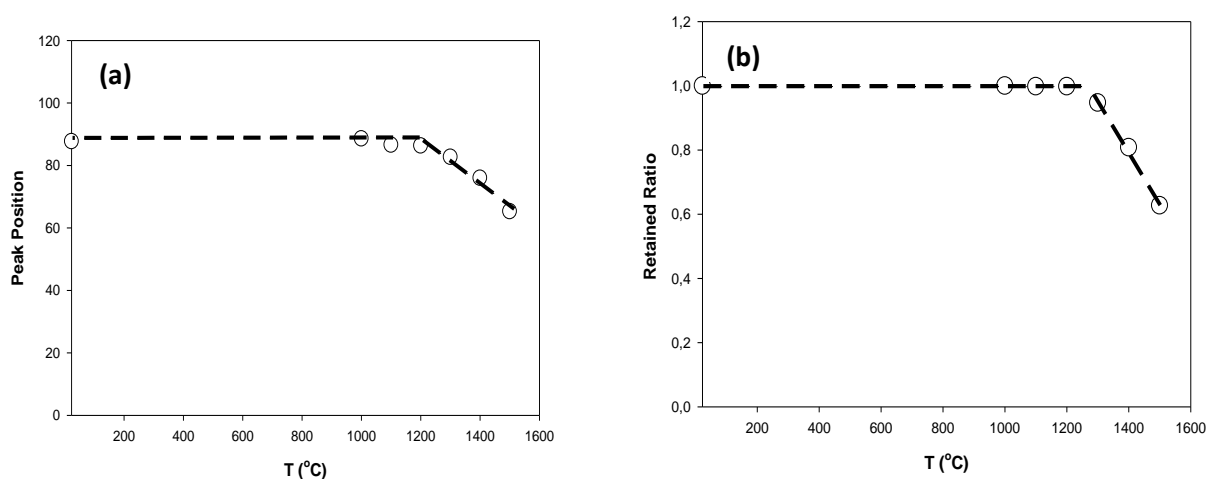


Figure 3. (a) The peak shift (b) retained ratio (calculated as the ratio of the total integrated counts of Se after annealing to that of as-implanted) of the Se profile as a function of annealing temperature.

To extract the diffusion coefficient of Se in polycrystalline SiC, the Se depth profiles obtained from RBS were fitted to the solution of the Fick diffusion equation for Gaussian as-implanted profile and with a perfect sink at the surface (see Fig. 4) [11]. The diffusion coefficients of $(8.0 \pm 0.24) \times 10^{-21}$ and $(1.1 \pm 0.33) \times 10^{-20} \text{ m}^2\text{s}^{-1}$ were extracted at 1400 and 1500°C, respectively. No previous Se

diffusion in SiC data were obtained in literature hence the obtained diffusion coefficients were not compared with any literature values.

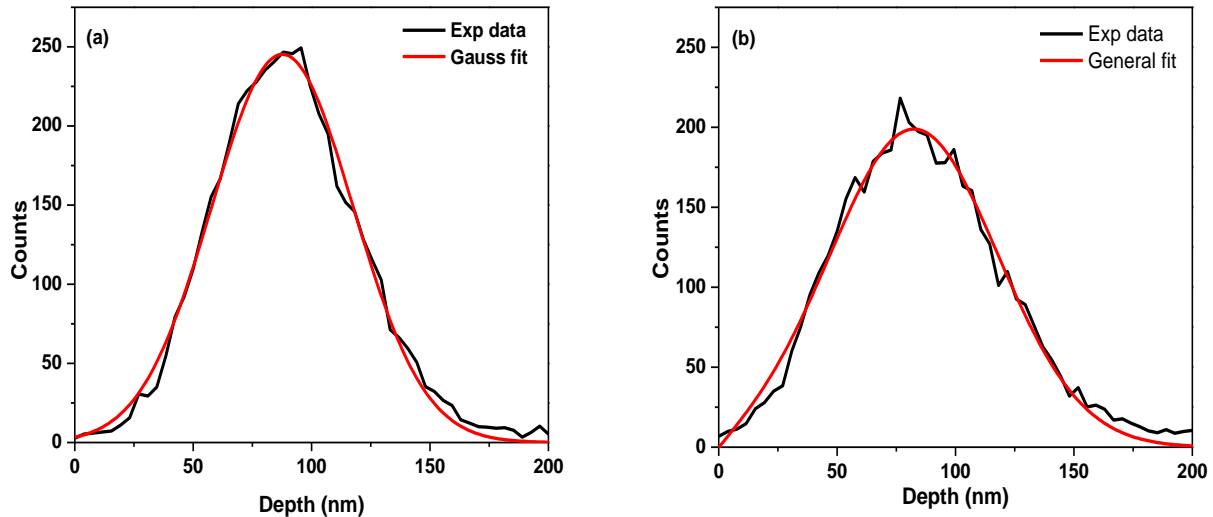


Figure 4. Example of the fitting of the diffusion equation solution to the depth profiles of the sample (a) as-implanted (Gaussian fit only) , (b) annealed at 1300°C

4. Conclusion

In this work, the migration behaviour of Se in polycrystalline SiC has been studied in terms of diffusion. Se^+ of 200 keV was implanted at RT to a fluence of $1 \times 10^{16} \text{ cm}^{-2}$. The implanted sample was isochronally annealed at temperatures ranging from 1000 to 1500°C in steps of 100°C for 10 h. The effect of annealing on Se implanted on SiC and its migration behaviour was investigated using RBS. No diffusion was observed after annealing at temperatures from 1000 up to 1300°C. The diffusion of Se began after annealing at 1400°C and increased with temperature. Also, the Se peak profile began shifting towards the surface after annealing at 1400°C and became more pronounced at 1500°C. This shift was accompanied by loss of Se from the surface. Significant loss, viz. about 40%, was observed at 1500°C. From fitting of the Se profile in the annealed samples, diffusion coefficients were extracted for the samples annealed at 1400°C and 1500°C.

Acknowledgement

Financial support by the National Research Foundation and The World Academy of Science is gratefully acknowledged.

References

- [1] Rashed AH, 2002 “*Properties and Characteristics of Silicon Carbide*,” *POCO Graphite, Inc*, vol. 5, no. 7.
- [2] Devanathan R, Weber WJ and Gao F, 2002 “Atomic scale simulation of defect production in irradiated 3C-SiC,” *J. Appl. Phys.*, vol. 90, no. 5, pp. 2303–2309.
- [3] Hlatshwayo TT, Van Der Berg NG, Msimanga M, Malherbe JB, and Kuhudzai R J, 2014 “Iodine assisted retainment of implanted silver in 6H-SiC at high temperatures,” *Nucl. Instruments Methods Phys. Res. Sect. B Beam Interact. with Mater. Atoms*, vol. 334, pp. 101–105.

- [4] Malherbe JB, 2013 “Diffusion of fission products and radiation damage in SiC,” *J. Phys. D Appl. Phys.*, vol. 46, no. 47, pp. 1–52.
- [5] Feltus MF, Poc, Winston P, and Poc T, 2014 “Fission Product Transport in TRISO Particle Layers Under Operating and Off-Normal Conditions,” no. 10, April 26.
- [6] Peterson J, MacDonell M, Haroun L and Monette F, 2007 “Selenium,” *Radiol. Chem. Fact Sheets to Support Heal. Risk Anal. Contam. Areas*, no. October, pp. 46–47.
- [7] American Elements, accessed March 09, 2019, *Selenium*, www.americanelements.com.
- [8] Katoh Y, Snead LL, Szlufarska I and Weber WJ, 2012 “Radiation effects in SiC for nuclear structural applications,” *Curr. Opin. Solid State Mater. Sci.*, vol. 16, no. 3, pp. 143–152.
- [9] Friedland E, Hlatshwayo TT and van der Berg N, 2013 “Influence of radiation damage on diffusion of fission products in silicon carbide,” *Phys. Status Solidi*, vol. 10, no. 2, pp. 208–215.
- [10] Van De Graaff RJ, Compton KT, Van Atta LC, Feb.1933 “The electrostatic production of high voltage for nuclear investigations,” *Physical Review*, vol. 43, no. 3, p.149.
- [11] Malherbe JB, Selyshchev PA, Odutemowo OS, Theron CC, Njoroge EG, Langa DF, Hlatshwayo TT, Sep. 2017 “Diffusion of a mono-energetic implanted species with a Gaussian profile,” *Nucl. Instruments Methods Phys. Res. Sect. B Beam Interact. with Mater. Atoms*, vol. 406, pp. 708–713.
- [12] Ziegler J, accessed May 16, 2018, SRIM 2012 computer code-2012, www.srim.org.
- [13] Gao F and Weber WJ, 2002 “Cascade overlap and amorphization in 3C-SiC: Defect accumulation, topological features, and disordering,” *Phys. Rev. B - Condens. Matter Mater. Phys.*, vol. 66, no. 2, pp. 1–10.

Photodynamic therapy using Sulfonated Aluminium Phthalocyanine mix for the eradication of cervical cancer: an *in vitro* study

E P Chizenga¹ and H Abrahamse^{1,2}

¹Laser Research Centre, Faculty of Health Sciences, University of Johannesburg, Doornfontein, 2028, Johannesburg, South Africa.

² NRF SARChI: Laser Applications in Health, South Africa

Email: habrahamse@uj.ac.za

Abstract. The use of phthalocyanines in Photodynamic Therapy (PDT) has greatly influenced the approach towards the treatment of cancer. PDT is very efficient in eradicating cancer cells but its efficacy depends on the correct choice of Photosensitizer (PS) used. This study, therefore, investigated the effectiveness of Sulfonated Aluminium Phthalocyanine mix (AlPcS_{mix}) in PDT of cervical cancer, which, in developing countries, including South Africa, is a common type of cancer. A working solution of AlPcS_{mix} was prepared in phosphate buffered saline, PBS. Cervical cancer HeLa cells (ATCC® CCL2™) were cultured in Dulbecco's Modified Eagle's Medium supplemented with 10% Foetal Bovine Serum and incubated at 37 °C, 5% CO₂ and 85% humidity. The cells were treated with varying concentrations of AlPcS_{mix} and irradiated using 673 nm diode laser at fluences of 5, 10 and 20 J/cm². Cellular responses were evaluated 24h post-irradiation to assess changes in cell structure, number and ability to survive after treatment. Results indicated that AlPcS_{mix} localized in cytoplasm, mitochondria and lysosomes, and cellular responses showed dose-dependent structural changes, with decreased cell numbers and impaired ability to grow. The study presented AlPcS_{mix} as an excellent choice of PS for use in PDT and the eradication of cervical cancer cells *in vitro*.

1. Introduction

Cervical cancer is a very common gynecologic malignancy in many parts of the world including South Africa. The burden of cervical cancer is due to lack of effective therapies which result in frequent cancer recurrences and migration to other organs (metastasis). Currently, surgery, chemotherapy and radiation are used for treatment. These therapies are associated with frequent recurrent rates and reduced quality of life for instance surgery, results in loss of fertility [1].

Modern advances in the field of applied physics in medicine, biomedical physics, has significantly modified methods of diagnosis and treatment of human diseases. Since antiquity, the use of light to treat skin diseases and other medical conditions has been in practice but only recently significant modern advances have been introduced to actively target specific diseases like cancer [2]. Photodynamic Therapy (PDT) is a treatment modality that uses light to activate a dye, referred to as Photosensitizer (PS) which reacts with molecular oxygen in its excited triplet state to produce singlet oxygen and other reactive oxygen species that cause damage to cancer cells [3]. This PS is administered into the body and actively localizes in the cancer tissue which upon light exposure, the cancer is eradicated. PDT has therefore gained much attention because of its specificity, noninvasiveness, minimal side effects and

tolerance to repeated doses [4]. It is therefore a potential treatment option for patients with both cervical intraepithelial lesions and advanced cases of cervical cancer

Numerous PSs have been used to treat various types of cancer since the beginning of the era of PDT. Among these PSs, Phthalocyanines have shown great potential in eradicating cancer cells in many studies. Like other PSs, the effectiveness of these PSs can however be further improved by chemical and biologic modifications e.g., addition of sulfur groups to the original chemical structure, and coupling to transition/poor metals. Metallation and sulfonation influences their cellular uptake by increasing solubility and also affect the intracellular distribution pattern, stability and pharmacokinetics, *in vivo* [5]. In this study we used Sulfonated Aluminium Phthalocyanine mix to treat cervical cancer.

2. Materials and methods

AlPcS_{mix} was prepared in phosphate buffered saline, PBS, to a final working concentration of 0.01M. The excitation/activation wavelength was determined using Uv-Vis Spectrophotometry detecting the spectrum of AlPcS_{mix} from 400 – 800nm wavelengths.

Cervical cancer cells were commercially purchased from the ATCC, HeLa cells (ATCC® CCL2™) and cultured in Dulbecco's Modified Eagle's Medium supplemented with 10% Foetal Bovine Serum, 1% pen-strep, 1% amphotericin B and incubated at 37 °C, 5% CO₂ and 85% humidity. For PDT experiments, 3×10⁵ cells were seeded in 3.4cm² cell culture dishes and treated with AlPcS_{mix} at concentrations of 5, 15 and 25 µM per plate. After 12 hours of incubation to allow maximum absorption of the PS by the cells, the cells were washed 3 times with pre-warmed Hank's Balanced Salt Solution, HBSS, to remove all traces of unabsorbed PS. Subcellular localization of the PS was observed using fluorescence microscopy. The treated cells were then irradiated using 673 nm diode laser (Oriel Corporation), supplied by the National Laser Center (NLC) of South-Africa. Cell groups were irradiated at fluences of 5, 10 and 20 J/cm² (Table 1).

Table 1. Laser parameters

Variable	Description/Value
Laser type	Semiconductor diode
Wavelength	673 nm
Pulsed or continuous	Continuous
Power Output	93 mW
Power density	10.25 mW/cm ²
Spot size	9.1cm ²
Fluence	5, 10, 20 J/cm ²
Irradiation times	8, 16, 32 minutes

Included in the experiments were a set of control groups that contained cells only without treatment with PS or irradiation. Laser negative control groups comprised of the three concentrations without laser irradiation and PS negative control groups comprised of cells that were irradiated with 5, 10 and 20 J/cm² without addition of PS. Each PS concentration was irradiated at all three fluences. After irradiation of cells, the plates were re-incubated at 37°C, 5% CO₂ and 85% humidity. Cellular responses were evaluated 24h post-irradiation using trypan blue viability assay to assess the cells survival (viability), adenosine triphosphate (ATP) assay, to determine cell number increase (proliferation) based on cellular ATP quantification, which indicates the presence of metabolically active cells, and bright field microscopy for structural changes (morphology).

All individual sets of experiments were repeated three times (n=3). Statistical analysis was performed using SigmaPlot software version 13.0. The student t-test was performed to determine the statistical difference between the control and experimental groups. One tailed student's t-test was performed to

compare different groups. Statistical significant difference between the untreated control and the experimental groups is shown in graphs as (*) for $p < 0.05$, (**) for $p < 0.01$, (***) for $p < 0.001$, and (ns) for no significant difference, where p denotes the probability. The standard error on all plotted graphs is represented by error bars, respectively

3. Results

Results indicated that AlPcS_{mix} accumulated in the cytoplasm was significantly localized in lysosomes and mitochondria. At the end of the investigation, control cells appeared healthy and maintained their normal cell structure and size. PDT on the other hand caused significant changes in morphology seen as cell rounding, blebbing and detachment from the surface of the culture dishes as shown in Figure 1 below.

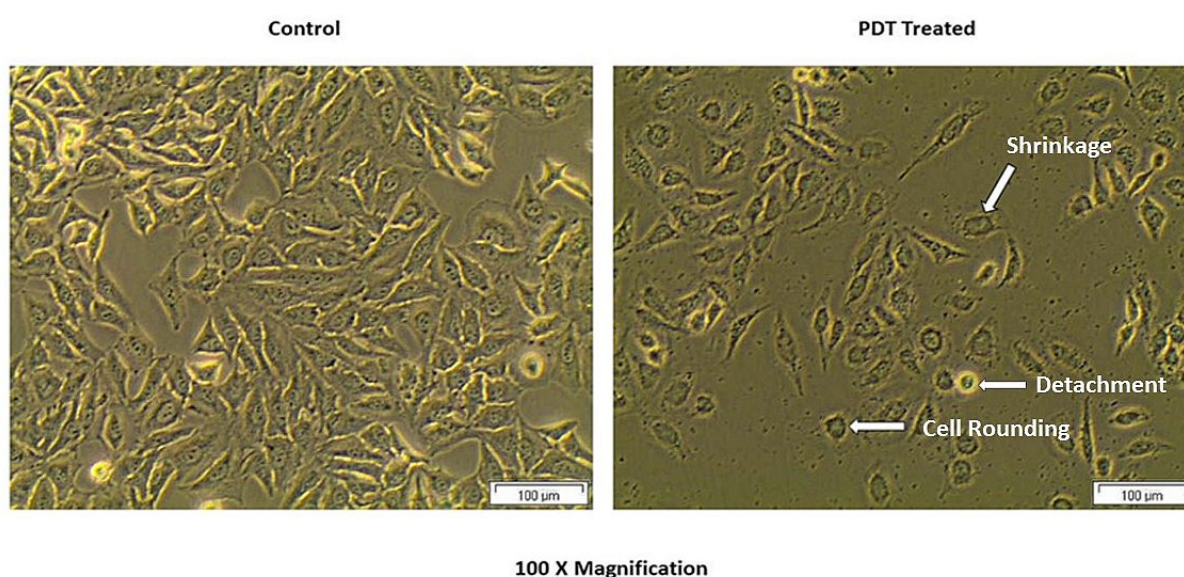


Figure 1. Cellular morphology of control and PDT treated cells seen under 100X magnification demonstrating the continuous growth of cells as a monolayer in the control group and a marked alteration of the morphology in PDT treated cells indicating cell shrinkage, blebbing and detachment from the surface.

Cellular responses showed dose-dependent structural changes, with significant ($p < 0.001$) decrease in cell viability (Figure 2) and proliferation (Figure 3) compared to the control. As shown in Figure 2 below, the control group (No PS, no irradiation) presented with a high cell viability indicating that the cells remained viable at the end of the experimental period. Cells treated with PS alone and those treated with laser alone showed similar results. PDT treated cells indicated a dose dependent decrease in cell survival ($p < 0.001$), with a marked decrease in viability seen in cells that received the highest dose of treatment (25 μ M of PS and 20 J/cm²).

The number of metabolically active cells was determined by detection of ATP. There was a marked decrease in cell proliferation in PDT treated cells, as compared to the control cells and untreated cells (Figure 3). The high luminescence signal seen with the control indicated increased proliferation of the cells, and the cells treated with either of the variables alone. PDT treated cells on the other hand showed a significant decrease in ATP production ($p < 0.001$), in a dose dependent manner with the highest decrease observed in cells that were treated with 25 μ M of AlPcS_{mix} at a fluence of 20J.

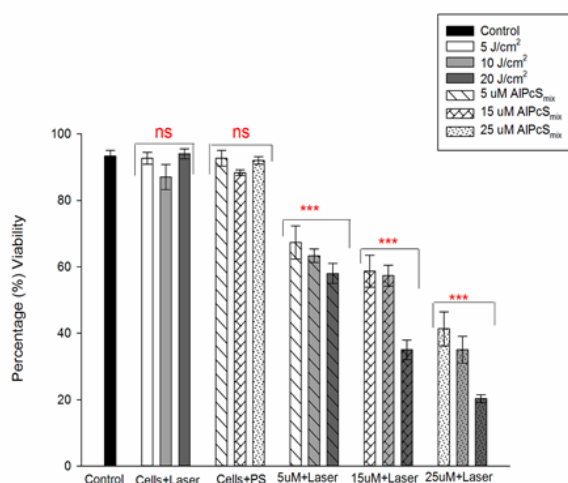


Figure 2. Post-irradiation cell viability showing a dose dependent decrease in cell survival. The control group and groups treated with either of the variables alone showed no significant decrease in viability (ns). All PDT groups compared to the control, indicated significant decrease in cell viability ($p < 0.001$) after 24 h incubation post treatment.

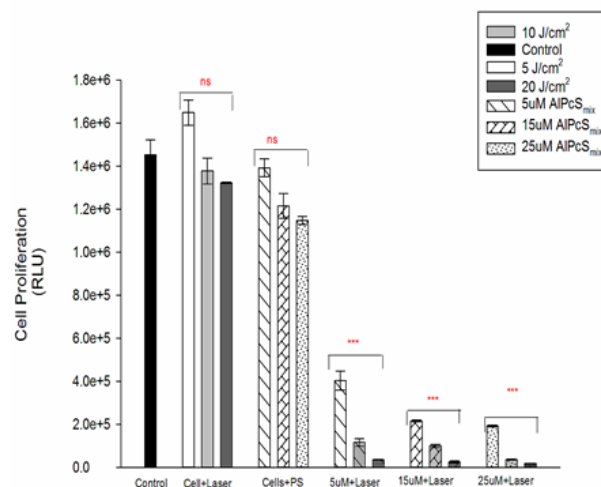


Figure 3. Post-irradiation ATP Luminescent signal of cells indicating proliferation. Control cells and groups treated with either of the variables alone did not show significant decrease in cell proliferation (ns). There was significant decrease in proliferation of PDT treated cells ($p < 0.001$) after 24 h.

4. Discussion and conclusion

Singlet oxygen and other reactive oxygen species are produced by the PS in its activated state. These highly reactive oxygen species directly cause cell death by interactions with cellular components and oxidation of biomolecules causing the observed cell damages [6]. In simple terms, PDT induces cell death by virtue of photochemical interactions of light and a PS which in the presence of molecular oxygen, yields a set of chemical reactions that generate ROS and other free radical species causing membrane damage. In this set up, the different concentrations of the PS caused a significant dose dependent damage upon activation by laser light, with the extent of damage directly proportional to the concentration used. Similarly, the different fluences activated the PS at different rates with higher fluences causing more damage to the cells. Decreased cell viability in PDT treated cells was observed using Trypan Blue viability assay which adequately represented the ability of PDT to cause cell death through ROS generation. To further confirm this observation, ATP proliferation assay significantly presented decreased proliferation of the treated cells. After 24 hours, PDT treated cells also completely lost their morphological characteristics and died.

AIPcS_{mix} has shown desired therapeutic effects in many solid tumours in previous studies [7, 8]. Zharkova et al used AIPcS_{mix} to treat patients with various types of cancer, *in vivo*, from which the majority showed complete regression of the tumours. In another study by Kresfelder et al [8], it was shown that AIPcS_{mix} induced sufficient cell death in oesophageal cancer cells with significant alteration of the post-irradiation cell proliferation. It was also demonstrated in the same study that AIPcS_{mix} had the most prominent effect when compared to a different PS, GePcS_{mix}.

Results obtained indicate the effectiveness of AIPcS_{mix} in PDT and the eradication of cervical cancer cells *in vitro*. Observable phenotypic changes with significant decrease in viability and proliferation were demonstrated. We therefore suggest in our study that AIPcS_{mix} can be considered for use as a photosensitizing agent for cervical lesions and cervical cancer cells. Future studies should consider checking this effect on normal cervical cells to adequately determine the specificity of PSs in treating cancer. Further research is now expected to examine the therapeutic effectiveness of AIPcS_{mix} *in vivo*.

Acknowledgements

This work is based on the research supported by the South African Research Chairs Initiative of the Department of Science and Technology and National Research Foundation of South Africa (Grant No 98337). The authors sincerely thank the University of Johannesburg, the National Research Foundation for their financial grant support, and the National Laser Centre for providing use of their lasers

References

- [1] Calixto G M, Bernegossi J, de Freitas L M, Fontana C R and Chorilli M. 2016 *Molecul*, **21** 3
- [2] Jadon G and Joshi K S 2012 Cervical Cancer a Review Article.*JBPR*, **1** 1
- [3] Ackroyd R, Kelty C, Brown N and Reed M 2001 *Photochem. and Photobio.* **74** 5
- [4] Boyle R W and Dolphin D 1996 *Photochem. Photobiol.* **64** 469
- [5] Abrahamse H and Hamblin M R 2016 *Biochem. J.* **473** 4
- [6] Sibata C H, Colussi V C, Oleinick N L and Kinsella T J 2000 *Braz J Med Biol Res.* **33** 8
- [7] Zharkova N N, Kozlov D N , Smirnov V V, Sokolov V V, Chissov V I, Filonenko E V, Sukhin G M, Galpern M G and Vorozhtsov G N 1995 Photodynamic Therapy of Cancer II International Symposium on Biomedical Optics Europe '94 Proc. SPIE ed D Brault, G Jori, J Moan, B Ehrenberg (Lille France 12 January 1995) SPIE Digital Library vol 2325 pp 367-374
- [8] Kresfelder T L, Cronje M J and Abrahamse H 2009 *Photomed Laser Surg.* **27** 4

Experimental and Numerical Measurement of the thermal performance for parabolic trough solar concentrators

Khaled Mohamad, Philippe Ferrer

School of Physics, University of the Witwatersrand, Johannesburg 2001, South Africa

khaled@aims.edu.gh

Abstract Parabolic trough mirror plants are a popular design for conversion of solar energy to electricity via thermal processes. The receiver unit (RU) for absorbing the concentrated solar radiation is limited to a maximum temperatures (580°C) and is responsible for efficiency losses mainly via thermal radiation. We built a RU in the laboratory to study the thermal performance for different designs and we accompanied this study with a mathematical module implemented on a simulation code. In this work, the simulation and the first set of experiments show a good agreement, validating applicability of the code.

1. Introduction

A parabolic trough solar thermal power plant consists of a series of parabolic mirrors concentrating solar radiation onto a linear focal line along which the receiver unit is positioned. The receiver heats up and in turn imparts a large portion of its heat to a heat transfer fluid circulating within. This heat transfer fluid can then be utilized in a steam cycle to generate electricity. The receiver is one of the most complex parts and the efficiency of the entire system is largely determined by it. It has to be carefully designed in such a way so as to minimize the energy losses. Every part of the receiver unit is a topic of ongoing research, such as the working fluid that can be used, and also the optical, chemical, and thermal properties of the concerned material [1].

Typically, the receiver unit consists of a blackened absorber pipe (AP) encapsulated by the glass cover (GC), (See Fig. (1a)). There is a vacuum in between to minimize convective heat losses [2]. For the conduction losses, the thermal contacts between the receiver pipe and the glass cover are kept to a minimum. The heat transfer fluid (HTF) inside the receiver pipe is heated by the concentrated solar radiation. The hot HTF can be used in generating electricity through a steam cycle or in thermochemical applications [3]. The dominant heat losses at high temperatures are due to the thermal emission (IR) from the receiver pipe. There is a conventional method to minimize the IR by painting the receiver pipe with a spectrally selective coating, a dielectric film that absorbs well in the visible region of the solar spectrum and emits poorly in the IR region. Much work has been published in regard to the selective coating and their properties [4]. The main weakness of selective coating is that it prevents the receiver pipe from being heated to high temperature, since it thermally decomposes at about 680 K [5], [6].

An alternative option to the selective coating is to reduce the thermal emission from the glass cover tube of a trough collector by trapping IR via a reflective surface on the part of the glass not facing the trough. The solar radiation inlet may be coated with a hot mirror type coating [7–10], i.e., Indium-Tin-Oxide and applying the reflective cavity around the absorber [11], which is shown in Fig. (1b).

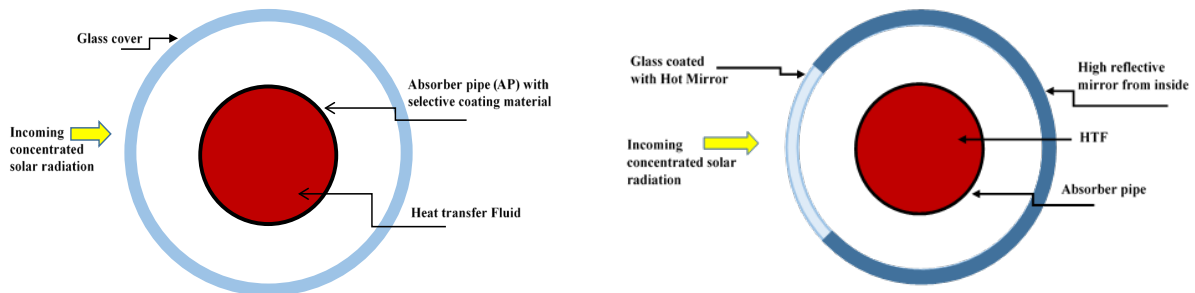


Figure 1. a) Receiver unit with a selective coating. b) Receiver unit with a cavity design [11].

Measuring the heat losses of the receiver unit of the parabolic trough is an effective way to determine the efficiency of the RU especially at a higher Heat transfer fluid (HTF) temperature. It allows us to judge the performance of different RU designs. In this work, we studied the thermal performance of the RU by measuring the heat losses experimentally and compared our results with our simulation code, which is based on a mathematical model of the system.

2. Experiment description

The Receiver Unit (RU) or heat collector element was tested indoor. Two heating elements inside the absorber pipe of the RU brought the HTF temperature to a desirable test temperature. In one experimental set, the glass tube was evacuated, in the other air was left inside the annulus. The heating element power was adjusted to a desired power value using a variac. Once the RU reached a steady state temperature, the electrical power required to maintain the HTF temperature equaled the heat loss of the RU at that temperature. Further, the temperatures along the RU elements were constant. The heat loss of the RU was tested at different temperatures corresponding to heating power generation of the heating elements from 50 W to 1.5 kW in roughly 50 W increments. Heat losses were reported per meter of RU. The temperature around the absorber pipe and the glass cover was measured with thermocouples and hence we could calculate the emittance of AP and the heat loss to the environment at different temperatures.

The length of the tested RU was 2.7 m at 25 °C (It will expand by about 9 mm at 300 °C with a mild steel absorber pipe outer/inner diameter of 3.2/2.8 cm and a two pieces of a Pyrex glass cover outer/inner diameter of 5.8/5.4 cm with a length of 1.35 m each. The Pyrex glass pieces were joined together with a brass section in the centre of the AP. We vacuum insulated the central brass piece, glass covers and the AP together using flame resistant high temperature silicon. The high temperature silicon also acted as a thermal insulator between the joints in this experiment.

The heating elements were two 1.2 m with 8 mm outer diameter. In order to prevent the heating element from touching the AP, we introduced spacers to center the heating elements. These spacers can be made from steel with a small size and sharp edge toward the AP inner surface to minimize the losses through it. Thermocouples measured the temperature of the outer surface of the AP and GC. Thermocouples were introduced to determine the average temperatures and heating behavior of the RU. The Absorber pipe and Glass cover temperatures were measured using two and four K-type thermocouples respectively. A good contact between the thermocouples and the surface was required for accurate measurement. Figs.2 and 3 show more details about the setup.

As indicated in Fig. 3, the thermocouples wires are insulated with a thermally resistance braided tube and grouped together at the end. Their ends are connected to the control and measurement unit. Furthermore, two holes through the end piece are made to allow the AP thermocouples wires get out and connected to the control and measurement unit via vacuum tight exits. The control and measurement unit allowed us to regulate and adjust the heater power in accordance to temperature requirements.

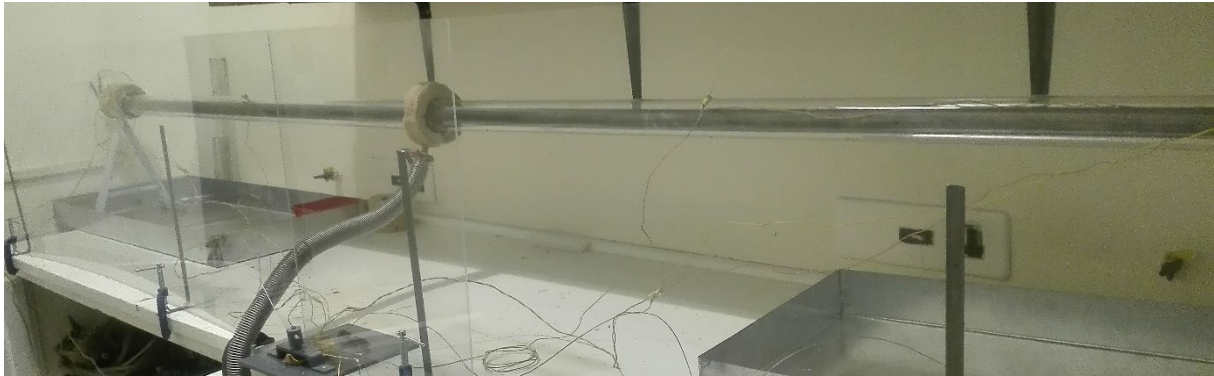


Figure 2: The receiver unit set up in the laboratory.

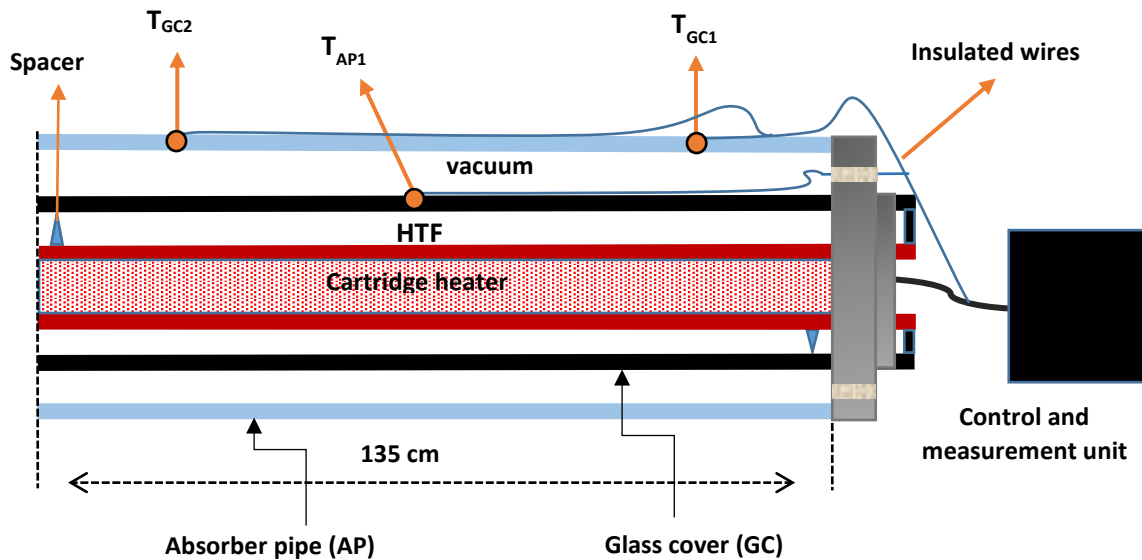


Figure 3: The right one-half of RU. T represents the thermocouple position.

3. Theory and simulation study

The source of the thermal energy is an electrical resistance heater wire with a constant rate of heat generation and can be modified by a variac. Fig. 3 shows the total heat transfer of the system and the interactions between its components. The physical basis of our model starts with a comprehensive description of the thermal interaction. Under steady operating conditions, the absorber pipe and the glass cover reach a different stagnation temperature. In addition, the heat loss and the heat gain of each element in the RU must equal the total rate of heat generation of the heating elements \dot{E}_{gen}

$$\dot{q}_{GC,amb} = \dot{q}_{GC,cond} = \dot{q}_{AP,GC} = \dot{q}_{AP,cond} = \dot{E}_{gen},$$

where $\dot{q}_{GC,amb}$ is the rate of the heat transfer from the glass cover (GC) to the surroundings, $\dot{q}_{GC,cond}$ is the conduction through the GC layer, $\dot{q}_{AP,GC}$ is the heat transfer from AP to GC, and $\dot{q}_{AP,cond}$ is the conduction through the AP.

The calculations start from the heat loss to the ambient because the ambient temperature is always known. We initially guess the unknown outer GC surface temperature $T_{g,o}$ iteratively, until the steady operating condition at which $\dot{q}_{GC,amb} = \dot{E}_{gen}$ is fulfilled. The heat rate $\dot{q}_{GC,amb}$ consists of natural convection and radiation heat transfer from the glass cover to the ambient.

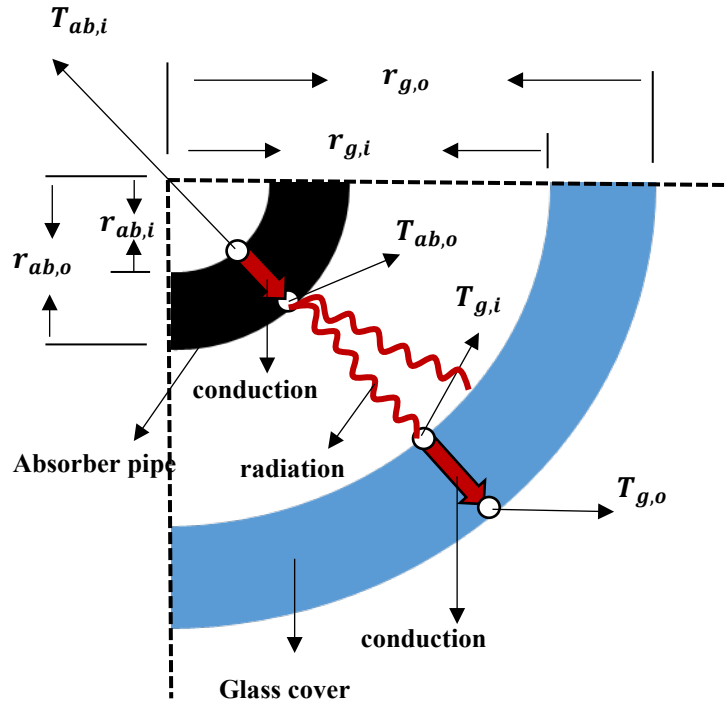


Figure 4: Receiver unit cross section.

The air properties during the calculation were selected at $T_{avg} = \frac{T_{g,o} + T_{amb}}{2}$. We could then evaluate $T_{g,i}$ at which the rate of heat loss due to the conduction through GC equal \dot{E}_{gen} . In the same way, $T_{ab,o}$ is evaluated through iteration until fulfilling $\dot{q}_{AP,GC} = \dot{E}_{gen}$, where $\dot{q}_{AP,GC}$ consists of the rate of the heat transfer between the AP and GC by convection and radiation. The convection heat transfer inside the evacuated annulus was ignored. Finally, $T_{ab,i}$ was evaluated such that the conduction heat loss through the AP equaled \dot{E}_{gen} . This simulation code was implemented using Python and is shown in Fig. 5.

4. Results

The initial experimental results tested for a normal RU reference unit without any coating. The aim was to validate our theoretical framework and simulation using experimental results. Two experiments were performed testing the thermal behaviour of the RU; 1) with air inside the annulus, and 2) with the annulus evacuated. The simulation predicted differing temperature readings for them, which we wanted to verify experimentally. The tested RU is shown in Fig. 2

In Fig. 6 and 7, the heat loss per meter of the RU length is depicted as a function of the absorber pipe and glass cover temperatures respectively. In the figures, “Sim” indicates simulation and “Exp” indicates experimental. In Fig. 6, the discrepancy between the simulation and experimental work in both cases vacuum and air in the annulus are 2% and 5.6% respectively.

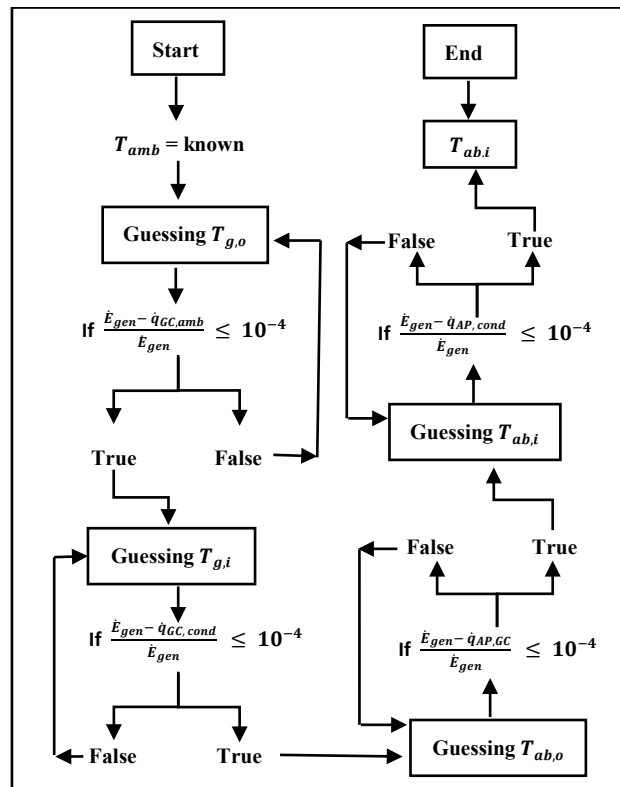


Figure 5: Algorithm for simulation code

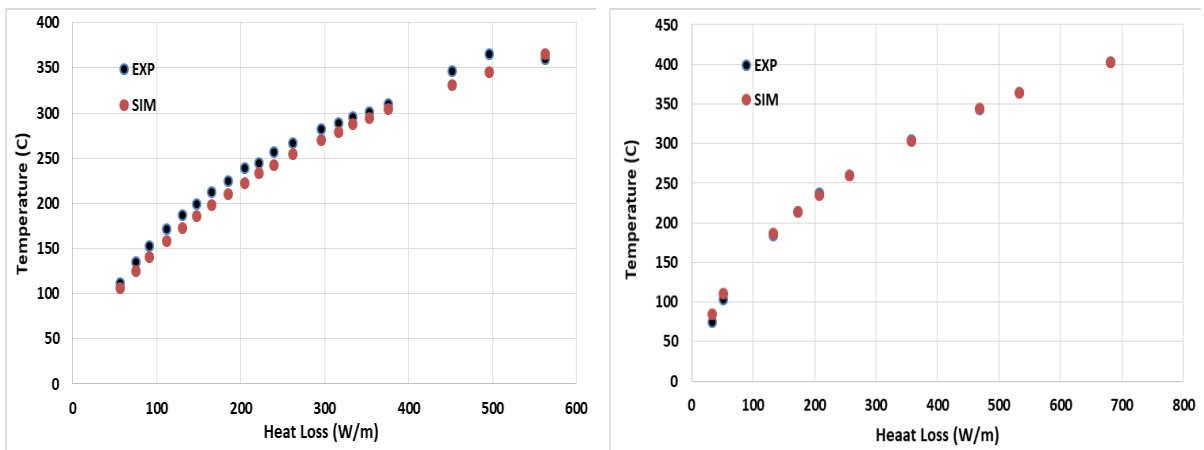


Figure 6: a) Heat loss versus AP temperature (Air in the annulus).

b) Heat loss versus AP temperature (Vacuum in the annulus).

The simulation predicted a higher AP temperature for the vacuum system, since there the convective heat transfer has been eliminated, and the only for heat to escape is via radiation. This is clearly shown in the experimental results, where the AP temperature is measurably higher in the vacuum case. In all cases the simulation seems to predict a greater heat loss. This seems to suggest that some of the material property values need to be re-evaluated. Further, the edge heat loss effects need to be incorporated.

In Fig. 7, the simulation predicts that the GC temperature for the case of vacuum and air in the annulus is the same at a fixed value of the heat power generation, since the heat dissipation mechanism from the

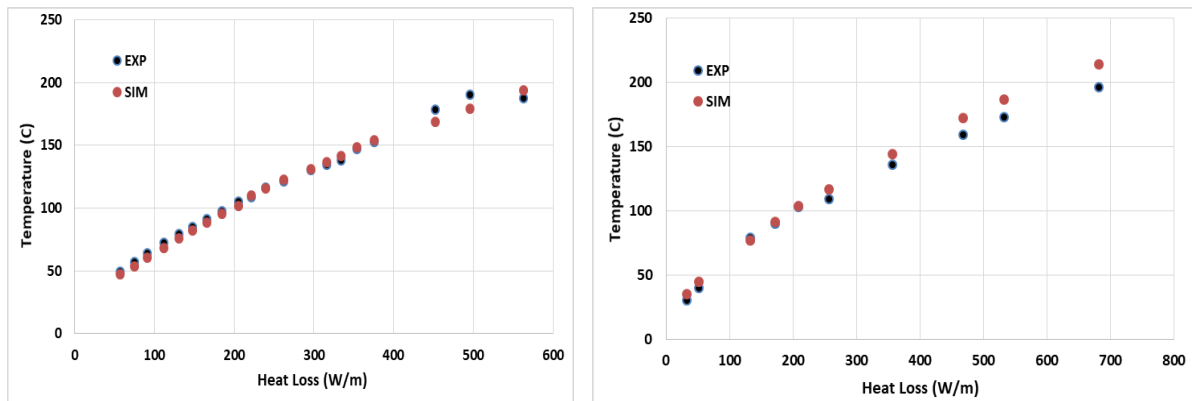


Figure 7: a) Heat loss versus GC temperature (Air in the annulus). b) Heat loss versus GC temperature (Vacuum in the annulus).

GC to the ambient is similar. Further, the discrepancy between the simulation and experimental work in both cases vacuum and air in the annulus are 6% and 3% respectively.

5. Conclusion

We tested a receiver unit (RU) of the parabolic trough collector indoor, in order to validate our theoretical and numerical framework. Two experiments were performed, for which the simulation predicted different results. Experimental data verified the results of the simulation to within 2 % and 6% discrepancy for the absorber pipe temperature in the case of vacuum and air in the annulus respectively. Also, a discrepancy of 6% and 3% for the glass cover in the case of vacuum and air in the annulus respectively. This successful set of validations encourages us to continue testing our proposed designs using this experimental setup.

References

- [1] Cyulinyana M C and Ferrer P 2011 Heat efficiency of a solar trough receiver with a hot mirror compared to a selective coating *South Afr. J. Sci.* **107** 01–7
- [2] Sargent and Lundy LLC Consulting Group 2003 *Assessment of Parabolic Trough and Power Tower Solar Technology Cost and Performance Forecasts* (Chicago, Illinois: DIANE Publishing)
- [3] Lampert C M 1979 Coatings for enhanced photothermal energy collection I. Selective absorbers *Sol. Energy Mater.* **1** 319–41
- [4] Burkholder F and Kutscher C 2008 *Heat-loss testing of Solel's UVAC3 parabolic trough receiver* (United States: National Renewable Energy Laboratory (NREL), Golden, CO.)
- [5] Kennedy C E and Price H 2005 Progress in Development of High-Temperature Solar-Selective Coating *ASME Int. Sol. Energy Conf. Sol. Energy* 749–55
- [6] Twidell J and Weir T 2015 *Renewable Energy Resources* (New York: Routledge)
- [7] Kreith F and Kreider J F 1978 *Principles of solar engineering* (United States: Hemisphere Pub. Corp.)
- [8] Cyulinyana M C and Ferrer P 2011 Heat efficiency of a solar trough receiver with a hot mirror compared to a selective coating *South Afr. J. Sci.* **107** 01–07
- [9] Liu D-S, Sheu C-S, Lee C-T and Lin C-H 2008 Thermal stability of indium tin oxide thin films co-sputtered with zinc oxide *Thin Solid Films* **516** 3196–3203
- [10] William S J 2000 Engineering heat transfer *CRC Press Boca Raton Lond. N. Y. DC*
- [11] Mohamad K and Ferrer P Computational comparison of a novel cavity absorber for parabolic trough solar concentrators *Submitt. Proc. 62th Annu. Conf. South Afr. Inst. Phys. SAIP2017*

Tuning the Bandgap of Bulk Molybdenum Disulphide using Defects

P V Mwonga¹, S R Naidoo¹, A Quandt¹ and K I Ozoemena²

¹School of Physics, University of the Witwatersrand, Private Bag 3, Wits 2050, Johannesburg, South Africa

²School of Chemistry, University of the Witwatersrand, Private Bag 3, Wits 2050, Johannesburg, South Africa

E-mail: mwongav@gmail.com

Abstract. This report highlights the use of defects to change the electronic properties of bulk molybdenum disulphide (MoS₂). The defects introduced also have significant effects on the thermal properties. We further demonstrate the effects of altering the atom arrangement or introducing other atoms in the lattice, has on the electronic properties of MoS₂ and other metal dichalcogenides. Pristine MoS₂ is p-type semiconductor and it can also be turned into an n-type semiconductor, depending on the choice of impurity introduced. We have demonstrate this by using plots of Seebeck coefficients against chemical potential. The high Seebeck coefficients observed suggest that defect modified MoS₂ is a potential candidate for thermoelectric applications. The anisotropic nature of the electronic properties of MoS₂ is demonstrated for the thermal conductivity and electronic conductivity as a function of chemical potential. The induced defects lead to bandgap reductions ranging between 10.7% and 100%, relative to the pristine MoS₂.

1. Introduction

Bulk MoS₂ is a quasi-2D Material. Subject to the coordination of Mo atoms within a single layer and the stacking order of single layers, there are three known polytypes: 1T, 2H, and 3R of MoS₂. The 2H polytype is reported to be abundant in the earth's crust [1, 2] and with the discovery of direct bandgap in 2D MoS₂, there was a shift in research, away from the traditional applications like dry lubricants, hydrodesulphurisation catalysts, and cathode materials for lithium ion batteries towards possible applications in electronics [3]. The indirect bandgap in multi-layered MoS₂ still finds utility in electronic devices, and it can also be utilised in chemical applications such as hydrogen evolution reaction and chemical sensing [4, 5, 6].

The properties of monolayer MoS₂ have been studied both theoretically and experimentally [7, 8]. Reports on field effect transistors and phototransistors based on monolayer MoS₂ have suggested monolayer MoS₂ as a promising candidate materials for novel electronics and photonics devices [9]. First-principles calculations demonstrated a bandgap tuning in bilayer MoS₂ sheets by applying a perpendicular external electric field and they predicted that the electronic properties of armchair MoS₂ weakly dependent on width of the ribbon, whereas the zigzag MoS₂ exhibits metallic behavior [10]. The electronic properties of monolayer and multilayer MoS₂ have also been engineered by imposing compressive and tensile strains and they have shown to lead to a reduction in bandgap [11, 12]. The introduction of functional

groups (H, CH₃, CF₃, OCH₃, NH₂) into MoS₂ has also been examined and yielded a bandgap of ≈ 1 eV for the 1T polytype of MoS₂, using density functional theory (DFT) [13]. Most of the DFT works on MoS₂ bandgap tuning have been done only on 1D or 2D of 1T polytype of MoS₂. This study focuses on bulk MoS₂ -2H polytype tunability, driven by these demands, and seeks ways of altering the bandgap of bulk MoS₂ using a simpler approach of altering the atomic positions by either removing or introducing mainly an extra Mo or S atoms, which are constituent elements of MoS₂. Working with only MoS₂ constituent elements also avoids the introduction of toxic elements in possible applications. However, tungsten (W) was introduced in the crystal lattice of MoS₂ for the sake of comparison, and the choice motivated by the fact that it also forms a layered material with sulphur (WS₂).

2. Methodology

The simulations were based on density functional theory (DFT) modeling method, as implemented in quantum espresso (QE) [14] code. We used Perdew-Burke-Ernzerhof (PBE) functionals [15], which belong to generalised gradient approximation (GGA) functionals for exchange correlation energy E_{XC} .

A supercell of $2 \times 2 \times 2$ was constructed, based on the six atoms unit cell for the hexagonal polytype (2H) of MoS₂. The convergence test was done using plane wave cutoff energy of 75 Ry, with energy and forces convergence thresholds set at 10^{-6} and 10^{-4} , respectively. Defects were then introduced by either adding or removing atoms to/from the lattice, translating to a 2 % defect concentration. After system relaxation, we evaluated the band structure and the density of states (DOS). The Boltzmann transport properties (BoltzTraP) code [16], was used to calculate thermal and electronic transport properties. The BoltzTraP code is based on Boltzmann transport equation (1), which self-consistently solves the perturbation $g(k)$ to the distribution $f(k, T)$, using smoothed Fourier expressions for periodic functions.

$$g(k) = \frac{S_i[g(k)] - \nu(k)\left(\frac{\partial f}{\partial z}\right) - \frac{eE}{\hbar}\left(\frac{\partial f}{\partial k}\right)}{S_o(k) + \nu_{el}(k)}, \quad (1)$$

where E is the local electric field, $\nu(k)$ is the group velocity, ν_{el} is the overall elastic scattering mobility, while S_i , S_o are the inelastic phonon scattering and f is the Fermi-Dirac distribution. ν_{el} is evaluated by applying Matthiessen's rule, given by Equation (2)

$$\nu_{el}(k) = \nu_{ii}(k) + \nu_{pe}(k) + \nu_{de}(k) + \nu_{dis}(k), \quad (2)$$

where el , ii , pe and dis denote elastic, ionized impurity, piezoelectric, deformation potential and dislocation scattering rates, respectively.

Various properties can be computed by setting several terms in Equation (1) to zero. For instance the Seebeck coefficient (S) can be calculated by setting the applied electric driving force $(-\frac{eE}{\hbar})(\frac{\partial f}{\partial k})$ to zero and considering only thermal force, $\nu(\frac{\partial f}{\partial z})$.

$$\nu(\vec{k}) \cdot \nabla_r f(\vec{k}, T) = \int [s(k', \vec{k}) f(\vec{k}', T) (1 - f(\vec{k}, T)) - s(k, \vec{k}') f(\vec{k}, T) (1 - f(\vec{k}', T))] d\vec{k}', \quad (3)$$

where $s(k, \vec{k}')$ is the differential scattering rate from the state k' to the state characterized by \vec{k} , implies that Equation 3 is an equation for S .

Equation 3 is then iteratively solved after which $f(\vec{k}, T)$ and $f(\varepsilon, T)$ are converted to each other by solving Kohn-Sham equation for $\varepsilon(\vec{k})$. This is achieved through setting fixed potential or by applying non-self consistent calculation approach. The transport properties are obtained from the conductivity distributions given by Equations 4, 5 and 6.

$$\sigma_{\alpha\beta}(T; \mu) = \frac{1}{\Omega} \int \sigma_{\alpha\beta}(\varepsilon) \left[-\frac{\partial f_{\mu}(T; \mu)}{\partial \varepsilon} \right] d\varepsilon, \quad (4)$$

$$\kappa_{\alpha\beta}(T; \mu) = \frac{1}{e^2 T \Omega} \int \sigma_{\alpha\beta}(\varepsilon) (\varepsilon - \mu)^2 \left[-\frac{\partial f_{\mu}(T; \mu)}{\partial \varepsilon} \right] d\varepsilon, \quad (5)$$

$$S_{\alpha\beta}(T; \mu) = \frac{(\sigma^{-1})_{\gamma\alpha}}{e T \Omega} \int \sigma_{\gamma\beta}(\varepsilon) (\varepsilon - \mu) \left[-\frac{\partial f_{\mu}(T; \mu)}{\partial \varepsilon} \right] d\varepsilon, \quad (6)$$

where $\sigma_{\alpha\beta}$, $\kappa_{\alpha\beta}$ and $S_{\alpha\beta}$ are the electrical conductivity, electronic thermal conductivity and thermopower, respectively. The projected energy conductivity $\sigma_{\alpha\beta}(\varepsilon)$ is defined as;

$$\sigma_{\alpha\beta}(\varepsilon) = \frac{1}{N} \sum_{i,k} \sigma_{\alpha\beta}(i, k) \frac{\sigma(\varepsilon - \varepsilon_{i,k})}{d\varepsilon}, \quad (7)$$

with

$$\sigma_{\alpha\beta}(i, k) = e^2 \tau_{i,k} \nu_{\alpha}(i, k) \nu_{\beta}(i, k), \quad \nu_{\alpha}(i, k) = \frac{1}{\hbar} \frac{\partial \varepsilon_{i,k}}{\partial k_{\alpha}}, \quad (8)$$

where τ is the electronic relaxation time, ν_{α} is the group velocity; which is calculated from the band structure $\varepsilon_{i,k}$. Since the electronic scattering is taken to be independent of energy, the transport properties are therefore integrated within the BoltzTraP code.

3. Results and Discussion

First we discuss the effects on electronic bandgap upon introduction or removal of atoms. This created vacancies or interstitial defects, intercalation.

3.1. Electronic properties

Figs. 1(a) and 1(b) show the supercell structure of hexagonal pristine MoS₂ of 48 atoms (16 Mo atoms and 32 S atoms) and its corresponding band structure, alongside its projected density of states (PDOS).

All the defect enhanced band structures (not included in this report) showed a decrease in energy band gap (E_g) compared to the E_g for pristine MoS₂. This is clearly shown in Table 1, whereby transition metal interstitials (Mo-interstitial and W-interstitial), lead to the highest energy bandgap reduction. The Mo-interstitials actually turned the semiconductor MoS₂ into a conductor [17].

Table 1. Comparison of bandgaps of pristine and defective MoS₂.

Structure defect	Bandgap E_g	%
	(eV)	Reduction
Pristine	1.32	
Mo-vacancy	0.551	58.2
Mo-intercalation	0.651	50.7
Mo-interstitial	0	100
S-vacancy	0.438	66.8
S-intercalation	1.18	10.7
W-interstitial	0.336	74.5

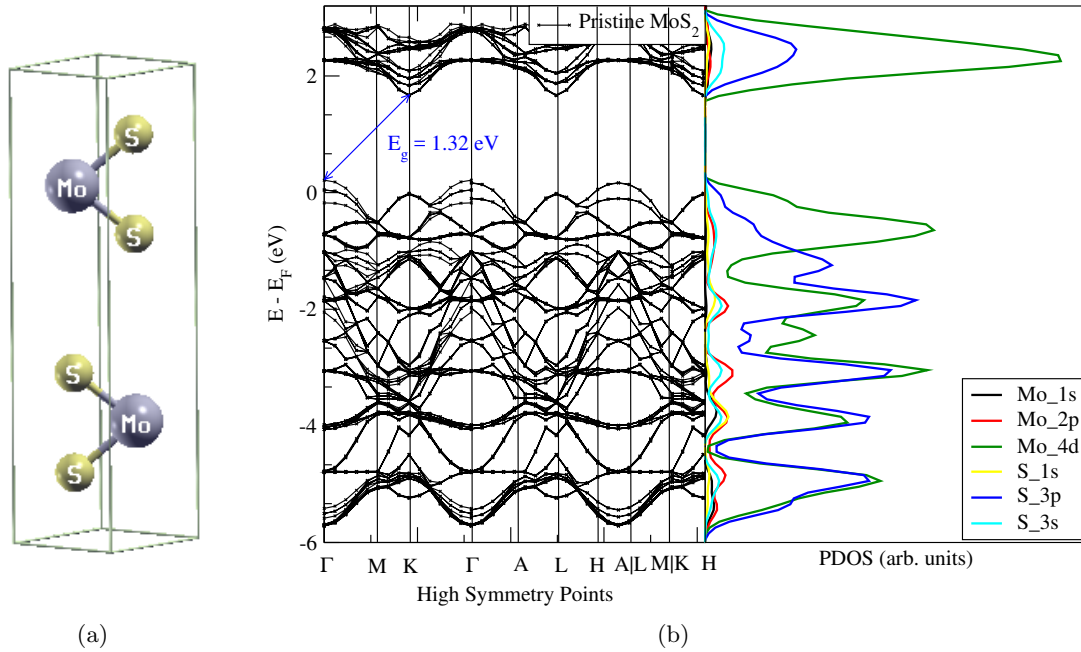


Figure 1. (a) Unit-cell structure of pristine MoS₂ (b) Band structure and PDOS of pristine MoS₂. An indirect bandgap of 1.32 eV is seen for pristine MoS₂. Based on the PDOS, Mo-4d orbitals are dominant in the conduction band of MoS₂.

3.2. Thermal and transport properties

Calculations of the electronic conductivities (σ), as well as of the electronic contribution to the thermal conductivity (κ), were also carried out for the pristine MoS₂, MoS₂ with Mo and W atom interstitials. We report both σ and κ at 300 K and in the xx direction, since xx and yy are the same. Major difference are found in the zz direction, where σ and κ diminishes due the anisotropic nature of MoS₂. MoS₂ remained anisotropic even after the introduction of Mo and W interstitials.

From Figure 2 the energy bandgaps calculated using BoltzTraP code are similar to what we got from QE code, except for the pristine material, with a difference of 0.04 eV. The σ for pristine MoS₂, MoS₂ with Mo and W atom interstitials (Mo_i and W_i, respectively), are as follows: 5.6×10^6 ; 3.534×10^6 and 2.918×10^6 ($\Omega \cdot m$)⁻¹, respectively. This implies that the introduction of Mo and W atoms increased the resistivity (ρ) of MoS₂, with W interstitial recording the highest values of ρ of 3.427×10^{-7} $\Omega \cdot m$.

Figure 2 also shows the effects after introducing defects in the lattice of MoS₂, on the thermal conductivity. The thermal conductivity decreased in the same order as the electronic conductivities, pristine MoS₂ with 36.8 W·m⁻¹·K⁻¹, MoS₂ with Mo interstitial, 23.43 W·m⁻¹·K⁻¹ and MoS₂ with W interstitial 20.67 W·m⁻¹·K⁻¹.

Another characteristic noted upon defect creation, was the ability to change a p-type semiconductor into an n-type semiconductor. When the Seebeck coefficient (S) is greater than zero at the chemical potential $\mu = 0$, then we have a p-type semiconductor; and if $S < 0$ at $\mu = 0$ we have a n-type semiconductor [18]. Figs. 3(a), 3(b) and 3(c) show how MoS₂ semiconductor behaviour is affected by the introduction of Mo and W ions at 300 K, 500 K and 800 K. Generally, increase in temperature shows decrease in S, except in Fig. 3(b) where temperature increase led to a rise in S, upto 500 K after which a reduction in S was observed at 800 K.

MoS₂ with a Mo interstitial changes from a p-type to an n-type as shown in Fig. 3(b). However, MoS₂ with a W interstitial remains a p-type semiconductor just like pristine MoS₂.

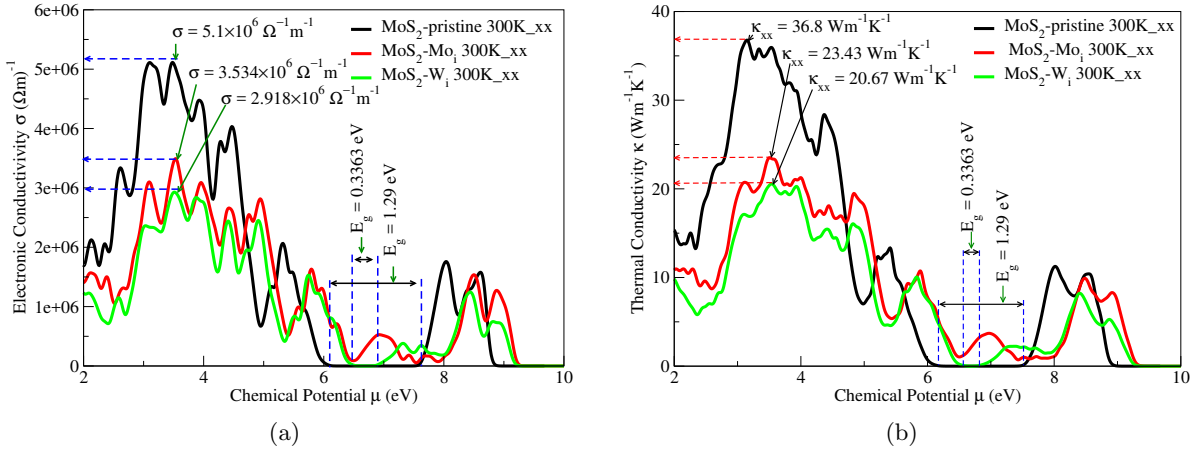


Figure 2. (a) Electronic conductivity vs chemical potential for pristine MoS₂ and MoS₂ Mo and W interstitials (b) Thermal conductivity vs chemical potential for pristine MoS₂ and MoS₂ Mo and W interstitials.

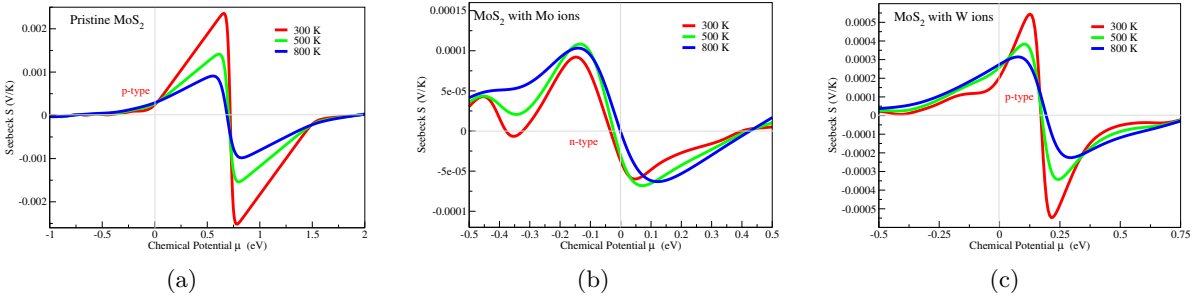


Figure 3. Seebeck coefficient vs chemical potential for temperatures; 300 K, 500 K and 800 K, for; (a) pristine MoS₂ (b) MoS₂ with Mo interstitial (c) MoS₂ with W interstitial.

An increase in temperature from 300 K to 800 K reduced the Seebeck coefficient (S) in both pristine MoS₂ and MoS₂ with Mo interstitial, but in the case of MoS₂ with W interstitial, increase in temperature increased Seebeck coefficient. At 300 K, we obtained S values of 2379 $\mu\text{V/K}$, 109 $\mu\text{V/K}$, and 544 $\mu\text{V/K}$ for pristine MoS₂, MoS₂ with Mo interstitial and MoS₂ with W interstitial, respectively. Our S values were quite high compared to the 1400 $\mu\text{V/K}$ reported by Lee *et al.*[19] at 300 K and using $\mu \approx \pm 0.1 \text{ eV}$, for pristine MoS₂. Since S is directly related to thermopower, our defect modified MoS₂ is good candidate for thermoelectric applications. High efficiency of a thermoelectric material is determined by the figure of merit (ZT) given by;

$$ZT = S^2 \sigma T / \kappa, \quad (9)$$

where S is the Seebeck coefficient, σ is the electrical conductivity, and κ is the thermal conductivity at a given temperature T . Note that $\kappa = \kappa_e + \kappa_p$, where κ_e and κ_p are the electronic and phononic contributions to the thermal conductivity. However, we didn't calculate ZT due to our computational resources limitation.

Thermal conductivities (κ) after introduction of Mo interstitials into MoS₂ dropped from $36.8 \text{ W}\cdot\text{m}^{-1}\cdot\text{K}^{-1}$ to $23.43 \text{ W}\cdot\text{m}^{-1}\cdot\text{K}^{-1}$. These findings are in agreement with a report by Jin *et al.* [20]. A similar drop in κ was noted with a W interstitial, which amounts to $20.67 \text{ W}\cdot\text{m}^{-1}\cdot\text{K}^{-1}$. The electronic conductivities (σ) dropped from $5.1 \times 10^6 \Omega^{-1}\cdot\text{m}^{-1}$ to $3.5 \times 10^6 \Omega^{-1}\cdot\text{m}^{-1}$, for MoS₂ with Mo interstitial; and to $2.9 \times 10^6 \Omega^{-1}\cdot\text{m}^{-1}$, for MoS₂ with W interstitial. Introduction of

defects in MoS₂ could be the key for new applications of MoS₂ [21]. A similar drop in κ was noted with a W interstitial, which amounts to 20.67 W·m⁻¹·K⁻¹. The electronic conductivities (σ) dropped from $5.1 \times 10^6 \Omega^{-1}\cdot\text{m}^{-1}$ to $3.5 \times 10^6 \Omega^{-1}\cdot\text{m}^{-1}$, for MoS₂ with Mo interstitial; and to $2.9 \times 10^6 \Omega^{-1}\cdot\text{m}^{-1}$, for MoS₂ with W interstitial. Introduction of defects in MoS₂ could be the key for new applications of MoS₂ [21]. The ability to change MoS₂ energy conversion devices, like solar cells from its usual p-type semiconductor to an n-type behaviour which could have applications in semiconductor junctions where higher conductivity is desired [22].

4. Conclusion

We have shown how the MoS₂ energy bandgap could be tuned, by defect creation. A reduction of the bandgap between 10.7% and 100% has been achieved where metal interstitials (Mo and W) show the highest reductions of 74.5% and 100% for tungsten and molybdenum atoms, respectively. Thermal conductivities (κ) after introduction of Mo and W interstitial into MoS₂ dropped by about 36% and 44 %, respectively. Similarly, a reduction of the electronic conductivities (σ) was noted as 31 % for Mo interstitial and 43 % in the case of MoS₂ with W interstitial. From the Seebeck coefficient results, the ability to change MoS₂ semiconductor type has the potential of being used in a wider range of energy conversion devices. Based on our results, the technique we used could be extended to other transition metal dichalcogenides (TMD) as well.

Acknowledgments

The authors would like to thank the University of the Witwatersrand for their support, and the Centre for High Performance Computing (CHPC) for granting us access to their facility, in order to carry out the simulations discussed in this paper. Finally we would like to thank the Materials for Energy Research Group (MERG) for support.

References

- [1] Braithwaite E, Reeves D and Haber J 2013 *Molybdenum* **19** 19–29
- [2] Song I, Park C, and Choi H 2015 *Rsc Advances* **5** 7495–7514
- [3] Radisavljevic B, Radenovic A, Brivio J, Giacometti I, and Kis A 2011 *Nature Nanotechnology* **6** 147
- [4] Jaramillo T, Jørgensen K, Bonde J, Nielsen J, Horch S, and Chorkendorff I 2007 *Science* **317** 100–102
- [5] Hinnemann B, Moses P, Georg B, Jørgensen K P Nielsen J H, Horch S, Chorkendorff I, and Nørskov J K 2005 *Journal of the American Chemical Society* **127** 5308–5309
- [6] Li H, Yin Z, He Q, Li H, Huang X, Lu G, Fam D, Wen H, Tok A I and Zhang Q and Zhang H 2012 *Small* **8** 63–67
- [7] Jing Y, Tan X, Zhou Z, and Shen P, 2014 *Journal of Materials Chemistry A* **2** 16892–16897
- [8] Li H, Zhang Q, Yap C, Tay B, Edwin T, Olivier A, Baillargeat D, 2012 *Advanced Functional Materials* **22** 1385–1390
- [9] Yin Z, Li H, Jiang L, Shi Y, Sun Y, Lu G, Zhang Q, Chen X, and Zhang H 2011 *ACS Nano* **6** 74–80
- [10] Pan H 2014 MoS₂ 1–35
- [11] Yue Q, Chang S, Kang J, Zhang X, Shao Z, Qin S and Li J 2012 *Journal of Physics, Condensed Matter* **24** 335501
- [12] Ramasubramanian A, Naveh D and Towe E 2011 *Physical Review B* **84** 205325
- [13] Tang Q and Jiang D 2015 *ACS Publications: Chemistry of Materials* **27** 3743–3748
- [14] Giannozzi P, Baroni S, Bonini N, Calandra M, Car R, Cavazzoni C, Ceresoli D, Chiarotti G, Cococcioni M, Dabo I et al. 2009 *Journal of Physics, Condensed Matter* **21** 395502
- [15] Wu Z and Cohen R E 2006 *Physical Review B* **73** 235116
- [16] Madsen G K and Singh D J 2006 *Computer Physics Communications* **175** 67–71
- [17] Wang Q H, Kalantar-Zadeh K, Kis A, Coleman J N, and Strano M S 2012 *Nature Nanotechnology* **7** 699
- [18] Jayaraman A, Bhat K A and Molli M 2016 *Indian Journal of Materials Science* **2016** 1155–1162
- [19] Lee C, Hong J, Lee W R, Kim D Y and Shim J H 2014 *Journal of Solid State Chemistry* **211** 113–119
- [20] Jin Z, Liao Q, Fang H, Liu Z, Liu W, Ding Z, Luo T and Yang N 2015 *Scientific Reports* **5** 18342
- [21] Choi, M S, Qu D Lee D, Liu X, Watanabe K, Taniguchi T and Yoo W J 2014 *ACS Nano* **8** 9332–9340
- [22] Mouri S, Miyauchi Y and Matsuda K 2013 *Nano Letters* **13** 5944–5948

DFT Study of selected croconate dye molecules for application in dye sensitized solar cells

T S Ranwaha¹, N E Maluta^{1,2} and R R Maphanga^{2,3}

¹University of Venda, Department of Physics, P/Bag X 5050, Thohoyandou, 0950.

²National Institute for Theoretical Physics (NITheP), Gauteng, South Africa.

³Council for Scientific and Industrial Research, P.O.Box 395, Pretoria, 0001

Email: funawahau@gmail.com

Abstract. Density functional theory (DFT) has been used to study the electronic and optical properties of selected Croconate dye molecules (CR2-I and CR3-Br). The generalized gradient approximation (GGA) was used in the scheme of Perdew-Burke Ernzerhof to describe the exchange-correlation function as implemented in the CASTEP package in material studio of BIOVIA. The calculations are based on the determinations of Absorption spectrum, UV-Vis spectrum, Light Harvesting Efficiency and HOMO-LUMO gap of the dye molecules. The calculated HOMO-LUMO gap was found to be 2.08 eV and 1.09 eV for CR2-I and CR3-Br respectively, the highest percentage of light harvesting efficiency was found to be 97 % for CR2-I and 98 % for CR3-Br. The results obtained shows that CR2-I and CR3-Br dye molecules can improve the efficiency of DSSCs as they shows absorption shift to the near infrared, which increase the absorption range from the visible on the solar spectrum.

1. Introduction

Solar energy is the perfect key to sustainable development for future energy requirements. Solar cells are promising devices to generate clean energy. Dye sensitive solar cells (DSSCs) consist of a photo electrode which combines semiconductor material (TiO₂) and sensitized dye molecule [1]. The dye molecule is a sensitizer material that absorbs photons from the sun, excites an electron into semiconductor, while the electrolyte regenerate the excited dye to complete the electron transport [2-3]. It's role requires well matched energy level to facilitate efficient electron injection and dye regeneration, strong physical anchoring to photoanode, sufficient absorption of solar light, and stable operation for a long period [1-3]. Corneliu *et al* [4] investigated various single and double deprotonated forms of the dye bound to a TiO₂ cluster, taking advantage of the presence of the carboxyl (–CO₂H), hydroxyl (–OH), and sulfonic (–SO₃H) groups as possible anchors. They reported that anchoring modes of the dye onto the TiO₂ surface are of crucial importance to the DSSCs performance through the bonding type and the extent of electronic coupling between the dye excited state and the conduction band edge of the semiconductor [4]. As most of the theoretical studies so far have been focused on the sensitizers with the carboxyl groups as anchors, with advantage of the opportunity offered by the protonated form of the Mordant Yellow 10 dye, which has –OH, –CO₂H and –SO₃H groups. These theoretical studies are based on understanding various anchors, binding configurations as well as propensities for electron transfer [4]. On the same work Corneliu *et al* [4] reported the results of density functional theory (DFT) and time-dependent DFT (TD-DFT) studies of several coumarin-based dyes, as well as complex systems consisting of the dye bound to a TiO₂ cluster. They provide the electronic structure and simulated UV-Vis spectra of the dyes and discussed the properties of the adsorbed dye molecule on the TiO₂ surface, which matches with the solar spectrum. Their results were compared with the experimental data available and discuss the key issues that influence the device performance like absorption spectra, the energy level alignment between the dye, the oxide and the electrolyte, and the adsorption of the dye to the substrate. In the current study we focuses on the understanding of different properties (electronic and optical properties) of selected Croconate dye molecules shown in figure 1 (CR2-I and CR3-Br) using the density functional theory (DFT).

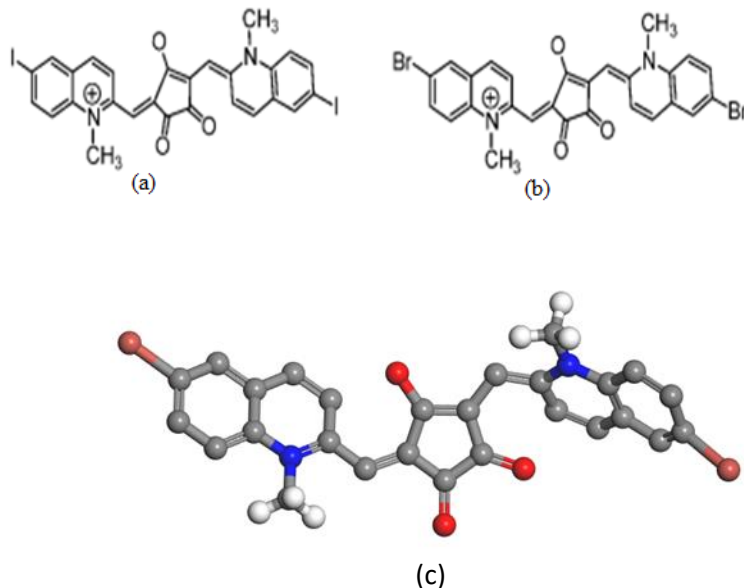


Figure 1: Structures of the Croconate Dyes molecules CR2-I and CR3-Br (a) and (b) from Ref [5], and (c) optimised geometry structure built using a Material Studio package and the colours used in this work (red is Oxygen, grey is Carbon, white is Hydrogen, blue is Nitrogen and brown is Iodine for CR 2- I and Bromine for CR 3-Br).

Figure 1 shows the structures of Croconate dye molecules investigated in this study, CR 2-I and CR 3-Br with halide functional group and containing the oxyallyl subgroup in the parent structure. CR 2- I and CR 3-Br exhibit strong absorption in the infrared, and possess donor–acceptor–donor type structure. These dye molecules can be synthesized easily and give rise to DSSCs that are flexible and interact strongly with light

2. Computational method

The structures of the selected Croconate dye molecules were built using a Material Studio package. The dye molecules structure was cleaned so that the atoms are reoriented in their lattice positions. Geometrical optimization and calculation of optical absorption of the dye molecules were performed by the CASTEP code in Material Studio package using density functional theory (DFT), which uses a plane-wave pseudopotential method of generalized gradient approximation (GGA) in the scheme of Perdew-Bruke-Ernzerhof (PBE) to describe the exchange-correlation functional using the coarse quality and all band/EDFT as electronic minimizer [6]. The ground state structures obtained through geometrical optimization structures were imported into a new 3D atomistic window and the calculation of electronic properties and UV-Vis of the dye molecule were performed using the VAMP module within the Material Studio package [7].

3. Results and discussion

3.1. Excitation and absorption spectrum of the Dyes

The UV-Vis spectrum of the two dye molecules used in this study shows that these molecules can absorb more photons at visible spectrum to the near infrared region of solar spectrum with a stronger peak at 610 nm with oscillator strength (Absorbance) of 1.78 for CR3-Bromine and a stronger peak at 635nm with oscillator strength (Absorbance) of 1.51 for CR2-Iodine. There are some weak absorption peaks near the infrared region for both CR2-iodine and CR3-Bromine. The following spectrum shows that there is an activity in visible to near infrared region of the solar spectrum, therefore these molecules can enhance the performance of solar cells.

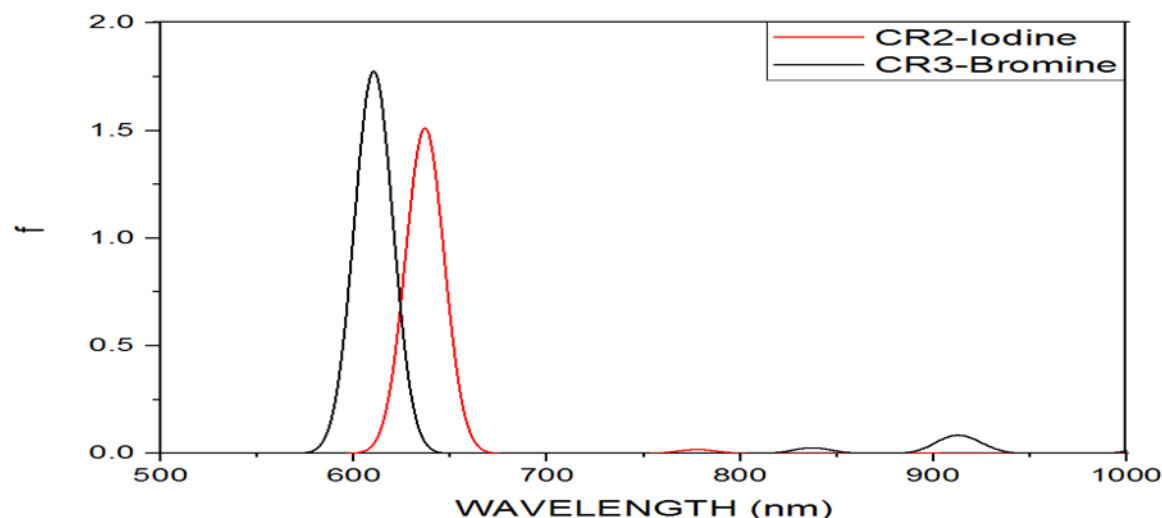


Figure 2: Calculated UV-Vis spectrum for CR2-Iodine and CR3-Bromine dye molecules.

Light harvesting efficiency of CR2-Iodine and CR3-Bromine at the absorption peaks was calculated using equation:

$$LHE(\lambda) = 1 - 10^{-f} \quad (1)$$

where f denotes the absorption also called the oscillator strength of sensitizer at a given wavelength (λ).

Table 1: LHE of CR2-Iodine at a particular wavelength

Wavelength (nm)	Absorption	LHE	LHE (%)
635	1.51	0.97	97
777	0.018	0.04	4

Table 2: LHE of CR3-Bromine at a particular wavelength

Wavelength (nm)	Absorption	LHE	LHE (%)
610	1.78	0.98	98
837	0.03	0.05	5
912	0.09	0.18	18

The light harvesting efficiency (LHE) of the sensitizer affects the short-circuit current density (J_{sc}), and hence, the overall power conversion efficiency (η). The calculated LHE values of CR2-I and CR3-Br found are shown in Table 1 and Table 2 respectively. The maximum values of LHE found to be 0.97 (97 %) at $\lambda_{max} = 635$ nm and 0.98 (98 %) at $\lambda_{max} = 610$ nm.

3.2. Optical absorption property of the dye molecules

Figure 3 illustrate the optical absorption property of CR2-I and CR3-Br dye molecules. The figure shows an absorption activity in the visible to near infrared region. The absorption in the ultraviolet region for CR2-I and CR3-Br are common for many synthesizer. The results illustrate that Croconate dyes CR2-I and CR3-Br as synthesizers in DSSCs can shift the absorption of photons from the ultraviolet region to the visible to near infrared region, hence improve the practical performance of DSSCs.

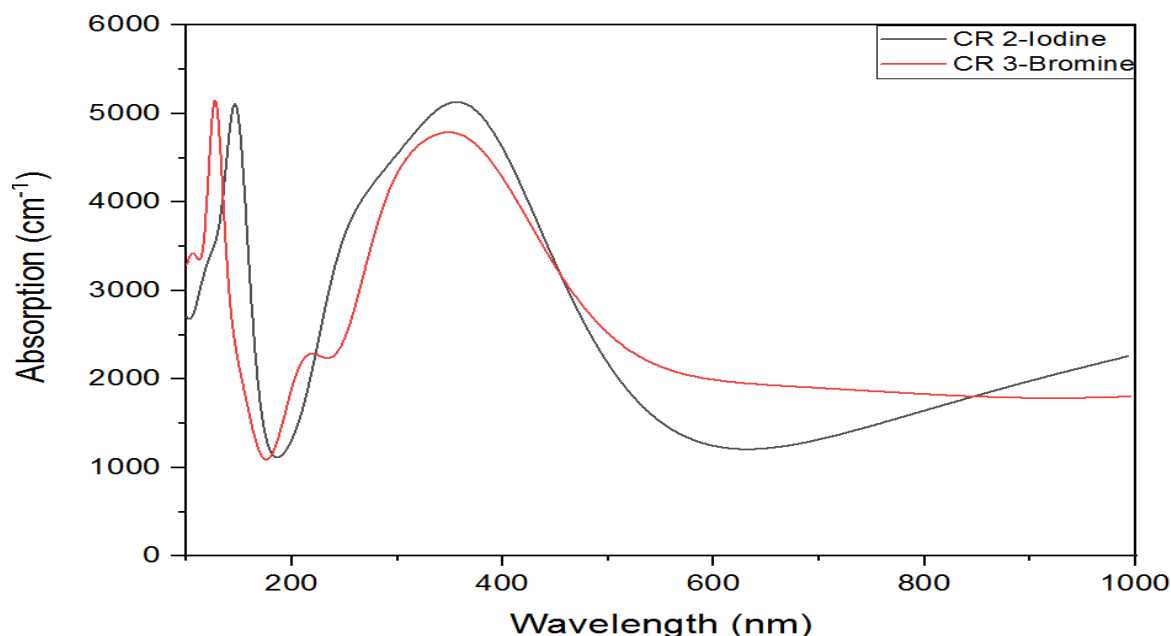


Figure 3: Calculated optical absorption for CR2-I and CR3-Br dye molecules.

3.3. Energy levels and isodensity surfaces of the dyes

Table 3: The HOMO, LUMO and HOMO-LUMO energy gap of CR 2-I and CR 3-Br dye molecules.

DYE MOLECULE	HOMO (eV)	LUMO (eV)	HOMO-LUMO GAP (eV)
CR2-I	-6.53	-4.45	2.08
CR3-Br	-6.88	-5.79	1.09

Table 3 shows the molecular orbitals of CR2-I and CR3-Br. The HOMO energies of CR2-I and CR3-Br are -6.53 eV and -6.88 eV respectively, the LUMO energies of CR2-I and CR3-Br are -4.45 eV and -5.79 eV respectively. The HOMO–LUMO energy gap (HLG) values of CR2-I and CR3-Br were 2.08 eV and 1.09 eV respectively. The smaller HOMO–LUMO gap favors the absorption of photons in the long-wavelength region. Figure 4 shows the molecular orbitals involved in the dominant electron transitions of CR2-I and CR3-Br.

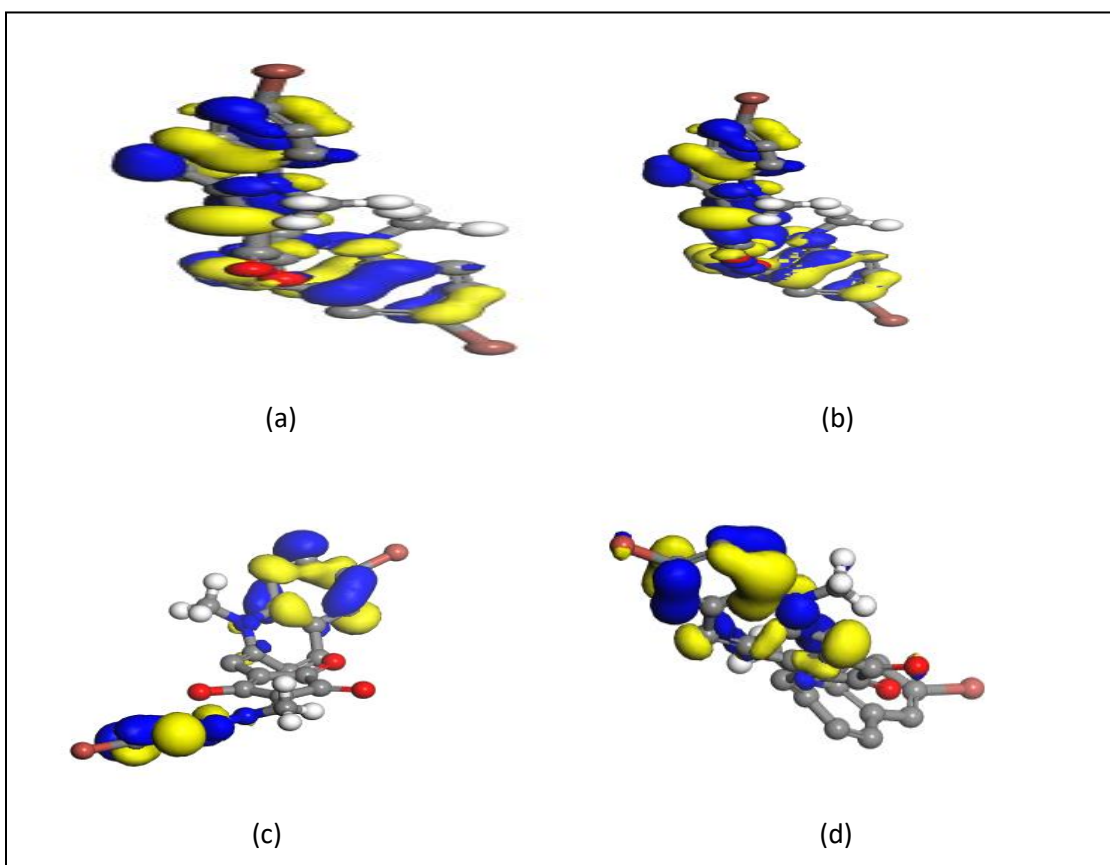


Figure 4: Isodensity surfaces of the molecular orbitals of (a) highest occupied molecular orbital of CR2-I (b) lowest unoccupied molecular orbital of CR2-I (c) highest occupied molecular orbital of CR3-Br (d) lowest unoccupied molecular orbital of CR3-Br

4. Conclusion

First principle DFT studies were used to investigate the electronic and optical properties of selected Croconate dye molecules (CR2-I and CR3-Br) with halide functional group. The HOMO-LUMO gap values of two molecules are less than the band gap values of TiO_2 semiconductors, and this means that electron injection from excited dye molecules to the conduction band of TiO_2 semiconductor will be efficient. The UV-Vis spectrum and optical absorption spectrum of the two molecules shows the photon absorption activity in the visible to near infrared region, hence the use of these dye molecules can improve the practical performance of DSSCs.

5. Acknowledgement

This work is financially supported through the NRF Thuthuka, DST Renewable Energy Funding, merSETA and the National institute for theoretical Physics (NiTheP). We would also like to thank the University of Venda for the support to carry out this research and Centre for High performance Computing (CHPC) for using their computing facilities.

References

- [1] Rokesh, K., Pandikumar, A., & Jothivenkatachalam, K. (2014). Dye sensitized solar cell: a summary. In *Materials Science Forum* (Vol. 771, pp. 1-24). Trans Tech Publications.
- [2] Wang, Y., Zhang, R., Li, J., Li, L., & Lin, S. (2014). First-principles study on transition metal-doped anatase TiO₂. *Nanoscale research letters*, 9(1), 46.
- [3] Triggiani, L., Munoz-Garcia, A. B., Agostiano, A., & Pavone, M. (2015). First-principles study of trimethylamine adsorption on anatase TiO₂ nanorod surfaces. *Theoretical Chemistry Accounts*, 134(10), 119.
- [4] Corneliu O. I., Panait, P., Lungu, J., Stamate, D., Dumbravă, A., Cimpoesu, F., & Gîrțu, M. A. (2013). DFT study of binding and electron transfer from a metal-free dye with carboxyl, hydroxyl, and sulfonic anchors to a titanium dioxide nanocluster. *International Journal of Photoenergy*, 2013.
- [5] Takechi, K., Kamat, P. V., Avirah, R. R., Jyothish, K., & Ramaiah, D. (2007). Harvesting infrared photons with croconate dyes. *Chemistry of Materials*, 20(1), 265-272.
- [6] Han, Y. X., Yang, C. L., Wang, M. S., Ma, X. G., & Wang, L. Z. (2015). Enhancing the visible-light absorption of TiO₂ with the use of key N, Co, and Na dopant concentrations. *Solar Energy Materials and Solar Cells*, 132, 94-100.
- [7] Clark, S. J., Segall, M. D., Pickard, C. J., Hasnip, P. J., Probert, M. I., Refson, K., & Payne, M. C. (2005). First principles methods using CASTEP. *Zeitschrift für Kristallographie-Crystalline Materials*, 220(5/6), 567-570.

DIVISION G

Division for Theoretical and Computational Physics

Quasi-normal modes of spin-3/2 fields in D -dimensional Reissner-Nordström black hole spacetimes using the continued fraction method

A S Cornell¹ and G E Harmsen²

National Institute for Theoretical Physics; School of Physics, University of the Witwatersrand, Johannesburg, Wits 2050, South Africa.

E-mail: ¹alan.cornell@wits.ac.za, ²gerhard.harmsen5@gmail.com

Abstract. In a recent paper we calculated the field equations of spin-3/2 fields in a D -dimensional Reissner-Nordström black hole spacetime whilst maintaining the gauge symmetry of the Rarita-Schwinger equation. We were also able to determine the quasi-normal modes of the associated gauge invariant variables using the WKB approximation and the asymptotic iteration method (AIM). However, it was found that for higher dimension, and especially for the near extremal cases, the effective potential developed another maximum. The shape of the potential posed difficulties for the WKB approximations, as well as the AIM. As such, in these proceedings we explore the connection between the AIM and the continued fraction method, and determine a possible reason for the difficulty in calculating the quasi-normal modes for spin-3/2 fields in this spacetime.

1. Introduction

The Rarita-Schwinger equation describes the equations of motion of spin-3/2 fields on a Reissner-Nordström (RN) spacetime by making use of a supercovariant derivative, that is:

$$\gamma^{\mu\nu\alpha}\tilde{\mathcal{D}}_\nu\psi_\alpha = 0, \quad (1)$$

where

$$\gamma^{\mu\nu\alpha} = \gamma^\mu\gamma^\nu\gamma^\alpha - \gamma^\mu g^{\nu\alpha} + \gamma^\nu g^{\mu\alpha} - \gamma^\alpha g^{\mu\nu} \quad (2)$$

is the antisymmetric product of Dirac matrices, ψ_α is the spin-3/2 field and

$$\tilde{\mathcal{D}}_\mu = \nabla_\mu + \frac{1}{2}\sqrt{\frac{D-3}{2(D-2)}}\gamma_\rho F_\mu^\rho + \frac{i}{4\sqrt{2(D-2)(D-3)}}\gamma_{\mu\rho\sigma}F^{\rho\sigma} \quad (3)$$

is the supercovariant derivative calculated in Ref.[1]. This equation preserves the gauge invariance of the Rarita-Schwinger equation that was noted in Refs.[2, 3]. However, when attempting to calculate the quasi-normal modes (QNMs) several parameter choices do not lead to convergent or reliable numbers when using the WKB approximation and the asymptotic iteration method (AIM) [1].

For the WKB approximation it was found that unreliable QNM results were those where the parameter choices led to higher order terms dominating over the lower order terms. Recall that

the WKB approximation is generated from a series expansion, and as such results where higher order terms dominate over lower order ones cannot be considered reliable. As for the AIM, the results did not converge for such choices of parameters, making them unreliable also, where it was found that as the number of iterations in this method were increased, these results did not converge to any one number. As such, in our previous work [1], no numbers for these QNMs were given for such parameter choices.

It was proposed that this peculiar behaviour was due to a second maxima developing in the effective potential, where this was clearly visible in higher dimensions ($D > 7$) and when the charge of the black hole approached its extremal value. Given that the WKB approximation, when applied to black hole studies, involves expanding the potential around its maximum value and then matching two WKB solutions from either side of this maximal region of the potential, having two maxima renders the approximation unreliable in its current form. However, it remains unclear as to why the AIM would break down, given all previous investigations have found it to be quite stable [4, 5, 6].

As such, it is the aim of this proceedings to investigate these unreliable quasi-normal frequencies with a third method for calculating QNMs, that of the continued fraction method (CFM) [7], and to test the claim that the AIM and the CFM are connected [8].

2. The spin-3/2 fields equations in a RN spacetime

Using the line element for the RN spacetime,

$$ds^2 = -f dt^2 + \frac{1}{f} dr^2 + r^2 d\bar{\Omega}_{D-2}^2, \quad (4)$$

where $f = 1 - 2M/r^{D-3} + Q^2/r^{2D-6}$, and $d\bar{\Omega}_{D-2}$ denotes the metric of the $D-2$ sphere (overbars will represent terms from this metric), our wave functions for the spin-3/2 fields can be constructed from “non TT eigenmodes” and “TT eigenmodes” [1, 2].

Focussing on the non-TT eigenfunctions, where a large number of the unreliable QNMs were observed in Ref.[1], the radial and temporal wave functions can be written as:

$$\psi_r = \phi_r \otimes \bar{\psi}_{(\lambda)} \quad \text{and} \quad \psi_t = \phi_t \otimes \bar{\psi}_{(\lambda)}, \quad (5)$$

where $\bar{\psi}_{(\lambda)}$ is an eigenspinor on the $D-2$ sphere with eigenvalue $i\bar{\lambda}$ given by $\bar{\lambda} = (j + (D-3)/2)$, where $j = 3/2, 5/2, 7/2, \dots$. Our angular wave function is written as:

$$\psi_{\theta_i} = \phi_{\theta}^{(1)} \otimes \bar{\nabla}_{\theta_i} \bar{\psi}_{(\lambda)} + \phi_{\theta}^{(2)} \otimes \bar{\gamma}_{\theta_i} \bar{\psi}_{(\lambda)}, \quad (6)$$

where $\phi_{\theta}^{(1)}, \phi_{\theta}^{(2)}$ are functions of r and t which behave like 2-spinors.

Using the Weyl gauge, $\phi_t = 0$, we introduce a gauge invariant variable

$$\Phi = - \left(\frac{\sqrt{f}}{2} i\sigma^3 + \frac{iQ}{2r^{D-3}} \right) \phi_{\theta}^{(1)} + \phi_{\theta}^{(2)}, \quad (7)$$

to determine the independent equations of motion. Component-wise we can write Φ as:

$$\Phi = \begin{pmatrix} \phi_1 e^{-i\omega t} \\ \phi_2 e^{-i\omega t} \end{pmatrix}, \quad (8)$$

where ϕ_1 and ϕ_2 are purely radially dependent terms. To simplify the equations we further set

$$\phi_1 = \frac{\left(\frac{D-2}{2}\right)^2 f - (\bar{\lambda} + C)^2}{Br^{(D-4)/2} f^{1/4}} \tilde{\phi}_1 \quad \text{and} \quad \phi_2 = \frac{\left(\frac{D-2}{2}\right)^2 f - (\bar{\lambda} - C)^2}{Ar^{(D-4)/2} f^{1/4}} \tilde{\phi}_2. \quad (9)$$

This leads to a set of decoupled second-order differential equations in the tortoise coordinates, defined by $dr_* = dr/f(r)$:

$$\begin{aligned} -\frac{d^2}{dr_*^2}\tilde{\phi}_1 + V_1\tilde{\phi}_1 &= \omega^2\tilde{\phi}_1, \\ -\frac{d^2}{dr_*^2}\tilde{\phi}_2 + V_2\tilde{\phi}_2 &= \omega^2\tilde{\phi}_2, \end{aligned} \quad (10)$$

where $V_{1,2} = \pm f(r)dW/dr + W^2$ and

$$\begin{aligned} W &= \frac{(D-3)\sqrt{f}}{rAB} \left[(\bar{\lambda} + C) \frac{2}{D-2} AB + \frac{D-2}{2} (C + \bar{\lambda}(1-f)) \right] \\ &\quad - \frac{D-4}{r(D-2)} \sqrt{f}(\bar{\lambda} + C), \end{aligned} \quad (11)$$

$$A = \frac{D-2}{2} \sqrt{f} + (\bar{\lambda} + C), \quad B = \frac{D-2}{2} \sqrt{f} - (\bar{\lambda} + C) \quad \text{and} \quad C = (D-2) \frac{Q}{2r^{D-3}}. \quad (12)$$

3. The asymptotic iteration method

In our previous works we had used the AIM to generate some of our QNMs. In the AIM we first single out the asymptotic behaviour, which is due to the QNM boundary condition that the wave function must have the form of $\tilde{\phi}_1 \sim e^{\pm i\omega r_*}$. Our first step is to determine the tortoise coordinates for the specific spacetime we are considering, that is the spacetime for specific values of Q and D . Plugging this into the wave function we then transform our wave function to the coordinates

$$\xi^2 = 1 - \frac{r_+}{r}, \quad (13)$$

where $r_+ = (M + \sqrt{M^2 - Q^2})^{1/(D-3)}$, such that $\xi \in [0, 1]$. Once our wave function has been written in terms of this new coordinate ξ we separate out the asymptotic behaviour and write our wave function as $\tilde{\phi}_1 = \beta(\xi)\chi(\xi)$, where $\beta(\xi)$ contains the asymptotic behaviour. In the case of $Q = 0$ and $D = 4$ we have that the wave function is written as

$$\tilde{\phi}_1 = \xi^{4iM\omega} (1 - \xi^2)^{-2iM\omega} e^{\frac{2iM\omega}{1-\xi^2}} \chi(\xi). \quad (14)$$

The lowest order coefficients on the AIM can be obtained as:

$$\begin{aligned} \lambda_0 &= 2 \frac{\beta'(\xi)}{\beta(\xi)} + \frac{\left(-(\xi)^{-2} (1 - \xi^2)^2 - 4(1 - \xi^2) \right) f\left(\frac{2M}{1-\xi^2}\right) + 4M f'\left(\frac{2M}{1-\xi^2}\right)}{\frac{1}{\xi} (1 - \xi^2)^2 f\left(\frac{2M}{1-\xi^2}\right)}, \\ s_0 &= \frac{\beta''(\xi)}{\beta(\xi)} + \frac{\beta'(\xi)}{\beta(\xi)} \left(\frac{\left(-(\xi)^{-2} (1 - \xi^2)^2 - 4(1 - \xi^2) \right) f\left(\frac{2M}{1-\xi^2}\right) + 4M f'\left(\frac{2M}{1-\xi^2}\right)}{\frac{1}{\xi} (1 - \xi^2)^2 f\left(\frac{2M}{1-\xi^2}\right)} \right) \\ &\quad + \frac{16M^2 \xi^2}{f\left(\frac{2M}{1-\xi^2}\right)^2 (1 - \xi^2)^4} \left(\omega^2 - V\left(\frac{2M}{1-\xi^2}\right) \right), \end{aligned} \quad (15)$$

where we have let

$$\beta(\xi) = \xi^{4iM\omega} (1 - \xi^2)^{-2iM\omega} e^{\frac{2iM\omega}{1-\xi^2}}, \quad (16)$$

and $f(x) = 1 - 2M/x^{D-3} + Q^2/x^{2D-6}$. As such the AIM differential equation is:

$$\frac{d^2\chi}{d\xi^2} = \lambda_0(\xi)\frac{d\chi}{d\xi} + s_0(\xi)\chi. \quad (17)$$

The higher order λ and s can be calculated from the relations:

$$\lambda_n = \lambda'_{n-1} + s_{n-1} + \lambda_0\lambda_{n-1} \quad \text{and} \quad s_n = s'_{n-1} + s_0\lambda_{n-1}, \quad (18)$$

with the quasi-normal frequencies, ω , being obtained from the equation:

$$s_n\lambda_{n+1} - s_{n+1}\lambda_n = 0. \quad (19)$$

Iterating this method for a sufficiently large number of iterations, the QNMs usually become stable, indicating that we have found the ω we are looking for. However, this was not the case for several modes in our previous work [1].

As was noted in Ref.[8], the AIM and CFM are closely connected. However, the correspondence espoused by Ref.[8] is overly simplistic given it only links two of the three terms of the typical CFM recurrence relation to the λ_0 and s_0 of the AIM. The third term remains unrelated (see Eq. (4) of Ref.[7]), despite its key role (see α_n defined below). Furthermore, it was noted in the earlier works on the CFM (see Ref.[7, 9]), that the coefficients should only depend on parameters, not variables, as is the case for the λ_0 and s_0 defined in this scenario.

4. The continued fraction method

To analyse the connection between the CFM and AIM, we first recall that in the original work on the CFM, where a power series expansion of the wave function was done after the removal of asymptotic behaviour (cf. Eq. (14) above), that is:

$$\chi(\xi) = \sum_{n=0}^{\infty} a_n \left(1 - \frac{1}{\xi}\right)^n, \quad (20)$$

where χ is the wave function of the AIM differential equation, Eq. (17). The expansion coefficients, a_n , are then defined by a three-term recurrence relation:

$$\alpha_n a_{n+1} + \beta_n a_n + \gamma_n a_{n-1} = 0, \quad n = 1, 2, \dots \quad (21)$$

The recurrence coefficients are in this case:

$$\begin{aligned} \alpha_n &= n(n+1), \\ \beta_n &= -n\xi(2 + \lambda_0\xi), \\ \gamma_n &= -s_0\xi^4 \end{aligned} \quad (22)$$

Note though that these coefficients should not depend on ξ [9], and furthermore γ_n has no n dependence, yet in Ref.[8] it was the α_n which was undefined in their correspondence (though we do see here that it is unrelated to the λ_0 and s_0 functions of the AIM). Furthermore, due to the complicated functionality of λ_0 and s_0 , it would seem impossible to remove all ξ dependencies from these coefficients, in general, even for other possible power series expansions. This could be why the AIM could not give reliable QNMs for higher dimension and near extremal cases, as these represent the most complicated forms for λ_0 and s_0 .

If it were possible to compute the quasi-normal frequencies, they would be the complex values of ω for which the series defined by [7]

$$F(\omega) = -\frac{\gamma_1}{\beta_1 - \frac{\alpha_1\gamma_2}{\beta_2 - \frac{\alpha_2\gamma_3}{\beta_3 - \dots}}}, \quad (23)$$

converges uniformly as $\xi \rightarrow \infty$ (where the convergence of this series is a separate issue from the convergence of the continued fraction). This analytic function is empirically found to converge for all ω that are not purely positive imaginary. This restriction is related to the absence of a minimal solution to recurrence relations, Eq. (21) [7].

Now when ω is a QNM, ω_n , the sequence of the expansion coefficients is the minimal solution to the recurrence relation, Eq. (21), and the ratio of the first two expansion coefficients is equal to the value of this continued fraction:

$$\frac{a_1(\omega_n)}{a_0(\omega_n)} = F(\omega_n). \quad (24)$$

Since this ratio is also given for any ω , we then have the equation

$$F(\omega_n) = -\frac{\beta_0(\omega_n)}{\alpha_0(\omega_n)}, \quad (25)$$

which holds whenever ω is a QNM. However, whenever ω is not a QNM (and also not purely positive imaginary), the continued fraction still converges and the expression

$$\frac{\beta_0(\omega)}{\alpha_0(\omega)} + F(\omega) \quad (26)$$

is an analytic function of ω whose zeroes are the QNMs. Note that being analytic makes this expression an ideal target for a numerical root search.

However, that the recurrence coefficients cannot seemingly be found in a ξ independent way means the whole CFM is not applicable [9]. And whilst we have shown that the AIM and CFM can be related, though not as trivially as espoused in Ref. [8], this correspondence breaks down when the recurrence coefficients do not depend solely on the parameters, but retain a variable dependence. This breakdown of a correspondence between the AIM and the CFM could explain the inability of the AIM to converge in this case, and warrants further investigation.

Acknowledgements

ASC and GEH are supported in part by the National Research Foundation of South Africa. We also wish to acknowledge the useful discussions with Prof. Hing-Tong Cho and Dr. Chun-Hung Chen, during the production of this short note.

References

- [1] Chen, C H, Cho, H T, Cornell, A S, Harmsen, G and Ngcobo, X, 2018 *Phys. Rev. D* **97**, no. 2, 024038.
- [2] Chen, C H, Cho, H T, Cornell, A S, and Harmsen, G, 2016 *Phys. Rev. D* **94**, no. 4, 044052.
- [3] Chen, C H, Cho, H T, Cornell, A S, Harmsen, G and Naylor, W, 2015 *Chin. J. Phys.* **53**, 110101.
- [4] Cho, H T, Cornell, A S, Doukas, J, Huang, T R and Naylor, W, 2012 *Adv. Math. Phys.* **2012**, 281705.
- [5] Cho, H T, Cornell, A S, Doukas, J and Naylor, W, 2010 *Class. Quant. Grav.* **27**, 155004.
- [6] Cho, H T, Cornell, A S, Doukas, J and Naylor, W, 2009 *Phys. Rev. D* **80**, 064022.
- [7] Leaver, E W, 1985 *Proc. Roy. Soc. Lond. A* **402**, 285.
- [8] Matamala, A R, Gutierrez, F A and Diaz-Valdés, J, 2007 *Phys. Lett. A* **361** 16-17.
- [9] Gautschi, W, 1967 *SIAM Rev.* **9**, 24.

Full phase space simulation of the relativistic Boltzmann equation in the context of heavy-ion collisions

E W Grunow and A Peshier

Department of Physics, University of Cape Town, Rondebosch 7700, South Africa

E-mail: william.grunow93@gmail.com

Abstract. Relativistic hydrodynamics has been the tool of choice to simulate the dynamics of the quark-gluon plasma produced in heavy-ion collisions. Despite the success of hydrodynamics, it has several shortcomings stemming from the fact that it assumes a system close to equilibrium. An alternative to hydrodynamics is solving the Boltzmann equation, which describes the evolution of the full distribution function of the system without the close to equilibrium requirement. The Boltzmann equation, however, has hitherto proved computationally intractable. By using a novel algorithm, and leveraging the computational power of graphics processing units, we numerically integrate the Boltzmann equation in the relaxation time approximation.

1. Introduction

Recent heavy-ion experiments have confirmed the existence of a deconfined plasma of quarks and gluons, the Quark Gluon Plasma (QGP) [1, 2]. This provides an excellent experimental opportunity to study the dynamics of the strong nuclear force, which due to confinement, has historically proved challenging.

The phenomenology of the QGP has most extensively been studied using the methods of viscous hydrodynamics [3]. Hydrodynamics, however, has limitations, most notably, it only tracks the evolution of the energy-momentum tensor, and not the more microscopic, distribution function.

Thus hydrodynamics would be unable to predict certain phenomena, for example, the possible formation of a Bose-Einstein condensate, as has been suggested by [4]. Given these considerations, we would like to go beyond hydrodynamics and have access to the full distribution function. In order to study the evolution of the distribution function, we would have to solve the Boltzmann equation, given by

$$\frac{d}{dt}f(x, p, t) = \mathcal{C}[f(p, t)] - v\nabla f(x, p, t), \quad (1)$$

where $f(x, p, t)$ is the distribution function evaluated at the point x , momentum p at time t . The $v\nabla f(x, p, t)$ term describes the flow of matter through space. $\mathcal{C}[f(p), t]$ is the so-called collision term which is a functional that describes the interaction between different particles, and in principle requires us to determine interaction probabilities using Quantum Chromodynamics (QCD), as our goal is to simulate gluon interactions.

There have been attempts to solve the Boltzmann equation, both analytically and numerically [5, 6, 7]. These attempts have, however, assumed highly symmetric initial conditions, typically assuming exact boost-invariance and cylindrical symmetry. We, however, know that boost-invariance is just an approximate symmetry, and we would want to consider deviations from exact boost-invariance. We also know that they are not cylindrically symmetric [8].

Our goal will be to solve the Boltzmann equation with these symmetry requirements relaxed.

We will, however, make a simplifying assumption regarding the collision term, instead of using a highly non-trivial collision term derived from QCD, we will rely on a simpler phenomenological model called the relaxation time approximation.

We will furthermore exclusively consider a plasma of gluons at this stage, neglecting quarks as they cannot participate in Bose-Einstein condensation.

2. The Relaxation Time approximation

The relaxation time approximation (RTA) is a staple of statistical physics and is conceptually very simple. We know by the Boltzmann H-theorem that the Boltzmann equation will, regardless of the details of the collision term, asymptotically drive the system into its equilibrium distribution. The RTA simply assumes that the system will asymptotically approach equilibrium with some characteristic relaxation time τ_{rel} .

The relativistically covariant form of the Boltzmann equation under relaxation time approximation, initially described here [9], is given by the following

$$p^\alpha \partial_\alpha f(x, p, t) = p^\alpha u_\alpha \frac{f_{eq}(x, p; T, u, \mu) - f(x, p, t)}{\tau_{rel}}. \quad (2)$$

where f_{eq} is the appropriate equilibrium distribution function for the species of particle under investigation, in our case, we will consider the Bose-Einstein equilibrium distribution

$$f_{eq}(x, p; T, u, \mu) = (\exp((p^\alpha u_\alpha - \mu)/T) - 1)^{-1}. \quad (3)$$

The spatial dependence of the distribution function is only present in the spatial dependence of the parameters T, u^α and μ .

Energy-momentum conservation is ensured by the requirement that the 4-divergence of the energy-momentum tensor ($T^{\alpha\beta}$) vanishes,

$$\partial_\alpha T^{\alpha\beta} = 0, \quad (4)$$

which under the RTA simplifies to

$$u_\alpha T_{[f]}^{\alpha\beta} = u_\alpha T_{eq}^{\alpha\beta}. \quad (5)$$

If we define the rest frame as the frame in which the net energy flux vanishes, also called the Landau rest frame (LRF), this becomes

$$T_{[f]}^\beta{}_\alpha u^\alpha = \mathcal{E}_{eq} u^\beta. \quad (6)$$

The (only) positive eigenvalue (\mathcal{E}_{eq}) of this eigenvalue equation corresponds to the energy density in the LRF, and the associated eigenvector is the flow velocity as in eq (3). We can, optionally, enforce particle number conservation as well, this would generate the additional requirement,

$$\partial_\alpha J^\alpha = 0, \quad (7)$$

where J^α is the 4-current density. Under the RTA, this condition becomes,

$$u_\alpha J^\alpha = \mathcal{N}_{eq} \quad (8)$$

where \mathcal{N}_{eq} is the local number density in the Landau rest frame. Using these we can determine the local temperature and chemical potential, using

$$\mathcal{E}_{eq} = \frac{3}{\pi^2} \text{Li}_4 \left(\exp\left(\frac{\mu}{T}\right) \right) T^4 \quad (9)$$

$$\mathcal{N}_{eq} = \frac{1}{\pi^2} \text{Li}_3 \left(\exp\left(\frac{\mu}{T}\right) \right) T^3, \quad (10)$$

where Li_n denotes the polylogarithm of order n .

Thus the parameters T , u^α and μ , the temperature, fluid flow velocity, and chemical potential respectively, are constrained and the only free parameter in the model is the relaxation time τ_{rel} .

Even though the Boltzmann equation under the relaxation time approximation is conceptually very simple, the temperature, flow velocity and, possibly, chemical potential are dynamic. The dynamic nature of these parameters have, thus far, rendered an exact analytic solution intractable without assuming a highly symmetric setting.

Thus we will resort to numerical methods to make headway.

3. Numerical Implementation

We want to simulate the evolution of the distribution function on a discretised phase-space. After setting up an initial grid of points, we perform free-streaming and relaxation steps independently. Free-streaming is performed by propagating the grid forward in time using the characteristic lines of the advection equation. In order to perform the relaxation step, we need access to the equilibrium parameters. We use a Gauss-Legendre integration scheme to calculate the energy-momentum tensor which is required to determine the equilibrium parameters. Which we can then use to update the function values using the right-hand side of eq (2).

There are a few significant numerical hurdles that need to be overcome.

Firstly, since we in general, do not want to be restricted to considering highly symmetric initial conditions (as other explorations of the Boltzmann equation tend to assume), we need to solve the Boltzmann equation in the full 6-dimensional phase space. The consequence of this high dimensionality is that the number of points that we a required to simulate to obtain a particular resolution of the distribution function scales rapidly with the size of the system. This is compounded by the fact that the system is rapidly expanding, especially in the longitudinal direction.

Another challenge is that we also have a large range of relevant momentum scales present in the problem. Typical initial conditions would be at least approximately boost-invariant, which would imply that the longitudinal momentum scale on which the distribution function has support grows exponentially with increasing rapidities. Thus for an accurate simulation, we require an appropriate resolution across all the relevant momentum scales.

Furthermore, due to time dilation, parts of the system at different rapidities evolve at possibly very different rates (in the lab frame). The consequence is that some parts of the system will conclude their evolution (*i.e.* thermalise) long before others, which is inefficient.

It will be convenient to choose the following set of coordinates,

$$t = \tau \cosh \eta \quad (11)$$

$$z = \tau \sinh \eta \quad (12)$$

$$k^0 = k_\perp \cosh Y \quad (13)$$

$$k^z = k_\perp \sinh Y. \quad (14)$$

As is convention, z denotes the axis parallel to the beam. We will henceforth refer to these coordinates as eigentime (τ), spacetime-rapidity (η) and momentum-rapidity (Y). In these coordinates, the Boltzmann equation reads,

$$\left(\frac{\partial}{\partial \tau} + \frac{1}{\tau} v_\eta \frac{\partial}{\partial \eta} + \mathbf{v}_\perp \frac{\partial}{\partial \mathbf{x}_\perp} \right) f = \frac{k_\mu u^\mu}{k_\perp \cosh(Y - \eta)} \frac{f - f_\infty}{\tau_{\text{rel}}}. \quad (15)$$

This set of coordinate transformations provide several benefits.

In the case of exact boost-invariance, and zero transverse flow velocity, the eigentime is equivalent to the local proper time, which is the natural timescale on which all parts of the system will evolve. Since physically relevant initial conditions must be approximately boost invariant, and the longitudinal flow velocity, in general, will be much larger than the transverse flow velocity, and thus the eigentime is still a good approximation of the local proper time.

Instead of continually expanding in the longitudinal direction, requiring an ever larger grid to accommodate the distribution function, the long term evolution is such that as $\tau \rightarrow \infty$, we have $\eta \rightarrow Y$, effectively a compression of the relevant phase space. Thus if the initial condition can be accommodated on the grid, the distribution function can be accommodated for all future times.

Due to locality, each cell can be independently updated, this allows us to develop an algorithm that computes these updates in parallel. This allows us to use Graphical Processing Units (GPUs) which have the ability to provide a large amount of computational power compared to traditional CPUs, as long as the algorithm used can be run in parallel.

4. Results

Using the RTA approximation and assuming boost invariance and cylindrical symmetry, we predict the temperature evolution in both the free-streaming ($\tau_{\text{rel}} \rightarrow \infty$) and hydrodynamic ($\tau_{\text{rel}} \rightarrow 0$) limits [7].

In particular in the free-streaming limit

$$\left(\frac{T(\tau)}{T(\tau_0)} \right) = \left(\frac{\tau}{\tau_0} \right)^{-\frac{1}{4}}, \quad (16)$$

and for the hydrodynamic limit,

$$\left(\frac{T(\tau)}{T(\tau_0)} \right) = \left(\frac{\tau}{\tau_0} \right)^{-\frac{1}{3}}. \quad (17)$$

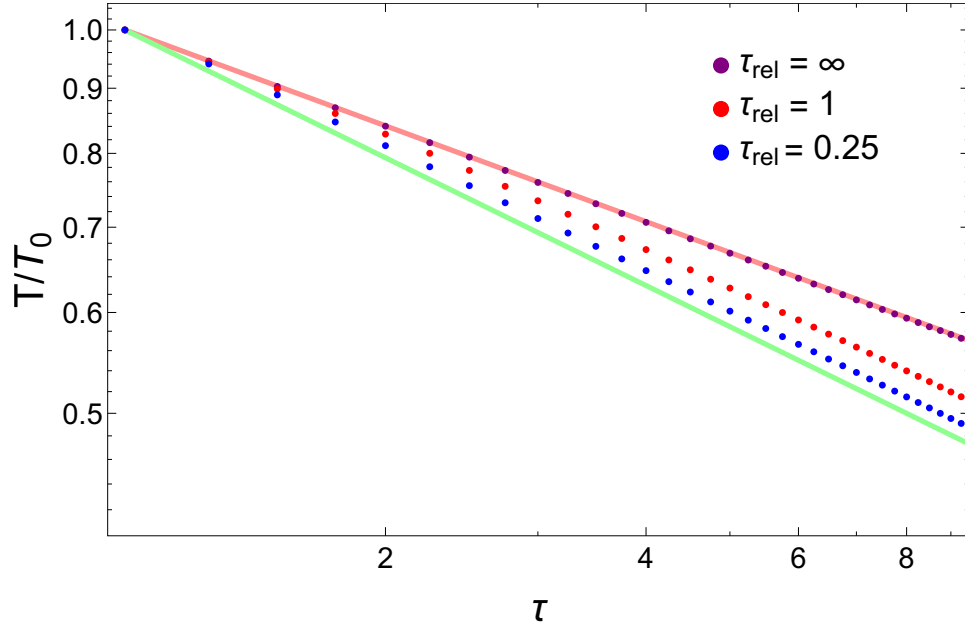


Figure 1: We compare the evolution of the temperature at mid rapidity of various relaxation times (dotted lines) to the hydrodynamic limit (solid green line), and the analytical free-streaming limit (solid red line).

We see that we can not only reproduce the limiting cases but also produce reasonable results for intermediate values of τ_{rel} .

This shows that our simulation is working as intended, and we can begin to investigate more interesting phenomena.

5. Conclusion and Outlook

In this work we have detailed our approach to numerically solving the Boltzmann equation under the relaxation time approximation, and showed preliminary success in reproducing analytical limits.

We hope to begin applying this new numerical tool to experimentally relevant initial conditions to investigate phenomena such as the possibility of Bose-Einstein condensation.

A natural extension of the project would be to consider more physically realistic collision terms. The modular nature of our software would allow us to rapidly prototype these collision terms.

References

- [1] Müller B and Nagle J L 2006 *Annu. Rev. Nucl. Part. Sci.* **56** 93–135
- [2] Aamodt K *et al.* (ALICE) 2010 *Phys. Rev. Lett.* **105** 252302 (*Preprint* 1011.3914)
- [3] Teaney D A 2010 Viscous Hydrodynamics and the Quark Gluon Plasma *Quark-gluon plasma 4* ed Hwa R C and Wang X N pp 207–266 (*Preprint* 0905.2433) URL <https://inspirehep.net/record/820552/files/arXiv:0905.2433.pdf>
- [4] Blaizot J P, Gelis F, Liao J F, McLerran L and Venugopalan R 2012 *Nucl. Phys.* **A873** 68–80 (*Preprint* 1107.5296)
- [5] Xu Z and Greiner C 2005 *Phys. Rev.* **C71** 064901 (*Preprint* hep-ph/0406278)
- [6] Scardina F, Perricone D, Plumari S, Ruggieri M and Greco V 2014 *Phys. Rev.* **C90** 054904 (*Preprint* 1408.1313)
- [7] Baym G 1984 *Physics Letters B* **138** 18–22
- [8] Schenke B and Schlichting S 2016 *Phys. Rev.* **C94** 044907 (*Preprint* 1605.07158)
- [9] Anderson J and Witting H 1974 *Physica* **74** 466–488

Bose-Einstein condensation from a gluon transport equation

B A Harrison and A Peshier

Department of Physics, University of Cape Town, Private Bag X3, Rondebosch 7701, South Africa

E-mail: hrrbre012@myuct.ac.za

Abstract. We present a novel numerical scheme to solve the QCD Boltzmann equation in the soft scattering approximation, for the quenched limit of QCD. Using this we can readily investigate the evolution of spatially homogeneous systems of gluons distributed isotropically in momentum space. We numerically confirm results of Blaizot et al [1, 2], in particular that for so-called “overpopulated” initial conditions, a (transient) Bose-Einstein condensate could emerge during equilibration, in a finite time. Beyond that, we analyze the dynamics of the formation of this condensate. The scheme is extended to systems with cylindrically symmetric momentum distributions, in order to investigate the effects of anisotropy. In particular, we compare the rates at which isotropization and equilibration occur. We also compare our results from the soft scattering scheme to the relaxation time approximation.

1. Introduction

The study of quark-gluon plasma (QGP), the phase of strongly interacting matter formed as a result of relativistic nuclear collisions and consisting of quasi-free quarks and gluons, is of increasing relevance in modern physics [3]. It represents a testing ground for the Standard Model, as well as for finite temperature field theory and possible grand unification theories. It is also of cosmological significance, as the early universe was dominated by this phase of matter.

Experiments at the Relativistic Heavy Ion Collider (RHIC) and Large Hadron Collider (LHC) allow us to probe the energy scales at which the QGP is produced. Inferring its properties and phenomenological behaviour is a central goal of the heavy ion programs at these facilities. The theoretical tools that have been developed to describe it are manifold, as the various stages of a heavy ion collision represent very different physical regimes that demand similarly diverse mathematical formalisms to describe (see Fig. 1).

Prior to the collision, the nuclei are accelerated to near-light speed, with a Lorentz factor on the order of 100. They are therefore subject to strong Lorentz contraction along the beam axis. At these energies, the lifetime of gluons emitted from the valence quarks or other gluons is long enough to allow additional emissions of soft gluons from themselves. This process keeps increasing the number density of gluons until saturation occurs as recombination of gluons becomes non-negligible, forming the state of matter called the Color Glass Condensate (CGC). This regime of large gluon number is well approximated by classical dynamics [4-6].

In the following stage, a large number of gluons are liberated from the CGC. These gluons form a dense, off-equilibrium state called the glasma. Extensive hydrodynamic analyses of HIC indicate that as the medium expands, rapid thermalization occurs (characteristic time on

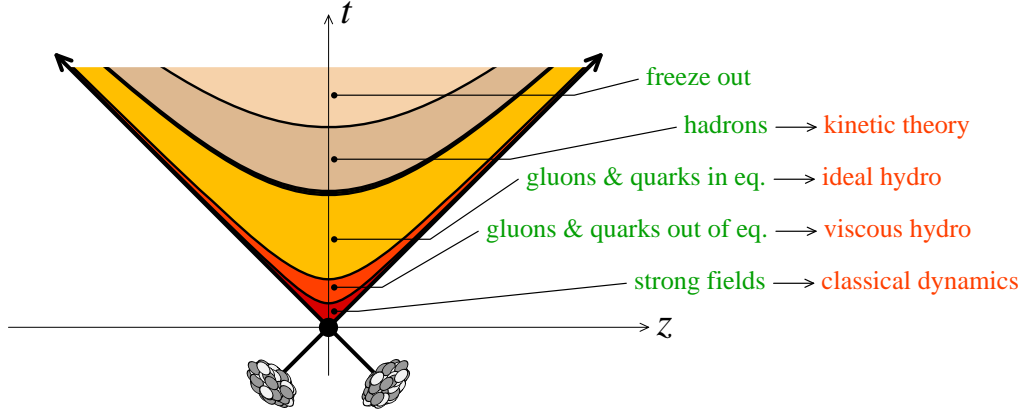


Figure 1. The stages of a heavy ion collision (from [3]).

the order of 1 fm) and a QGP in local equilibrium forms. The speed of this thermalization is indicative of strong interactions. As the medium continues to expand and decrease in temperature, it eventually drops below the deconfinement temperature ($T_c \approx 170$ MeV) and hadronization occurs [7-10].

Using relativistic kinetic theory as an alternative, in some respects more fundamental, approach to viscous hydrodynamics, we aim to describe the collective behaviour of the QGP from the earliest pre-equilibrium stages through thermalization and eventual freeze-out. To this end we numerically solve the relativistic Boltzmann equation.

2. The Boltzmann Transport Equation

The fundamental equation of kinetic theory is the Boltzmann transport equation. It is a non-linear integro-differential equation, for our purposes governing the evolution of the distribution function of a dilute gas of gluons “in a box”. (Quarks are omitted as the relevant regime is gluon-dominated). For a spatially homogeneous system under the assumption that $2 \rightarrow 2$ processes dominate, it can be written as

$$\partial_t f = \frac{1}{2} \int \frac{d^3 p_2}{(2\pi)^3 2E_2} \frac{d^3 p_3}{(2\pi)^3 2E_3} \frac{d^3 p_4}{(2\pi)^3 2E_4} \frac{|\mathcal{M}_{12 \rightarrow 34}|^2}{2E_1} (2\pi)^4 \delta(p_1 + p_2 - p_3 - p_4) (f_3 f_4 \bar{f}_1 \bar{f}_2 - f_1 f_2 \bar{f}_3 \bar{f}_4). \quad (1)$$

Here f_i is the distribution function of particle i with 4-momentum $p_i = (E_i, p_i)$. As shorthand, we write $\bar{f}_i \equiv 1 + f_i$. The transition amplitude \mathcal{M} of binary gluon scattering reads at tree level

$$|\mathcal{M}_{12 \rightarrow 34}|^2 = 72g^4 \left[3 - \frac{tu}{s^2} - \frac{su}{t^2} - \frac{st}{u^2} \right], \quad (2)$$

where s , t and u are the familiar Mandelstam variables and g is related to the QCD coupling constant α by $g^2 = 4\pi\alpha$.

For small scattering angles, $|t| \ll s$ and expression (2) simplifies to

$$|\mathcal{M}_{12 \rightarrow 34}|^2 \approx 144g^4 \frac{s^2}{t^2}, \quad (3)$$

which is to be regulated, e.g. by making the substitution

$$\frac{1}{t^2} \rightarrow \frac{1}{(t - \mu^2)^2}, \quad (4)$$

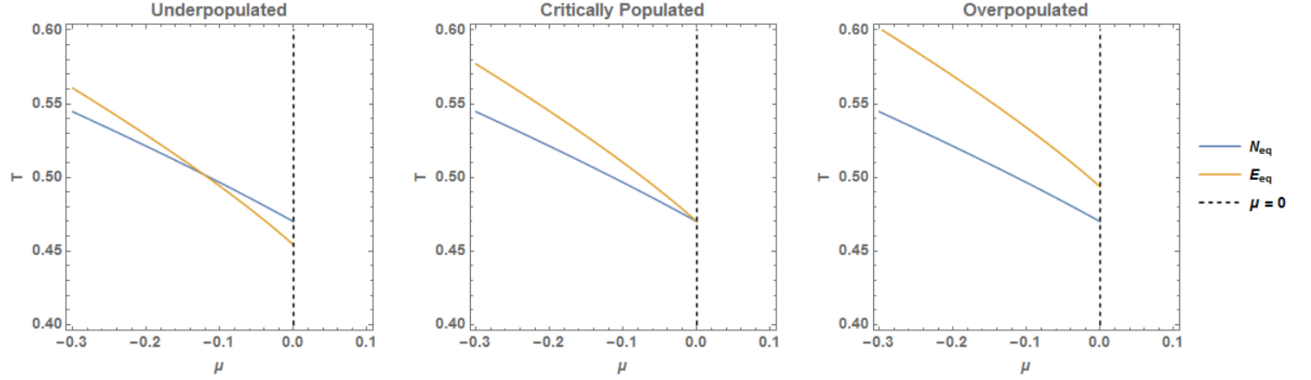


Figure 2. Contours of constant particle number and energy density at equilibrium. In the under- and critically populated cases, the values of the equilibrium parameters T and μ are found where the lines intersect. In the critically populated case, the intersection occurs at the maximum possible value of $\mu = 0$. In the overpopulated case, no real solution for $\mu < 0$ exists and a condensate is necessary to contain the excess particles.

where μ is the screening mass. While this equation is a challenge to solve, the Boltzmann H-Theorem guarantees that regardless of initial condition, the equilibrium distribution function will be a Jüttner distribution [11],

$$f_{eq}(x, p) = \left[e^{\frac{p^\alpha u_\alpha(x) - \mu(x)}{T(x)}} - 1 \right]^{-1}. \quad (5)$$

Here T , u and μ parameterize the temperature, collective flow velocity and chemical potential, respectively.

There is one caveat; there exists a class of “overpopulated” initial distribution functions (see Fig. 2) which contain more gluons than can be “accommodated” in a Jüttner distribution while maintaining particle number and energy conservation. It has been argued [1] that under the assumption of gluon number conservation, a transient equilibrium state may form with a Bose-Einstein condensate.

3. The Fokker-Planck and Relaxation Time approximations

Under the assumption that small-scattering angles dominate, it is possible to write the RHS of Eq. 1 as the divergence of a current in momentum space [1],

$$D_t f = -\nabla \cdot \mathcal{J}(p), \quad (6)$$

where \mathcal{J} reads

$$\mathcal{J}_i(p) = \frac{9}{4\pi} g^4 \mathcal{L} \int_k \mathcal{V}_{ij}(p, k) \left\{ f_p \bar{f}_p \nabla_k^j f_k - f_k \bar{f}_k \nabla_p^j f_p \right\}. \quad (7)$$

Introduced here is

$$\mathcal{V}^{ij} = (1 - v \cdot w) \delta^{ij} + (v^i w^j + v^j w^i), \quad (8)$$

where to lighten notation we have defined $p \equiv p_1$, $k \equiv p_2$ and denoted the corresponding unit vectors by $w \equiv p/p$ and $v \equiv k/k$.

In Eq. 7, \mathcal{L} is the so-called Coulomb logarithm emerging in screened interactions with vector boson exchange, $\mathcal{L} = \int_{q_{min}}^{q_{max}} \frac{dq}{q} = \ln \frac{q_{max}}{q_{min}}$ where q_{max} and q_{min} are cutoffs of the order of the

equilibrium temperature T and Debye screening mass m_D , respectively [1]. We take \mathcal{L} to be a constant of order 1 in our analysis.

It is convenient to rescale the time variable in Eq. 6 as $\tau = \frac{9}{4\pi} g^4 \mathcal{L} t$ to eliminate the constant factor in Eq. 7. The integral in currentIntegral can then be performed and yields [12]

$$\mathcal{J}(p) = I_a \nabla f + I_b f \bar{f} \hat{p} + (\nabla f \cdot \hat{p}) \mathcal{I} + (\nabla f \times \hat{p}) \times \mathcal{I}, \quad (9)$$

where $I_a = \int f \bar{f}$, $I_b = \int \frac{2f}{p}$ and $\mathcal{I} \equiv (\mathcal{I}_x, \mathcal{I}_y, \mathcal{I}_z) = \int \frac{\vec{p}}{p} f \bar{f}$ are functionals of the distribution function f .

We have constructed an efficient flux-conservative numerical scheme [12] that allows us to solve the Boltzmann equation in the Fokker-Planck approximation, (6) + (9), for initial conditions cylindrically symmetric in momentum space.

It is worth comparing this scheme to the well-known Relaxation Time Approximation (RTA),

$$\partial_t f = \frac{p^\mu u_\mu}{p_0} \frac{f_\infty - f}{\tau_r}. \quad (10)$$

where the constant τ_r is the characteristic relaxation time for which the approximation is named.

The RTA is easily solvable (and converges to the same equilibrium distribution); however it lacks QCD-specific features and as we will see yields qualitatively different behavior to the Fokker-Planck approximation, which we argue is more physically motivated.

4. Results

Figs. 3-6 show the evolution in the special case of spherically symmetric, CGC-inspired initial conditions of the form

$$f(p) = f_0 \frac{1}{e^{(p-Q)/C} + 1}, \quad (11)$$

where f_0 and C are constants and Q sets the momentum scale. For these figures, we have chosen $f_0 = 0.225$ and $C = 0.05Q$ (and $Q \rightarrow 1$), which is a moderately overpopulated initial condition where some 8% of the particles asymptotically condense. We denote the number density of the condensate by n_c .

Of particular note is the qualitative difference between the results from the Fokker-Planck and Relaxation Time Approximations. In particular, the condensate begins to form immediately in the RTA scheme, whereas the Fokker-Planck scheme exhibits a characteristic “lag”.

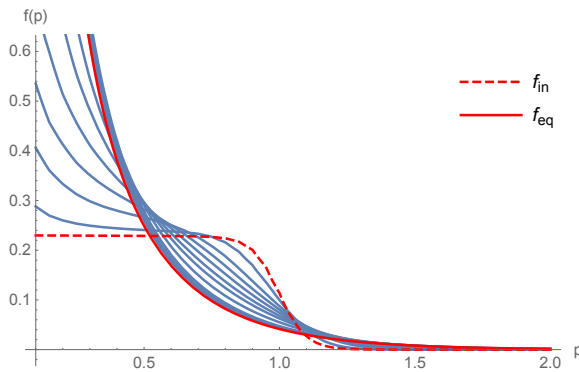


Figure 3. Evolution of an overpopulated initial condition using the Fokker-Planck approximation.

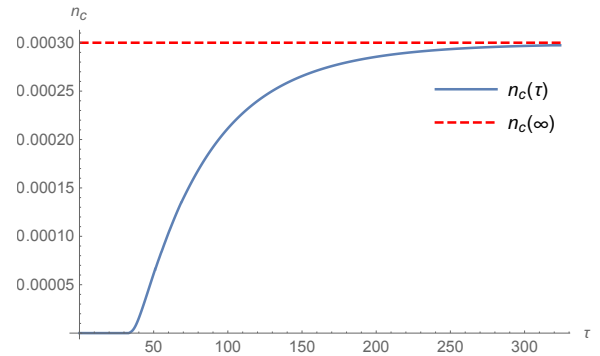


Figure 4. Corresponding evolution of the condensate for the system in Fig. 3.

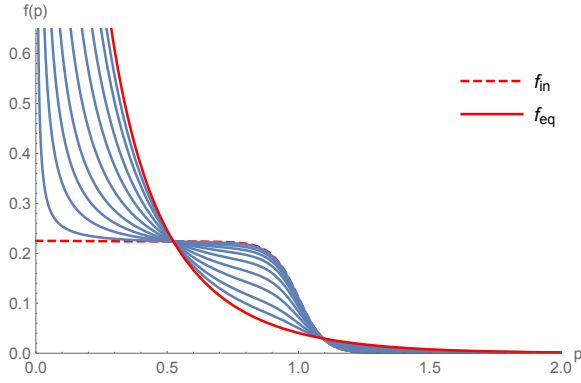


Figure 5. Evolution of an overpopulated initial condition using the Relaxation Time Approximation.

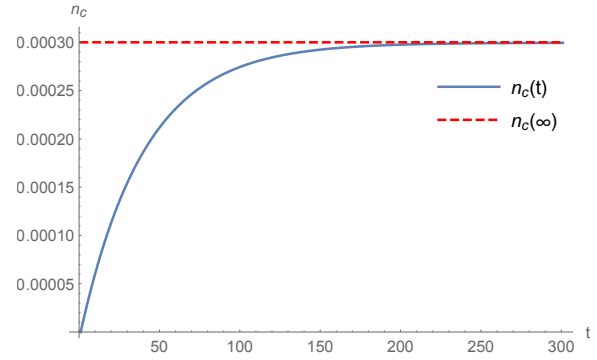


Figure 6. Corresponding evolution of the condensate for the system in Fig. 5.

Generalizing from spherically symmetric to cylindrically symmetric initial conditions, it becomes possible to explore the effects on anisotropy on the evolution of the distribution function. It is important to differentiate between isotropic distribution functions just boosted out of their rest frame and distribution functions that are “generically” anisotropic, i.e. even in their rest frame.

In order to study anisotropy of the second kind, we follow Strickland [13] and consider initial conditions of the form

$$f(\omega, p_z) \rightarrow (\sqrt{1+\xi}) f\left(\sqrt{\omega^2 + \xi p_z^2}, p_z\right), \quad (12)$$

where $\xi > -1$ specifies the anisotropy and the factor of $\sqrt{1+\xi}$ is a normalization to preserve particle number and energy density while varying ξ .

We can generalize our spherically symmetric initial condition (Eq. 11) using this anisotropization. Additionally (as we will see in Eq. 13) we introduce a boost parameter b which introduces a net flow in the z -direction. This can be interpreted as a boost out of the rest frame.

We are therefore interested in the family of initial conditions

$$f(\omega, p_z) = (\sqrt{1+\xi}) \frac{f_0}{e^{\frac{1}{T}(\sqrt{\omega^2 + \xi p_z^2} + b p_z - Q)} + 1}, \quad (13)$$

where $\omega = |p|$. We extract the equilibration time by studying the entropy, evaluated towards final equilibrium. In particular we would like to compare it to the time taken for the initially anisotropic distribution function to isotropize.

To this end, as a measure of the anisotropy of a distribution function, we define the “anisotropy parameter”

$$\alpha = \frac{T_{LRF}^{22}}{T_{LRF}^{33}}, \quad (14)$$

where $T_{LRF}^{\mu\nu}$ is the energy-momentum tensor in the local rest frame. In the rest frame, for a cylindrically symmetric distribution function with some anisotropy, $T^{11} = T^{22} = P_{\perp}$ is the transverse pressure of the fluid, while $T^{33} = P_z$ is the longitudinal pressure. For an isotropic distribution they are equal; thus the ratio α must approach 1 as the system isotropizes. Analogously, the ratio of the system’s entropy S to its equilibrium entropy S_{∞} approaches 1 as the system equilibrates.

In Fig. 7, as a proof of concept we plot the evolution of the normalized entropy and anisotropy parameters associated with a representative initial condition. Fig. 8 shows a linearization of this evolution.

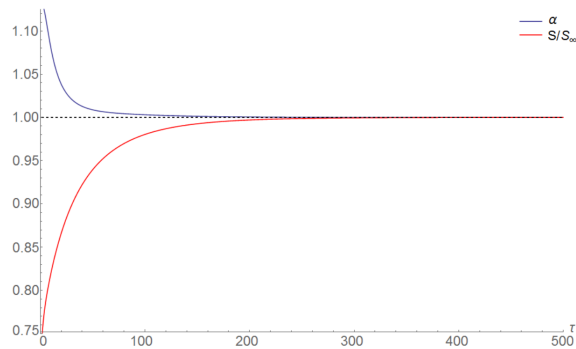


Figure 7. Evolution of the normalized entropy and anisotropy parameters.

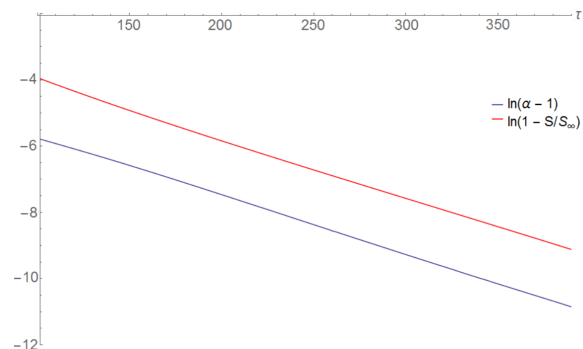


Figure 8. Linearized evolution of the normalized entropy and anisotropy parameters.

The gradients of the lines of best fit associated with the plots in Fig. 8 are identical within uncertainty (obtainable e.g. using statistical resampling methods) which corroborates that the rates of isotropization and equilibration are strongly correlated.

5. Conclusion

In summary, we have developed a numerical scheme to solve the relativistic Boltzmann equation for gluons in the small-scattering approximation under the assumption of cylindrically symmetric initial conditions and spatial homogeneity. Among our results, we have presented an argument for the formation of a transient Bose-Einstein condensate state for certain initial conditions. We have investigated the rate at which an anisotropic distribution function becomes isotropic and compared it to the rate of thermalization. Further, we have compared these results to the relaxation-time approximation to the Boltzmann equation.

Scope for further extension of this scheme exists, and such an extension is planned. In particular, it is desirable to extend the scheme to remove the assumption of spatial homogeneity and describe systems without symmetry assumptions in which the above scheme would essentially represent a single spatial cell. A challenge is the fact that the computational complexity scales geometrically with each additional degree of freedom - the so-called “curse of dimensionality”. (Boltzmann equation solvers as well as hydro-codes typically rely on assumptions of symmetry, and for good reason).

References

- [1] Blaizot J-P, Liao J and McLerran L 2013 *Nuclear Physics A* **920** 58
- [2] Blaizot J-P, Liao J and Mehtar-Tani Y 2017 *Nuclear Physics A* **961** 37
- [3] Gelis F 2012 *Journal of Physics: Conference Series* **381** 12021
- [4] McLerran L and Venugopalan R *Physical Review D* 1994 **49** 2233
- [5] Gelis F 2016 *Quark-Gluon Plasma* 5 67
- [6] Weigert H 2005 *Progress in Particle and Nuclear Physics* **55** 461
- [7] Heinz U W and Kolb P F 2002 *Nuclear Physics A* **702** 269
- [8] Romatschke P and Romatschke U 2007 *Physical Review Letters* **99** 172301
- [9] Ollitrault J-Y 2008 *European Journal of Physics* **29** 275
- [10] Romatschke P and Romatschke U 2017 arXiv:1712.05812[nucl-th]
- [11] Rezzolla L and Zanotti O 2013 *Relativistic Hydrodynamics* (Oxford: OUP)
- [12] Harrison B and Peshier A 2019 *Particles* **2** 231
- [13] Schenke B and Strickland M 2006 *Physical Review D* **74** 65004

Quantitative Predictions of Heavy Flavor Photon Bremsstrahlung in Heavy Ion Collisions from AdS/CFT

W A Horowitz

Department of Physics, University of Cape Town, Private Bag X3, Rondebosch 7701, South Africa

E-mail: wa.horowitz@uct.ac.za

Abstract. We present quantitative predictions for the spectra of photon bremsstrahlung from heavy quarks propagating through a strongly-coupled quark-gluon plasma using the techniques of AdS/CFT. The spectra are the result of including both drag and diffusion terms in the heavy flavor propagation in the plasma. The predictions show that future experimental upgrades and high-luminosity runs at the Large Hadron Collider at CERN will allow for a quantitative comparison between data and our calculations, providing novel insight into the non-trivial, emergent many-body dynamics of a non-Abelian gauge theory.

1. Introduction

Experimental indications give a mixed picture of the relevant dynamics of the quark-gluon plasma (QGP) created at the Relativistic Heavy Ion Collider (RHIC) and the Large Hadron Collider (LHC). In particular, measurements of the distribution of low transverse momentum ($p_T \lesssim 2$ GeV/c) particles can be understood through near perfect viscous hydrodynamics with a rapid hydrodynamization time [1–7] or from parton cascades [8–13]. Similarly, observables related to single partons at high transverse momentum ($p_T \gtrsim 15$ GeV/c) can also be qualitatively described using energy loss models based on either strong-coupling AdS/CFT [14–22] or weak-coupling pQCD [23–39].

We therefore seek novel experimental handles to provide insight into the relevant dynamics of the quark-gluon plasma (QGP) produced at the temperatures $T_{QGP} \sim 400$ MeV accessible at RHIC and LHC. In particular with the massive increase in luminosity and detector sensitivity that will come to the LHC after upgrades, the study of rare observables becomes possible.

A natural observable of potential interest is the measurement of the *photon* bremsstrahlung associated with open heavy flavor propagation in QGP. Presumably the radiation pattern for photons will differ depending on whether the heavy quark undergoes rare hard scattering events as one expects from pQCD or if it rather is plowing through a strongly-coupled soup as described by AdS/CFT. (Note that photon tagged heavy flavor production is different and refers to the $2 \rightarrow 2$ or $2 \rightarrow 3$ prompt hard photon production at heavy ion collision time $t = 0$ that is clearly well described by standard perturbative field theory methods [40, 41].)

We provide here quantitative predictions for the photon bremsstrahlung produced by an open heavy quark strongly-coupled to a strongly-coupled plasma. In this exploratory study we use

leading order heavy quark drag as derived from a steady state string setup in AdS/CFT [42, 43]. The influence of fluctuations [44–46] in the momentum loss experienced by the heavy quark may be an important contribution, but we leave it to future work.

2. Setup

We treat the heavy quark–anti-quark pair produced at the initial nuclear overlap at $t = 0$ and moving in opposite directions as a classical current [47]

$$j^\mu(x) = Q e \theta(t) [v^\mu(t) \delta^{(3)}(\vec{x} - \vec{x}(t)) - \tilde{v}^\mu(t) \delta^{(3)}(\vec{x} + \vec{x}(t))]. \quad (1)$$

coupled to the electromagnetic field

$$\mathcal{L} = -\frac{1}{4} F_{\mu\nu} F^{\mu\nu} + j_\mu A^\mu. \quad (2)$$

In Eq. 1, Q is the fractional electric charge carried by the heavy quark, $\theta(t)$ is the usual Heaviside step function, and

$$\begin{aligned} v^\mu(t) &= (1, \vec{v}(t))^\mu \\ \tilde{v}^\mu(t) &= (1, -\vec{v}(t))^\mu \\ \vec{x}(t) &= \vec{x}_0 + \int_0^t dt' \vec{v}(t'). \end{aligned} \quad (3)$$

For any generic current coupling to the electromagnetic field given by Eq. 2, one finds [16, 48] that the momentum differential energy distribution of the emitted electromagnetic radiation is given by

$$\frac{dE}{d^3k} = -\frac{1}{2} \frac{1}{(2\pi)^3} \tilde{j}^\mu(k) \tilde{j}_\mu(-k), \quad (4)$$

where

$$\tilde{j}^\mu(k) \equiv \int d^4x e^{-ik \cdot x} j^\mu(x). \quad (5)$$

2.1. Hard Production Electromagnetic Radiation

Since we will ultimately wish to compare to pQCD-based energy loss calculations for which there are usually non-trivial UV and IR catastrophes associated with the factorization of the hard production and subsequent dynamics, we wish to compute the *difference* in the radiated energy in medium as compared to the vacuum. For the vacuum case, we have that, in the soft radiation approximation, the heavy quark pair does not lose momentum after it is produced. In this case we then take $\vec{v}(t) \equiv \vec{v}_0$ and $\vec{x}(t) = \vec{v}_0 t$ in Eq. 1. To perform the Fourier transform in Eq. 5 one must insert a small convergence factor η . Evaluation of Eq. 5 then yields

$$\begin{aligned} \tilde{j}_{vac}^\mu(k) &= \lim_{\eta \rightarrow 0} \int d^4x e^{-i[(\omega - i\eta)t + \vec{k} \cdot \vec{x}(t)]} j^\mu(x) \\ &= \lim_{\eta \rightarrow 0} Q e \left[\frac{v_0^\mu}{i\omega - i\vec{k} \cdot \vec{v}_0 + \eta} - \frac{\tilde{v}_0^\mu}{i\omega + i\vec{k} \cdot \vec{v}_0 + \eta} \right] \\ &= -i Q e \left[\frac{v_0^\mu}{\omega - \vec{k} \cdot \vec{v}_0} - \frac{\tilde{v}_0^\mu}{\omega + \vec{k} \cdot \vec{v}_0} \right]. \end{aligned} \quad (6)$$

After some manipulation and taking the motion of the quarks to be along the z direction, with $\vec{k} \cdot \vec{v}_0 = \omega v_0 \cos \theta$, $\omega \equiv k^0$, and $v_0 \equiv |\vec{v}_0|$, we find Eq. 4 yields for the differential energy radiated in vacuum

$$\frac{dE_{vac}}{d^3k} = \frac{2}{(2\pi)^3} (Qe)^2 \frac{1}{\omega^2} \frac{v_0^2 \sin^2 \theta}{(1 - v_0^2 \cos^2 \theta)^2}. \quad (7)$$

As is usual, we see that the total integrated energy radiated by the vacuum current grows linearly with an artificially imposed UV cutoff ω_{max} . Interestingly, the inclusion of the *pair* of quarks has tamed the usual IR divergence: the long wavelength physics knows that the total charge remains 0 as the $q\bar{q}$ pair separates.

2.2. AdS/CFT Induced Electromagnetic Radiation

The leading order energy loss of a heavy quark in a strongly-coupled $\mathcal{N} = 4$ SYM plasma is given by [42, 43]

$$\frac{d\vec{p}}{dt} = -\mu \vec{p}, \quad \mu = \frac{\pi\sqrt{\lambda}}{2} \frac{T^2}{M_Q}, \quad (8)$$

where $\lambda = g^2 N_c$ is the 't Hooft coupling, T is the temperature of the plasma, and M_Q is the mass of the heavy quark.

From Eq. 8, and assuming motion is only in one dimension, we may solve for

$$\begin{aligned} p(t) &\equiv |\vec{p}(t)| = p_0 e^{-\mu t} \\ E(t) &= \sqrt{m^2 + p^2(t)} \\ v(t) &= p(t)/E(t) \\ x(t) &= \frac{1}{2\mu} \ln \left[\frac{E_0 + p_0}{E_0 - p_0} \times \frac{E(t) - p(t)}{E(t) + p(t)} \right]. \end{aligned} \quad (9)$$

We may plug in our results from Eq. 9 into our equation for the Fourier transform of the current, Eq. 5, to find the Fourier transform of the current when the heavy quarks are subject to the AdS/CFT heavy quark drag. Unfortunately, the result cannot be evaluated analytically.

3. Results

Once we have the Fourier transform of the current associated with a heavy quark pair separating in a strongly-coupled AdS/CFT plasma, we may compute the difference in energy radiated by the heavy quark in medium minus the energy radiated in vacuum. We show in Fig. 1 (left) the result for $m_c = 1.5 \text{ GeV}/c^2$ charm quarks and (right) $m_b = 4.75 \text{ GeV}/c^2$ bottom quarks. Not surprisingly, the biggest medium modification to $\omega^2 dE/d^3k$ is centered at $\theta_{max} \sim m_Q/p_T$; one can show numerically that the depth of the difference at θ_{max} is a function of $(m_Q/p_T)^2$.

One can understand the reduction in emitted photon radiation shown in the plot as follows. In vacuum, the quarks are accelerated from rest to some non-zero velocity v_0 associated with the initial p_T of the particles. The quarks in medium, on the other hand, immediately begin decelerating due to the presence of the plasma. The produced photons will always have some non-zero formation time. For the photons produced in-medium, the effective acceleration of the quark is smaller than that for the quark in vacuum because of the immediate deceleration. Therefore there is less radiation emitted from the in-medium quarks, and thus the suppression observed in the subtracted spectrum.

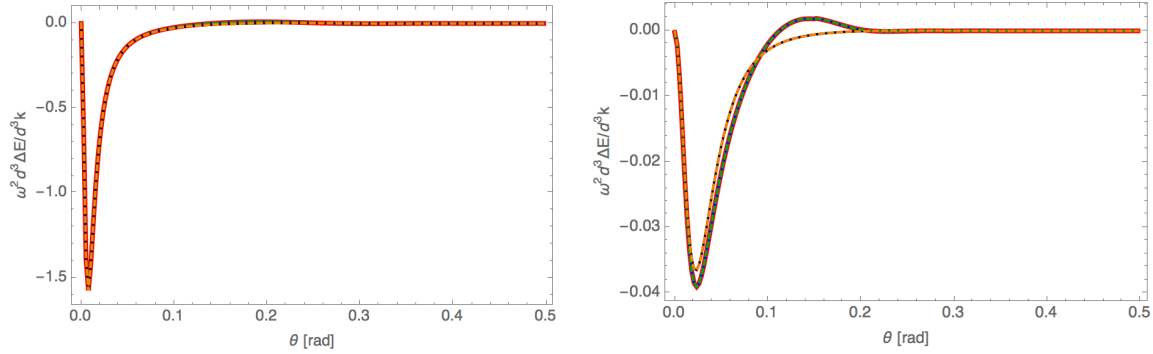


Figure 1: (Colour online) $dE/d^3k|_{med} - dE/d^3k|_{vac}$ for $T = 400$ MeV strongly-coupled $\mathcal{N} = 4$ SYM plasma for (left) $m_c = 1.5$ GeV/ c^2 charm quarks and (right) $m_b = 4.75$ GeV/ c^2 bottom quarks. For both plots the quarks have $p_T = 200$ GeV/ c , the photon has energy 20 GeV, and $\lambda = 12$. In both plots, the thicker red curve corresponds to both quarks traversing an infinite length plasma, the thick blue curve to both quarks traversing up to 5 fm of plasma, and the thick black curve to both quarks traversing up to 1 fm of plasma. For the dashed green curve, the quark moving in the z direction traverses a distance of up to 5 fm while the away side quark traverses a 1 fm thick plasma; for the dashed orange curve, the distances are reversed.

4. Conclusions and Outlook

We presented the first prediction of photon bremsstrahlung for heavy quarks produced in a strongly-coupled $\mathcal{N} = 4$ SYM plasma. We derived the spectrum of emitted QED radiation dE/d^3k for a classical point current of given (potentially) time-dependent velocity in Eq. 4. We then focused on the trajectory of a heavy quark strongly coupled to a strongly coupled plasma as predicted by leading order AdS/CFT, in which case the momentum of the heavy quark is modified according to the usual drag result $dp/dt = -\mu p$, where $\mu = \pi\sqrt{\lambda}T^2/m_Q$. We plotted the difference in the spectra of the photons produced in medium compared to those produced in vacuum, $\omega^2 dE/d^3k|_{med} - \omega^2 dE/d^3k|_{vac}$, in Fig. 1. The presence of the medium suppresses the radiation emitted by heavy quark compared to that in the vacuum. Given the very small angle at which the modification is significant, $\theta_{max} = m_Q/p_T \ll 1$, it is currently unclear whether the current experiments at the LHC could distinguish between a modification to the production bremsstrahlung as shown here or a potential modification to the photons generated in the hadronization process in which the heavy quarks become heavy mesons.

Acknowledgments

The author wishes to thank the South African National Research Foundation and the SA-CERN Collaboration for generous support.

References

- [1] Teaney D 2003 *Phys. Rev.* **C68** 034913 (*Preprint* nucl-th/0301099)
- [2] Chesler P M and Yaffe L G 2011 *Phys. Rev. Lett.* **106** 021601 (*Preprint* 1011.3562)
- [3] Song H, Bass S A, Heinz U, Hirano T and Shen C 2011 *Phys. Rev. Lett.* **106** 192301 [Erratum: *Phys. Rev. Lett.* 109,139904(2012)] (*Preprint* 1011.2783)
- [4] Gale C, Jeon S, Schenke B, Tribedy P and Venugopalan R 2013 *Phys. Rev. Lett.* **110** 012302 (*Preprint* 1209.6330)
- [5] Bernhard J E, Moreland J S, Bass S A, Liu J and Heinz U 2016 *Phys. Rev.* **C94** 024907 (*Preprint* 1605.03954)

- [6] Alqahtani M, Nopoush M, Ryblewski R and Strickland M 2017 *Phys. Rev.* **C96** 044910 (*Preprint* 1705.10191)
- [7] Weller R D and Romatschke P 2017 *Phys. Lett.* **B774** 351–356 (*Preprint* 1701.07145)
- [8] Molnar D and Gyulassy M 2002 *Nucl. Phys.* **A697** 495–520 [Erratum: *Nucl. Phys.*A703,893(2002)] (*Preprint* nucl-th/0104073)
- [9] Lin Z w and Ko C M 2002 *Phys. Rev.* **C65** 034904 (*Preprint* nucl-th/0108039)
- [10] Bzdak A and Ma G L 2014 *Phys. Rev. Lett.* **113** 252301 (*Preprint* 1406.2804)
- [11] Orjuela Koop J D, Adare A, McGlinchey D and Nagle J L 2015 *Phys. Rev.* **C92** 054903 (*Preprint* 1501.06880)
- [12] He L, Edmonds T, Lin Z W, Liu F, Molnar D and Wang F 2016 *Phys. Lett.* **B753** 506–510 (*Preprint* 1502.05572)
- [13] Lin Z W, He L, Edmonds T, Liu F, Molnar D and Wang F 2016 *Nucl. Phys.* **A956** 316–319 (*Preprint* 1512.06465)
- [14] Horowitz W A and Gyulassy M 2008 *Phys. Lett.* **B666** 320–323 (*Preprint* 0706.2336)
- [15] Akamatsu Y, Hatsuda T and Hirano T 2009 *Phys. Rev.* **C79** 054907 (*Preprint* 0809.1499)
- [16] Horowitz W A 2010 *Probing the Frontiers of QCD* Ph.D. thesis Columbia U. (*Preprint* 1011.4316) URL <https://inspirehep.net/record/878251/files/arXiv:1011.4316.pdf>
- [17] Horowitz W A and Gyulassy M 2011 *J. Phys.* **G38** 124114 (*Preprint* 1107.2136)
- [18] Horowitz W A 2012 *AIP Conf. Proc.* **1441** 889–891 (*Preprint* 1108.5876)
- [19] Morad R and Horowitz W A 2014 *JHEP* **11** 017 (*Preprint* 1409.7545)
- [20] Horowitz W A 2015 *Phys. Rev.* **D91** 085019 (*Preprint* 1501.04693)
- [21] Hambrock R and Horowitz W A 2017 *Nucl. Part. Phys. Proc.* **289-290** 233–236 (*Preprint* 1703.05845)
- [22] Brewer J, Rajagopal K, Sadofyev A and van der Schee W 2017 *Nucl. Phys.* **A967** 508–511 (*Preprint* 1704.05455)
- [23] Gyulassy M, Levai P and Vitev I 2002 *Phys. Lett.* **B538** 282–288 (*Preprint* nucl-th/0112071)
- [24] Vitev I and Gyulassy M 2002 *Phys. Rev. Lett.* **89** 252301 (*Preprint* hep-ph/0209161)
- [25] Wang E and Wang X N 2002 *Phys. Rev. Lett.* **89** 162301 (*Preprint* hep-ph/0202105)
- [26] Majumder A, Wang E and Wang X N 2007 *Phys. Rev. Lett.* **99** 152301 (*Preprint* nucl-th/0412061)
- [27] Dainese A, Loizides C and Paic G 2005 *Eur. Phys. J.* **C38** 461–474 (*Preprint* hep-ph/0406201)
- [28] Armesto N, Cacciari M, Dainese A, Salgado C A and Wiedemann U A 2006 *Phys. Lett.* **B637** 362–366 (*Preprint* hep-ph/0511257)
- [29] Wicks S, Horowitz W, Djordjevic M and Gyulassy M 2007 *Nucl. Phys.* **A784** 426–442 (*Preprint* nucl-th/0512076)
- [30] Majumder A, Nonaka C and Bass S A 2007 *Phys. Rev.* **C76** 041902 (*Preprint* nucl-th/0703019)
- [31] Zhang H, Owens J F, Wang E and Wang X N 2009 *Phys. Rev. Lett.* **103** 032302 (*Preprint* 0902.4000)
- [32] Vitev I and Zhang B W 2010 *Phys. Rev. Lett.* **104** 132001 (*Preprint* 0910.1090)
- [33] Schenke B, Gale C and Jeon S 2009 *Phys. Rev.* **C80** 054913 (*Preprint* 0909.2037)

- [34] Young C, Schenke B, Jeon S and Gale C 2011 *Phys. Rev.* **C84** 024907 (*Preprint* 1103.5769)
- [35] Majumder A and Shen C 2012 *Phys. Rev. Lett.* **109** 202301 (*Preprint* 1103.0809)
- [36] Horowitz W A and Gyulassy M 2011 *Nucl. Phys.* **A872** 265–285 (*Preprint* 1104.4958)
- [37] Buzzatti A and Gyulassy M 2012 *Phys. Rev. Lett.* **108** 022301 (*Preprint* 1106.3061)
- [38] Horowitz W A 2013 *Nucl. Phys.* **A904-905** 186c–193c (*Preprint* 1210.8330)
- [39] Djordjevic M and Djordjevic M 2014 *Phys. Lett.* **B734** 286–289 (*Preprint* 1307.4098)
- [40] Stavreva T, Arleo F and Schienbein I 2013 *JHEP* **02** 072 (*Preprint* 1211.6744)
- [41] Huang J, Kang Z B, Vitev I and Xing H 2015 *Phys. Lett.* **B750** 287–293 (*Preprint* 1505.03517)
- [42] Herzog C P, Karch A, Kovtun P, Kozcaz C and Yaffe L G 2006 *JHEP* **07** 013 (*Preprint* hep-th/0605158)
- [43] Gubser S S 2006 *Phys. Rev.* **D74** 126005 (*Preprint* hep-th/0605182)
- [44] Gubser S S 2008 *Nucl. Phys.* **B790** 175–199 (*Preprint* hep-th/0612143)
- [45] Casalderrey-Solana J and Teaney D 2007 *JHEP* **04** 039 (*Preprint* hep-th/0701123)
- [46] Moerman R W and Horowitz W A 2016 (*Preprint* 1605.09285)
- [47] Adil A, Gyulassy M, Horowitz W A and Wicks S 2007 *Phys. Rev.* **C75** 044906 (*Preprint* nucl-th/0606010)
- [48] Peskin M E and Schroeder D V 1995 *An Introduction to quantum field theory* (Reading, USA: Addison-Wesley) ISBN 9780201503975, 0201503972 URL <http://www.slac.stanford.edu/~mpeskin/QFT.html>

Oscillating cosmological correlations in $f(R)$ gravity

Neo Namane, Heba Sami and Amare Abebe

Center for Space Research & Department of Physics, North-West University, Mafikeng, South Africa

E-mail: nechnotick@gmail.com

Abstract. The purpose of this paper is to investigate the oscillatory behavior of the universe through a Schrödinger-like Friedmann equation and a modified gravitational background described by the theory of $f(R)$ gravity. The motivation for this stems from the observed periodic behaviour of large-scale cosmological structures when described within the scope of the general theory of relativity. The analysis of the modified Friedmann equation for the dust epoch in power-law $f(R)$ models results in different behaviors for the wave-function of the universe. These oscillatory instances of the wave-function point towards a possible ordered pattern in the manner in which clustering occurs during the universe's evolution.

1. Introduction

According to the Cosmological Principle (CP), matter in the universe is homogeneously and isotropically distributed; a principle that is confirmed by observations on sufficiently large scales ($1000h^{-1}\text{Mpc}$). However, observations show that the CP breaks on scales of the order $\sim 100h^{-1}\text{Mpc}$ and below, and the clustering property of cosmological objects (galaxies, clusters, superclusters, filaments) shows there exists some sort of hierarchy. Thus, there are suggestions that the distribution of galaxies is not random and that some fundamental mechanism has led to the formation of large-scale structure. Such an idea is built from the notion that the density inhomogeneities that are the primordial causes of the formation of structure in the universe are as a result of quantum fluctuations generated during inflation. One proposal is cosmological solutions with an overall Friedmannian expanding behaviour, corrected by small oscillatory regimes [1]. Given the cosmological scale factor $a(t)$ and redshift z , we have the Hubble parameter H given by

$$\frac{\dot{a}}{a} = \frac{\Theta}{3} \equiv H = -\frac{\dot{z}}{1+z}, \quad (1)$$

wherein Θ represents the cosmological (volume) expansion parameter. Oscillations at a particular redshift can be considered as some sort of quantization [1, 2] and all quantities containing H or z have to oscillate. These oscillations affect several observational quantities, such as the number count of galaxies

$$\frac{dN}{d\Omega dL dz} = n(L, t_0) a_0^2 H^{-1} d^2, \quad (2)$$

where dN is the number of galaxies in the solid angle $d\Omega$ having redshift between z and $z + dz$ and luminosity between L and $L + dL$, $n(L, t_0)$ that represents the number density of galaxies with luminosity L that an observer sees at time t_0 , a_0 is the value of the cosmological scale

factor today and d is the comoving distance defined as $d = \int_t^{t_0} \frac{dt}{a}$.

There have also been recent attempts to link gravitation with quantization, largely motivated by the need to unify two of theoretical physics' most fundamental theories into one overarching framework. There are generally two main approaches in this endeavor:

- The whole universe as a quantum system of co-existing and non-interacting universes [4, 5]
- The universe as a classical background: where primordial quantum processes gave rise to the current macroscopic structures [3, 6]

Following Capozziello [1] and Rosen [7], one can recast the cosmological Friedmann equation

$$\left(\frac{\dot{a}}{a}\right)^2 = \frac{1}{9}\Theta^2 = \frac{\mu}{3} - \frac{k}{a^2} \quad (3)$$

as some sort of a Schrödinger equation (SE). To do so, we can rewrite the above equation as the equation of motion of a “particle” of mass m :

$$\frac{1}{2}m\dot{a}^2 - \frac{m}{6}\mu a^2 = -\frac{1}{2}mk, \quad (4)$$

where $\Theta \equiv 3H$, μ and k are, respectively, the cosmological (volume) expansion parameter, the energy density and spatial curvature of the universe. The total energy E of the particle can be thought of as being the sum of the kinetic T and potential V energies:

$$E = T + V \quad (5)$$

where

$$T = \frac{1}{2}m\dot{a}^2, \quad V = -\frac{1}{6}m\mu a^2, \quad E = -\frac{1}{2}mk. \quad (6)$$

One can also rewrite the Raychaudhuri (acceleration) equation

$$\frac{\ddot{a}}{a} = -\frac{1}{2}(\mu + 3p) \quad (7)$$

in a way that mimics the equation of motion of the particle, otherwise given by

$$m\ddot{a} = -\frac{dV}{da}, \quad (8)$$

where p is the isotropic pressure, related to the energy density of a perfect fluid through the equation of state parameter w as $p = w\mu$. The particle's momentum and Hamiltonian are defined, respectively, as

$$\Pi \equiv m\dot{a}, \quad H \equiv \frac{\Pi^2}{2} + V(a). \quad (9)$$

From the “first quantization” scheme, we have

$$\Pi \rightarrow -i\hbar \frac{\partial}{\partial a}. \quad (10)$$

Thus the SE for the wavefunction $\Psi = \Psi(a, t)$ is given by

$$i\hbar \frac{\partial \Psi}{\partial t} = -\frac{\hbar^2}{2m} \frac{\partial^2 \Psi}{\partial a^2} + V(a)\Psi. \quad (11)$$

We can think of m as the mass of a galaxy, and $|\Psi|^2$ as the probability of finding the galaxy at $a(t)$ or at a given redshift

$$1 + z = \frac{a_0}{a} , \quad (12)$$

and thus, in the language of quantum physics, $\Psi = \Psi(z, t)$ defines the probability amplitude to find a given object of mass m at a given redshift z , at time t . The stationary states of energy E are given by

$$\Psi(a, t) = \psi(a)e^{-iEt/\hbar} , \quad (13)$$

and the time-independent Schrödinger equation (TISE) reads

$$-\frac{\hbar^2}{2m} \frac{d^2\psi}{da^2} + V\psi = E\psi . \quad (14)$$

2. $f(R)$ Gravitation

$f(R)$ models are a sub-class of *fourth-order* theories of gravitation, with an action given by [9]¹

$$\mathcal{A}_{f(R)} = \frac{1}{2} \int d^4x \sqrt{-g} [f(R) + 2\mathcal{L}_m] , \quad (15)$$

where R , g and \mathcal{L}_m are the Ricci scalar, the determinant of the metric tensor, and the matter Lagrangian. The $f(R)$ -generalized Einstein field equations can be given by

$$f'G_{ab} = T_{ab}^m + \frac{1}{2}(f - Rf')g_{ab} + \nabla_b \nabla_a f' - g_{ab} \nabla_c \nabla^c f' . \quad (16)$$

Here primes symbolize derivatives with respect to R , whereas G_{ab} and T_{ab}^m are the Einstein tensor and the energy-momentum tensor of matter respectively. These models provide the simplest generalizations to GR, and come with an extra degree of freedom. The cosmological viability of the models can be determined through observational and theoretical constraints. Some generic viability conditions on f include [8]:

- To ensure gravity remains attractive

$$f' > 0 \quad \forall R \quad (17)$$

- For stable matter-dominated and high-curvature cosmological regimes (nontachyonic scalaron)

$$f'' > 0 \quad \forall R \gg f'' \quad (18)$$

- GR-like law of gravitation in the early universe (BBN, CMB constraints)

$$\lim_{R \rightarrow \infty} \frac{f(R)}{R} = 1 \Rightarrow f' < 1 \quad (19)$$

- At recent epochs

$$|f' - 1| \ll 1 \quad (20)$$

The matter-energy content of a universe filled with a perfect fluid is specified by

$$T_{ab} = (\mu + p)u_a u_b + pg_{ab} . \quad (21)$$

The background curvature and total perfect fluid thermodynamics is described by [10]

$$\begin{aligned} \mu_R &= \frac{1}{f'} \left[\frac{1}{2}(Rf' - f) - \Theta f'' \dot{R} \right] , \\ p_R &= \frac{1}{f'} \left[\frac{1}{2}(f - Rf') + f'' \ddot{R} + f''' \dot{R}^2 + \frac{2}{3} \Theta f'' \dot{R} \right] , \\ \mu &\equiv \frac{\mu_m}{f'} + \mu_R , \quad p \equiv \frac{p_m}{f'} + p_R . \end{aligned} \quad (22)$$

¹ In geometrized units: $c = 8\pi G \equiv 1$.

3. The Cosmological Schrödinger Equation

In $f(R)$ gravity, the Raychaudhuri equation generalizes to

$$\frac{\ddot{a}}{a} = -\frac{1}{6} \left(\frac{\mu_m}{f'} + \mu_R + \frac{3p_m}{f'} + 3p_R \right) \quad (23)$$

which in terms of the expressions for μ_R , p_R and the trace equation ($R = \mu - 3p$) can be simplified as

$$\frac{\ddot{a}}{a} = -\frac{1}{6f'} \left(2\mu_m - f - 2\Theta f'' \dot{R} \right). \quad (24)$$

Similarly, the corresponding modified Friedmann equation in $f(R)$ gravity is given by

$$\frac{1}{9}\Theta^2 + \frac{k}{a^2} = \frac{1}{6f'} \left(2\mu_m + Rf' - f - 2\Theta f'' \dot{R} \right). \quad (25)$$

But for FLRW models, it is also true that

$$\frac{1}{9}\Theta^2 + \frac{k}{a^2} = \frac{1}{6}R - \frac{\ddot{a}}{a}, \quad (26)$$

one can therefore re-write equation (4) as

$$\frac{1}{2}m\dot{a}^2 - \frac{1}{2} \left(\frac{R}{6} - \frac{\ddot{a}}{a} \right) ma^2 = -\frac{1}{2}mk, \quad (27)$$

with the potential

$$V(a) = -\frac{1}{2} \left(\frac{R}{6} - \frac{\ddot{a}}{a} \right) ma^2. \quad (28)$$

Now rearranging the TISE (14) for $f(R)$ gravity yields

$$\frac{d^2\psi}{da^2} = -\frac{2m}{\hbar^2} [E - V(a)] \psi = \left[C - \frac{m^2}{6f'\hbar^2} (2\mu_m + Rf' - f - 2\Theta f'' \dot{R}) a^2 \right] \psi, \quad (29)$$

where $C \equiv \frac{m^2 k}{\hbar^2}$.

4. Oscillating Solutions

Let us now consider power-law $f(R)$ models of the form

$$f(R) = R^n, \quad (30)$$

admitting scale factor solutions

$$a(t) = a_0 t^{\frac{2n}{3(1+w)}}. \quad (31)$$

For dust ($w = 0$) models, we get

$$\Theta = \frac{2n}{t}, \quad R = \frac{4n(4n-3)}{3t^2}, \quad \mu_m = \frac{\mu_0}{a^3}. \quad (32)$$

Here a_0 and μ_0 are integration constants that can be normalized to unity when considering current values of the scale factor and the energy density of matter. Thus, for such models, the TISE (29) takes the form

$$\begin{aligned} \frac{d^2\psi}{da^2} = & \left\{ C - \frac{m^2}{3n\hbar^2 a^3} \left[\frac{4n(4n-3)}{3a^{\frac{3}{n}}} \right]^{1-n} + \frac{4nm^2(4n-3)}{18\hbar^2 a^{\frac{3-2n}{n}}} \right. \\ & \left. - \frac{4m^2(4n-3)}{18\hbar^2 a^{\frac{3-2n}{n}}} + \frac{32nm^2(n-1)}{24a^{\frac{3-2n}{n}}} \right\} \psi. \end{aligned} \quad (33)$$

For $n = 1$, the above equation reduces to

$$\frac{d^2\psi}{da^2} = \left[C - \frac{B}{a} \right] \psi, \quad (34)$$

where $B \equiv \frac{m^2}{3\hbar^2}$ and we recover the GR solutions [1] obtained by Capozziello et al. For example, for a flat universe, $C = 0$ and we get a combination of Bessel functions as the general solution:

$$\psi(a) = C1 \sqrt{a} J_1 \left(2 \sqrt{-B} \sqrt{a} \right) + C2 \sqrt{a} Y_1 \left(2 \sqrt{-B} \sqrt{a} \right). \quad (35)$$

For $n = 3$, it can be shown that

$$\frac{d^2\psi}{da^2} = \left[C - Ba \right] \psi, \quad (36)$$

and the corresponding solutions are Airy functions of the form

$$\psi(a) = C3 \text{Ai} \left(\frac{C - Ba}{B^{2/3}} \right) + C4 \text{Bi} \left(\frac{C - Ba}{B^{2/3}} \right). \quad (37)$$

Figure (1) below shows the oscillatory behaviour of such exact-solution wavefunctions. Our investigations for the power-law models suggest that exact solutions are possible only for $n = 1$ and $n = 3$. Also, our numerical computations show no oscillatory behaviour of the solutions for $n < 1$, whereas oscillating solutions for $n = 1.5$ and $n = 2$ are presented in figure (2).

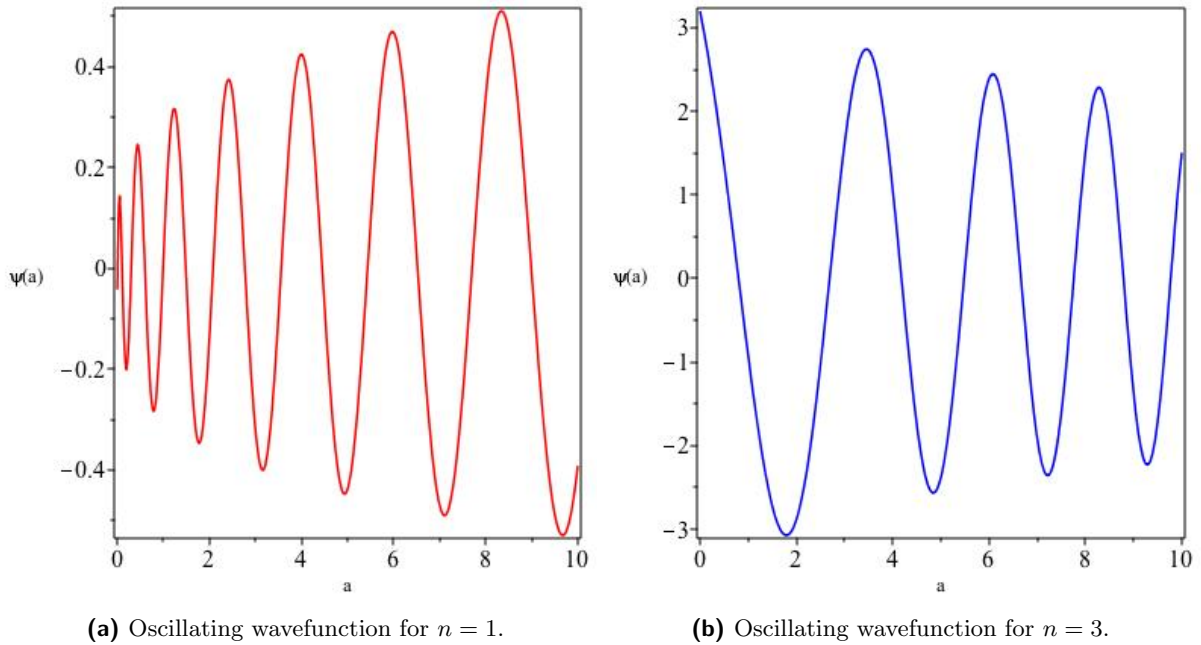


Figure 1: Exact solutions for $n = 1$ and $n = 3$.

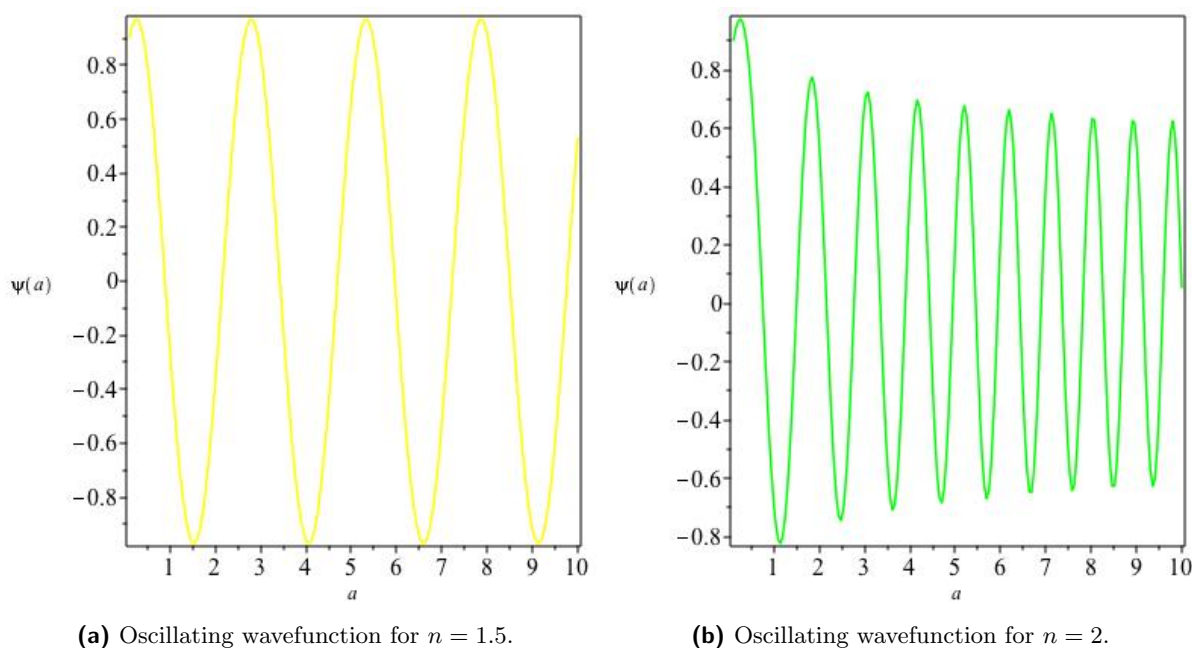


Figure 2: Numerical solutions for $n = 1.5$ and $n = 2$.

5. Conclusion

A breaking of homogeneity and isotropy on small scales with oscillating correlations between galaxies can be achieved with a Schrödinger-like equation. This work reproduces existing GR solutions and provides an even richer set of solutions for $f(R)$ gravity models, thus providing possible constraints on such models using observational data. For the power-law $f(R)$ model considered in this work, exact solutions have been obtained for $n = 1$ and $n = 3$ in the flat FLRW background, as well as numerical solutions for the $n = 1.5$ and $n = 2$ dust scenarios. A more detailed analysis of such oscillatory solutions with more viable $f(R)$ models and under more realistic initial conditions is currently underway.

Acknowledgments

NN and HS acknowledge the Center for Space Research of North-West University for financial support to attend the 63rd Annual Conference of the South African Institute of Physics. NN acknowledges funding from the National Institute of Theoretical Physics (NITheP). HS and AA acknowledge that this work is based on the research supported in part by the National Research Foundation (NRF) of South Africa.

References

- [1] Capozziello S, Feoli A and Lambiase G 2000 *International Journal of Modern Physics D* **9** 143–154
- [2] Tift W 1977 *The Astrophysical Journal* **211** 31–46
- [3] Calogero F 1997 *Physics Letters A* **228** 335–346
- [4] Witt B D 1967 *Phys. Rev* **160** 1143
- [5] Everett III H 1957 *Reviews of modern physics* **29** 454
- [6] Birrell N D and Davies P 1984 *Quantum fields in curved space* 7 (Cambridge University Press)
- [7] Rosen N 1993 *International Journal of Theoretical Physics* **32** 1435–1440
- [8] Amare A 2015 *Beyond concordance cosmology* (Scholars' Press)
- [9] Abebe A 2014 *Classical and Quantum Gravity* **31** 115011
- [10] Ntahompagaze J, Abebe A and Mbonye M 2017 *International Journal of Geometric Methods in Modern Physics* **14** 1750107

Using the Ultra-relativistic Quantum Molecular Dynamics (UrQMD) model to extract the thermal conductivity transport coefficient of hadron gas

T Nemakhavhani¹ and A Muronga²

¹Physics Department, University of Johannesburg, P.O.Box 524. Auckland Park 2006, Johannesburg, RSA

² Faculty of Science, Nelson Mandela University, Summerstrand, Port Elizabeth, 6031, South Africa

E-mail: tenemakhavhani@gmail.com

Abstract. The thermal conductivity of hadronic matter is studied using a microscopic transport model, which will be used to simulate ultra-relativistic heavy ion collisions at different energy densities ϵ , namely the Ultra-relativistic Quantum Molecular Dynamics (UrQMD). The molecular dynamics simulation is performed for a system of zero baryon number density and light meson species (π , ρ and K) in a box with periodic boundary conditions. The equilibrium state is investigated by studying the chemical equilibrium and the thermal equilibrium of the system. The particle multiplicity equilibrates with time, and the energy spectra of different light mesons species have the same slopes and common temperatures when thermal equilibrium is reached. The thermal conductivity transport coefficient is calculated from the heat current - current correlations using the Green-Kubo relations.

1. Introduction

A large number of studies in heavy ion physics and high energy physics have been done using the results from the Relativistic Heavy Ion Collider (RHIC). Now with the restart of the Large Hadron Collider (LHC) physics programme, the field of high energy nuclear physics, and especially heavy ion physics, has gone into a new era. It is now possible to explore the properties of Quantum-Chromo-Dynamics (QCD) at unprecedented particle densities and temperatures, and at much higher energies than that produced at RHIC, from $\sqrt{s} = 200$ GeV to $\sqrt{s} = 14$ TeV at the LHC [1].

High energy heavy ion reactions are studied experimentally and theoretically to obtain information about the properties of nuclear matter under extreme conditions at high densities and temperatures, as well as about the phase transition to a new state of matter, the quark-gluon plasma (QGP) [2, 3]. This work reports on a transport coefficient, namely the thermal conductivity of hadron matter. Other transport coefficients such as shear and bulk viscosity are well discussed and documented [3, 4], but the study of the thermal conductivity transport coefficient is poorly documented, especially with the use of UrQMD model to simulate ultra-relativistic heavy ion collisions. The knowledge of this transport coefficient plays an important role in the development of a model such as the UrQMD model, and also the development of high energy heavy ion experiments such as LHC and RHIC.

Equilibration of the system is studied by evaluating particle number densities from chemical equilibrium, energy spectra as well as the temperatures from thermal equilibrium of different

light meson species in a cubic box, which imposes periodic boundary conditions. The infinite hadronic matter is modelled by initializing the system with light meson species namely, the pion (π), the rho (ρ) and the kaon (K). We focus on the hadronic scale temperature ($100 \text{ MeV} < T < 200 \text{ MeV}$) and zero baryon number density, which are expected to be realized in the central high energy nuclear collisions [5]. We then change energy density from $\varepsilon = 0.1 - 2.0 \text{ GeV/fm}^3$ and for each energy density we run the system with 200 events while keeping the volume and baryon number density constant until the equilibrium state is reached. The thermal conductivity transport coefficient is calculated from the heat current - current correlations using the Green-Kubo relations.

The rest of the paper is organized as follows: In section 2 we study the description of the UrQMD model. In section 3 we study equilibration properties of the system. In section 4 we calculate the thermal conductivity transport coefficient around the equilibrium state through the UrQMD model using Green-Kubo relations.

2. Short Description of the UrQMD Model

The Ultra-relativistic Quantum Molecular Dynamic model (UrQMD) is a microscopic model based on a phase space description of nuclear reactions. We use version 3.3 of the UrQMD model for this study. The UrQMD 3.3 hybrid approach extends previous ansatzes to combine the hydrodynamic and the transport models for the relativistic energies. The combination of these approaches into one single framework, it is done for a consistent description of the dynamics

The UrQMD model describes the phenomenology of hadronic interactions at low and intermediate energies from a few hundreds MeV up to the new LHC energy of $\sqrt{s} = 14 \text{ TeV}$ per nucleon in the centre of mass system [6, 7]. The UrQMD collision term contains 55 different baryon species and 32 meson species, which are supplemented by their corresponding anti-particles and all the isospin-projected states [6, 8]. The properties of the baryons and the baryon-resonances which can be populated in UrQMD can be found in [8], together with their respective mesons and the meson-resonances. A collision between two hadrons will occur if

$$d_{\text{trans}} \leq \sqrt{\frac{\sigma_{\text{tot}}}{\pi}}, \quad \sigma_{\text{tot}} = \sigma(\sqrt{s}, \text{type}), \quad (1)$$

where d_{trans} and σ_{tot} are the impact parameter and the total cross-section of the two hadrons respectively [6]. In the UrQMD model, the total cross-section σ_{tot} depends on the isospins of colliding particles, their flavour and the centre-of-mass energy \sqrt{s} . More details about the UrQMD model is presented in [6, 7, 8].

3. Equilibration of Hadronic Matter

To investigate the equilibration of a system, the UrQMD model is used to simulate the ultra-relativistic heavy ion collisions. A multi-particle production plays an important role in the equilibration of the hadronic gas [3]. The cubic box used for this study is initialised according to the following numbers of baryons and mesons: zero protons, 80 pions, 80 rhos and 80 kaons. For this study a cubic box with volume V and a baryon number density $n_B = 0.00 \text{ fm}^{-3}$ is considered. The energy density ε , volume V and the baryon number density n_B in the box are fixed as input parameters and are conserved throughout the simulation. The energy density is defined as $\varepsilon = \frac{E}{V}$, where E is the energy of N particles and the three-momenta p_i of the particles in the initial state are randomly distributed in the centre of mass system of the particles as shown in the equations below.

$$E = \sum_{i=1}^N \sqrt{m_i^2 + p_i^2}, \quad \sum_{i=1}^N p_i = 0. \quad (2)$$

3.1. Chemical Equilibrium

In this subsection the chemical equilibrium is studied from the particle number densities of different light meson species in a box with $V = 1000 \text{ fm}^3$, zero net baryon number density $n_B = 0.0 \text{ fm}^{-3}$ at different energy densities using UrQMD box calculations. Figure 1 (a) and (b) represents the time evolutions of the various meson number densities at $\varepsilon = 0.3$ and 0.4 GeV/fm^3 energy densities.

In figures 1 (a) and (b), the meson species indicate that the system does indeed reach chemical equilibrium. It is observed that the pions have large particle number densities and the reason could be the decay in the heavier mesons and other particles produced in the system to form pions. The saturation of the particle number densities indicate the realization of a local equilibrium. In conclusion, the chemical equilibrium of the system has been reached, as in both figures the saturation times are the same for all three mesons, regardless of the shape of each meson. In figure 1 (a) where $\varepsilon = 0.3 \text{ GeV/fm}^3$, the equilibrium time for all meson species is around $t = 22 \text{ fm/c}$ and for figure 1 (b) at a higher energy density of $\varepsilon = 0.4 \text{ GeV/fm}^3$, the equilibrium time is observed to have increased to $t = 32 \text{ fm/c}$. These results show that an increase in energy density influences the particle multiplicity inside the periodic box, which affect the equilibration time.

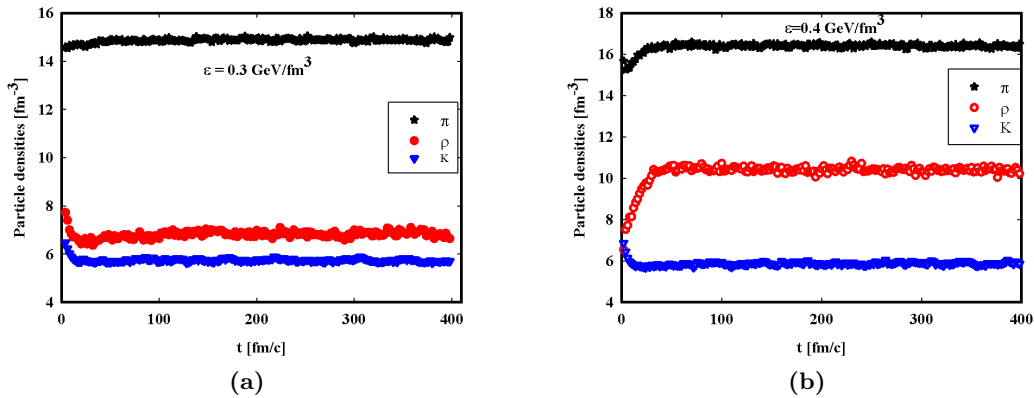


Figure 1: The time evolution of particle number densities of light meson species (π , ρ and K) at (a) $\varepsilon = 0.3 \text{ GeV/fm}^3$ and (b) $\varepsilon = 0.4 \text{ GeV/fm}^3$.

3.2. Thermal Equilibrium and Temperature

In this subsection the thermal equilibrium and the temperature from the energy distributions of different light meson species are studied. The possibility of the thermal equilibrium of the hadronic matter is studied by examining the energy distribution of the system in a box with periodic boundary conditions using the UrQMD model. The particle spectra are given by the momentum distribution as

$$\frac{dN_i}{d^3p} = \frac{dN}{4\pi E p dE} \propto C e^{(-\beta E_i)}. \quad (3)$$

Figure 2 (a) and (b) represent the time evolutions of energy spectra of different meson species. The linear lines are fitted using the Boltzmann distribution, which is approximated by $C \exp(-\beta E_i)$ from Eq. 3, where $\beta = 1/T$ is the slope parameter of the distribution and E_i is the energy of particle i . The results are plotted as a function of kinetic energy $K = E - m$, so that the horizontal axes for all the particle species coincide [9]. In figure 2 (a) and (b) it is

observed that the slopes of the energy distribution converge to common values of temperatures at different times above $t = 180$ fm/c for $\varepsilon = 0.2$ GeV/fm³ and above $t = 250$ fm/c for $\varepsilon = 0.3$ GeV/fm³. In thermal equilibrium the system is characterized by unique temperature T [9]. The thermal temperatures were extracted from the equilibrium state using the Boltzmann distribution such that $T = 118.3$ MeV for $\varepsilon = 0.2$ GeV/fm³ and $T = 150.1$ MeV for $\varepsilon = 0.3$ GeV/fm³.

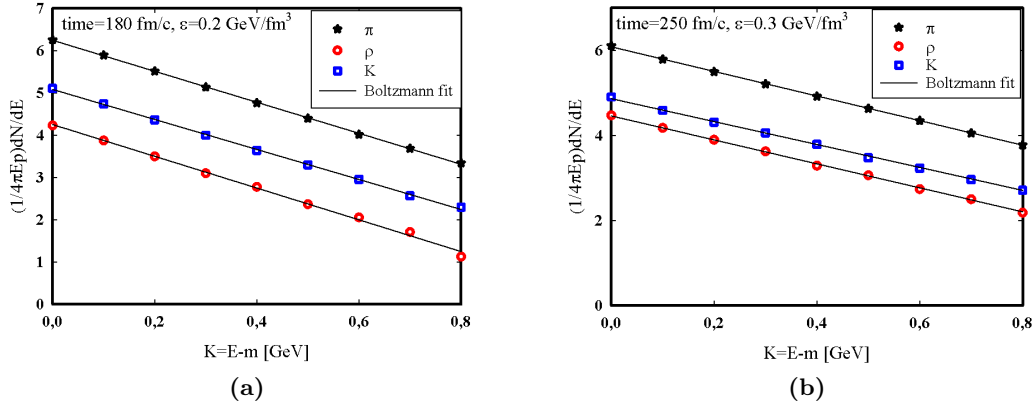


Figure 2: The energy distributions of light meson species (π , ρ and K) at (a) $\varepsilon = 0.2$ GeV/fm³ and $t = 180$ fm/c and (b) $\varepsilon = 0.3$ GeV/fm³ and $t = 250$ fm/c. The lines are the Boltzmann fit which gives the extracted temperatures of $T = 118.3$ MeV for (a) and $T = 150.1$ MeV for (b).

4. Thermal Conductivity Transport Coefficient

The transport coefficients, such as the thermal conductivity κ and the shear viscosity η , characterize the dynamics of the fluctuations of the dissipative fluxes in a medium [3]. The most often used method to investigate these coefficient is either through employing the kinetic theory or the field theory using the Green-Kubo formula [3].

The knowledge of various transport coefficients is important for the dissipative fluid dynamical model. One can calculate the coefficient of thermal conductivity from the fluctuation-dissipation theorem. The fluctuation-dissipation theorem tells us that the thermal conductivity is given by the heat current-current correlations [10]. Green and Kubo showed that the transport coefficients like heat conductivity, shear and bulk viscosity can be related to the correlation functions of the corresponding flux or the tensor in the thermal equilibrium [11]. The Green-Kubo formalism relates linear transport coefficients to near-equilibrium correlations of dissipative fluxes and treats dissipative fluxes as perturbations to local thermal equilibrium [12]. The relevant formular for the Green-Kubo relation for thermal conductivity can be written as [13]

$$\kappa = \frac{V}{3T^2} \int_0^\infty \langle \mathbf{q}_i(0) \cdot \mathbf{q}_i(t) \rangle dt. \quad (4)$$

In Eq. (4) the brackets $\langle \dots \rangle$ stand for the equilibrium average, and no summation is implied over the repeated indices [3, 13]. κ is the thermal conductivity. The vector \mathbf{q}_i is the Eckart's heat current along the $i = x, y$ and z axes which is defined as

$$\mathbf{q}^i = \frac{1}{V} \sum_{k=1}^N \mathbf{p}^i \left(\frac{\mathbf{p}^2}{\mathbf{p}_0^2} \right), \quad (5)$$

where \mathbf{p}^i is the momentum along the $i = x, y$ and z axes, and $\mathbf{p}^2 = \mathbf{p}_0^2 - \mathbf{p}_x^2 - \mathbf{p}_y^2 - \mathbf{p}_z^2$, which can be extracted from the UrQMD model output file. If the evolution of the fluctuations of the fluxes is described by the Maxwell-Cattaneo equation [13]. We adopt a relativistic microscopic model, namely the UrQMD [8] and perform molecular-dynamics for a hadron gas of mesons in a box to compute the thermal conductivity coefficient of the hadron gas.

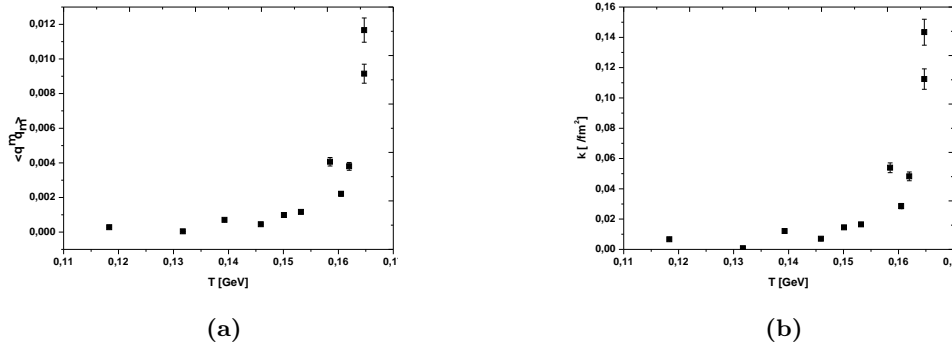


Figure 3: (a) The square expectation value of the heat current and (b) the thermal conductivity of the hadronic gas as a function of temperature.

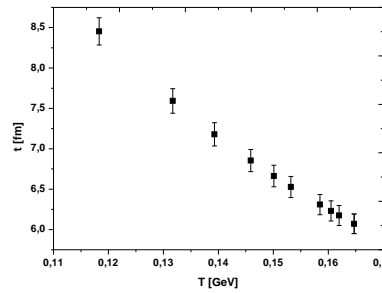


Figure 4: The relaxation time for the heat conductivity of a the hadronic gas as a function of temperature.

Figure 3 (a) shows the square expectation of the heat current results obtained from the UrQMD model. The heat current increases with increase in temperature. These results are in good comparison with those obtained in [10], where a different model named URASIMA was used. The UrQMD square expectation of heat current is much smaller than that obtained in [10]. The reason might be that for this study we considered a situation with only meson species and zero baryon number.

Figure 3 (b) shows the thermal conductivity κ of a hadronic gas, which increases with an increase in temperature. Saturation is reached below $T = 0.17$ GeV, where the hadronic gas with zero baryon number density is expected to be realized in the central high energy nuclear collisions [3]. According to our simulation, we observed a strong temperature dependence. The temperature behavior of the thermal conductivity is $\kappa \sim T^{2.88}$. The temperature dependence of thermal conductivity in this study is greater ($T^{2.88} > T^2$) than the one reported by [14], where the author used Effective Field Theory, and it is less ($T^{2.88} < T^5$) than the one reported by [10],

where the author used a different simulation model called URASIMA and a different system which includes the baryon number densities.

Due to the smaller number of studies done on the thermal conductivity coefficient, it is difficult to make a proper conclusion from the results obtained, but from a comparison with the few related studies, one can agree that the results are in good comparison with those reported by [10]. At the moment it is not very clear where the large fluctuation around $T = 160$ MeV come from in the above figures. Thus a similar study will be done in the future which will include the baryon number density and different mesons species at higher energies and large number of events in order to check if one of these factors does play a role for this large fluctuation. Figure 4 shows the relaxation time for the heat flux of a hot hadronic gas as a function of the temperature calculated from the UrQMD model by fitting the heat correlation functions. The heat relaxation time decreases with an increase in temperature similarly to the one reported in [3, 10].

5. Conclusion

From the presented results, it can be concluded that it is possible to calculate thermal conductivity transport coefficient using the UrQMD model. More study is still required for a better understanding of the results and the coefficient. The future studies will focus on how the thermal conductivity transport coefficient is affected by adding different numbers of meson species in the box, including baryon number density, in order to compare with other studies such as that reported by [10, 15], as well as to compare to those who used different models and statistical approach [14, 16].

6. Acknowledgments

I would like to thank everyone who helped me with this paper in terms of corrections and discussions. Financial support from NITheP is acknowledged.

References

- [1] Campbell J M, Ellis R K and Williams C 2011 *Journal of High Energy Physics* **2011** 1–36
- [2] Bratkovskaya E, Cassing W, Greiner C, Effenberger M, Mosel U and Sibirtsev A 2000 *Nuclear Physics A* **675** 661–691
- [3] Murgola A 2004 *Physical Review C* **69** 044901
- [4] Gorenstein M, Hauer M and Moroz O 2008 *Physical Review C* **77** 024911
- [5] Mitrovski M, Schuster T, Gräf G, Petersen H and Bleicher M 2009 *Phys. Rev. C* **79**(4) 044901 URL <http://link.aps.org/doi/10.1103/PhysRevC.79.044901>
- [6] Bleicher M, Zabrodin E, Spieles C, Bass S A, Ernst C, Soff S, Bravina L, Belkacem M, Weber H, Stöcker H *et al.* 1999 *Journal of Physics G: Nuclear and Particle Physics* **25** 1859
- [7] collaboration P *et al.* 2005 *Technical Progress Report, GSI, Darmstadt*
- [8] Bass S A, Belkacem M, Bleicher M, Brandstetter M, Bravina L, Ernst C, Gerland L, Hofmann M, Hofmann S, Konopka J *et al.* 1998 *Progress in Particle and Nuclear Physics* **41** 255–369
- [9] Sasaki N 2001 *Progress of theoretical Physics* **106** 783–805
- [10] Muroya S 2007 *arXiv preprint hep-ph/0702220*
- [11] Wesp C, El A, Reining F, Xu Z, Bouras I and Greiner C 2011 *Physical Review C* **84** 054911
- [12] Demir N and Bass S A 2009 *The European Physical Journal C* **62** 63–68
- [13] Murgola A 2008 *The European Physical Journal-Special Topics* **155** 107–113
- [14] Torres-Rincon J M 2012 *arXiv preprint arXiv:1205.0782*
- [15] Rougemont R, Noronha J and Noronha-Hostler J 2015 *Physical Review Letters* **115** 202301
- [16] Greif M, Reining F, Bouras I, Denicol G, Xu Z and Greiner C 2013 *Physical Review E* **87** 033019